Etude de la couronne solaire en 3D et de son évolution avec SOHO/EIT

Fabrice Portier-Fozzani

Etude de la couronne solaire en 3D et de son evolution avec SOHO/EIT

par Fabrice Portier-Fozzani

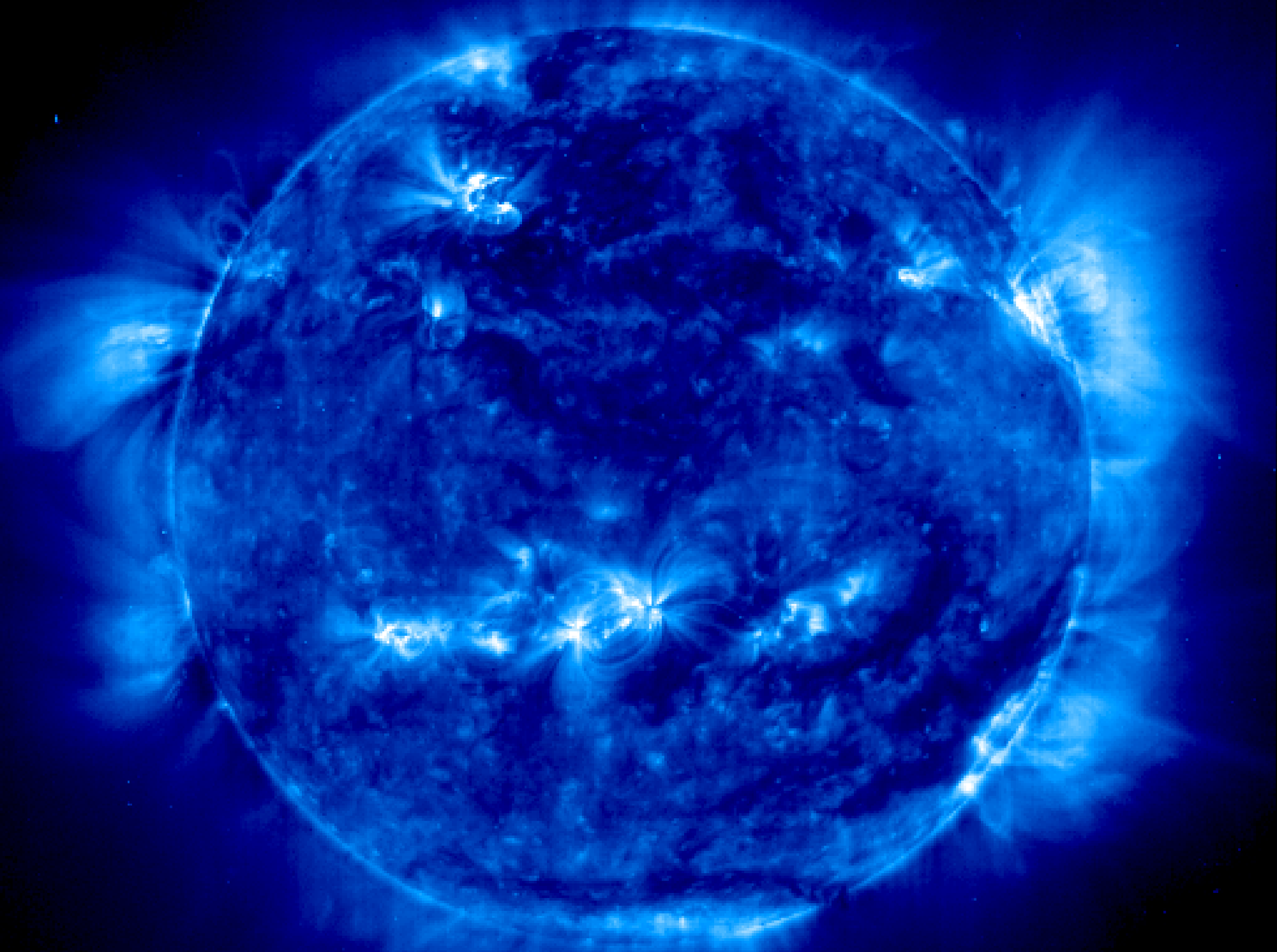

CD-ROM de la these de doctorat en sciences de l'univers (Astrophysique & Imagerie)

Résumé : Pour mieux comprendre les structures de la couronne solaire —de température élevée— et leurs évolutions, des méthodes de vision à 3 dimensions à partir des images EUV de SOHO/EIT ont été développées. Des anaglyphes ont servi à mieux comprendre le rôle du champ magnétique et des intéractions entre champ fermés et ouverts. Il est apparu que la reconnection entre des trous coronaux (CH) et des régions actives (AR) peut expliquer certaines disparitions de boucles coronales fermées. De plus, des analyses multi-instruments ont montré que la structuration des CHs résulte parfois de changements dans l'activité magnétique voisine.

Les mesures d'incertitudes sur les reconstructions par stéréovision n'ont pas permis de valider une méthode générale pour visualiser la couronne globalement en 3D. Par contre, le principe a pu être utilisé avec succès pour la reconstruction en 3 dimensions de boucles coronales. Ainsi après analyse des paramètres physiques de 30 boucles EUV de températures intermédiaires d'une région active, il est apparu que contrairement aux boucles chaudes en X, elles étaient en équilibre hydrostatique.
Les boucles d'une région active émergentes sont apparues comme se détorsadant au fur et à mesure de son grandissement ce qui correspond à un transfert de l'hélicité.
Des corrélations entre des brusques détorsadages et des éruptions ont aussi été établis dans les cas où la torsion initiale est trop importante et permet le développement d'instabilités.

Ces études 3D vont pouvoir permettre de mieux contraindre les bilans énergétiques pour le chauffage coronal gràce à la conservation de l'hélicité et d'améliorer la prévision de la météorologie spatiale. L'utilisation de techniques d'imageries adaptées (comme le dégrillage ou le Modèle de Vision Multi-échelle) a permis de faire ressortir certains détails dans la formation de CMEs par exemple.

Les instructions relatives à l'utilisation du CD-Rom sont données dans les fichiers README de chaque répertoire

---

Summary This thesis deals with 3D evolution of coronal structures based upon the ultraviolet telescope of SOHO : EIT.
Anaglyphs and incertainties on a complete stereovision reconstruction are described. Stereoscopic methods for loop reconstruction were successfully made to find 3D parameters. With dynamical stereoscopy, physical conditions were derived for 30 loops of temperature around 1MK.
A method which is able to derive twist variation were also built. Emerging loops were found highly twisted and they detwist as they grow. According to helicity conservation, this correspond to a transfert of twist into expansion.
Long time twist evolution of magnetic flux tubes are followed in relation with flares as relaxation.
Interaction between magnetic field lines were analysed. An example of reconnection between open and closed field line were observed. Other interactions were found with multi-wavelength observations : coronal holes borders (and thus CH) are better defined when an active region nearby is growing.
Other imaging techniques were used to better take profit as possible of SOHO/EIT. A multiscale vision model (MVM) was applied with success to show small coronal structures evolutions hidden by the noise level.

Instructions to use the CD-Rom are given in each directory inside the README files

UNIVERSITÉ DE NICE-SOPHIA ANTIPOLIS (UNSA)
FACULTÉ DES SCIENCES

Laboratoire d'Astronomie Spatiale
(LAS-CNRS, Marseille)

THESE

présentée pour obtenir le titre de
Docteur en SCIENCES
(discipline : Imagerie en Sciences de l'Univers, Astrophysique)

par

PORTIER-FOZZANI FABRICE

Etude de la couronne solaire en 3D et de son évolution avec SOHO/EIT

Soutenue le 15 Decembre 1999 devant le jury composé de :

- R. F. Malina (Directeur de these)
- A. Bijaoui (Président du jury)
- J. P. Delaboudinière (1er Rapporteur)
- M. Pick (2ème Rapporteur)
- J. C. Vial (Examinateur)
- B. Schmieder (Examinatrice)
- J. C. Noens (Examinateur)
- E. Fossat (Examinateur)
- S. Pohjolainen (Examinatrice)

au Laboratoire d'Astronomie Spatiale à 14h

Contents

List of Figures

List of Tables

.

Liste des publications Articles Publiés : AP
Articles Soumis ou en cours de soumission : AS
Colloques : C

- III.1.1 : PORTIER-FOZZANI, F., MAUCHERAT, A. J. & THE EIT TEAM, *First Year of Observations with SOHO/EIT of the "Quiet" Sun Corona*, 1998, (AP + C), PASP Conf. Ser.
- III.1.2 : PORTIER-FOZZANI, F.; MOSES, J. D.; DELABOUDINIERE, J. P.; GURMAN, J. B.; CLETTE, F.; MAUCHERAT, A., *EIT Images of the EUV Solar Atmosphere*, 1997, (AP + C), PASP Conf. Ser.
- III.3 : DELABOUDINIERE, J.-P.; STERN, R. A.; MAUCHERAT, A.; PORTIER-FOZZANI, F.; *et al.*, 1997, AP + C, AdSR
- IV.3 : ASCHWANDEN, MARKUS J. *et al.*, *Three-dimensional Stereoscopic Analysis of Solar Active Region Loops.*, 1999, (AP), ApJ. 515-842
- IV.3.3 : Portier-Fozzani, Démoulin, Neupert, Aschwanden, Maucherat, *Measurement of coronal magnetic twist during loops emergeance of NOAA 8069*, 1999, (AS), A&A
- IV.3.3 : Portier-Fozzani, Neupert, Aschwanden, Maucherat, Newmark, *Variations in the twist in coronal loops and association with flare activity during the solar cycle minimum*, 2000, (AS), A&A
- ex V.2 : Portier-Fozzani, *A possible role of magnetic reconnections in the decay of coronal loops*, 1998-99, (AS), A&A
- V.1 : Neupert *et al.*, *Observations of Coronal Structures Above an Active Region by Eit and Implications for Coronal Energy Deposition*, 1998, (AP), Sol. Phys.
- V.2 : Pohjolainen S., Portier-Fozzani F., Ragaigne D., *Radio Bright Structures near the Solar Poles at Millimeter Wavelengths*, 1999, (AP), NRO Report
- V.2 : Pohjolainen S., Portier-Fozzani F., Ragaigne D., *Comparison of 87 GHz solar polar structures with EUV emission*, 1999, accepte par A&A Sup. Ser.
- V.3 : Moses *et al.*, *Eit Observations of the Extreme Ultraviolet Sun*, 1997, (AP), Sol. Phys.
- V.4 : Portier-Fozzani F., *3D loops evolutions (twist and expansions) and magnetic fields interactions studied with SOHO/EIT*, 1999, SOHO 8, ESA, SP-446
- C : NOENS J.C. & PORTIER-FOZZANI, F., *Coordinated Observations made with SOHO/EIT*, 1997, (AP), Obs. Paris Edts

Communications non présentes dans la these

1. Talk du colloque de Vienne
2. Talk du colloque de Preveza
3. Poster 1 du colloque du CESRA
4. Poster 2 du colloque du CESRA
5. Poster de SOHO8

.

A mes proches

.

Préambule à la deuxième édition de la thèse

A la demande de certains lecteurs, pour faciliter la lecture, cette deuxième édition se retrouve allégée de l'ancien chapitre 5 et d'une partie du chapitre 4 (soit d'une trentaine de pages). Cela correspond à un recentrage de la thèse sur l'étude en 3 dimensions des boucles ce qui a permis d'approfondir dans cette version du manuscript l'importance du rôle des boucles dans la physique solaire coronale et dans leurs implications dans les relations Terre-Soleil. Les conclusions ont été aussi retravaillées en ce sens.

Les lecteurs interessés par la structuration des trous coronaux à cause de régions actives se repporteront au CDROM et à la version originale de la thèse. Il ressort de cette étude que l'hélicité magnétique joue un role fondamental dans l'ouverture des champs et que l'apport d'hélicité via une région active torsadée peut contraindre une région de champ magnétique faible à se structurer en une région de champ magnétique ouvert. Cela peut expliquer ainsi les observations de la structuration de mini-trous coronaux en vastes trous coronaux bien definis lorsqu'une région active apparaît. D'autres observations peuvent venir completer utilement cette étude, aussi cela fera partie d'une publication ultérieure.

Il est temps désormais de se pencher sur l'étude de notre étoile et de profiter de sa proximité pour essayer de mieux comprendre la physique qui la règle.

Réver à l'impossible rêve.
...
Tenter, sans force et sans armure,
D'atteindre l'inaccessible étoile
Telle est ma quête.
Suivre l'étoile
...
Jacques Brel, la Quête

Remerciements

Tout d'abord, je souhaite remercier M Roger Malina d'avoir accepté d'être mon directeur de thèse. Son travail a dépassé celui initialement prévu de directeur administratif; malgré son emploi du temps chargé comme directeur du Laboratoire d'Astronomie Spatiale et du CEA de Berkeley, il a toujours pu consacrer du temps pour mon encadrement. Je remercier aussi M André Jean Maucherat pour toute son aide pendant ces mois de thèse.

Je voudrais aussi remercier M Jean Pierre Delaboudinière pour son accueil dans l'équipe SOHO/EIT. J'ai pu apprécier ses talents de manageur qui ont permis d'unifier des personnalités scientifiques riches de leurs diversités ainsi que ses conseils qui m'ont été fort utiles. Je le remercie également d'avoir accepté d'être rapporteur de ma thèse.

Je souhaite aussi fortement remercier Mme Monique Pick qui a accepté d'être rapporteur de ma thèse et a largement dépassé ce rôle. Elle m'a accueilli chaleureusement au sein de l'équipe du Radiohéliographe au DASOP. J'ai ainsi pu trouver à Meudon les compétences sur la couronne solaire nécessaires pour établir les éléments scientifiques afin de finaliser cette these.

Je remercie aussi M Albert Bijaoui qui accepté d'être président du jury et M Eric Fossat -qui en tant que directeur du DAUNSA m'a permis un accès à l'indispensable revue "Solar Physics" sur Nice-.
Je remercie M Jacques-Clair Noens pour sa collaboration, la lecture attentive de la thèse et ses avis judicieux. Les échanges scientifiques tant à Cannes qu'au Pic du Midi ont été fructueux même s'ils n'ont pas toujours donné lieu à publication.
Je remercie Mme Brigitte Schmieder pour avoir accepté d'être membre du jury et m'avoir donné des conseils en conséquences.
Je remercie M Jean-Claude Vial pour son très sympatique accueil au MEDOC (IAS), d'avoir accepté d'être membre du jury et des nombreuses discussions.
Je remercie Mme Silja Pohjolainen du radio-télescope de Metsähovi pour sa collaboration.

Cette thèse n'aurait pu se réaliser sans les bons offices de M Francis Rouard qui m'a aidé dans la quête aux financements possibles. Je tiens à remercier aussi chaleureusement M Pierre Baude et le Rotary Club de Roquefort Les Pins (près de Sophia Antipolis) d'avoir accepter de participer financièrement et administrativement à l'élaboration de cette thèse. Leur confiance a permis l'élaboration de ce manuscript. Merci aussi à M Bernard Kohl et

le cercle d'étude "La Pensée Complexe : Edgar Morin," pour son soutien moral.

La richesse des échanges scientifiques avec Werner Neupert, Pascal Demoulin, Markus Aschwanden, Jeff Neumark, Jean Heyvaerts et bien d'autres a permis de donner matière à la consitution d'un terrain de travail très fertile. Après m'avoir donné la base nécessaire de la physique solaire, les discussions ont permis de conforter et d'affiner l'analyse des données faites.

Je remercie l'équipe du DASOP de m'avoir tres bien accueilli et d'avoir été très disponible (Dalmiro Maia, Alain Kerdraon, Ludwig Klein, Pierre Mein, Vilmer Nicole, Marie Pierre Issartel, Antoinette Raoult, Arturo Lopez, Anne Buttighoffer, Trottet Gérard, Van Driel-Gesztely Lydia et tellement d'autres...). Mes nombreuses periodes meudonnaises m'ont permis d'apprécier la gentillesse et les nombreuses compétences de chacun.

Je remercie Jo Gurman, Barbara Thompson et Creg De Forest pour leur accueil au Goddard (NASA, Washington DC). La réussite totale de SOHO provient en grande partie de l'ambiance et de la cohésion des centres européens et américains, aussi merci à Catherine Cougrand, Karine Bocchellini, Spiros, Frederic, Vincent... pour la bonne ambiance du MEDOC.
Je remercie M Julien Borgnino pour son travail pour l'école doctorale.

Cette these n'aurait pu être realisée pleinement sans le concours des differents services du LAS :
Administratif (Mme Babeth Harmitt, Mme Odile Candela, Mme Dominique Maccari, M Raphael Oloron, Mme Andrée Laloge et Mme Patricia Bentoza).
Imagerie (notre mimi nationale alias Mme Martinis, M Antoine Llebaria, Liliane Leporati,...)
Informatique (M Jacques Pons et M Jean Paul Marteau)
Je pense aussi à tous ceux qui font des choses utiles sans forcément être en avant scène.
Qu'ils en soient tous remercié.

Je remercie aussi mes amis du LAS (Serge List et Etienne Baudino) pour leur aide precieuse. Ce temps passé au LAS m'a aussi permis d'apprécier l'éfficacité et la rigueur du sous directeur du LAS Jean Michel Deharveng qui fut toujours de bons conseils.

Meme si pour des raisons de place je ne cite pas tout le monde, je tiens à signifier à tous ceux qui ont été proches ma reconnaissance.

Chapter I

Introduction

O Soleil! toi sans qui les choses
Ne seraient que ce qu'elles sont !
E. Rostand, Chantecler

Sommaire

I.1 Motivation de la thèse dans le cadre actuel de la physique solaire : situation de la question

La très haute température coronale – qui peut atteindre plusieurs millions de degrés Kelvins dans certaines structures – ne trouve actuellement aucune explication complètement satisfaisante. Divers processus sont évoqués qui mettent en jeu le champ magnétique et les évolutions des lignes de champs. En effet, dans la couronne solaire, le plasma se retrouve figé par le champ magnétique. Aussi la structure 3D du plasma coronal permet de cartographier la topologie et la morphologie du champ coronal et permet de comprendre ses évolutions. Par exemple, les boucles coronales —structures fermées— sont susceptibles de devenir instables et d'engendrer des phenomènes éruptifs et d'éjections. Aussi, la détermination de la physique 3D des structures est importante pour faire les bilans énergétiques.

L'étude des structures 3D de la couronne solaire et de leurs évolutions apparaît donc comme un thème important pour comprendre le rôle du champ magnétique. La formation des tubes de flux, les conséquences de leurs émergences dans la couronne, l'évolution des structures fermées ou ouvertes peuvent être étudiés en relation avec le

chauffage coronal à partir du champ magnétique, le développement d'instabilités qui sont sources de nombreuses questions.

En cela le lancement du satellite SOHO entièrement dedié aux observations solaires a permis d'accumuler des données pour une analyse précise et d'actualiser nos connaissances sur le Soleil. A son bord l'imageur EUV EIT avec une résolution temporelle et spatiale plus importante que les fusées ou missions embarquées précédentes montre la richesse d'activité coronale même pour le Soleil calme.

I.2 Etapes de travail

Avant de pouvoir s'intéresser au thème choisi de l'étude des structures 3D de la couronne solaire et de leurs évolutions, il a fallut tout d'abord qualifier les données et les outils d'analyses.

La première priorité pour l'équipe EIT fut donc de mettre en place des outils performants pour dépouiller les données. Dans ce cadre, afin d'obtenir des images sans artefact, après avoir diagnostiqué sur les images du vignettage périodique — dû principalement à une grille support de filtre—, avec M Jean Maucherat, nous avons développé une méthode de filtrage local pour les ôter numériquement.

Ensuite pour étudier les évolutions temporelles en 3D des structures coronales, plusieurs études ont alors été réalisées concernant la vision en 3D. Des techniques de stéréovision (*eg* anaglyphes) ont permis de définir les régions d'intérets en visualisant la morphologie des structures 3D, —boucles, évolution de structures, ...—. Cela met en évidence par exemple la complexité des boucles des régions actives supportant des protubérances et avoisinant des trous coronaux.

Une étude préliminaire sur les possibilités de reconstruction totale par stéréovision basée sur la géométrie projective fut entreprise. A partir des résultats obtenus par l'INRIA sur les inversions d'objets ordinaires, nous avons défini les contraintes dans le cadre de structures "diffuses" — ce qui est le cas pour les ions coronaux étudiés —. Le taux d'erreur de reconstruction pour des structures coronales estimé à partir des reconstructions d'objets réels fut jugé comme trop important pour continuer actuellement l'étude dans le cadre général.

Dans le cas des boucles coronales, il est par contre possible de définir la géométrie 3D de ces structures et de les reconstruire par stéréoscopie. Pour cela a été mis en place en collaboration avec M. Markus Aschwanden des programmes d'ajustement en 3D de boucles EUV. Tout d'abord des programmes d'ajustements a priori permettent de convenablement ajuster les projections des boucles sur des modèles circulaires ou torsadés. Les anisotropies observées pour les boucles comme le torsadage et le cisaillement sont apparues comme étant des paramètres importants liés à l'énergie disponible dans la région active. Nous avons ainsi pu établir des liens entre les paramètres des boucles et leurs stabilités.

2 types de methodes distinctes ont été mises en place : la stéréovision statique et la stéréovision dynamique.

Le calcul des températures le long et transversalement aux boucles a pu être réalisé pour des boucles circulaires. Des comparaisons sur la cospatialité des boucles de différentes températures ont été réalisées en collaboration avec d'autres instruments (eg avec M Peter Young pour CDS).

Une étude exhaustive se servant de la stéreovision dynamique pour contraindre les paramètres des boucles, a permis d'analyser 30 boucles et de trouver les relations physiques qui régissent ces boucles.

Afin de mieux suivre l'évolution et de choisir les périodes correspondant à nos sujets d'études, nous avons développé des catalogues d'images sélectionnées selon les dates et longueurs d'ondes. Dans d'autres cas, nous nous sommes servis des programmes de films existants.

La contrainte avec succès de l'algorithme de filtrage en ondelettes de M. Albert Bijaoui a fait ressortir des phénomènes d'évolutions de structures noyés initialement dans le bruit de l'image.

Des études en collaborations multi-instruments ont permis de définir avec exactitude la nature des objets et d'étudier leurs évolutions (structuration de trous coronaux,...). Cela fut aussi le cas pour l'étude des phénomènes éruptifs et éjections. Des observations coordonnées entre plusieurs instruments (EIT, Coronographes du Pic Du Midi —avec M. Jacques-Clair Noens—, Radio de Metsähovi —avec Mme Silja Pohjolainen—,...) ont ainsi pu être programmées.

A partir de ce thème scientifique principal sont aussi venus se greffer des thèmes secondaires connexes comme le cisaillement avec responsabilité scientifique au sein de l'équipe[1]. De même, lorsque les données EIT étaient privées, chaque membre de l'équipe a eu un rôle d'arbitre[2] et de conseil auprès des personnes extérieures à l'équipe qui demandaient des données. Cette tache de service scientifique — qui recoupait un rôle administratif, scientifique et technique— fut l'occasion d'échanges et discussions très intéressantes sur différents aspects de la physique solaire.

I.3 Plan de thèse

Après avoir rappelé dans le chapitre suivant des notions de physiques solaires coronales, les instruments utilisés sont présentés.

Le chapitre 3 précise les techniques d'imageries employées pour visualiser en 3 dimensions. De plus, des techniques se servant de vision multi-échelles pour retrouver des détails fins noyés dans le bruit sont aussi mises en oeuvre.

En se servant de ces outils, l'étude physique se porte d'abord sur les structures fermées — chapitre 4—. Tout d'abord le développement d'une méthode basée sur la stéréoscopie permet de retrouver les principaux paramètres physiques des boucles. Une première méth-

[1] Durant 1996, les membres de l'équipe SOHO/EIT se sont répartis les thèmes scientifiques en fonctions de leurs thèmes propres d'études [57]

[2] on dit aussi "de referee"

ode, à partir d'un à priori de circularité pour les boucles, permet de regarder l'évolution dynamique des tubes de flux. Ainsi des statistiques sont réalisées pour l'ensemble des boucles d'une région active.

Or certains ajustements justifient un nouveau modèle de boucle qui prend en compte le fait que les boucles ne sont pas toutes circulaires. Une deuxième méthode basée sur la stéréovision statique permet de mesurer ces écarts via le degré de torsion d'une boucle et d'étudier leurs évolutions. L'observation de l'apparition rapide d'une boucle avec un torsadage diminuant lors de son expansion est ainsi analysee. A partir des tubes de flux de Parker, l'émergence d'une région active est reanalysé d'un point de vue observationnel et théorique. Pour une région de boucles stables, l'augmentation observée du torsadage est attribuée en partie à la rotation différentielle. Enfin les observations sont venues confirmer la théorie sur la possibilité de création de phénomenes éruptifs lorsque le torsadage des boucles devient trop important.

L'évolution de structures coronales à partir d'observation multi-instruments est décrite au chapitre 5. Elle complète l'ancien chapitre 5 sur la structuration des régions magnétiques coronales. Ces analyses permettent de mieux comprendre, la formation de phénomènes éruptifs et des éjections de matières coronales.

Une synthèse du travail est rédigée au chapitre 6. Elle reprend de manière succincte les grandes lignes de l'étude.

Un bilan et les perspectives de ce travail sont tracés au chapitre 7.

Chapter II

Notions Générales Requises

La Science consiste à oublier ce que l'on croit savoir;
et la Sagesse à ne pas s'en soucier
Ch. Nodier, Léviathan le Long

Sommaire

Dans un premier paragraphe nous allons rappeler les lois physiques qui régissent la couronne solaire. Le second paragraphe sera consacré aux moyens modernes d'observation du soleil en particulier les observations multi-longueurs d'ondes, ainsi que l'apport du satellite SOHO et en particulier de l'instrument EIT.

II.1 Physique de la couronne solaire

Si l'atmosphère solaire est vue comme une sphère symétrique (*i.e.* plan parallèle), alors la couronne solaire est la partie extérieure de l'atmosphère solaire au dessus d'une certaine altitude ou d'une certaine température. Mais en fait la couronne est loin d'être homogène et le modèle précédant sera précisé par rapport à ses structures. Comme nous allons le voir l'aspect de la couronne et son activité sont commandés par le champ magnétique. La compréhension de sa physique nécessite quelques rappels sur la structure du soleil et sur les plasmas dans les champs magnétiques.

II.1.1 Le soleil et son champ magnétique

La proximité de la Terre vis à vis du Soleil a permis d'obtenir sur cette étoile moyenne (de type G2V) des connaissances sur ses structures spatiales.

L'intérieur du Soleil se compose d'un noyau chauffé par les réactions thermonucléaires. Selon les densités, l'énergie est transmise de manière radiative ou convective. La structuration de ces zones est connue grace aux ondes qui s'y propagent (héliosismologie).

Figure II.1: Eclipse du Soleil du 11 Aout 1999 à Vouziers (France) : La Lune a caché pendant 2 minutes 14s la photosphère, rendant visible la couronne en blanc, des protubérances en rouge. Noter la forte activité coronale présente et la haute protubérence au Sud Ouest (*Photo personnelle* ©*Association NOVAE*)

L'atmosphère du Soleil se compose de couches structurées de la manière suivante:

- La photosphère : c'est la surface visible du soleil avec une température voisine de 5800K.
- La chromosphère : elle se situe au dessus de la photosphère et s'observe en H_α
- La région de transition : c'est une région intermédiaire où la température croit très fortement sur une faible "épaisseur". Son étude permet de faire le lien entre les mesures du champ magnétique photosphérique et les structures coronales.
- La couronne solaire : Observable pendant longtemps uniquement pendant les éclipses —où la Lune cache la photosphère 10^6 fois plus brillante en visible—, elle tire son nom de son aspect (Fig. II.1). La spectrométrie a montré une température très élevée de plusieurs millions de degrés pour certaines de ces activités. Les processus physiques formant de telles températures sont encore sujets à de nombreuses interrogations.

Le champ magnétique joue un role important dans l'atmosphère solaire. Parmi les structures de la photosphère, les taches solaires sont des parties refroidies (3800K) par le champ magnétique important qui bloque les mouvements convectifs subphotosphériques. La variation du nombre de taches solaires ([87]) selon un demi-cycle de 11ans ([213]) se conjugue avec une migration de même periodicité de ces taches en latitude de l'équateur (au minimum de l'activité) vers les poles ([44]).

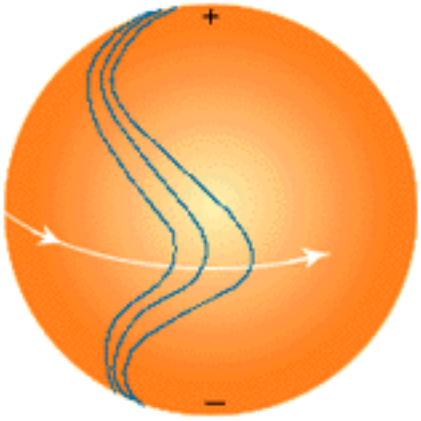

Figure II.2: Vitesse différentielle des taches en latitude (d'après [225])

La période de rotation des taches solaires est de 26,24 jours à l'équateur et augmente avec la latitude : cela induit une rotation différentielle (Fig. II.2).

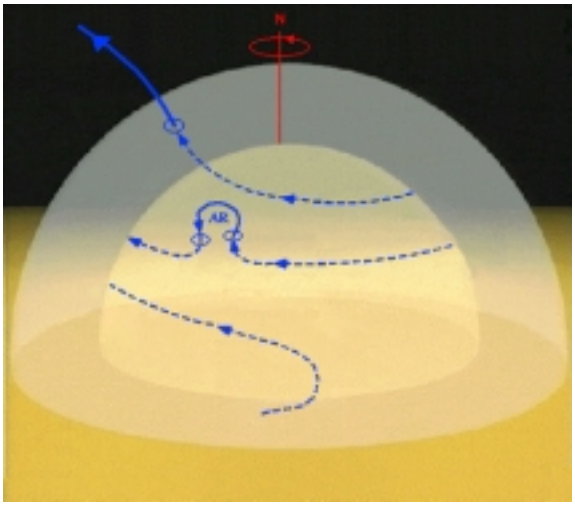

Figure II.3: Emergence de bipolarité (d'après [230])

Les taches apparaissent par paires [99]. La force de Coriolis via l'effet dynamo (où le champ magnétique toroidal se conjuge avec le champ poloidal) forme les "cordes magnétiques emergentes" [66].
Des travaux récents (par exemple [235]) semblent montrer que le stockage des champs

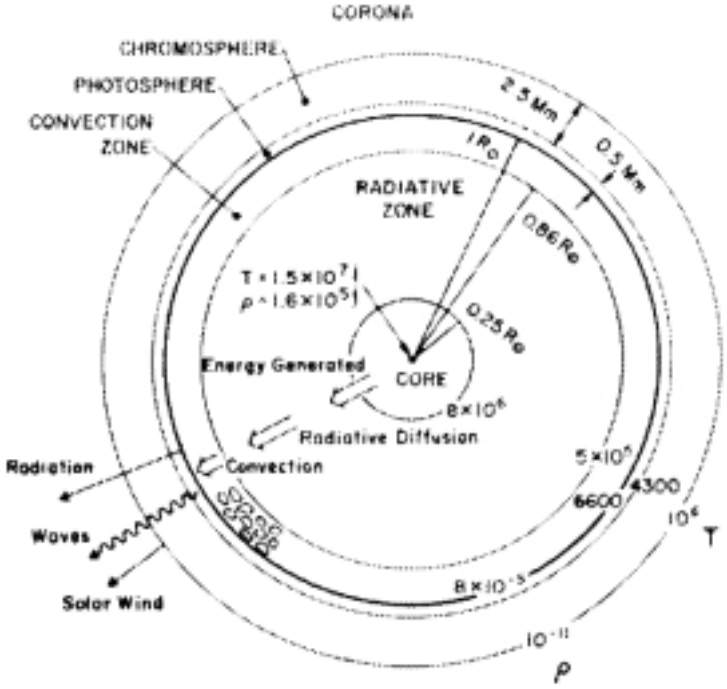

Figure II.4: Structure du soleil

magnétiques toroidaux intervient dans la zone à l'intérieur du Soleil où la rotation differentielle égale la rotation rigide et correspond aux latitudes d'émergences des taches (rôle de la tachocline). Nous reviendrons là dessus pour discuter de la morphologie des boucles coronales Ω (Fig. II.3).

D'autres structures photosphériques sont observables telles que les plages, les granules (diamêtre 1000km, durée de vie 8mn) et supergranules (diamêtre 30000-35000km, durée de vie 20h -[210]-). Ces 2 dernières structures traduisent le "bouillonnement" convectif de zones plus internes qui transporte ainsi l'énergie des réactions nucléaires vers l'exterieur.

Dans la chromosphère, des protubérances brillantes dépassant du bord du soleil suivent les lignes de neutralité du champ magnétique et correspondent à des filaments sombres lorsqu'ils sont vus sur le disque. Des spicules de durée de vie de 5mn et de diamêtre de 500-1500km, et un réseau chromosphérique (de diamêtre 30000-35000km et de temps caractéristique 20h) composé de mottes -brillantes ou sombres- et fibrilles sont aussi classiquement observés ([210]).

Les structures de la haute atmosphère sont décrites au paragraphe suivant.

II.1.2 La physique de la couronne et de la région de transition

Aspect

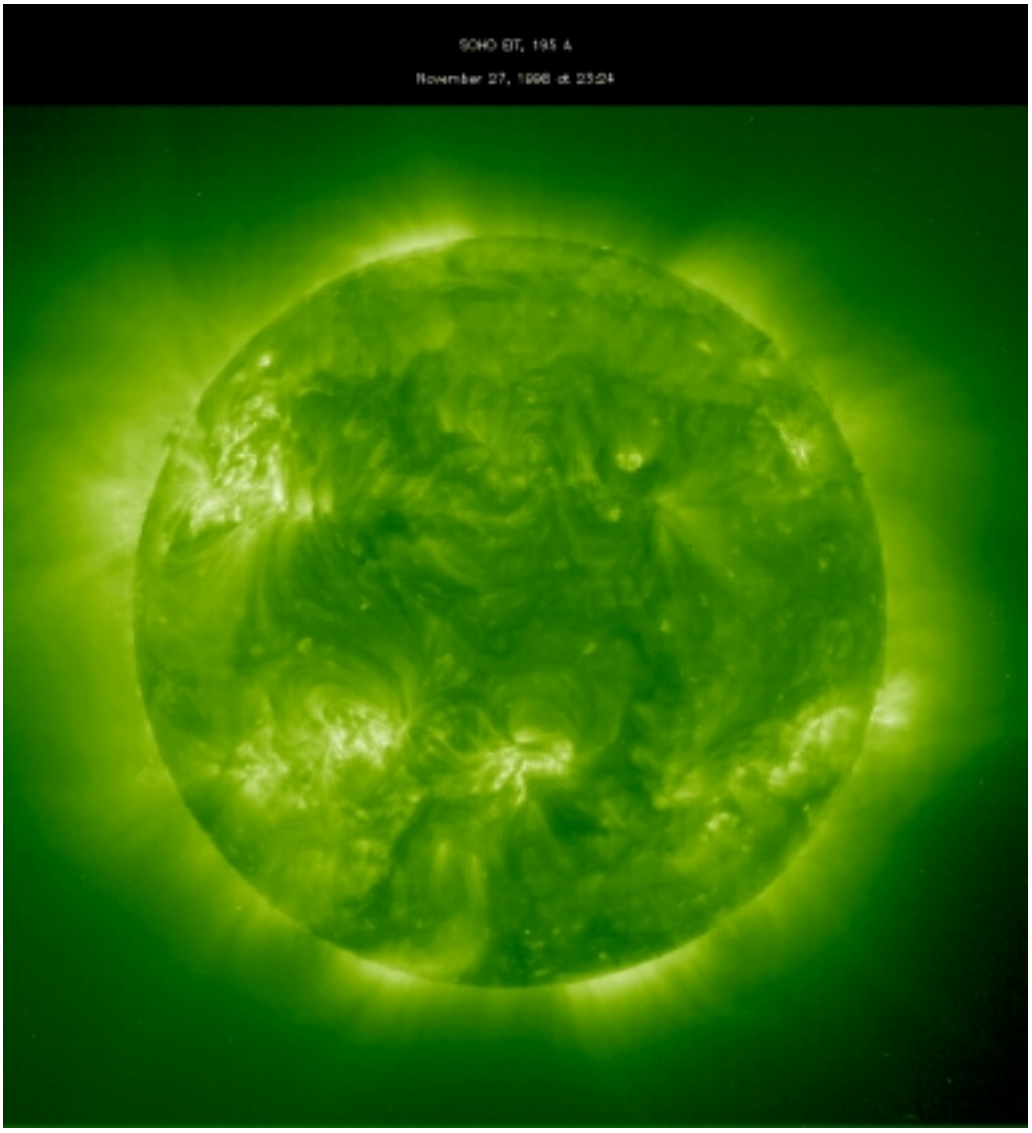

Figure II.5: Image EIT de la couronne (Fe XII, le 27 Novembre 1998 à 23h 24mn)

La couronne solaire (Fig. II.5), un milieu très chaud de plusieurs millions de K, Fig. II.6, se décompose classiquement en 4 parties ([94]) :

- La couronne K (continue) causée par la diffusion Thomson du rayonnement photosphérique sur les électrons coronaux rapides.
- La couronne F (de Fraunhofer) est le résultat de la diffusion de la lumière photosphérique par les poussières interplanétaires (entre Mercure et la Terre).

- La couronne E (émission) provient de l'émission de la radiation des particules hautement ionisées de la couronne

- La couronne T (thermale), principalement observable en InfraRouge, est de la poussière interplanétaire chauffée. Il s'agit de la même poussière que celle qui produit la composante F coronale.

La couronne que nous analyserons en détail est la partie chaude qui émet en UV et en X. A cause des températures élevées, les longueurs d'ondes ultraviolettes sont particulièrement bien adaptées à l'imagerie de la couronne solaire. Le rapport de transitions de raies permet de calculer les températures et les densités des différentes structures ([61],[62],[60]).

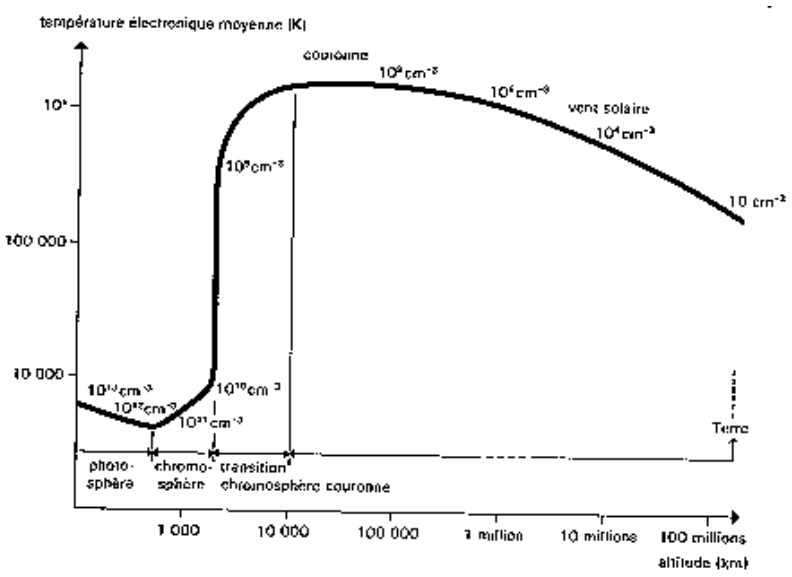

Figure II.6: Température versus altitude

Les structures de la haute atmosphère solaire

Températures et densités varient selon les structures. La Table II.1 résume quelques paramètres typiques de structures coronales observées en rayon X.

Selon les auteurs les bornes de la région de transition (centrés sur 10^5K) et de la couronne (plusieurs MK) sont variables. Par exemple, on peut donc considérer que les structures vues par SOHO/EIT et TRACE en Fe IX/X sont soit la région de transition, soit la partie basse de la couronne. Nous reviendrons lors du chapitre sur les boucles sur cette séparation physique de l'atmosphère solaire.

Les structures coronales peuvent être fermées (régions actives de boucles aussi notées ARL) ou ouvertes (trous coronaux — notés CH—, plumes polaires,...). Afin de compren-

Composante	Taille caractéristique	Température maximale atteinte	Part de contribution dans la luminosité en X (respectivement au maximum et minimum du cycle)
Régions Actives (AR)	4.10^7 m	3MK	40-5
Structure à large échelle	10^8 m	2 MK	20-70
Trous coronaux (CH)	$< 10^8$ m	$< 2.10^6$K	< 1

Table II.1: Composantes coronales (d'après [94])

dre le rôle du champ magnétique précisons comment se comportent les particules chargées (ionisées) de la haute atmosphère solaire en présence d'un champ magnétique.

II.1.3 Rappels de physique des plasmas et MHD

Définitions et équations de base

Un plasma est un fluide dans lequel les particules chargées (ions et électrons liés) sont suffisamment nombreuses pour influencer son comportement. Il se décrit ainsi d'après son comportement collectif ([46]). Un exposé extensif décrivant le plasma coronal solaire est disponible dans Velli ([244]).

L'équation de Poisson permet de définir l'écrantage électronique (ie distance limite d'influence) aussi appellé longueur de Debye :

$$\lambda_D = \sqrt{\frac{\varepsilon_0.K.T}{n.e^2}} \tag{II.1}$$

Comme les structures étudiées sont de tailles caractéristiques $L \gg \lambda_D$, on considèrera le plasma coronal comme monofluide.

Les équations de Maxwell décrivent le systeme (E étant le champ électrique, B le champ magnétique, $\vec{D} = \varepsilon.\vec{E}$ et $\vec{B} = \mu\vec{H}$) :

$$\begin{cases} Div(\vec{D}) = \rho \\ \vec{Rot}(\vec{E}) = -\frac{\partial \vec{B}}{\partial t} \\ Div(\vec{B}) = 0 \\ \vec{Rot}(\vec{H}) = \vec{j} + \frac{\partial \vec{D}}{\partial t} \end{cases} \tag{II.2}$$

auxquelles on rajoute la loi d'Ohm avec le courant J :

$$\vec{J} = \rho.(\vec{E} + \vec{v}\Delta\vec{B}) \tag{II.3}$$

En combinant les équations précédentes, on écrit la loi d'induction

$$\frac{\partial \vec{B}}{\partial t} = \vec{\nabla} \times (\vec{v} \times \vec{B}) + \eta \vec{\nabla}^2 \vec{B} \tag{II.4}$$

avec $\eta = \frac{1}{\mu\rho}$ = diffusivité magnétique. Le premier terme de la loi d'induction (Eq. II.4) est un terme dynamique, le second est un terme résistif. Le nombre de Reynolds magnétique est défini comme étant le rapport entre ces 2 termes. Dans le cas de la physique solaire il est environ $R_m \sim 10^6 - 10^9 m >> 1$ et on peut donc souvent négliger le terme résistif : c'est le cadre de la MHD idéale.

A partir de là il est donc possible de faire les bilans énergétiques des transferts entre structures magnétiques.

La materialisation de $\vec{B}$

Les concepts de lignes de champ et de tube de flux magnétique matérialisent par leurs représentations les configurations magnétiques. En effet, une ligne de champ décrit la variation de $\vec{B}(\vec{r},t)$ dans l'espace où $\vec{r} = (x,y,z)$ c'est à dire par définition

$$\frac{B_x}{dx} = \frac{B_y}{dy} = \frac{B_z}{dz} \tag{II.5}$$

.
La force de Lorentz ($\vec{F} = q(\vec{v} \otimes \vec{B} + \vec{E})$) s'exerce sur les particules de charge q et de masse m et de vitesse v. Dans le cas de la couronne solaire la gyration de la matière est tres faible ([197]) donc on considère que les particules suivent les lignes de champ magnétique.
Un tube de flux magnétique est par définition un groupe de lignes de champ coupant une surface (ou section) ouverte S occupant un volume V. On peut définir son flux

$$\Phi = \int\int_S \vec{B}.\vec{dS} \tag{II.6}$$

.
D'après le théoreme mathématique de la divergence, on a

$$\int\int \vec{B}\vec{dS} = \int\int\int_V div(\vec{B}) dV(S) \tag{II.7}$$

Cette valeur est nulle puisque $div(\vec{B}) = 0$ (Eq. II.2). Donc pour un tube de flux entre des surfaces S_1 et S_2,

$$\Phi = \int\int_{S1} \vec{B}.\vec{dS}_1 + \int\int_{S2} \vec{B}.\vec{dS}_2 = 0 \tag{II.8}$$

, c'est à dire $\Phi_1 = -\Phi_2$, ce qui veut dire que *Le flux magnétique se conserve sur toute la longueur du tube de flux*. Priest [197] résume différentes propriétes magnétiques.

Confinement

Le rapport entre l'énergie thermique et l'énergie magnétique

$$\beta = \frac{E(thermique)}{E(magnetique)} = \frac{\frac{3}{2}nKT}{\frac{B^2}{\mu}} \tag{II.9}$$

détermine le confinement ou non du plasma par le champ magnétique. Dans le cas des structures magnétiques coronales, comme $n \sim 10^9 cm^{-3}$, $T \sim 10^6$ K, et $B \sim$ quelques Gauss on trouve

$$\beta \prec\prec 1 \tag{II.10}$$

A partir de l'équation d'induction (Eq. II.4), lorsque la diffusivité magnétique η est nulle (cadre de la MHD idéale), on a la variation de flux magnétique Φ qui s'écrit :

$$\frac{d\Phi}{dt} = \frac{d}{dt}\int_S \vec{B}\vec{n}dS = \int_S (\frac{\partial \vec{B}}{\partial t} - \vec{\nabla} \times (\vec{v} \times \vec{B}))\vec{n}dS = 0 \tag{II.11}$$

Les lignes de champs se déplacent donc avec la matière : le plasma se retrouve "gelé" par le champ magnétique ([210]).

La magnétohydrodynamique permet de décrire les structures coronales. Nous détaillerons au chapitre 4 le cas des boucles coronales.

II.2 Instrumentation et utilisation des données

Comme nous allons nous intéresser au champ magnétique au niveau de la couronne, nous allons utiliser les instruments qui sont susceptibles de tracer ces structures. En imagerie spatiale nous nous servirons principalement des observations UV et X c'est à dire de SOHO/EIT, de SOHO/CDS, de Yohkoh/SXT et de TRACE. Les données coronographiques de SOHO/LASCO ainsi que des observations terrestres viendront compléter ces données.

II.2.1 Présentation des instruments utililisés

Le satellite SOHO : SOlar Heliospheric Observatory

Le lancement du satellite SOHO (SOlar Heliospheric Observatory, Fig. II.7) en décembre 1995 a fourni un nouvel outil performant pour mieux comprendre le Soleil. Les 12 instruments qui se trouvent à son bord profitent du positionnement au point de Lagrange L1 Terre-Soleil pour observer de manière continue divers aspects de notre étoile. L'héliosismologie, l'étude de l'atmosphére extérieure du soleil, et la mesure du vent solaire in situ au niveau du satellite sont les 3 composantes principales de la mission.

Figure II.7: Le satellite SOHO : au premier plan au centre l'instrument EIT

Parmi les instruments nous nous servirons de MDI pour étudier le champ magnétique, d'EIT pour imager les structures coronales, de CDS pour observer les variations spatiales en température des structures éventuellement des coronographes LASCO et du spectro-coronographe UVCS pour comprendre les structures coronales étendues. Des relations avec d'autres instruments de SOHO seront éventuellement évoquées le moment venu. Comme nous allons principalement utiliser SOHO/EIT et mettre en oeuvre de nouveaux outils adaptés à cet imageur EUV, une description s'impose.

L'imageur EUV de SOHO : EIT

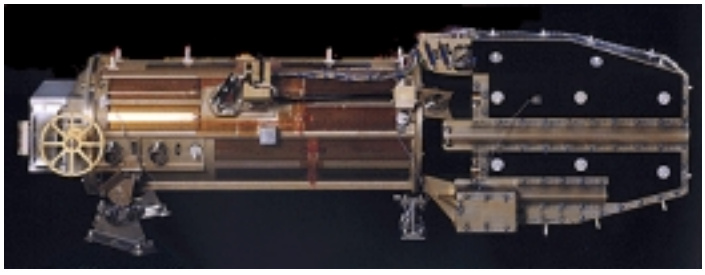

Figure II.8: L'instrument EIT

L'instrument EIT (Extreme ultraviolet Imaging Telescope, Fig. II.8) image en 4 longueurs d'ondes centrées respectivement sur 171 Å(Fe IX–X), 195 Å(Fe XII), 284 Å(Fe XV), 304 Å(He II) la couronne solaire.

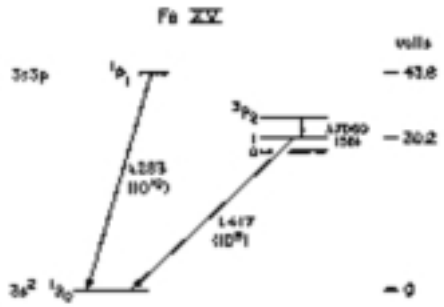

Figure II.9: Transition UV pour le Fe XV ([270])

Le choix des raies La formation des raies est décrite dans l'*Annexe I*. 4 raies ont été judicieusement choisies pour couvrir une gamme de température entre la chomosphère et la couronne moyenne (Fig. II.6).

- La raie chromosphérique He II à 304 Å([118]) a été utilisée lors des missions SERT-S 91. Comme le montre les images EIT, une raie coronale -chaude- de Si IX étant proche, la séparation de ces 2 raies se trouve impossible à réaliser. Cela rend l'analyse de ce filtre quelquefois complexe ([157]). En première approximation le bouillonnement de la partie convective subchromosphérique est "pollué" par les points brillants coronaux des régions actives.

- Au voisinage de 171 Å, les transitions de $S_0^1 - P_1^1$ à 171.01 Åpour le Fe IX, et $2P_{\frac{3}{2}}^2 - D_{\frac{5}{2}}^2$ à 174.53 Åpour le Fe X (Dere [62]) permettent d'analyser la région de transition dont l'intéret du Fe IX apparut lors de Skylab à 241 et 244 Å(Feldman *et al.*, [78]). Les structures observées dans cette raie sont généralement fines (boucles étoites,...).

- Le quadrant de filtre spectral centré sur le Fe XII à 195 observe la raie $3s^2 3p^3 - 3s^2 3p^2 3d$ ainsi que 2 autres transitions $S_{\frac{3}{2}}^4 - P_{\frac{5}{2}}^4$ et $D_{\frac{3}{2}}^2 - D_{\frac{3}{2}}^2$ à 195.13 Å. D'autres raies peuvent être aussi présentes dans ce filtre ([62]). Des CMEs sont observées dans cette raie.

- Le Fe XV $3s^2 - 3s3p$ a comme transition atomique (Fig. II.9): $S_0^1 - P_1^1$ à 284.17. Les boucles chaudes sont alors tracées et apparaissent moins précises spatialement.

La technique de l'instrument Le télescope est de type Ritchey-Chrétien (Fig. III.3) avec à son foyer une caméra CCD 1024x1024 pixels qui couvre $45 \times 45 arcmin^2$. La focale de l'instrument est de 1652mm.

Chaque pixel de la CCD couvre $21 \mu m^2$, ce qui donne une résolution de $2.62 \times 2.62 arcsec^2$ avec un temps de lecture de la CCD de 21 s.
Les miroirs sont formés de couches multiples Mo-Si et la sélection des bandes passantes

Télescope	de Ritchey-Chrétien
Longeur effective	165.2 $\pm$ 0.2 cm
Diamêtre du primaire	12 cm
Aire Géométrique par quadrant	13 cm2
CCD	(refroidie à environ -80 C)
Taille de la matrice	1024 x 1024 (45 x 45 arcmin)
Taille des pixels	$21\mu m^2$ (2.6 arcsec)
Temps de lecture	21 s
Filters	
Filtre d'entrée 1500	Al/700 A cellulose/1500 A Al
Roue à Filtre	à plusieurs positions
Télémetrie	*durant la première année avant d'être augmentée*
Taux habituel moyen	1 Kbps
Taux combiné EIT/LASCO	5.2 Kbps
Taux mélangé (avec CDS et SUMER)	26.2 Kbps (30 mn par 24 h)
Compression des données	
Racine carré	de 14 à 7 bits
Avec algorithme ADCT	jusqu'à un facteur de compression de 10
Temps de transmission	*d'une image entière pleine résolution (à 7 bits/px)*
pendant télémétrie normale (5.2 Kbps)	23.5min (toutes les 2h)
Temps de transmission	*d'une image de résolution* 4×4 *pixels*
pendant télémétrie normale	1.5 min
Télémetrie	*moyenne après 1997*
Temps de transmission d'une image entière	environ 12 minutes

Table II.2: Caractéristiques techniques d'EIT ([58])

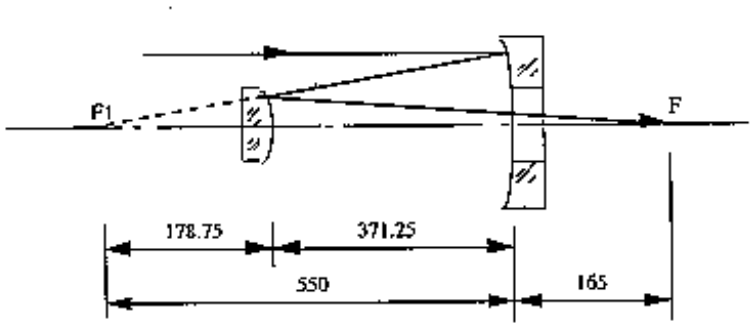

Figure II.10: SOHO/EIT : Trajet Optique ([228])

s'effectue par un cache ouverture, cache qui ne laisse passer que la lumière du quadrant choisi (Fig. II.10).

Les caractéristiques principales Tables II.3 et II.2 et le schéma optique Fig. II.10 de l'instrument viennent compléter la description (*cf.* aussi [58], [228], [56]).

Longueur d'onde	Ion	Température	Observation
304 Å	He II	8.0×10^4 K	Le réseau chromosphérique
171 Å	Fe IX,X	1.3×10^6 K	la région de transition
195 Å	Fe XII	1.6×10^6 K	la couronne calme
284 Å	Fe XV	2.0×10^6 K	les régions actives

Table II.3: Les filtres EIT ([58])

Quelques possibilités observationnelles : Le calcul des températures Lorsque EIT prend des images dans les 4 longueurs d'ondes de façon quasi-simultanée [1] , il est théoriquement possible de mesurer les températures et les densités ([162], [15]). En effet, Mason *et al.*, (ref. in [60]) ont développé un code atomique (CHIANTI) qui à partir de la température et de la densité de diverses espèces chimiques (dont les ions du Fer) donne l'intensité émise dans toutes les raies du spectre EUV. (*cf.* Annexe). Cette émission est proportionnelle à une quantité indépendante de l'ion considéré : la mesure d'émission différentielle qui est le carré du nombre d'électrons dans un domaine de température donné. En renversant le code à partir d'images dans plusieurs longueurs d'ondes d'EIT, on peut — moyennant quelques précautions — obtenir les températures et les densités ([162]) des structures.
Ce même principe est utilisé aussi par l'instrument CDS qui observe simultanément en plusieurs longueurs d'onde de l'EUV pour faire des diagnostics de plasma.

[1] Le temps raisonnable entre les poses doit etre tel que les structures auxquelles on s'intéresse n'ont pas eu le temps de varier c'est à dire hors formation de CMEs

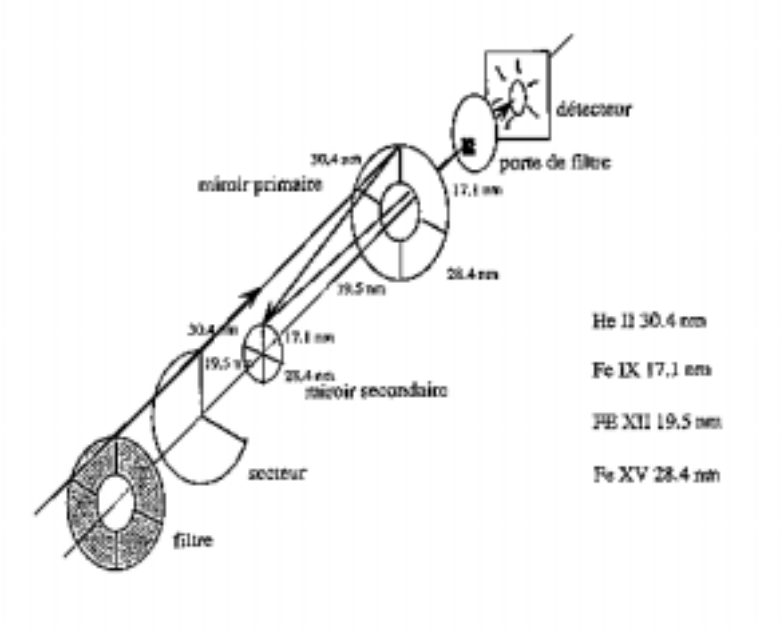

Figure II.11: SOHO/EIT : Positions des filtres UV ([228])

II.2.2 Les autres instruments utilisés

Les observations multi-longueurs d'ondes sont nécessaires pour déterminer les paramètres physiques des régions étudiées. Sans décrire en détail les instruments, nous précisons quels sont leurs apports dans notre étude.

1. **Disques en lumière "Blanche" :** L'observation de la photosphère (Big Bear Solar Observatory -BBSO-, Le Grand Equatorial Coudée de l'observatoire de Nice,...) permet de décrire la morphologie des taches solaires (*e.g.* configuration en δ,...)

2. **Disques en filtres spécifiques :**

   (a) H_{alpha} **:** Filaments et protubérances sont mis en évidence à $\lambda = 6563A$ (*e.g.* Bass 2000, BBSO,...)

   (b) **He I :** La raie He I à $\lambda = 10830A$ trace les trous coronaux (CH) depuis le sol car son mécanisme de formation met en jeu le rayonnement coronal qui vient de la couronne vers la chromosphère [210]. (Exemple : Observatoire de Kitt Peak)

3. **Magnétogrammes :** Les magnétogrammes permettent de déterminer l'importance, la polarité et la structure du champ magnétique photosphérique. (Exemple : Na $\lambda = 5896A$ et Fe $\lambda = 5250A$ au Mont Wilson, ...).

   A bord de SOHO, MDI dispose d'une résolution de 4 arcsec ([79]) ce qui permet des modélisations "force free" des lignes de champs d'une région active. De plus, l'observation des polarités des régions magnétiques renseigne sur les possibilités d'interactions.

4. **Radio :** Les observations radio à 17GHz du Nobeyama Radio Observatory permettent de distinguer entre les protubérances (en sombres sur le disque [96]) et les trous coronaux —CH— (brillants [97]) qui sont tous deux sombres en UV.

   Nous verrons ulterieurement que la comparaison avec le radiotélescope de Metsähovi à 87GHz permet de mieux comprendre la structuration des trous coronaux.

5. **Les imageurs UV**

   (a) **SOHO/CDS**

   Sur le satellite SOHO, le spectro-imageur CDS mesure les températures et les densités coronales à partir d'images simultanées en plusieurs longueurs d'ondes UV ([79]).

   L'utilisation simultanée de son canal à incidence normale et d'EIT permet d'avoir une gamme complète de température entre 10^5 et 10^6 K (Fig. II.12) et de suivre l'évolution de la morphologie d'une structure en fonction de sa

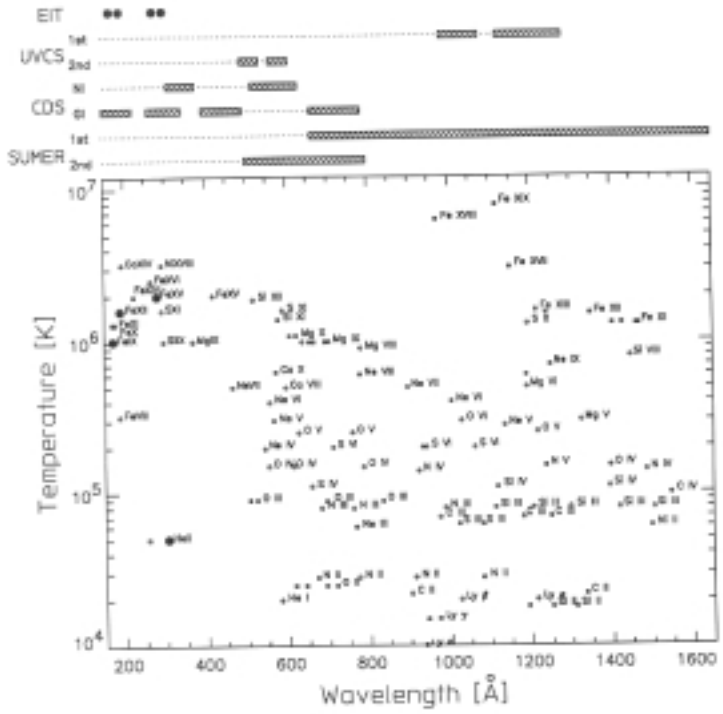

Figure II.12: Spectres des instruments UV de SOHO ([79])

température. (*cf.* par exemple le chapitre sur les boucles).

(b) **Le satellite TRACE** Par rapport à EIT, l'instrument TRACE (Transition Region And Coronal Explorer, [236]) grace à sa forte résolution (entre 0.5 et 1 arcsec /pixels) est capable en UV d'agrandir certaines régions son champ de vue étant 8.5×8.5 arcmin (avec une CCD 1024 X 1024 refroidie à -65C).
Les longueurs d'ondes d'observations de Trace sont les 3 mêmes raies coronales qu'EIT (Fe IX/X, Fe XII, Fe XV), plus la région de transition (1550 Å), la chromosphère (1700 Å, 1216 Å), et la photosphère (2500 Å).

Pour observer le soleil entier, TRACE est obligé de faire une mosaique —c'est à dire des prises successives d'images en changeant le cadrage–. Après avoir repéré sur EIT les régions d'intérets, cet instrument permet de regarder en détail les structures à petites échelles (par exemple les détails dans les boucles).

6. **Le satellite YOHKOH** Le satellite Yohkoh observe en X la couronne chaude (2-20MK) depuis une orbite autour de la Terre.

   4 instruments se trouvent à son bord ([168]), le plus connu étant SXT (Table II.4):

   - HXT : Hard X Ray Telescope : imageur à transformée de Fourier de Rayons X durs ($\simeq$ 15–100 KeV) , Champ de vue 2x2', résolution 5" ([127])

Instrument:	Miroir à incidence Rasante
Plusieurs longueurs d'ondes	entre 2.3-10
Résolution angulaire	2.45 arcsec pixel
Champ de vue:	42 x 42 arcmin
Résolution temporelle maximale:	0.5 s
Résolution temporelle typique:	2.0 s pour les éruptions, 8.0s dans les régions calmes

Table II.4: L'imageur SXT à bord de Yohkoh [94]

- SXT : Soft X Ray Telescope : Télescope Rayons X mous à incidence, CCD 1024×1024, pixels 2.46 arcsec ([237])
- WBS : Wide Band Spectrometer : spectromètre depuis les SXR (1KeV) jusqu'au rayons γ (< 100 MeV) ([269])
- BCS : Bragg Crystal Spectrometer pour le spectre complet ([54])

L'analyse des données du satellite Yohkoh [267] a montré que la structure à grande échelle varie fortement avec les phases du cycle d'activité solaire. En outre, les boucles coronales chaudes interviennent fortement dans l'activité.
A partir de ces constatations, la couronne en UV étant de température intermédiaire entre la couronne en X et la chromosphère vue en H_α, mes axes principaux de recherches avec SOHO/EIT sont établis comme étant : **la structuration et l'évolution de la couronne EUV globale**, ainsi que **les changements observés dans les boucles**.
De plus les variations ou non de températures dans les structures sont analysées en corrélant les images de Yohkoh et EIT.

7. **Coronographes** Les coronographes réalisent artificiellement des éclipses de soleil selon le principe de l'occulteur de Lyot. L'occultation permet d'imager en lumière visible et proche IR les structures coronales environ 10^{-6} à 10^{-12} fois moins brillante que la photosphère suivant la distance au centre du soleil.
Des observations coordonnées entre SOHO/EIT et les coronographes du Pic du Midi ont été organisées. Le petit coronographe image en H_α les protubérances. Le spectromètre du grand coronographe mesure l'intensité des structures dans la raie verte (Fe XIV : $\lambda = 5303A$, transition en lumière visible [94] de la raie interdite $2p.^2P_{\frac{3}{2}} - .^2P_{\frac{1}{2}}$) et 2 raies InfraRouge du Fe XIII $\lambda = 10747A$, transition en lumière visible de la raie interdite $3p^2.^2P_1 -^3 P_0$ et $\lambda = 10798A$, *ie* $3p^2.^3P_2 -^3 P_1$. Leur rapport permet de déduire les densités de ces structures.
Les coronographes de SOHO ([79]) appelés LASCO (entre 1.1 et 30 $R_\odot$) et UVCS (entre 1.3 et 10 $R_\odot$) permettent d'observer les éjections de matières coronales (CMEs), les "helmets streamers" —où est supposé se former le vent solaire—, et les trous coronaux. Il est possible de remonter sur EIT à l'observation des activités qui forment les CMEs. Ces mécanismes exacts de formation sont encore un sujet ouvert.

8. **Les satellites GOES :**
   Les satellites GOES mesurent les éruptions solaires avec des capteurs en rayons X, éruptions souvent vues par SOHO/EIT. Une échelle quantitative de flux reçu est alors mise en place.

Les bulletins quotidiens d'organismes spécialisés comme le Space Environment Center (SEC, [222]) résument l'ensemble de l'activité observée depuis les différents observatoires (Eruptions, Disparition Brusque des Filaments, ...), ce qui peut servir de première base pour l'analyse multi-longueurs d'onde d'une évolution de structure.

II.2.3 Un exemple d'observation multi-longueurs d'onde avec SOHO/EIT

A titre d'exemple nous allons analyser quelles sont les activités présentes le 27 novembre 1998 (Fig. II.13) au niveau de la couronne.

1. **Régions Actives :**
   Correspondant aux taches solaires photosphériques, elles apparaissent comme bipolaires sur les magnétogrammes (AR4). Sur EIT, souvent des tubes de plasma confinés par le champ magnétique rejoignent ces bipolarités et forment des "boucles coronales" (AR3). Elles ont tendance à s'etaler avec le temps (AR1, AR2, AR5).

2. **Les Trous Coronaux :**
   Il s'agit de régions correspondant à des champs magnétiques ouverts, le plasma s'échappant apparait sombre en UV et brillant sur les cartes radio de Nobeyama. Généralement polaires (CH1, CH2) ils peuvent aussi être quelquefois présents à basse latitude.

3. **Les Filaments ou Protubérances :**
   Ce materiel plus froid est visible en H_α comme sombre sur le disque (on parle alors de filament —FC1—) ou brillant sur le limbe solaire (on parle alors de protubérance). En fait, il s'agit du même objet —cf FC2— dénommé différement par les observateurs pour des raisons historiques.

Le champ magnétique se manifeste de nombreuses autres manières que nous analyserons le moment venu.

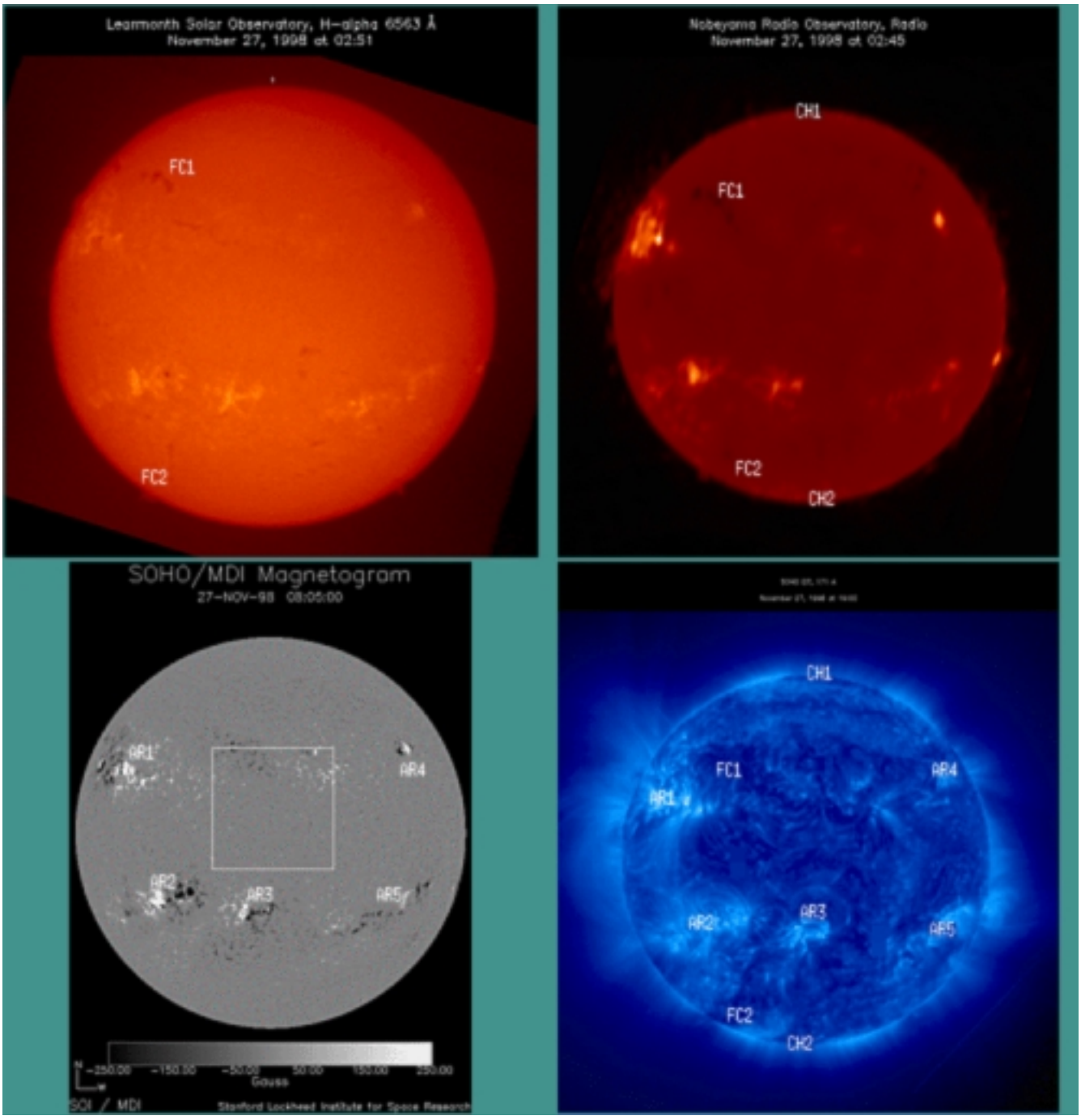

Figure II.13: Image composite de différents instruments solaires

Chapter III

Techniques d'imageries spécifiques

Le Sage voit, fait et transmet
Anonyme

Sommaire

Dans ce chapitre nous présentons les techniques d'imageries spécifiques que nous avons employées dans notre recherche sur les structures coronales. La mise en place de catalogues d'images facilitera la recherche des données. La calibration des données a comporté la mise au point d'une méthode de dégrillage. Afin d'améliorer la compréhension physique des structures coronales présentes, des structures cachées dans le bruit de fond de l'image ont pu être révélées après une utilisation adéquate du Modèle de Vision Multi-échelle. De plus des méthodes 3D ont été étudiées pour être appliquées sur les images SOHO/EIT.

III.1 Imagerie EIT

L'instrument SOHO/EIT a été présenté au chapitre précédent. Le grand nombre de données reçues quotidiennement a motivé la création d'outils qui permettent de suivre les évolutions avec le temps. Ainsi on peut utiliser la procédure movie_maker pour faire des films. Des procédures permettant d'archiver des films sur Video-cassettes ont aussi été réalisées. En complément, nous avons développé et mis en place un programme de catalogue par imagettes.

III.1.1 Mise en place du catalogue d'images

Pour comparer efficacement et analyser les données nous avons conçu et mis en place un catalogue par imagettes.

Ce catalogue par imagettes réunit sur une seule planche les images caractéristiques correspondant aux données choisies par des critères de sélections tels que la longueur d'onde, la taille de l'image, la date. Un exemple du catalogue d'images est donné Fig. III.1. Les lignes générales de la programmation sont précisées en annexe. Ce programme de catalogue d'image réalisé au LAS, fut commencé par le stagiaire Martial André au printemps 1996, avant que je modifie profondémment sa structure afin d'y introduire certains critères de selections et de pouvoir lire les données précalibrées (Level Zero : EFZ) et non plus seulement les données de vision rapide ("quicklook": EFR). La programmation du catalogue par imagette ne se sert que des entêtes de chaque image disponible puisque pour des raisons de rapidité d'accès lors de l'écriture, le catalogue "officiel" EIT est écrit en binaire ce qui necessite un script adapté pour le transformer en fichier texte lorsque l'on cherche des paramètres précis (taille image, longueur d'onde,...). Les imagettes permettent de définir et de suivre temporellement les régions d'intérets.

Pendant près de 2 ans[1], ce programme fut adapté pour aller chercher directement sur la base de données aux USA uniquement celles répondant aux critères d'entrées pour en faire les imagettes diminuant de facto le temps de transmission et l'espace mémoire nécessaire.

Après avoir été fiabilisé pour Unix, la version a été installé sur les sites du Médoc en Septembre 1997 et puis inclus au soft EIT du Goddard. Cela permet désormais de cataloguer l'ensemble de la base de donnée des images EIT disponibles selon des critères précis (longueur d'onde, taille,...) à partir des entêtes des images en FITS.
Des catalogues obtenus pour le Fe IX/X sont présentés sur le CD-Rom en Annexe. Ces catalogues sont des images au format gif regroupant les Années 1996, 1997, et début 1998.
Ces catalogues par imagettes ont permis l'étude de la couronne solaire à grande échelle lors du minimum de 1996. Un choix adéquat des données (Fig. III.1) correspondant à la recherche physique du moment a pu être réalisé à partir des milliers d'images de cette période. L'article présenté ci dessous résume l'intérêt de son utilisation pour faire une analyse de l'évolution temporelle des structures coronales.

[1] jusqu'à l'abandon par Renater des transmissions Outre-Atlantique via *DEC-VMS*

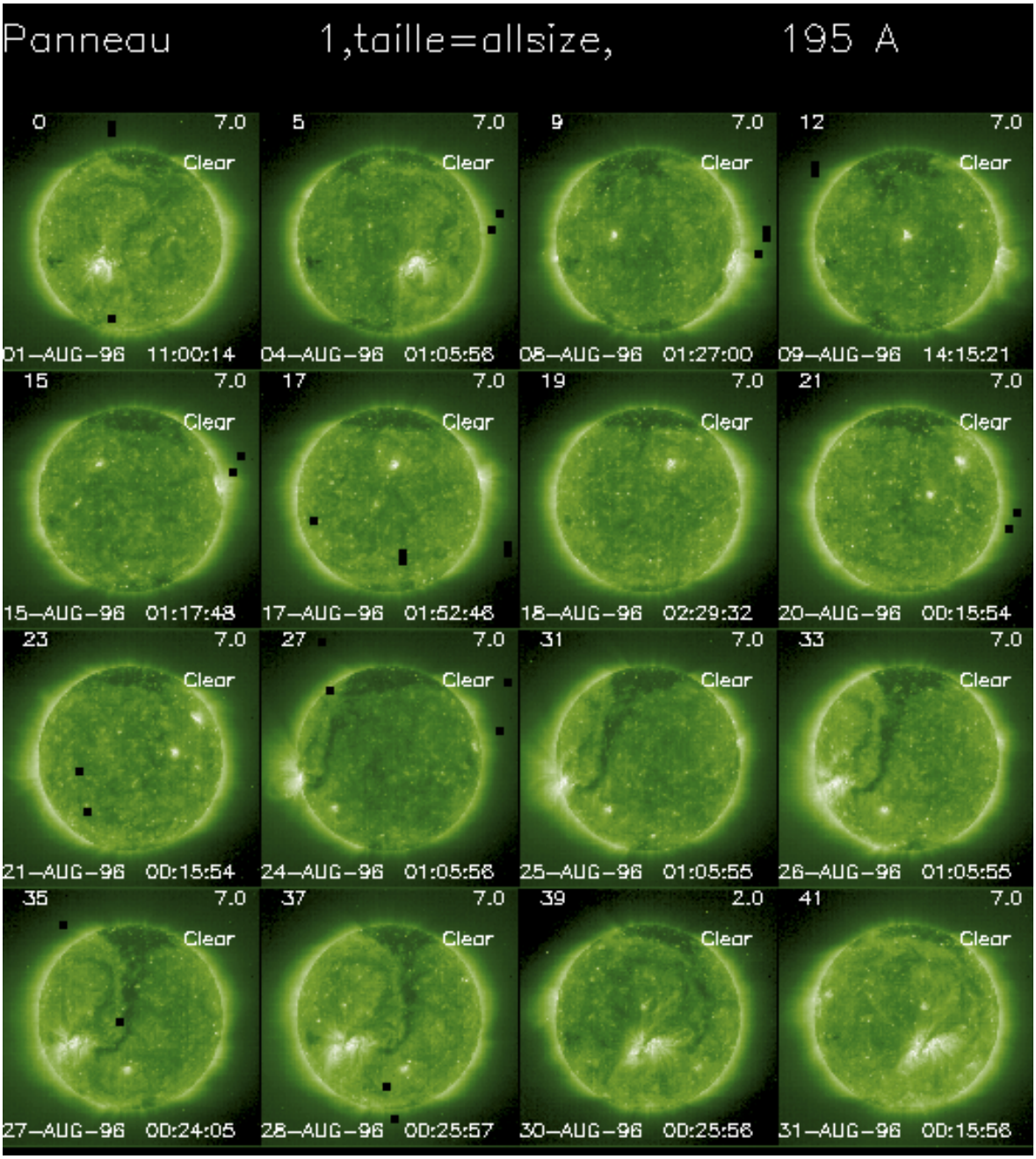

Figure III.1: Catalogue par imagettes d'images 1024 $\times$ 1024 du Fe XII pour Aout 1996

- **First Year of Observations with SOHO/EIT of the "Quiet" Sun Corona**
- by PORTIER-FOZZANI, F., MAUCHERAT, A. J. & THE EIT TEAM
- published in New Perspectives on Solar Prominences, proceedings of a meeting held in Aussois, France (ASP Conference Series, Vol. 150, IAU Colloquium 167) 28 April- 4 May 1997. Edited by David F. Webb, Brigitte Schmieder, and David M. Rust, p. 41.
- Code ADS : 1998npsp.conf...41P

New Perspectives on Solar Prominences, IAU Colloquium 167
ASP Conference Series, Vol. 150, 1998
David Webb, David Rust, and Brigitte Schmieder (eds.)

First Year of Observations with SOHO/EIT of the "Quiet" Sun Corona

F. Portier-Fozzani, A. J. Maucherat and the EIT Team
Laboratoire d'Astronomie Spatiale, CNRS, BP8, 13376 Marseille Cedex 12, France

Abstract. Since January 1996 (EIT first light) the Extreme Ultraviolet Telescope aboard SOHO has produced about 20,000 wide-field images of the corona and transition regions. Four different emission lines (He II, Fe IX/X, Fe XII, Fe XV) were selected to detail morphologies of magnetic structures in the corona. They show the different structures present in the corona with information about their topologies (Neupert et al. 1998). They provide the global temperature distribution in the quiet corona in the range 0.5 to 3×10^6 K.

The evolution of the corona during the first year of the SOHO mission revealed its nonuniform aspect and the nonregularity of the appearance of new active regions. Changes observed in active regions and coronal holes (e.g., August–September 1996) showed the complex role of magnetic fields including magnetic interactions and possible reconnections needed to explain some loop morphology evolution.

1. Introduction

A full description of the EIT Telescope aboard SOHO can be found in Delaboudiniere et al. (1995). Since February 1996 at least one image per day in all 4 wavelengths of the whole Sun have been taken (except during CCD bakeout done to increase efficiency). Movies were made on smaller areas to give shorter time evolution. The satellite observes the Sun 24 hours per day but, due to telemetry sharing, precise targets have to be chosen.

The Sun was at the minimum level of the 11 year cycle during 1996, but even at that time, some activity was present. Comparison between the amount of activity (determined by active region counts) with time and the sunspot number shows the well known links via magnetic fields. We followed the evolution with studies of 3D coronal structures (Portier-Fozzani et al. 1996).

2. 1996: A Full Year of Observations of the Quiet Sun's Corona

During January 1996 three Active Regions (ARs) were present. There was also another active fuzzy area, in which two new ARs appeared the next month. A decrease of activity was noted in March with only two large and two small ARs.

The lowest activity occurred in April with 4 small ARs: the "Quiet" Sun's

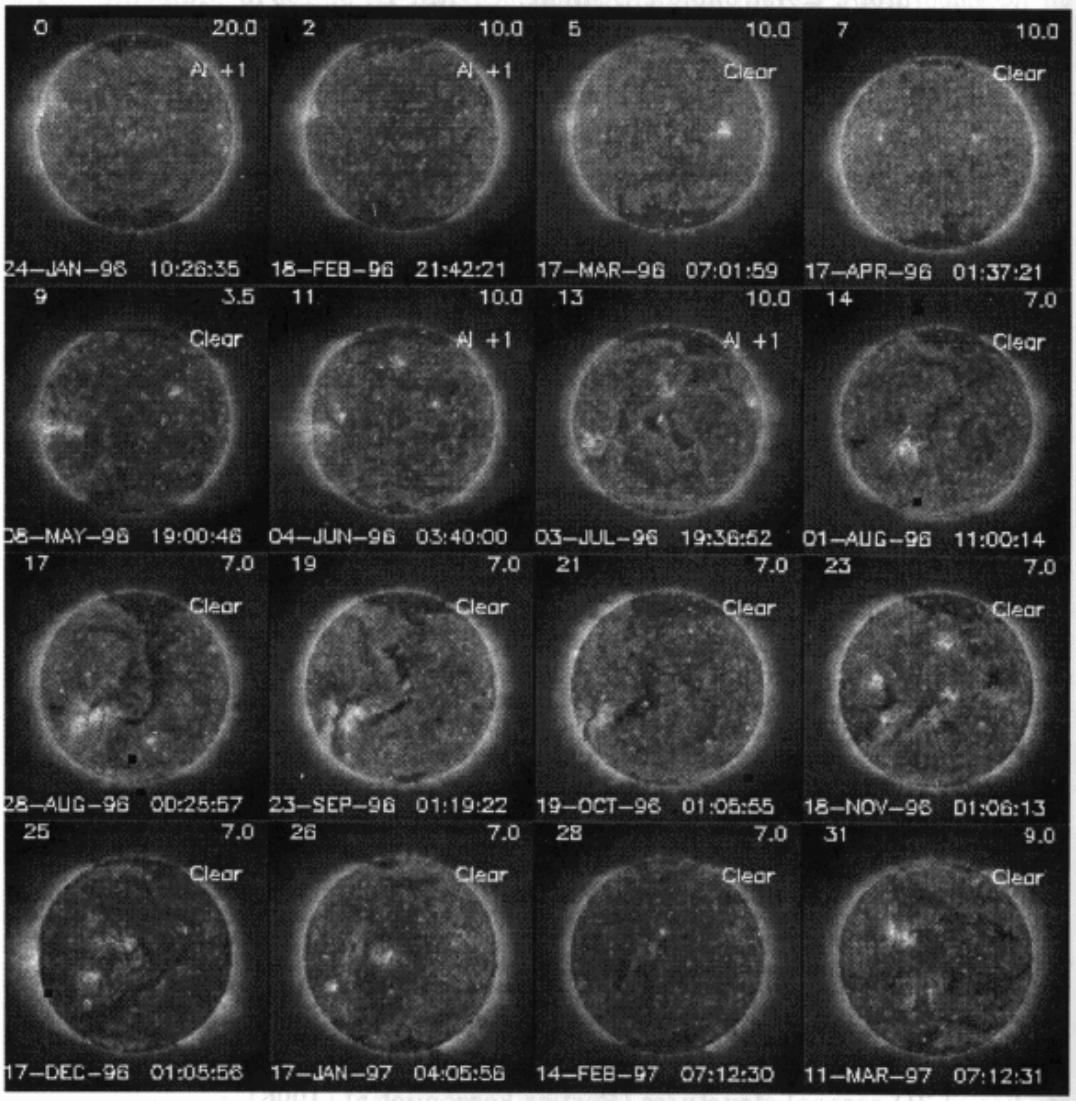

Figure 1. Activity of the corona observed with SOHO EIT in FeXII at 195Å during the January 1996–March 1997 period.

corona remained in fact still active. During May, two large ARs were present, both shared and spread in four parts in June. July showed an increase of activity. ARs and Coronal Holes (CHs) became more frequent, introducing strong nonuniformity in the corona. An interaction between CHs and ARs began in August. A strong Equatorial Coronal Hole (ECH) developed from the North polar CH toward an AR loop present in the southern hemisphere (Figure 1). Then, in September, the morphology of the AR changed completely, with fewer loops inside. By October, the ECH had decreased. In November, 5 ARs were present and 7 in December, showing the increase of activity of the cycle.

K. Harvey (1997, private communication) found that the minimum of the sunspot number was in May 1996, but the appearance of the new cycle activity was unusual. From EIT results, the AR number was minimum around April 1996 (Portier-Fozzani 1997). On the other hand, the main presence of a large CH suggests that the minimum of coronal activity occurred during June–October.

3. Global Evolution of the Coronal Activity

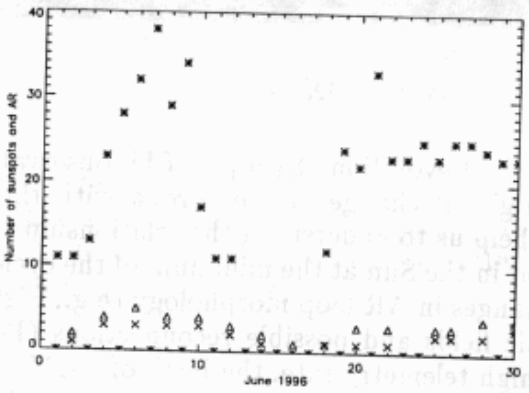

Figure 2. Coronal and photospheric activity during June 1996: (* represents the sunspot number, △ the AR number and X the number of big ARs)

During that minimum period the corona appeared very nonuniform. An example is given by mid-February when the Sun had an active region on one side while the other side had nothing. Apparitions of AR were nonlinear with time; sometimes 1, 2 or 3 could appear during a short time like in October–December.

Phillips (1995) mentioned that ARs do not always correspond to sunspots despite the expected link via the magnetic field. This is mainly the case in 1996, except for the weak activity in June 1996 (Figure 2), where coronal numbers were proportional to sunspot numbers. The reason is probably that only a part of the sunspots influence strongly coronal activity and are able to build via the magnetic field some loops with high enough temperature to be seen at all wavelengths.

The number of large active regions seen on the disk are proportional to the absolute value of the magnetic field. This was expected because the plasma is frozen to the strong magnetic field and then creates large ARs (Klimchuk et al. 1998). Finally, by studying C,M,X flare eruptions, no observed links are noted between the numbers of ARs and flares. As there was no relation with

the time of the flares, this activity could be linked to AR's stability and not to their statistical numbers (Portier-Fozzani and Noens 1997).

4. Conclusions

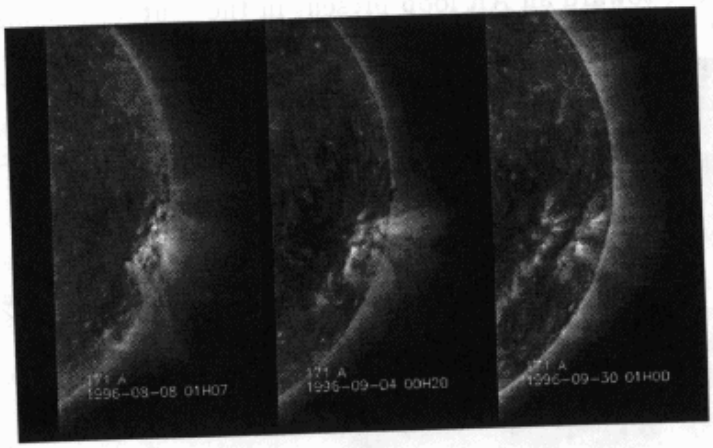

Figure 3. Loop evolution in Fe IX/X

Magnetic fields drive coronal evolution. Synoptic EIT observations give us the possibility to study the global change of the corona with time. Comparison with other observations help us to understand the relationship between different physical processes present in the Sun at the minimum of the cycle. The evolution of the corona, such as changes in AR loop morphology (e.g., Figure 3), recall the role of different magnetic fields and possible reconnections (Portier-Fozzani et al. 1998). Thanks to a high telemetry rate, the birth of a CME was recorded on December 24, 1996 (Moses et al. 1998). In conclusion, observations will certainly yield more and more surprises as the activity cycle grows toward maximum, but even at the minimum lots of events occurred in the corona.

References

Delaboudiniere, J.-P. et al. Solar Phys., 162, 291

Klimchuk, J., D. Moses and F. Portier-Fozzani 1998, ApJ, submitted

Portier-Fozzani, F. et al. 1996, in Magnetic Reconnection in the Solar Atmosphere, (eds.) R. Bentley and J. Mariska, San Francisco, p. 402

Portier-Fozzani, F. and J.C. Noens 1997, in Science with Themis, Publication of Paris-Meudon Observatory, p. 281

Portier-Fozzani, F. June 1997, LAS Internal Report

Portier-Fozzani, F. 1998, A&A, submitted

Phillips, K. 1995, Guide to the Sun, Cambridge University Press

Neupert, W.M. et al. 1998, JGR, in press

Moses, D. et al. 1998, Solar Phys., submitted

III.1.2 Dégrillage

De manière usuelle, l'étalonnage d'un instrument comporte outre les tests mécaniques de solidité, la mesure de la fonction de transfert de l'optique (CCD incluse). Afin de déterminer la fonction d'étalement d'un point (PSF), on envoie une source brillante quasi-ponctuelle sur l'instrument. Pour EIT, cela a été mesuré en envoyant un faisceau collimaté de lumière UV produit par un rayonnement synchrotron sur EIT [228]. Pour pouvoir utiliser les images, il faut en plus connaître la carte de sensibilité de l'ensemble instrument optique et de son récepteur. Idéalement on souhaite regarder l'image d'une source uniforme obtenue par un instrument optique et son récepteur ce qui permet de cartographier les défauts de l'instrument comme la différence de sensibilités dans les pixels de la CCD, les anisotropies introduites dans le chemin optique, etc... On obtient ainsi la carte de sensibilité de l'ensemble du champ. Les images observées sont alors corrigées à l'aide de cette carte afin d'obtenir des données étalonnées. Mais il est très difficile techniquement de réaliser, une source étendue uniforme rayonnant dans l'UV. Pour SOHO/EIT les champs plats [2] de l'instrument n'ont pu être complètement mesurés avant le vol. Le champ plat de la CCD seule a été mesuré ([157]).

On peut aussi chercher à se servir du soleil, qui est un objet étendu, pour mesurer la carte de sensibilité. Mais, l'intensité de la couronne solaire — même en dehors de structures — n'est pas constante entre le centre et le bord du disque (*cf.* histogrammes ou sections d'intensités dans [184]), et donc il n'est pas possible de mesurer les variations de l'instruments sans connaitre celles du soleil. Par contre, le lancement en 1998 et en 2000 d'une fusée d'étalonnage dont on connait les cartes de sensibilités, permet en comparant les images simultannées du soleil avec les 2 instruments de parfaire la connaissance technique de l'instrument ([56]).

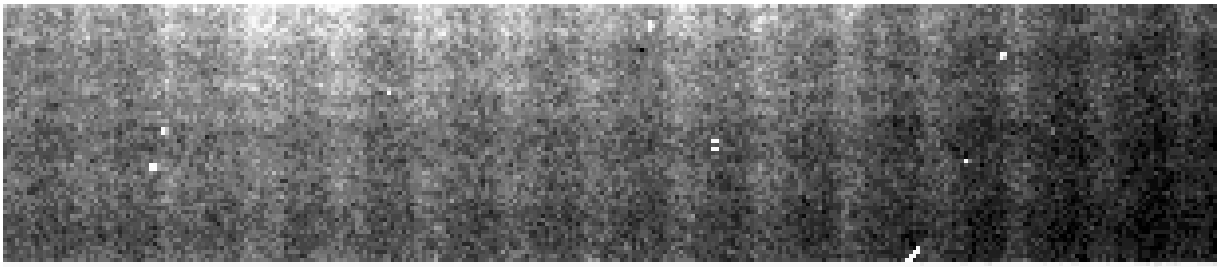

Figure III.2: Extrait d'une image EIT et sa grille

Ainsi, sur les images SOHO/EIT, une grille brillante [3] est visible (Fig. III.2). Ceci est le résultat d'un phénomène d'ombrage introduit par le support d'une feuille aluminium qui sert à empêcher la CCD de recevoir la lumière visible solaire (Figure III.3). A cause de sa position sur le trajet optique proche de la CCD ([199]) cette grille intervient comme un masque de transmission multiplicatif. Etant donné les fréquences respectives du faisceau

[2] ou Flat Field

[3] En fait 3 grilles sont visibles mais celle qui est proche de la CCD est la principale source du bruit sur les images [109].

et de la grille celle ci apparaît en émission [56] suite à un phénomène d'aliasing. L'aspect de la grille ne peut être totalement décrit uniquement que lors du vol car le "champ plat" incluant la grille n'était pas réalisable au sol.

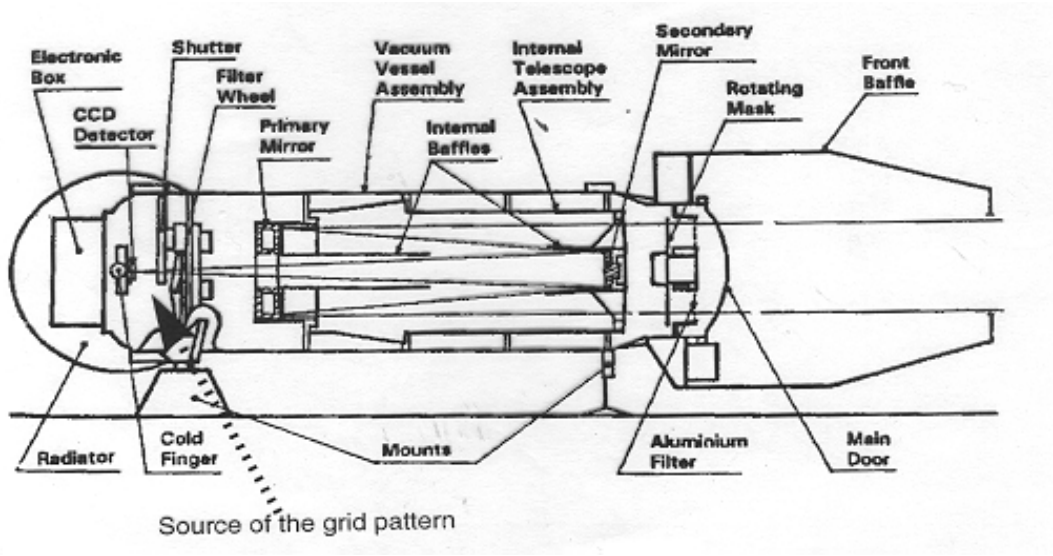

Figure III.3: Schéma de l'instrument EIT

Il va donc falloir déterminer cette ombre parasite pour la supprimer numériquement afin de reconstruire l'image "originale" du soleil dans les longueurs d'ondes qui nous intéressent.

Propriétés de la grille Nous allons déterminer les propriétés de la grille en regardant la transformation de Fourier de l'image. Après avoir séparé la composante image de la composante grille dans l'espace fréquence, il est théoriquement possible de reconstruire l'image dégrillée.

Propriété d'une grille idéale Prenons une grille idéale (c'est à dire grille de taille infinie, de pas et d'espacement réguliers) à 1 dimension. Sa fonction de transmission optique s'écrit comme un assombrissement de largeur e régulièrement espacé de a. La fonction "porte" de largeur e, $\Pi_e(x)$, est telle que $\Pi_e(x) = 1$ pour $-\frac{e}{2} < x < \frac{e}{2}$ et nulle en dehors de cet intervalle.
Par analyse de Fourier, nous savons que convoluer une fonction par $\delta(x-a)$ revient à translater de a. La fonction de transmission de l'optique de la grille 1D peut donc se formaliser de la manière suivante :

$$t(x) = \sum_n \Pi_e(x) * \delta(x - n.a) = \Pi_e(x) * \amalg_a(x)$$

où la fonction $\amalg_a$ est définie comme le peigne de Dirac d'espacement a.
On peut démontrer ([199]) que la transformée de Fourier (TF) d'une porte d'épaisseur e

est un sinus cardinal, que la TF d'un Π de période a est un Π de période 1/a, et que la TF d'une convolution est un produit ordinaire. On obtient donc dans le plan fréquence

$$\hat{t}(u) = TF(t(x)(u)) = e\frac{sin\pi ue}{\pi ue} \times \Pi_{\frac{1}{a}}(u)$$

, le produit d'une fonction périodique de période 1/a nulle presque partout et d'une fonction pseudo-périodique d'amplitude décroissante.

Il s'agit maintenant de connaître l'espacement des fréquences. $\hat{t}(u) = 0$ en dehors du support[4] de Π et lorsque le sinc n'est pas nul sur le support du Π. Ces deux fonctions sont simultanément nulles pour $sin(\pi.n.a.e) = 0$ avec n entier puisque cela dépend du support de Π. Cela s'écrit $\pi nae = k2\pi \Rightarrow n = \frac{2*k}{a.e}$ avec k et n entier. Pour a et e donnés, un calcul montre que ces cas sont rares. On s'attend donc à observer des fréquences régulièrement espacées [5].

Le cas de la grille à 2 dimensions se traite de la même manière et on obtient des fréquences spatiales dans le plan (u,v) régulièrement espacées [6].

En divisant la fonction régulière de la grille dans le plan fréquence par une fonction de grille synthétique il est théoriquement possible de retrouver toutes les fréquences initiales. C'est le principe du filtrage global par analyse de Fourier, où l'on choisit dans le plan des fréquences les structures à cacher ou à faire ressortir.

Le filtre focal, disposé à une distance de 14.5mm du plan focal, a une grille support constitué de fils de nickels de $40\mu m$ de diamêtre de diamêtre avec des mailles de $440\mu m$ de coté. Compte tenu de ces valeurs, un calcul complet est présenté par [56] chapitre 4 et annexe 2.
Si la grille était contre le filtre, on aurait bien le résultat obtenu précédemment. La grille se trouvant à une distance z du filtre, le calcul par la convolution montre le déphasage induit par le trajet optique induit par la distance supplementaire z à parcourir et donc que la grille apparait en surbrillance ([56]).

Aspect de la grille sur les images et motivation d'une méthode locale de dégrillage Nous allons donc pouvoir maintenant comparer la TF de la grille théorique avec les fréquences de la grille réelle.

[4] Le support d'une fonction est le lieu où la fonction est non nulle

[5] La mesure approximative de a et e sur les images montre que l'on est bien dans ce cas là

[6] La Transformation de Fourier 2D d'une fonction f est par définition

$$\hat{f}(u,v) = \int_{-\infty}^{+\infty} f(x,y).e^{-2.i.\pi(xu+yv)}dx.dy$$

, d'où $\hat{t}(u,v) \sim \Pi_(1/a, 1/b)(u,v) \times Sinc(u,v)$.

L'aspect exact de la grille est obtenu en regardant la transformation de Fourier d'une image. En effet, soit t(x,y) le facteur de transmission de la grille, soit O(x,y) l'objet d'entrée (le soleil issu de l'instrument), l'image s'écrit $I(x,y) = t(x,y).O(x,y)$ car la grille intervient comme un facteur multiplicatif. Sa transformée de Fourier s'écrit $\hat{I}(u,v) = \hat{t}(u,v) * \hat{O}(u,v)$. L'image de la TF est donc la fonction de transfert de la grille convoluée avec la TF du soleil.

La transformation de Fourier des images (Fig. III.4) nous donne, outre les fréquences du soleil, les différentes fréquences de la grille. La période spatiale de la grille dans le plan de Fourier doit être 1/a selon l'axe u et 1/b selon l'axe v

Figure III.4: TF d'une image SOHO/EIT à 171A (Fe IX/X).
Remarquez l'aspect irrégulier de la grille pour la partie Fe IX/X du télescope EIT

Or sur la Fig. III.4 les espacements mesurés entre 2 points de l'image de la grille sont irréguliers. La grille à donc des pas irréguliers dans l'espace direct ([182]).

De plus, l'image de la grille evolue suivant la longueur d'onde d'observation λ. En effet, le trajet optique est différent suivant λ puisque le miroir du télescope est séparé en 4 quadrants (Fig. II.10. Une éventuelle déformation (position par rapport au miroir, support non plan ou irrégulier) se répercute au niveau de l'image.

Un filtrage global donc n'est pas adapté pour enlever numériquement cette grille irrégulière des images. Par contre, les variabilités mesurés du pas de la grille étant observées localement, un filtrage local est plus adéquat ([182]).

Sur une image, on mesure le pas moyen de la grille à 1 pixel près : il avoisine les 21 pixels. L'épaisseur de la grille est d'un pixel d'épaisseur environ.

La méthode la plus simple initiale réalisée pour supprimer cette grille ([182]) est un filtre médian en croix sur 5 points de l'image. Le filtre médian remplace le pixel traité par le pixel de la fenêtre ayant la valeur médiane. Lorsqu'une valeur isolée est aberrante

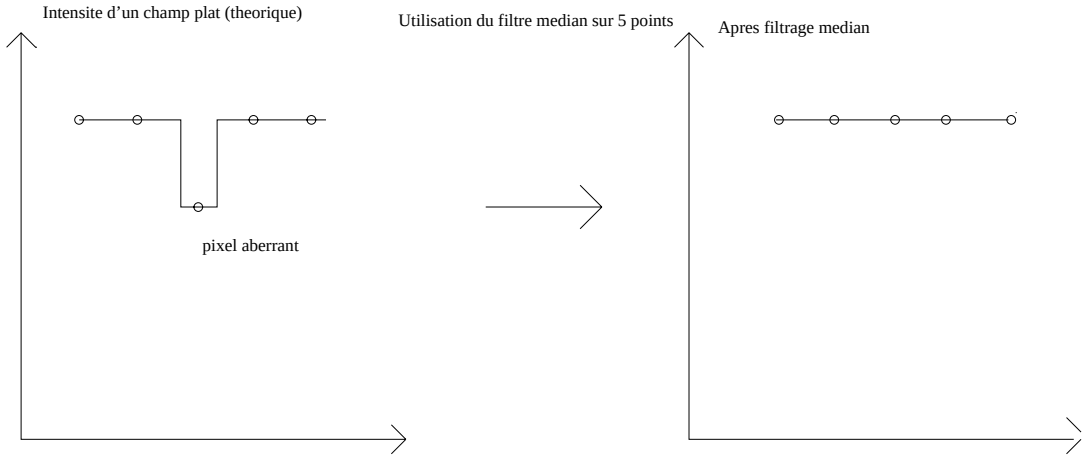

Figure III.5: Principe du filtre médian :
(la largeur choisie du filtre est de 5 pixels;
les pixels aberrants ont une épaisseur d'un pixel.)

(trop grande ou trop faible), elle disparaît (Fig. III.5). Cette méthode a l'avantage de la simplicité de la mise en oeuvre (même en 2D) mais elle supprime toutes les structures fines d'un pixel d'épaisseur.

De plus, même avec 1 pixel de large la grille ne "tombe" pas nécessairement sur 1 pixel de la CCD mais peut se projeter entre deux. Il faut alors corriger 2 pixels de large pour ôter les effets de la grille. Pour remédier à cela, un filtrage adaptatif [7] et local peut être plus approprié. Il s'agit d'isoler la grille et de faire subir aux points de la grille — et à ces points seulement — un filtrage médian sur 5 points (2 de chaque coté de la grille). Ainsi on ne supprime plus les éventuelles structures fines présentes. Cette dernière amélioration de la technique fut proposée par J. Maucherat et collaborateurs en Fevrier 1996. L'ensemble de la méthode fut inclus au Software EIT sous le nom (*eit_degrid_smooth.pro*).

Des mesures calibrées

Les filtres médians étant non linéaires, cela peut être un inconvéniant pour les valeurs trouvées. La méthode précédante peut être aussi appliquée pour trouver l'aspect de la grille : Il suffit de soustraire une image ainsi lissée à une image brute. En sommant l'ensemble des grilles ainsi obtenues pour un grand nombre de données on obtient une grille moyenne qui lorsque le nombre d'images de grilles sommées est important, devient indépendant du signal d'entrée. Il suffit alors de soustraire cette grille moyenne à une image pour obtenir ainsi une image calibrée dégrillée.
La partie "moyennage" de grille a été calculée sur des modèles théoriques de grilles par F. Clette ([157]). L'évolution de la sensibilité des CCD avec l'activité croissante du soleil

[7] *ie.* qui adapte ses coefficients au cours du temps en fonction des conditions non stationnaires du signal d'entrée

montre désormais l'intéret du calcul de la grille par la méthode non linéaire et la sommation de toutes les grilles ainsi obtenues malgré le long temps de calculs sur chaque image (environ 3mn).
Dans la procédure eit_degrid_smooth.pro, des options permettent de sauvegarder la grille pour chaque image.

- **EIT Images of the EUV Solar Atmosphere**
- by PORTIER-FOZZANI, F.; MOSES, J. D.; DELABOUDINIERE, J. P.; GURMAN, J. B.; CLETTE, F.; MAUCHERAT, A.
- Magnetic Reconnection in the Solar Atmosphere. ASP Conference Series; Vol. 111; 1997; ed. R. D. Bentley and J. T. Mariska (1997), p.402
- 1997mrsa.conf..402P

Magnetic Reconnection in the Solar Atmosphere
ASP Conference Series, Vol. 111, 1996
R.D. Bentley and J.T. Mariska, (eds.)

EIT Images of the EUV Solar Atmosphere

F. Portier-Fozzani

Laboratoire d'Astronomie Spatiale, CNRS, BP 8, 13376 Marseille Cedex 12, France

J.D. Moses

Naval Research Laboratory, Washington, DC 20375, USA

J.P. Delaboudiniere

Inst. d'Astrophysique Spatiale, Universite Paris XI, 91405 Orsay Cedex, France

J.B. Gurman

NASA/Goddard Space Flight Center, Greenbelt, MD, USA

F. Clette

Observatoire Royal de Belgique, B-1180 Bruxelles, Belgique

A. Maucherat

Laboratoire d'Astronomie Spatiale, CNRS, BP 8, 13376 Marseille Cedex 12, France

Abstract. The Extreme-ultraviolet Imaging Telescope (EIT) was one of several instruments launched on board the *SOHO (Solar and Heliospheric Observatory)* satellite on 1995 December 2. It was stationed in a halo orbit around the L1 Earth-Sun Lagragian point on 1996 February 14, and has already produced thousands of wide-field images of the low corona at 4 wavelengths (171, 195, 284 and 304 Å). These wavelengths correspond to different emission lines (Fe IX-X, Fe XII, Fe XV and He II), formed over a wide range of plasma temperatures, from 8×10^4 K (transition region) to 2×10^6 K (quiet corona and active regions). In this respect, the EIT experiment is fully complementary to the *Yohkoh* mission which studies hot active corona. The first EIT images and movies, presented during this meeting, reveal how this sensitive instrument will provide unprecedented information about the dynamics of small scale phenomena in the quiet solar corona and inside coronal holes. Results of a local deconvolution method, used to correct a grid pattern present in raw EIT images, were also presented.

1. The EIT Instrument

The Extreme-ultraviolet Imaging Telescope (EIT), shown schematically in Figure 1, produces images of the corona and transition region with 2.6 arcsec pixels and a wide 45×45 arcmin full field of view. The telescope uses two normal-incidence hyperboloid mirrors in a Ritchey-Chretien telescope. The effective focal length of the instrument is 1.652m with a primary diameter of 0.12m. Each mirror has 4 sectors (geometrical area per quadrant = $0.0013 m^2$), coated with different multilayers which define 4 different bandpasses (spectral resolution 10–100). The working wavelength is selected by a rotating occulter placed in the entrance aperture. A set of aluminium filters in the entrance pupil and near the focal plane completely block off long (UV-visible) wavelength radiation.

The selected emission lines are produced either in the transition region (He II at 304 Å, $T \sim 8 \times 10^4$ K) or in the corona. The Fe IX-X lines at 171 Å ($T = 1.3 \times 10^6$ K) are emitted in the cool corona (holes), the Fe XII line at 195 Å ($T = 1.6 \times 10^6$ K) shows the quiet sun outside coronal holes, while the Fe XV line at 284 Å ($T = 2.0 \times 10^6$ K) is mainly produced in hot loops inside active regions and in bright points. These lines are imaged on a 1024×1024 CCD, which is cooled to about −65 C by a cold finger attached to a passive radiator facing deep space. A full description of the instrument can be found in Delaboudiniere et al. (1995)

Full disk full resolution images at all four wavelengths are made on a daily basis as part of the basic synoptic program, but subfield or reduced spatial resolution modes can be implemented to increase the image cadence, in order to study fast local phenomena. Using Rice compression, full-field high resolution images can be read out and transferred to the ground in about 22 minutes. Partial images (160×160) at different wavelengths can be taken approximately one minute apart for intervals up to 2 hours.

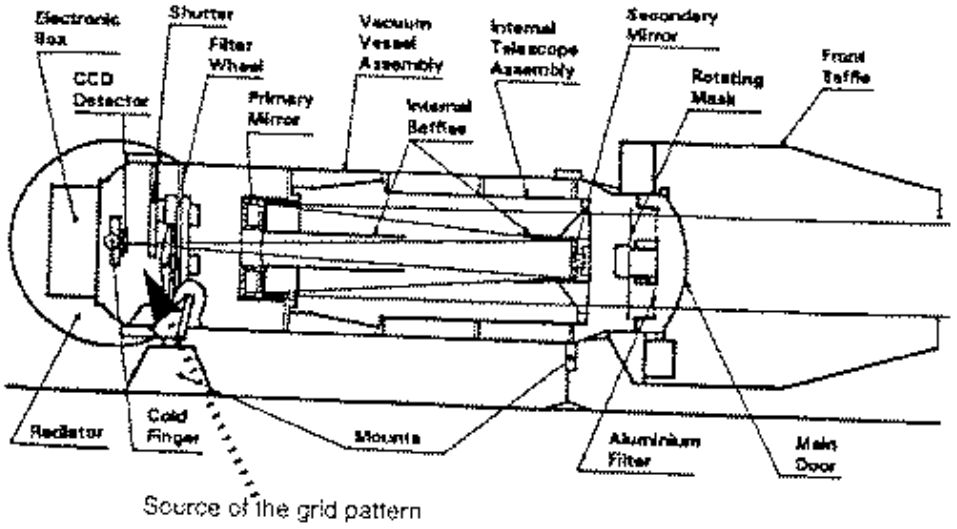

Figure 1. The EIT instrument

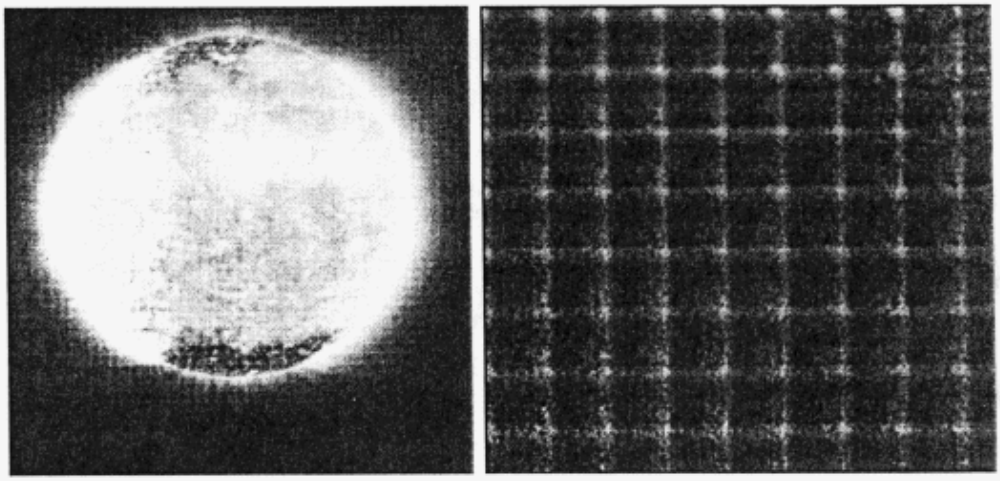

Figure 2. An uncorrected image taken at 195 Å showing the pattern caused by the nickel supporting grid (left); an expanded extract of the grid pattern (right).

2. EIT Images

A GIF format representation of each 'raw quicklook' EIT image (as well as each quicklook LASCO image) can be viewed as it is recieved via the LASCO homepage URL `http://lasco-www.nrl.navy.mil/lasco.html`. Full disk synoptic images corrected for shadowing by the support grids of the aluminum visible light rejection filters near the focal plane are available via the EIT homepage URL `http://umbra.nascom.nasa.gov/eit/`. This shadow pattern was expected but could not be characterized accurately in the EUV before launch. It is thus extracted from the in-flight solar images. Figure 2 shows the appearance of the grid pattern on the raw images. Results of filtering and local deconvolution methods are shown in the pictures in Figure 3.

3. Physics with EIT

The consortium of EIT investigators has developed a list of science topics which will be investigated through EIT observations and analysis such as morphology and evolution of loops in the corona (quiescent features), signatures of coronal heating (including waves, nanoflares, emerging flux regions, and magnetic shear), sources of the solar wind and interplanetary disturbances (including coronal plumes, transient events), properties of He II emission and structures, properties and evolution of the large scale corona.

4. Temporal Evolution of the Quiet Corona

The movies presented during the Bath meeting were assembled from images covering the commissioning phase, between January and April 1996. This period

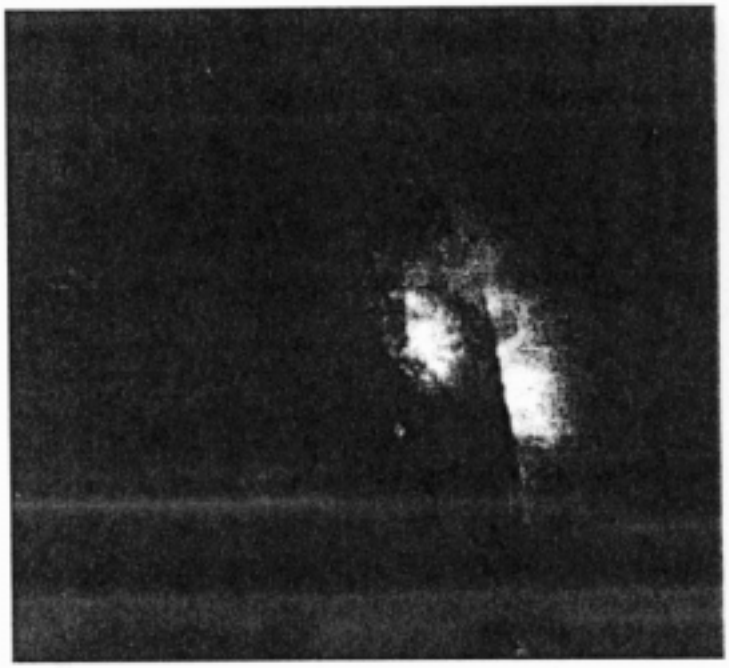

Figure 4. Extract of a loop observation movie (1996, February 3 at 18:25 UT) at 195 Å.

was characterized by very low levels of solar activity. Nevertheless, EIT images reveal continuous changes of the structures inside quiet regions and the large polar holes. The so-called "quiet" corona now appears as a highly dynamical medium, which completely changes on timescales of few hours.

Flaring activity was also observed in an active region between 1996 January 28 and February 4 (Figure 4). Multi-temperature data from EIT contain unique information concerning magnetic reconnection processes daily at work over a range in the solar corona.

References

J.-P. Delaboudiniere et al. 1995, Solar Phys., 162, 291

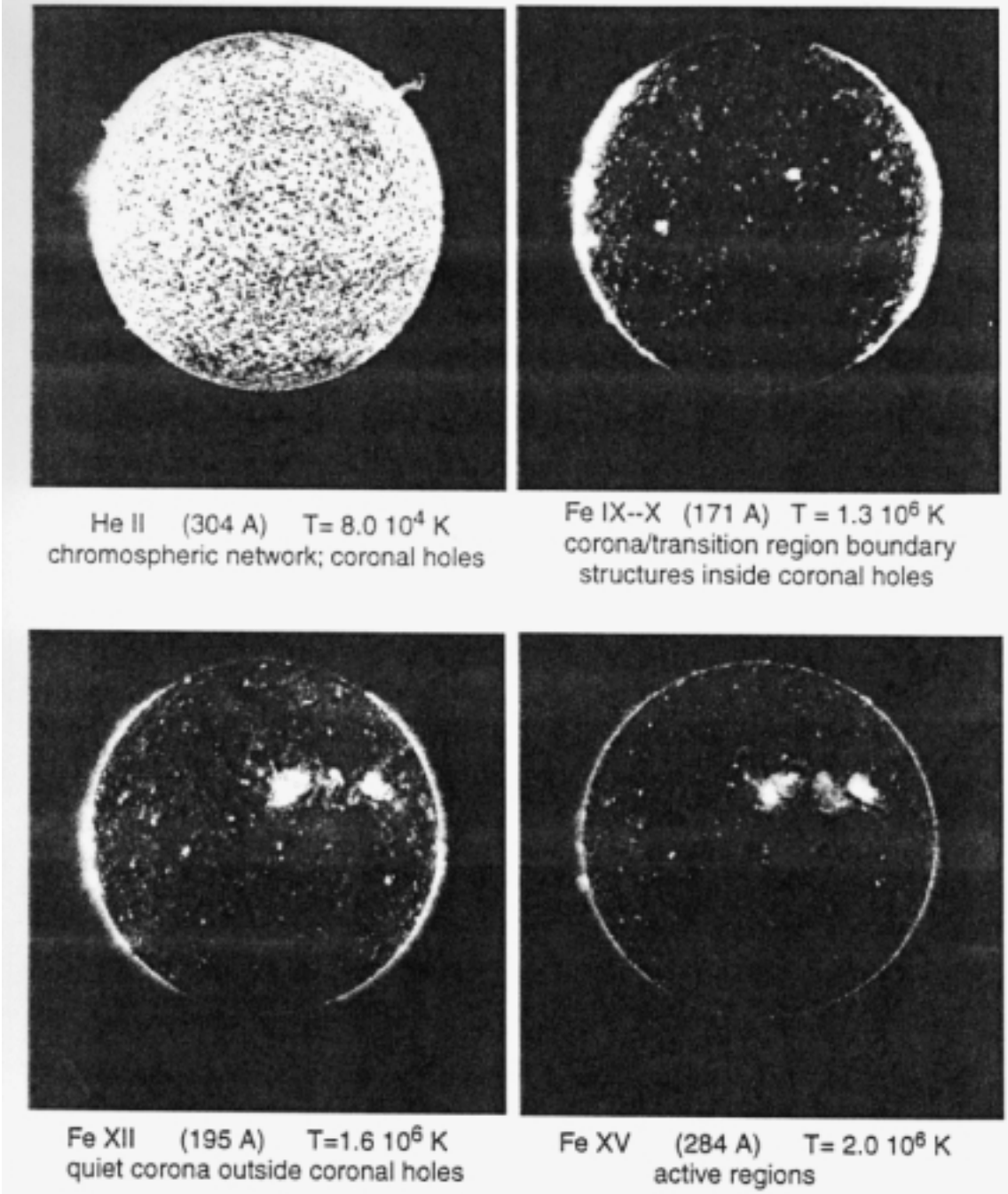

Figure 3. Results of the deconvolution: these images taken on 1996, February 16 have had the grid pattern removed

III.2 Vision multi-échelles basée sur une transformation en ondelettes

La méthode de vision multi-échelle (MVM) —élabore par M. Albert Bijaoui & son équipe—, qui utilise les ondelettes spatiales, permet de mettre en évidence sur des images de galaxies des structures fines. Nous avons élaboré des contraintes dans l'utilisation de cette technique pour l'imagerie solaire.

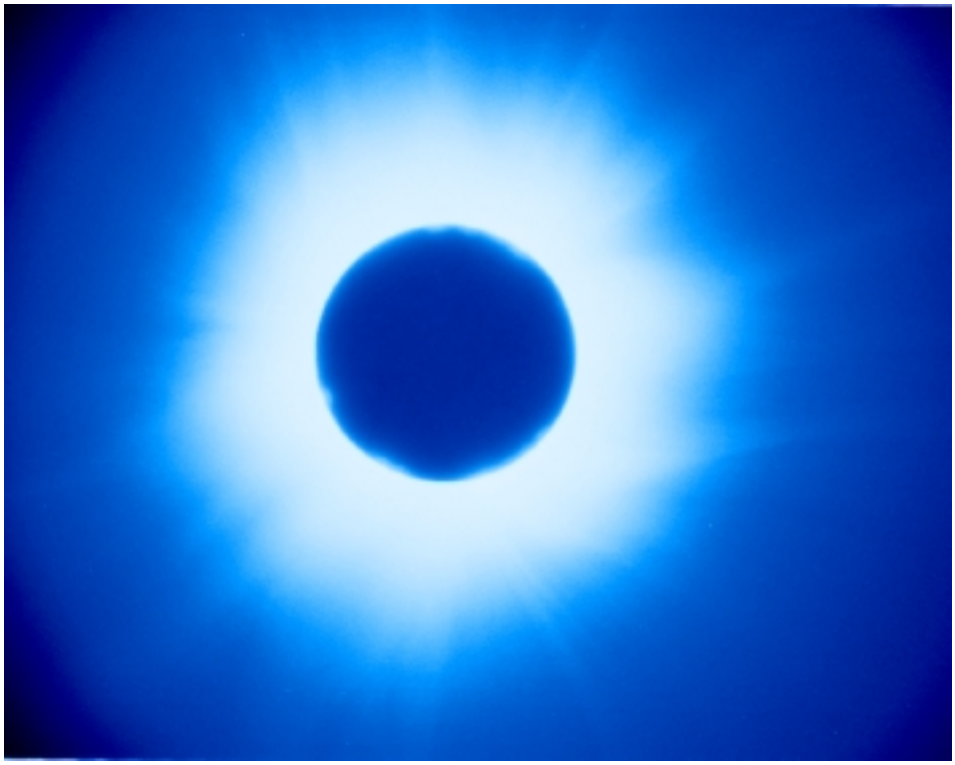

Figure III.6: Premiers résultats de MVM appliqués sur des photos de l'éclipse du 11 Aout 1999 (Original : négatif couleur Konica 100 ISO, lunette 80/400 mm + doubleur de focale)

La Figure III.6 montre une première ébauche de l'application de cette technique, réalisée avec des photographies personnelles de l'éclipse du 11 Aout 1999.

L'utilisation de cette méthode avec SOHO/EIT a permis de mettre en évidence certaines structures coronales. Les aspects techniques (contraintes) de son utilisation et les apports scientifiques sont discutés dans l'article suivant.

- **A Multiscale Vision Model applied to analyse EIT images of the solar corona**
- by Portier-Fozzani, Vandame, Bijaoui, Maucherat
- Article soumis a Solar Physics (Novembre 1999)

A MULTISCALE VISION MODEL APPLIED TO ANALYZE EIT IMAGES OF THE SOLAR CORONA

F. PORTIER-FOZZANI[1], B. VANDAME[2], A. BIJAOUI[3], A. J. MAUCHERAT[4] and the EIT TEAM[5]

[1]*Max Planck Institut fur Aeronomie (MPAE), Max-Planck-Straße 2, D-37191 Katlenburg-Lindau, Germany*

[2]*European Southern Observatory, Karl Schwarzschild Straße 2, D-85748 Garching bei München, Germany*

[3]*Observatoire de la Cote d'Azur (OCA), Departement Cerga, UMR-CNRS 6527, BP 4229, 06304 Nice Cedex 04, France*

[4]*LAS-CNRS, BP 8, 13376 Marseille Cedex 12, France*

[5]*with J.P. Delaboudinière P.I.*

(Received 15 December 1999; accepted 8 January 2001)

Abstract. The large dynamic range provided by the SOHO/EIT CCD (1 : 5000) is needed to observe the large EUV zoom of coronal structures from coronal homes up to flares. Histograms show that often a wide dynamic range is present in each image. Extracting hidden structures in the background level requires specific techniques such as the use of the Multiscale Vision Model (MVM, Bijaoui *et al.*, 1998). This method, based on wavelet transformations optimizes detection of various size objects, however complex they may be. Bijaoui *et al.* built the Multiscale Vision Model to extract small dynamical structures from noise, mainly for studying galaxies. In this paper, we describe requirements for the use of this method with SOHO/EIT images (calibration, size of the image, dynamics of the subimage, etc.). Two different areas were studied revealing hidden structures: (1) classical coronal mass ejection (CME) formation and (2) a complex group of active regions with its evolution. The aim of this paper is to define carefully the constraints for this new method of imaging the solar corona with SOHO/EIT. Physical analysis derived from multi-wavelength observations will later complete these first results.

1. Introduction

The solar corona is a complex, hot part of the solar atmosphere (a few million degrees kelvin) with plasma structured by the magnetic field due to a low β parameter. SOHO/EIT extreme ultraviolet wavelengths reveal mainly:

– Active regions (ARs) : they are seen in emission in all 4 EIT wavelengths. The simplest case occurs when the bipolar magnetic field is seen as a loop. For a group of ARs the aspect could be more complex involving several loops with different footpoints (Bray *et al.*, 1991; Klimchuk and Porter, 1995 and references therein).

– Coronal holes (CHs) : they correspond to regions with open field lines (Bohlin and Sheeley, 1978). Due to lower density (escaping plasma along the magnetic lines) and temperature, they correspond to an intensity depression in EUV lines.

Solar Physics **201:** 271–288, 2001.

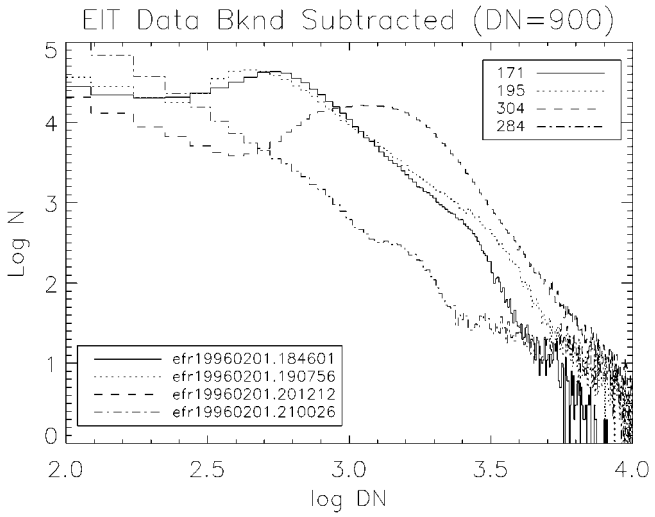

Figure 1. Histogram of 4 SOHO/EIT EUV full-disk full-resolution images (1024×1024) taken on 1 February 1996.

– Prominences and filaments : they are always found above inversion lines (i.e., neutral line) of the photospheric magnetic field. They are usually seen in absorption – except during eruption – in coronal lines over the disk as lower temperature material in front of the hot corona and are called filaments. Outside the limb, they are seen in emission in the chromospheric 304 Å line and called prominences.

Usually, by comparing space data with ground-based observations one can define and delimit these areas. For example, CHs are seen in He I, prominences and filaments in Hα, etc.

The magnetic evolution of an active area (increase of AR shear, twist variation for active region loops (ARL), interactions between magnetic field lines), leads sometimes to eruptive events such as flares, CMEs, etc. (Canfield, Hudson, and McKenzie, 1999, and references therein)

Delaboudinière *et al.* (1995) fully described the instrument SOHO/EIT. Defise, Moses, and Clette (1998) derived some aspects of the preflight and in-flight calibration. Moses *et al.* (1997) described the calibration methods for EIT. This includes the smooth de-gridding pattern procedure that we will use.

The SOHO/EIT 1024 × 1024 pixel CCD provides a resolution of about 2.6 × 2.6 arc sec^2 over the full solar disk. The CCD's dynamic range is 1:5000 and the whole dynamic range is needed to observe different structures from coronal holes up to flares. Stern and Portier-Fozzani (1996) show by analysis of histogram images that the wide dynamic range of the CCD is often completely used. Histograms in Figure 1 show pixel numbers versus intensity level. The distribution appears almost log-normal over more than 1 magnitude. Intensity values range from 10^2 up to 10^4 in DN units. Therefore, when images are displayed on standard devices, very tiny coronal structures are sometimes hidden by the neighborhood level. These

structures cannot be revealed by classical methods such as changing the look up table (LUT) to have better dynamic, thresholding, etc. We test here a new approach using multiresolution to dissociate large and smooth structures from small details.

Astronomical image-processing software is often based on a single spatial scale with adapted smoothing and background mapping. Bijaoui, Rué, and Vandame, (1998) built a Multiscale Vision Model (MVM) in order to find small structures which could not be detected due to the background level. This method is very successful in revealing thin structures such as weak galaxies over a wide Schmidt photograph. The multiscale method used in this vision model is based on the notion of significant structures. An object is defined and rebuilt when wavelet coefficient values significantly different from zero are present simultaneously in different planes of the wavelet transform space. Objects and sub-objects are thus found from trees and subtrees in the graph.

This method was applied to the solar corona with images taken by SOHO/EIT. Data for scientific analysis were prepared with the EIT package of the IDL solar software. Very efficient local smooth-filtering of EIT images avoids taking into account shadow artifacts given by grids placed in the foreground of the CCD (Portier-Fozzani *et al.*, 1997, 1998). Thus to obtain the best structure reconstruction, we checked different parameters with the MVM method to have the most efficient tree reconstruction.

2. Reconstruction Method Derived from Multiscale Vision Model

2.1. Multiscale approach

The multiscale approach (Bijaoui, Rué, and Vandame, 1998) is performed using wavelet transformations. The classical discrete wavelet transform results from *Multiresolution Analysis* (Mallat, 1989). But this method is not shift-invariant (i.e., contrary to the continuous wavelet transform, these analyses are not covariant under translation) and does not lead to an isotropic vision. That is why, among the extensions of *Mallat's algorithm*, the '*à trous*' algorithm (Holschneider *et al.*, 1989; Bijaoui, 1991) was preferred. It does not favor any direction in the image and maintains the sampling at each scale.

At a given scale, we derive a number of wavelet coefficients decimated by a factor 4. Due to this decimation the transform depends on the origin. In the case of the *à trous* algorithm, no direction is favored, no decimation occurs and the shift-invariance is verified.

In this method, the sampled data, $F(k, l)$, are assumed to be the scalar product of a continuous function $\mathcal{F}$ with a scaling function ϕ:

$$F(k, l) = \langle \mathcal{F}(x, y), \phi(x - k, y - l) \rangle; \tag{1}$$

$F(k, l)$ is also denoted $F(0, k, l)$ in order to be compatible with the equations that follow.

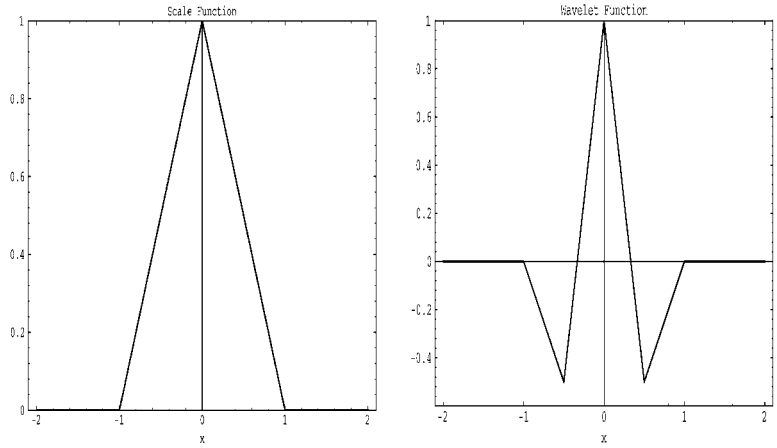

Figure 2. Scaling function (*on the left*) and the wavelet function (*on the right*) associated.

Let us consider the following scalar products that give the smoothed image of $F(k, l)$ at scale i:

$$F(i, k, l) = \frac{1}{4^i}\left\langle \mathcal{F}(x, y), \phi\left(\frac{x-k}{2^i}, \frac{y-l}{2^i}\right)\right\rangle, \tag{2}$$

ϕ is chosen to satisfy the dilation equation (Strang, 1989).

$$\frac{1}{2}\phi\left(\frac{x}{2}, \frac{y}{2}\right) = \sum_n \sum_m h(n, m)\phi(x-n, y-m), \tag{3}$$

where h is the low pass filter (Bijaoui and Rué, 1995). The wavelet coefficients are chosen as the difference between two smoothed images. They correspond to the details lost between two scales:

$$W(i, k, l) = F(i-1, k, l) - F(i, k, l). \tag{4}$$

We choose the following scaling function:

$$\phi(x, y) = B_1(x)B_1(y), \tag{5}$$

where B_1 is the B-spline function of degree 1 (Unser and Aldroubi, 1992). In Figure 2 the scaling function ϕ (a triangle) is shown on the left. On the right we see the wavelet function ψ associated.

2.2. Object definition in the wavelet transform space

The wavelet transform space (WTS) is a 3D space. In an image, an object occupies a physically connected region. Each pixel of the region can be linked to the others (Bijaoui and Rué, 1995). The connectivity in direct space has to be transferred to the WTS. At each scale, structures associated with an object are also connected.

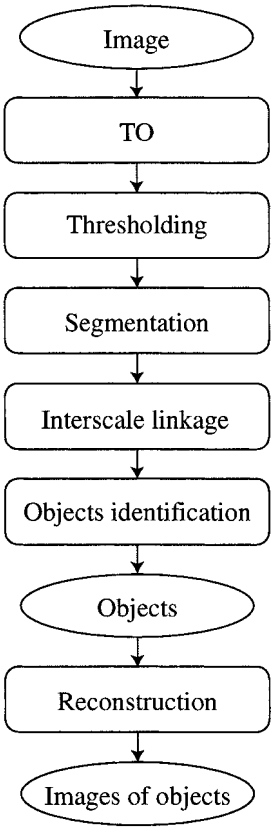

Figure 3. MVM algorithm.

All these structures form a 3D connected set which is hierarchically organized: for a given scale, structures are linked to smaller structures of the previous scale. This set gives the description of an object in the WTS. The steps of the multiscale model can now be defined (Figure 3).

After applying the wavelet transform to the image (i.e., the '*à trous algorithm*'), to identify the statistically significant coefficients we performed a thresholding in the WTS. A wavelet coefficient is significant if its value is such that the probability to be only due to the noise is smaller than a given thresholding ϵ. These are gathered in connected fields using a scale-by-scale segmentation procedure in order to define the object structures.

At a given scale the thresholding leads to connected fields. Each one can display many local maxima coefficients. Each field is decomposed in different sub-fields using a ridge line algorithm in order to get a decomposition for which we have only one maximum, i.e. one peak, per field.

An interscale connectivity graph is established and the object identification procedure then extracts each connected sub-graph corresponding to 3D connected sets

TABLE I

Graph statistics for the image efr19980407-010014.fits. The image chosen is 1024 × 1024 pixels (full-disk full-resolution image), SOHO/EIT Fe IX/X on 7 April 1998 at $01^{h}00^{m}14^{s}$. The exposure time was 7 s with the Al+1 filter. The threshold coefficient was chosen to be 3σ.

Wavelet plane number	Noise level	Number of defined elements
1	4.7148	31962
2	2.4551	12206
3	2.0568	2747
4	1.1133	670
5	0.55663	90

of pixels in the WTS. By referring to the object definition, these can be associated with the objects. Finally, from each set of pixels the corresponding object image can be reconstructed using MVM algorithms.

3. Utilization of the Multiscale Vision Model to Analyze Solar images

3.1. THE ALGORITHM

The MVM program (Bijaoui, Rué, and Vandame, 1998) is a C++ program running on a Digital Alpha (Unix). Input data are FITS files and the output consists of five FITS files for the different wavelet transform planes and another one for the final reconstructed image. Different parameters can be adjusted for the best performance.

The procedure's first step determines structures in all wavelet planes (Table I).

The second step compares structures and defines a structure which is present in 2 different wavelet planes as an object – or a sub-object – (Table II).

As each wavelet plane is a 'filtering for some frequencies', by rebuilding all structures present in at least 2 planes, noise – which is a random structure – disappears because it is not present simultaneously at two WTS, and low-level structures are now visible.

3.2. CONSTRAINTS OF UTILIZATION

(1) The first step is to degrid an EIT raw image with a smooth method. All EIT images include the shadow of a fine grid that supports an aluminum filter standing in front of the CCD camera.

TABLE II
Statistics concerning object numbers for the image efr19980407-010014.fits.

Wavelet plane number	Number of objects	Number of sub-objects
1	26560	13045
2	1668	531
3	756	120
4	108	3
5	12	0

This procedure removes perfectly the grid pattern with local filtering. Without it, as Multiscale Vision Model is rebuilding all structures, the grid pattern would appear first on the image (Figure 5).

(2) We remark (Figure 4) that the simple model does not work correctly for large images and must be adapted. This is due to the way we decompose the trees to define the objects. The apparent small-scale object could be hidden by larger scale objects. Even if the wavelet transform is a local method, the rules which allow us to define an object in MVM are adapted to favor the largest objects. In this case the smallest structures are swamped in the largest ones. In order to avoid that, we limit the largest scale by working only on small images.

Otherwise for large images, we need to compute the MVM twice. The first computation creates the large scale branching. The large reconstruction objects are removed, then the second computation made with higher wavelet frequency planes builds the small branching. Then we overplot the 2 reconstructions of the MVM and obtain a good image with the whole tree. If we do not do that, when there is too much information on the image, small details disappear.

(3) Choosing an area with less dynamic range is the third constraint to increase the algorithm precision. It is recommended that portions of the image with high intensity compared to the area of interest (Figure 6) be excluded.

As the EUV coronal lines of EIT are optically thin (Portier-Fozzani, 1999, and references there), intensity comes from the integration along the line of sight. At the limb, due to integration with more plasma material, there is limb brightening. Thus, the limb diffusion light could have the same intensity as the structures (Figure 4) and then the use of MVM method is very convenient to extract coronal structures at the limb from the noise (Figure 6).

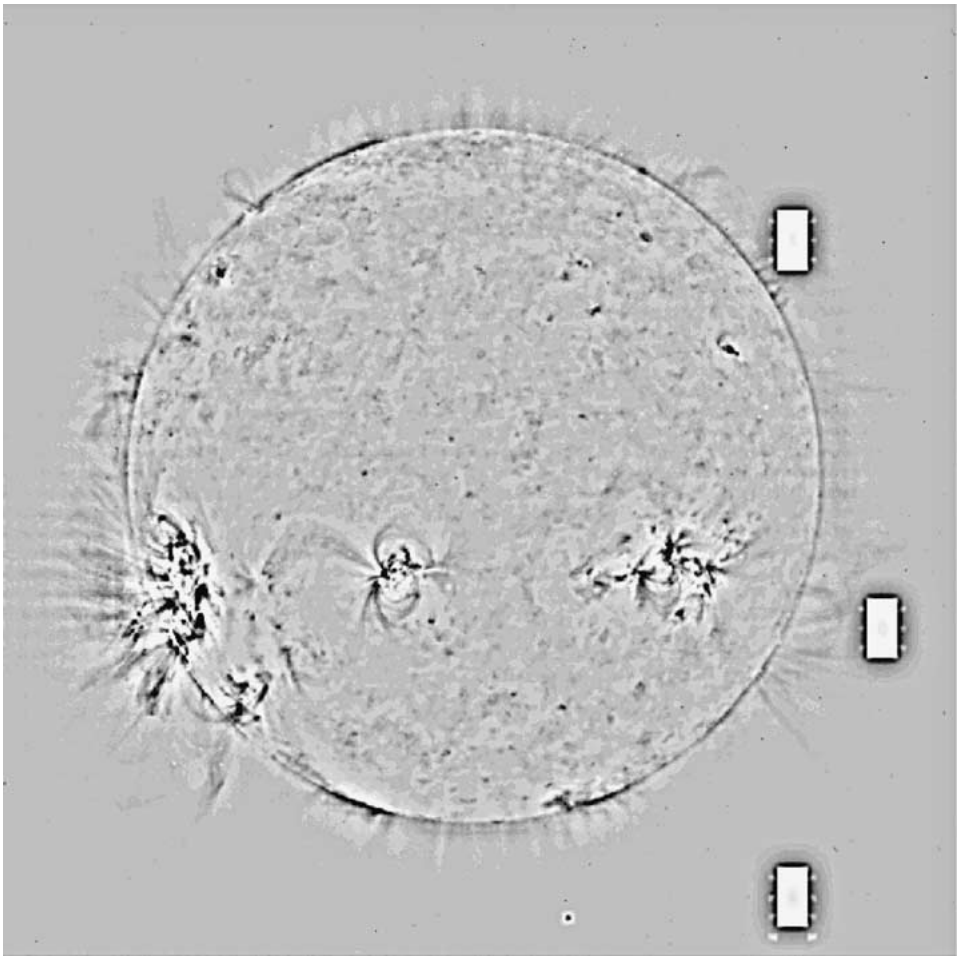

Figure 4. Processed full SOHO/EIT Fe IX/X image of 7 April 1998 at 01:00 UT (negative look up table, hereafter LUT).

3.3. COMPARISON WITH OTHER USUAL FILTERING METHODS TO ENHANCE STRUCTURES ON IMAGES

Tiny structures can sometimes be enhanced using their characteristic spatial frequencies. Usually, in basic vision models, small intensity gradients are used to define an object. For example, the edge of a table appears clearly with high filtering. Sobel filtering uses advanced high space frequency filters. Results for this EIT image are given in Figure 7. The comparison with MVM methods in Figure 6 shows clearly the advantage of using the multiscale vision model (i.e., which use different spatial frequencies for the reconstruction).

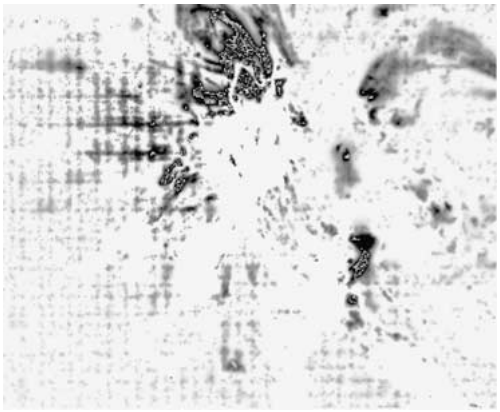

Figure 5. Magnification of the rebuilt wavelet image processed with the rough EIT image: The grid pattern appears clearly and hides some structures. Negative LUT.

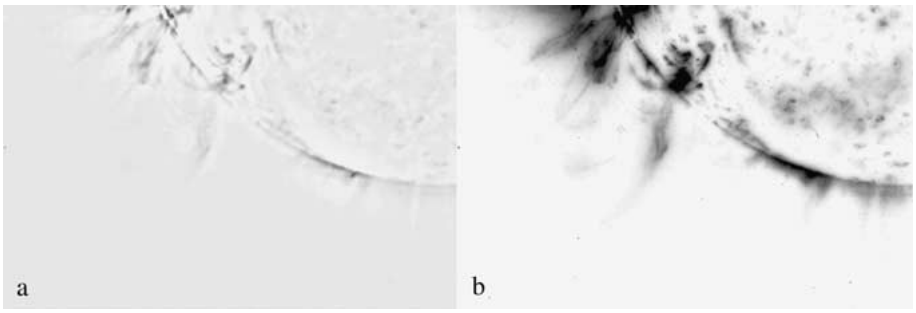

Figure 6. Size and dynamic range comparison with the same restricted area processed: SOHO/EIT Fe IX/X taken the 7 April 1998 at 01:00 UT (negative LUT). (a) Reconstruction using the complete data set 1024 × 1024 (b) Reconstruction using a restricted portion of the image.

4. Application: Link between Loops and Material Ejecta

We analyze now the active region NOAA 8100 from 5 November 1997, 20:00 UT to the 6th before 12:00 UT. During that period, loop evolution appears to have slower variations than we will describe below.

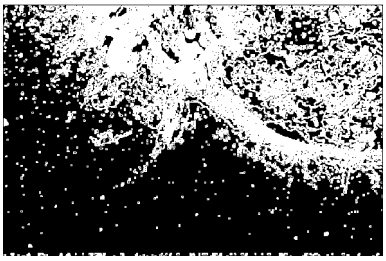

Figure 7. Sobel image of EIT image of Figure 6(a).

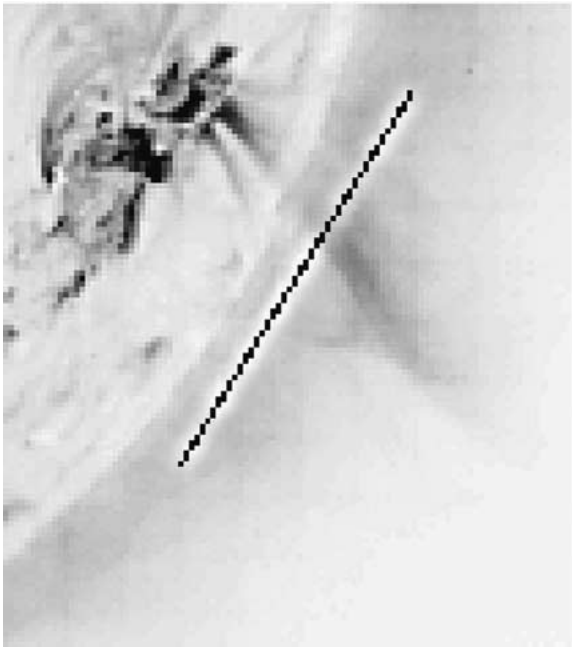

Figure 8. Initial image: south west zoomed on a 512 × 512 pixel SOHO/EIT Fe XII image taken on 6 November 1997 at 00:15 UT (exposure time: 4.8 s; filter: clear, negative LUT).

After that time, an eruption followed by a CME (with coat-hanger shape) is observed. In this paper, we will focus on only the first part of the event, prior to the main changes.

From 22:00 UT and lasting 3 hrs, EIT images taken every 12 min show a morphological change in the coronal loop structures which cannot be completely described only with these images (cf., for example, MPEG movies on the CD-ROM).

As the active region is on the (west) limb, MVM can be used to enhance the structures hidden by the noise. We hide the bright part of the AR by putting a mask over the line plotted in Figure 8. The MVM reconstruction of the EIT image at 00:30 UT (Figure 10) then shows a Y structure. This Y structure's footpoints correspond to the AR, while the edge corresponds to the helmet seen with LASCO/C2 in the SW quadrant.

By reversing the time to 22:00 UT, we found that the Y corresponds to the evolution of the loops which expand and deform (Figure 11). After 01:00 UT, structures become too tiny to be followed on EIT even with the help of MVM.

On LASCO/C2 at 02:00 UT (see movie on the CD-ROM), outward material above 1.5 $R_{\odot}$ and structures with helicity escaping are seen along the streamer area denoted (1) in Figure 12.

As the Y structure constitutes the continuity between the EUV data and coronagraphic data, Figure 13 sketches a possible evolution of the loops into the streamer

Figure 9. Aspect of NOAA 8100 with loops on 4 November, 1997. SOHO/EIT Fe XII (195 Å) with negative LUT processed with smooth de-gridding and image enhancement by MVM.

direction. Portier-Fozzani *et al.* (2000) have studied loop expansion in relation with twist decrease during ARL emergence. They analyzed the observations of loop expansion and twist decrease during the emergence of a new active region, as a consequence of magnetic helicity conservation while the twist is transferred to a larger volume (i.e., a longer loop). Here, helicity transfer from the loop to the streamer seems to be observed.

5. Application to Complex Structures

We studied a complex AR on the south-east limb on 6–7 April 1998. Filaments – which follow the neutral magnetic lines – appear here in absorption in Hα (Figure 14, right) as He II (Figure 14, left) due to low temperature. Two filaments are present between the 2 polarities of each bipolar AR NOAA 8194 and NOAA 8195 (Figure 14).

On the SOHO/EIT image sequence shown in Figure 15 coronal activities present in NOAA 8194, NOAA 8195 and between these numbered areas (hereafter named area (1)) as defined on the image in Figure 15 there is a change of morphology but their structures are hidden by the noise level from the surrounding corona. As the activities are present on the limb, it is then possible to extract the structures from the 'coronal diffusion noise' by using MVM (Figure 16).

With MVM, an arcade can be observed in the lower part of area (1) on 6 April 1998 at 02:06 UT (Figure 16(a)). Over the arcade, closed twisted structures connect NOAA 8194 to 8195. The observed connection becomes weaker with time (15:02 UT, Figure 16(b)). Perpendicular to this axis and replacing the loop arcade, a tiny coronal structure normal to the surface is observed on 7 April at 07:00 UT (Figure 16(c)). Area (1) is completely open at 13:16 UT (Figure 16(d)).

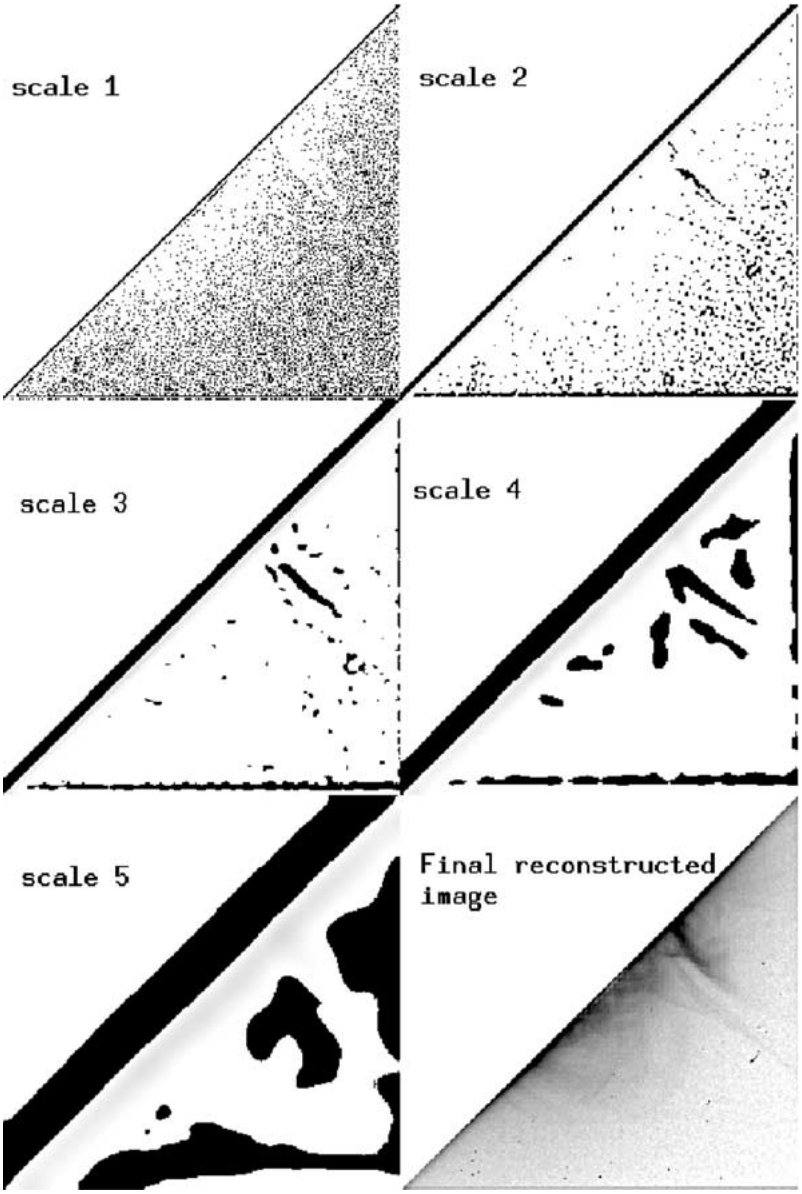

Figure 10. Wavelet reconstruction of NOAA 8100, 6 November, 1997 (SOHO/EIT Fe XII with negative LUT). The 5 wavelet transform planes and the rebuilt object (double Y shape). Only half of the image was used to avoid large intensity gradients. Scales 1 to 5 give, respectively, small to large scale for sub-objects. The large-scale background appears in the scale 5 picture.

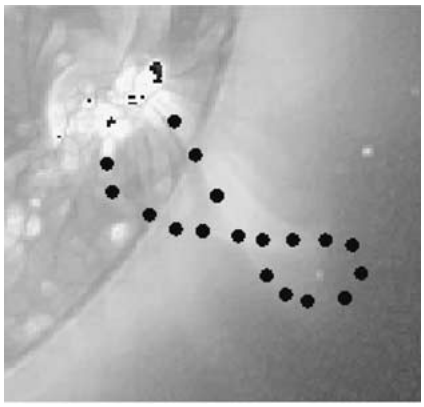

Figure 11. Aspect of NOAA 8100 with SOHO/EIT Fe XII (195 Å) on 5 November, 1997 at 23:02 UT. We emphasized the structure which is a twisted loop (as analyzed with a 'stereoscopic' method) (Portier-Fozzani, 1999).

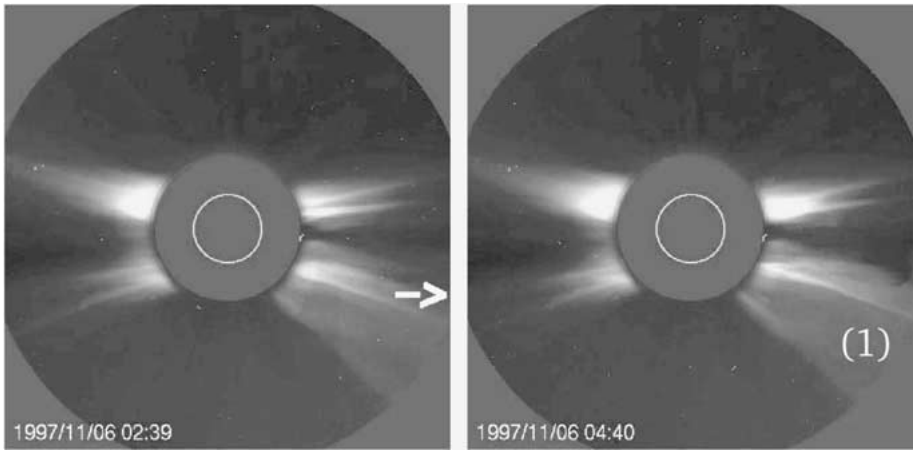

Figure 12. Coronagraphic LASCO C2 images taken on 6 November 1997 at 02:39 UT (*left*) and 04:40 UT (*right*). Outward materials follows the arrow. On the movie, we note that the escaping structure is twisted with an Y shape.

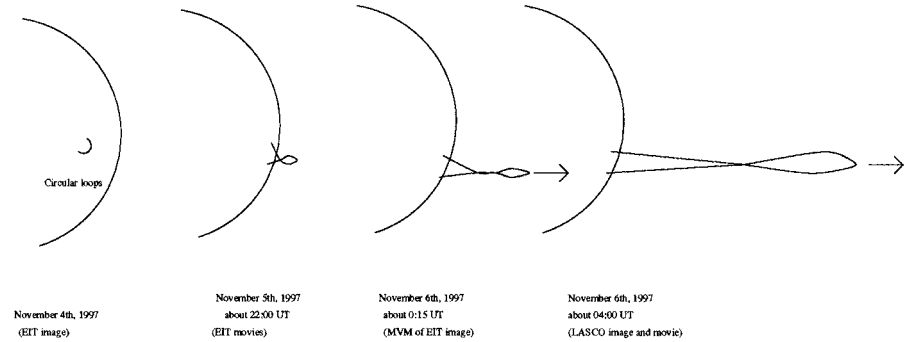

Figure 13. Possible outward ejection of coronal materials from highly twisted loop: aspect of NOAA 8100 in EUV and consequences for coronagraphic images.

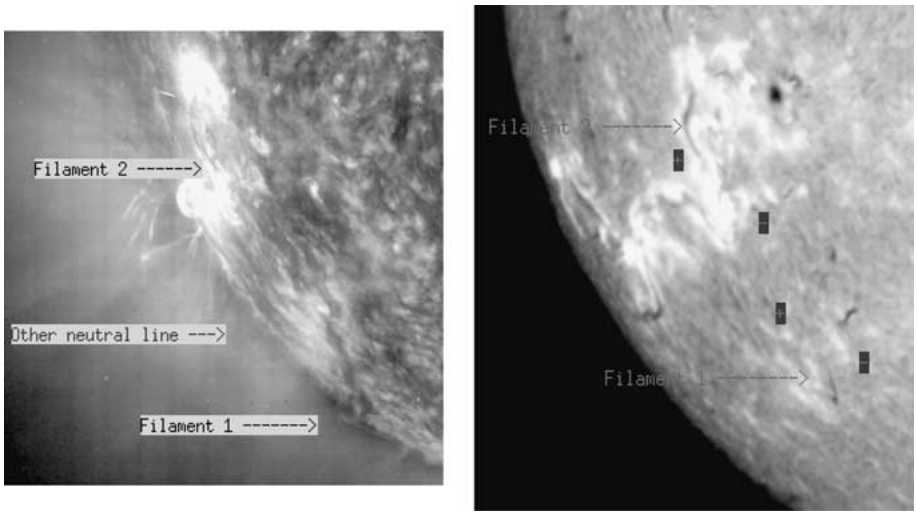

Figure 14. Aspect of the area NOAA 8194 and 8195 and their filaments with multi-wavelength observations on 8 April, 1998. *Left:* SOHO/EIT He II (304 Å) at 17:00 UT. *Right:* Meudon spectroheliograph Hα.

In our field of view, we have 2 filaments and an area (area (1)) which contains a neutral line. Area (1) does not appear to be filled by any prominence material (Figure 14). During the same time, openings of closed structures in area (1) are observed. Martin (1998) reviewed conditions for the formation and maintenance of filaments. Existence comes from the association between chirality of the filament, the presence of a filament channel and an arcade. In area (1) we have the arcade only. At present, the condition of filling a neutral line which will become a filament is still open. We analyze in area (1) the conditions of arcade loop stability which would have supported the filament material if it existed. The simplest coronal loops can be described by the magnetic lines of a potential field configuration which corresponds to a minimum of the magnetic energy for a given vertical field at the photosphere (e.g., Aly, 1991). Loop arcades are formed with parallel plane loops. Higher-energy configurations correspond to sheared or twisted structures. In certain cases, Aly (1991) showed that sheared or twisted magnetic closed field lines can become open according to magnetic helicity conservation. In area (1), over the arcade, we have a twisted structure. With time, NOAA 8194 and NOAA 8195 are no longer connected. The structure might have been opened by transferring the extra twist into the opening of the field through the magnetic helicity. This would explain why such an arcade could not exist too long as the shear destroys the possibility of filling a neutral line channel. The link with chirality has to be made. This discussion has to be finalized with other data.

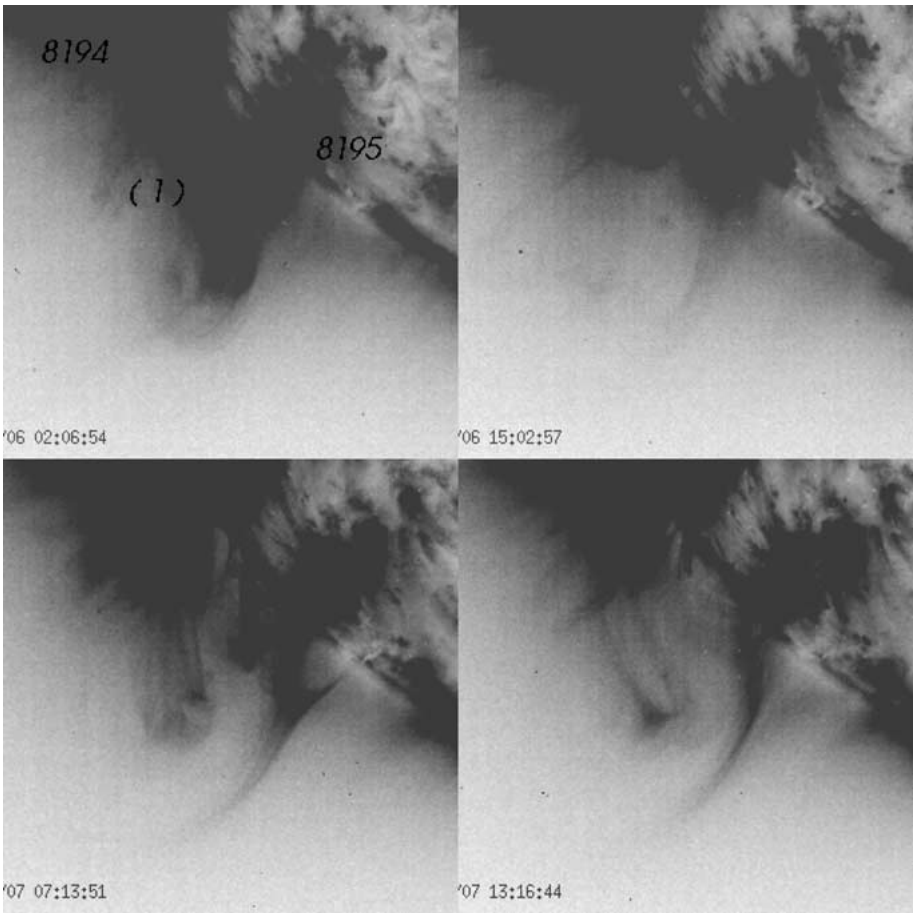

Figure 15. SOHO/EIT Fe IX/X original images taken on 6 April 1998 at 02:06 UT, 15:02 UT, and on 7 April 1998 at 07:13 UT and 13:16 UT (negative LUT).

6. Conclusion

Usual image-processing methods enhance images up to some values limited by the noise level. So, even if the dynamic range of an instrument is important, such as the EUV imager SOHO/EIT, not all the structures are seen. While analyzing images as the sum of different objects, the multiscale vision model extracts structures from the diffuse background and highlights details concerning some thin coronal structures which were not seen with usual filtering.

The method used can be summarized as follows:

(1) The wavelet transform with the 'à trous algorithm' is computed.

(2) Wavelet coefficient deviations due to the noise are determined.

(3) Thresholds at each scale are deduced.

(4) The wavelet coefficient maxima in the wavelet space are determined.

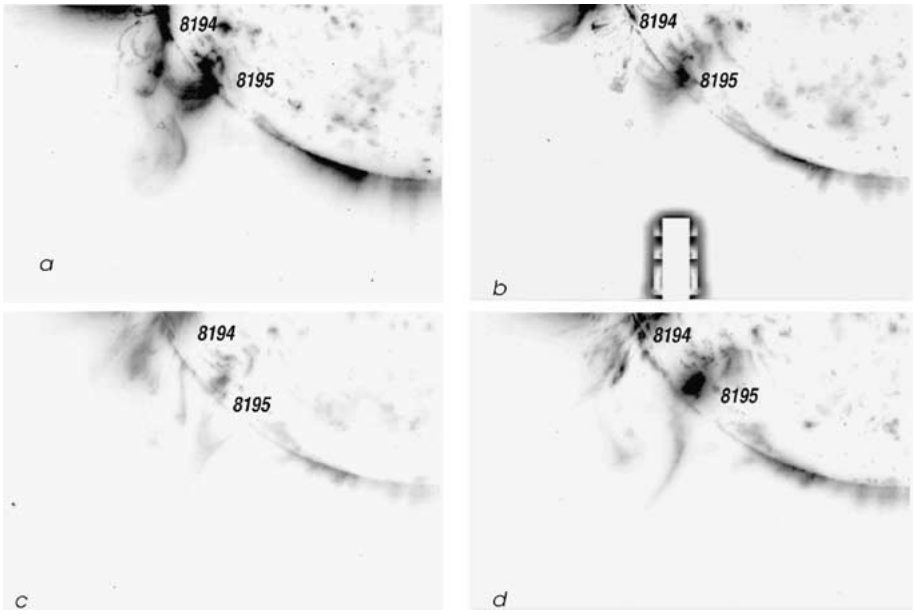

Figure 16. SOHO/EIT Fe IX/X rebuilt by wavelet imaging taken on 6 April 1998 at (a) 02:06 UT, (b) 15:02 UT, and on 7 April 1998 at (c) 07:13 UT and (d) 13:16 UT (reverse LUT).

(5) Image labeling is done taking into account a multi-peak decomposition.

(6) Interscale relations are determined.

(7) Trees are deduced from the maximum in each wavelet frequency space plane.

Thus sub-objects and objects are rebuilt.

The method is very efficient when the area studied has a low dynamic range. Constraints for the method with SOHO/EIT images were derived with success. Efficient applications of the method are obtained when the images are small with low contrast.

Our first example took place on 5 – 6 November 1997. On EUV processed images, highly sheared or twisted loops progressively form a Y-shape. The Y-shape usually characterizes fast magnetic reconnection with plasmoid ejections. At the same time on a coronagraphic movie, a helicoidal structure observed in the streamer, escapes. Then injection of material in a coronal streamer in relation with coronal loop evolution is established.

Our second example happened on 6 –7 April 1998. Original images show global coronal modifications with time. With MVM processed images, it becomes possible to identify which structures show a change of morphology. In a complex active region, openings of arcade loops are observed. Such phenomena are possible due to helicity transfer. Consequences for filament stability and relations with shear, twist and chirality will be discussed in a later paper.

Additional material can be found on the CD-ROM.

References

Aly, J. J.: 1991, *Dynamics of Solar Flares*, Flares 22 Workshop, Obs. Paris-Meudon DASOP Editors, p. 29.

Anscombe, F. J.: 1948, *Biometrika* **15**, 246.

Amari, T., Luciani, J. F., Aly, J. J., and Tagger, M.: 1996a, *Astrophys. J.* **466**, L39.

Amari, T., Luciani, J. F., Aly, J. J., and Tagger, M.: 1996b, *Astron. Astrophys.* **306**, 913.

Claude Berge: 1967, *Théorie des Graphes et Ses Applications* **16**, Ed. Dunod, Paris, p. 154.

Bijaoui, A.: 1978, *Traitement des Images et Reconnaissance des Formes*, Ed. INRIA, pp. 848–854.

Bijaoui, A.: 1991, *Ondelettes et Paquet d'Ondes, Algorithmes de la transformation en ondelettes. Applications en Astronomie*, Ed. INRIA, pp. 115–140.

Bijaoui, A. and Rué, F.: 1995, *Signal Processing* **46**, 345.

Bijaoui, A., Rué, F., and Vandame, B.: 1998, in M. C. Maccarrone *et al.* (eds.), *Data Analysis in Astronomy*, World Scientific, Singapore, pp. 337–344.

Bijaoui, A., Bobichon, Y., Fang, Y., and Rué, F.: 1996, *Traitement du Signal, Méthodes multi-échelles appliqués à l'analyse des images SAR*.

Bohlin, J. D. and Sheeley, N. R.: 1978, *Solar Phys.* **56**, 125.

Bray, R. J., Cram, L. E., Durrant, C. J., and Loughhead, R. E.: 1991, *Plasma Loops in the Solar Corona*, Cambridge University Press, Cambridge.

Canfield, R. C., Hudson, H. S., and McKenzie, D. E.: 1999, *Geophysical Research Letters* **26**, No. 6, 627.

Defise, J. M., Moses, J. D., and Clette, F.: 1998, *Proc. SPIE* **3442**, 126.

Delaboudinière, J. P. *et al.*, 1995, *Solar Phys.* **162**, 291.

Démoulin, P.: 1998, *PASP Conf. Ser.* **150**, 78.

Dere, K., Brueckner, G. E., Howard, R. A., Michels, D. J., and Delaboudinière, J. P.: 1999, *Astrophys. J.* **516**, 465.

Forbes, T. and Malherbe, J. M.: 1986, *Astrophys. J.* **302**, L67.

Harman, W. W.: 1963, *Principles of the Statistical Theory of Communication*, Vol. 11, 217, MacGraw Hill, New York, p. 217.

Holschneider, M., Kronland-Martinet, R., Morlet, J., and Tchamitchian, P.: 1989, *Wavelets: Time-Frequency Methods and Phase-Space*, Springer-Verlag, Berlin, pp. 286–297.

Klimchuk, J. A. and Porter, L. J.: 1995, *Nature* **377**, 131.

Lascaux, P and Théodor, R.: 1994, *Analyse numérique matricielle appliquée à l'art de l'ingénieur*, Vol. 2, Ch. 8, Ed. Masson, pp. 405–458.

Lin, J., Forbes, T., Isenberg, P., and Démoulin, P.: 1998, *Astrophys. J.* **504**, 1006.

Mallat, S., 1989, *IEEE Transactions on Pattern Analysis and Machine Intelligence* **11**, 574.

Martin, S.: 1998, *Solar Phys.* **182**, 107.

Moses, D. *et al.*: 1997, *Solar Phys.* **175**, 571.

Murtagh, F., Starck, J. L., and Bijaoui, A., 1995, *Astron. Astrophys. Suppl. Ser.* **112**, 179.

Parker, E. N.: 1974, *Astrophys. J.* **191**, 245.

Portier-Fozzani, F.: 1999, PhD Thesis, *Étude de la couronne solaire en 3D et de son évolution avec SOHO/EIT*, Université de Nice Sophia Antipolis, Laboratoire d'Astronomie Spatiale Marseille, France.

Portier-Fozzani, F., Moses, J. D., Delaboudinière, J. P., Gurman, J. B., Clette, F., and Maucherat, A. J.: 1997, *PASP Conf. Ser.* **111**, 402.

Portier-Fozzani, F., Maucherat, A. J., and the EIT Team: 1998, *PASP Conf. Ser.* **150**, *IAU Colloq.* **167**, 41.

Portier-Fozzani, F., Démoulin, P., Neupert, W., Aschwanden, M., and the EIT Team: 2000, *Astron. Astrophys.* (submitted).

Starck, J. L. and Bijaoui, A.: 1994, *Signal Processing* **35**, 195.

Stern, R. and Portier-Fozzani, F.: 1996, Internal report concerning EIT histograms and calibration.

Stetson, P. B.: 1987, *Publ. Astron. Soc. Pacific* **99**, 191.
Stobie, R. S.: 1986, *Pattern Recognition Lett.* **4**, 317.
Strang, G.: 1989, *SIAM Rev.* **31**, 614.
Unser, M. and Aldroubi, A.: 1992, in C. K. Chui (ed.), *Wavelets: a Tutorial in Theory and Applications*, Academic Press, New York, pp. 91–122.
Webb, D. F.: 1998, *IAU Colloq.* **167**, *PASP Conf. Ser.* **150**, 463.

La méthode a aussi été testée avec moins de succès sur des données LASCO/C2 pour comprendre des Ejections de Matieres Coronales (CME). Il apparaît que des problèmes de lumières parasites entrent alors en compte et empéchent la recherche fructueuse de structures fines.

III.3 Vision 3D : Généralités

III.3.1 Problématique

Les images correspondent à une représentation en 2 dimensions du monde en 3 dimensions. Le problème de la reconstruction de cette 3ème dimension se pose à partir de groupes d'images en 2D.

En préambule précisons ce que signifie la "connaissance 3D d'un objet". Un objet est représenté différemment en 3D selon si on s'interresse à son contour ou à son contenu. Comme pour une orange avec son écorce, la connaissance de 2 angles distincts permet seulement de disposer de l'aspect extérieur de sa peau (ie son enveloppe) éventuellement légèrement bosselée. Toutefois pour connaître son intérieur il faut impérativement réaliser des coupes. La haute atmosphère solaire (couronne et région de transition) est une sorte d'écorce épaisse. On peut donc soit déterminer l'aspect d'une enveloppe donnée, soit comparer en coupe l'aspect des enveloppes des différentes parties de la couronne solaire. Cela aboutit donc à 2 possibilités de "vision 3D" assez différentes :

1. utiliser des coupes différentes pour connaître l'intérieur de l'écorce (eg. le "3 D par couche"). Cette approche est retranscrite symboliquement sur les cartes IGN où les isocontours de plusieurs plans d'altitudes différentes sont reportés sur un même plan (pseudo-2D)

2. utiliser des angles de vues différents pour déterminer l'enveloppe 3D de la structure donnée (*e.g.* stéréovision, tomographie, ...). En médecine, gràce à des traceurs adéquats, la tomographie ([147]) permet de déterminer la structure 3D d'organes internes. Utilisée par Davila ([55]) sur la couronne solaire, l'algorithme de reconstruction tomographique ART permet de retrouver l'enveloppe externe des structures coronales. Batchelor ([18]) se sert de paires d'images de Skylab X-ray Spectrographic Telescope, distantes de 12h pour visualiser de manière quasi-stéréoscopique l'enveloppe de la couronne chaude.

Dans ces 2 manières de concevoir la 3D (intérieur ou enveloppe), l'échantillonnage (ie le nombre de coupes ou angles) joue un rôle essentiel dans la possibilité de reconstruire l'objet initial à partir de ces informations 2D.

La difficulté dans le cadre de la couronne solaire vient du fait que les ions du plasma considérés étant optiquement mince, l'intensité d'un point est définie par l'intégration sur

une certaine épaisseur. La position d'un point sur une image 2d est donc la résultante d'une intégration sur la ligne de visée qui devra être prise en compte lors de la reconstruction par chacune des méthodes.

III.3.2 Le "3D par couche"

Cette méthode ne peut être réalisée que dans le cas très particulier de la couronne en dehors des structures. Cela est donc uniquement valable au moment du minimum du cycle et en dehors de toutes régions actives. D'après la relation température versus altitude donnée par la Fig. II.6, une image prise avec un filtre EIT correspond à une[8] température (Fig. III.7). On peut ainsi définir les couches d'altitudes à partir des filtres en températures.

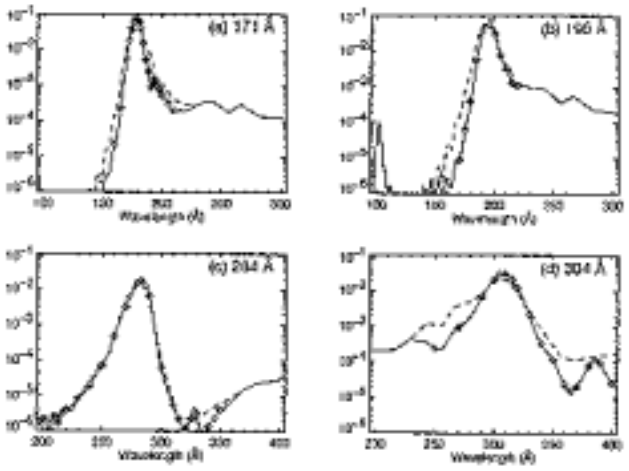

Figure III.7: Bande Passante des filtres pour EIT

En dehors des structures, les 4 longueurs d'ondes disponibles donnent 4 coupes de la "couronne" en couches parallèles à la surface de la photosphère (Fig III.8).

Les séquences synoptiques de prises de vues SOHO/EIT prévoient au moins 1 image pour chacune des 4 longueurs d'ondes par jour. Elles permettent donc de construire ces coupes (Fig. III.8). **En pratique ces coupes en températures sont rarement applicables pour trouver la structure 3D. Par contre la comparaison des 4 longueurs d'ondes d'EIT sert pour correller les structures entre la région de transition et la couronne**, ainsi qu'à mesurer les températures (cf chapitre 2).

Pour avoir une vision 3D de la haute atmosphère solaire, les méthodes de vision basées sur la stéréoscopie sont plus efficaces.

[8]Plus précisément, la bande passante de chaque filtre recouvre, de manière plus ou moins piquée, des gammes des fréquences qui caractérisent des températures.

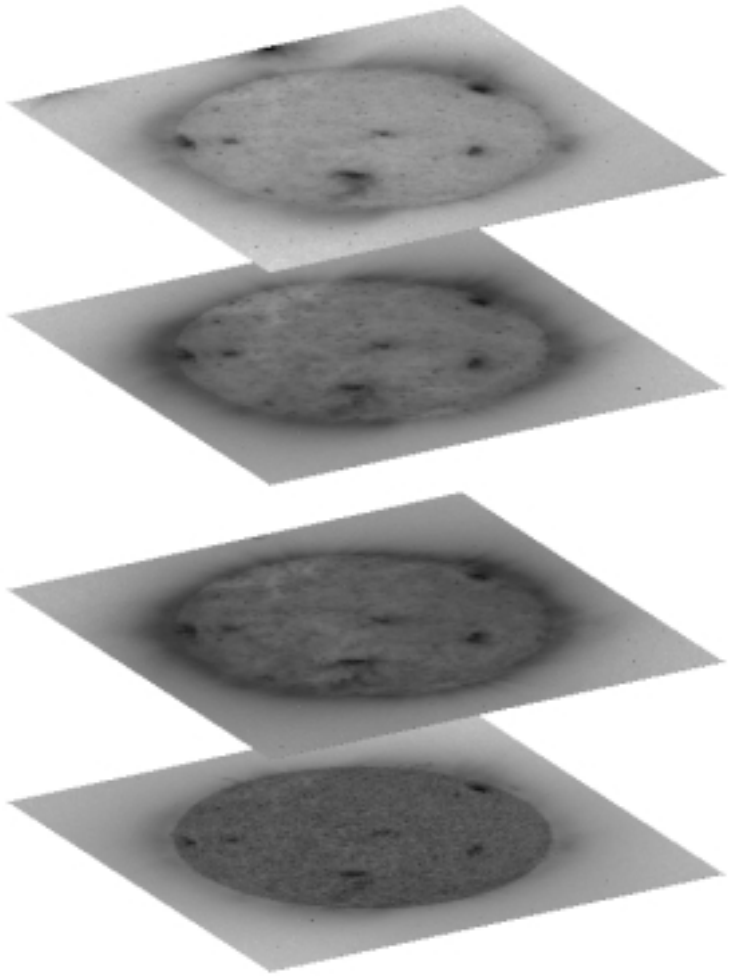

Figure III.8: Le soleil en 4 coupes UV de température :
De bas en haut : He II, Fe IX/X, Fe XII, Fe XV.

III.3.3 Principe de la vision en relief : “3D par différence d’angle” : Methodes stéréoscopiques et Anaglyphes

Le relief d’un objet est conceptualisé au niveau des 2 yeux grace à des différences d’angle de vue (Fig. III.9) entre chacune des images reçues.

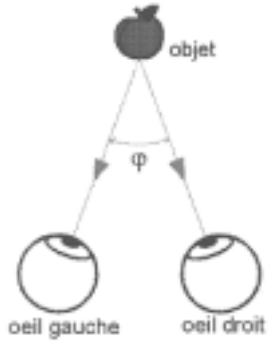

Figure III.9: La vision binoculaire : la base —définit comme la distance entre les recepteurs (yeux)— et la distance à l’objet, interviennent dans l’angle sous lesquels l’objet est vu.

Les différences (Fig. III.10) entre les images gauches (G) et droites (D) sont interprétées par le cerveau comme une profondeur déterminée. Ainsi à partir de 2 images 2D on a une connaissance de la 3ème dimension.

Figure III.10: La vision binoculaire : perspectives

Plusieurs techniques ([93]) sont alors possibles pour reconstituer le relief à partir de photos d’angle différents (c’est le sens étymologique du mot stéréoscopie : stereo = solide, scopie = observer) .
1/ Soit on prend des photos simultanées avec 2 appareils semblables séparés de quelques degrés
2/ soit les photos sont prises du même appareil en le déplaçant (il faut alors que le temps caractéristique de variation de l’objet soit négligeable par rapport au temps nécessaire entre les poses)

Dans notre cas, nous disposons d’un seul récepteur (EIT). Le satellite observant dans une direction fixe, ce sera la rotation du soleil qui donnera l’angle nécessaire entre 2 ob-

servations pour retrouver la profondeur et donc permettra l'étude des structures stables du soleil. La vitesse de rotation variant en fonction de la latitude, l'angle minimal[9] nécessaire est de quelques degrés soit 3-4 heures environ à l'équateur solaire (13.45 degrés par jour [2]).

Figure III.11: 2 méthodes utilisées permettant une vision stéréoscopique:
(a) en bas pour des diapositives,
(b) en haut pour des anaglyphes

Il faut alors affecter le couple d'images prises à une vision quasi-naturelle pour faire le rendu du relief. Ainsi pour voir avec la profondeur les couples d'images, il faut que chaque oeil (respectivement Droit et Gauche) observe une image (respectivement Droite et Gauche). Cela peut se faire soit par des

- systèmes optiques séparant en permanence le trajet optique des 2 yeux (par exemple : 2 visionneuses diapos mises ensembles, Fig. III.11a)

- systèmes optiques qui redécomposent les objets. Par exemple, dans la vision colorée (aussi appelée **anaglyphe**), la complémentarité des couleurs est utilisée pour superposer les deux images sur le même tirage papier avant que les lunettes à verres colorés (Fig. III.11b) séparent les voies de chaque oeil (Fig. III.12).

Un anaglyphe d'EIT obtenu à partir des images EIT est présenté figure III.13.

Signalons aussi qu'il existe d'autres techniques 3D comme les stéréogrammes, les hologrammes, etc...

[9]Les variations sur cet angle accentuent ou diminuent l'effet de relief dans la limite d'accommodation de l'oeil. L'homme à une sensation de relief à 0.01—100m environ pour un écartement entre les yeux de 6,4 cm en moyenne.

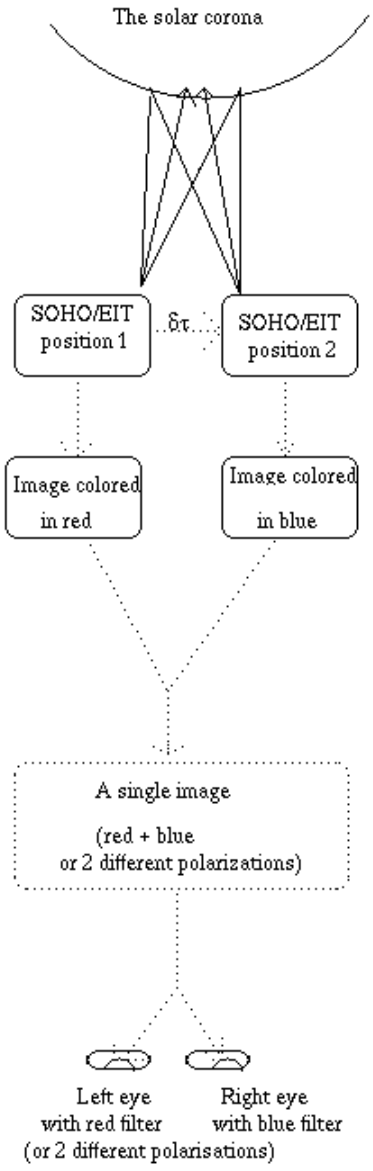

Figure III.12: Principe de la stéréovision avec EIT (Extrait du Poster de Portier-Fozzani & al. de SOHO 8)

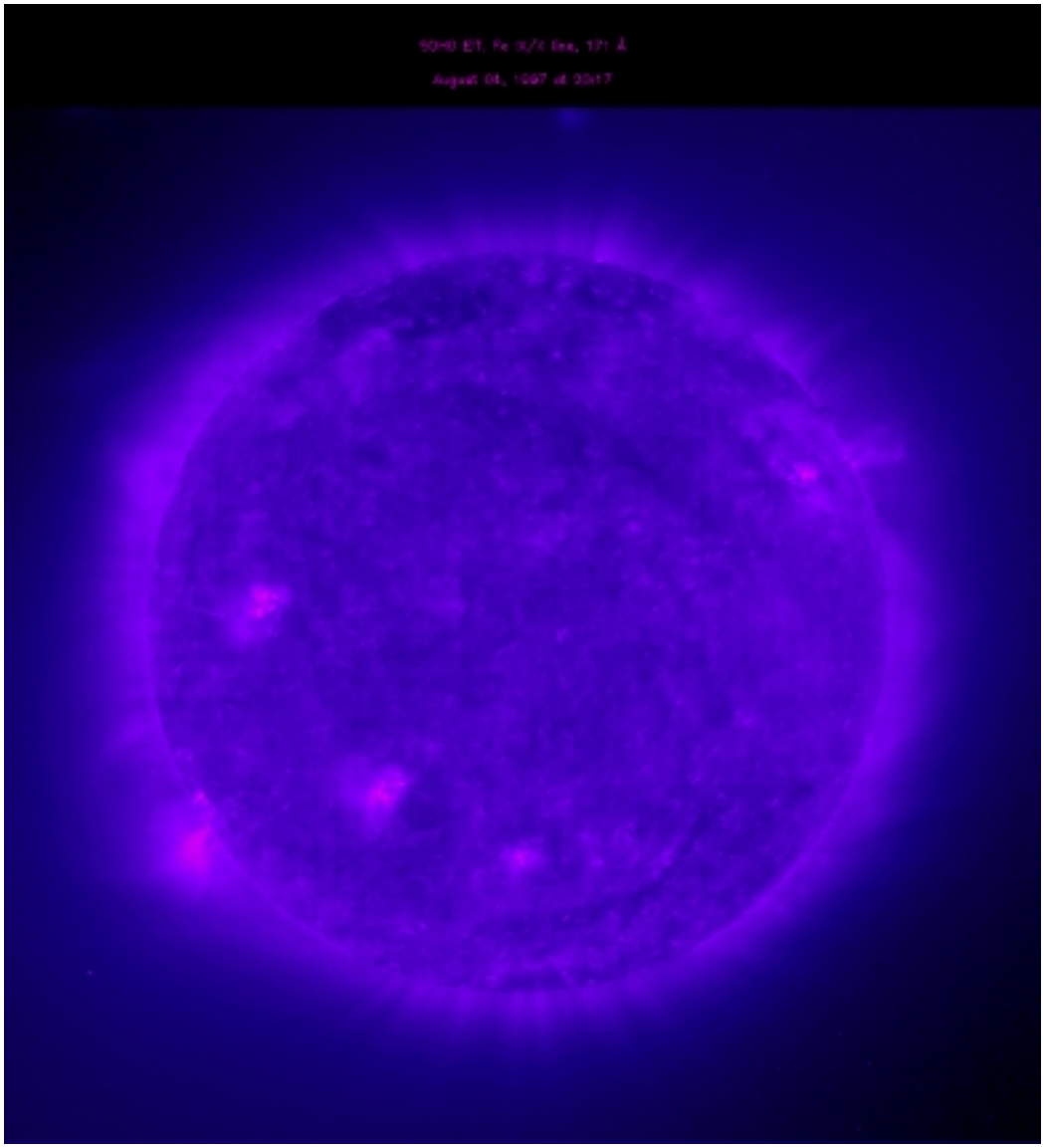

Figure III.13: Anaglyphe d'EIT

III.4 Vision 3D (2ème partie) : reconstructions stéréographiques

Aprés avoir considéré la vision “simple” en 3D, étudions maintenant les possibilités de reconstruction en 3 dimensions.

III.4.1 Structures visionnées par stéréovision avec un modèle à priori

Lorsque l’on connait partiellement la forme des structures que l’on souhaite observer, on peut approximer ces structures avec des modèles connus à priori (segments de droites,...). En particulier, l’approximation des structures en 1D par des segments de droites permet de retrouver facilement leurs positions dans l’espace. En effet, les coordonnées des points sont mesurées sur une grille héliocentrique et les structures sont déduites par rapport à la normale du lieu. Dans l’approche plus formalisée que nous aborderons ensuite pour essayer de généraliser la connaissance des structures quelconques à partir de représentation géométrique, on dit que c’est une approximation à 1 Dimension de Delaunay plongée, au sens mathématique des sous variétés, dans un espace de dimension 3. On peut ainsi approximer les plumes polaires par des modèles géométriques simples (droite centrale, ou cône de révolution) et retrouver les paramètres géométriques de taille et d’inclinaison par stéréoscopie. Un exemple de ce type de résultats est donné dans l’article suivant.

- **Imaging the solar corona in the EUV**

- DELABOUDINIERE, J.-P.; STERN, R. A.; MAUCHERAT, A.; PORTIER-FOZZANI, F.; NEUPERT, W. M.; GURMAN, J. B.; CATURA, R. C.; LEMEN, J. R.; SHING, L.; ARTZNER, G. E.; BRUNAUD, J.; GABRIEL, A. H.; MICHELS, D. J.; MOSES, J. D.; AU, B.; DERE, K. P.; HOWARD, R. A.; KREPLIN, R.; DEFISE, J. M.; JAMAR, C.; ROCHUS, P.; CHAUVINEAU, J. P.; MARIOGE, J. P.; CLETTE, F.; CUGNON, P.; VAN DESSEL, E. L.

- Advances in Space Research, Volume 20, Issue 12, p. 2231-2237.

- 1997AdSpR..20l2231D (**COSPAR**)

Imaging the solar corona in the EUV

J.-P. Delaboudiniere

Inst. d'Astrophysique Spatiale, Universite Paris XI, 91405 Orsay Cedex, France

G. E. Artzner, J. Brunaud, A. H. Gabriel

Inst. d'Astrophysique Spatiale, Universite Paris XI, 91405 Orsay Cedex, France

B. Au, K. P. Dere, R. A. Howard, R. Kreplin, D. J. Michels, J. D. Moses

Naval Research Laboratory, Washington, DC 20375, USA

J. M. Defise, C. Jamar, P. Rochus

Centre Spatial de Liege, Liege, Belgium

J. P. Chauvineau, J. P. Marioge

Institut d'Optique Theorique et Appliquee, 91403 Orsay, France

R. C. Catura, J. R. Lemen, L. Shing, R. A. Stern

Solar and Astrophysics Laboratory, Lockheed Martin, Palo Alto, CA 94304, USA

J. B. Gurman, W. M. Neupert

NASA/Goddard Space Flight Center, Greenbelt, MD, USA

A. Maucherat, F. Portier-Fozzani

Laboratoire d'Astronomie Spatiale, Marseille, France

F. Clette, P. Cugnon, E. L. Van Dessel

Observatoire Royal de Belgique, Brussels, Belgium

Abstract. The SOHO (SOlar and Heliospheric Observatory) satellite was launched on December 2nd 1995. After arriving at the Earth-Sun (L1) Lagrangian point on February 14th 1996, it began to continuously observe the sun. As one of the instruments onboard SOHO, the EIT (Extreme ultraviolet Imaging Telescope) images the Sun's corona in 4 EUV wavelengths. The He II filter at 304 Å images the chromosphere and the base of the transition region at a temperature of $5-8\times10^4$ K; the Fe IX-X filter at 171 Å images the corona at a temperature of $\sim 1.3\times10^6$ K; the Fe XII filter at 195 Å images the quiet corona outside coronal holes at a temperature of $\sim 1.6\times10^6$ K; and the Fe XV filter at 284 Å images active regions with a temperature of $\sim 2.0\times10^6$ K. About 5000 images have been obtained up to the present. Images and movies of all the wavelengths allow a look at different phenomena present in the sun's corona, and in particular, magnetic field reconnection.

1. Introduction

The SOHO (SOlar and Heliospheric Observatory) satellite, which is completely dedicated to understanding the physics of the Sun, was launched December 2nd 1995.

Having arrived at its working orbit on February 14th 1996, it is now able to continuously observe the Sun from the Lagrangian L1 (Earth-Sun) point. The EIT (Extreme ultraviolet Imaging Telescope), one of the instruments onboard SOHO, images the Sun's corona and transition region in 4 EUV wavelengths. EIT's first light occured on January 2, 1996 and the instrument was declared operational on January 15th,1996. In this paper we discuss the instrument, the operations and the first results of EIT observations.

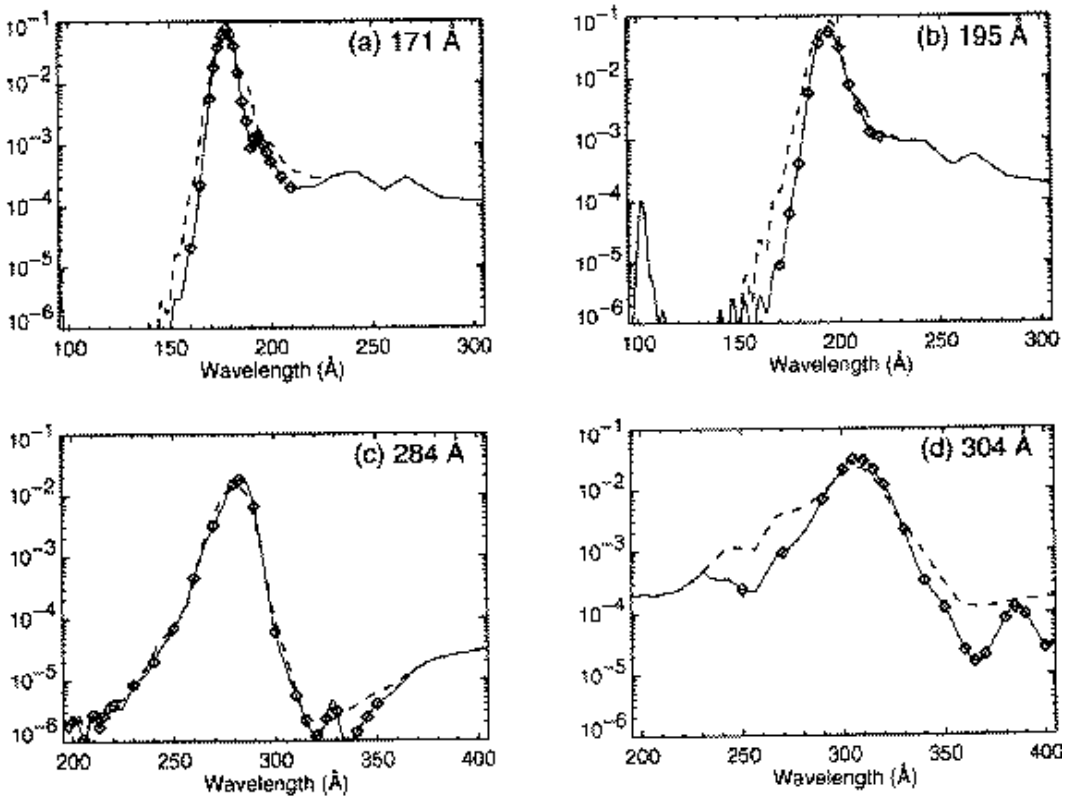

Figure 1. The two-mirror reflection efficiency for each EIT quadrant. Measured values are shown as data points; dashed and solid curves represent the predicted and adopted values respectively.

2. The EIT Instrument

The EIT telescope uses a modified wide-field Ritchey-Chretien design, (Delaboudinière 1989b, Chauvineau 1991). With a full field of view of 45 × 45 arcmin, the telescope has an effective focal length of 1.652 m and a primary diameter of 0.12 m.

The mirror is divided into 4 sectors (geometrical area per quadrant = 0.0013 m^2), to isolate with appropriate filters the emission in narrow wavelength ranges. Four separate multilayers are deposited on the matched quadrants of both the primary and secondary mirrors of the telescope. A rotating mask allows only a single multilayer-coated quadrant of the telescope to be illuminated by the Sun at any time. The image from a selectable single EIT quadrant is focused on a back-illuminated CCD (1024 × 1024 pixels, 1 pixel = 21 × 21 μm^2 = 2.6 × 2.6 $arcsec^2$) with good efficiency at extreme-ultraviolet (EUV) wavelengths. The CCD is also sensitive to visible light, so 2 aluminium filters were used as visible blockers. These blocking aluminium filters in EIT are mechanically supported by nickel meshes which create a grid pattern in the focal plane. Another Al filter on a filter wheel can also be introduced in the field, if necessary. The telescope is contained in a vacuum enclosure for cleanliness and to reduce acoustical loads on the thin-film filters during launch. The main door at the front of the telescope was opened after spacecraft outgassing and may be re-closed when thrusters are fired for SOHO station keeping. The CCD is cooled to about −65 C by a cold finger attached to a passive radiator facing deep space. The CCD was calibrated at Orsay and Lockheed Martin and the entire instrumented was calibrated at IAS, using the Orsay synchrotron (Song 1995). A more detailed decription of the EIT instrument and calibration may be found in Delaboudinière et al. (1995).

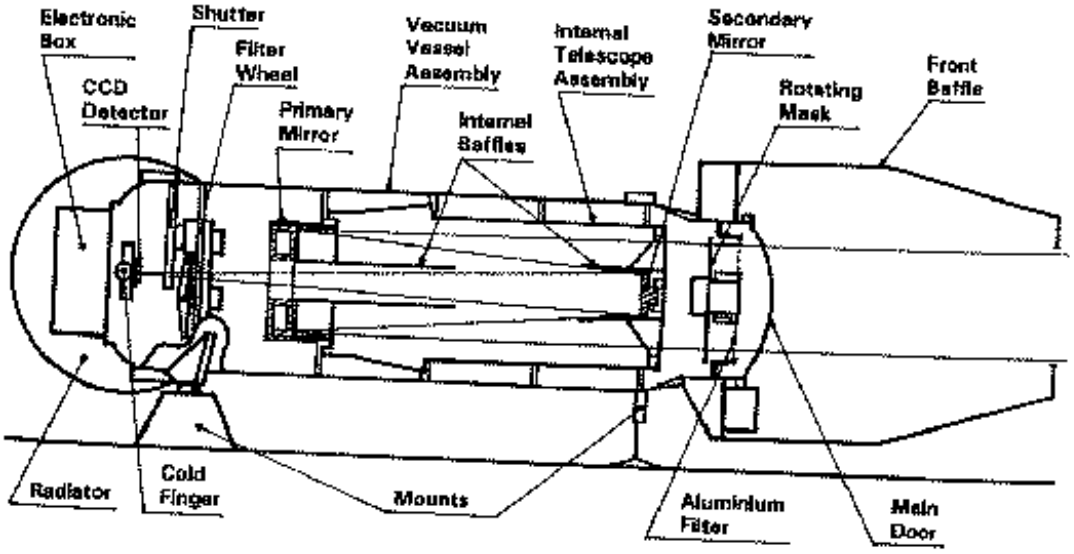

3. Instrument operations and performance

3.1. Operations

The baseline observation plan consists of taking full field of view images in all four bandpasses one to three times per day (joint EIT/LASCO synoptic plan). In addition, smaller size images can also be obtained.

LASCO and EIT have the same electronic box. The telemetry of EIT is shared with the 3 coronographs of LASCO which observes the corona in visible wavelengths. EIT uses, on average, about 20 percent of the total telemetry capability and computer resources available to the EIT/LASCO experiments. The combined telemetry rate is $5.2 Kbps$. For short time periods 26.2 Kbps can be made available using the telemetry allocation of the other instruments.

Data compression routines allow the storage/transmission requirements for an image to be reduced by a factor of 2-4 using a loss-less Rice compression algorithm. It then takes 22 minutes to transmit a full 1024×1024 image. To study smaller regions on the Sun at faster rate, sub-arrays of pixels, each 32×32 (83×83 arcsec) in size, may be read out while the rest of the CCD field is discarded. Missing pixels due to transmission problems represent less than 1 percent of the total image.

3.2. Extraction of the grid from images:

The grid pattern created by the filter support mesh must be removed from the images prior to scientific analysis.
One appraoch to this problem uses the classical Fourier method with a FFT followed by filtering. Results obtained by adding many images permit removal of the grid pattern (F.Clette, 1996, in preparation).

3.3. Response of the CCD with time:

During the first months of EIT operations, it became apparent that the instrument response was decreasing with time. This effect can be seen by plotting counts per unit time in full-field EIT images in each of the four sectors from the start of operations (see Appendix). Note that the 304 Å channel shows the greatest change with time, and the greatest recovery after periods of warming up the CCD (bakeouts). Bakeouts were performed on 1996 May 23 - 25 and 1996 June 23 - 24. After the second bakeout, the 304 Å response returned to approximately the same level as after the first bakeout. Given the shorter duration of the second bakeout (24 hours vs. 48), this may be considered supporting evidence that we are seeing the effects of (organic ?) ice condensing on the detector. However, the phenomenology of the response variations is not well understood at present.

4. EIT Science Topics

The consortium of EIT investigators has developed a list of science topics which will be investigated through EIT observations and analysis. These are not meant to be exclusive or to indicate permanent rights of any sort, but it would benefit any prospective Guest Investigator (official or otherwise) to read the full list of science topics and lead consortium members (available on the World Wide Web at: http://umbra.nascom.nasa.gov/eit/) and to contact them prior to requesting use of EIT data.

Some of the science areas to be investigated are:

- Morphology and evolution of loops in the corona (quiescent features)
- Signatures of coronal heating, including waves, nanoflares, emerging flux regions, and magetic shear

- Properties of He II emission and structures
- Properties and evolution of the large scale corona
- EUV proxies and EUV source modeling; correlations with SEM,LASCO, and ground based images

5. Stereoviews and movies

By using coronal rotation, we obtained a pair of stereoviews (1 to 5 hours between right and left views) that give an idea of long lived coronal morphologies (loops,coronal holes,plumes) (Koutchmy 1994).

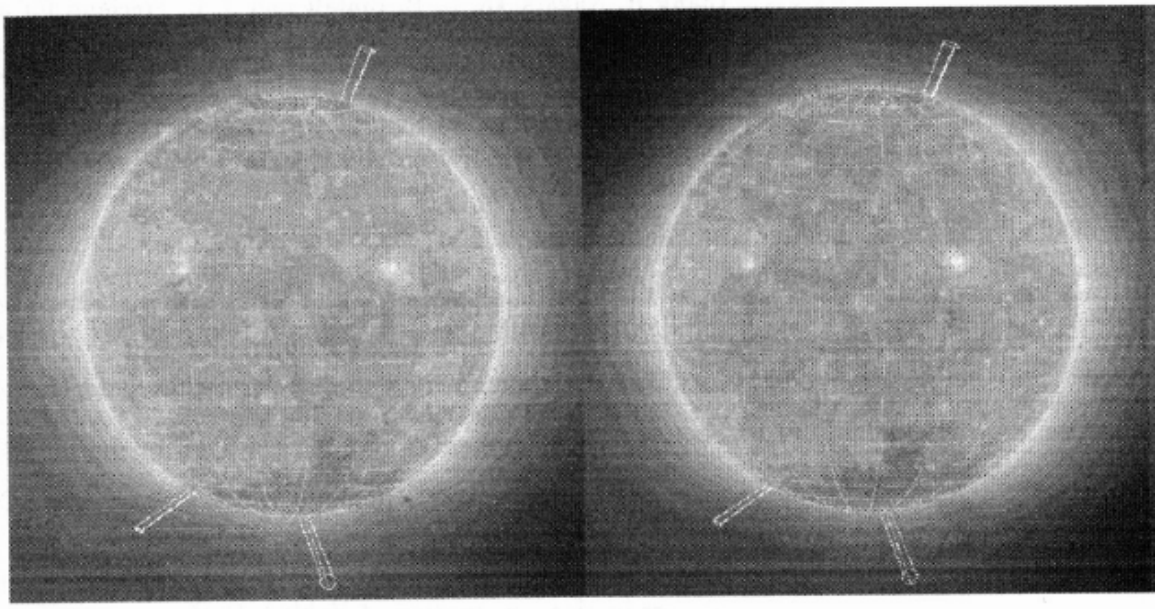

Figure 3. Respectively the left and right pictures for stereovision effect (full images of the sun at 195 $\AA$ (Fe XII) taken april 17th, 1996

A special Carrington grid that appears to vanish under bright plasma clouds (providing a visual reference for the solar surface) is superposed on the images. Stereo movies can be also created with help of numerous intermediate images generated by interpolation between two consecutives images. Stereomodels of polar plumes adapted from Walker and Deforest (1993) are developed and compared with stereoviews to obtain morphology,orientation and evolution of polar plumes.

6. Activity in Coronal Holes and Polar Plumes

One of the most exciting results to have come from early EIT observations has been the realization that solar activity continues at all levels, even during Solar Minimum and even in coronal holes. EIT movies made of the south polar coronal hole during the early operational phases of EIT demonstrate transient brightenings in coronal holes on surprisingly short (2 - 10 minutes) time scales. In addition, the EIT movies have revealed the source areas of polar plumes as regions of possible magnetic flux reconnection and at least in some cases, of mass ejections in "microjets."

7. Conclusion

The EIT is a very versatile instrument that provides full-Sun EUV images covering temperatures characteristic of the chromosphere to the corona. EIT's spatial (2.6 arcsec pixels) and diagnostic capabilities allows us to study a wide range of coronal problems

and enhances the studies made by other diagnostic instruments on the SOHO spacecraft. The EIT images are an important link between observations of the inner and outer corona and will also play an important role in correlating SOHO data with ground-based observations.

Acknowledgments. French laboratories (IAS, IOTA and LAS) were supported by CNRS and CNES. Belgian laboratories were funded by SPPS via PRODEX. NRL received support from the Office of Naval Research and from NASAthrough contract DPR S-19506-E. LSAL acknowledges NASA support through contract NAS5-32627 and NRL contract N00014-90-C-2346 and from the Lockheed Independent Research Program. We benefited greatly from the work of Dr. Barry Labonte of the Yohkoh SXT team who provided an IDL version of the flat-field algorithm of Kuhn et al. (1991). We thank R. Nakatsuka, E. E. Einfalt and S. L. Freeland for aid in developing the ground data analysis system and software. G. Holland contributed greatly to this project by his extensive innovation in vacuum related technologies. We are indebted to the Scientific Imaging Technologies Inc., Tektronix for fabricating the CCDs used in this investigation. We acknowledge the work of the Physikalisch-Technische Studien G.M.B.H. (Germany) and the Luxel Corporation (USA) in fabricating the thin-film filters for the EIT.

8. references

- J.-P. Delaboudinière & al . , EIT: Extreme ultraviolet imaging telescope for the SOHO mission, Solar Physics, n 162, p 291-312, december 1995
- J.-P. Delaboudinière & al . , Solar corona synoptic observations from SOHO with an extreme ultraviolet imaging telescope, ESA (european space agency) & NASA (national aeronautics and space administration), 1989, esa sp-1104
- Eds by B. Fleck, V. Domingo & A.I. Poland, The SOHO Mission, Solar Physics, vol 162, n 1-2, 1995
- F. Portier-Fozzani & al . , EIT images of the EUV solar atmosphere : initial data reduction, proceeding of Yohkoh Bath reconnection meeting, March 1996, to be published in PASJ 1996
- A. Maucherat, F. Portier-Fozzani & A. Martial, June 1996, internal note about stereovision
- W. Neupert & al., May 1996, internal note about science with EIT
- Song, X.Y.(1995)Thesis, Universite d'Orsay (France)
- Walker A.B.C., Jr., DeForest,C.,E., Hoover,R.B., Barbee,T.W. ,Jr. (1993) Sol.Phys.,1
- Koutchmy,S., Molodensky, M.M., Vial, J.C.(1994) IAU Colloq.144"Solar Structures", V.Rusin, P.Heinzel, Vial,J.C. p585 VEDA Bratislava
- Batchelor D.,"Quasi-stereoscopic imaging of the solar X-ray corona", 1994, Solar Physics, 155, 57B

9. Appendix

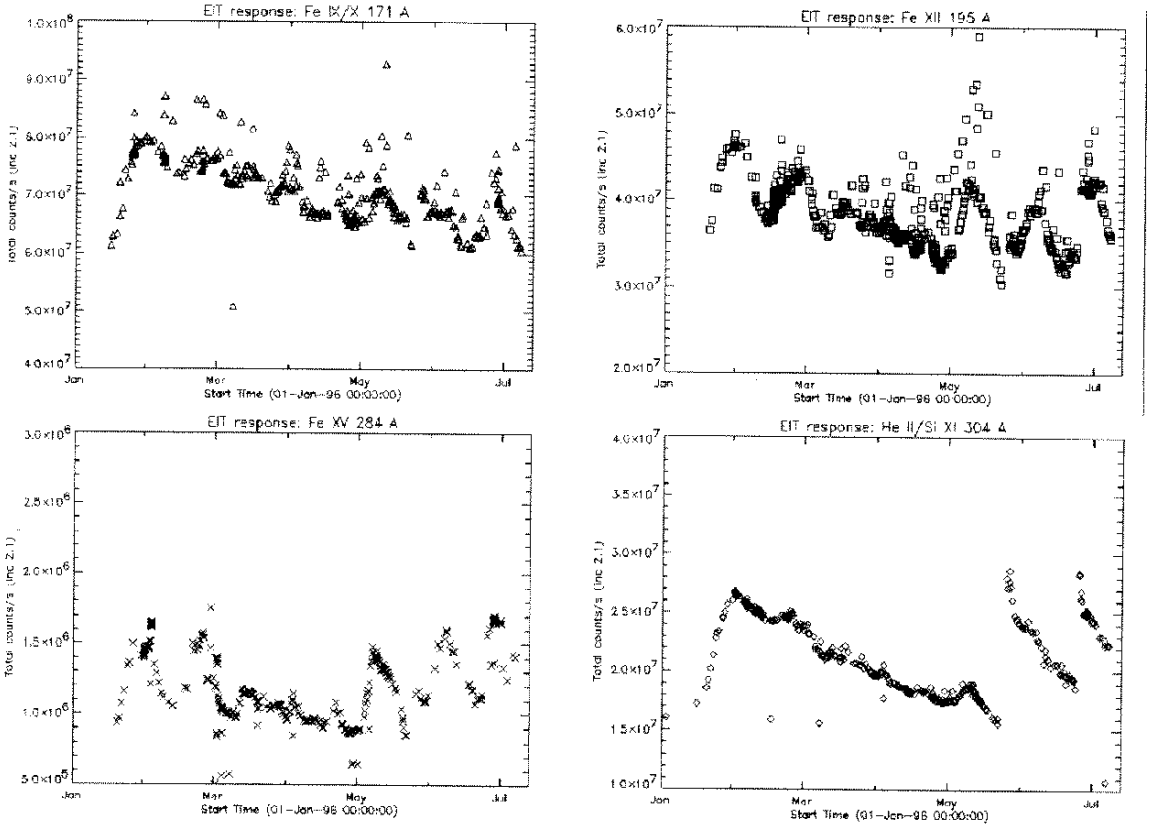
EIT response: Fe IX/X 171 A
EIT response: Fe XII 195 A
EIT response: Fe XV 284 A
EIT response: He II/Si XI 304 A
Total counts/s (inc 2.1)
Start Time (01-Jan-96 00:00:00)
Jan
Mar
May
Jul

Nous reviendrons au chapitre suivant sur la possibilité de contraindre par des modéles géométriques à priori les structures que nous voulons observer en stéréovision.

III.4.2 Limitations actuelles des reconstructions par inversion stéréographique

Vision et vision par ordinateur

L'oeil et le cerveau réalisent pour la "stéréo vision" de nombreux calculs parmis lesquels la mesure des angles de projections et l'inversion de l'image 2D $\Rightarrow$ 3D.

Les limitations interviennent dans la précision sur la définition des droites de fuites, ce qui peut entraîner une certaine incertitude dans la reconstruction et donc une impression de flou dans la définition des "objets". Néanmoins le cerveau arrive à corriger jusqu'à des valeurs angulaires importantes.

Le calcul de paramètres précis en 3D nécessite la formalisation des objets présents dans les images. En effet, les objets doivent être bien définis (taille, structure, position) pour pouvoir être calculés car il n'est plus question de faire "accommoder l'oeil" lors de la reconstruction.

La vision par ordinateur ([233]) définit des concepts présents dans chaque image tels que les textures, les structures principales, etc... L'extraction de primitives d'une image permet de définir celle ci et de mathématiser les objets présents dans l'image. On peut alors appliquer différentes transformations sur chacun des objets.

La formalisation des transformations permettant la reconstruction 3D à partir d'images 2D conceptualisées s'explique à partir de notions de géométrie projective ([152]) dont la base est exposée au paragraphe suivant.

Deux principales étapes constituent le départ des algorithmes de reconstruction par stéréovision tel que celui de l'INRIA :

1. Il faut d'abord échantillonner l'objet (comme en imagerie classique). Le plus simple est de considerer que chaque objet 3D -si complexe soit il- est composé de petites facettes planes (2D) définies par 3 points. On appelle cela la triangulation.
2. Il suffit alors connaître l'image de ces 3 points par la transformation. Cette étape de mise en correspondance est décrite dans Chabbi [45].

Précisons maintenant quels types de transformations projectives nous allons pouvoir utiliser dans la reconstruction.

Mise en équation de la stéréovision et techniques de géométries projectives : les premiers pas

1. Le point M représente l'objet à observer (Fig. III.14). Ses images respectives prises par les caméras C_1 et C_2 sur les plans (u_1, v_1) et (u_2, v_2) sont m_1 et m_2. Le problème

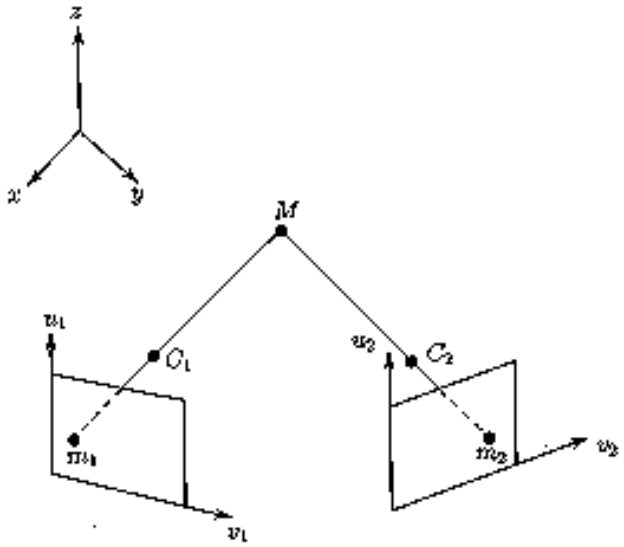

Figure III.14: Stéréovision : La vision 3D

posé est celui de la reconstruction c'est à dire connaissant m_1 et m_2 trouver M. Connaissant les matrices de passage des caméras P_i (*i.e.* $m_1 = P_1.M$ et $m_2 = P_2.M$) et les centres optiques (*i.e.* $P_i.C_i = 0$ par définition de C_i [77]), on trouve M comme étant $P_1^{-1}m_1$ ou $P_2^{-1}m_2$ (où P^{-1} sont les matrices "inverses").

2. Lorsque l'on a 2 points M et N (Fig. III.15) la question d'appartenance ou non au même objet se pose. Il s'agit donc de classer les objets par ordre. La notion mathématique de connexité[10] permet de résoudre cela.

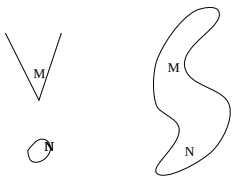

Figure III.15: Connexité ou non de M & N

3. Il s'agit alors de reconstruire l'ensemble de l'objet. Pour cela, on va choisir un échantillonnage adéquat sur les images, faire l'inversion de ses points et ensuite

[10] La connexité est une généralisation à 3D de la notion de continuité d'une fonction. On distingue connexe = en un morceau ; et simplement connexe = sans trou.
Les démontrations formelles mathématiques utilisent l'analyse et la topologie. On prend pour cela une famille de lacet (fonction continue) de M à N, et on regarde la continuité de la famille de fonctions. S'il est toujours possible de construire une famille continue de fonction entre M et N, la surface qui regroupe M et N est simplement connexe. Si par contre, il existe des fonctions qui vont de M à N mais il n'existe pas d'application continue permettant de passer d'une fonction à une autre alors, M et N sont connexes. Si enfin il n'existe aucune fonction permettant d'aller de M à N, alors ces 2 points font parties de surfaces disjointes.

interpoler en 3 dimensions.
La triangulation de Delaunay (qui consiste à approximer l'objet par des éléments triangulaires contigus –Fig. III.16–) et les squelettes sont adaptés à cette étape. En effet, il faut creer des echantillonages représentatifs tels que leurs maillages permettent une reconstruction optimale. Le choix de triangles conjoints s'apparente à la définition d'une surface (ou facette) calculée avec la "norme inf" (*ie* la distance inférieure). On obtient ainsi des miniplans que l'on peut reconstruire facilement : il suffit de déterminer l'image des 3 points sommets.

Figure III.16: Triangulation de Delaunay d'une main ([246]) : Il s'agit de générer sur chaque image une triangulation 2/3 (c'est à dire un assemblage de triangle 2D dans un espace euclidien $\mathbb{R}^3$) qui fait donc un pavage dense de l'image. Il suffit alors de reconstruire chaque petit plan facette, c'est à dire connaître les images de 3 points par une application (transformation affine donnée)

L'approche explicite

1. Dans le cas général l'étape suivante consiste à déterminer la géométrie épipolaire et définir le plan (C_1MC_2).

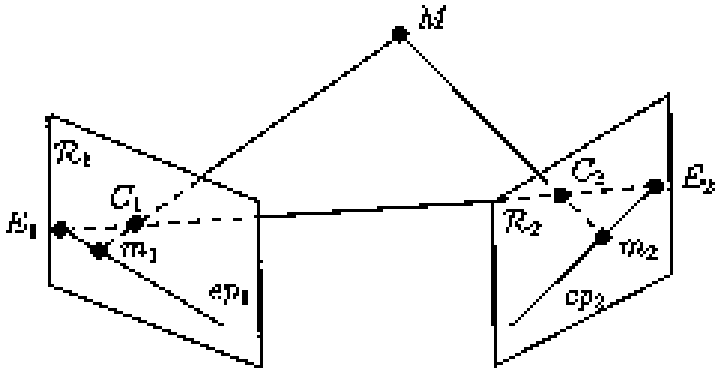

Figure III.17: Stéréovision : La géométrie épipolaire

2. Un cas simple pour la compréhension du problème et sa mise en équations, est celui des caméras parallèles. On utilise les notations de la Figure III.18 (en particulier on

note les coordonnées sur les plans images $m_1 = (\nu_1, \mu_1)$ et $m_2 = (\nu_2, \mu_2)$). D'après le théorème de Thalès on a :

$$\frac{\nu_2 - \nu_1}{d_{1.2}} = \frac{f}{z} \tag{III.1}$$

et

$$\frac{x}{d_{1.2}} = \frac{1}{2}\frac{\nu_1 + \nu_2}{\nu_1 - \nu_2} \tag{III.2}$$

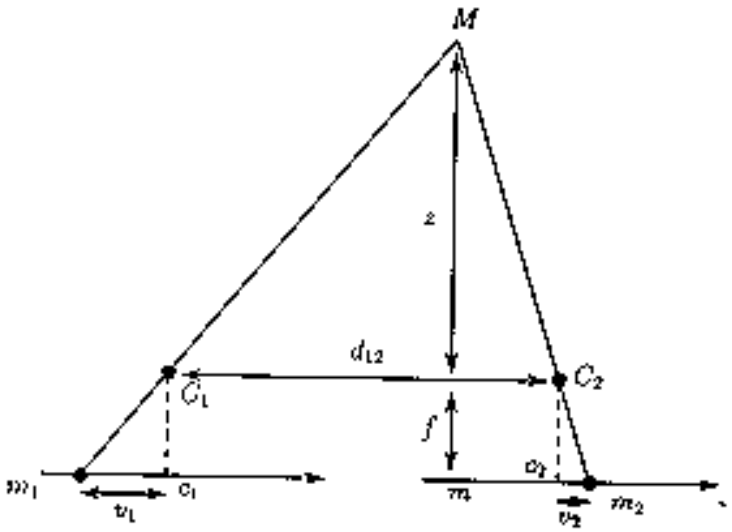

Figure III.18: Stéréovision : Les relations entre la profondeur et la disparité

On obtient donc des relations entre les coordonnées sur les 2 images $(\nu_1, \nu_2, \mu_1, \mu_2)$ et les coordonnées réelles du point 3D (x,y,z). Cela permet de recalculer la position du point en 3D à partir de 2 images.

3. Dans le cas général, les caméras se trouvent dans des plans quelconques avec une distance connue. L'approche explicite suit le même principe que ci-dessus. Faugéras [77] présente les lignes générales de ce calcul.

Géométrie projective

Il existe une autre approche pour résoudre ce problème : l'approche implicite.
Son nom vient du fait que les transformations employées pour la reconstruction ne sont pas explicitées.

Par définition, un espace projectif $\tilde{X}$ est la "somme" de l'espace affine X auquel on rajoute l'ensemble des points à l'infini (c'est à dire l'ensemble des directions des droites de X).

Ainsi 2 droites parallèles en géométrie affine correspondent à 2 droites sécantes au point Ω en géométrie projective. (Cela se résume dans le langage courant en disant que 2 droites parallèles se coupent à l'"infini". Dans le langage de la géométrie projective cela signifie que 3 droites projectives se coupent alors au point Ω, la dernière étant l'horizon de l'espace affine précédant.)[11].

Il s'agit alors de définir entre ces espaces les transformations (ou applications) possibles. Par exemple le choix de l'"infini" détermine l'espace affine de travail mais par l'intermédiaire des espaces projectifs, on peut déterminer des applications bijectives entre espaces affines et donc des transformations entre séquences temporelles. En effet, une image à un instant peut être représentée comme un graphe contenu dans un espace affine de dimension 2. La variation temporelle nous donne une variation des lignes de fuites, c'est à dire des autres espaces affines de dimension 2. Une fois définies les transformations adéquates pour passer d'un plan affine à un autre, on peut ainsi tout reconstruire dans un ensemble affine de dimension 3.

Le développement de certaines de ces équations est donné dans [152]. Nous allons toutefois motiver notre démarche en montrant la possibilité de telles transformations dans ces espaces. A titre d'exemple, pour définir les coordonnées, montrons que l'ensemble des directions de droites dans un espace de dimension 2 est isomorphe à un espace de dimension 1 plus 1 point : On appelle couramment ce dernier espace la droite achevée.

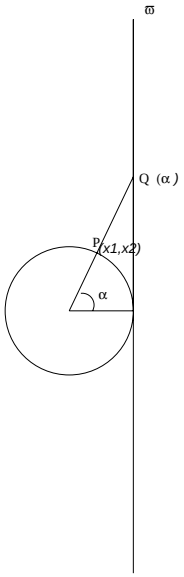

Figure III.19: Isomorphisme entre un cercle et une droite plus un point

- Dans $\mathfrak{P}^1 =$ l'ensemble des droites de $\mathbb{R}^2$, on a:

[11]Cette notion de perspective formalisée en mathématique fut utilisée dès la Renaissance en peinture, et plus récemment pour construire des images "impossibles" (*e.g.* Escher, [74])

$$\vec{e_1} = \begin{pmatrix} 1 \\ 0 \end{pmatrix}$$

et

$$\vec{e_2} = \begin{pmatrix} 0 \\ 1 \end{pmatrix}$$

d'où $\vec{x} = x_1.\vec{e_1} + x_2.\vec{e_2}$ si $x_2 \neq 0$ alors $\vec{x} \sim \alpha\vec{e_1} + \vec{e_2}$ avec $\alpha = \frac{x_1}{x_2}$.

On a donc

$$G : \begin{cases} \mathbb{R}^2 \longrightarrow \mathfrak{P}^1 \\ (x_1, x_2) \longrightarrow \alpha \end{cases}$$

L'isomorphisme entre $\mathfrak{P}$ et $\mathbb{R} \bigcup \{\infty\}$ résulte de la bijectivité de l'application qui transforme un point P du cercle en un point Q de la droite (Fig. III.19). C'est à partir de cette application que l'on construit l'ensemble des directions de droites (y compris la verticale) et donc l'espace projectif associé.

- Soit par définition $\mathfrak{P}^m$ = l'ensemble des droites de $\mathbb{R}^{m+1}$. On a alors $\mathfrak{P}^m \sim \mathbb{S}^m \subset \mathbb{R}^{m+1}$ avec $\mathbb{S}^m$ la sphère unité de l'espace $\mathbb{R}^m$

La définition de telles applications bijectives dans ces nouveaux espaces permet donc de définir la transformation des coordonnées. En stéréovision, pour des "plans affines non parallèle" la transformation se fait directement comme au paragraphe précédent. Par contre pour des plans parallèles, il faut définir entre espaces projectifs la transformation projective de passage de l'image ([152]).

III.4.3 Problèmes et contraintes de la stéréovision

Généralités

1. La définition des mini-objets à mettre en correspondances peut être arbitraire et difficile comme le relève [246]. En effet, en théorie de la vision, l'extraction des primitives est quelquefois non unique ce qui empêche la modélisation automatique par relation biunivoque.

2. La définition des paramètres des caméras (les matrices P_i) doit être connue avec précision ([143]).

3. Les projections sont non linéaires rajoutant du "bruit" à la méthode et impliquant des incertitudes dans l'inversion ([45]).

Les problèmes et contraintes sur les objets solides ont été étudiés dans le cadre du projet Syntim par l'INRIA. Ce projet a abouti au développement d'algorithmes d'inversions décrits par ([246]) dans le but de pouvoir diriger des robots.

Sans rentrer dans les détails de ces algorithmes mais afin de déterminer la faisabilité de la méthode envisagée pour la couronne solaire dans son ensemble, nous avons mesuré les écarts observés entre les images originales et les images reconstruites afin de connaître les incertitudes de la méthode de reconstruction pour des objets solides.

La méthode d'inversion de l'INRIA

L'algorithme de l'INRIA tout d'abord extrait de l'image originale (respectivement Fig. III.20 à gauche et Fig. III.21 à gauche) les primitives de l'image (respectivement Fig. III.20 au centre et Fig. III.21 au centre). A partir de là sont extraits et numérotés les objets (respectivement Fig. III.20 à droite et Fig. III.21 à droite).

La totalité de la méthode est expliqué dans [45] p. 55 et p. 61.

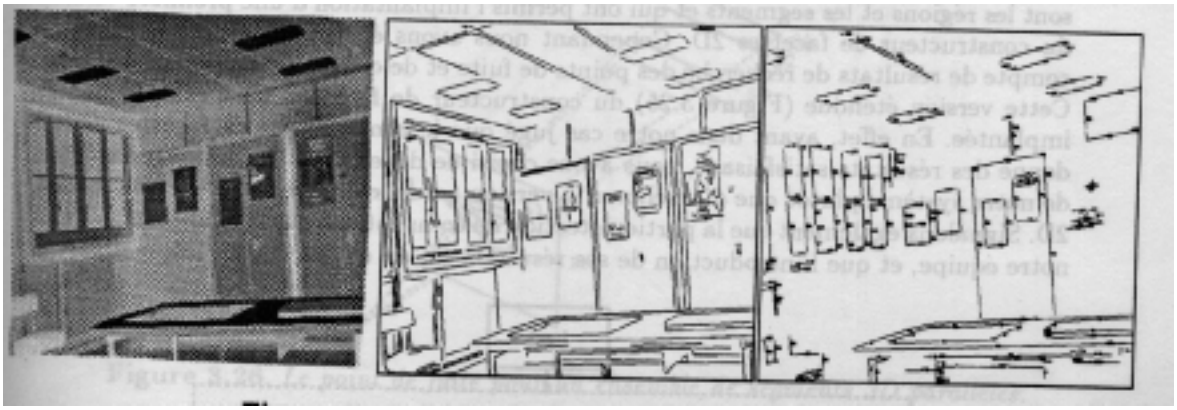

Figure III.20: Photo originale (orientation 1), extraction des primitives

Figure III.21: Photo originale (orientation 2), extraction des primitives

On mesure les variations de distance entre les objets de la figure III.20 à droite avec les objets reconstruits de la figure III.22 à gauche. On fait de même pour ceux de la figure

III.21 à droite avec ceux reconstruit de la III.22 à droite.

Pour cela, on mesure l'erreur définie par $\sigma^2 = \Sigma \|\vec{p}_{original} - \vec{p}_{reconstruit}\|^2$ où $\vec{p}_{original}$ et $\vec{p}_{reconstruit}$ sont respectivement les points originaux et reconstruits.

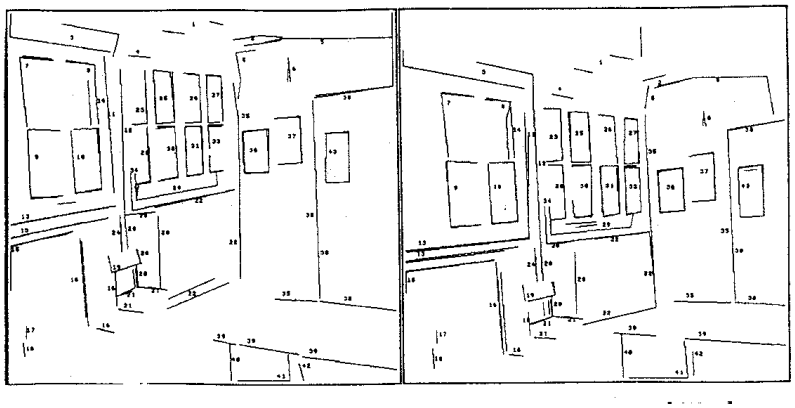

Figure III.22: Reconstruction orientation 1 et orientation 2 : Les erreurs sont mesurées entre Fig. III.20 et Fig. III.21

Les resultats d'inversions dans le cas optiquement épais

Soient (x_1, y_1) les coordonnées du point P_1 dans le référentiel de l'image et $(\tilde{x_1}, \tilde{y_1})$ coordonnées du point $\tilde{P_1}$ reconstruit dans le référentiel de l'image reconstruite. La figure III.23 donne le lieu de $\tilde{P}$ "autour de P" c'est à dire l'ensemble des points reconstruits.

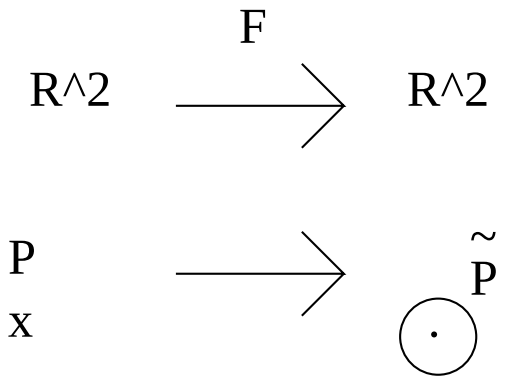

Figure III.23: Limitations actuelles des méthodes d'inversions :
On considère l'application mathématique dans le plan image qui a partir du point réel (à gauche) aboutit à un ensemble de points reconstruits (à droite). C'est une application $F : \mathbb{R}^2 \longrightarrow \mathbb{R}^2$

L'erreur sur la reconstruction pour un point "solide" s'écrit
$||P_1\tilde{P_1}|| = \sqrt{(x_1 - \tilde{x_1})^2 + (y_1 - \tilde{y_1})^2}$

Problèmes rencontrés pour l'inversion 3D de la couronne solaire

Aux problèmes précédents de reconstruction d'objet "solide", se rajoute les incertitudes intrinsèques sur la position puisque la couronne est optiquement mince avec SOHO/EIT. On a $I(x,y) = \int EM\vec{dl}.\vec{n}$ (*c.f.* Annexe).
Diverses méthodes pour mesurer la colonne d'intégration existent ([15]). Le positionnement d'un point sur une image s'écrit en fait $(x(\vec{\xi}), y(\vec{\xi}))$ avec $\vec{\xi}$ la direction d'intégration (vecteur 3d).

Pour borner l'erreur nous allons utiliser l'astuce suivante : on considère chacun des points de la ligne de visée de manière séparée et on les reconstruits. On trace alors le contour des lieux des $\tilde{P}$. Celui ci se retrouve donc être -par construction- comme la plus mauvaise reconstruction possible. Ainsi, on obtient une borne supérieure de l'erreur.

La figure III.24 résume les résultats trouvés.
L'erreur ainsi trouvée dans un cas général est trop importante (Fig. III.25).

Une autre erreur vient s'ajouter à celle ci : le calcul précédent à été fait en supposant que les structures varient peu entre 2 images stéréographiques. En pratique la dynamique

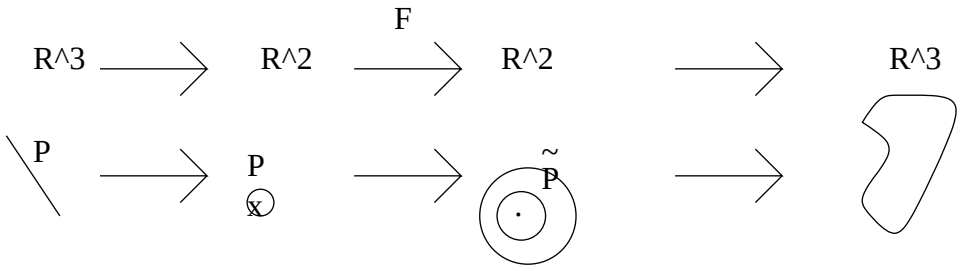

Figure III.24: Limitations actuelles des méthodes d'inversion: La reconstruction en 3 dimensions dans le cas des ions coronaux ou des nuages atmosphérique optiquement mince est une application $G : \mathbb{R}^3 \longrightarrow \mathbb{R}^3$. Elle est composée d'une projection selon une ligne de visée, de l'application F précédante Fig. III.24, et de la recomposition en 3D selon la ligne de visée. A partir du point réel (à gauche) on mesure les différentes erreurs cumulatives qui aboutissent à un ensemble de points reconstruits (à droite).

de la couronne est telle que en analysant de nombreux anaglyphes, il ressort une impression de "flou" fréquente qui se traduit par un manque de corrélation entre les structures. Toutefois l'oeil arrive à acclimater ce que ne peut faire une méthode complètement automatique. Donc la reconstruction complète de la couronne par stéréovision semble prèmaturée à moins de pouvoir prendre réellement 2 images en même temps (ce qui est le but de la futur mission STEREO).

Par contre si l'on se limite à vouloir reconstruire certaines structures uniquement (comme les boucles par exemple), nous pouvons introduire une forme à priori pour faire converger le modèle avec moins d'erreur. C'est le principe de la reconstruction avec contraintes que nous développerons au chapitre suivant.

III.5 Vision 3D : Conclusion sur les méthodes stéréo

Nous nous sommes servis de cette étude pour analyser la faisabilité de telles techniques en UV. En plus de la difficulté de trouver des couples d'images où les structures n'ont pas varié spatialement avec le temps, il est très vite apparu que

1. comme pour SOHO/EIT un "point" M de la couronne vu en Fe IX/X,
   Fe XII, Fe XV est en fait le résultat d'une intégration sur une ligne de vue à cause de la profondeur optique de la raie. Cela induit une incertitude sur la position du "point".

2. Les méthodes d'inversion actuellement disponibles pour des objets solides génèrent des erreurs importantes dans la reconstruction ([45], [246], [77])

L'inversion totale (autre que visuelle) pour des raies UV est prématurée (Fig. III.25). Les évolutions des structures coronales viennent encore rajouter des incertitudes. La simultanéité des données avec la mission STEREO devrait lever ce problème. De plus les

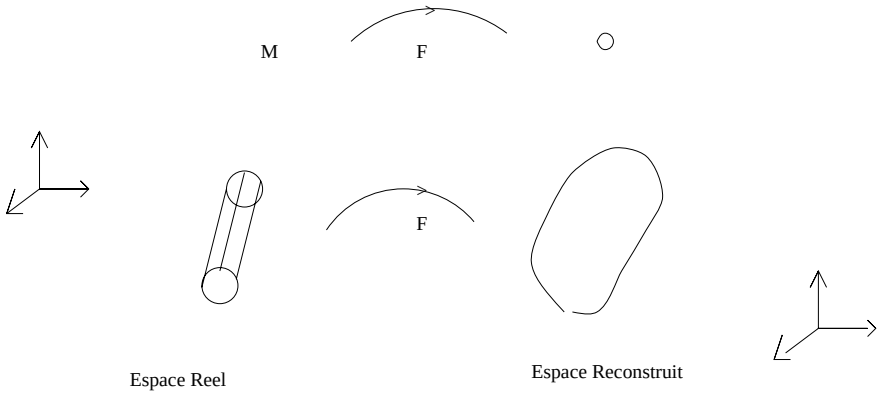

Figure III.25: Stéréovision : Limitations théoriques actuelles des méthodes d'inversion:
A gauche : point réel, à droite : point reconstruit.
En haut, Inversion obtenue pour un point précis défini spatialement
(Mesuré sur [45] p. 55 et p. 61 en comparant respectivement III.20 avec III.22a d'une part, et III.21 avec III.22b d'autre part)
En bas, Inversion dans un cas type EIT où l'intégration à lieue sur une Ligne de Visée -LdV- augmentant l'ensemble des solutions possibles.
(Extrapolation d'après les incertitudes de la LdV et la mesure de [246]).

techniques d'inversion auront été améliorées. Cela devrait donc permettre de donner lieu a de meilleurs résultats.

Toutefois la prise en considération d'un modèle à priori permet d'hors et déjà de reconstruire par stéréovision les structures considérées. Dans le chapitre suivant nous présenterons une méthode que nous avons développée qui permet de reconstruire en 3D des boucles coronales.

Chapter IV

Les Boucles Coronales

Ote toi de mon soleil
Diogène (413-323 avt JC),
Réponse à Alexandre Le Grand

Sommaire

Après avoir présenté les propriétés principales des boucles coronales, nous analyserons certaines de ces boucles. Les boucles sont présentes à différentes températures et à différentes échelles. L'étude de leurs morphologies est importante car les boucles sont un moyen de transfert de l'énergie magnétique en chauffage. Nous allons mettre en place dans ce chapitre des outils 3D permettant cette étude et nous analyserons des données de SOHO/EIT afin de mieux comprendre leurs propriétés physiques et leurs évolutions.

IV.1 Différents types de boucles

Les boucles de plasma, en forme d'arcs de "cercles", sont les structures dominantes dans la haute atmosphère solaire. Elles se situent généralement au dessus des taches solaires et

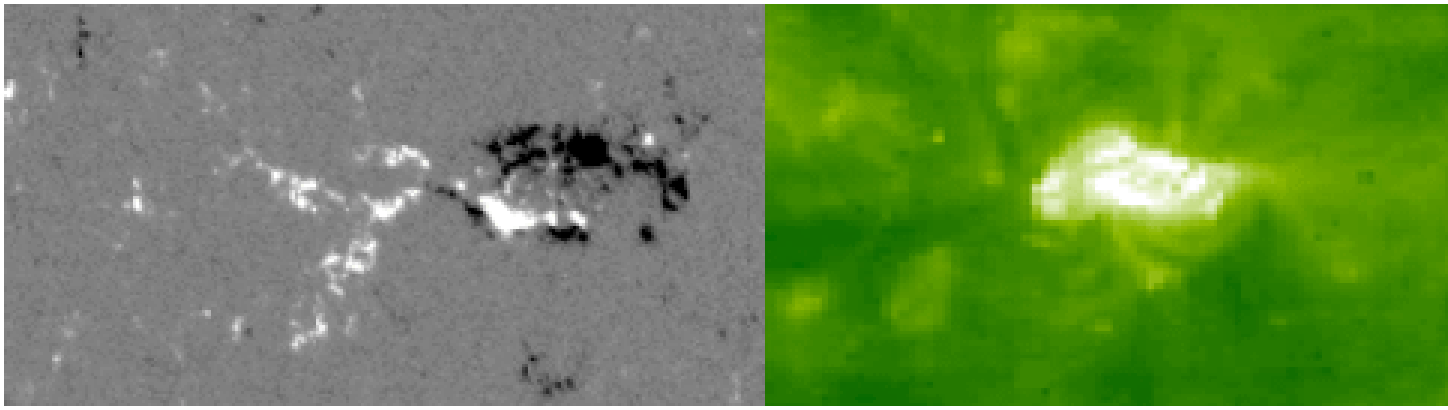

Figure IV.1: Boucles du 02/02/1997 vues en EUV par SOHO/EIT Fe XII et magnétogramme de SOHO/MDI correspondant. Chaque boucle de plasma suit les lignes du champ magnétique et relie une polarité positive (en blanc sur le magnétogramme) à une polarité négative (en noir)

connectent des régions de polarités magnétiques opposées (Fig. IV.1). Les boucles correspondent au confinement du plasma le long des lignes de champ magnétique fermées. Les boucles peuvent être très variées en taille (1 à 70Mm), en température ($10^4 - 10^6 K$) et en durée de vie (de quelques minutes à quelques mois) et coexister. Les boucles coronales peuvent être plus chaudes d'un million de degrés que l'environnement [101]. Il faut véritablement attendre le lancement de SOHO et de Yohkoh, pour avoir une résolution temporelle et spatiale importante pour bien etudier ces structures dont l'intérêt et l'importance dans la couronne ont été révélés lors de fusées (X), ou de la mission Skylab (EUV) et tenter de comparer aux morphologies observées en H_α.

On distingue classiquement 2 types de boucles :

- **Les boucles chaudes :** $T > 10^6 K$
  La table IV.1 résume leurs principaux paramètres. Elles sont vues en EUV et X. Les lois d'échelles des boucles en X ont été définies grâce a Yohkoh (Klimchuk et Porter, [125]). Yoshida & Tsuneta ([268]) avec Yohkoh ont montré que les structures en boucles avec un court temps de vie (inférieur à quelques heures) ont en général de plus hautes températures (5-8 MK) que les boucles avec des durées de vie plus longues (3-4MK).

- **Les boucles froides :** $T < 10^6 K$ La table IV.2 résume les principaux paramètres. Bray & Loughhead ([30]) ont montré que les pieds des boucles froides (H_α) correspondent à l'ombre photosphérique des taches solaires c'est à dire au plus fort champ magnétique.

Toutefois les structures des régions actives ne sont que rarement des boucles à une seule température.
Dans le cas de la Fig. IV.2, les boucles sont présentes simultanément sur des images prises avec différents filtres d'EIT. La partie la plus chaude se trouve au centre du "cylindre".

Température	$Te = 2.0 \times 10^6 - 3.2 \times 10^6$ K
Densité	$Ne = 8.0 \times 10^8 - 6.0 \times 10^9 cm^{-3}$
Pression du gaz	2.4 dyne cm^{-2}
hauteur (projetée)	25000-200000km
Séparation des pieds	250000-500000km
Diamètre	5000-30000km
Durée de vie	heures-jours

Table IV.1: Valeurs usuelles des boucles chaudes non éruptives observées en rayons X (d'après [31])

Température	Te = 21000 K
Densité électronique	$Ne \sim 5.6 \times 10^{10} cm^{-3}$
Pression du gaz	0.36 dyne cm^{-2}
Hauteur (véritable)	40000-53000 km
Séparation des pieds	71000-86000 km
Diamètre	de 1600 (habituellement) à 500 km.

Table IV.2: Valeurs usuelles des boucles froides non éruptives observées en $H\alpha$ (d'après [31])

Cela peut être analysé comme comme la conséquence de la conduction thermique de la partie chaude vers la partie froide (Yoshida [268] et Kano [121]).
Le plasma confiné par le champ magnétique peut être parfois aussi chauffé localement.

La comparaison de boucles à différentes températures peut aussi faire apparaître un gradient entre les pieds et le haut des boucles. Sur la Fig. IV.1, les observations simultanées par SOHO/EIT et SOHO/CDS le 24 et 25 Mars 1996 d'une même région active de boucles montrent que la température en haut de la boucle (I) est plus chaude que les pieds de celle ci (*cf.* la grande boucle vue en Fe XVI dont seulement la partie basse est vue en Fe IX/X).

Rosner, Tucker, & Vaiana [202], Serio *et al.* [214] ont montré par une analyse avec une large bande en X et des calculs théoriques que les boucles chaudes avaient une température maximale au sommet. Kano & Tsuneta [121] ont ainsi trouvé une température au sommet 1.2 fois supérieure à celle des pieds de la boucle. Rosner *et al.* ([202]) ont établi que pour ce type de boucles, la température au sommet de la boucle est liée à la pression p et à la longueur L de la boucle :

$$T_{Max} = 1.4 \times 10^3 (pL)^{\frac{1}{3}} \tag{IV.1}$$

Kano & Tsuneta ([119]), à partir de statistiques sur des observations de Yohkoh, trouvent un exposant se rapprochant davantage de $\sim 1/5$.

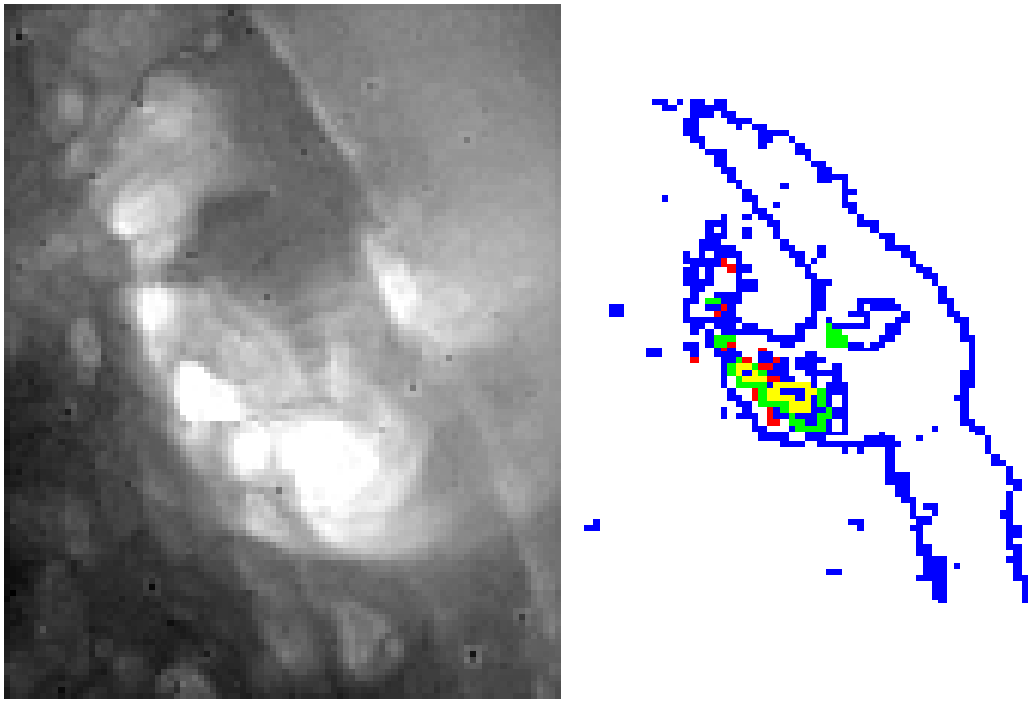

Figure IV.2: SOHO/EIT 08 Aout 1998 : A gauche, une image EIT en Fe XII.
A droite : Superposition du contour transverse des boucles à différentes températures. A cause de la position de la région active, on obtient en fait une coupe en tranche en température :
Le rouge correspond au contour de la boucle en He II, le bleu en Fe IX/X, le vert en Fe XII, le jaune en Fe XV.
On notera que le centre des tubes de flux magnétiques de l'ARL coincide avec les boucles les plus chaudes.

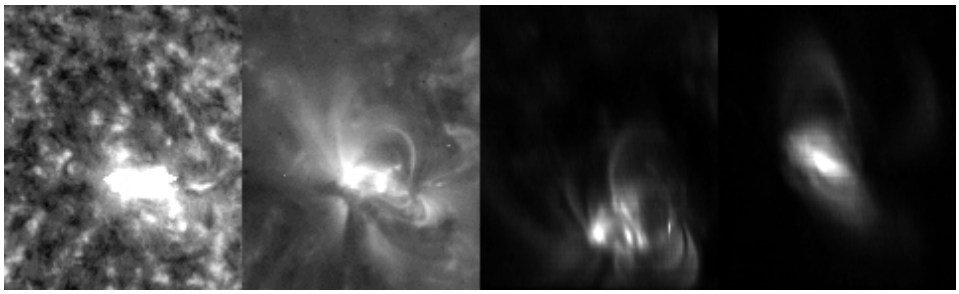

Figure IV.3: Comparaison d'images SOHO/EIT et CDS : (collaboration avec P. Young)
De gauche à droite par température croissante (cf. Fig. II.12).
Respectivement He II et Fe IX/X d'EIT; Mg IX et Fe XVI de CDS

La petite boucle (II) de l'AR est vue uniquement en Fe IX/X. Il n'y a donc sans doute pas de gradient de température[1]. Si on essaye d'appliquer la formule précédente en considérant que $T_{Boucle\ II} = T_{Max}$ les pressions des 2 boucles (la petite de température

[1]Nous démontrerons rigoureusement au paragraphe suivant de ce chapitre que de telles boucles sont effectivement isothermes.

inférieure et la grande boucle (I) observée à plus haute température) peuvent être très voisines.
Les boucles plus froides ont été mesurées comme étant des structures isothermales et hydrostatiques par Gabriel & Jordan [85].
Nous venons de voir que des boucles pouvaient coexister avec des températures différentes en ayant des conditions de pressions voisines. D'autres études montrent en comparant l'UV et l'X que des boucles de températures différentes peuvent être très proches et que les plus tièdes ne semblent pas provenir du refroidissement du plasma chaud [150]. Cela impliquerait le résultat suivant : chaque boucle est chauffée individuellement par sa ligne magnétique propre.
L'étude sur les variations de températures en fonction des boucles nécessite une bonne connaissance de leurs géométries. Il convient donc dans un premier temps d'élaborer des outils performants permettant de trouver les paramètres physiques pertinents.
D'un point de vue modélisation théorique, jusqu'a nos jours structures et dynamiques des boucles étaient traitées dans l'approximation d'un plasma mono fluide (par *e.g.* Landini & Monsignori Fossi [129], Rosner, Tucker & Vaiana [202], Serio et al. [214], Wragg & Priest [263],). Ces approches ont permis de mettre en évidence de maniere théorique des conditions physiques d'existance des boucles (rôle de la gravité, asymétries,...).
Récemment des approches bifluides avec des ondes (Wu & Fang [264]) ont montré pourquoi les boucles X les plus brillantes étaient ancrées dans la pénombre des taches solaires (Klimchuk & Porter, [125]) où le champ magnétique normal à la photosphère est plus faible que dans l'ombre des taches solaires (Solanki [226]).
Klimchuk *et al.* ([123]) ont trouvé que la section transverse[2] des boucles X est relativement constante. Des courants électriques qui contraignent le plasma peuvent expliquer cela (Wang & Sakurai, [251]).
Le facteur de remplissage[3] du plasma dans le tube de flux estimé à partir de données Yohkoh multi-filtres, reste controversé ([123]).
La section transverse sera calculée pour les boucles EUV vues par EIT ([15]). Le facteur de remplissage nécessite plusieurs filtres simultanément et une étude préliminaire réalisée en collaboration avec Jim Klimchuk a montré l'intéret de CDS pour de telles mesures. Les programmes utilisés dans cette étude sont présentés dans l'annexe.
Les boucles coronales ne sont généralement pas statiques. La couronne solaire est parfois la source d'évènements très énergétiques appellés éruptions, à partir desquels on observe parfois des boucles d'après éruptions. Schmieder et collaborateurs ([220]) ont proposé un modèle dans lequel les boucles froides en H_α sont formées à partir des boucles chaudes (vues par SXT).

Les boucles constituent donc une partie très importante de la couronne solaire. De différentes tailles, elles jouent un rôle très important dans le processus de transfert d'énergie magnétique en chauffage. Certaines peuvent d'érupter soit par le développement d'instabilités internes soit par reconnection avec d'autres lignes de champ. Dans ce chapitre nous allons essayer d'établir des liens observationnels entre la morphologie des boucles et la possibilité de développement d'instabilités. La théorie MHD prévoit que certaines ondes sont

[2]"cross section" en langue anglaise, couramment appelé largeur des boucles
[3]filling factor

favorisées dans certains cas d'assymétries. Afin d'étudier le rôle des assymétries, nous allons mettre en place un modèle d'ajustement des boucles qui permet de trouver différents paramètres de taille et de torsion. Ces paramétres seront étudiés pour faire de la statistique sur une région active et trouver d'autres paramètres physiques tels que la température le long de la boucle, pour étudier l'émmergence d'une region active, enfin pour étudier à long terme l'évolution d'une région active. La résolution maintenant disponible permet désormais de faire de telles mesures qui permettont de mieux comprendre le rôle des ARL et leurs stabilités, celles ci pouvant entrainer des processus de chauffage. De plus, cette étude portera sur des boucles de température intermédiaire entre la partie chaude de la couronne et celle plus froide en H_α ce qui permettra de mieux comprendre les changements de températures.

IV.2 Les boucles EUV : des maillons intermédiaires pour comprendre le chauffage coronal

Notre étude va se centrer sur les boucles intermédiaires en température (1MK—1.5MK) qui peuvent être bien étudiées avec SOHO/EIT. L'intéret de ces boucles est qu'elles peuvent permettre de mieux comprendre la région de transition et la partie "froide" de la couronne. La formation et l'évolution de telles structures peuvent améliorer la compréhension du processus de chauffage.

IV.2.1 Les différents comportements des boucles EUV

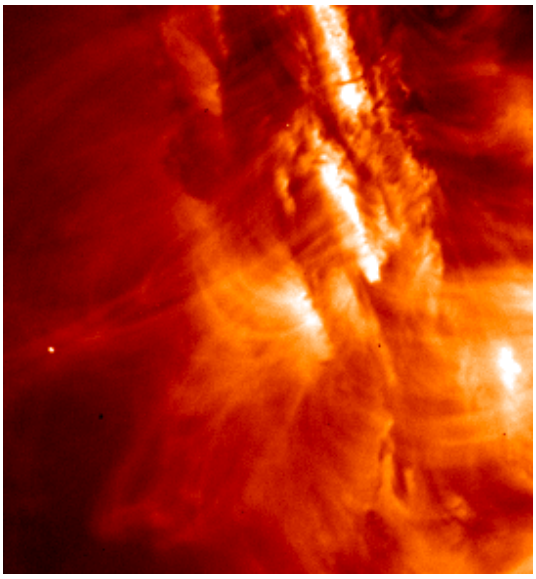

Figure IV.4: Boucles vues par TRACE Fe XII : le champ magnétique bien que continu ne trace que certaines boucles

Comme le paramètre plasma est petit ($\beta << 1$), les boucles tracent en 3 D le champ magnétique coronal puisque $div(\vec{B}) = 0$. Dans les régions actives, alors que le champ magnétique est continu de maniere transverse, les observations montrent des boucles individuelles bien séparées et définies. Certaines images montrent que le tube de flux ainsi révélé n'émet pas forcément sur toute sa longeur. Le plasma est ainsi confiné mais pas forcément (suffisamment) chauffé pour émettre. C'est le même phénomène qui rend seulement certains tubes de flux magnétiques visibles dans une région active (Fig. IV.2.1) alors que le champ magnetique est partout présent (avec un gradiant d'intensité). En effet, seules certaines lignes de champs sont fortement chauffées et le plasma émet alors en EUV. Les processus entrant en jeu sont encore partiellement incompris. Les ondes qui se développent dans les tubes de flux peuvent aussi influer sur leur luminosité.

IV.2.2 Durée de vie des tubes de flux et des boucles

Plusieurs échelles de temps interviennent :

1. le temps d'existence τ_{ib} individuel d'une boucle (qui correspond au maintient du plasma en densité moyenne et température moyenne le long de la ligne de champ)

2. le temps d'existence τ_{tf} du tube de flux (les boucles se créent, disparaissent et se recréent le long des tubes de flux).

En suivant la region active de boucle numérotée NOAA 8026 le 1997-04-02 on constate qu'entre 8h et 23h la bipolarité reste stable mais les boucles se forment et se déforment sans cesse (Fig. IV.5). Les boucles se reforment en permanence autour de tubes de flux "moyens" qui conservent les propriétés globales à travers le temps. Cet effet a été étudié en X par Porter & Klimchuk, [180]. Les calculs réalises pour l'article [15] montrent que $\tau_{ib} \sim 35mn$ et que $\tau_{tf} >$ quelques dizaines de jours ce qui est conforme aux résultats trouvés dans la littérature.

Donc, par abus de langage —sauf indication contraire— nous conviendrons d'appeler "boucles" les tubes de champs magnétiques "moyens". Pour des échelles temporelles courtes —quelques heures— les notions de tubes de flux et des boucles de plasma chauffé coïncident. A plus grande échelle de temps, on considère que le tube peut être ou ne pas être rempli.

IV.2.3 Aspect des boucles : Torsadage, Cisaillement, Gauchissement

L'aspect des boucles peut être très différent. Comme nous allons le voir, il traduit souvent l'énergie interne du champ magnétique. A cause du manque de résolution spatiale sur les instruments jusqu'alors disponibles, peu d'études ont porté sur l'aspect énergétique impliqué par des contraintes morphologiques. Pourtant depuis la boucle potentielle circulaire jusqu'à la boucle fortement cisaillée prête à érupter, la morphologie des boucles joue un rôle important. Avant de définir les critères énergétiques nous allons décrire les divers

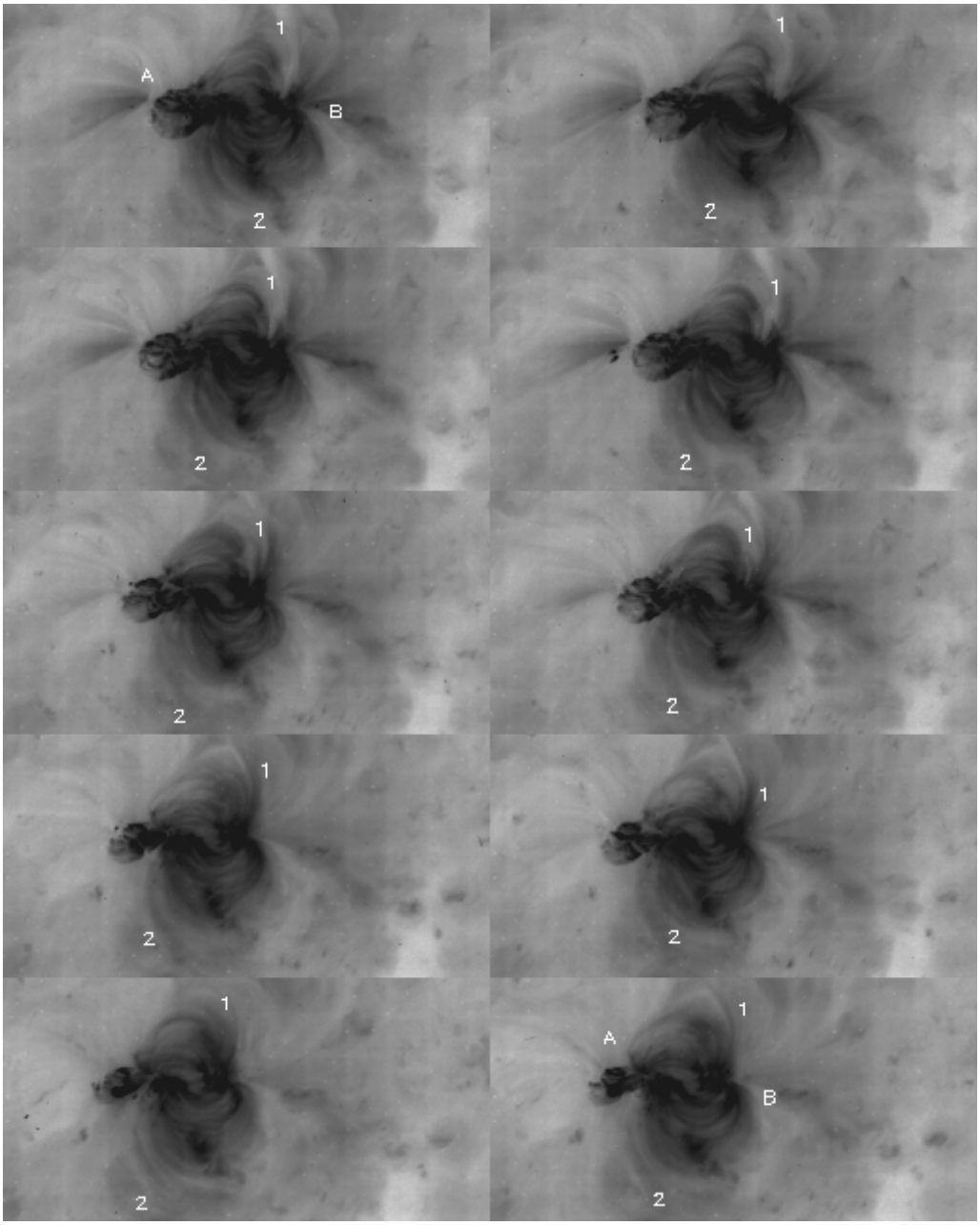

Figure IV.5: Les boucles se forment et se déforment sans cesse avec les mêmes paramètres (taille, torsadage,...) ceux des tubes magnétiques remplis ou non de plasma (SOHO/EIT Fe XII, le 1997-04-02 (NOAA 8026) : évolution régulière entre 8h et 23h)

aspects possibles que peuvent avoir les boucles pour un observateur.

Figure IV.6: Exemples de differents aspects pour les boucles :
De gauche à droite : boucle circulaire, tiltée, cisaillée, torsadée
La boucle tiltée est une projection de la boucle circulaire normale. La boucle cisaillée et la boucle torsadée nécessitent des déformations physiques importantes par rapport au cas circulaire.

Tilt Pour une structure, le tilt est l'inclinaison du plan de la structure par rapport à la normale (Fig. IV.6). Une boucle tiltée ne change pas ses paramètres intrinsèques par rapport à une boucle "normale", seul l'aspect pour l'observateur varie à cause de l'inclinaison.

Cisaillement Le cisaillement[4] se réfère au champ magnétique d'une région et pas uniquement à des boucles en particulier. Toutefois comme nous nous servirons de cette notion pour établir des propriétés relatives aux boucles, nous avons choisi de présenter ici cette notion.
L'équation d'Euler s'écrit $\vec{j} \times \vec{B} = 0$ ce qui implique que le courant électrique est aligné avec le champ magnétique. En combinant avec la loi d'Ampère on obtient que $\vec{\nabla} \times \vec{B} = \alpha \vec{B}$.
Dans une telle configuration à l'équilibre, aussi appelée champ sans force (fff), le plasma n'est soumis qu'à la force de Lorentz.
Le cisaillement magnétique $\alpha = \frac{\mu . j}{B}$ en m^{-1}. est constant le long de chaque ligne de champ puisque pour un champ sans force en prenant la divergence de l'equation fff on trouve $(\vec{B}\vec{\nabla})\alpha = 0$ c'est à dire $\vec{B}$ orthogonal aux gradients de α. La configuration d'un champ sans force (ie $\vec{rot}(\vec{B}) = \alpha \vec{B}$ avec $\alpha = Cste$ ou nulle) est la configuration qui requiert le minimum d'énergie pour une ligne de champ ([232]).
Le minimum absolu d'énergie d'un champ sans force est donne par le cas où $\alpha = 0$. Un tel champ s'appelle un champ potentiel puisqu'alors $\vec{\nabla} \times \vec{B} = 0$ implique $\vec{B} = \vec{\nabla} U$.
Dans le cas où $\alpha(x, y, z)$, l'équation devient non linéaire et est difficile à résoudre. Cette non-linéarité introduit des courants non parallèles aux lignes de champ magnétique.
Wilkinson, Emslie & Gary [261] définissent le cisaillement magnétique en un point comme la différence d'angle entre le champ magnétique transverse photosphérique observé et le champ potentiel.
Observationnellement un fort cisaillement correspond à un gradiant important du paramètre α dans une région active. Cela se décrit souvent comme un basculement relatif des boucles par rapport à la ligne de neutralité (souvent perpendiculaire aux pieds des boucles). En absence de cisaillement, les boucles (potentielles) restent perpendiculaires à la ligne neutre. Le cisaillement d'une AR est vu comme une variation globale pour chaque ligne de

[4] Shear

flux.

Le cisaillement peut provenir de la rotation différentielle dans les régions actives qui penche les lignes de neutralité et modifie la répartition topologique des α si les boucles ne sont pas à la même latitude. Les mouvements stochastiques des pieds des tubes de flux peuvent aussi intervenir.

Lorsque le cisaillement d'une ligne de champ magnétique est trop important, il peut se relaxer sous forme d'éruption solaire (cf par exemple [203]).

Torsadage Le torsadage[5] se refère à l'aspect d'une boucle. Il traduit le nombre de tours que les boucles font sur elles mêmes.

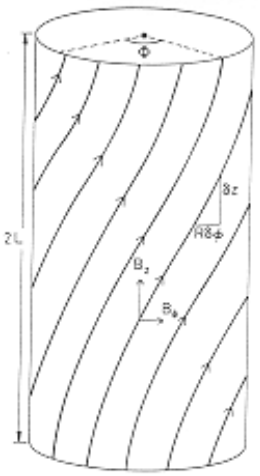

Figure IV.7: Le champ magnétique se décompose en une composante toroidale (B_Φ) et une composante longitudinale (B_z). En coordonées cylindriques :
$\vec{B} = B_z.\vec{z} + B_\Phi.\vec{\Phi}$.

Les lignes de champs magnétiques peuvent s'enrouler autour d'un axe principal (ie le champ magnétique longitudinal) à cause d'un champ annexe (le champ magnétique toroidal). Les lignes de champs sont alors torsadées et on définit (Fig. IV.2.3) en géométrie plan-parallèle sur un cylindre de longueur L et de rayon r [197] l'angle de torsion

$$\Phi(R) = \frac{LB_\Phi(R)}{rB_z(R)} \tag{IV.2}$$

Le torsadage est issu souvent d'un mouvement local de rotation de chacun des pieds d'une boucle.
Robertson, Hood et Lothian [201] ont montré sur des modèles 2D et 3D que des torsadages

[5] ou twist en langue anglaise

importants étaient sources d'instabilités. Browning & Hood [39] ont calculé les évolutions vers l'équilibre de boucles faiblement torsadées. Parker [172] a établi la forme du champ magnétique toroidal et poloidal dans le cas de boucles uniformément ou non torsadées. Vu comme un cylindre de rayon R et $2\pi\delta$ la longueur d'onde de l'hélice, $\omega = (x^2 + y^2)^{\frac{1}{2}}$ la distance à l'axe z, il obtient que

$$B_z = B_0 . \frac{(1 + \frac{R^2}{\delta^2})^{\frac{1}{2}}}{(1 + \frac{\omega^2}{\delta^2})^{\frac{1}{2}}} \tag{IV.3}$$

$$B_\Phi = B_z \frac{\omega}{\delta} \tag{IV.4}$$

Lothian & Hood [140] ont montré que même pour un faible torsadage, les boucles coronales torsadées ne pouvaient rester à l'équilibre que si elles étaient confinées par un champ magnétique externe et pas par la pression gazeuse.

Des instablilités de types kink peuvent se développer à partir de certaines valeurs du torsadage [19]. La possibilité d'ouverture rapide de boucles torsadées est modélisée par Amari et coauteurs [5].

Autres remarques observationnelles Il existe des cas où il peut être difficile de séparer cisaillement et torsadage. Par exemple pour des formes coronales en S, on peut considérer qu'il s'agit de boucles circulaires torsadées d'un tour ou de champs magnétiques fortement cisaillés. Hormis ce cas ambigu les anisotropies engendrées étant différentes, il est possible de séparer les situations.

Sur cet exemple de région active nous allons montrer comment il est possible -en premiere approximation- de comparer la théorie aux observations. Dans le cadre d'une collaboration, Stephane Regnier a réalisé les modélisations de lignes de champs magnétiques suvantes (Fig. IV.8). Certaines correspondent à des cas linéaires force free (c'est à dire les lignes de champs ont été programmées sur une boite tel que $\vec{\nabla} \times \vec{B} = \alpha \vec{B}$ avec α constant) d'autres non force free linéaires (c'est à dire que α varie suivant les lignes de champs).
Le groupe de boucles I est quasiment circulaire. Le groupe de boucle II a pratiquement les mêmes pieds et a des structures très variées en son interieur. Comme vérifié d'après le code numérique, le groupe I est linéaire force free. Le groupe II a un gradiant de α ce qui se traduit par cette déformation importante. Nous avons donc pu faire le lien entre observation et théorie. Il est toutefois à noter qu'en théorie avec un dipole magnétique il est possible d'obtenir même pour des champs force free des lignes qui ne sont pas circulaires. Mais par rapport à des boucles initialements circulaires, les variations induites permettent de connaitre le cisaillement et le courant induit.

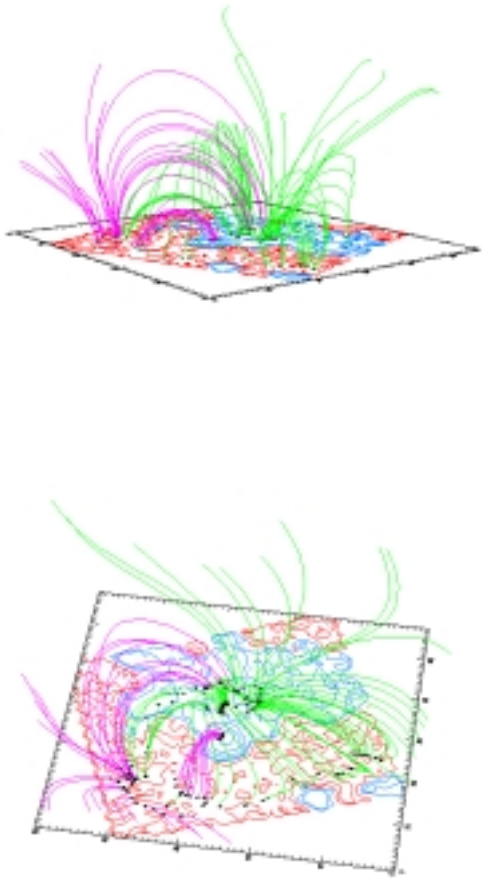

Figure IV.8: Modélisation de lignes de champs magnétiques

Nous reviendrons en précisant ces arguments dans les articles au moment venu.

IV.2.4 Hélicité et énergie

Il nous faut faire ici le lien entre les critères précédents et les lois de conservation définies pour le plasma.
On définit l'hélicite magnétique par

$$H = \int H_m = \int \vec{A}.\vec{B} = \int \vec{A}.(\vec{\nabla} \times \vec{A}) \tag{IV.5}$$

L'hélicité ([21]) se limite souvent à une somme de termes qui nécessitent une mesure du torsadage (twist), du cisaillement (shear) et du degré de lien (linking). L'hélicité est conservé en MHD idéale — car elle est longue à dissiper [23]—, dans de nombreux cas de reconnection [41].

Elle se calcule indépendamment du référentiel de l'observateur ce qui permet de quantifier les 3 notions qu'elle fait intervenir. Le lien avec la chiralité des régions actives et

filaments se fait via le signe de l'intégrale. Le nombre de lien L est une description topologique entre 2 courbes : L est multiplié par -1 uniquement quand une boucle croise la direction de notre boucle de référence. L'expression en forme d'intégrale à été établie par Moffatt [156].
Le cas de 3 boucles qui se croisent, s'écrit :

$$H = T_1(\Phi_1)^2 + T_2(\Phi_2)^2 + T_3(\Phi_3)^2 + 2L_{12}(\Phi_1)(\Phi_2) + 2L_{13}(\Phi_1)(\Phi_3) + 2L_{23}(\Phi_3)(\Phi_2) \tag{IV.6}$$

avec Φ_i le flux magnétique du tube i (i=1,2,3). Dans le cas d'une boucle uniformément torsadée, T_i mesure le nombre de tours faits sur elle même (c'est à dire : torsion/2pi). Noter que l'on peut considerer les premiers termes comme de l'auto inductance de torsion, les autres termes étant de l'inductance mutuelle entre tous les cas possibles.
Globalement, on peut donc écrire

$$H = 2\int_0^{\Phi} T(\phi)\phi d\phi \tag{IV.7}$$

Introduisons maintenant le cisaillement de structure, Wr [6] qui mesure la deformation (torsion) de l'axe de la structure elle même [24].
L'hélicité s'écrit

$$H = \Sigma(T_w + W_r) \tag{IV.8}$$

On a donc un moyen dans des cas de reconnections de transformer du cisaillement en flux et en torsion. De plus dans le cadre de la MHD, il est donc possible de faire évoluer un fort torsadage sur un petit volume vers une diminution de torsadage sur un volume plus grand. Nous reviendrons en détail dans les articles de ce chapitre sur ces possibilites.

[6] writh en anglais

IV.3 Etude des boucles EUV

Afin de pourvoir déterminer les paramètres physiques des boucles, nous allons définir la géométrie de celles-ci en utilisant la stéréovision avec contrainte par l'ajustement à un modèle. Nous allons développer 2 techniques distinctes se servant de la stéréovision; puis une étude multi-longueurs d'ondes permettra de calculer les lois d'échelles pour analyser la physique des tubes de flux.

IV.3.1 Des boucles EUV circulaires

Les paramètres 3D pour un modèle circulaire

Dans un premier temps, il s'est agi de développer un modèle d'ajustement de boucles circulaires afin de trouver les paramètres 3D de celles ci. Les programmes écrits en collaboration avec M. Aschwanden sous IDL pour Unix et se servent des routines de "Solar SoftWare" (sswidl). Leur développement a eu lieu au Goddard (NASA, Washington DC) en 1997 à partir de routines pré-existantes pour Yohkoh SXT ([10]).
A partir d'une séquence temporelle d'images 2 D de SOHO/EIT, nous allons reconstruire en 3D des boucles coronales dont les temps caractéristiques d'évolution auront été très grands par rapport au temps entre 2 images. La base du principe de stéréovision ayant déja été développée au chapitre 2, nous allons ici directement nous intéresser au cas particulier de structures circulaires.
En considérant dans un premier temps que les sections transverses [7] des boucles EUV sont constantes — ce qui a été observé par Klimchuk [123] pour les boucles chaudes de Yohkoh— on peut définir géométriquement une boucle à partir du tracé du centre de son tube de flux. Il s'agit ensuite d'identifier et de tracer des boucles dans les images ce qui passe par le désenboitement des boucles mélangées (1), la séparation des boucles proches (2), voire même la discrimination des boucles multiples présentes le long de la ligne de vue (3) (cf Fig. IV.9).
Une fois toutes ces étapes considérées, on peut reconstruire à trois dimensions la géométrie et déprojetter la boucle.
L'algorithme initial développé est donc le suivant :

1. On ajuste visuellement à la souris la boucle (coordonnée s)
2. On obtient donc un tableau $[x(s), y(s)]$ des coordonnées (les extrêmes sont les pieds : donc sur la surface).
3. On entre les coordonnées (soit directement, soit calculées depuis l'entete de l'image). On connaît donc les latitudes et longitudes de la portion d'image
4. L'intersection entre les équations cercle (ou tore) et de la surface donnent alors les conditions aux limites
5. D'où on obtient en sortie les valeurs du modèle ajusté

[7] cross section en langue anglaise

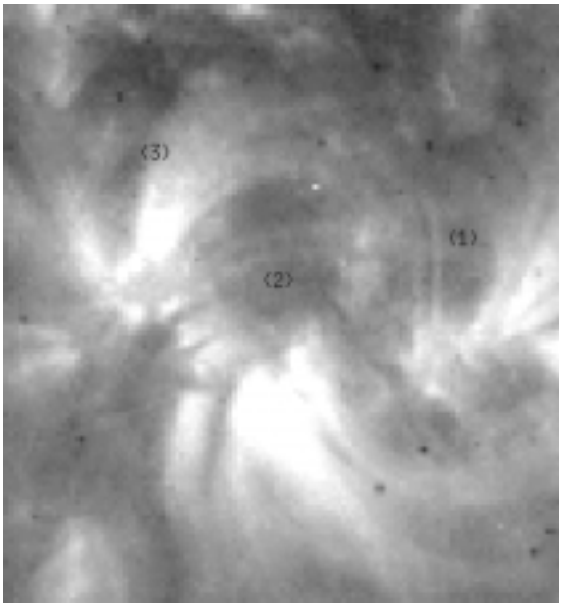

Figure IV.9: Extrait d'une image d'une région active SOHO/EIT Fe IX/X le 11 Aout 1999 :
(1) Plusieurs boucles se croisent.
(2) Des boucles voisines (avec champs magnétiques parallèles) sont très proches.
(3) Plusieurs boucles sont présentes sur la même ligne de visée

Mais il faut encore s'assurer d'avoir trouver la bonne solution...

Unicité par contrainte stéréographique dans l'ensemble des solutions de la modélisation précédente

La méthode précédente utilisée directement sans précaution aboutit à une non unicité des résultats. En effet selon les angles de vue, une boucle de petite taille peu inclinée (*e.g.* boucle numéro 3 de la Fig. IV.10) peut avoir la même projection qu'une grande boucle fortement inclinée (*e.g.* boucle numéro 1, Fig. IV.10).
L'ambiguïté est levée grace au changement de perspective avec le temps (Fig. IV.11) . En effet, le changement de direction de la ligne de visée avec la rotation des boucles sur la "surface solaire", fait projetter les boucles de manières différentes (*eg.* P_1 différent de P_3). On peut donc contraindre le modèle de boucle à partir d'une séquence temporelle d'image : c'est le principe de la *stéreoscopie*.

En suivant les tubes de flux magnétiques d'un bord à l'autre du soleil, les solutions issues de mauvaises projections sont éliminées. On obtient ainsi une solution unique.

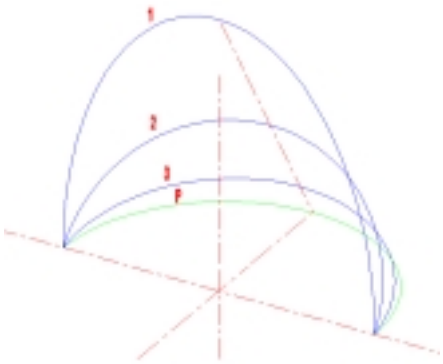

Figure IV.10: Non unicité de la projection (mathématique) : Les boucles 1, 2, 3 de taille différentes ont la même projection P

Meilleur ajustement possible

La méthode employée consiste à minimiser l'écart entre le modèle et les points cliqués sur le plan. Cet ajustement s'effectue par une méthode de type "moindres carrés" en optimisant le gradient. La convergence de la méthode peut être insuffisante et avoir une erreur supérieure à la tolérance admissible (1 pixel d'ecart sur l'image). Il faut donc rechercher une autre solution. Ce cas peut arriver si la solution arrive à un minimum local et non global (ex A au lieu de B dans la Fig. IV.12). Il faut donc alors appliquer une méthode type minimum d'entropie en autorisant la recherche de solution avec une plus grande barre d'erreur pour ensuite permettre un meilleur résultat (*ie* depuis A, on autorise le passage du maxima local C pour atteindre le minimal global B).

Evidemment, on élimine les résultats non physiques (boucle sous la surface par exemple).
A noter que l'entrée manuelle de valeurs initiales visuellement adéquates permet souvent de faire converger plus vite la méthode avec des valeurs physiquement acceptables.

Cette méthode s'appelle la *stéréovision statique*. En effet les structures suivies avec le temps, sont supposés ne pas varier. En pratique, en rajoutant des hypothèses sur différents paramètres obtenus en comparant plusieurs images prises à des temps différents, on peut permettre certaines variations dynamiques des tubes de flux.

Stéréoscopie dynamique

Nous allons proposer une amélioration de la méthode précédente (stéréoscopie statique) dans le cas où les boucles étudiées sont circulaires. Avec ce modèle à priori, il est possible d'étudier les cas où le tube de flux se reforme de maniére parallèle au cas précédent. Pour cela lorsque nous disposons du premier ajustement circulaire, on linéarise la boucle sous forme de bande ("stripe"). Un tube de flux qui se reformerait ulterieurement serait donc

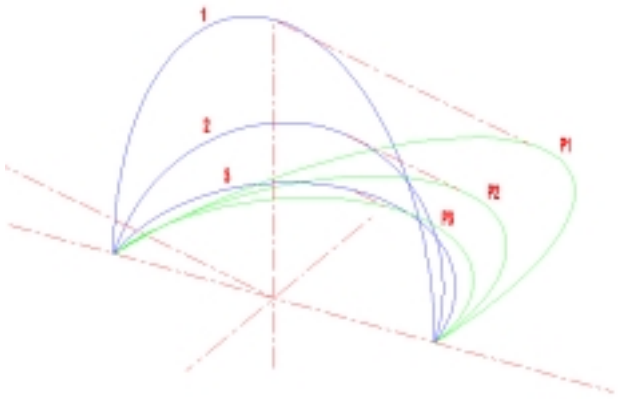

Figure IV.11: Possibilité de rétro-projection (mathématique) : Evoluant en fonction du temps, la direction de projection tourne et maintenant les boucles 1, 2 et 3 se projettent en 3 boucles distinctes. Inversement, en considérant des temps différents on peut remonter par rétroprojection aux véritables paramètres 3D de la boucle.

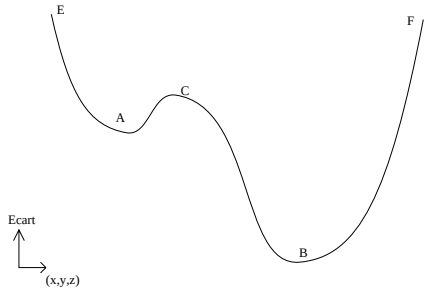

Figure IV.12: Critère d'erreur (ici : la différence par rapport au tracé)

parrallèle au précédant. Cette méthode appellée "stéréoscopie dynamique" est complètement décrite dans l'article ci dessous. Sa mise en oeuvre a permis l'analyse des paramètres 3D de 30 boucles d'une région active. Leurs profils de températures, leurs densités et différents paramètres physiques ont pu ainsi être déterminés. Nous avons calculés que ces boucles d'une région active proche du minimum du cycle sont circulaires et en équilibre hydrostatique.

- **Three-dimensional Stereoscopic Analysis of Solar Active Region Loops. I. SOHO/EIT Observations at Temperatures of (1.0-1.5) x 10^6 K**
- by ASCHWANDEN, MARKUS J.; NEWMARK, JEFFREY S.; DELABOUDINIERE, J.-P.; NEUPERT, WERNER M.; KLIMCHUK, J. A.; GARY, G. ALLEN; PORTIER-FOZZANI, F.; ZUCKER, ARIK
- The Astrophysical Journal, Volume 515, Issue 2, pp. 842-867.
- Code ADS : 1999ApJ...515..842

La recherche qui a abouti à cet article a permis de **définir la gémétrie des boucles** et de **confronter ces paramètres observationnels avec des modèles théoriques**.

THE ASTROPHYSICAL JOURNAL, 515:842–867, 1999 April 20

THREE-DIMENSIONAL STEREOSCOPIC ANALYSIS OF SOLAR ACTIVE REGION LOOPS. I. *SOHO*/EIT OBSERVATIONS AT TEMPERATURES OF (1.0–1.5) × 10^6 K

MARKUS J. ASCHWANDEN[1]
Department of Astronomy, University of Maryland, College Park, MD 20742; markus@astro.umd.edu
JEFFREY S. NEWMARK
Space Applications Corporation, Vienna, VA 22180
JEAN-PIERRE DELABOUDINIÈRE
Institute d'Astrophysique Spatiale, Université Paris XI, 91405 Orsay Cedex, France
WERNER M. NEUPERT
Hughes SXT Corporation, Lanham, MD 20706
J. A. KLIMCHUK
Space Science Division, Code 7675, Naval Research Laboratory, Washington, DC 20375-5352
G. ALLEN GARY
ES82-Solar Physics Branch, Space Science Laboratory, NASA/MSFC, Huntsville, AL 35812
FABRICE PORTIER-FOZZANI
Laboratoire d'Astronomie Spatiale, CNRS, BP 8, 13376 Marseille Cedex 12, France
AND
ARIK ZUCKER
ETH, Institute Astronomy, Häldeliweg 15, CH-8092 Zurich, Switzerland
Received 1998 May 13; accepted 1998 November 23

ABSTRACT

The three-dimensional structure of solar active region NOAA 7986 observed on 1996 August 30 with the Extreme-Ultraviolet Imaging Telescope (EIT) on board the *Solar and Heliospheric Observatory* (*SOHO*) is analyzed. We develop a new method of *dynamic stereoscopy* to reconstruct the three-dimensional geometry of dynamically changing loops, which allows us to determine the orientation of the mean loop plane with respect to the line of sight, a prerequisite to correct properly for projection effects in three-dimensional loop models. With this method and the filter-ratio technique applied to EIT 171 and 195 Å images we determine the three-dimensional coordinates $[x(s), y(s), z(s)]$, the loop width $w(s)$, the electron density $n_e(s)$, and the electron temperature $T_e(s)$ as a function of the loop length s for 30 loop segments. Fitting the loop densities with an exponential density model $n_e(h)$ we find that the mean of inferred scale height temperatures, $T_e^{\lambda} = 1.22 \pm 0.23$ MK, matches closely that of EIT filter-ratio temperatures, $T_e^{\rm EIT} = 1.21 \pm 0.06$ MK. We conclude that these cool and rather large-scale loops (with heights of $h \approx 30$–225 Mm) are in hydrostatic equilibrium. Most of the loops show no significant thickness variation $w(s)$, but we measure for most of them a positive temperature gradient ($dT/ds > 0$) across the first scale height above the footpoint. Based on these temperature gradients we find that the conductive loss rate is about 2 orders of magnitude smaller than the radiative loss rate, which is in strong contrast to hot active region loops seen in soft X-rays. We infer a mean radiative loss time of $\tau_{\rm rad} \approx 40$ minutes at the loop base. Because thermal conduction is negligible in these cool EUV loops, they are *not in steady state*, and radiative loss has entirely to be balanced by the heating function. A statistical heating model with recurrent heating events distributed along the entire loop can explain the observed temperature gradients if the mean recurrence time is $\lesssim 10$ minutes. We computed also a potential field model (from *SOHO*/MDI magnetograms) and found a reasonable match with the traced EIT loops. With the magnetic field model we determined also the height dependence of the magnetic field $B(h)$, the plasma parameter $\beta(h)$, and the Alfvén velocity $v_A(h)$. No correlation was found between the heating rate requirement E_{H0} and the magnetic field $B_{\rm foot}$ at the loop footpoints.

Subject headings: Sun: activity — Sun: corona — Sun: UV radiation — techniques: image processing

1. INTRODUCTION

The evolution of coronal plasma loops, beginning from the well-kept secret of the elusive heating mechanism, to the somewhat better understood conductive and radiative cooling processes, and the various transitions from steady state to nonequilibrium states, still represents a key problem of coronal plasma physics. Because the average temperature of the solar corona ranges around $T_e \approx 1.5$ MK, this temperature seems to reflect the most likely steady state condition of coronal structures, demarcating at the same time a watershed where cooling and heating processes start to lose equilibrium. It is therefore a physically meaningful choice to distinguish between *cool*[2] and *hot* loops

[1] Current address: Lockheed-Martin ATC, Solar and Astrophysics Laboratory, Department H1-12, Building 252, 3251 Hanover Street, Palo Alto, CA 94304; aschwanden@sag.lmsal.com.

[2] The temperature range of $T_e \lesssim 1.5$ MK that we denote as *cool* here is sometimes also termed *intermediate* temperatures (e.g., Brown 1996), whereas loops with temperatures of $T_e \lesssim 10^5$ K are referred to as *cool* loops (e.g., Martens & Kuin 1982).

with respect to this *maximum likelihood temperature* $T_e \approx$ 1.5 MK, which also separates roughly the line-formation temperatures in the EUV/XUV and soft X-ray (SXR) wavelength regimes. Coronal loops in EUV/XUV wavelengths could only be studied with few instruments, mainly from the spacecraft missions *Skylab*, *SOHO*, *Transition Region And Coronal Explorer* (*TRACE*), and from a few short-duration rocket flights (e.g., American Science and Engineering [AS&E], High-Resolution Telescope and Spectrograph [HRTS], or Solar EUV Rocket Telescope and Spectrograph [SERTS]). The scarce EUV observations before the launch of *SOHO* provided little systematic information on the physical structure of cooler active region loops in the temperature regime of $T_e \lesssim 1.5$ MK, as opposed to the much more frequently studied hotter loops ($T_e \gtrsim 1.5$ MK) in SXR (with *OSO 8*, *P78-1*, *Hinotori*, *SMM*/XRP, *Yohkoh*/SXT, *Coronas*, etc.). A number of statistical studies exist on hot active region loops observed in SXRs (e.g., Pallavicini, Serio, & Vaiana 1977; Rosner, Tucker, & Vaiana 1978; Cheng 1980; Porter & Klimchuk 1995; Klimchuk & Gary 1995; Kano & Tsuneta 1995, 1996), but there are no comparable statistics available on cooler active region loops observed at temperatures of $T_e = 1.0$–1.5 MK in EUV. Moreover, not much effort has been invested in the three-dimensional reconstruction of coronal loops at any wavelength so far (although the technology is ready; see, e.g., Gary 1997). This work represents a first comprehensive statistical study on physical parameters of *cool* active region loops in the $T_e = 1.0$–1.5 MK temperature range, measured with unprecedented accuracy using a newly developed three-dimensional reconstruction method called *dynamic stereoscopy*.

Let us quickly review some highlights of earlier work on EUV loops in the $T_e \approx 1.0$–1.5 MK temperature range. A comprehensive account on literature before 1991 can be found in Bray et al. (1991). The *Skylab* XUV spectroheliograph provided images with 2″–3″ resolution at wavelengths of 180–630 Å, including the Mg IX line with a formation temperature of $T_e = 0.9$ MK. Dere (1982) analyzed such XUV loops and found (1) that they are close to hydrostatic equilibrium (within the uncertainties of the unknown three-dimensional geometry) and (2) that hot ($T_e > 1$ MK) loops do not have a cool core structure as suggested by Foukal (1975). Sheeley (1980) studied the temporal variability of EUV loops and found lifetimes of ≈ 1.5 hr for 1 MK loops, somewhat longer than those of 0.5 MK loops. This lifetime of 1 MK loops, estimated by Sheeley from time-lapse movies, is actually close to the value we infer for the radiative cooling time from *SOHO*/EIT data. Observations with SERTS revealed that the brightest structures seen in Mg IX are not spatially coincident with hotter coronal loops seen in SXR but are rooted in chromospheric He II features and thus seem to trace out cooler coronal loops with apex temperatures of $T_e \lesssim 1$ MK (Brosius et al. 1997). The existence of numerous cooler loops has also been postulated from the observed discrepancy between SXR-inferred temperatures of active regions and simultaneous radio brightness temperature measurements because the former include only the contributions from hot loops, whereas the latter are sensitive to the combined free-free opacity of both hot and cool loops (Webb et al. 1987; Nitta et al. 1991; Schmelz et al. 1992, 1994; Brosius et al. 1992; Klimchuk & Gary 1995; Vourlidas & Bastian 1996). The most recent work on EUV loops comes from *SOHO*/EIT (Neupert et al. 1998; Aschwanden et al. 1998a, 1998b) and *SOHO*/CDS (Fludra et al. 1997; Brekke et al. 1997). Neupert et al. (1998) analyzed a long-lived loop structure and an open-field radial feature and found (1) that they are close to hydrostatic equilibrium (within the uncertainties of the unknown three-dimensional geometry), and (2) that radiative energy loss strongly dominates conductive energy loss at these loop temperatures of $T_e = 1.0$–1.5 MK, requiring a heating function that scales with the squared density, $E_H \propto n_e^2$. The temporal variability and lifetime of EUV loops can now best be studied from *SOHO*/EIT movies (Newmark et al. 1997).

What progress can we expect from a new analysis of active region loops, using the most recent EUV data available from *SOHO*/EIT? To accomplish sensible tests of theoretical models on heating and cooling processes, accurate physical parameters from *resolved single loops* are needed. However, most of the previous literature deals with line-of-sight averaged quantities without discriminating between single loops. For a proper determination of physical parameters from single active region loops, a number of analysis problems have to be overcome.

1. Geometric loop definition
2. Identification and tracing of loops in images
3. Disentangling of nested loops
4. Separation of overlying or closely spaced loops
5. Discrimination of multiple loops along the line of sight
6. Three-dimensional reconstruction of loop geometry and deprojection
7. Temperature discrimination along the line of sight
8. Reliable temperature and emission measure determination.

Most of these problems have not been treated in a systematic way in previous studies. Here we present the results of a new approach, making use of the principle of dynamic stereoscopy to reconstruct the three-dimensional orientation of loops, which provides a reliable method to obtain more accurate physical parameters as a function of the loop length, properly corrected for line-of-sight related projection effects. The enhanced accuracy is expected to allow for more rigorous tests of theoretical loop models.

In § 2 we describe the stereoscopic data analysis of 30 loops observed with *SOHO*/EIT at a wavelength band centered around Fe IX, Fe X at 171 Å. In § 3 we apply physical loop models to the data and investigate loop scaling laws. A summary and conclusions are given in § 4.

2. STEREOSCOPIC DATA ANALYSIS

2.1. *Data Set*

The investigated active region is a long-lived coronal structure that was present during several solar rotations, from its apparition in 1996 July until its disappearance in 1996 September (Hudson et al. 1998; Harvey & Hudson 1998), numbered as NOAA 7978, 7981, 7986 during consecutive rotations. We concentrate here on the central meridian transit on 1996 August 30, when the dipolar magnetic field structure offered the most favorable perspective to disentangle the "jungle" of nested loops.

An Fe IX/Fe X image recorded with *SOHO*/EIT (Delaboudinière et al. 1995) at a wavelength of 171 Å on 1996 August 30, 0020:14 UT is shown in Figure 1 (*top*). For stereoscopic correlations we will also use EIT images from

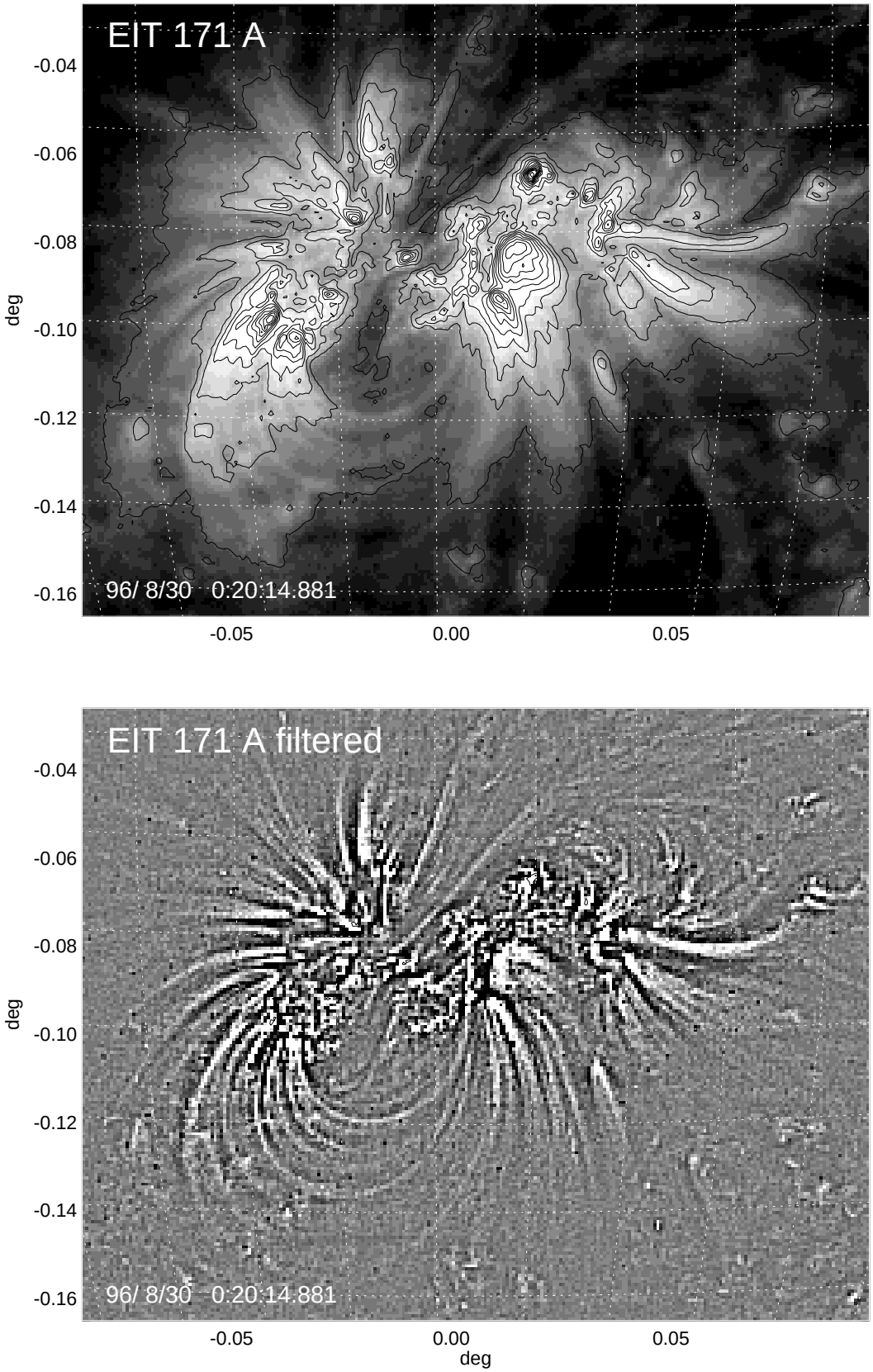

FIG. 1.—*SOHO*/EIT Fe IX/Fe X image of active region AR 7986, recorded on 1996 August 30, 0020:14 UT, at a wavelength of 171 Å, sensitive in the temperature range of $T_e = 1.0$–1.5 MK (*top*). The gray scales of the image is scaled logarithmically in flux, the contours correspond to increments of 100 DN (data numbers). The heliographic grid has a spacing of 5°. The filtered image (*bottom*) was created by subtracting a smoothed image (using a boxcar of 3×3 pixels) from the original image, in order to enhance the loop fine structure.

the previous (1996 August 29, 0015:15 UT) and following day (1996 August 31, 0010:14 UT). The multiloop structure of this active region is clearly visible in the high-pass filtered rendering shown in Figure 1 (*bottom*). The filtered image is simply created by subtracting a smoothed image (with a boxcar average over 3 × 3 pixels) from the original image. The original (full disk) image has a pixel size of 2.″616 and was recorded with an exposure time of 3.5 s. The absolute coordinate system of the full-disk image was established by fitting a circle to the solar limb (at 30 limb positions). The accuracy of the so-defined Sun center position is estimated to be $\sigma_x \approx 1$ pixel$/30^{1/2} \approx 0.2$ pixel. The offset of the Sun center position (x'_0, y'_0) provided (by an automatic limb-fitting routine) in the FITS header of the archive EIT image with respect to our value (x_0, y_0) is found to be $(x'_0 - x_0) = +0.5$ and $(y'_0 - y_0) = -3.9$ pixels. For the solar radius we find a difference of $(r'_0 - r_0) = -1.2$ pixels. Part of the discrepancy probably results from the automatic limb-fitting routine that can fail in the presence of active regions near the limb. The discrepancy in the solar radius has a more fundamental reason related to the problem of defining the radius of a fuzzy EUV limb, which is moreover found to be asymmetric in equator and polar direction (Zhang, White, & Kundu 1998). The EIT pixel size of $\Delta x = 2.''616$ is derived for a spacecraft distance of $d = 0.01$ AU from Earth and based on the assumption that the solar limb seen in EIT 171 Å corresponds to the top of the chromosphere ($h =$ 2500 km).

2.2. *Dynamic Stereoscopy Method*

In order to analyze the three-dimensional structure of coronal loops we develop a new technique we might call dynamic stereoscopy, as opposed to static stereoscopy, where the solar rotation is used to vary the aspect angle of otherwise *static* structures (e.g., Loughhead, Chen, & Wang 1984; Berton & Sakurai 1985; Aschwanden & Bastian 1994a, 1994b; Davila 1994; Aschwanden et al. 1995; Aschwanden 1995). The innovative feature of this new technique is that spatial structures, e.g., coronal loops, are allowed to evolve dynamically during the time interval over which the stereoscopic correlation is performed.

In the dynamic stereoscopy method we take advantage of the fact that the global magnetic field is slowly evolving (say during a day) compared with heating and cooling processes in coronal loops. Consequently, the coronal magnetic field $\boldsymbol{B}(\boldsymbol{x}, t)$ can be considered as invariant over short timescales, whereas the confined plasma can flow through "magnetic conduits" in a highly dynamic manner. If a specific coronal flux tube following a field line $\boldsymbol{B}(\boldsymbol{x}, t_1)$ is loaded with bright plasma at time t_1, the same flux tube may be cooled down at time t_2 (say a few hours later) and invisible at the same observed wavelength, whereas heating may occur in an adjacent flux tube $\boldsymbol{B}(\boldsymbol{x} + \Delta\boldsymbol{x}, t_2)$, which was dark at time t_1 and appears now bright at time t_2. For adjacent flux tubes, the two field lines $\boldsymbol{B}(\boldsymbol{x})$ and $\boldsymbol{B}(\boldsymbol{x} + \Delta\boldsymbol{x})$ will run almost parallel, a property we will exploit in our dynamic stereoscopy method. Our method is applicable to coronal structures that meet the following two conditions.

1. The global magnetic vector field $B(\boldsymbol{x}, t)$ is static (or slowly varying) during the time interval over which stereoscopic correlations are performed (typically 1 day). The magnetic field can be traced out by optically thin emission (e.g., in SXR or EUV wavelengths).

2. At least one footpoint of an observed coronal loop is identifiable, which can be used as a reference level of the altitude. For EUV emission we assume that the altitude of a loop footpoint is located in the lower corona above the chromosphere, at an altitude of $h_{\rm foot} \approx 2500$ km above the photosphere.

We outline briefly the numerical procedure of our implementation of the dynamic stereoscopy method, and the mathematical coordinate transformations are given in Appendix A. The projected geometry of a loop segment in an image at time t_1 is traced out by a series of image coordinates (x_i, y_i), $i = 1, \ldots, n$, starting at footpoint position (x_1, y_1), assumed to be anchored at height $h_{\rm foot}$ (Fig. 2). Two additional variables to characterize the three-dimensional geometry of the loop segment are the azimuth angle α of the footpoint baseline and the inclination angle ϑ of the mean loop plane (intersecting the footpoint baseline; see Fig. 2). The procedure of stereoscopic correlation (illustrated in Fig. 3) includes the following steps.

1. Measuring of positions (x_i, y_i), $i = 1, \ldots, n_j$ by tracing a loop segment in an image recorded at time t_1, starting with the primary footpoint at (x_1, y_1).

2. Estimating the position of the secondary footpoint (x_{F_2}, y_{F_2}) to obtain the azimuth angle α of the footpoint baseline. If the full length of the loop can be traced, the secondary footpoint is just given by the last point x_n, y_n, and the tangent of the azimuth angle α corresponds to the ratio of the latitude $(b_{F_2} - b_{F_1})$ and longitude difference $(l_{F_2} - l_{F_1})$ of the two footpoints, i.e.,

$$\tan \alpha = \frac{(b_{F_2} - b_{F_1})}{(l_{F_2} - l_{F_1})} . \tag{1}$$

However, most of the loops analyzed here can only be reliably traced over 1 density scale height, whereas the apex segment is generally so weak that some uncertainty results in the localization of the secondary, magnetically conjugate,

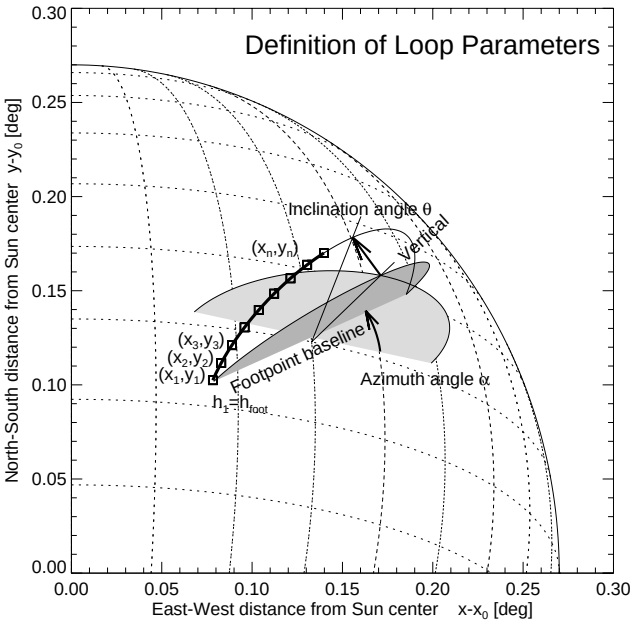

FIG. 2.—Definition of loop parameters: loop point positions (x_i, y_i), $i = 1, \ldots, n$ starting at the primary footpoint at height $h_1 = h_{\rm foot}$, the azimuth angle α between the loop footpoint baseline and heliographic east-west direction, and the inclination angle ϑ between the loop plane and the vertical to the solar surface.

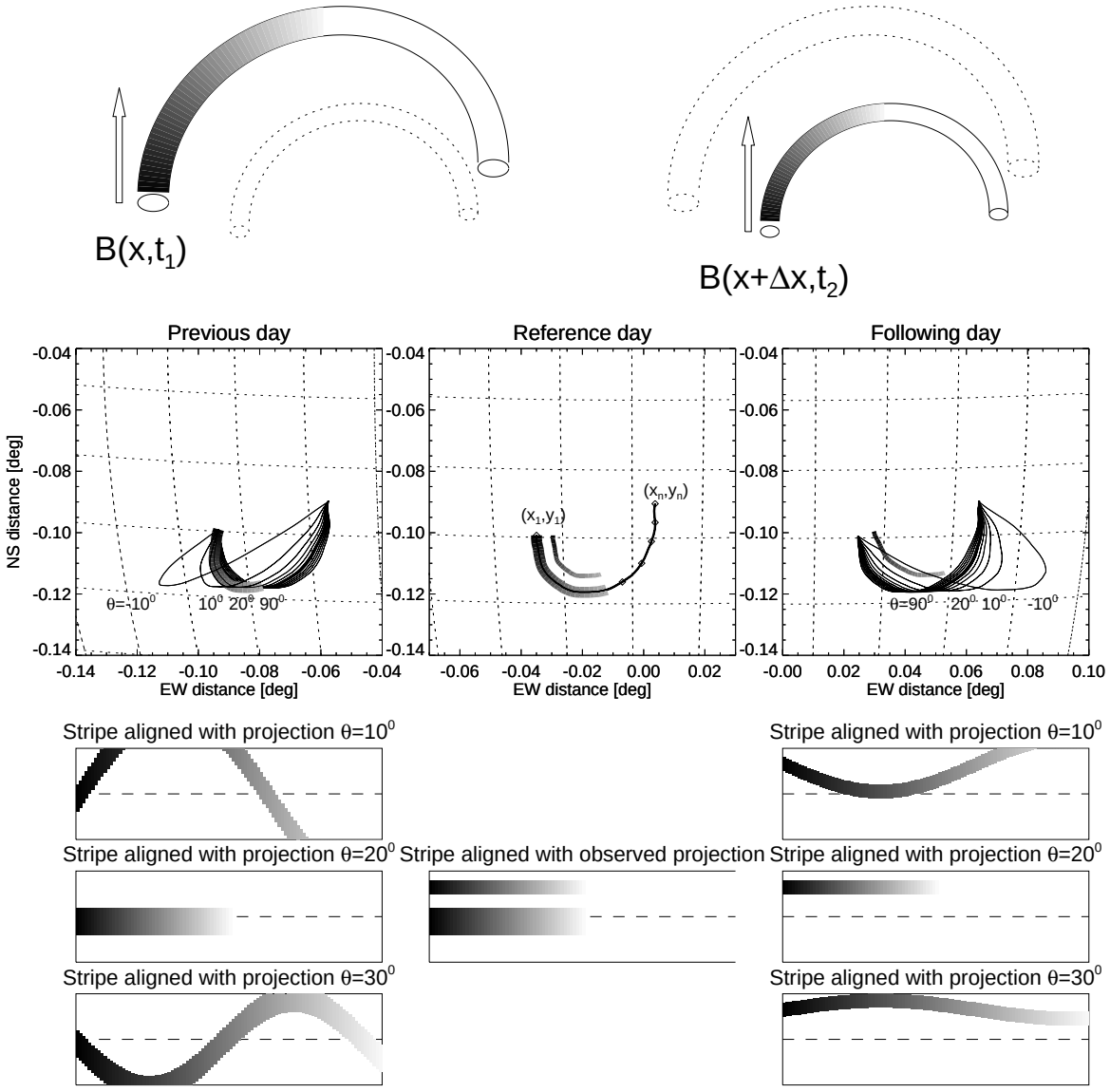

FIG. 3.—Principle of dynamic stereoscopy is illustrated here with an example of two adjacent loops, where a thicker loop is bright at time t_1, whereas a thinner loop is brightest at time t_2. From the loop positions (x_i, y_i) measured at an intermediate reference time t, i.e., $t_1 < t < t_2$ (*middle panel in middle row*), projections are calculated for the previous and following days for different inclination angles ϑ of the loop plane (*left and right panel in middle row*). By extracting stripes parallel to the calculated projections $\vartheta = 10°$, 20°, 30° (*bottom*) it can be seen that both loops appear only co-aligned with the stripe axis for the correct projection angle $\vartheta = 20°$, regardless of the footpoint displacement Δx between the two loops. The co-alignment criterion can therefore be used to constrain the correct inclination angle ϑ, even for dynamically changing loops.

footpoint. However, the general dipole characteristic of the magnetic field in this active region provides sufficient guidance to localize the secondary footpoint with an accuracy of $\lesssim 10\%$ of the loop length. In order to obtain an error estimate of the location of the secondary footpoint, we repeat the loop tracing procedure five times for each loop and obtain from the measured azimuth angles a_j, $j = 1, \ldots, 5$ a mean and standard deviation $\alpha \pm d\alpha$.

3. The loop positions (x_i, y_i) measured in the image at time t_1 are then transformed into heliographic longitude and latitude coordinates (l_{ij}, b_{ij}) and altitudes (h_{ij}), based on the azimuth angle α of the footpoint baseline and the variable inclination angle ϑ_j, which is varied over a range of $-90° < \vartheta_j < +90°$ in increments of $\Delta\vartheta = 1°$.

4. The heliographic coordinate $l_{ij}(t_1)$ is then transformed to the time t_2 of the second stereoscopic pair image, $l'_{ij}(t_2)$, using the solar differential rotation rate applied to the time interval $(t_2 - t_1)$. We use the differential rotation rate specified by Allen (1973),

$$l'(t_2) = l(t_1) + [13.^\circ 45 - 3^\circ \sin^2 b] \frac{(t_2 - t_1)}{1 \text{ day}} . \qquad (2)$$

The heliographic latitude b_{ij} and altitude h_{ij} are assumed to be constant during the considered time interval.

5. In the stereoscopic pair image at time t_2 we calculate the image coordinates (x'_{ij}, y'_{ij}) of the projected loop structure. Parallel to these loop curves (with typical lengths of $n_s = 50$–200 pixels) we extract image stripes of some width ($n_w = 16$ pixels) by interpolating the image brightness $F(x, y)$ at the positions of the curved coordinate grid.

6. The stretched two-dimensional image stripes ($n_s \times n_w$ pixels) are then scanned for parallel brightness ridges, caused by "dynamic" structures that are co-aligned (or parallel-displaced) to the loop projection in image t_2 (for

illustration see examples shown in Fig. 3, *bottom*). This scanning process is numerically performed by measuring the total lengths $L(\vartheta_k)$ of parallel contiguous brightness ridges detected in each image stripe k for a given angle ϑ_k. As the examples in Figure 3 (*bottom*) show, loop projections in stripes with angles ϑ (e.g., $\vartheta = 10°$ or 30°) that deviate from the mean loop plane $\vartheta = 20°$) appear as curved features and thus have shorter parallel segments than those projections in stripes with inclination angles that coincide with the mean loop plane ($\vartheta = 20°$). The numerical detection of the length of parallel segments is therefore a reliable indicator of whether the inclination angle ϑ_k used in the coordinate transformation matches the effective loop plane ϑ. We evaluate this criterion in our algorithm by maximizing the sum of all detected contiguous parallel brightness ridges, i.e., by maximizing the quantity (max $[\sum L(\vartheta_k)]$) as a function of the variable inclination angle ϑ_k used in the coordinate transformation. This way we infer the most likely value of the inclination angle ϑ of the mean loop plane.

7. The same procedure is repeated in forward and backward directions in time. The mean and standard deviation of $\vartheta \pm d\vartheta$ is determined by averaging the two stereoscopic solutions (± 1 day).

The independent stereoscopic correlation in forward ($+1$ day) and backward (-1 day) direction provides a useful redundancy of the solution. The time difference of ± 1 day corresponds to an aspect angle change of $\pm 13.^{\circ}5$. Except for steps 1–2, which constitute the definition of a selected loop feature, all other steps (3–7) of the stereoscopic correlation are performed automatically by a numeric code without human interaction. The determination of the loop inclination angle ϑ is therefore achieved in a most objective way, within the principle of dynamic stereoscopy.

2.3. *Loop Geometry*

With the dynamic stereoscopy method described above we analyzed the three-dimensional coordinates of 30 loops from the EIT 171 Å image on 1996 August 30 (Fig. 4, *middle column*). The true three-dimensional geometry of (the central axis of) a coronal loop can be characterized with three orthogonal spatial coordinates $[x(s_i), y(s_i), z(s_i)]$, $i = 1, \ldots, n$, parametrized by the loop length parameter s_i. When we trace a loop structure in an image (see Fig. 4, *middle column*), we can accurately measure the two coordinates $[x(s_i), y(s_i)]$, without imposing any geometric constraint on its shape, as opposed to a method that fits a predefined geometric model (e.g., a circular geometry or its elliptic projection). We impose only some constraints on the third coordinate $z(s_i)$, namely, assuming that the loop segment is mathematically described in a plane, whose orientation we quantify with two free parameters (Fig. 2): with the azimuth angle α (of the loop footpoint baseline) and the stereoscopically measured inclination angle ϑ (with respect to the

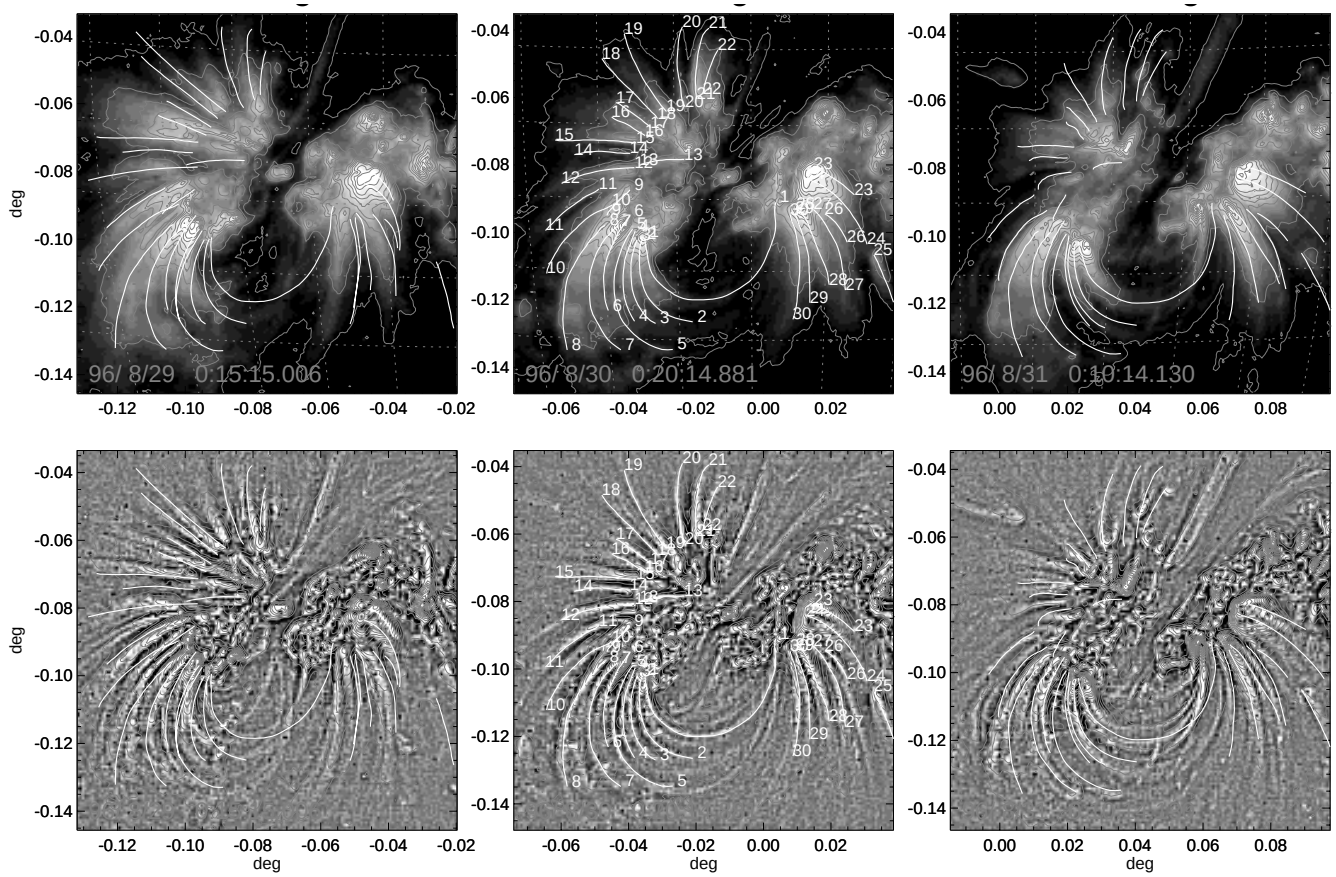

FIG. 4.—Projections of 30 stereoscopically reconstructed loop segments (numbered white curves) are shown overlaid on the *SOHO*/EIT 171 Å images (*top*) and the filtered images (*bottom*) of 1998 August 29 (*left*), 30 (*center*), and 31 (*right*). The 30 loop segments were traced from the filter image of August 30 (*bottom middle*), whereas the projections on the previous and following day were calculated from the inclination angles ϑ obtained from the dynamic stereoscopy method. Note that the overall magnetic field structure is almost invariant during the 3 days, but dynamic changes of the loops produce slight displacements between the calculated projections forward and backward in time and the actually observed fine structure.

vertical). However, the planar approximation serves only for mathematical convenience and defines a mean loop plane but does not require that the actual loop is exactly confined in a plane because our dynamic stereoscopy method allows for near-parallel displacements in time and space within some range. One additional constraint is also introduced by the reference level $h(s_1)$ of the first footpoint position, assumed to be located at a fixed height of $h(s_1) = h_{\rm foot} \approx 2.5$ Mm.

Some geometric elements of the analyzed 30 loops are listed in Table 1: the heliographic longitude (l_1) and latitude (b_1) position of the primary footpoint [$x(s_1)$, $y(s_1)$, $h(s_1) = h_{\rm foot}$], the azimuth angle α of the footpoint baseline measured at the primary footpoint, and the inclination angle ϑ of the loop plane. The average heliographic position of the 30 loop footpoints is $\langle l_{F_1} \rangle = 251\overset{\circ}{.}0$, $\langle b_{F_1} \rangle = -11\overset{\circ}{.}8$, which is slightly southward of the Sun center position at this time, $l_0 = 255\overset{\circ}{.}8$, $b_0 = 7\overset{\circ}{.}2$.

The average azimuth angle (modulo 180°) of the 30 loop footpoint baselines is $\alpha = -3° \pm 10°$, which represents the global orientation of the large-scale dipolar magnetic field that dominates the active region, which was used as a guide to estimate the azimuth angle of the footpoint baseline for individual loop segments. The only complete loop that could be traced out (without gaps between the footpoints) is loop 1, which has an azimuth angle of $\alpha = 15° \pm 1°$.

The inclination angles ϑ of the loop planes cover a large range from $\vartheta = -56°$ to $\vartheta = +69°$, having an average of $\langle \vartheta \rangle = 7° \pm 37°$. The southern loops (loops 1–11, 23–30) all show an inclination toward south (with ϑ negative if the primary footpoint is to the east), whereas the northern loops (loops 12–22) show a systematic inclination toward north (with ϑ positive if the primary footpoint is to the east). This fan-shaped divergence of loop planes is consistent with the overall magnetic dipolar field, having the dipole axis aligned to the east-west direction.

We visualize the three-dimensional structure of the stereoscopically reconstructed 30 loops in Figure 5, where different perspectives and viewing angles are displayed. The traced segments (Fig. 4) of the reconstructed loops are marked with thick lines in Figure 5, whereas the thin lines represent circular segments in the loop plane, constrained by the two footpoints and the endpoint of the traced segment. We rotated these reconstructed 30 loops by −7.2 days to the east (Fig. 5, *bottom left*), in order to illustrate the distribution of inclination angles. The group of loops that are inclined to the south in our EIT image of 1996 August 30 are also found to have a similar configuration (with similar loop heights and loop plane inclinations) in an EIT image observed 7.2 days earlier, when this active region crossed the east limb (Fig. 5, *top left*).

2.4. *Loop Background Subtraction*

We parametrize the positions of the traced loop segments from the image coordinates [$x(s_i)$, $y(s_i)$] as a function of the (projected) loop length parameter s_i, by interpolating the

TABLE 1

GEOMETRIC PARAMETERS OF 30 CORONAL LOOPS (1996 AUGUST 29, EIT 171 Å)

Loop Number	Heliographic Coordinates l_1, b_1 (deg)	Azimuth Angle α (deg)	Inclination Angle ϑ (deg)	Loop Radius R_0 (Mm)	Center Offset Z_0 (Mm)	Loop Trace L_1 (Mm)	Loop Length L (Mm)	Scale Height λ (Mm)	Loop Width w (Mm)
1	247.9, −15.4	15 ± 1	−42 ± 1	56	−14	149	149	49	6.8
2	247.7, −15.5	13 ± 1	−49 ± 5	62	18	91	234	50	6.1
3	247.4, −15.6	12 ± 1	−34 ± 1	68	31	89	282	57	7.4
4	247.3, −15.0	8 ± 2	−26 ± 1	77	45	104	338	57	6.9
5	247.1, −14.9	8 ± 3	−49 ± 1	73	37	121	309	56	6.3
6	247.0, −13.9	2 ± 2	−56 ± 1	84	53	80	381	42	7.0
7	246.1, −14.7	4 ± 2	−36 ± 1	89	51	125	389	62	7.1
8	245.2, −14.7	9 ± 2	−33 ± 2	113	80	124	534	57	7.1
9	247.0, −12.2	−3 ± 3	−12 ± 1	86	44	41	366	60	8.1
10	245.8, −13.3	1 ± 2	−23 ± 1	124	95	90	609	53	7.9
11	244.9, −12.2	1 ± 3	−31 ± 2	144	116	56	725	66	6.8
12	247.3, −10.7	−6 ± 2	10 ± 1	116	94	153	585	60	7.8
13	250.6, −10.1	−9 ± 7	11 ± 1	73	60	62	373	60	6.4
14	247.1, −9.8	−8 ± 3	10 ± 1	113	87	70	554	33	6.4
15	247.5, −9.0	−8 ± 1	12 ± 1	125	105	103	643	47	6.8
16	248.1, −8.5	−11 ± 3	25 ± 1	85	59	63	400	53	6.7
17	248.5, −8.0	−14 ± 4	32 ± 1	93	71	52	455	47	7.4
18	249.0, −7.4	−9 ± 4	40 ± 3	92	79	109	483	93	5.6
19	249.6, −6.9	−18 ± 3	39 ± 1	116	95	130	590	65	7.9
20	250.7, −6.6	−24 ± 6	52 ± 6	78	64	103	399	56	7.7
21	251.5, −6.1	−21 ± 6	58 ± 3	67	47	85	318	45	7.6
22	251.9, −5.7	−25 ± 5	58 ± 3	49	29	53	217	58	7.2
23	259.1, −10.7	−4 ± 4	0 ± 1	102	71	69	479	60	8.0
24	258.6, −11.4	−1 ± 4	14 ± 6	114	90	106	568	64	8.7
25	263.2, −16.6	−1 ± 5	43 ± 1	138	70	59	582	42	8.1
26	259.9, −13.8	−8 ± 4	13 ± 2	100	60	39	446	59	5.1
27	259.1, −13.4	−2 ± 3	50 ± 2	101	68	72	471	58	7.1
28	258.0, −13.4	0 ± 2	27 ± 2	90	63	86	423	57	7.5
29	257.9, −13.7	5 ± 2	36 ± 1	78	45	88	344	60	6.0
30	257.5, −13.8	−2 ± 3	69 ± 1	76	44	86	336	38	7.4
Average...	251.0 (±5.4), −11.8 (±3.3)	−3 (±10)	7 (±37)	93 (±23)	62 (±27)	89 (±29)	433 (±136)	55 (±10)	7.1 (±0.8)

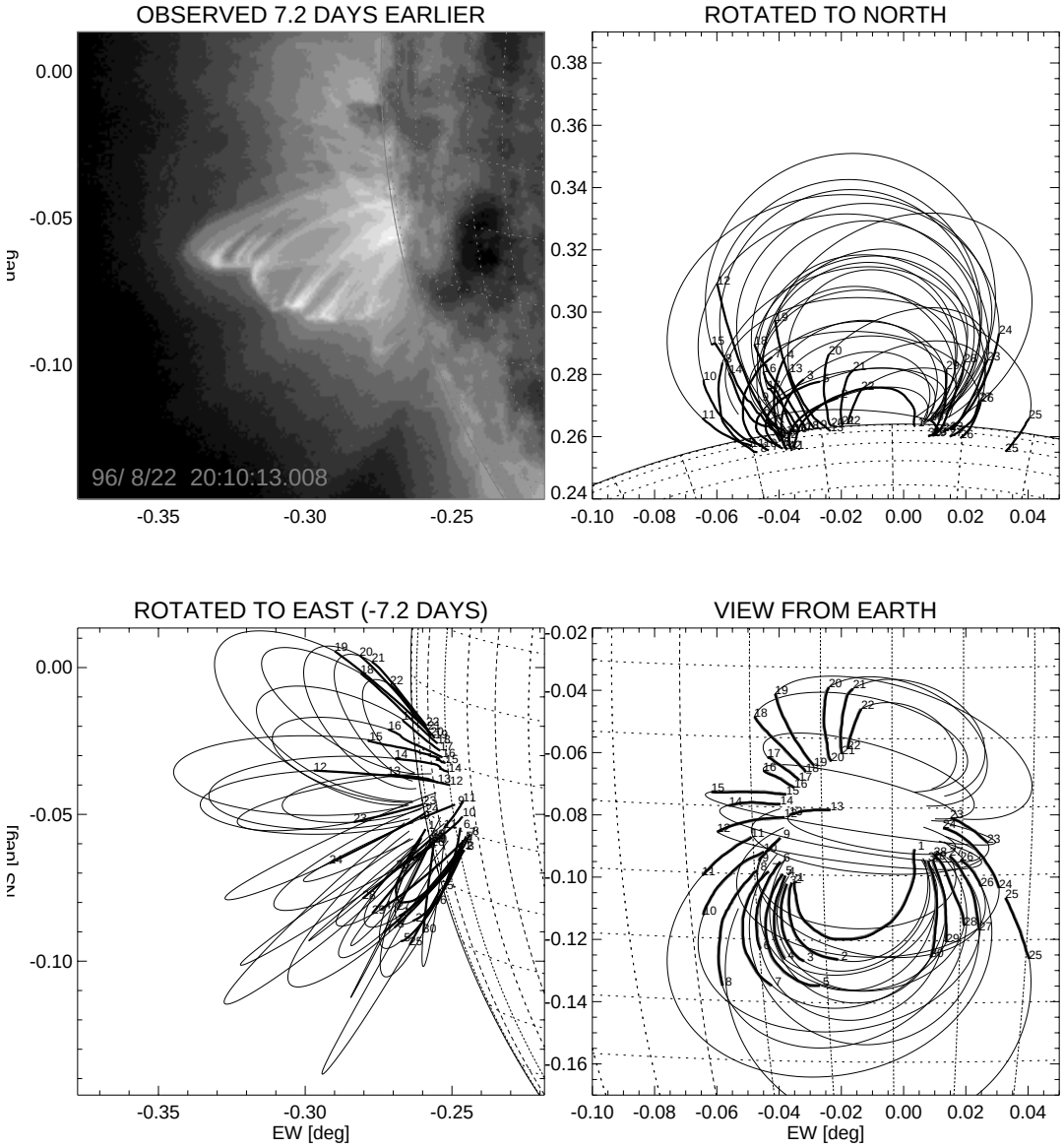

FIG. 5.—Three different projections of the stereoscopically reconstructed 30 loops of AR 7986 are shown. The loop segments that were traced from the 1996 August 30, 171 Å image are marked with thick solid lines, whereas the extrapolated segments (*thin solid lines*) represent circular geometries extrapolated from the traced segments. The three views are (1) as observed from Earth with l_0, b_0 (*bottom right*), (2) rotated to north by $b_0' = b_0 - 100°$ (*top right*), and (3) rotated to east by $l_0' = l_0 + 97.^\circ 2$ (corresponding to -7.2 days of solar rotation, *bottom left*). An EIT 171 Å image observed at the same time (-7.2 days earlier) is shown for comparison (*top left*), illustrating a similar range of inclination angles and loop heights as found from stereoscopic correlations a week later. The heliographic grid has a spacing of 5° degrees or 60 Mm.

coordinates with a constant resolution of $\Delta s_i = s_{i+1} - s_i = 1$ pixel in the image plane. These positions mark the central axes of the analyzed loops. For single-loop analysis it is convenient to introduce a coordinate grid $[s_i, t_j]$ that is co-aligned with the loop axis s_j, and t_j is the coordinate orthogonal to the loop axis. The projections $[x(s_i, t_j), y(s_i, t_j)]$ of these curved coordinate grids are shown in Figure 6 (*top right*). We parametrized both coordinates $[s_i, t_j]$ with a uniform resolution of 1 pixel and have chosen a width of 16 pixels for the width of the stripes (t_j), symmetrically bracketing the central loop axis. We show the radiative flux $F(t_j)$ as a function of the loop cross section t_j for each loop (1–30) and for each position s_i along the central loop axis with an incremental step of $\Delta s_i = 1$ pixel in Figure 6, measured from the EIT 171 Å image of 1996 August 30.

In a next step we attempt to separate the loop-associated fluxes from the loop-unrelated background. This is a very crucial step to determine the correct emission measure and electron density in a given loop. This task is difficult because most of the loops are very closely spaced and separated only by a few pixels at their primary footpoint (see Fig. 6). Very few loops occur in an isolated environment (e.g., such as loop 25; see Figs. 4–6). For many cross sections there is not enough separation between adjacent loops to model the loop-unrelated background properly. The fact that the flux-unrelated background makes up typically 50%–90% of the total EUV flux measured at a given line of sight (see Fig. 7) indicates that we can separate out only a fraction of superposed and nested loops, like the topmost elements on the topological surface of a "strand of spaghetti."

We tested various methods and found the following to be least susceptible to confusion by adjacent loops. We calculated the background profile $F_B(t_j)$ to the observed flux $F(t_j)$

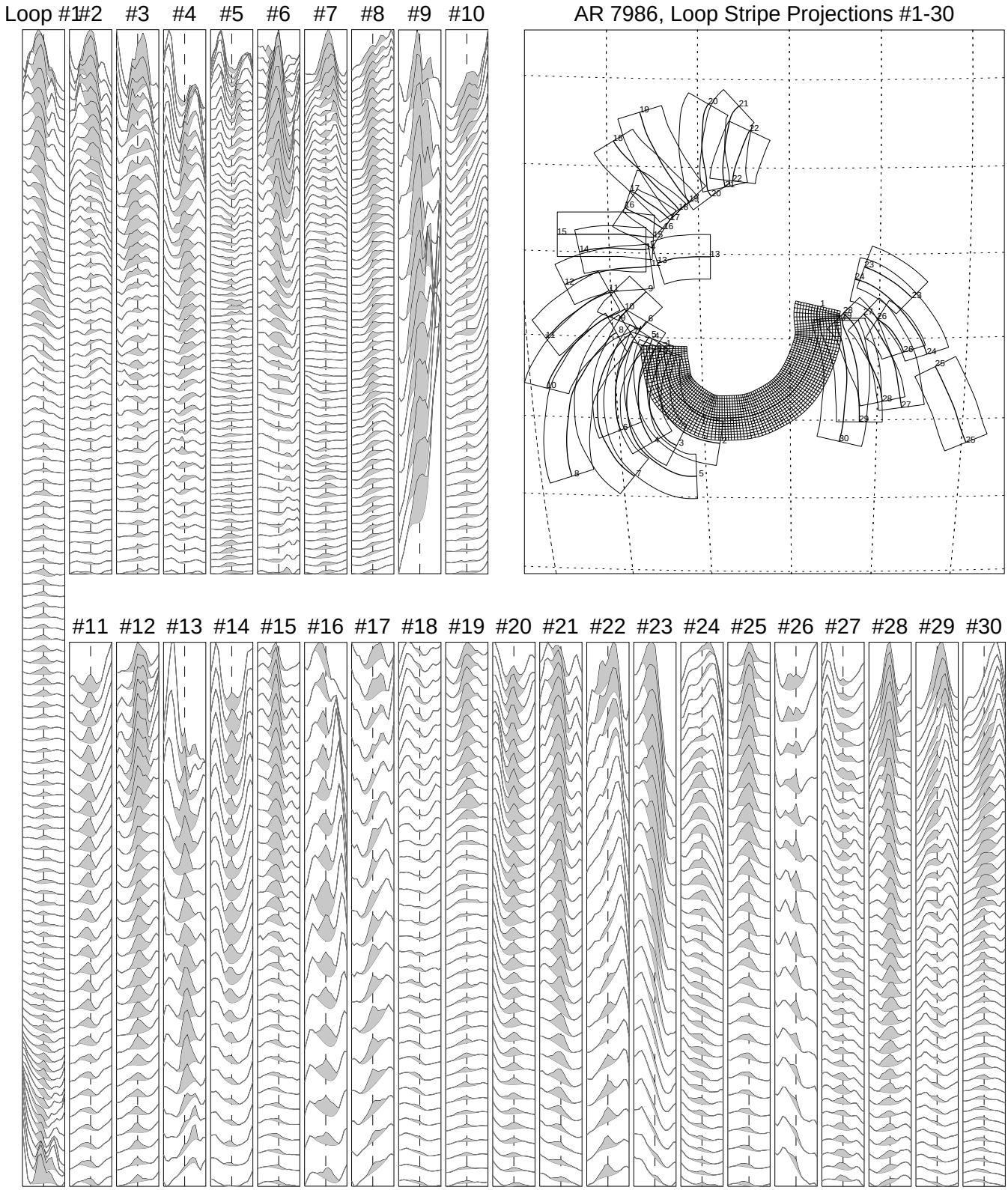

FIG. 6.—Positions of the curved coordinate grids of the 30 analyzed loop segments are shown in the top right panel, which has the same orientation as the 1996 August 30 map shown in Fig. 4 (*middle*). The coordinate grid of loop 1 is represented with 1 pixel resolution, whereas only the outer borders and central axes are indicated for the other loop segments. The vertically oriented panels represent the coordinate grids of the analyzed 30 loops, stretched out along the loop axis. The top of the panels corresponds to the primary footpoint (see positions l_1, b_1 in Table 1). In each panel we show the EIT 171 Å flux loop cross sections measured perpendicularly to the loop axes. Successive cross sections are separated by a distance of 1 pixel along the loop axis. The flux associated with each loop is marked with a gray area, obtained by background subtraction with a cubic spline interpolation between both sides of the loop cross section.

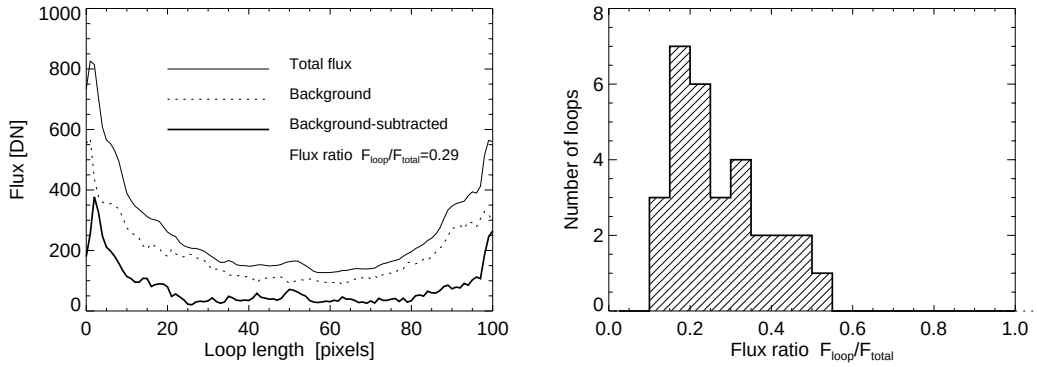

FIG. 7.—Loop-associated EUV flux [$F_{\rm loop}(s)$, *thick line*], the total EUV flux [$F_{\rm total}(s)$, *thin line*], and the background [$F_{\rm total}(s) - F_{\rm flux}(s)$, *dotted line*] measured along the loop is shown for loop 1 (*left*). A histogram of the relative fractions $F_{\rm loop}/F_{\rm total}$ (integrated over the traced loop lengths) is shown from all 30 analyzed loops (*right*).

by cubic spline interpolation between various cross section boundaries $[t_1, t_2]$, which were varied over a range of 1, ..., 4 pixels (or 2–7 Mm for the half-width of the loop cross section) on both sides of the central loop axis. From the varied loop boundaries $[t_1, t_2]$ those were used for the background envelope that maximize the flux integrated over loop cross section, i.e., the maximum of $\int [F(t_j) - F_B(t_j)]dt_j$ because this quantity is invariant to lateral displacements (in transverse direction t) and is least susceptible to changes of the functional form $F(t)$ along the loop coordinate s. This method has the advantage of adjusting for loop thickness variations, for offsets in tracing of the central axis, and for co-alignment errors between the 171 and 195 Å image in the use of the filter-ratio technique. The so-determined loop-associated fluxes are shown with gray areas for each cross section $F(t_j)|_{s=s_i}$ in Figure 6. The results show that the allowed loop half-width range of ± 1, ..., 4 pixels separates most of the loops reasonably, except for occasional double loop detections (e.g., 22 or 26 in Fig. 6) near the primary footpoint. Such loop segments where the loop separation fails will be excluded in further analysis.

2.5. *Loop Cross Sections*

We measured the loop width $w(s)$ as a function of the loop length parameter s, using the definition of the *equivalent width* $w(s)$,

$$w(s) = \frac{\int F(s, t_j) - F_B(s, t_j)\, dt_j}{\max\,[F(s, t_j) - F_B(s, t_j)]} \,. \qquad (3)$$

These loop widths $w(s)$ are shown as a function of the loop length s in Figure 8 for the 10 loops that are least confused by adjacent loops, as can be judged from the cross sections $F(t_j)|_{s=s_i}$ shown in Figure 6 (loop 1, 8, 11, 14, 15, 19, 20, 21, 25, 28). Performing a linear regression fitted to the observed values $w(s)$, we find a significant variation of the loop thickness only for two of them (loop 20 and 28). To quantify the variation of the loop thickness we calculated a *loop divergence factor*, defined by the average width in the upper part ($s_{\rm max}/2 < s < s_{\rm max}$) to the lower part ($0 < s < s_{\rm max}/2$) of the traced loop segment. We remind the reader that the traced loop segments generally extend over about 1 density scale height but often do not reach the loop top (except for the smallest loop, 1). The loop divergence factors and their uncertainties are shown in Figure 8 (*bottom right*) for each loop. We caution that some of the loop thickness variation near the footpoints is due to separation problems of closely spaced adjacent loops (as can be judged from Fig. 6). A histogram of average loop widths is shown in Figure 8 (*top right*), whereas the individual values w and their mean and standard deviation ($w = 7100 \pm 800$ km) are also listed in Table 1. The preference for such a narrow range of loop diameters is perhaps an instrumental resolution bias because the finest recognizable structures are most likely to be seen at a scale corresponding to the size of a few pixels.

2.6. *Loop Densities and Scale Heights*

For electron density and temperature diagnostics we are using a filter-ratio technique applied to the EIT 171 and 195 Å wavelength images, based on the most recent EIT standard software (status of 1998 February, Newmark et al. 1996; *SOHO* EIT User's Guide). The resulting emission measures EM and temperatures $T_e^{\rm EIT}$ are based on the calculation of synthetic spectra using the CHIANTI database, containing some 1400 emission lines in the 150–400 Å wavelength range (Dere et al. 1997). For details of the EIT calibration and error analysis, the reader is referred to Delaboudinière et al. (1995), Moses et al. (1997), and Neupert et al. (1998). Further cross calibrations of the EIT instrument with NRL rocket flights carrying an EIT duplicate instrument are in progress (led by D. Moses). In brief, we note that the main errors at this stage are systematic and due to calibration questions. This has a larger effect on the emission measure than on the temperature because the latter is determined from a ratio, in which systematic errors cancel out to some extent. Our estimate of the absolute error in the temperature determination is about 0.2 MK, whereas the emission measure has a systematic error of up to a factor of 4. The abundances in the above calculations are those given by Meyer (1985) for the corona. As iron is a low–first ionization potential (FIP) element, abundance questions play a minor role in the uncertainties.

To determine the electron density $n_e(s)$ along individual loops, we use the background-subtracted EIT fluxes $F_{\rm loop}(s) = F(s) - F_B(s)$ in the filter ratios and the loop widths $w(s)$. An additional important loop parameter is the line-of-sight angle $\psi(s)$, which provides a correction factor of the effective column depth for a loop with circular cross section specified by a diameter $w(s)$, i.e., $w_z(s) = w(s)/\cos\,[\psi(s)]$ (see Appendix B). With this parametrization we define the density $n_e(s)$ along a loop (normalized to a filling factor of unity) by

$$n_e(s) = \sqrt{\frac{\rm EM(s)}{w_z(s)}} = \sqrt{\frac{\rm EM(s)\,\cos\,[\psi(s)]}{w(s)}} \,, \qquad (4)$$

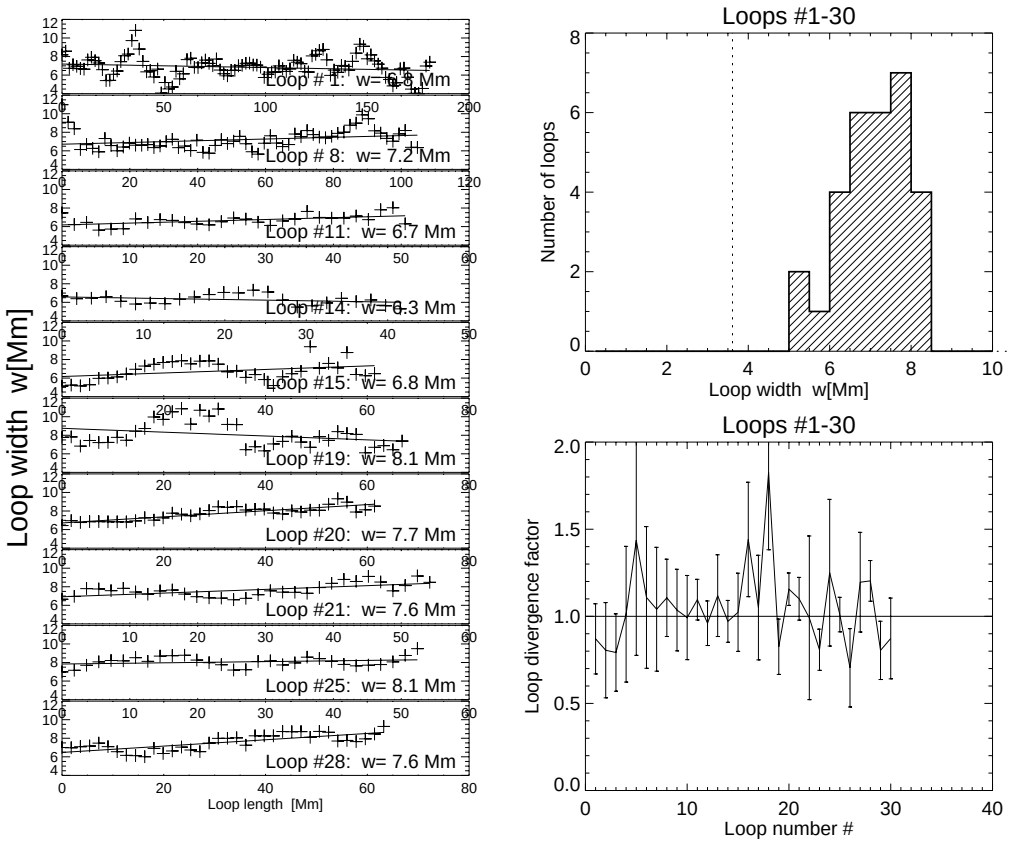

FIG. 8.—Variation of the loop thickness is shown for the 10 loops with the least confusion by adjacent loops (see cross sections in Fig. 6) as a function of the loop length s (*left*). A linear regression fit is indicated (*solid line in left panels*). The average (equivalent) width w is histogrammed for all 30 analyzed loops (*top right*). A loop divergence factor is calculated from the ratio of the average width in the upper half and lower half (*traced*) loop segments (*right bottom*). Note that most of the loops show no significant loop thickness variation.

with the loop length $s(x, y)$ parametrized as a function of the image position (x, y), from which the EIT emission measure $\mathrm{EM}(x, y)$ is measured. Because the line-of-sight angle $\psi(s)$ is very sensitive to the loop orientation, correct values of the electron density $n_e(s)$ can only be obtained from an appropriate three-dimensional model of the loop (constrained by stereoscopic correlations here). The projection effect of the loop curvature on the effective column depth $w_z(s)$, and the effect of the inclination angle ϑ of the loop plane on the inferred density scale height $\lambda(\vartheta)$ are illustrated in Figure 9 (see also discussion in Alexander & Katsev 1996).

The electron density $n_e(s)$ calculated from equation (4) is shown graphically for the 10 least-confused loops (1, 8, 11, 14, 15, 19, 20, 21, 25, 28) in Figure 10 (*left*). Because the height dependence $s(h)$ of the loop length is known from our stereoscopic reconstruction (displayed in Fig. 5), we can directly obtain the parametrization $n_e[s(h)] \mapsto n_e(h)$ and fit an exponential density model,

$$n_e(h) = n_{e0} \exp\left[-\frac{h}{\lambda(T_e)} \right] \tag{5}$$

to obtain a scale height temperature T_e^{λ}, which is defined by (e.g., Lang 1980, p. 285)

$$\lambda(T_e) = \frac{k_B T_e}{\mu m_H g} \approx 46 \left(\frac{T_e}{1\ \mathrm{MK}} \right) [\mathrm{Mm}] , \tag{6}$$

with k_B the Boltzmann constant, μ the mean molecular weight ($\mu \approx 1.4$ for the solar corona), m_H the mass of the hydrogen atom, and g the acceleration of gravity at the solar surface. The so obtained scale height λ, with a mean of $\lambda = 55 \pm 10$ Mm, and the inferred scale height temperature T_e^{λ}, with a mean of $T_e^{\lambda} = 1.22 \pm 0.23$, are listed in Tables 1 and 2 for each of the analyzed 30 loops. Loop segment ranges that are obviously confused by adjacent or crossing loops (as can be judged from Fig. 6), have been excluded in the fitting of the scale height model. We find that most of the analyzed loop segments fit closely an exponential density model (see Fig. 10, *left*). Deviations from an exponential density model can often be explained by uncertainties in the background subtraction or by confusion from adjacent or overlying loops. A correction to the local scale height temperature would also result from temperature gradients (§ 2.8), which are of the order $(dT/ds)/(T/\lambda) \approx 0.05 \pm 0.20$ and are neglected here.

2.7. *Loop Temperatures*

Independently of the scale height temperature T_e^{λ}, we can also determine the temperature directly from the EIT filter ratio (as described in § 2.6), which moreover provides a temperature differentiation along the loop, $T_e^{\mathrm{EIT}}(s)$. Since our loop definitions are based on tracing of an EIT 171 Å image, we use only the filter ratio of EIT 171 Å (Fe IX, Fe X) and 195 Å (Fe XII), which is sensitive in the temperature regime of $T_e = 1.0$–1.5 MK. We are using the spatial loop definition $[x(s), y(s)]$ based on the 171 Å image and apply the same background-subtraction technique to the 195 Å

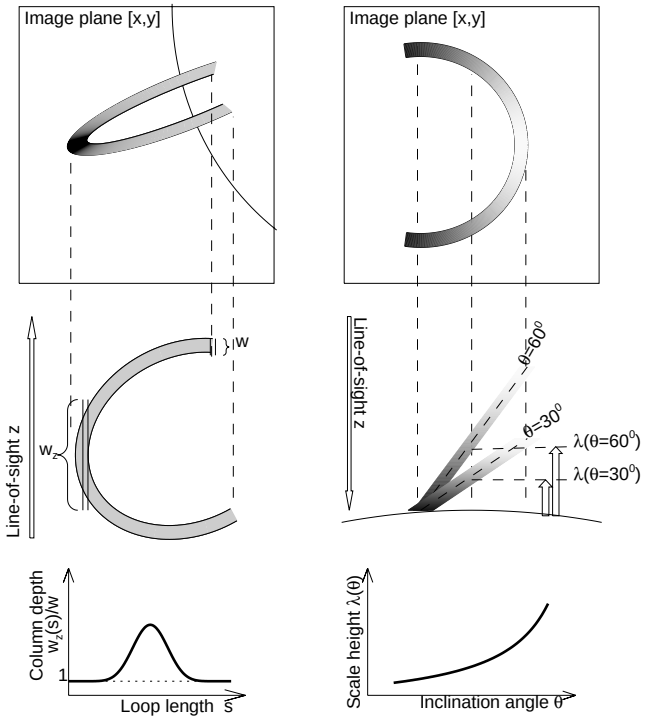

FIG. 9.—*Left:* The effect of the variable column depth $w_z(s)$ measured parallel to the line of sight z is illustrated as a function of the loop length parameter s, for a loop with a constant diameter w. *Right:* The effect of the inclination angle ϑ of the loop plane on the inferred density scale height $\lambda(\vartheta)$ is shown. Both effects have to be accounted for the determination of the electron density $n_e(s)$ along the loop.

image before we determine the temperature from the filter ratio $(F^{195} - F_B^{195})/(F^{171} - F_B^{171})$. Because our background-subtraction technique has some tolerance (of $\pm 1, \ldots, 4$ pixels) in the localization of the loop cross section (by maximizing the flux integrated over the loop cross section), the filter-ratio is not susceptible to small co-alignment errors between the 171 and 195 Å image. The employed background-subtraction technique also requires a correlated structure (with a width of 2–8 pixels) in both wavelengths, whereas larger or diffuse structures with possibly different temperatures are safely subtracted out.

The filter-ratio temperatures $T_e^{\rm EIT}$ averaged over the loop segments are tabulated in Table 2, with a mean of $T_e^{\rm EIT} = 1.21 \pm 0.06$ MK. The distribution of filter-ratio temperatures $N(T_e^{\rm EIT})$ is shown in Figure 11 (*bottom left*), along with the distribution of scale height temperatures $N(T_e^{\lambda})$ (Fig. 11, *top left*), both having almost identical means. The range of scale height temperatures (± 0.23 MK) is broader than the range of EIT filter-ratio temperatures (± 0.06 MK), probably because of systematic errors in background subtraction and loop separation. This is also consistent with the scatter plot of the two temperature definitions (Fig. 11, *top right*), where no obvious correlation is seen. Despite these unavoidable uncertainties in the background subtraction, it is remarkable that the means of the two independently determined temperatures coincide so closely.

2.8. *Loop Temperature Gradients*

The detailed variation of the temperature $T_e^{\rm EIT}(s)$ along the loop length s is shown for the 10 least-confused loops in

TABLE 2

PHYSICAL PARAMETERS OF 30 CORONAL LOOPS (1996 AUGUST 29, EIT 171 Å)

Loop Number	Emission Measure EM_0 log (cm^{-5})	Electron Density $n_e/10^9$ (cm^{-3})	Scale Height Temperature T_e^{λ} (MK)	Filter-Ratio Temperature $T_e^{\rm EIT}$ (MK)	Temperature Gradient dT/ds (K km^{-1})	Conductive Loss Rate $\nabla F_c \times 10^3$ (ergs cm^{-3} s^{-1})	Radiative Loss Rate $E_R \times 10^3$ (ergs cm^{-3} s^{-1})	Steady State Heating Rate $E_H \times 10^3$ (ergs cm^{-3} s^{-1})	Magnetic Field $B_{\rm foot}$ (G)
1	27.71	2.5	1.08 ± 0.07	1.25 ± 0.09	2.2 ± 0.5	−0.001	−0.718	0.716	−413
2	27.93	2.3	1.09 ± 0.12	1.27 ± 0.10	1.7 ± 1.0	−0.001	−0.607	0.607	−413
3	27.79	2.1	1.25 ± 0.13	1.22 ± 0.10	−0.1 ± 0.8	−0.000	−0.506	0.506	−285
4	27.60	2.6	1.26 ± 0.14	1.27 ± 0.11	3.7 ± 0.8	−0.004	−0.776	0.773	−285
5	27.34	2.5	1.22 ± 0.33	1.23 ± 0.10	−1.1 ± 0.4	−0.000	−0.718	0.718	−270
6	29.68	3.7	0.93 ± 0.08	1.30 ± 0.12	7.9 ± 2.7	−0.015	−1.572	1.557	−298
7	27.88	1.7	1.36 ± 0.17	1.19 ± 0.09	0.9 ± 0.3	−0.000	−0.332	0.332	−261
8	27.45	2.2	1.26 ± 0.10	1.23 ± 0.06	0.9 ± 0.2	−0.000	−0.556	0.555	−114
9	27.52	2.1	1.32 ± 0.53	1.15 ± 0.03	0.6 ± 1.0	−0.000	−0.506	0.506	−333
10	27.49	1.4	1.16 ± 0.30	1.21 ± 0.11	2.2 ± 0.5	−0.001	−0.225	0.224	−148
11	27.11	1.6	1.44 ± 0.18	1.20 ± 0.09	4.9 ± 0.4	−0.006	−0.294	0.288	7
12	27.56	2.0	1.31 ± 0.07	1.10 ± 0.06	0.5 ± 0.2	−0.000	−0.459	0.459	−208
13	27.41	1.8	1.31 ± 0.17	1.21 ± 0.11	4.6 ± 1.3	−0.006	−0.372	0.366	−252
14	27.18	1.7	0.73 ± 0.08	1.12 ± 0.05	1.2 ± 0.7	−0.000	−0.332	0.331	−157
15	27.48	2.0	1.04 ± 0.08	1.18 ± 0.09	1.8 ± 0.3	−0.001	−0.459	0.458	−294
16	27.28	1.4	1.15 ± 0.32	1.24 ± 0.12	−6.4 ± 0.7	−0.000	−0.225	0.225	−269
17	27.04	1.7	1.03 ± 0.30	1.18 ± 0.04	2.2 ± 0.6	−0.001	−0.332	0.330	−178
18	26.90	1.1	2.03 ± 0.41	1.30 ± 0.06	0.7 ± 0.6	−0.000	−0.139	0.139	−159
19	27.28	1.3	1.43 ± 0.17	1.18 ± 0.04	0.0 ± 0.4	−0.000	−0.194	0.194	−129
20	27.43	1.8	1.22 ± 0.05	1.22 ± 0.04	1.2 ± 0.2	−0.000	−0.372	0.372	−140
21	27.51	2.1	0.98 ± 0.11	1.15 ± 0.04	0.8 ± 0.3	−0.000	−0.506	0.506	−97
22	27.32	1.0	1.27 ± 0.82	1.22 ± 0.12	−4.5 ± 1.9	−0.000	−0.115	0.115	−159
23	27.61	2.3	1.31 ± 0.28	1.23 ± 0.15	11.4 ± 1.0	−0.024	−0.607	0.584	54
24	28.29	1.3	1.41 ± 0.22	1.20 ± 0.08	−7.3 ± 4.0	−0.000	−0.194	0.194	951
25	27.38	1.8	0.93 ± 0.04	1.18 ± 0.11	5.4 ± 0.5	−0.007	−0.372	0.365	76
26	26.95	1.4	1.30 ± 0.36	1.15 ± 0.08	5.9 ± 1.8	−0.009	−0.225	0.216	60
27	27.20	1.5	1.26 ± 0.30	1.21 ± 0.07	−1.7 ± 0.5	−0.000	−0.258	0.258	61
28	27.79	2.6	1.24 ± 0.05	1.12 ± 0.04	0.0 ± 0.3	−0.000	−0.776	0.776	128
29	27.76	2.4	1.31 ± 0.06	1.36 ± 0.07	−1.2 ± 0.6	−0.000	−0.661	0.661	128
30	29.48	1.7	0.84 ± 0.10	1.16 ± 0.08	−9.7 ± 4.8	−0.000	−0.332	0.332	142
Average...	27.61 (±0.61)	1.92 (±0.56)	1.22 (±0.23)	1.21 (±0.06)	0.960 (±4.265)	−0.003 (±0.005)	−0.458 (±0.285)	0.455 (±0.283)	−108 (±257)

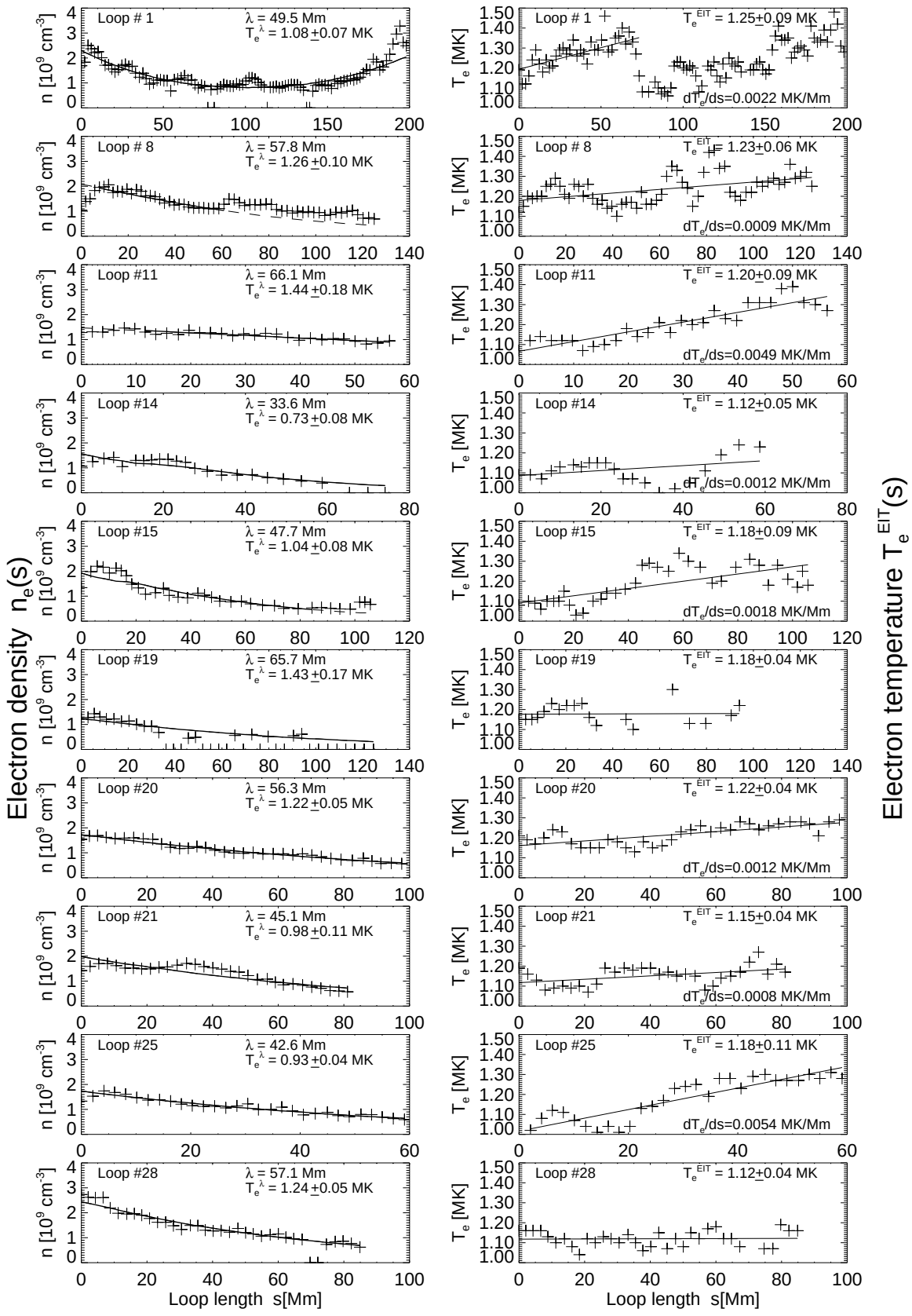

FIG. 10.—Electron density $n_e(s)$ (*left*) and the EIT filter-ratio electron temperature $T_e(s)$ (*right*) as a function of the loop length s for the same 10 loops selected in Fig. 8. An exponential model $n_e(h)$ is fitted, yielding the density scale height λ and scale height temperature T_e^{λ} indicated in the left panels. The average EIT filter-ratio temperature T_e^{EIT} (obtained from 171/195 Å images) is indicated in the right panels. A temperature gradient dT_e/ds is listed if the gradient is significant.

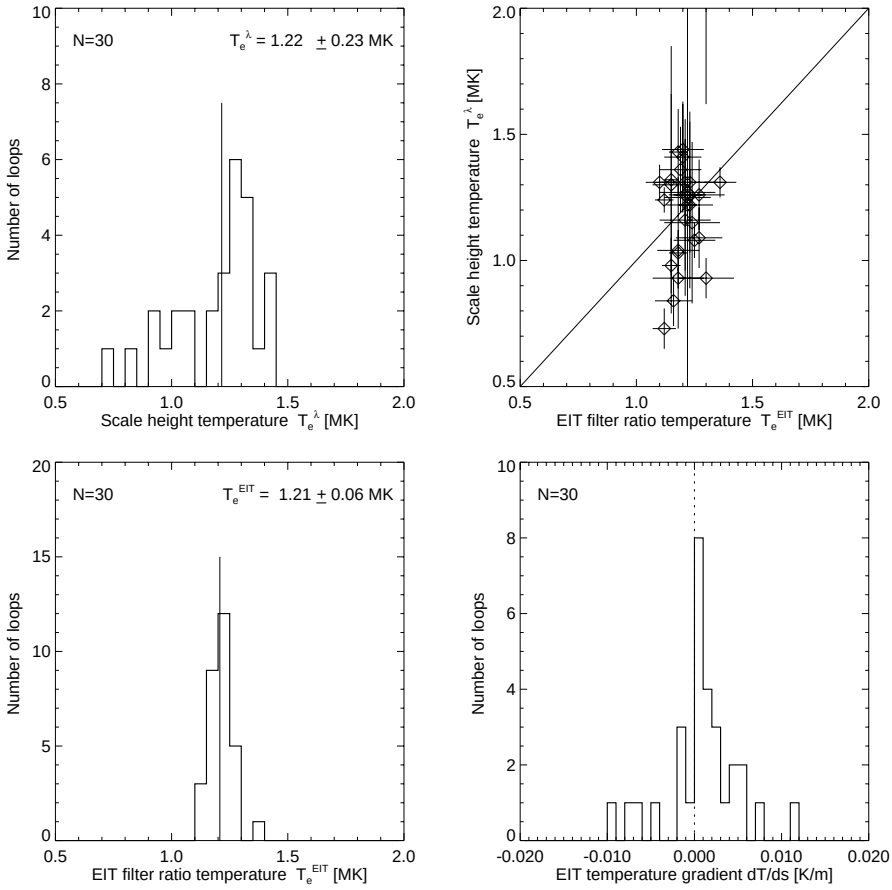

FIG. 11.—Statistics of scale height temperatures T_e^{λ} (*left top*), EIT filter-ratio temperatures $T_e^{\rm EIT}$ (*left bottom*), scatter plot of these two temperatures (*right top*), and EIT temperature gradients dT/ds (*right bottom*) for all analyzed 30 loops.

Figure 10 (*right*). We note that the filter-ratio temperature varies sometimes discontinuously along the loop, e.g., there is a jump from $T_e = 1.35$ MK to $T_e = 1.1$ MK at $s = 70$ Mm in loop 1 (Fig. 10, *top right*), which may be caused by contamination from a hotter loop that is located almost parallel to loop 1 at $s < 70$ Mm (see cross sections in Fig. 6). Such confusion problems can only be identified in hindsight. Despite such confusion problems, there seems to be a trend of a positive temperature gradient $dT/ds > 0$ above the footpoint for most of the loops (Table 2). To estimate these average temperature gradients (without correcting for multiloop confusion) we performed a linear regression $T_e(s)$ for all loops. The most significant temperature gradients are found for loop 11 ($dT/ds = +0.0049$ K m^{-1}), for loop 20 ($dT/ds = +0.0012$ K m^{-1}), and for loop 25 ($dT/ds = +0.0054$ K m^{-1}); see examples in Figure 10 and Table 1. The distribution of temperature gradients $N(dT/ds)$ is shown in Figure 11 (*bottom right*), revealing that $\approx 75\%$ of the loops have a positive temperature gradient $dT/ds > 0$ across the first scale height above their footpoints. Higher parts ($h \gtrsim 1\lambda$) of these loops are not detectable in EIT images due to insufficient density contrast (1 scale height corresponds to a factor of ≈ 3 in density or a factor of ≈ 10 in emission measure or EIT flux).

2.9. *Magnetic Field, Plasma-β Parameter, and Alfvén Velocity*

There is no accurate method available yet to determine the height dependence of the coronal magnetic field, nor to trace the magnetic field along a particular active region loop. Some attempts are in progress to match loop geometries observed in SXR or EUV with potential field models (constrained by the photospheric boundary and projections of coronal loops; Gary 1997; Gary & Alexander 1999). As a first approximation to investigate the magnetic field along the observed EUV loops, we calculate here a potential field model of AR 7986, using the code of Sakurai (1982) applied to a *SOHO*/Michelson-Doppler Imager (MDI) magnetogram, recorded on the same day as the EIT image (with a time difference of 20 hr). The potential field model is shown in Figure 12, overlaid on the MDI magnetogram, and coaligned with the traced EIT loops (by transforming the three-dimensional field lines according to the solar rotation rate during the time difference). Note that the EUV loops represent independent tracers of the plasma along magnetic field lines and thus convey an important test of how well the coronal magnetic field is represented with a potential field model. The match of the traced EUV loops with the potential field shown in Figure 12 is remarkably good, given the time difference of 20 hr and the nonpotential structure implied by currents that are likely to be present in this active region, imposed by the observed filament along the neutral line. Detailed modeling with potential and force-free magnetic fields and investigating the best match with individual loops traced from EIT and SXT images will be pursued in a subsequent study.

To estimate the magnetic field along the traced EIT loops we localize those potential field lines that have the closest

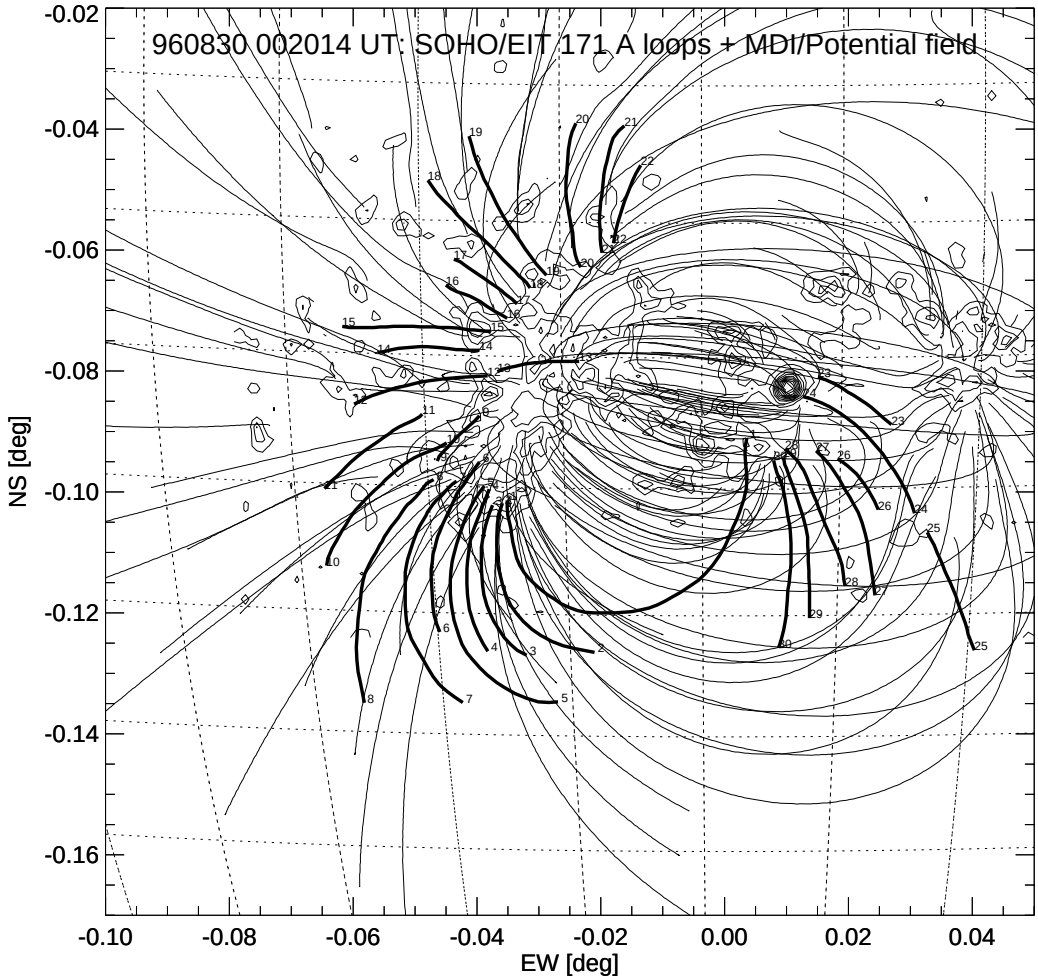

FIG. 12.—*SOHO*/MDI magnetogram recorded on 1996 August 30, 2048 UT, rotated to the time of the analyzed EIT image (1996 August 30, 0020:14 UT), with contour levels at $B = -350, -250, \ldots, +1150$ G (in steps of 100 G). Magnetic field lines calculated from a potential field model are overlaid (*thin lines*) onto the 30 loops (*thick lines*) traced from the *SOHO*/EIT image.

footpoints to the EIT loop footpoints and take the height dependence of their magnetic field strength $B(h)$ as a proxy for the EIT loops. The height dependence of the magnetic field $B(h)$ of the 30 potential field lines closest to the analyzed EIT loops is shown in Figure 13 (*top*). It can be approximated with a dipole model,

$$B(h) = B_{\rm foot}\left(1 + \frac{h}{h_D}\right)^{-3}, \qquad (7)$$

with a mean dipole depth of $h_D = 75$ Mm and a range of footpoint field strengths $B_{\rm foot} \approx 20, \ldots, 230$ G (dashed lines in Fig. 13, *top*), or a mean of $B_{\rm foot} \approx 100$ G.

With the potential field $B(h)$ and the measured density $n_e(h)$ and temperature profiles $T_e(h)$ we can now determine the height dependence of the plasma-β parameter for each of the 30 analyzed loops,

$$\beta(h) = \frac{n(h)kT_e(h)}{[B(h)^2/8\pi]} \approx 3.47 \times 10^{-15}\,\frac{n_e(h)T_e(h)}{B(h)^2}, \qquad (8)$$

which quantifies the ratio of the thermal to the magnetic pressure and thus provides a crucial criterion for magnetic confinement. The plasma-β parameter is shown in Figure 13 (*middle*), ranging typically at $\beta \lesssim 0.1$ in the entire coronal range ($h \lesssim 200$ Mm) of the EUV loops. We find only 2 (out of 30 loops) that exceed the critical limit of $\beta \geq 1$, possibly implying currents and nonpotential magnetic fields along the loops. Gary & Alexander (1999) found such regimes with $\beta \gtrsim 1$ in the upper corona at $h \gtrsim 0.2\,R_\odot$ from analysis of SXR loops, in contrast to the common belief that the coronal value is always $\beta \ll 1$ (Dulk & McLean 1978; Priest 1981; Sakurai 1989; Gary 1990; McClymont, Jiao, & Mikić 1997). Reliable measurements of the plasma-β parameter require fully resolved structures, such as single loops analyzed here (save for unknown filling factors), whereas line-of-sight averaged densities are expected to underestimate the density in loop structures and thus are biased toward too low β values.

A further plasma parameter that is of interest for coronal loop dynamics is the Alfvén velocity, which can be computed along individual loops thanks to the knowledge of the magnetic field $B(h)$ and density $n_e(h)$,

$$v_{\rm A}(h) = \frac{B(h)}{\sqrt{4\pi n_i(h) m_i}} \approx 2.18 \times 10^{11}\,\frac{B(h)}{\sqrt{n_e(h)}}\ {\rm cm\ s^{-1}}. \qquad (9)$$

This quantity is shown in Figure 13 (*bottom*). The Alfvén velocity is found to be highest near the footpoints of the analyzed EUV loops, ranging from $v_{\rm A}(h = 0) \approx 2000$ to 6000 km s^{-1}, and is dropping off steadily with larger height

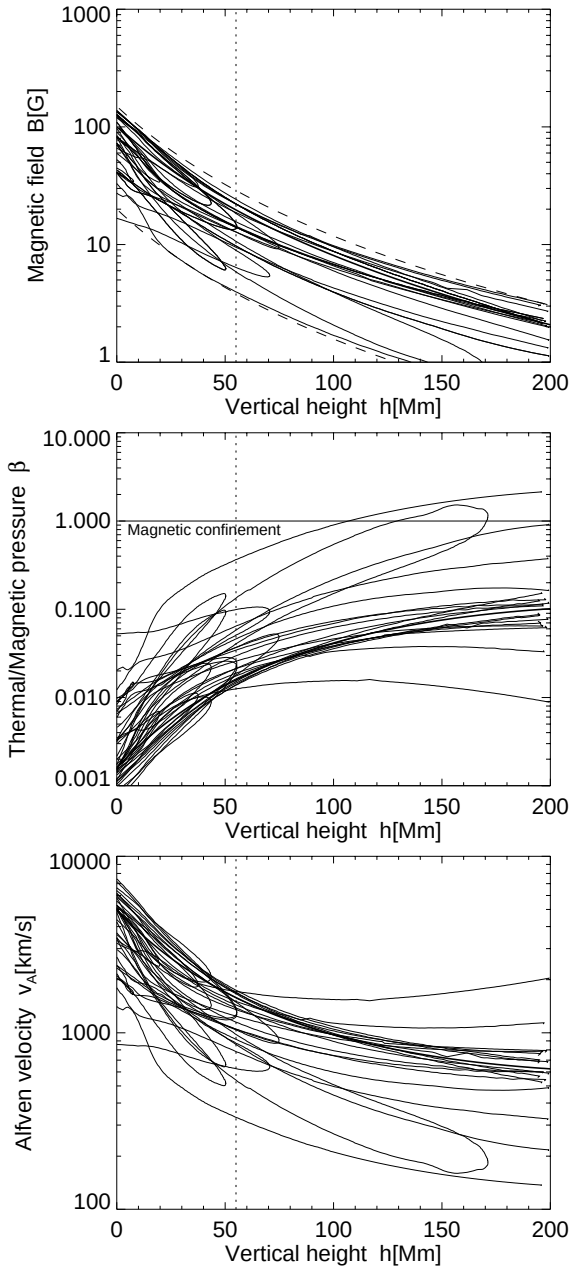

FIG. 13.—Magnetic field $B(h)$ (*top*), the plasma-β parameter or ratio of thermal to magnetic pressure, $\beta(h)$ (*middle*), and the Alfvén velocity $v_A(h)$ (*bottom*) determined as a function of height h for the 30 analyzed EIT loops. The magnetic field $B(h)$ is taken from the nearest potential field line (see Fig. 12). The vertical density scale height $\lambda = 55$ Mm is marked with a dotted line. A potential field model is indicated with dashed curves (*top*).

to a characteristic value of $v_A(h \gtrsim 100 \text{ Mm}) \approx 500$–$1000$ km s^{-1}.

3. PHYSICAL MODELS AND DISCUSSION

The density and temperature diagnostics obtained as functions of three-dimensional space coordinates allow us to investigate the physical conditions in the analyzed loops and to test some theoretical loop models and scaling laws. The major benefit of this study is that the loop geometry is well determined by the data, so that no geometric assumptions have to be made in the application of theoretical loop models.

3.1. *Loop Length Parametrization*

Because the thermal energy is generally much smaller than the magnetic energy in the corona [plasma parameter $\beta = n_e k_B T_e/(B^2/8\pi) \ll 1$], energy transport in coronal loops can be reduced to one dimension, as a function of the loop length parameter s. In our analysis we detected, except for one complete loop, only segments of loops that extend about 1 scale height above the primary footpoint. We will denote the start of the traced loop segments at the primary footpoint with $s = 0$, the end of the traced loop segment with $s = L_1$, and the full loop length extending all the way to the secondary footpoint with $s = L$. By localizing the secondary footpoint of traced loops from the global dipolar magnetic field of the active region, we obtained the approximate azimuth angle and length of the footpoint baseline. Using the stereoscopically determined inclination angle ϑ and the azimuth angle α of the footpoint baseline (Fig. 2), we were able to project the three-dimensional loop coordinates into the loop plane X-Z (eq. [A5]). In this loop plane we can approximate the loop geometry with a circular function, by interpolating the three loop positions ($s = 0, L_1, L$) with the circle parametrization $[X(\varphi), Y(\varphi)]$,

$$X = R_0 \cos \varphi \,, \tag{10}$$

$$Z = R_0 \sin \varphi + Z_0 \,, \tag{11}$$

yielding the circular loop radius R_0 and the offset Z_0 of the circle center from the footpoint baseline. The loop length $s(\varphi)$ can now be parametrized as a function of the circular angle φ,

$$s(\varphi) = R_0(\varphi + \varphi_0) \,, \quad -\varphi_0 \le \varphi \le (\pi + \varphi_0) \,, \tag{12}$$

where the starting angle φ_0 is defined by the loop radius R_0 and center offset Z_0,

$$\varphi_0 = \arcsin \frac{Z_0}{R_0} \,. \tag{13}$$

The full loop length L is then

$$L = R_0(\pi + 2\varphi_0) \,. \tag{14}$$

The geometric elements R_0, Z_0, L_1, and L are listed in Table 1 for all 30 loops. The same circular geometry was also used to visualize the extrapolated loop segments in Figure 5.

For the application of the hydrostatic equilibrium equation we need also to quantify the height dependence $h(s)$ of the loop length, which is determined by the loop plane inclination angle ϑ and equations (11)–(12),

$$h(s) = Z \cos \vartheta = \left[Z_0 + R_0 \sin \left(\frac{s}{R_0} - \varphi_0 \right) \right] \cos \vartheta \,. \tag{15}$$

The apexes or loop tops, $h_{\text{top}} = (Z_0 + R_0) \cos \vartheta$, have a range of $h_{\text{top}} = 30$–225 Mm in our sample of 30 loops and thus extend up to 4 scale heights (with $\lambda = 55 \pm 10$ Mm).

3.2. *Static Loop Model*

In static loop models it is assumed that mass flows can be neglected, leading to the basic steady state energy balance equation, e.g., derived by Rosner et al. (1978),

$$E_H(s) + E_R(s) - \nabla F_C(s) = 0 \,, \tag{16}$$

where E_H denotes the rate of heat deposition, E_R the energy radiated from the loop, and F_C is the thermal conductive flux, to be balanced at each location s of the loop in a static model.

The conductive flux term can be expressed in one-dimensional form (with the Spitzer thermal conductivity $\kappa = 0.92 \times 10^{-6}$ ergs s^{-1} cm^{-1} K$^{-7/2}$; Spitzer 1962, p. 144) by

$$\nabla F_C(s) = \frac{d}{ds}\left[-\kappa T^{5/2}(s)\,\frac{dT(s)}{ds}\right] \approx -\frac{5}{2}\,\kappa T^{3/2}(s)\left[\frac{dT(s)}{ds}\right]^2 \text{ ergs cm}^{-3}\text{ s}^{-1}\,, \quad (17)$$

where the approximation on the right-hand side includes only the linearized temperature dependence $T(s)$. The linearized temperature dependence can be written in terms of our measured temperature gradients (dT/ds) and mean temperatures $T_e^{\rm EIT}$ listed in Table 2 by

$$T(s) = T_e^{\rm EIT} + \left(\frac{dT}{ds}\right)\left(s - \frac{L_1}{2}\right). \quad (18)$$

The conductive flux term $\nabla F_C(s)$ in the energy balance equation (17) is calculated for $s = 0$ in Table 2, having a mean of $\langle \nabla(F_c)\rangle = (-0.003 \pm 0.005) \times 10^{-3}$ ergs cm^{-3} s^{-1}.

The radiative loss term $E_R(s)$ can be written in terms of the electron density $n_e(s)$ and the radiative loss function $\Lambda(T)$,

$$E_R(s) = -n_e(s)^2 \Lambda[T(s)] \text{ ergs cm}^{-3}\text{ s}^{-1}\,, \quad (19)$$

which can be approximated with a constant value in our relatively narrow temperature range of interest ($T_e =$ 0.5–2.0 MK),

$$\Lambda[T] = 10^{-21.94} \text{ ergs cm}^{-3}\text{ s}^{-1} \quad (10^{5.75} < T < 10^{6.3})\,, \quad (20)$$

as calculated by Raymond, Cox, & Smith (1976) for solar abundances (Rosner et al. 1978; Fig. 10; and eq. [A1]). The radiative loss rate $E_R(s)$ is calculated for $s = 0$ in Table 2, having a mean of $\langle E_R\rangle = (-0.46 \pm 0.29) \times 10^{-3}$ ergs cm^{-3} s^{-1} for our 30 analyzed loops, surpassing the conductive loss rate by about 2 orders of magnitude (under the assumption of a filling factor of unity).

Static hydrodynamic loop models assume steady state conditions, i.e., the heating rate has to balance the energy losses by conduction and radiation according to equation (16). Because we find here that the conductive loss rate is much smaller than the radiative loss for this set of analyzed EUV loops, the required steady state heating rate has to balance essentially the radiative loss rate, i.e., $E_H \approx -E_R$. This steady state heating rate requirement E_H (defined by eq. [16]) is listed in Table 2, having a mean of $\langle E_H\rangle = (+0.46 \pm 0.28) \times 10^{-3}$ ergs cm^{-3} s^{-1}. Because the radiative loss rate is proportional to the squared density (eq. [19]), for which we found an exponential decrease with height (eq. [5]), the steady state heating rate requirement follows a similar exponential relation,

$$E_H(s) \approx -E_R(s) \approx n_{e0}^2\,\Lambda(T)\,\exp\left[-\frac{2h}{\lambda(T)}\right], \quad (21)$$

with an exponential scale height that equals half the density scale height. Such an exponential heating scale height s_H, or heat-deposition length, has been introduced, for instance in loop models of Serio et al. (1981),

$$E_H(s) = E_{H0}\,\exp\left(-\frac{s}{s_H}\right), \quad (22)$$

which has a mean value of $s_H = \lambda/2 = (55 \pm 10$ Mm$)/2 = 28 \pm 5$ Mm (see Table 1) for our group of EUV loops. This is a very stringent requirement for the spatial distribution of the heating function. It is very unlikely that the heating function always adjusts to the gravitational stratification without thermal conduction. However, because we found that conductive loss is 2 orders of magnitude smaller than radiative loss, the observed temperature and density structure of EUV loops can only be controlled by a combination of heating and radiative loss. Because these two terms cannot be balanced in a natural way, we conclude that the observed EUV loops *are not in steady state* and thus cannot be explained with static models.

Coronal loops in steady state conditions have also been simulated numerically, where solutions of the static energy equation yield the result that the conductive energy loss is about equivalent to twice the radiative loss (e.g., Vesecky, Antiochos, & Underwood 1979). Consequently, for loops in steady state condition, the heating rate, the conductive loss, and the radiative loss are all of about the same order. The fact that we find the conductive loss to be 2 orders of magnitude smaller than radiative loss violates this rule of thumb for steady state condition. Therefore, we conclude that the observed EUV loops are not in steady state condition but rather in a cooling phase, far off the equilibrium.

3.3. *Loop Lifetime*

To investigate the lifetime of loops we have to consider the fastest of the energy loss timescales. The conductive loss time,

$$\tau_{\rm cond} = \frac{E_{\rm th}}{dE_C/dt} = \frac{3 n_e k_b T_e}{\nabla F_C} \approx 1.1 \times 10^{-9} n_e T^{-5/2} L_0^2 \text{ [s]}\,, \quad (23)$$

is found to be $\tau_{\rm cond} \approx 9 \times 10^5$ s (or 10 days), using the average parameters from Table 1, $n_e = 1.92 \times 10^9$ cm^{-3}, $T_e^{\rm EIT} = 1.22 \times 10^6$ K, and $L_0 = L/2 = 2.2 \times 10^{10}$ cm. The conductive loss time of EUV loops is therefore substantially longer than for SXR loops, for two reasons (1) the temperature is cooler, and (2) the loop length is somewhat larger. If we compare typical SXR loops as observed with *Yohkoh*/SXT, where typical temperatures of $T_e^{\rm SXR} = 5$ MK, densities of $n_e = 3 \times 10^9$ cm^{-3}, and loop lengths of $L^{\rm SXR} = 10^{10}$ cm were measured (Kano & Tsuneta 1995), we find conductive loss times of $\tau_{\rm cond}^{\rm SXR} \approx 8 \times 10^3$ s (or 2.4 hr). The huge difference in the conductive loss times of EUV and SXR loops comes mainly from the temperature factor, $(T^{\rm SXR}/T^{\rm EUV}) \approx 5$, which raised to the $T^{-5/2}$ power yields a ratio of

$$\frac{\tau_{\rm cond}^{\rm EUV}}{\tau_{\rm cond}^{\rm SXR}} \approx \left(\frac{T^{\rm EUV}}{T^{\rm SXR}}\right)^{-5/2} \approx 55\,, \quad (24)$$

i.e., the conductive loss time is about 55 times longer for EUV loops than for SXR loops.

Let us now estimate the radiative loss time of EUV loops (under the assumption of a filling factor of unity). The radi-

ative lifetime is

$$\tau_{\rm rad} = \frac{E_{\rm th}}{dE_R/dt} = \frac{3 n_e k_b T_e}{n_e^2 \Lambda(T_e)}, \quad (25)$$

yielding a mean lifetime of $\tau_{\rm rad} \approx 2.3 \times 10^3$ s or about 40 minutes, based on our mean values $\langle n_e \rangle = 1.92 \times 10^9$ cm^{-3}, $\langle T_e \rangle = 1.22$ MK, and $\Lambda(T) = 10^{-21.94}$ ergs cm^{-3} s^{-1}. Comparing the radiative lifetime of EUV loops with SXR loops, there is less of a difference than for the conductive loss time. This similarity is because the mean electron densities are comparable, i.e., $n_e^{\rm EUV} \approx 2 \times 10^9$ cm^{-3} versus $n_e^{\rm SXR} \approx 3 \times 10^9$ cm^{-3} (Kano & Tsuneta 1995), and the radiative loss function has only a slightly smaller value at SXR temperatures, i.e., $\Lambda(T^{\rm EUV}) \approx 10^{-21.94}$ ergs cm^{-3} s^{-1} (eq. [17]) versus $\Lambda(T^{\rm SXR}) \approx 10^{-22.18}$ ergs cm^{-3} s^{-1} (Kano & Tsuneta 1995), whereas the temperatures differ by a linear factor $T^{\rm SXR}/T^{\rm EUV} \approx 5$. The ratio of radiative loss times between EUV and SXR loops is therefore mainly determined by the temperature ratio,

$$\frac{\tau_{\rm rad}^{\rm EUV}}{\tau_{\rm rad}^{\rm SXR}} \approx \left(\frac{T^{\rm EUV}}{T^{\rm SXR}} \right) \approx 0.2 , \quad (26)$$

yielding a radiative cooling time of $\tau_{\rm rad}^{\rm SXR} \approx 10^4$ s (or about 3 hr) for SXR loops. The mean physical loop parameters of EUV and SXR loops and the resulting timescales are also summarized in Table 3 for convenience.

From these average physical parameters of our 30 analyzed EIT loops we find therefore that the conductive cooling time is at least 2 orders of magnitude larger than the radiative cooling time, a result that we have already noticed by comparing conductive loss rates versus the radiative loss rates in Table 2. This extreme ratio for EUV loops is in marked contrast to SXR loops, where the ratio $\tau_{\rm cond}^{\rm SXR}/\tau_{\rm rad}^{\rm SXR} = 8 \times 10^3/10^4 \approx 1$ is close to unity if we use the mean loop parameters of Kano & Tsuneta (1995). An even greater difference was found by Porter & Klimchuk (1995) and Priest et al. (1998), who measured ratios $\ll 1$ for individual SXR loops. Note that, for many of these loops, the ratio may actually be near unity if we allow for the possibility of small filling factors (see § 3.5). It is therefore possible that a majority of SXR loops are in quasi-static equilibrium. This is definitely not the case for the EUV loops, since small filling factors make the discrepancy between the radiative and conductive loss rates even larger. The ratio of conductive to radiative cooling times of EUV loops is even more different with respect to large-scale SXR loops, where the opposite ratio was found, i.e., the conductive loss being 2 orders of magnitude stronger than radiative loss (Priest et al. 1998).

We have only limited information on the real lifetime of the analyzed loops. A lower limit is constrained by the radiative cooling time, amounting to 40 minutes at the loop base. The real lifetime can be a few times longer, if radiative cooling is partially balanced by heating. However, the real lifetime cannot be much longer than the radiative cooling time because the required heating function would then have to be extremely fine tuned close to the steady state condition, which is implausible without the effect of thermal conduction. Based on this argument we conclude that the real lifetime cannot exceed a few radiative cooling times, say a few hours. This conclusion is somewhat supported by the localization capability of our dynamic stereoscopy method. The stereoscopic correlation over time intervals of ± 24 hr clearly shows spatial displacements of loops. It is therefore conceivable that the heating function is not cospatial over 24 hr, but rather spreads over multiple neighbored field lines, where individual loop strands cool off on timescales as short as the radiative cooling time ($\approx$40 minutes). Short-term fluctuations in $T_e \lesssim 1.0$ MK on the order of 5–10 minutes were also reported by Habbal, Ronan, & Withbroe (1985). A conceivable scenario is quasi-periodic microflare heating as simulated by Peres (1997).

3.4. *Loop Scaling Laws*

Scaling laws have been derived among physical loop parameters (such as the temperature T_e, the loop pressure p, the loop length L, the steady state heating rate requirement E_H [in a steady state model], and the magnetic field B), to test the internal self-consistency of the energy balance equation for a given set of observed loops. We show the relationships between these parameters in the form of correlation plots for our sample of 30 EUV loops in Figure 14, including the loop length L, the loop base pressure $p_0 = p(h = 0)$, the steady state heating rate at the footpoint $E_{H0} = E_H(h = 0)$, and the magnetic field $B_{\rm foot}$ at the footpoint. The footpoint field strengths $B_{\rm foot}$ have been measured from the MDI magnetogram by taking the maximum field values among the nearest MDI pixels to the EIT loop footpoints (see values of $B_{\rm foot}$ listed in Table 2).[3] We omit correlations with the temperature because this parameter is almost constant ($T_e^{\rm EIT} = 1.21 \pm 0.06$) for our data set. Linear regres-

[3] The cautious reader may make a distinction between a photospheric and coronal footpoint definition, which can be related using flux conservation as $\langle B_{\rm cor} \rangle r_{\rm cor}^2 = \langle B_{\rm phot} \rangle r_{\rm phot}^2$, in case of a canopy-like divergence from photospheric flux tube radius $r_{\rm phot}$ to coronal footpoint radius $r_{\rm cor}$. This effect is not considered here.

TABLE 3

COMPARISON OF MEAN PHYSICAL LOOP PARAMETERS IN EUV AND SXR

Parameter	EUV (This Work)	SXR (Kano & Tsuneta 1995, 1996)
Objects	*Cool* loops	*Hot* loops
Observations	*SOHO*/EIT 171 Å	*Yohkoh*/SXT
Electron temperature T_e (MK)	1.2	5
Electron density n_{e0} (cm^{-3})	2×10^9	3×10^9
Loop half-length L (cm)	2×10^{10}	1×10^{10}
Loop pressure p_0 (dyne cm^{-2})	0.6	4
Conductive loss time $\tau_{\rm cond}$ (s)	9×10^5	8×10^3
Radiative loss time $\tau_{\rm rad}$ (s)	2×10^3	1×10^4
Ratio $\tau_{\rm cond}/\tau_{\rm rad}$	450	1

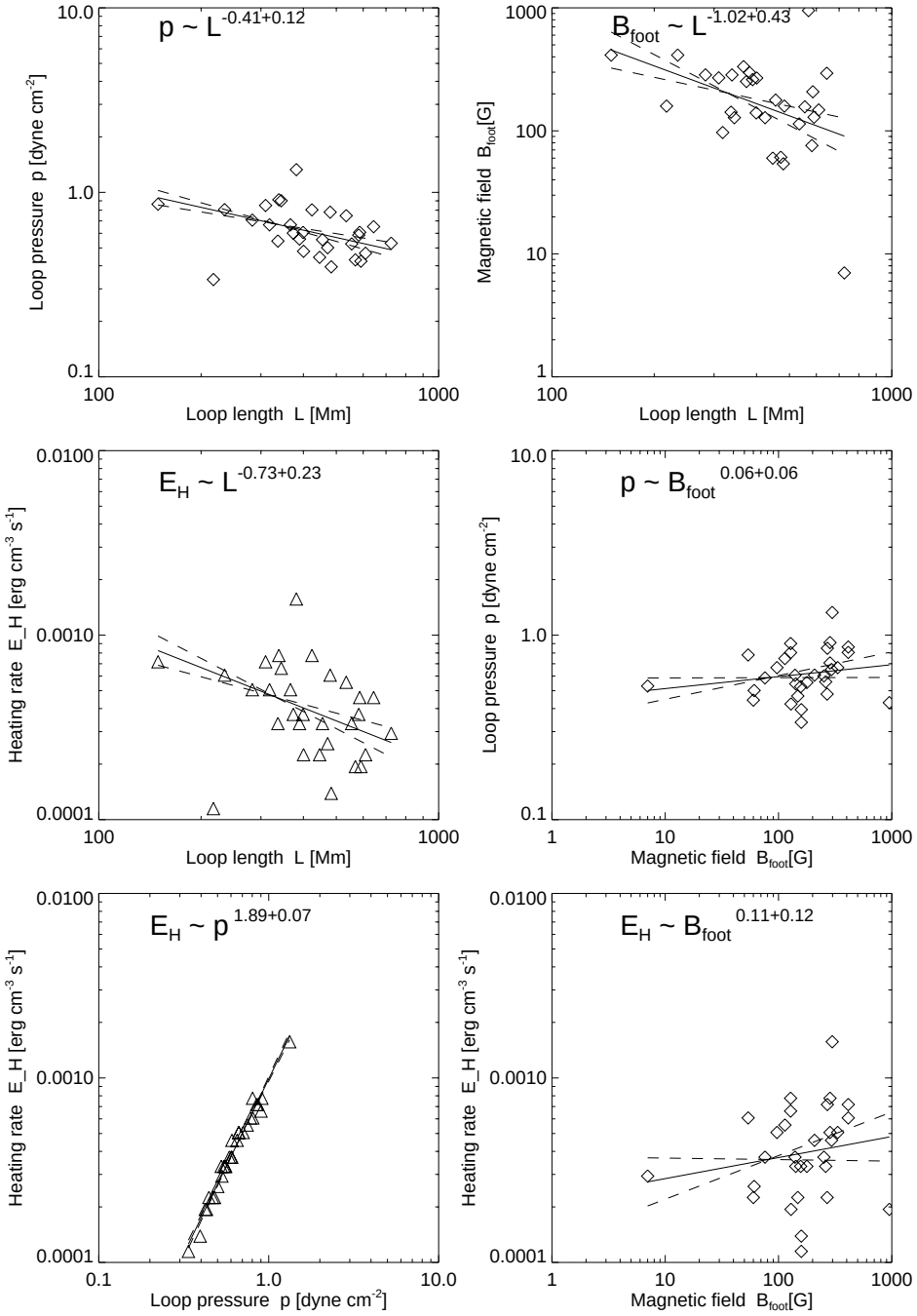

FIG. 14.—Scaling laws between the steady state heating rate requirement E_{H0}, loop base pressure p_0, loop length L, and magnetic field strength $B_{\rm foot}$ for our sample of 30 EUV loops. Linear regression fits are indicated with solid lines, the standard deviations of the slopes are marked with dashed lines.

sion fits reveal the following correlations

$$p_0 \propto L^{-0.41\pm0.12}\,, \tag{27}$$

$$B \propto L^{-1.02\pm0.43}\,, \tag{28}$$

$$E_{H0} \propto L^{-0.73\pm0.23}\,, \tag{29}$$

$$E_{H0} \propto p_0^{1.89\pm0.07}\,. \tag{30}$$

We do not find a significant correlation between the loop pressure p_0 and the magnetic field $B_{\rm foot}$ (Fig. 14, *middle right*), or between the heating rate E_{H0} and the magnetic field $B_{\rm foot}$ (Fig. 14, *bottom right*).

First, let us discuss the scaling between loop pressure and loop length. From the analysis of SXR loops (Porter & Klimchuk 1995; Klimchuk & Porter 1995), a power-law index of $-1.82 \le \beta \le -0.22$ (90% confidence range) was found for the correlation $p_0 \propto L^{\beta}$. This result is consistent with our findings from EUV loops, with $\beta = -0.41 \pm 0.12$ (1 σ standard deviation, eq. [27]). The theoretical interpretation of this value β depends on the heating deposition length in the context of a specific heating model. In the simplest case where the heating source is localized in a point source and does not depend on any other physical parameters, i.e., the same amount of thermal energy is deposited in loops of different lengths, the volumetric heating rate would scale as $E_H \propto L^{-1}$. If we additionally assume that the heating rate has to balance the radiative loss, $E_H \propto p^2$, as supported by the observed correlation (eq. [30]), then the pressure is expected to scale with loop length by $p_0 \propto L^{-0.5}$,

or $\beta = -0.5$, for one-dimensional loops. This is consistent with our observed relation $p_0 \propto L^{-0.41 \pm 0.21}$ (eq. [27]).

Second, we discuss the physical interpretation of correlations with the heating rate E_{H0}. Inserting the definition of the loop base pressure p_0,

$$p_0 = p(h = 0) = 2n_{e0}\, k_B\, T_e^{\rm EIT}\,, \tag{31}$$

into the steady state heating rate E_H that is required to balance the dominant radiative loss $-E_R$ (eq. [21]), we find immediately

$$E_{H0} \propto n_{e0}^2 \approx p_0^2\,, \tag{32}$$

since the temperature $T_e^{\rm EIT}$, as well as the radiative loss function $\Lambda(T)$, can be approximated by a constant for the given data set. This explains, by definition, the correlation found for EUV loops (eq. [30]). Such a dependence ($E_{H0} \propto p^2$) was also inferred for soft X-ray bright points (Kankelborg, Walker, & Hoover 1997). Note that this scaling law is distinctly different from that derived by Rosner et al. (1978), or Galeev et al. (1981),

$$E_{H0} \approx 10^5 p_0^{7/6} L_0^{-5/6}\,, \tag{33}$$

which was derived under the assumption of quasi-static equilibrium, in which radiative and conductive losses are necessarily comparable (e.g., Vesecky et al. 1979). The same applies to the generalized scaling law of Serio et al. (1981), who account for a nonconstant pressure $p(h)$, parametrized by a pressure scale height s_p and a heading deposition scale height s_H,

$$E_{H0} \approx 10^5 p_0^{7/6} L_0^{-5/6} \exp\left[0.5L\left(\frac{1}{s_H} - \frac{1}{s_p}\right)\right]. \tag{34}$$

Also Kano & Tsuneta (1996) derived an energy scaling law by equating radiative and conductive energy loss, for the special case of the heating source is located at the loop top,

$$E_{H0} = 4.0 \times 10^3 (p_0\, T_m^{1/2}) L_0 \text{ ergs cm}^{-3}\text{ s}^{-1} \tag{35}$$

with T_m the maximum temperature at the loop top. Similarly, Ofman, Klimchuk, & Davila (1998) derive a heating rate scaling law for resonant absorption of Alfvén waves under the assumption of quasi steady state equilibrium. Consequently, because all these energy scaling laws are based on the assumption of quasi-static equilibrium, in which radiative and conductive losses are necessarily comparable, they are not applicable to our set of EIT loops, where conductive loss is completely negligible compared with the radiative loss.

Third, we discuss the physical meaning of correlations with the magnetic field. For models where loop heating is accomplished by dissipation of magnetic energy (e.g., nanoflare heating model of Parker 1988), one would expect a relation $E_H \propto B^2$, which is not consistent with our findings because we did not find any significant correlation between E_H and $B_{\rm foot}$ (Fig. 14, *bottom right*). In many coronal heating models, the dissipated energy E_H depends also on the loop length L. It is then useful to investigate the specific dependence of the magnetic field B on the loop length L from observations, e.g., specified by a power law (Porter & Klimchuk 1995),

$$B \propto L^{\delta}\,. \tag{36}$$

Theoretically, a power-law index of $\delta = -3$ is expected for a point dipole, or $\delta = -2$ for a line dipole, in the far-field approximation. In the near field, i.e., for field lines comparable with the dipole separation, these relations are strongly modified (approaching a regime of $\delta \approx 0$). The distinction between the near-field and far-field approximations should therefore be taken into account in the application of a $B(L)$ relation. Klimchuk & Porter (1995) inferred that $\delta \approx -0.7$ by combining their $P \propto L^{-1}$ result for SXR loops with the *Skylab* result of Golub et al. (1980) that $P_{\rm AR} \propto B_{\rm AR}^{1.6}$, where the subscripts refer to averages over entire active regions. Recent work with more detailed magnetic field modeling yields a value of $\delta = -0.97 \pm 0.25$ (Mandrini, Demoulin, & Klimchuk 1999). This recent value obtained from magnetic field extrapolations of many active regions agrees very well with the value found here from EUV loops, $\delta \approx -1.02 \pm 0.42$ (eq. [28]). The value of $\delta \approx -1$ for both SXR and EUV loops indicates that the observed loops belong to the near-field regime rather than to the far-field case. Interestingly, no correlation was found between $B_{\rm foot}$ and L for large-scale magnetic fields of the global corona, which extends out to the heliosphere (Wang et al. 1997).

3.5. *Loop Filling Factors*

So far we assumed a filling factor of unity in our derivation of physical loop parameters. However, there is some indirect evidence that coronal loops may consist of many unresolved thin strands (Golub et al. 1990), which suggests a higher electron density inside the strands than obtained from the volume-averaged emission measure across a macroscopic loop diameter. If we denote the true density inside the strands with n_e^* and the volume filling factor of strands by f, the two densities relate by

$$n_e^*(s) = \sqrt{\frac{\text{EM}(s)}{w_z(s)}\frac{1}{f}} = \frac{n_e(s)}{\sqrt{f}}\,. \tag{37}$$

This filling factor affects the radiative loss rate (eq. [19]), but not the conductive loss rate (eq. [17]). Numerical solutions of the static energy equation in coronal loops have shown that the conductive energy loss to the chromosphere is about twice as much as the radiative loss in the corona (Vesecky et al. 1979). Based on this argument, the filling factor can be derived by equating twice the conductive loss rate with the radiative loss rate, $2\nabla F_C(s) \approx E_R(s)$. Porter & Klimchuk (1995) used this approach to infer filling factors $\ll 1$ for most of the 47 SXR loops they analyzed. Several had filling factors greater than 1, an unphysical situation that led them to conclude that those particular loops cannot be in quasi-static equilibrium. We find a similar situation for our EUV loops. Introducing a filling factor less than 1 would increase the radiative loss rate, but not the conductive loss rate, and so the 2 order of magnitude discrepancy that already exists would become even larger. Thus, our conclusion that the loops are not in equilibrium seems inescapable. It is interesting to note that the nonequilibrium loops of the Porter and Klimchuk study are relatively cool at $T \approx 2$ MK. They may belong to a separate class of loops (Cargill & Klimchuk 1997) that includes the EIT loops presented here.

3.6. *Hydrostatic Equilibrium*

The exponential density profiles $n_e(h)$ of our analyzed sample of EUV loops together with the finding that the resulting scale height temperature ($T^{\lambda} = 1.22 \pm 0.23$ MK) matches exactly the filter-ratio temperature ($T^{\rm EIT} = 1.21 \pm 0.06$ MK) in the statistical average, clearly proves that these EUV loops are in hydrostatic equilibrium. On the

other hand we found that these EUV loops are not in steady state condition, but are dominated by radiative cooling. The question arises then how pressure changes due to unbalanced heating or cooling processes can always adjust to hydrostatic equilibrium. Pressure gradients propagate with sound speed,

$$v_s = \sqrt{\frac{\gamma k_B T_e}{\mu m_H}} \approx 1.51 \times 10^4 \sqrt{T_e} \text{ cm s}^{-1}, \quad (38)$$

which amounts to $v \approx 165$ km s^{-1} for the observed EUV loops with an average temperature of $T_e \approx 1.2$ MK. Based on the mean scale height of $\lambda = 55$ Mm, the sound travel time across a scale height is $t_s = \lambda/v_s = 330$ s, or about 5 minutes. Because this sound travel time is therefore always much shorter than the radiative cooling time, with a minimum value of $\tau^0_{\rm rad} \approx 40$ minutes at the loop base, increasing to $\tau_{\rm rad}(h = \lambda) \approx 110$ minutes at a height of 1 scale height, pressure changes can always be adjusted to hydrostatic equilibrium, so that we expect these loops always to be close to hydrostatic equilibrium. This is also consistent with results based on numerical simulations of the thermal stability. Although uniform-pressure loops were found to be thermally unstable under some conditions (e.g., if the base heat flux is too small), the influence of gravity (or hydrostatic equilibrium) was found to have a stabilizing effect (Wragg & Priest 1982). These arguments may partially explain the numerous existence of hydrostatic EUV loops observed by EIT during four solar rotations in this active region.

3.7. *A Statistical Heating Model for EUV Loops*

Our measurements have shown two important findings: (1) EUV loops are in hydrostatic equilibrium, and (2) radiative energy loss dominates conductive loss completely. The second finding is in strong contrast to SXR loops, which are found to be close to steady state condition, where radiative cooling and thermal conduction are comparable. Consequently, EUV loops are far off the steady state equilibrium, and their temperature structure cannot be explained by steady state models. Although it is mathematically possible to construct a heating function that exactly balances the radiative loss (eq. [21]), the conductive loss rate cannot be increased (given the observed temperature gradients) to match the radiative loss, a necessary condition for static equilibrium. It is therefore more reasonable to invoke a model that does not require static equilibrium, e.g., a dynamic model with a time-dependent heating function.

Because thermal conduction is demonstratedly not essential in EUV loops, we cannot assume a single localized heating source, e.g., at the loop top, but rather have to assume a heating function that acts in all parts of the loop, either uniformly or randomly distributed, but affecting all parts of the loops in the temporal average. The loop can be subdivided into multiple strands, where the heating function acts randomly in different strands, or along the loop strands (Fig. 15, *top*). Let us characterize such a heating function with a fragmented topology, where each elementary heating event has a dissipation length l_h (Fig. 15, *top*) and occurs with a mean recurrence rate $R = 1/t_R$ at a given loop position h. The duration of the heating event has to be shorter than the local radiative cooling time $\tau_{\rm rad}$ because the loops would cool off faster than they can be heated otherwise. The radiative cooling time depends primarily on the

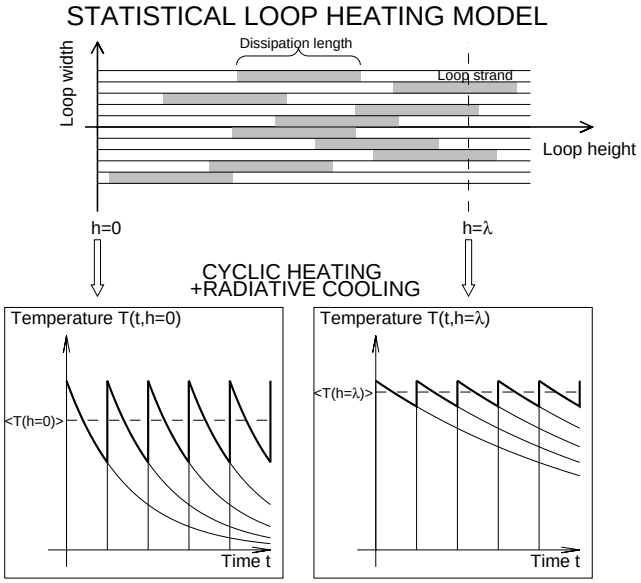

FIG. 15.—Cartoon of a statistical loop heating model, where heating events are uniformly or randomly distributed along and across a loop (possibly in different loop strands) and occur cyclically with a mean recurrence time. Because the heated loop portions cool off faster at the loop footpoints (due to the shorter radiative cooling time, *bottom left*) than in larger heights, i.e., at 1 scale height, $h = \lambda$ (*bottom right*), a positive temperature gradient arises in the statistical average.

density and has therefore a height dependence that is related to the hydrostatic equilibrium, i.e.,

$$\tau_{\rm rad}(h) = \frac{3 n_e(h) k_b T_e}{n_e(h)^2 \Lambda(T_e)} \approx \tau^0_{\rm rad} \exp\left(\frac{h}{\lambda}\right), \quad (39)$$

where $\tau^0_{\rm rad}$ refers to the radiative cooling time at the loop base ($h = 0$). Since the heating timescale has to be shorter than the radiative cooling time, we can neglect it to first order and obtain a sawtooth-like temperature profile $T_e(t)$ for a recurrent sequence of heating events, i.e., the loop is heated cyclically to a temperature $T_{\rm max}$ and cools off with an exponential decay time $\tau_{\rm rad}$ (Fig. 15, *bottom*). Because the radiative cooling time increases with height due to the hydrostatic density dependence, the loops will cool off slower in larger heights and thus maintain a higher temperature in the temporal average. This simple model already explains the basic mean temperature structure of EUV loops, producing a positive temperature gradient with height (without invoking thermal conduction). We can now derive the mean loop temperature $\langle T_e(h) \rangle$ as a function of the height by averaging the time-dependent temperature evolution during one heating cycle t_R (the mean recurrence time of a heating event),

$$\langle T_e(h) \rangle = \frac{\int_0^{t_R} T_{\rm max} \exp\left[-t/\tau_{\rm rad}(h)\right] dt}{\int_0^{t_R} dt} = T_{\rm max} \left[\frac{\tau_{\rm rad}(h)}{t_R}\right] \left\{1 - \exp\left[-\frac{t_R}{\tau_{\rm rad}(h)}\right]\right\}. \quad (40)$$

Inserting the height dependence of the radiative cooling time $\tau_{\rm rad}(h)$ from equation (39) yields then the following temperature profile,

$$\langle T_e(h) \rangle = T_{\rm max} \frac{1}{q_R} \exp\left(\frac{h}{\lambda}\right) \left\{1 - \exp\left[-\frac{q_R}{\exp(h/\lambda)}\right]\right\}, \quad (41)$$

where we defined a dimensionless recurrence time ratio q_R by

$$q_R = \frac{t_R}{\tau_{\rm rad}^0} . \quad (42)$$

The average temperature gradient dT/dh over a scale height λ is then

$$\frac{dT}{dh} \approx \frac{T_e(h=\lambda) - T_e(h=0)}{\lambda} = \frac{T_{\rm max}}{\lambda} \frac{1}{q_R} \left\{ e \left[1 - \exp\left(-\frac{q_R}{e} \right) \right] - [1 - \exp(-q_R)] \right\} , \quad (43)$$

which can be related to the measured temperature gradients dT/ds described in § 2.8 (see also Table 2). We see that the temperature gradient depends only on one free model parameter, the recurrence time ratio q_R. For very short recurrence times, $q_R \ll 1$, the temperature gradient becomes zero because heating is almost continuous and thus maintains the loop temperature everywhere near $T_{\rm max}$ and is therefore constant along the loop. On the other side, the rarer the heating events, the more the loop will cool off before onset of the next heating event, and thus the steeper a temperature gradient will arise due to the hydrostatic dependence of the radiative cooling time. A comparison of the measured temperature gradient with this model allows therefore to constrain the recurrence time. We show the theoretical temperature profiles $\langle T_e(h) \rangle$ (eq. [41]) in Figure 16 (*left*), for a set of recurrence ratios $q_R = 0, \ldots, 1$, with the maximum temperature $T_{\rm max}$ adjusted for each case in such a way that the loop base has a temperature of $T_e(h=0) = 1.2$ MK, as observed for our set of EIT loops. The resulting temperature gradients $dT/dh(h=0)$ at the loop base are shown as a function of the recurrence time t_R in Figure 16 (*right*), where we find the following behavior: (1) the temperature gradient is very shallow ($dT/dh < 0.01$ K m^{-1}) for fast recurrence times ($t_R < t_{\rm rad}^0$), and (2) a maximum temperature gradient of $(dT/dh)_{\rm max} \lesssim 0.04$ K m^{-1} is predicted for long recurrence times. We mark the observed temperature gradients dT/ds in this diagram (crosses in Fig. 16, *right*), to infer the recurrence times that are consistent with the observations. We find that most of the EIT loops (20 out of 30) have temperature gradients that require recurrence time ratios of $q_R \lesssim 0.25$, or recurrence times of $t_R = q_R \times \tau_{\rm rad}^0 \lesssim 10$ minutes (based on $\tau_{\rm rad}^0 \approx 40$ minutes). From this model we predict that heating events should occur with a mean rate of about 5 minutes in a given loop location to maintain the observed temperature gradient in EUV loops. The predicted correlation between temperature gradients (dT/dh) and temperature fluctuation rates R could possibly be checked with high-cadence EIT movies (Newmark et al. 1997).

This heating model is entirely constrained by the observed temperature $T_e(s)$ and density profile $n_e(s)$ and predicts a recurrence rate R at a given loop location. In order to affect the entire length of a loop strand, the total rate R of heating events has to be multiplied by the ratio of the loop length L to the dissipation length $l_{\rm heat}$ of an individual heating event,

$$R_{\rm strand} = R \frac{L}{l_{\rm heat}} . \quad (44)$$

If the loop is composed of $N_{\rm strand}$ strands, the required total number $R_{\rm loop}$ of heating events scales with the ratio of strand cross sections to the loop cross section, i.e.,

$$R_{\rm loop} = R_{\rm strand} \left(\frac{w}{w_{\rm strand}} \right)^2 = R \frac{L}{l_{\rm heat}} \left(\frac{w}{w_{\rm strand}} \right)^2 , \quad (45)$$

where $w_{\rm strand}$ indicates the width of a strand. If the width of individual strands is very small, the total rate of heating events becomes so large that the variability of individual heating events cannot be resolved with currently available time cadences, and the temperature profile of the loop will appear smooth in space and time. Future investigations will reveal whether individual heating events can be resolved or not.

The purpose of this simple statistical heating model without conduction is just to illustrate that the observed temperature gradients can naturally be explained with recurrent heating events uniformly distributed all over the entire loop. A heating source that is confined to a small part of the loop cannot explain the temperature structure of EUV loops. For instance, a heating source localized at the loop-top cannot balance the radiative energy loss in the lower part of the loop (because thermal conduction is inefficient in EUV loops), an argument that was used by Neupert et al. (1998) against the heat-deposition model at large heights (e.g., Wheatland, Sturrock, & Acton 1997). A conductionless heating model necessarily requires a heating

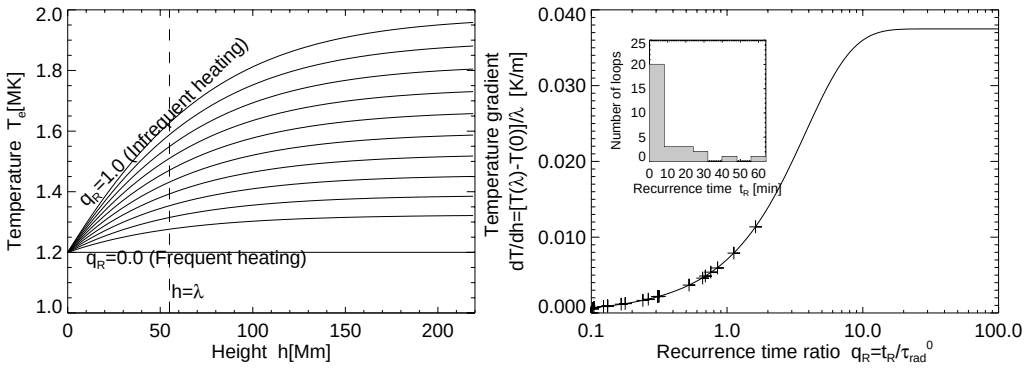

FIG. 16.—Temperature profiles $T_e(h)$ along a loop predicted by the statistical loop heating model (Fig. 15) are shown for different recurrence time ratios $q_R = 0, 0.1, 0.2, \ldots, 1.0$ (*left*). The resulting temperature gradients dT/dh are shown as a function of the recurrence time ratio q_R (*right*). The crosses mark the temperature gradients observed in the 30 EIT loops, and the resulting distribution of recurrence times t_R is shown in the form of a histogram (insert). Note that most of the required recurrence times are $\lesssim 10$ minutes.

function that covers the entire loop, either uniformly or randomly distributed (in space and time). Because a uniform heating function requires an implausible fine tuning with the hydrostatic equilibrium, we invoke a statistical heating function. At this point we leave it open whether the statistical heating events can be interpreted by nanoflares (Parker 1988), by resonant dissipation of Alfvén waves (Ofman et al. 1998), or by cyclically driven mass flows (e.g., chromospheric evaporation cycles, spicules, surges, jets, injections). A scenario with quasi-periodic microflare heating has been modeled, e.g., by Cargill (1994), Cargill & Klimchuk (1997), or Peres (1997). In the nanoflare concept, dominant radiation loss (with a ratio of $\tau_{\rm rad}/\tau_{\rm cond} \approx 10^{-2}$), as observed for the EIT loops here, would occur in the final cooling phase of a nanoflare event, according to a model of Cargill (1994).

3.8. *Mass Flows in EUV Loops*

In the discussion of heating requirements we neglected mass flows, which could play a significant role. Downflows were found from Doppler shift measurements at EUV temperatures of $T_e \approx 1$ MK that carry an energy flux comparable with radiative energy loss (Foukal 1978). Upflows with (Doppler shift) velocities of 50 km s^{-1} have been reported in Mg IX and Mg X lines ($T_e \approx 1$ MK) in an active region recently observed with *SOHO*/CDS (Brekke et al. 1997). Brown (1996) performed hydrodynamic simulations of loops that cool from an initial temperature of $T_e = 2$ MK down to temperatures of $T_e = 0.1$ MK, with subsequent heating back to the original temperatures of $T_e = 2$ MK (in cycles of 3000 s). These simulations demonstrate that downflows with velocities of 7–45 km s^{-1} occur during the cooling phase due to coronal condensation.

4. SUMMARY AND CONCLUSIONS

We developed a three-dimensional analysis method designed to determine geometric and physical parameters of loop structures in solar EUV or SXR images. This method, called dynamic stereoscopy, makes use of stereoscopic correlations of dynamically evolving loop structures that can be traced from high-pass filtered images. The method is designed to separate closely spaced, nested loops, in the plane of the sky, as well as along the line of sight, by suitable background subtraction. With this method we analyzed *SOHO*/EIT Fe IX, Fe X, and Fe XII observations of active region AR 7986, obtained on 1996 August 30. We traced 30 loop segments of this active region and determined the three-dimensional Cartesian space coordinates $[x(s), y(s), z(s)]$, the loop widths $w(s)$, the electron density $n_e(s)$, and the electron temperature $T_e(s)$ as a function of the loop length s. The vertical density scale height λ of these loops was properly corrected for the inclination angle ϑ of the loop plane to the vertical, and the column depth $w_z(s)$ of loops was corrected for the projection angle $\psi(s)$ between the loop axis and the line of sight, which enters the conversion of emission measures EM(s) into electron densities $n_e(s)$. From potential field lines neighbored to the selected EUV loops we estimated also the magnetic field $B(h)$, the plasma-β parameter $\beta(h)$, and the Alfvén velocity $v_{\rm A}(h)$ along the loops. The physical parameters obtained with this stereoscopic three-dimensional method have therefore an unprecedented accuracy. The statistical results of geometric and physical parameters of the analyzed 30 EUV loops of AR 7986 are listed in Table 4.

The major findings and conclusions of this analysis are as follows:

1. The analyzed cool EUV loops are in *hydrostatic equilibrium*, i.e., the mean scale height temperature is identical to the filter-ratio temperature, $T_e^{\lambda} \approx T_e^{\rm EIT}$, and the density profile $n_e(h)$ is nearly exponential. The high accuracy of this result could only be accomplished by proper reconstruction of the three-dimensional loop geometry, in particular by the stereoscopic measurement of the inclination angle ϑ of the loop planes. The existence of hydrostatic equilibrium is physically plausible because pressure gradients can be quickly adjusted to the gravitational scale height, since the loop cooling times are found to be much longer than the sound travel time across a scale height.

2. The *loop width* $w(s)$ is found to be almost *constant* for most of the analyzed loops. Only four out 30 loops show a significant divergence with height, as is expected for dipolar fields. The constant thickness of EUV loops indicates the presence of current-induced nonpotential magnetic fields (Wang & Sakurai 1998), consistent with the findings from SXR loops (Klimchuk et al. 1992). However, we cannot make a statement about the magnitude of nonpotential fields because we measure the geometric divergence only over a segment of 1 scale height.

3. The *potential magnetic field* is found to convey an adequate representation of the coronal magnetic field traced out by EIT loops in some parts of the active region, whereas significant deviations are present in other parts. The ratio of the thermal to the magnetic pressure is found to be always $\beta \lesssim 1$ up to the apexes of the EIT loops, warranting magnetic confinement in all parts of the EUV loops. The Alfvén velocity is found to be highest near the loop footpoints and reaches asymptotically values in the range of $v_{\rm A} \approx$ 500–1000 km s^{-1} in the upper parts of the loops.

4. We find the following scaling laws between the loop length L, the loop base pressure p_0, the footpoint magnetic field $B_{\rm foot}$, and the steady state heating requirement E_{H0}: $p_0 \propto L^{-0.41\pm0.12}$, $B_{\rm foot} \propto L^{-1.02\pm0.43}$, $E_{H0} \propto L^{-0.73\pm0.23}$, $E_{H0} \propto p_0^{1.89\pm0.07}$. These scaling laws are distinctly different from steady state loop models usually applied to SXR loops, where radiative loss is comparable with conductive loss, e.g., the Rosner et al. (1978) loop scaling laws.

5. The conductive loss rate ∇F_C is found to be about 2 orders of magnitude smaller than the *radiative loss rate* E_R for these cool EUV loops, a fact that is in marked difference to hot SXR loops, where it is generally the case that $\nabla F_C \approx E_R$. The dominance of radiative cooling over conductive cooling is mainly an effect of the cooler temperature of EUV loops. As a consequence, the heating rate has to balance only the radiative loss in steady state, implying that the heating rate scales with the squared density, $E_H \propto n_e^2$, and that the heating scale height s_H corresponds to the half-density scale height λ, $s_H = \lambda/2$. However, because a steady state solution requires that radiative and conductive loss are comparable, these cool EUV loops *cannot be in steady state* equilibrium.

6. The non–steady state of cool EUV loops requires a heating function that heats uniformly or randomly along the loops because thermal conduction from a localized heating source is inefficient. This excludes heating models where the heating source is strongly localized, either at the loop top or at the footpoints. A plausible possibility is statistical heating events distributed along the entire loop that

TABLE 4

STATISTICAL RESULTS OF GEOMETRIC AND PHYSICAL PARAMETERS OF THE ANALYZED 30 EUV LOOPS OF AR 7986

Parameter	Value
Loop radius (Mm)	$R_0 = 93 \pm 23$
Offset of circular loop center from baseline (Mm)	$Z_0 = 62 \pm 27$
Loop height (Mm)	$h = 128 \pm 56$
Loop length (Mm)	$L = 433 \pm 136$
Length of traced loop segments (Mm)	$L_1 = 89 \pm 29$
Loop width (Mm)	$w = 7.1 \pm 0.8$
Loop aspect ratio	$L/w = 61 \pm 20$
Azimuth angle of loop baselines (deg)	$\alpha = 3 \pm 10$
Inclination angle of loop planes (deg)	$\vartheta = 7 \pm 37$
Base emission measure (cm^{-5})	$EM_0 = 10^{27.61 \pm 0.61}$
Base electron density (cm^{-3})	$n_{e0} = (1.92 \pm 0.56) \times 10^9$
Base pressure (dyne cm^{-2})	$p_0 = 0.61 \pm 0.17$
Density scale height (Mm)	$\lambda = 55 \pm 10$
Scale height temperature (MK)	$T_e^{\lambda} = 1.22 \pm 0.23$
EIT 171/195 Å filter-ratio temperature (MK)	$T_e^{\rm EIT} = 1.21 \pm 0.06$
Temperature gradient (K km^{-1})	$dT/ds = 0.96 \pm 4.26$
Conductive loss rate (ergs cm^{-3} s^{-1})	$\nabla F_C = (-0.003 \pm 0.005) \times 10^{-3}$
Radiative loss rate (ergs cm^{-3} s^{-1})	$E_R = (-0.458 \pm 0.285) \times 10^{-3}$
Steady state heating rate (ergs cm^{-3} s^{-1})	$E_H = (+0.455 \pm 0.283) \times 10^{-3}$
Conductive cooling time (s)	$\tau_{\rm cond} = 9 \times 10^5$ (10 days)
Radiative cooling time (s)	$\tau_{\rm rad} = 2 \times 10^3$ (40 minutes)
Ratio of conductive to radiative loss time	$\tau_{\rm cond}/\tau_{\rm rad} = 450$
Magnetic field strength at footpoints (G)	$\lvert B_{\rm foot} \rvert = 20, \ldots, 230$
Magnetic dipole depth (Mm)	$h_D \approx 75$
Ratio thermal/magnetic pressure at footpoints	$\beta(h = 0) = 0.001, \ldots, 0.01$
Ratio thermal/magnetic pressure at loop tops	$\beta(h = 100$ Mm$) = 0.04, \ldots, 0.15$
Alfvén velocity at loop footpoints (km s^{-1})	$v_A(h = 0) = 2000, \ldots, 6000$
Alfvén velocity at loop tops (km s^{-1})	$v_A(h = 100$ Mm$) = 500, \ldots, 1000$

balance the local radiative loss. The radiative cooling time increases with loop height because of the hydrostatic density structure and thus leads naturally to a positive temperature gradient along the loop. A mean recurrence time of $\lesssim 10$ minutes for individual heating events at a given location can reproduce the observed temperature gradients measured in EUV loops. Possible candidates for such a statistical heating function are nanoflares, dissipated Alfvén waves, or mass injections.

The obtained conclusions rely on the correctness of the density and temperature measurements, for which we quoted accountable uncertainties. The quoted uncertainties do not include possible systematic errors that could not be quantified in this study, such as calibration errors of the EIT instrument, uncertainties of coronal abundances used in the computation of the EIT response function, including FIP effects of some elements, or newer calculations of the radiative loss function (e.g., currently computed by J. Cook). The major progress of this study lies in a more rigorous reconstruction of the three-dimensional geometry of coronal loops (which has virtually not been attempted in earlier studies) and thus should provide more reliable values of electron densities free from projection and line-of-sight convolution effects. In future work we will analyze the hotter loops $T_e \gtrsim 1.5$ MK of this active region with stereoscopic methods. A further goal is to investigate the time variability of cool and hot active region loops, their steady state phases, and transitions to nonequilibrium states.

We thank the anonymous referee and a number of people for suggestions and helpful discussions, including John Cook, Dan Moses, Charles Kankelborg, Stephen White, Tim Bastian, Arnold Benz, and Pascal Demoulin. *SOHO* is a project of international cooperation between ESA and NASA. The work of M. J. A. was supported by NASA grants NAG-54551 and NAG-57233 through the *SOHO* Guest Investigator Program. W. M. N. was supported by NASA Contract NAS5-32350 with the Hughes STX Corporation. A. Z. was supported by a summer internship at GSFC through grant NCC5-83 with the Catholic University of America (CUA).

APPENDIX A

HELIOGRAPHIC COORDINATE SYSTEMS AND TRANSFORMATIONS

For analysis of observed images, for time-dependent coordinate transformations that take the solar rotation into account (as needed in stereoscopic correlations), and for convenient definitions of loop geometries we define three different coordinate systems:

Image coordinate system (x, y, z).—The (x, y) coordinates refer to the x-axis and y-axis of an observed image, whereas the coordinate (z) is orthogonal to the image, or parallel to the line-of-sight direction, defined positive toward the observer. The origin $(x, y, z) = (0, 0, 0)$ of this coordinate system is most conveniently assumed at the Sun center position. A solar FITS image should contain the position of the Sun center in pixel units (i_{x0}, j_{y0}) (in FITS header *CRPIX1*, *CRPIX2* or *E_XCEN*, *E_YCEN*), the pixel size $(\Delta x, \Delta y)$ in units or arcseconds (in FITS header *CDELT1*, *CDELT2*), and the solar radius i_{r0} in pixel units (in FITS header *SOLAR_R*, or *E_XSMD*, *E_YSMD* if the semidiameters of an ellipse are fitted). With this information, a pixel position (i, j) can then be converted into the coordinate system (x, y) by

$$x_i = \Delta x(i - i_{x0}) , \tag{A1}$$

$$y_i = \Delta y(j - j_{y0}) , \tag{A2}$$

where Δx = arcseconds pixel^{-1} for (x, y) in units of arcseconds, or $\Delta x = R_\odot / i_{r0}$, with $R_\odot = 696{,}000$ km, if physical length units (km) are preferred.

Heliographic coordinate system (l, b, r).—The heliographic coordinate system is corotating with the solar surface. A position on the solar surface is generally specified by heliographic longitude and latitude coordinates (l, b) (in units of heliographic degrees), with reference to the Carrington rotation grid. The heliographic longitude and latitude $[l_0(t), b_0(t)]$ of the Sun center and the position angle $P(t)$ of the solar rotation axis for a given time t are published in The Astronomical Almanac (Nautical Almanac Office, NRL, Washington DC). The two-dimensional spherical coordinate system (l, b) can be generalized into a three-dimensional coordinate system by incorporating the height h above the solar surface, which can be expressed as a dimensionless distance to the Sun center (in units of solar radii),

$$r = \left(1 + \frac{h}{R_\odot}\right) . \tag{A3}$$

The transformation from the three-dimensional heliographic coordinate system (l, b, r) into image coordinates (x, y, z) can be accomplished by applying a series of four rotations to the (normalized) vector $(0, 0, r)$ (see also Loughhead, Wang, & Blows 1983),

$$\begin{pmatrix} x/R_\odot \\ y/R_\odot \\ z/R_\odot \end{pmatrix} = \begin{pmatrix} \cos(P + P_0) & -\sin(P + P_0) & 0 \\ \sin(P + P_0) & \cos(P + P_0) & 0 \\ 0 & 0 & 1 \end{pmatrix} \begin{pmatrix} 1 & 0 & 0 \\ 0 & \cos b_0 & -\sin b_0 \\ 0 & \sin b_0 & \cos b_0 \end{pmatrix}$$

$$\begin{pmatrix} \cos(l_0 - l) & 0 & -\sin(l_0 - l) \\ 0 & 1 & 0 \\ \sin(l_0 - l) & 0 & \cos(l_0 - l) \end{pmatrix} \begin{pmatrix} 1 & 0 & 0 \\ 0 & \cos -b & -\sin -b \\ 0 & \sin -b & \cos -b \end{pmatrix} \begin{pmatrix} 0 \\ 0 \\ r \end{pmatrix} , \tag{A4}$$

where (l_0, b_0) are the heliographic longitude and latitude of the Sun center, P is the position angle of the solar rotation axis with respect to the north-south direction (defined positive toward east), and P_0 is the image rotation (roll) angle with respect to the north-south direction ($P + P_0 = 0$ for images rotated to solar north). In stereoscopic correlations, only the longitude of the Sun center, $l_0(t)$, is time-dependent in first order (according to the solar rotation rate), whereas $b_0(t)$ and $P(t)$ are slowly varying and thus almost constant for short time intervals.

Loop plane coordinate system (X, Y, Z).—To parametrize coronal loops it is also convenient to introduce a Cartesian system that is aligned with the loop footpoint baseline (X-axis) and coincides with the loop plane (X-Z plane, $Y = 0$). For instance, a circular loop model defined in the X-Z plane is specified in equations (10)–(11). The transformation of loop coordinates $(X, Y = 0, Z)$ into Cartesian coordinate system (X', Y', Z') that is aligned with the heliographic coordinate system (l, b, r) can simply be accomplished with help of two rotations,

$$\begin{pmatrix} X' \\ Y' \\ Z' \end{pmatrix} = \begin{pmatrix} \cos\alpha & -\sin\alpha & 0 \\ \sin\alpha & \cos\alpha & 0 \\ 0 & 0 & 1 \end{pmatrix} \begin{pmatrix} 1 & 0 & 0 \\ 0 & \cos\vartheta & \sin\vartheta \\ 0 & -\sin\vartheta & \cos\vartheta \end{pmatrix} \begin{pmatrix} X \\ Y \\ Z \end{pmatrix} , \tag{A5}$$

where the *azimuth angle* α denotes the angle between the loop footpoint baseline and the east-west direction and ϑ represents the inclination or tilt angle between the loop plane and the vertical to the solar surface (Fig. 2). Placing the origin of the loop coordinate system $[X = 0, Y = 0, Z = 0]$ (which is also the origin of the rotated coordinate system $[X' = 0, Y' = 0, Z' = 0]$ at heliographic position (l_1, b_1) at an altitude $h_{\rm Foot}$ above the solar surface, the transformation into heliographic coordinates is then given by

$$\begin{pmatrix} l \\ b \\ r \end{pmatrix} = \begin{pmatrix} l_1 + \arctan\left[X'/(Z' + h_{\rm foot} + R_\odot)\right] \\ b_1 + \arctan\left[Y'/(Z' + h_{\rm foot} + R_\odot)\right] \\ \sqrt{\left[X'^2 + Y'^2 + (Z' + h_{\rm foot} + R_\odot)^2\right]}/R_\odot \end{pmatrix} . \tag{A6}$$

APPENDIX B

LINE-OF-SIGHT CORRECTION ON LOOP COLUMN DEPTH

Column depth of loops with constant cross section.—In order to convert observed emission measures $\mathrm{EM}(x, y) = \int n_e^2(x, y, z)\, dz$ into local electron densities $n_e(x, y, z)$ we need information on the column depth $\int dz$. An approximation that is often useful is coronal loops with a constant cross section w, which can be measured from the FWHM as it appears perpendicular to the line of sight in the plane of the sky. For three-dimensional models of loops parametrized by coordinates (x_i, y_i, z_i), the angle ψ between the line of sight and a loop segment can then directly be derived by the ratio of the projected to the effective length of a loop segment $[i, i + 1]$.

$$\cos(\psi[x_i, y_i, z_i]) = \frac{\sqrt{(x_{i+1} - x_i)^2 + (y_{i+1} - y_i)^2}}{\sqrt{(x_{i+1} - x_i)^2 + (y_{i+1} - y_i)^2 + (z_{i+1} - z_i)^2}} \tag{B1}$$

yielding the column depth w_z along the line-of-sight axis z,

$$w_z[x_i, y_i, z_i] = \frac{w}{\cos(\psi[x_i, y_i, z_i])} \quad . \tag{B2}$$

REFERENCES

Alexander, D., & Katsev, S. 1996, Sol. Phys., 167, 153
Allen, C. W. 1973, Astrophysical Quantities (London: Athlone)
Aschwanden, M. J. 1995, Lect. Notes Phys., 444, 13
Aschwanden, M. J., & Bastian, T. S. 1994a, ApJ, 426, 425
———. 1994b, ApJ, 426, 434
Aschwanden, M. J., Bastian, T. S., Nitta, N., Newmark, J., Thompson, B. J., & Harrison, R. A. 1998a, in ASP Conf. Ser. 155, Second Advances in Solar Physics Euroconference: Three-Dimensional Structure of Solar Active Regions, ed. C. Alissandrakis & B. Schmieder (San Francisco: ASP), 311
Aschwanden, M. J., Lim, J., Gary, D. E., & Klimchuk, J. A. 1995, ApJ, 454, 412
Aschwanden, M. J., et al. 1998b, in ASP Conf. Ser. 155, Second Advances in Solar Physics Euroconference: Three-Dimensional Structure of Solar Active Regions, ed. C. Alissandrakis & B. Schmieder (San Francisco: ASP), 145
Berton, R., & Sakurai, T. 1985, Sol. Phys., 96, 93
Bray, R. J., Cram, L. E., Durrant, C. J., & Loughhead, R. E. 1991, Plasma Loops in the Solar Corona (Cambridge: Cambridge Univ. Press)
Brekke, P., Kjeldseth-Moe, O., Brynildsen, N., Maltby, P., Haugan, S. V. H., Harrison, R. A., Thompson, W. T., & Pike, C. D. 1997, Sol. Phys., 170, 163
Brosius, J. W., Davila, J. M., Thomas, R. J., Saba, J. L. R., Hara, H., & Monsignori-Fossi, B. C. 1997, ApJ, 477, 969
Brosius, J. W., Willson, R. F., Holman, G. D., & Schmelz, J. T. 1992, ApJ, 386, 347
Brown, S. F. 1996, A&A, 305, 649
Cargill, P. J. 1994, ApJ, 422, 381
Cargill, P. J., & Klimchuk, J. A. 1997, ApJ, 478, 799
Cheng, C. C. 1980, ApJ, 238, 743
Davila, J. M. 1994, ApJ, 423, 871
Delaboudinière, J. P., et al. 1995, Sol. Phys., 162, 291
Dere, K. P. 1982, Sol. Phys., 75, 189
Dere, K. P., Landi, E., Mason, H. E., Monsignori-Fossi, B. F., & Young, P. R. 1997, A&AS, 125, 149
Dulk, G. A., & McLean, D. J. 1978, Sol. Phys., 57, 279
Fludra, A., Brekke, P., Harrison, R. A., Mason, H. E., Pike, C. D., Thompson, W. T., & Young, P. R. 1997, Sol. Phys., 175, 487
Foukal, P. 1975, Sol. Phys., 43, 327
———. 1978, ApJ, 223, 1046
Galeev, A. A., Rosner, R., Serio, S., & Vaiana, G. S. 1981, ApJ, 243, 301
Gary, G. A. 1990, Mem. Soc. Astron. Italiana, 61, 457
———. 1997, Sol. Phys., 174, 241
Gary, G. A., & Alexander, D. 1999, Sol. Phys., in press
Golub, L., Herant, M., Kalata, K., Lovas, I., Nystrom, G., Pardo, F., Spiller, E., & Wilczynski, J. 1990, Nature, 344, 842
Golub, L., Maxson, C., Rosner, R., Serio, S., & Vaiana, G. S. 1980, ApJ, 238, 343
Habbal, S. R., Ronan, R., & Withbroe, G. L. 1985, Sol. Phys., 98, 323
Harvey, K. L., & Hudson, H. S. 1998, in Proc. *Yohkoh* Workshop, Observational Plasma Astrophysics: Five Years of *Yohkoh* and Beyond, ed. T. Watanabe, T. Kosugi, & A. C. Sterling (Astrophys. and Space Science Library; Dordrecht: Kluwer), 229, 315
Hudson, H. S., LaBonte, B. J., Sterling, A. C., & Watanabe, T. 1998, in Proc. *Yohkoh* Workshop, Observational Plasma Astrophysics: Five Years of *Yohkoh* and Beyond, ed. T. Watanabe, T. Kosugi, & A. C. Sterling (Astrophys. and Space Science Library; Dordrecht: Kluwer), 229, 237
Kankelborg, C. C., Walker, A. B. C., II, & Hoover, R. B. 1997, ApJ, 491, 952
Kano, R., & Tsuneta, S. 1995, ApJ, 454, 934
———. 1996, Publ. Astron. Soc. Japan, 48, 535
Klimchuk, J. A., & Gary, D. E. 1995, ApJ, 448, 925
Klimchuk, J. A., Lemen, J. R., Feldman, U., Tsuneta, S., & Uchida, Y. 1992, PASJ, 44, L181
Klimchuk, J. A., & Porter, L. J. 1995, Nature, 377, 131
Lang, K. R. 1980, Astrophysical Formulae (Berlin: Springer)
Loughhead, R. E., Chen, C. L., & Wang, J. L. 1984, Sol. Phys., 92, 53
Loughhead, R. E., Wang, J. L., & Blows, G. 1983, ApJ, 274, 883
Mandrini, C. H., Demoulin, P., & Klimchuk, J. A. 1999, ApJ, submitted
Martens, P. C. H., & Kuin, N. P. M. 1982, A&A, 112, 366
McClymont, A. N., Jiao, L., & Mikić, Z. 1997, Sol. Phys., 174, 191
Meyer, J. P. 1985, APJS, 57, 173
Moses, D., et al. 1997, Sol. Phys., 175, 571
Neupert, W. M., et al. 1998, Sol. Phys., 183, 305
Newmark, J. S., Delaboudinière, J. P., Dere, K. P., Gurman, J. B., Lemen, J. R., & Thompson, B. J. 1996, EOS, Vol. 77, 46, 557
Newmark, J. S., Thompson, B., Gurman, J. B., Delaboudinière, J. P., Aschwanden, M. J., & Mason, H. 1997, BAAS, 29/5, 1321, 73.07
Nitta, N., et al. 1991, ApJ, 374, 374
Ofman, L., Klimchuk, J. A., & Davila, J. M. 1998, ApJ, 493, 474
Pallavicini, R., Serio, S., & Vaiana, G. S. 1977, ApJ, 216, 108
Parker, E. N. 1988, ApJ, 330, 474
Peres, G. 1997, in Proc. 5th *SOHO* Workshop on The Corona and Solar Wind Near Minimum Activity (Nordwiijk: ESA SP-404), 55
Porter, L. J., & Klimchuk, J. A. 1995, ApJ, 454, 499
Priest, E. R. 1981, Solar Flare Magnetohydrodynamics (New York: Gordon & Breach)
Priest, E. R., Foley, C. R., Heyvaerts, J., Arber, T. D., Culhane, J. L., & Acton, L. W. 1998, Nature, 393, 545
Raymond, J. C., Cox, D. P., & Smith, B. W. 1976, ApJ, 204, 290
Rosner, R., Tucker, W. H., & Vaiana, G. S. 1978, ApJ, 220, 643
Sakurai, T. 1982, Sol. Phys., 76, 301
———. 1989, Space Sci. Rev., 51, 11
Schmelz, J. T., Holman, G. D, Brosius, J. W., & Gonzalez, R. D. 1992, ApJ, 399, 733
Schmelz, J. T., Holman, G. D., Brosius, J. W., & Willson, R. F. 1994, ApJ, 434, 786
Serio, S., Peres, G., Vaiana, G. S., Golub, L., & Rosner, R. 1981, ApJ, 243, 288
Sheeley, N. 1980, Sol. Phys., 66, 79
SOHO EIT User's Guide. 1998, http://umbra.nascom.nasa.gov/eit/eit_guide/guide.html
Spitzer, L. 1962, Physics of Fully Ionized Gases (New York: Interscience)
Vesecky, J. F., Antiochos, S. K., & Underwood, J. H. 1979, ApJ, 233, 987
Vourlidas, A., & Bastian, T. S. 1996, ApJ, 466, 1039
Wang, H., & Sakurai, T. 1998, PASJ, 50, 111
Wang, Y. M., et al. 1997, ApJ, 485, 419
Webb, D. F., Holman, G. D., Davis, J. M., Kundu, M. R., & Shevgaonkar, R. K. 1987, ApJ, 315, 716
Wheatland, M. S., Sturrock, P. A., & Acton, L. W. 1997, ApJ, 482, 510
Wragg, M. A., & Priest, E. R. 1982, A&A, 113, 269
Zhang, J., White, S. M., & Kundu, M. R. 1998, ApJ, 504, L127

Conclusion Provisoire

Récemment, Lenz et collaborateurs ([134]) ont analysé avec la haute résolution de TRACE des boucles EUV a 171A et 195A. Ils ont retrouvé et confirmé notre résultat, à savoir, qu'il n'y a pas de variation en température le long de certaines boucles EUV. Il va donc falloir comprendre à l'avenir pourquoi des boucles EUV isothermiques d'une part et des boucles X plus chaudes au sommet d'autre part peuvent toutes 2 correspondre au confinement de plasma le long de lignes magnétiques fermées.

IV.3.2 Role du torsadage pour les boucles coronales

En analysant les données il est apparu la nécessité de prendre en compte par un nouveau modèle d'ajustement les anisotropies sur les boucles EUV. L'introduction du torsadage a permis d'ajuster des boucles dont le modèle circulaire ne pouvait rendre compte.

Nous allons donc faire de la stéréoscopie statique avec un modèle à priori non circulaire.

Dans le cas d'un modèle simple, on approxime la boucle par un cercle dont on calcule le rayon, et la hauteur du centre par rapport à la photosphère.

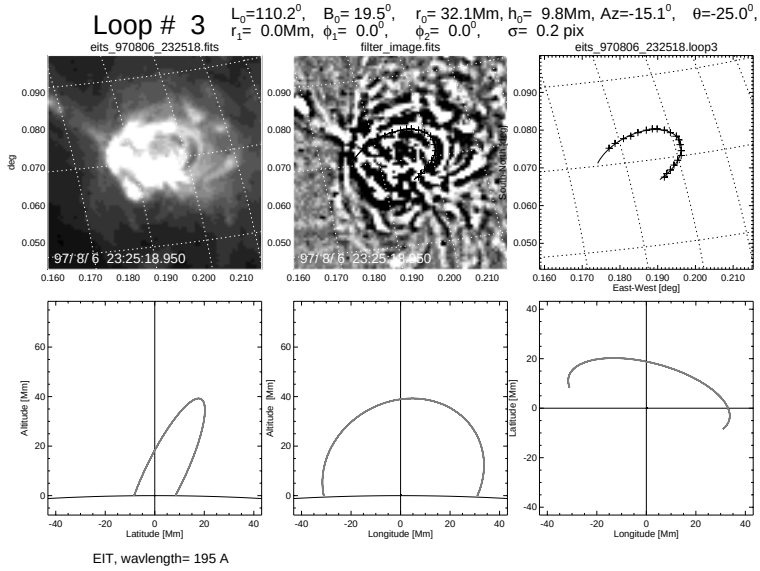

Figure IV.13: Exemple où le modèle circulaire convient pour ajuster une boucle

Certaines boucles s'ajustent parfaitement sur ce modèle circulaire (Fig. IV.13).

Afin de prendre en compte les écarts à la circularité observés (Exemple Fig. IV.14), on peut être amené à considérer que le flux de plasma se retrouve torsadé inclus à la surface d'un tore (cf [261]).

En effet, lorsque la boucle est torsadée, elle n'est plus nécessairement coplanaire. Dans le cas d'un modèle plan photosphérique parallèle la boucle se retrouve comme une

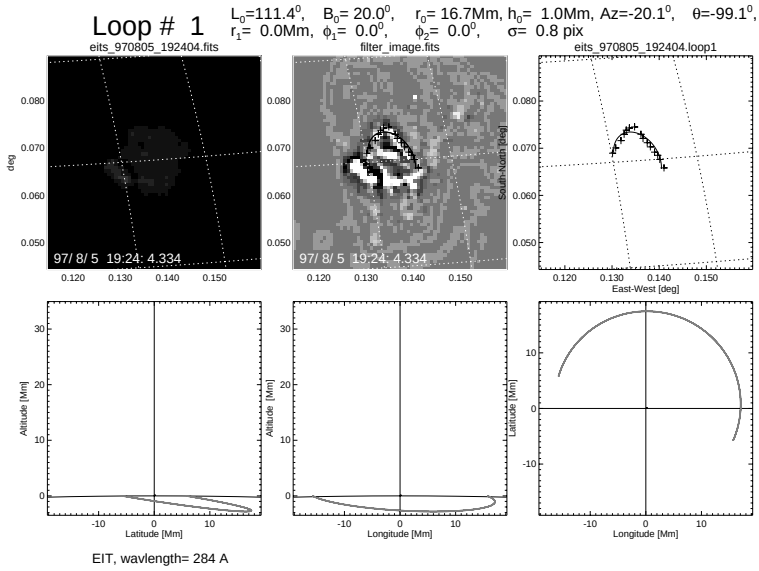

Figure IV.14: Exemple où le modèle circulaire ne suffit plus pour ajuster une boucle

ligne. Lorsqu'il y a torsadage cette ligne évolue dans un tube cylindrique. En retransformant en 3D cela revient à dire que la boucle se trouve sur la surface d'un tore (Fig. IV.15). On peut donc mesurer les angles de départ et d'arrivée de la courbe sur le tore ainsi que les paramètres du tore (rayons, hauteurs,...).

La suite de l'algorithme basé sur la stéréoscopie est le même. Toutefois au niveau des contraintes, lorsqu'il existe plusieurs types de solutions possibles on préférera la solution la plus simple (sans torsion). La continuité des paramètres avec le temps dans l'ensemble des solutions possibles donnera l'existence et l'unicité de la solution physique.

La méthode a été appliquée aux cas ci dessous : une émergence rapide de boucles et une évolution à long terme de tubes de flux dans une région active.

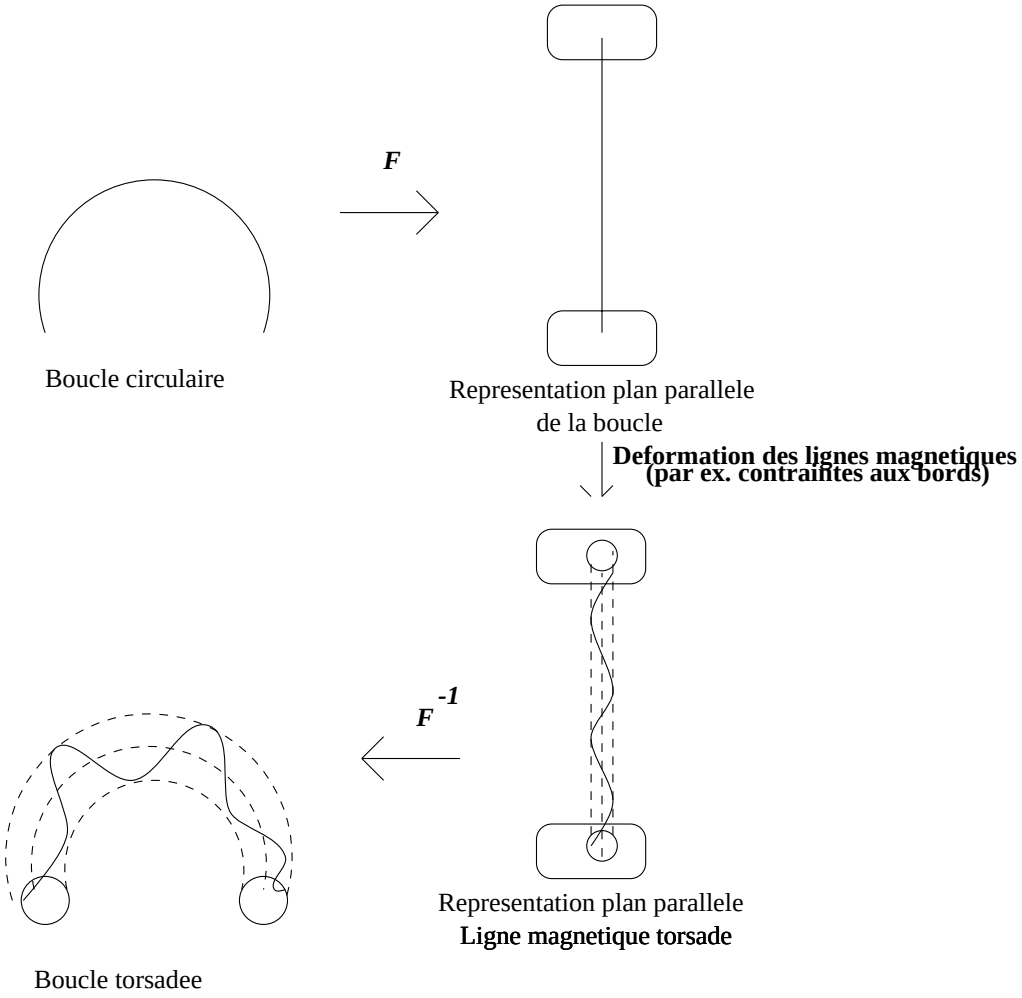

Figure IV.15: Du cercle à la ligne sur le tore (Justification du modèle torique)

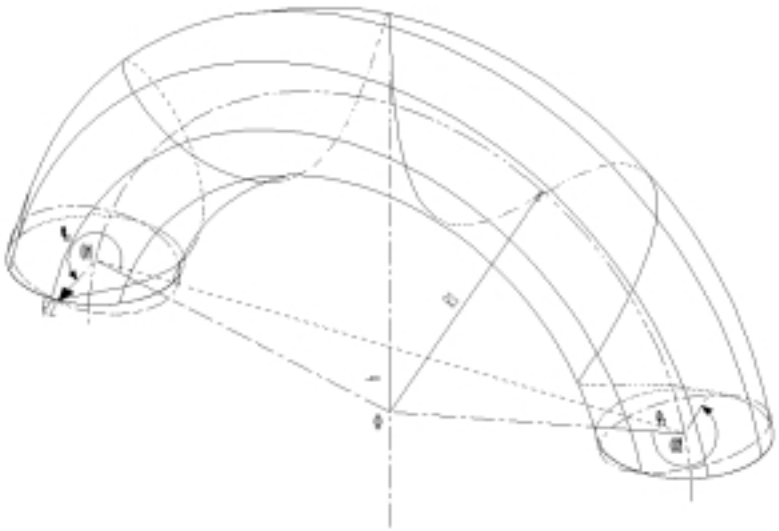

Figure IV.16: Définition des paramètres des boucles torsadées :
r_0 le rayon principal du tore, h la hauteur du centre du tore par rapport à la surface, r_1 le rayon secondaire du tore, Φ_1 et Φ_2 les angles par rapport à une origine arbitraire de la position de la boucle par rapport à la coupe horizontale.

Validation de la méthode

Algorithme A titre d'exemple considérons les données du 2 Aout 1998 à 07:24 TU. Le fichier eits_960802_072407.loop1 comprend les coordonnées de la boucle 1 telles que obtenues après ajustement à l'ecran sur l'image EIT. Ces coordonnées vont être transformées en fonction des éphémerides et de la position héliographique de l'image pour obtenir differents ajustements.

Plusieurs exemples de resultats d'ajustements des paramètres sont données dans la table IV.3 (Fichier eits_960802_072407.para1).

l_0	b_0	r_0	h_0	az	th	r_1	$\Phi 1$	$\Phi 2$	dev
254.24	-7.95	57.16	9.77	18.91	-92.56	2.92	301.73	138.35	1.15
256.29	-7.58	58.11	1.39	32.67	-86.87	25.01	145.79	-39.05	1.73
254.26	-8.02	54.65	10.11	28.99	-74.45	1	0.0	1	0.73
254.52	-7.79	64.93	16.49	16.09	-97.01	19.21	228.96	118.75	1.22
254.62	-9.27	52.61	24.22	14.21	-94.59	0.12	39.00	55.27	1.13
254.51	-6.35	62.26	13.31	15.56	-57.93	18.71	122.27	104.08	2.85
254.52	-6.34	62.28	13.48	15.47	-58.02	18.91	122.60	103.49	2.84

Table IV.3: Différentes solutions géométriques pour 1 boucle avec 1 seul angle de vue (La déviation entre le modèle et l'ajusté - dev - est exprimé en pixels)

Certains valeurs de ce tableau sont non physiques comme par exemple lorsque la boucle est trouvée comme étant sous la surface (*i.e.* ! th ! > 90 degres). On élimine alors ces solutions.
On obtient nénamoins plusieurs valeurs pour l'ajustement. L'unicité de la solution est obtenue en comparant l'évolution temporelle. Les valeurs alors doivent être proches puisque le tube de flux magnetique se déforme de manière continue (au sens mathématique).

On peut alors retracer la boucle ainsi correctement ajustée sur le graphique.

Incertitudes On verifie (Fig. IV.17 et IV.18) pour chacun des paramètres calculés les barres d'incertitudes.
A titre d'exemple sur les données du 30 Aout 1996, si au lieu d'avoir $\phi 2 = -197.10$ on avait $\phi 2 = -190$, on passerait d'une déviation de 0.32 pixel à une déviation de 2.78 pixels. En minimisant le paramètre de déviation on est bien capable de voir les différences de torsadages même lorsqu'elles sont inférieures à 7 degrés.

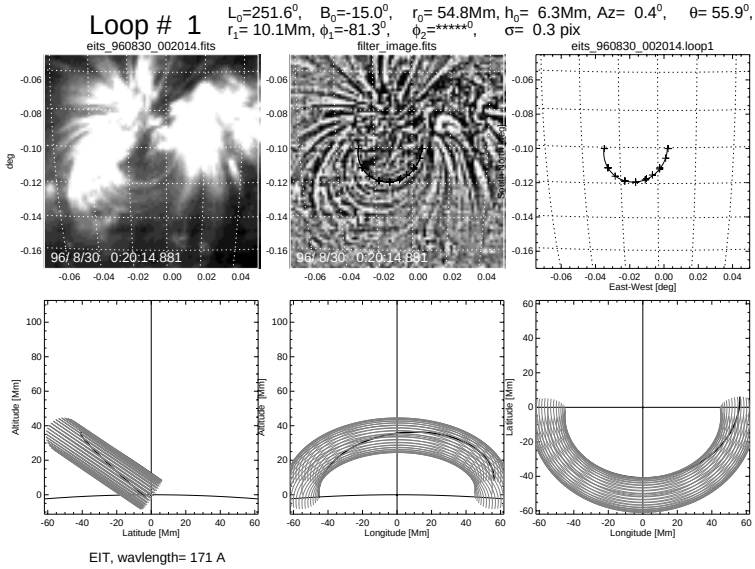

Figure IV.17: SOHO/EIT le 96-08-30 à 00h 20mn 14s (UT) boucle 1, Les parametres d'ajustement sont l0 = 251.62, b0 = -15.02, r0 = 54.84 Mm, h0 = 6.28 Mm, az = 0.45, th = 55.86, r1 = 10.05 Mm, $\phi 1 = -81.33$ degrés, $\phi 2 = -197.10$ degrés. L'erreur mesurée entre le modèle et l'ajustement est dev = 0.32 pixel

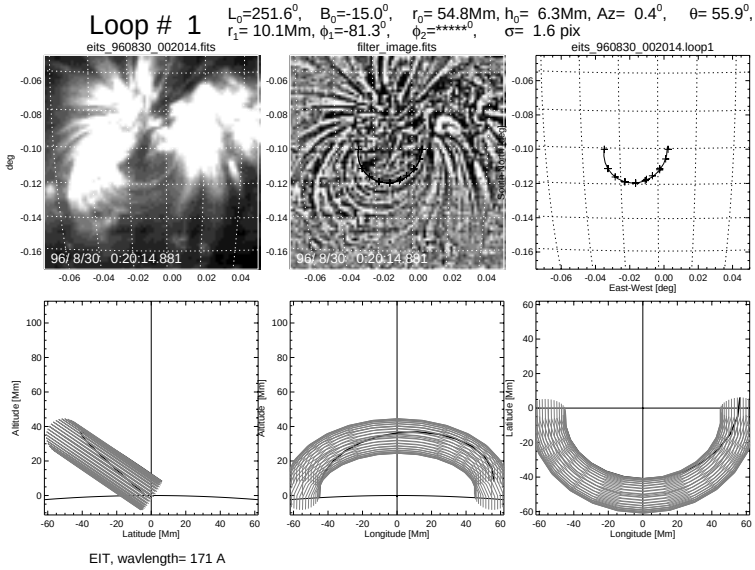

Figure IV.18: SOHO/EIT le 96-08-30 à 00h 20mn 14s (UT) boucle 1. Les parametres d'ajustement sont l_0 = 251.62, b_0 = -15.02, r_0 = 54.84, h_0 = 6.28, az = 0.45, th = 55.86, r_1 = 10.05, $\Phi 1 = -81.33$, $\Phi 2 = -190$. L'erreur mesurée entre le modèle et l'ajustement est dev = 2.78 pixels

Vérification de la convergence vers un minimum global On prend le cas du 96-08-30 à 00h20mn14s. La Table IV.4 donne la solution trouvée par la méthode.

l_0	b_0	r_0	h_0	az	th	r_1	$\Phi 1$	$\Phi 2$	dev
251.62	-15.02	54.84	6.28	0.45	55.86	10.05	-81.33	-197.10	0.32

Table IV.4: Valeur de convergence trouvée par la méthode

Nous allons nous assurer que cela est bien un minimum sur l'ensemble des paramètres en prenant comme valeur

```
l0      b0      r0      h0      az      th
262     -15      55    6       0       56
```

et en faisant varier r1 de 5 à 15 Mm avec des pas de 1 Mm, $\phi 1$ de -90 à -80 degrés avec des pas de +1 degré, $\phi 2$ de -200 à -190 degrés avec des pas de +1 degré.

Ainsi on va analyser la déviation en fonction de ($\phi 1$,$\phi 2$) pour r1=10Mm. De même on prendra 2 autres plans de r1 pour verifier la dependance.

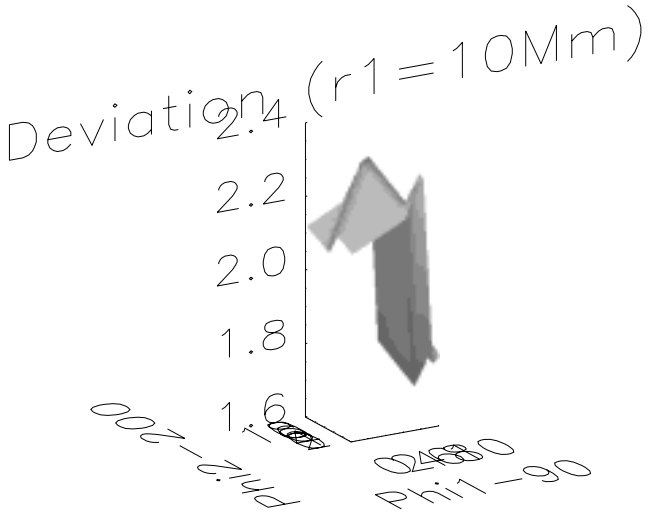

Figure IV.19: Pour r1 fixé à 10Mm, mesure de la variation minimale pour $\phi 1$ variant de -90 à -80 degrés, $\phi 2$ de -200 à -190 degrés: Le minimum de déviation correspond à $\phi 1 \sim -81$ degrés et $\phi 2 \sim -197$ degrés.

Le minimum est atteint sur la fig.IV.19 pour les valeurs $\Phi_1 = -81$ degrés et $\Phi_2 = -197$ degrés. En comparant les figures IV.19, IV.20 et IV.21 ce minimum semble être un mimimum sur un certain voisinage topologique. Afin de vérifier cela on regarde aussi les variations avec r1 qui varient IV.22 et IV.23. Cela confirme la necessité de faire le calcul variationnel sur l'ensemble des variables.

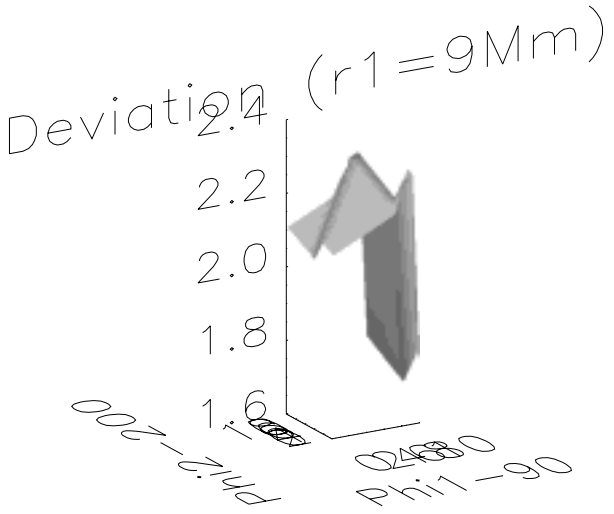

Figure IV.20: Pour r1 fixé a 9Mm, mesure de la variation minimale pour $\phi 1$ variant de -90 à -80 degrés, $\phi 2$ de -200 à -190 degrés.

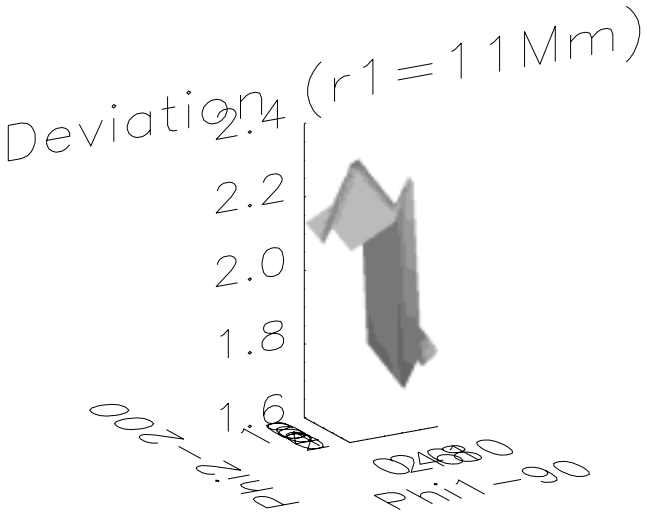

Figure IV.21: Pour r1 fixé a 11Mm, mesure de la variation minimale pour $\phi 1$ variant de -90 à -80 degrés, $\phi 2$ de -200 à -190 degrés.

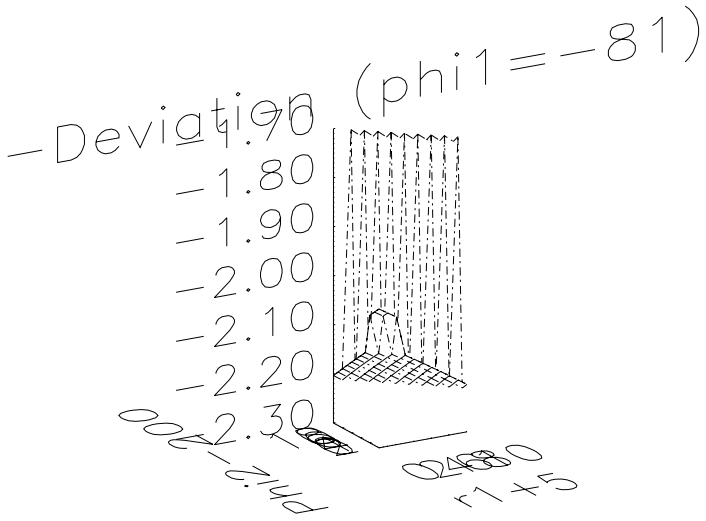

Figure IV.22: Pour ϕ_1 fixé a -81 degré, déviation en fonction de r1 et ϕ_2 : Le minimum est atteint pour $r1 \sim 10$ et $\phi_2 \sim -197$

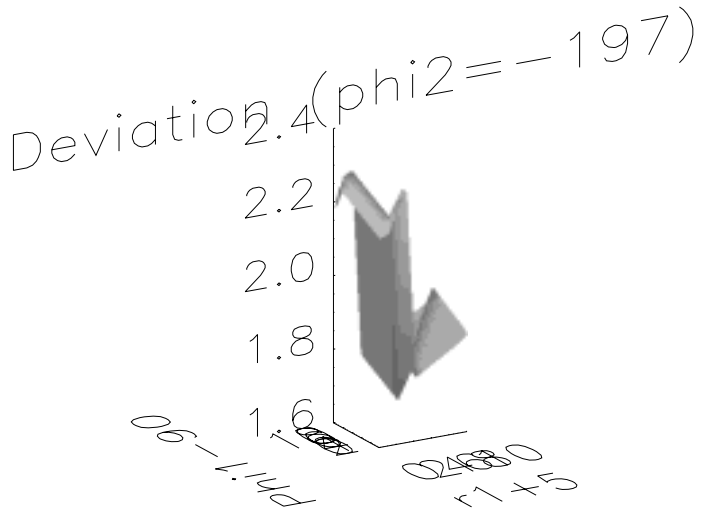

Figure IV.23: Pour ϕ_2 fixé a -197 degré, déviation en fonction de r1 et ϕ_1 : Le minimum est atteint pour $r1 \sim 10$ et $\phi_1 \sim -81$

Convergence La convergence de la méthode se fait en minimisant le paramètre d'erreur dev. Différentes itérations de la méthode sont présentés figures IV.24 et IV.25.

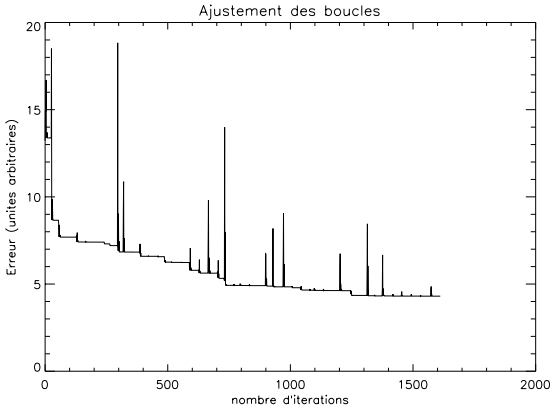

Figure IV.24: Minimisation de dev en fonction de l'itération

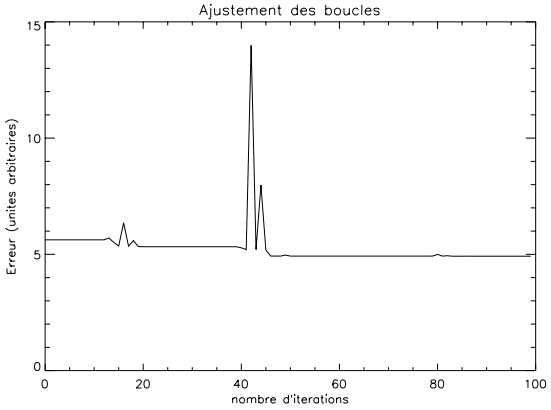

Figure IV.25: Minimisation de dev par mimimum d'entropie (deviation en fonction de l'itération)

IV.3.3 Quelques exemples

Après avoir qualifié la méthode en y ayant introduit des asymétries, nous allons maintenant étudier plusieurs possibilités d'évolution. Tout d'abord, nous prendrons le cas de l'émergence rapide de nouveaux tubes de flux. Ensuite nous regarderons le cas de l'évolution de tube de flux sur une plus longue durée (plusieurs rotations solaires)

Cas d'une évolution rapide

- **Emerging flux and short time loop expansion August 5th-6th, 1997**
- par Portier-Fozzani, Démoulin, Neupert, Aschwanden, Maucherat
- Soumis à Astronomy & Astrophysics (Novembre 1999)

Dans cet article nous nous sommes interessé à l'émergence de boucles et à l'évolution de leur torsadage en fonction de l'expansion.
Nous avons comparé les résultats observationnels ainsi obtenus avec les théories d'évolution de tubes de flux.

MEASUREMENT OF CORONAL MAGNETIC TWISTS DURING LOOP EMERGENCE OF NOAA 8069

F. PORTIER-FOZZANI[1], M. ASCHWANDEN[2], P. DÉMOULIN[3], W. NEUPERT[4] and the EIT Team with J.-P. DELABOUDINIÈRE P.I.
[1]*Max Planck Institut fur Aeronomie (MPAE), Max-Planck-Straβe 2, D-37191 Katlenburg-Lindau, Germany*
[2]*Lockheed Martin Palo Alto Advanced Technology Center, Palo Alto, California, U.S.A.*
[3]*DASOP, Observatoire de Paris-Meudon, France*
[4]*NOAA – SEC, Boulder, Colorado, U.S.A.*

(Received 22 May 2001; accepted 4 July 2001)

Abstract. Emerging coronal loops were studied with extreme ultraviolet observations performed by SOHO/EIT on 5 and 6 August 1997 for NOAA 8069. Physical parameters (size and twist) were determined by a new stereoscopic method. The flux tubes were measured twisted when first observed by EIT. After emerging, they de-twisted as they expanded, which corresponds to a minimization of the energy. Different scenarios which take into account the conservation of the magnetic helicity are discussed in relation with structure and temperature variations.

1. Introduction

The solar magnetic field (Solanki, 1998), which drives solar activity, emerges over the photosphere as flux tubes which confine the plasma (Klimchuk and Porter, 1996; Parker, 1974).

Different types of loops with fast or slow evolution – between days up to months – coexist (Bray *et al.*, 1991). Their morphologies can change a lot due to shearing and twisting of the flux tubes. Shear, measured along the inversion line of the vertical field component (between the two footpoints of a bipolar AR), plays a major role in flares as reviewed by Heyvaerts and Hagyard (1991). In other cases, loops are sometimes seen to be twisted which indicates a perturbation from a lower energy state. Energy release within very hot loops observed in X-rays and also highly twisted – i.e., with an S shape called a sigmoid – happens sometimes as flares (Rust and Kumar, 1996). Difficulties in measuring the loop twist accounts for the small number of articles concerning it. With new stereoscopy techniques and the actual resolution of EUV instruments it has become possible to estimate the magnetic helicity by twist measurement.

After describing the instruments and the active region loops (hereafter denoted ARL) that we observed, we explain the stereoscopic method that we used to deduce the 3D shape of the observed EIT loops. We focus this study on the measurement of twist and its evolution with time during the short period of time when the loops

Solar Physics **203:** 289–308, 2001.

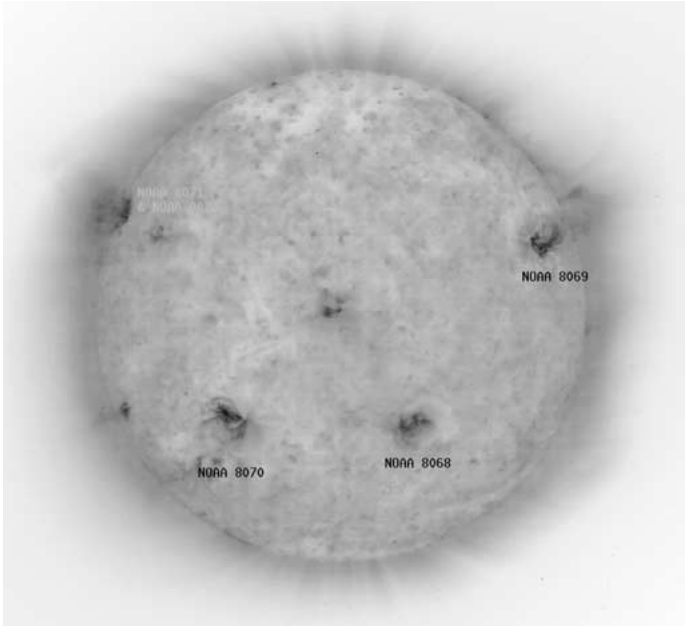

Figure 1. Active regions observed with SOHO/EIT Fe IX/X on 7 August 1997 at 19:54 UT with their NOAA numbers (with reversed intensity table: dark on the figure is bright on the Sun).

emerge. We will then discuss the energy and helicity transfer during the evolution of the geometrical morphology of the loops.

2. Instruments and Target

2.1. Instruments

Multiwavelength observations were used for this study.

– SOHO/EIT images the solar corona in four EUV wavelengths (Delaboudinière *et al.*, 1995). Loops with temperature around 1 MK are clearly visible and their evolution can be studied (e.g., Portier-Fozzani *et al.*, 1997).

– *Yohkoh* SXT images the hot corona in X rays (temperature between 2–10 MK e.g., Uchida, 1992; Bentley, Mariska, and Sakao, 1996).

– Magnetograms: SOHO/MDI gives the longitudinal component of the photospheric magnetic fields with two arc sec resolution for full disk images.

Temperature maps are derived with SOHO/EIT using the atomic CHIANTI code (Dere *et al.*, 1997) with quasi simultaneous image ratios of different EIT filters (Figure 6, cf., Newmark, 1997; Neupert *et al.*, 1998).

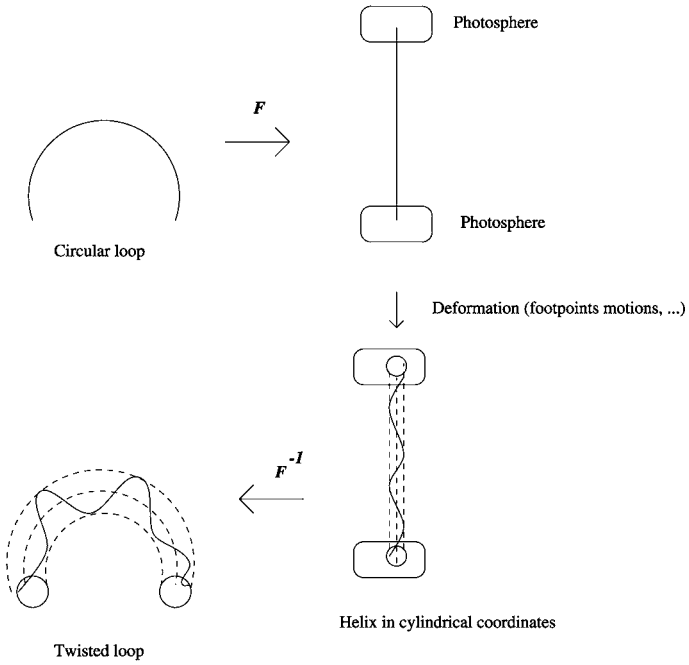

Figure 2. The torus shape approximation for coronal loops: *Top*: simple circular model with its linear representation. *Bottom*: footpoint vortex motion consequences: loops are approximately transformed respectively to a helix shape on a cylinder and into a line on a torus surface.

2.2. TARGET

The rapid emergence of a new active region (NOAA 8069) on August 5, 1997 made possible a study of the growth of its coronal loop system. This area – emerging shortly after the 1996 solar minimum cycle (Harvey and Hudson, 1998) – was far enough away from other active regions (Figure 1) to provide a good example of emerging flux tubes with rapid expansion and without interaction with other active regions (cf., also the MPEG movie in the CD-ROM).

3. Method to Compute the Size and Twist

3.1. THE GEOMETRY OF THE LOOP FITTING MODEL

A plasma loop traces the magnetic field from a positive polarity to a negative polarity. The simplest coronal loops can be described by the magnetic lines of a potential field configuration which corresponds to a minimum of the magnetic energy for a given vertical field at the photosphere (e.g., Aly, 1991). In many cases (Aschwanden *et al.*, 1999), loops can be fitted approximately with a circular model (i.e., constant radius without torsion in an Eulerian frame). A geometrical approxi-

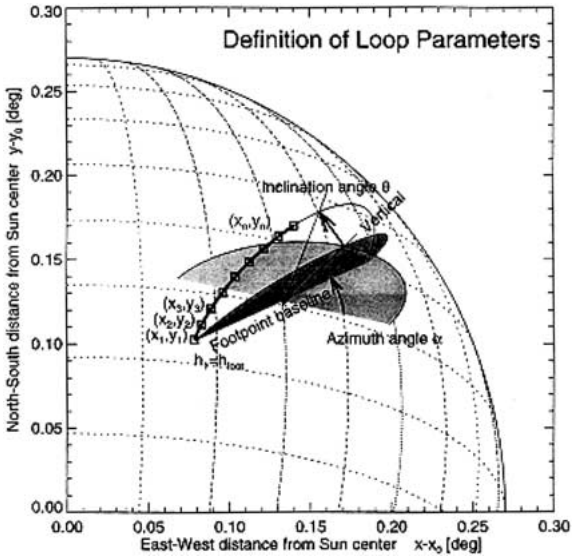

Figure 3. Geometric circular parameters definition with the standard circular approximation.

mation often used to describe a coronal loop is to neglect the global curvature of the loop, so the configuration is stretched and contained in a line between two 'half' planes representing the photosphere (Figure 2 top). We call F the transformation which, if applied to a circular loop, transforms it into a straight line.

In simple cases, footpoint motion will introduce torsion. In cylindrical coordinates, field lines are then transformed to a helix. By applying the reverse application F^{-1}, in 3D the field lines will approximately appear as lines upon a torus surface (Figure 2 bottom). It is worth noting that the force balance will be changed by this transformation. We neglect these effects here.

These non-circular and non-coplanar models are needed to describe twisted loops. More complex loop shapes, present even in bipolar magnetic regions are not considered in this paper.

3.2. ALGORITHM

As a first step, we consider that the loop is circular. We then determine the 3D parameters from *static stereoscopy*. In static stereoscopy, the solar rotation is used to vary the aspect angle of otherwise static structures (e.g., Loughhead, Chen, and Wang, 1984; Berton and Sakurai, 1985; Aschwanden and Bastian, 1994a, b; Davila, 1994; Aschwanden, 1995).

Recently, Aschwanden *et al.* (1999) have developed a method called *dynamic stereo vision* where the fit can be obtained even if the circular loops traces are not completely visible all the time (for the case where the closed magnetic field lines are not permanently traced). In this paper we want to take into account that the loop could be non circular. To be able to keep that possibility, our software uses

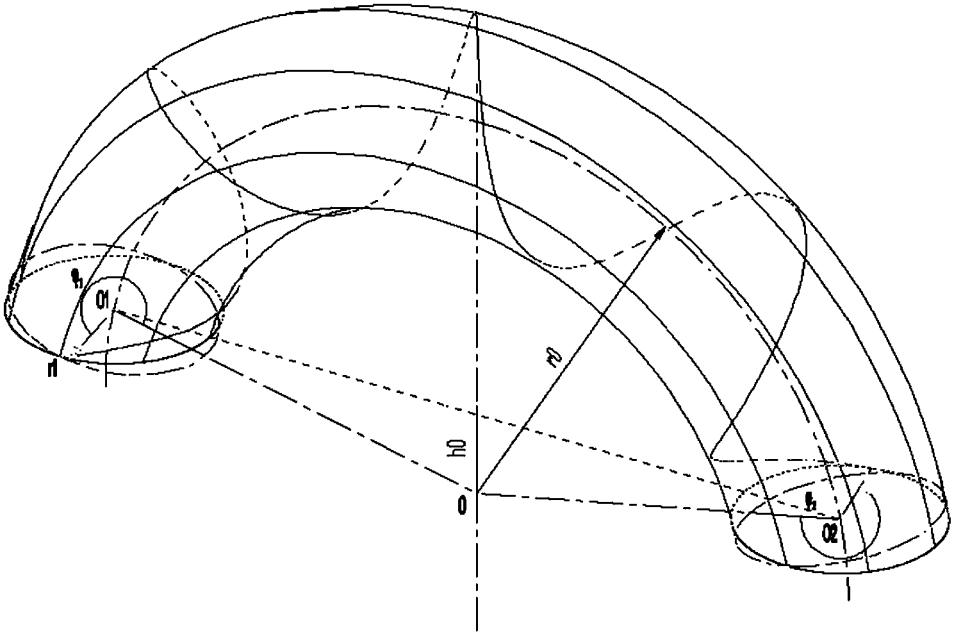

Figure 4. Definition of the parameters used to define a helix wound on a torus.

almost the same formula derived in steps 1 to 4 of paragraph 2.2 in Aschwanden *et al.* (1999, pp. 845–846). Each fitting is divided into 2 parts:

(1) A forward-fitting method of a given geometric model. The work is done on a single image where a geometric form is defined *a priori* and a best fit to one projection is done.

(2) Using pairs of images separated in time and assuming continuous change of parameters with time, we calculate the 3D geometry for twisted loops.

Afterwards if the circular fit shows a significant deviation from the observed loop we assume that the loop is on the torus to check if this deviation could be interpreted as a magnetic twist (as justified above).

The first model of coronal loop fitting (Figure 3) describes in a simplified way the morphology of the loops as circular arcs where radius r_0, altitude of the center over the photosphere h_0, azimuth and inclination angle (Az and ϑ) are determined. Different fitting parameters are found with an improved least square method (Powell function of IDL). Heliographic transformations used are presented in the Appendix A of Aschwanden *et al.* (1999).

When the loop is non circular, we replace the circular fitting (e.g., radius found R) by a *torus fitting* with the initial main radius $r_0 = R$, the small radius r_1 starts from zero and is fitted as the twist. This final fitting gives then, with time evolution: the torus radius r_0, its section radius r_1, the altitude above the photosphere h_0 and the position centers of the 2 cuts of the torus with the solar surface (S1 and S2). The program then gives how the line (loop) is twisted along the torus with Φ_1 and

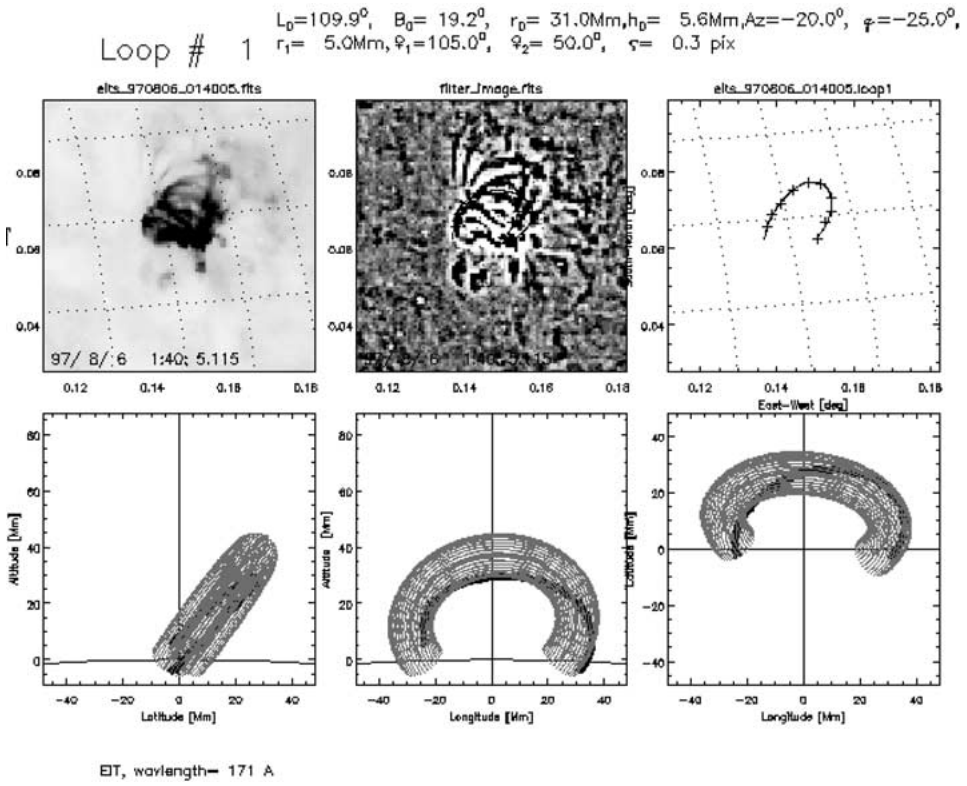

Figure 5. Example of the fit of one loop for 6 August 1997 at 01:40 UT. *On the upper left*: the EIT image and its transform with a Sobel filter which emphases the high spatial frequencies on the image. *On the upper right*: the determination of the loop on the image. *Lower images*: 3 different view points of the loop fit.

Φ_2 phase angles over sections S1 and S2. The complete twist Ψ is given by the difference between the two angles at the footpoints (Figure 4). The definitions of the origin of Φ_1 and Φ_2 are carefully chosen in such a way that if there is no twist Ψ is zero. It is important to note that each loop asymmetry is fully described by r_1, Φ_1, and Φ_2 or in an equivalent way by r_1, Φ_1, and Ψ (see Figure 4).

The fit is non linear, so in general there are several sets of parameters which minimize the distance between the observation and the model. Let us call s_i^j the jth solution for the fitted parameters ($(L_0)_i^j$, $(B_0)_i^j$, Az_i^j, ϑ_i^j, $(r_0)_i^j$, $(h_0)_i^j$, $(r_1)_i^j$, $(\Phi_1)_i^j$, $(\Phi_2)_i^j$) for the image number i.

From the different set of solutions we use the continuity obtained by stereo vision to derive the unique solution. For that, we select from the set of solutions s_i^j, the one with most continuous evolution of parameters. In practice, we first consider that the loops are circular. The heliographic latitude and longitude can be estimated by putting a spherical grid on the Sun. From two different images, it is easy to derive an initial estimation of the azimuth and inclination angles. These are the two

parameters that we derive first because the line of sight gives us a strong constraint. The sizes are then deduced. These provide starting values for the circular fit. If the deviation from the circular fit is too large we evaluate the twist as a perturbation of the circular model.

3.3. APPLICATION OF THE METHOD

As an example, the method is applied to the SOHO/EIT Fe IX/X image of 6 August 1997 at 01:40 UT (Figure 5). Loops (Figure 5(a)) are emphasized by Sobel filtering techniques (Figure 5(b)) as a high pass band filter. Loops are fitted with the described method. The tracing of a loop is established interactively on the image. It is plotted with crosses on Figure 5(c) while the result of the fitting obtained is drawn with a full line. Three different viewpoints are presented in Figures 5(d–f) to show the 3D geometry. The parameters deduced from the fitting are given at the top of Figure 5.

3.4. UNCERTAINTIES

To determine the exact coordinates and then the real morphology of the loops, we need to know with high accuracy the Sun center on the EIT images. The coordinates of the Sun center given by the FITS header is provided by an automatic fitting routine in which asymmetries, such as an active region on the limb introduce errors. Instead, we determine the Sun center by fitting a solar limb by a circle with 30 positions. It gives an accuracy of $\sigma = 1$ pixel$/30^{0.5} = 0.2$ pixel (EIT pixel size is about 2.616 arc sec). A more complete discussion can be found in Aschwanden *et al.* (1999).

We now discuss the error estimation of the values derived. As the precision on the image is 1 pixel and we fit loops with more than 10 points, the standard error introduced by describing the loop by a series of points is $\sigma = 1$ pixel$/10^{0.5} \approx 0.3$. Errors concerning the determination of latitude, longitude of loop position, azimuth angle and inclination angle are already discussed in Aschwanden *et al.* (1999). To derive the error for every other parameter, we measured successive images of each loop and analyzed the variation in each variable (while the other parameters were kept fixed). As EIT resolution is 2.6 arc sec, we obtained uncertainties of 2 Mm in linear dimensions. The loops studied have a size around 36 Mm, thus we are able to distinguish loops with 5 deg of twist differences (within the torus hypothesis). See the Appendix for details concerning measurement uncertainties.

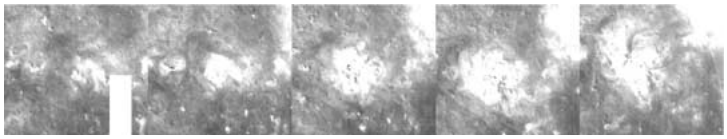

Figure 6. Intensity ratios 195Å/171Å, i.e., temperature between 0.7–1.5 MK (respectively *dark* – *bright*): 5 August 1997 at 07:00 UT, 13:00 UT, 19:00 UT, and 6 August 1997 at 01:00 UT, 15:00 UT.

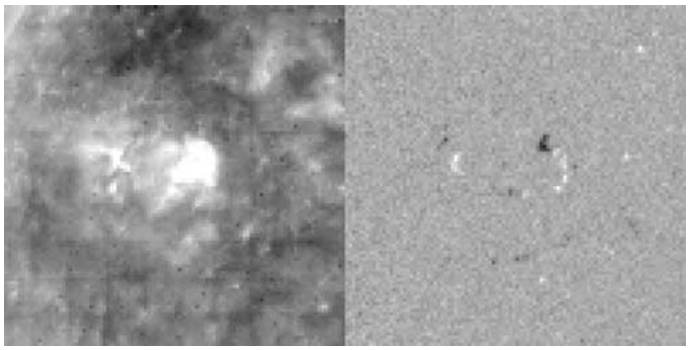

Figure 7. Aspect of the area with SOHO/EIT Fe IX/X et SOHO/MDI, 30 July 1997, i.e., 5 days before the appearance of the active region.

4. Observations of NOAA 8069

4.1. Before emergence

Active region NOAA 8069 emerged in an old activity location (Figure 7), as seen in some other cases (van Driel-Gesztelyi *et al.*, 1998). The remnant of the old active region (NOAA 8066) was weak. For example, on 30 July 1997, this coronal activity was seen by EIT as a diffuse area without distinguishable loops in agreement with MDI observations which showed a small bipolar magnetic field with weak intensity (Figure 7). The sunspot area in NOAA 8066 appeared at the limb on 25 July 1997 (*Solar Geophysical Data* Report, 1997) and was no longer visible on 31 July 1997 although it should have been near the disk center. The photospheric magnetic field remained weak but detectable (cf., iso-contours of the Stanford Magnetogram in *Solar Geophysical Data* Report, 1997). No structure was visible at the highest temperatures in X-rays with *Yohkoh*. No activity was reported until 5 August (*Solar Geophysical Data* Report, 1997) when the sunspot NOAA 8069 appeared there. New bright loops appeared on the EIT images on 5 August 1997 at 07:18 UT.

4.2. Active-region evolution

Loops were observed simultaneously in EUV-structures with temperatures around 10^6 K, and in X-rays $T_e \approx 5 \times 10^6$ K. The loops observed by EIT in NOAA 8069 do not appear to be simple potential loops corresponding to the bipolar photospheric

Figure 8. SOHO/MDI magnetic evolution of the bipolar AR: 5 August 1997 at 14:29 UT, 5 August 1997 at 15:27 UT, 6 August 1997 at 09:41 UT, 6 August 1997 at 17:28 UT. Magnetic field: *white* = positive polarity, *black* = negative polarity.

TABLE I

Loop size and twist evolution. Average of 5 different loops (the results for the different loops exhibit the same variations). We obtained uncertainties of 2 Mm for the maximum altitude and 5 deg for the twist. The small radius of the torus remains about 5 Mm.

Date time	5 Aug. 1997 19:07 UT	6 Aug. 1997 01:40 UT	6 Aug. 1997 15:51 UT	6 Aug. 1997 23:25 UT
Maximum altitude ($r_0 + h_0$ in Mm)	34	37	40	46
Twist: $\Psi = \Phi_2 - \Phi_1$	210	55	27	10
E.g., Loop 1a : Φ_2	230	105	70.1	50.3
E.g., Loop 1a : Φ_1	18	50	43	40

field observed (Figure 8). The fitting technique developed in Section 3 was used to estimate the twist in these loops.

From EIT images, first an increase of temperature was observed (Figures 6(a–c)). The increase of the temperature coincides with the position of the magnetic field lines which emerge. During the same time, magnetograms showed an enlargement of the bipolarity and an increase in the magnetic field intensity. This revealed strong development of photospheric magnetic activity (Figure 8) which is followed by an increase of temperature observed in the neighborhood of the loops and not only along the magnetic field lines (Figures 6(d) and 6(e)).

Five similar loops were fitted on each image. Then, the 3D loop geometry was obtained for 5 August 1997 at 19:07 UT (Figure 9(a)), the 6th at 01:40 UT (Figure 5), 6 August at 15:51 UT (Figure 9(b)), 6 August at 23:25 UT (Figure 9(c)).

Within the uncertainties, latitude, longitude and inclination angles were found to be the same for each loop which is consistent with the expected continuity in the evolution of loop parameters. Measured loop sizes and twists are summarized in Table I. The average loop expansion increased in height which is consistent with the development of the polarities observed at the photosphere (Figure 8). The loop size (altitude + main radius) increases with time.

The velocity of the average loop expansion is found to be less than a few km s^{-1}. After 2 days of quick expansion, the AR stabilizes in size.

The results of the fit (see Figure 5) give a left-handed helix (cf., definitions in Berger, 1998). This corresponds to a negative twist (T_w) and a negative helicity as the magnetic helicity is proportional to $T_w \Phi^2$ (Berger, 1985). As the region studied is in the northern hemisphere, this chirality agrees with the usual rules by hemisphere: for the northern hemisphere, the magnetic helicity is negative (Seehafer, 1990; Pevtsov, Canfield, and Metcalf, 1995).

The main result is that the measured twist (Table I) decreased continuously with time during the increase of loop size. The coherent evolution found for the fitting parameters gives some confidence in the technique developed in Section 3. The main result is that the measured twist is decreasing with time during the emergence of AR 8069. The difference of sign between T_w and ψ comes from the geometrical definition. The evolution is analyzed in the next section.

5. Analysis

5.1. Active-region emergence

We have analyzed the formation of a new active region where a set of loops was visible in UV. Our observations show that these loops were twisted when they first appeared in the corona (Table I). In the same way as Leka *et al.* (1996), we interpret our observations as the emergence of a twisted flux tube. However, one difference is that Leka *et al.* observed the emergence of 5 small bipoles in an already existing active region, while in our case it is the full active region which is emerging.

Such emergence of a twisted flux tube is expected from the recent development of the theory analyzing the transport of magnetic flux from the bottom of the convection zone to the photosphere. Indeed both Emonet and Moreno-Insertis (1998) and Fan, Zweibel, and Lantz (1998) show independently that a minimum of magnetic twist is needed in order that the flux tube keeps its coherence during its rise through the convective zone.

5.2. Evolution in the corona

What is the expected evolution in the corona of such a flux tube? As the emergence proceeds, a larger part of the twisted flux tube is present in the corona, thus, without dissipation, the twist is expected to grow up to a maximum value (when the remaining part of the flux tube in the convective zone is no longer buoyant). This increase of coronal twist has probably happened in our analyzed case earlier in time but it was difficult to visualize the loop in EUV in this early stage of the emergence (before 19:00 UT on 5 August). Rather, when we were able to follow the loops, a continuous decrease of twist was observed (Table I). Since the magnetic twist is closely related to the non-potentiality of the magnetic field and thus to its free energy, the decrease of twist may be interpreted as the consequence of magnetic dissipation. In particular it is well known that a potential magnetic field, with no

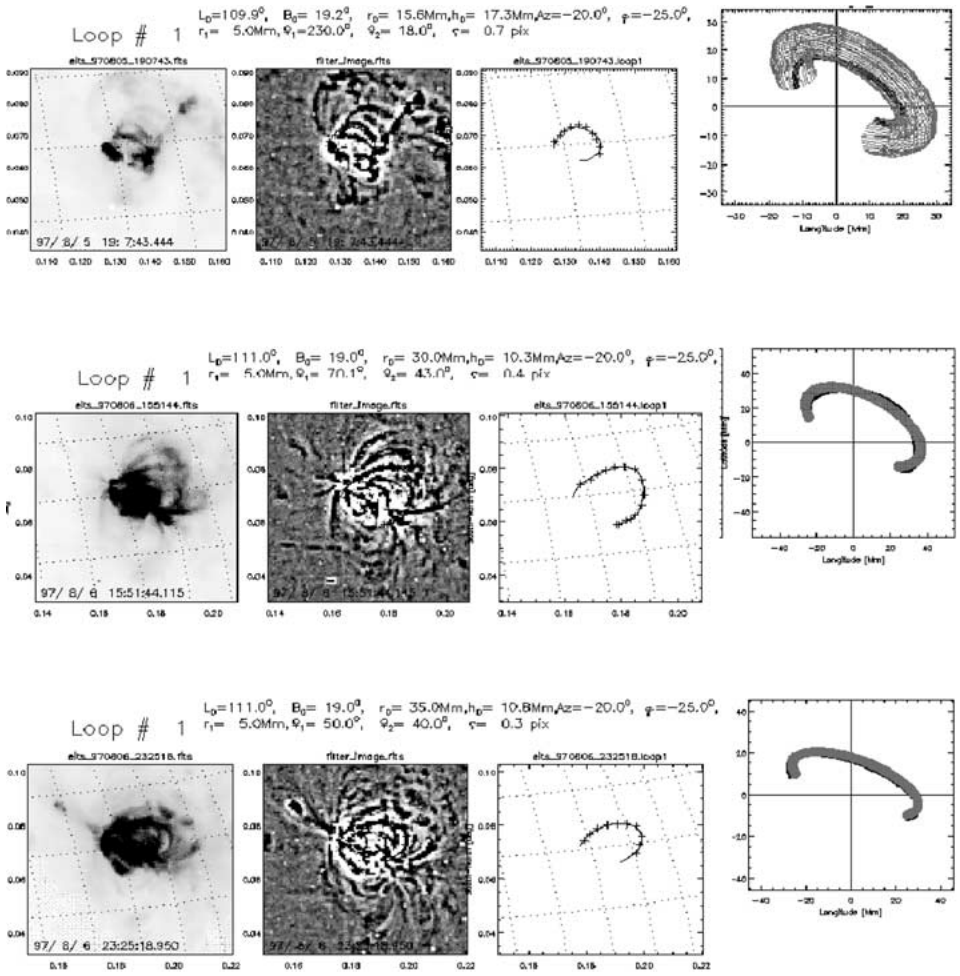

Figure 9. Loops fitting: radius, altitude and twist measured for the 3 other images. *From left to right*: the EIT image studied, its Sobel transformed with the loop pointing overlaying, the pointing and the result of the fitting. *From up to down*: the results are given for 5 August 1997 at 19:07 UT, the 6 August at 15:51 UT, and 23:25 UT.

twist, minimizes the magnetic energy for a given distribution of the vertical component of the photospheric magnetic field. Before further analyzing this scenario, we describe the constraints given by the observations on the dissipation mechanism.

How was the energy dissipated? In the case of NOAA 8069 flares were detected only after 6 August (as shown by EIT and GOES data). So the excess of energy was not realized in flares or it could be that the event intensities were less than the instrument sensitivity.

No CME either was detected in association with this active region (LASCO Team, 1999). The only evidence of dissipation is the presence of hot loops in the active region (Figure 6) which expand. This corresponds to a global heating of the

loops and may explain the decrease of magnetic twist (while the energy budget of the emission is difficult to estimate from observations with the narrow pass-band filters of EIT).

5.3. Relaxation of the magnetic field

According to the above section, the dissipation of the magnetic energy, associated with the twist, appears to be the most plausible interpretation of the twist evolution. However, this needs further analysis because a constraint arises from the conservation of magnetic helicity H in resistive MHD. It is dissipated much more slowly than the magnetic energy in magnetized plasma with a high Lundquist number such as the coronal medium, (Biskamp, 1993). For a closed magnetic volume (i.e., without flux exiting from the surface of the volume), magnetic helicity is simply defined by the integral over the volume $\mathbf{H} = \int\int\int \mathbf{A} \cdot \mathbf{B}\, \mathrm{d}^3\mathbf{r}$, where $\mathbf{A}$ is the vector potential of $\mathbf{B}$.

For an open system, like the magnetic field of an AR above the photosphere, this definition needs a generalization : the definition of a relative helicity. But the important point here is that this relative helicity is also preserved provided there is no injection of helicity through the boundary – here the photosphere (Berger and Fields, 1984). The conservation of helicity implies that the lowest energy level (the potential field) cannot be reached if the field is contained in a finite volume. The field with minimum energy, with the same photospheric distribution of the vertical field component, is instead a non-linear force-free field (Sakurai, 1981). The relaxation to this field still allows a decrease of the magnetic twist. However in the corona the plasma beta is low so that the magnetic field is space-filling. The newly emerged field will expand until there is a force balance with the ambient coronal field. In general this will produce current sheets where magnetic energy will be dissipated, and where part of the helicity will be transfered to the ambient field.

We finally conclude that the magnetic twist of the emerging flux tube could plausibly decrease to a low value, both because of the large expansion of the flux tube in the corona and because part of the magnetic helicity is transferred to the surrounding corona (so cascading to large spatial scales, see, e.g., Biskamp, 1993). This proposition needs however to be tested quantitatively with MHD numerical simulations.

6. Conclusion

With the development of a new fitting technique based upon stereoscopy of EIT images we are able to find 3D parameters for loops such as their size and twist. The emergence and the evolution of active region loops without magnetic neighborhood interaction is tracked.

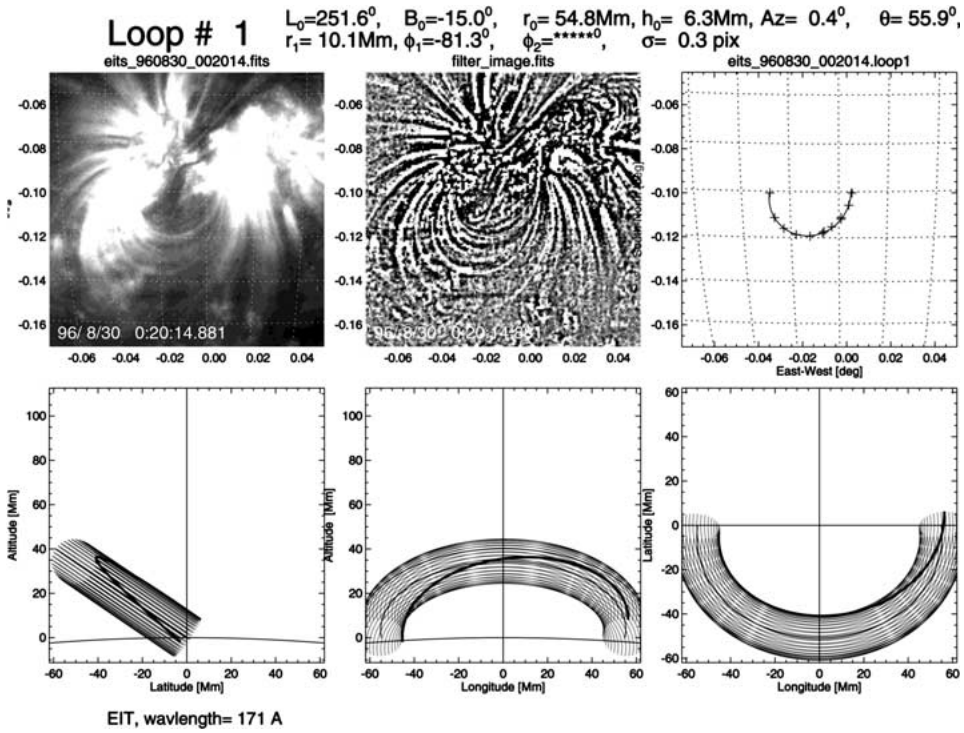

Figure 10. SOHO/EIT 30 August 1996 at 00:20:14 UT, loop 1. Parameter fitting gives $l_0 = 251.62$, $b_0 = -15.02$, $r_0 = 54.84$ Mm, $h_0 = 6.28$ Mm, az $= 0.45$, th $= 55.86$, $r_1 = 10.05$ Mm, $\phi_1 = -81.33$ deg, $\phi_2 = -197.10$ deg. Measured error between the model and the fit is 0.32 pixel.

Active region loops in NOAA 8069 were twisted (almost one turn) when first observed and de-twisted with time as the loops expanded. The de-twisting with expansion can be explained by considering the conservation of helicity while the twist is transfered into an adjacent volume of the corona.

We can try to speculate about what happens if the anisotropy of the emerging flux is too large to be relaxed in a decent time scale. Thus the expansion could happen very quickly and create a plasmoid ejection. Amari *et al.* (1996a,b) have already discussed the impact of the shear to CMEs. Some flares are related with twisted or shared emerging flux (Ambastha, 1997; Ishii and Kurokawa, 1997). Measurement of twist between flare and emergence needs to be done in the future to confirm this possible scenario. This method could better constrain loop flare prediction for space weather forecasting.

Additional Material on the CD-ROM

The MPEG arem97 movie was made from the EIT full-disk full-resolution (1024×1024 pixels) images available in the transition region Fe IX/X line (171Å). Images

were taken 5 August at 01:05, 07:18, 13:23, 19:18, and 6 August at 01:40, 07:53, 15:39, 17:35, 19:00, 19:54, 22:46 UT. The movie displays the emergence and growth of the ARLs of NOAA 8069.

Acknowledgements

F. Portier-Fozzani thanks for support during the PhD thesis – which partially led to this work – Francis Rouard, the Rotary-Club of Roquefort Les Pins (president Pierre Baude) and the philosophical circle: 'Edgar Morin, la Pensée Complexe' (president Bernard Kohl). He also thanks Serge List for graphics, Roger Malina and Andre Jean Maucherat for advice in writing the paper. Part of the work has been done while the main author was at the Laboratoire d'Astronomie Spatiale in Marseilles (CNRS UPR, France) with the support of the laboratory and the EIT Team. The authors also wish to thank an anonymous referee for comments which helped to improve the paper.

Appendix : Method Validation and Uncertainty Measurement

A complete analysis concerning validation of the method and the uncertainty measurement has been done using August 1996 data (Portier-Fozzani, 1999). The file eits_960802_072407.loop1 for 2 August 1996 at 07:24 UT includes loop 1 coordinates as on a screen showing the SOHO/EIT image. These coordinates will be transformed with the ephemerides and the heliographic position for the different fitting.

Several examples of parameter fitting are given in Table II (file eits_960802_072407.para1).

Some of these values, which are not physical (such as an inclination angle more than 90 deg which would correspond to a structure under the solar surface), are suppressed. Meanwhile, we obtain several values for the fitting with only one image. The uniqueness of the solution is obtained in comparing data from images given in a time sequence. Values obtained with different images must be close while the magnetic flux is continuously moving (in the mathematical sense). It is then possible to re-plot the corrected fitted loop.

A.1. Uncertainties

We check the uncertainties (Figures 10 and 11) for all the processed parameters.

As an example on the data of 30 August 1996, if instead of $\phi_2 = -197.10$ deg we would have $\phi_2 = -190$ deg, then the difference between the model and the fitting plot will grow 0.32 pixel up to 2.78 pixels. So the minimization of these differences is effective down to 7 degrees of twist difference.

TABLE II

Several geometrical solutions obtained for one loop with one angle only (variation between the model and the fit -dev- is given in pixels).

l_0	b_0	r_0	h_0	az	th	r_1	$\Phi 1$	$\Phi 2$	dev
254.24	−7.95	57.16	9.77	18.91	−92.56	2.92	301.73	138.35	1.15
256.29	−7.58	58.11	1.39	32.67	−86.87	25.01	145.79	−39.05	1.73
254.26	−8.02	54.65	10.11	28.99	−74.45	1	0.0	1	0.73
254.52	−7.79	64.93	16.49	16.09	−97.01	19.21	228.96	118.75	1.22
254.62	−9.27	52.61	24.22	14.21	−94.59	0.12	39.00	55.27	1.13
254.51	−6.35	62.26	13.31	15.56	−57.93	18.71	122.27	104.08	2.85
254.52	−6.34	62.28	13.48	15.47	−58.02	18.91	122.60	103.49	2.84

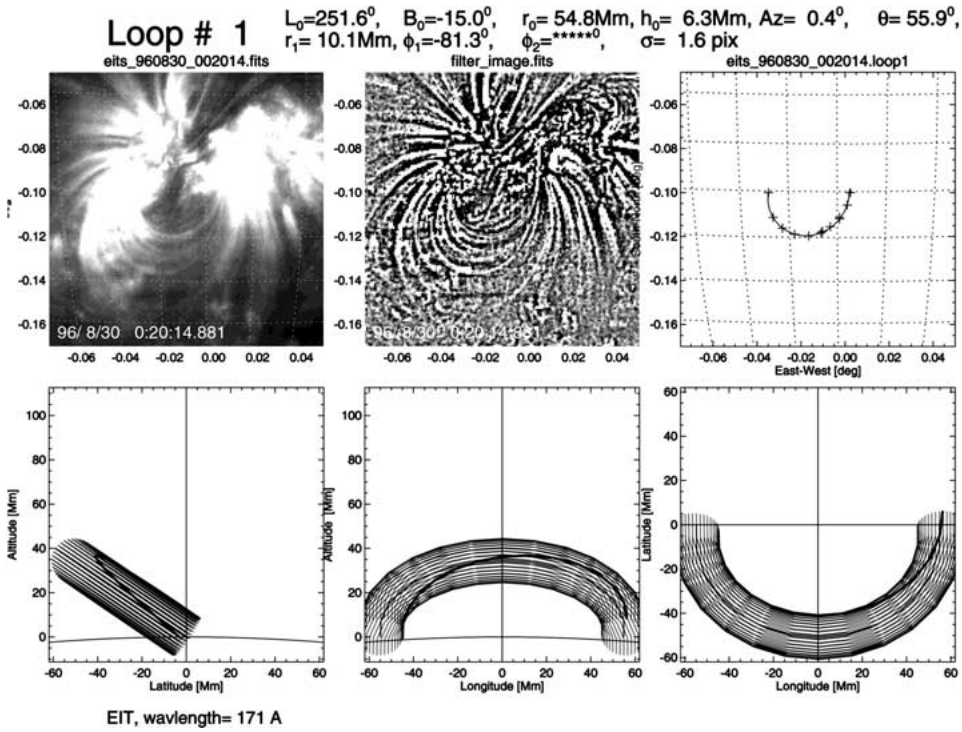

Figure 11. SOHO/EIT 30 August 1996 at 00:20:14 UT, loop 1. Parameters fitted are chosen such as $l_0 = 251.62$, $b_0 = -15.02$, $r_0 = 54.84$, $h_0 = 6.28$, $az = 0.45$, $th = 55.86$, $r_1 = 10.05$, $\Phi_1 = -81.33$, $\Phi_2 = -190$, giving a measured error between the model and the fit of 2.78 pixels.

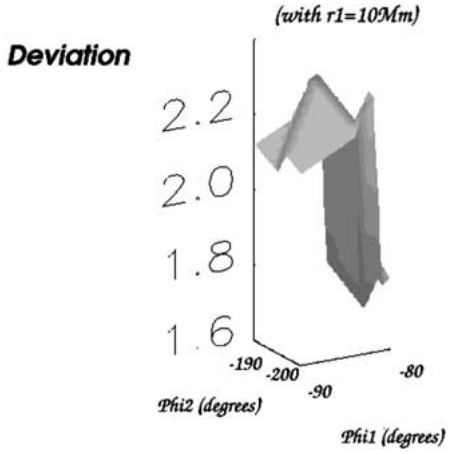

Figure 12. For r_1 given at 10 Mm, minimal variation obtained for ϕ_1 from -90 to -80 deg, ϕ_2 from -200 to -190 deg: minimum deviation correspond to $\phi_1 \sim -81$ deg and $\phi_2 \sim -197$ deg.

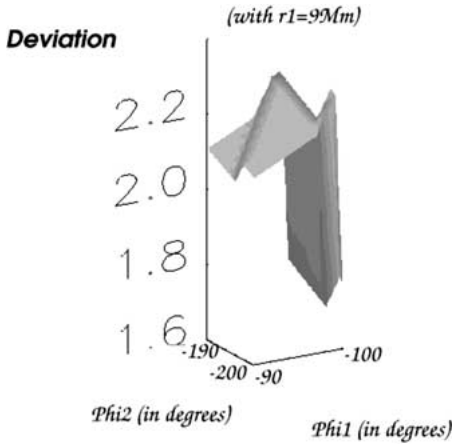

Figure 13. For r_1 given at 9 Mm, measurement of the minimum variation for ϕ_1 from -90 up to -80 deg, ϕ_2 from -200 up to -190 deg.

The uncertainty calculation is given by the sum of all uncertainties for each of the parameters. With 30 points, a previous calculation (in the main text) shows that the most discernible difference between the sampled loop and the model is an error of 0.2 pixels. If s_1 is the solution and s_2 can be a solution if $\text{Error}(\text{Norm}(s_2 - s_1)) \leq 0.2$ pixels. Then for all fixed parameters except Φ_2, this cooresponds numerically to $\Delta\Phi \sim 4.7$ deg (Portier–Fozzani, 1999). Numerical simulations for the uncertainties is used because even if the torus is a correct analytical function, a line over a torus is not a simple function and the error cannot be easily derived.

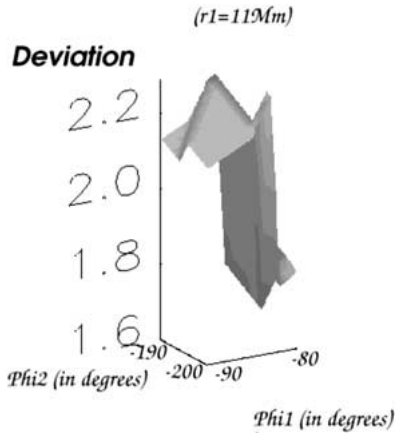

Figure 14. For r_1 fixed at 11 Mm, measurement of the minimum variation for ϕ_1 from -90 to -80 deg, ϕ_2 from -200 to -190 deg.

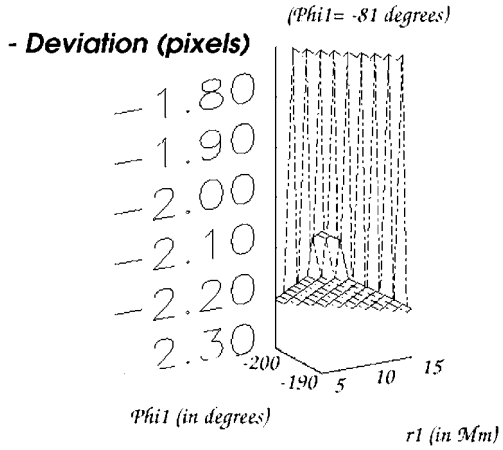

Figure 15. For ϕ_1 fixed at -81 deg, deviation as a function of r_1 and ϕ_2: The minimum is reached for $r1 \sim 10$ Mm and $\phi_2 \sim -197$ deg.

A.2. Global Minimization convergence

Table III gives the solution found for 30 August 1996 at 0 h 20 min 14 s.

TABLE III
Converged values found by the method.

l_0	b_0	r_0	h_0	az	th	r_1	$\Phi1$	$\Phi2$	dev
251.62	−15.02	54.84	6.28	0.45	55.86	10.05	−81.33	−197.10	0.32

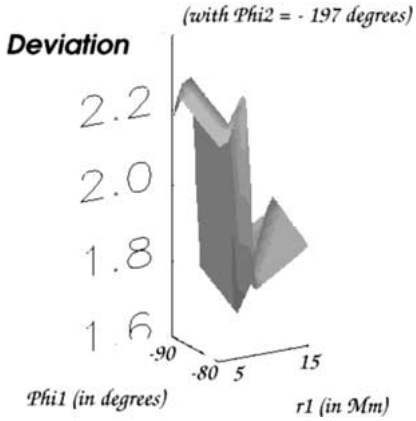

Figure 16. For ϕ_2 fixed at -197 deg, deviation as a function of r_1 and ϕ_1: the minimum is reached for $r_1 \sim 10$ Mm and $\phi_1 \sim -81$ deg.

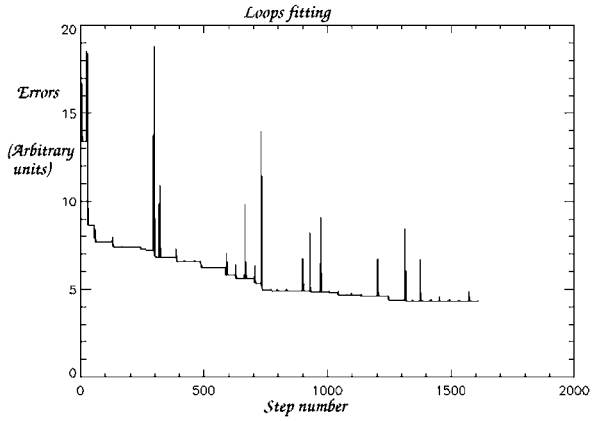

Figure 17. Minimization of dev as a function of the step number.

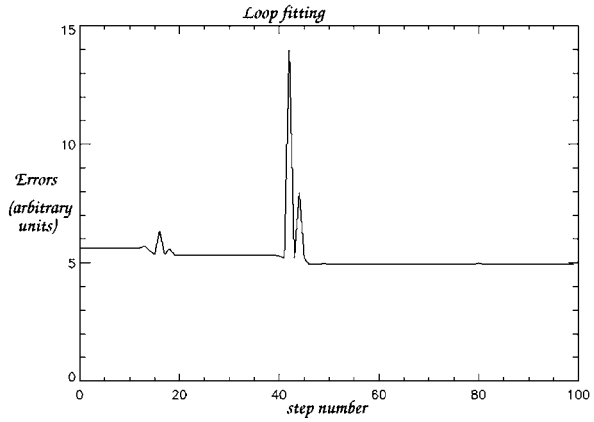

Figure 18. Minimization of dev with entropy minimum method (deviation as function of the step).

We show that this solution completely minimizes the error over all sets of parameters by analyzing how the method works.

Let us take the initial value as $l_0 = 262$ deg, $b_0 = -15$ deg, $r_0 = 55$ Mm, $h_0 = 6$ Mm, $az = 0$, $th = 56$, while r_1 goes from 5 to 15 Mm with 1 Mm step, ϕ_1 from -90 to -80 deg with $+1$ deg step, ϕ_2 from -200 to -190 degrees with $+1$ deg step. Then we can analyze the deviation versus (ϕ_1,ϕ_2) for $r_1 = 10$ Mm. In practice, we would try 2 other values of r_1 to look at the variations of the other parameters.

The minimum is reached (Figure 12) for $\Phi_1 = -81$ deg and $\Phi_2 = -197$ deg. While comparing Figures 12–14, this minimum is a minimum over a certain topological neighborhood. To check that, we have to consider also variations with r_1 (Figures 15 and 16), and thus a global formula is derived from the variational calculation over the set of all variables.

A.3. Convergence

The method is converged by minimizing the error parameter dev. Several steps for the method are shown in Figures 17 and 18.

Because the Powell function uses a kind of entropy minimalization, the program is able to jump over a local gap from a local minimum to the global minimum. Then the program converges toward the absolute minimum of the deviation over the set of all variables.

A.4. Conclusion for the method

The method, based on Powell procedures, reaches a global minimum of the difference between a graphical fit and a model. Complete uncertainty formulas can not be calculated directly by analytical mathematics but errors can be estimated by looking at the difference introduced by a small change in the parameters. Reasonable values obtained (e.g., with a big difference change while the angle does not change more than 5 degrees) confirm the good accuracy of the method.

References

Aly, J. J.: 1991, in B. Schmieder and E. Priest (eds.), *Dynamics of Solar Flares*, Flares 22 Workshop, Obs. Paris-Meudon, p. 29.

Amari, T., Luciani, J. F. *et al.*: 1996a, *Astron. Astrophys.* **306**, 913.

Amari, T., Luciani, J. F., Aly, J. J. *et al.*: 1996b, *Astrophys. J.* **466**, L39.

Ambastha, A.: 1997, in K. S. Balasubramaniam, J. Harvey, and D. Rabin (eds.), *18th NSO/Sacramento Peak Summer Workshop Synoptic Solar Physics*.

Aschwanden, M. J.: 1995, *Lecture Notes Physics* **444**, 13.

Aschwanden, M. J. and Bastian, T. S.: 1994a, *Astrophys. J.* **426**, 425.

Aschwanden, M. J. and Bastian, T. S.: 1994b, *Astrophys. J.* **426**, 434.

Aschwanden, M. J., Newmark J. S., Delaboudinière, J. P. *et al.*: 1999, *Astrophys. J.* **515**, 842.

Bentley, R., Mariska, J. T., and Sakao, T.: 1996, *Publ. Astron. Soc. Pacific* **109**, 107.
Berger, M.: 1985, *Astrophys. J. Suppl. Ser.* **59**, 433.
Berger, M. and Fields, 1984, *Geophys. Astrophys. Fluid Dyn.*, **30**, 79.
Berton, R. and Sakurai, T.: 1985, *Solar Phys.* **96**, 93.
Biskamp, D., 1993, *Nonlinear MHD*, Cambridge Monographs on Plasma Physics.
Bray, R. J., Cram, L. E., Durrant, C. J., Loughhead R. E.: 1991, *Plasma Loops in the Solar Corona*, Cambridge Astrophysics Series.
Davila, J. M.: 1994, *Astrophys. J.* **423**, 87.
Delaboudinière, J. P. *et al.*: 1995, *Solar Phys.* **162**, 291.
Dere, K. P., Brueckner, G. E., Howard R. A. *et al.*: 1997, *Solar Phys.* **175**, 601.
Emonet, T. and Moreno-Insertis, F.: 1998, *Astrophys. J.* **492**, 804.
Fan, Y., Zweibel E. G., and Lantz, S. R.: 1998, *Astrophys. J.* **493**, 480.
Harvey, K. L. and Hudson, H. S.: 1998, in *Observational Plasma Astrophysics: Five Years of Yohkoh and Beyond*, Astrophysics and Space Science Library, Dordrecht Kluwer Academic Publishers, pp. 229, 315.
Heyvaerts, J. and Hagyard, M.: 1991, in B. Schmieder and E. Priest (eds.), *Dynamics of Solar Flares*, Flares 22 Workshop, Obs. Paris-Meudon, p. 1.
Ishii, T. T. and Kurokawa, H.: 1997, *Physics of the Sun and Heliosphere in the Era of Space Probes: Scientific Highlights of SOHO, Ulysses, and Yohkoh*, 23rd IAU Meeting.
Klimchuk, J. and Porter, L.: 1996, 'Magnetodynamic Phenomena in the Solar Atmosphere', *IAU Colloquium* **153**, 39.
LASCO Team, 1999, http://lasco-www.nrl.navy.mil/cmelist.html.
Leka, K. D., Canfield, R. C., McClymont, A. N., and van Driel-Gesztelyi, L.: 1996, *Astrophys. J.* **462**, 547.
Loughhead, R. E., Chen, C. L., and Wang, J. L.: 1984, *Solar Phys.* **92**, 53.
Newmark, J., 1997, *Temperature and density with SOHO/EIT*, EIT internal report.
Neupert, W., Delaboudinière, J. P., Thompson, B. *et al.*: 1998, *Solar Phys.* **183**, 305.
Parker, E. N.: 1974, *Solar Phys.* **36**, 249.
Pevtsov, A. A., Canfield, R. C., and Metcalf, T. R.: 1995, *Astrophys. J.* **440**, L109.
Portier-Fozzani, F.: 1999, Ph.D. Thesis (in French), *The 3D Solar Corona and its Evolution with SOHO/EIT*, University of Nice Sophia Antipolis and Laboratoire d'Astronomie Spatiale (France), (available on CD-ROM and online http://www.linmpi.mpg.de/ fabrice/)
Portier-Fozzani, F. *et al.*: 1997, *Publ. Astron. Soc. Pacific Conf. Ser., IAU Colloq.* **167**.
Rust, D. and Kumar, A.: 1996, *Astrophys. J.* **464**, L199.
Sakurai, T.: 1981, *Solar Phys.* **69**, 343.
Seehafer, N.: 1990, *Solar Phys.* **125**, 219.
Solanki, S.: 1998, *Lecture Notes in Physics*, **507**, 41.
Solar Geophysical Data Report, *NOAA*, 1997.
Uchida, Y.: 1992, *Publ. Astron. Soc. Japan* **44**, L181.
Van Driel-Gesztelyi, L. *et al.*: 1998, *Publ. Astron. Soc. Pacific Conf. Ser.* **155**, 202.

Cas d'une évolution lente

Il est apparu interessant d'étudier l'évolution 3D à long terme des boucles coronales et de comparer avec le moment des éruptions. A part lors de reconnection entre régions actives, il est rarement possible (pas assez de résolution spatiale ou temporelle) de décrire parfaitement les éruptions. Velli ([244]) a rappellé l'influence théorique des ondes MHD qui peuvent déstabiliser des tubes de flux lorsqu'ils sont torsadés ([136]).
Nous avons ainsi suivi la région qui s'est successivement appellée NOAA 7978, 7981, 7986 de l'été 1996 lors du minimum du cycle. Cette région est formée de nombreuses boucles. Nous nous sommes servis des images SOHO/EIT pour déterminer les différents paramètres des boucles (comme expliqué au chapitre précédent). Les valeurs trouvées à petite échelle de temps qui traduisaient la continuité des variables, ont montré la forte stabilité des boucles. Cette stabilité peut être observée aussi en réalisant des films de séquences temporelles.
2 boucles ont ainsi pu être modélisées et nous avons étudié leur évolution. Ces résultats préliminaires seront développés dans un article ulterieur mais d'hors et déjà, on a pu remarquer que

1. la torsion mesurée sans impact exterieur à tendance à croitre avec le temps
2. Lorsqu'elle atteint une valeur critique, elle décroit brusquement. Cette chute est correllée avec une éruption GOES.

Les lecteurs interessés retrouveront cette étude dans la premiere version de la thèse, disponible sur le CD-ROM, puisque la rédaction de l'article est encore en cours.

IV.4 Conclusion et liens éventuels dans les phénomènes énergetiques

L'évolution des tubes de flux magnétiques se traduit au niveau de la couronne par le comportement en 3D des boucles. Les boucles ont tendance à émerger torsadées et s'expandent progressivement vers une forme plus lisse. Elles peuvent être parfois très circulaires et en équilibre thermodynamique. Lorsque de fortes asymétries dues au cisaillement induit par les mouvements de leurs pieds sont observées, cela peut conduire à des éruptions avec une forte libération d'énergie.

Tous ces comportements sont cohérents avec une conservation de l'hélicité globale. Le torsadage peut être ainsi transformé en expansion. Des valeurs importantes du torsadage peuvent avoir des conséquences sur la stabilité des structures ainsi que sur le chauffage coronal. Nous allons étudier maintenant d'autres critères importants pour la stabilité des structures 3D coronales.

Chapter V

Diverses structures coronales

Soleil éblouissant : ta belle chevelure est couronnée de rayons.
Les Véda, Inde, 2000 avt J.C.

Sommaire

Pour completer l'étude sur la couronne 3D et son évolution, après avoir décrit le comportement physique des boucles EUV et les interactions entre lignes du champ magnétique ouvertes et/ou fermés, nous allons maintenant préciser pour des cas précis l'aspect de diverses structures coronales.

Dans un premier temps nous allons revenir sur l'étude de la région active de l'été 1996 (NOAA 7981) dont nous avons étudié les changements morphologiques et topologiques au chapitre précédent et dont nous avons établi différents paramêtres sur les boucles. Nous établirons ainsi un bilan énergétique pour cette région et les structures avoisinantes.

Ensuite afin de mieux comprendre quels types de structures sont détectés par le radiotélescope de Metsähovi à 87 Ghz, nous comparons ces données à celles de SOHO/EIT. D'autres observations multi-longueurs d'ondes viendront completer ces données.

Enfin nous regarderons la diversité de l'évolution de la couronne (éruptions, Ejections de Matières Coronales,...). Nous analyserons les éruptions de filaments, en considérant cette fois-ci la stucture torsadée propre du filament.

V.1 Régions ouvertes et fermées

L'étude de la région du minimum de 1996 a permis de mettre en évidence des structures ouvertes et des structures fermées. L'article ci dessous publié dans Sol. Phys. (Neupert & al., [158]) précise les conditions physiques que nous avons pu déterminer grâce à SOHO/EIT.

- **Observations of Coronal Structures Above an Active Region by Eit and Implications for Coronal Energy Deposition**

- by NEUPERT, W. M.; NEWMARK, J.; DELABOUDINIERE, J.-P.; THOMPSON, B. J.; CATURA, R. C.; MOSES, J. D.; GURMAN, J. B.; PORTIER-FOZZANI, F.; GABRIEL, A. H.; ARTZNER, G.; CLETTE, F.; CUGNON, P.; MAUCHERAT, A. J.; DEFISE, J. M.; JAMAR, C.; ROCHUS, P.; DERE, K. P.; HOWARD, R. A.; MICHELS, D. J.; FREELAND, S.; LEMEN, J. R.; STERN, R. A.

- Solar Physics, v. 183, Issue 2, p. 305-321 (1998).

- Code ADS : 1998SoPh..183..305N

Cette article complète l'étude de la région active de l'été 1996. Les aspects de géométrie, topologie et évolution sont abordés en relation avec le bilan énergétique.

OBSERVATIONS OF CORONAL STRUCTURES ABOVE AN ACTIVE REGION BY EIT AND IMPLICATIONS FOR CORONAL ENERGY DEPOSITION

W. M. NEUPERT[1], J. NEWMARK[2], J.-P. DELABOUDINIÈRE[3], B. J. THOMPSON[2], R. C. CATURA[4], J. D. MOSES[5], J. B. GURMAN[6], E. PORTIER-FOZZANI[7], A. H. GABRIEL[3], G. ARTZNER[3], F. CLETTE[8], P. CUGNON[8], A. J. MAUCHERAT[7], J. M. DEFISE[9], C. JAMAR[9], P. ROCHUS[9], K. P. DERE[5], R. A. HOWARD[5], D. J. MICHELS[5], S. FREELAND[4], J. R. LEMEN[4] and R. A. STERN[4]

[1]*Raytheon STX Corp., Lanham MD, 2070 U.S.A.**
[2]*Space Applications Corp, Vienna, VA 22180, U.S.A.*
[3]*IAS, U. Paris-Sud, Orsay, France*
[4]*LMPARL, Palo Alto, CA 94304, U.S.A.*
[5]*NRL, Washington, DC 203751, U.S.A.*
[6]*NASA-GSFC, Greenbelt, MD 20771, U.S.A.*
[7]*LAS-CNRS, Marseille, France*
[8]*ORB, Brussels, Belgium*
[9]*CSL, Liege, Belgium*

(Received 20 April 1998; accepted 19 June 1998)

Abstract. Solar EUV images recorded by the EUV Imaging Telescope (EIT) on SOHO have been used to evaluate temperature and density as a function of position in two largescale features in the corona observed in the temperature range of 1.0–2.0 MK. Such observations permit estimates of longitudinal temperature gradients (if present) in the corona and, consequently, estimates of thermal conduction and radiative losses as a function of position in the features. We examine two relatively cool features as recorded in EIT's Fe IX/X (171 Å) and Fe XII (195 Å) bands in a decaying active region. The first is a long-lived loop-like feature with one leg, ending in the active region, much more prominent than one or more distant footpoints assumed to be rooted in regions of weakly enhanced field. The other is a near-radial feature, observed at the West limb, which may be either the base of a very high loop or the base of a helmet streamer. We evaluate energy requirements to support a steady-state energy balance in these features and find in both instances that downward thermal conductive losses (at heights above the transition region) are inadequate to support local radiative losses, which are the predominant loss mechanism. The requirement that a coronal energy deposition rate proportional to the square of the ambient electron density (or pressure) is present in these cool coronal features provides an additional constraint on coronal heating mechanisms.

1. Introduction

A primary objective of the SOHO mission is the investigation of mechanisms of coronal heating. Soft X-ray instrumentation on *Skylab*, SMM, and *Yohkoh* have

*Present and mailing address: Code R/E/SE, NOAA/SEC, 325 Broadway, Boulder, CO 80303, U.S.A.

Solar Physics **183:** 305–321, 1998.

contributed much to a description of the corona at $T_e > 2$ MK and EUV instruments on the OSOs, *Skylab*, and SMM have done likewise for the transition region $T_e < 1$ MK) (see Webb, 1981, and references therein). Coronal structure between 1 and 2 MK has been less extensively studied, due primarily to the lack of appropriate emission lines in the spectral ranges of the space instrumentation. The introduction of a new technology—multilayer normal incidence optics (Walker *et al.*, 1988; Golub *et al.*, 1990) — has made it possible to achieve high spatial resolution at EUV wavelengths that was unattainable with earlier grazing incidence optics. The EIT on SOHO is the first instrument in space to apply this technology to extended observations of the Sun (Delaboudinière *et al.*, 1995). Initial scientific results of the investigation have been presented in Moses *et al.* (1997). In this paper we demonstrate that energy deposition in two large emission features scales with the square of the local electron density (or pressure). This result is contrary to the dependence expected for typical wave-mode energy deposition processes (Rosner, Tucker, and Vaiana, 1978; Craig, McClymont, and Underwood, 1978).

Observational progress in detecting the signatures of heating processes requires a concerted observing program utilizing both SOHO's spectroscopic and imaging capabilities that provide a comprehensive description of the coronal plasma, including non-thermal emission line widths, and the EIT has supported such spectroscopic investigations via Joint Observing Programs (JOPS). However, it is also useful to provide a characterization of features as recorded by EIT itself (Aschwanden *et al.*, 1998a, b). In this paper we examine two features in the temperature range of 1.0–2.0 MK that extend to heights greater than their nominal pressure scale heights in an effort to evaluate radiative and conductive energy losses and their implications for coronal energy deposition.

2. Observations

The EIT provides the capability for multi-wavelength imaging of the corona in four spectral bands, centered at 171, 195, 284, and 304 Å using multilayer telescope technology (Delaboudinière *et al.*, 1995; Moses *et al.*, 1997). These bands encompass coronal temperatures from 1 MK to 2.5 MK as well as upper chromospheric temperatures at about 60 000 K. In particular, nearly simultaneous imaging in passbands centered near 171 Å and 195 Å bands, the former including major Fe IX and Fe X emission lines, the latter including a strong Fe XII line, provides a capability to infer the morphology and characteristics of the corona at temperatures of 1.0–1.5 MK, a temperature regime below the principal sensitivity range of the Soft X-ray Telescope (SXT) on *Yohkoh*.

EIT observations of an active region at Carrington Longitude 260° were made at its initial appearance in July 1996 and continued on successive solar rotations through October (Portier-Fozzani *et al.*, 1998). By late September the region was in decline with no evidence of sunspots or flare activity (no NOAA number was

assigned) and with only dispersed magnetic fields of opposite polarity separated by a filament channel that was particularly evident in the 171 Å and 195 Å bands. To establish the three-dimensional geometry of the large-scale features over this active region remnant, we observed the region from day-to-day during its September transit. While changing in small detail over time scales of tens of minutes to hours (as verified with several seven-minute cadences of observations), the overall structure of the active region appeared to change little as it moved from the central meridian to the West limb. That stability was important as it provided the opportunity to estimate the lateral extent of features from disk observations and their range of heights from limb observations.

Figure 1 shows EIT images of the region near central meridian in the 171 Å and 195 Å bands while Figure 2 shows the same region as it neared the west limb. The image pairs were taken closely together in time (5 min or less) so that spatial shifts due to solar rotation were negligible at EIT's spatial resolution (pixel size = 2.6 arc sec). The filament channel separating opposite magnetic polarities was clearly visible on 25 September and was still discernable near the limb on 30 September. Coronal emission over this filament channel consisted principally of high loops connecting regions of enhanced magnetic field (i.e., loops over the magnetic neutral line). These loops were clearly detected in SXT soft X-ray images and to a lesser extent in EIT's 284 Å (Fe XV) channel. Portier-Fozzani *et al.* (1998) discuss the evolution of these loops during the September transit of the region. Such loops are generally detectable over their entire length, have two footpoints of comparable brightness, and can have temperatures as low as 1×10^6 K (Sheeley, 1980). A three-dimensional analysis of such features has been presented by Aschwanden *et al.* (1998a).

EIT also observes features that emanate from the strong magnetic fields of an active region toward distant regions of presumably weakly enhanced field preceding and trailing the active region. Such features display obvious longitudinal brightness gradients. In such features the leg of the (presumed) loop associated with a strongly enhanced field is prominent whereas the opposite leg is often so faint that it cannot be reliably traced to a specific region of the photosphere. An example of such an asymmetric feature in the September active region is designated (a) in Figure 1. This feature varied little in its overall configuration from day-to-day and its limb appearance (Figure 2) was consistent with a system of loops as viewed in the plane of the loops, with the trailing bright footpoints visible on the disk. No fine structure that would be evidence for an array of diverging loops is present in Figure 1, although some detail was observed at other times. *Skylab* EUV observations (Sheeley, 1980) did detect fan-like collections of loops, and high resolution (1 arc sec) soft X-ray observations (Sams, Golub, and Weiss, 1992; Figure 6) show similar collections of loops emanating from the penumbra of a large sunspot. Feature (a) may therefore alternatively be interpreted as a bundle of loops diverging from a compact region associated with an enhanced photospheric magnetic field in the active region but connecting to distant and well separated footpoints in regions

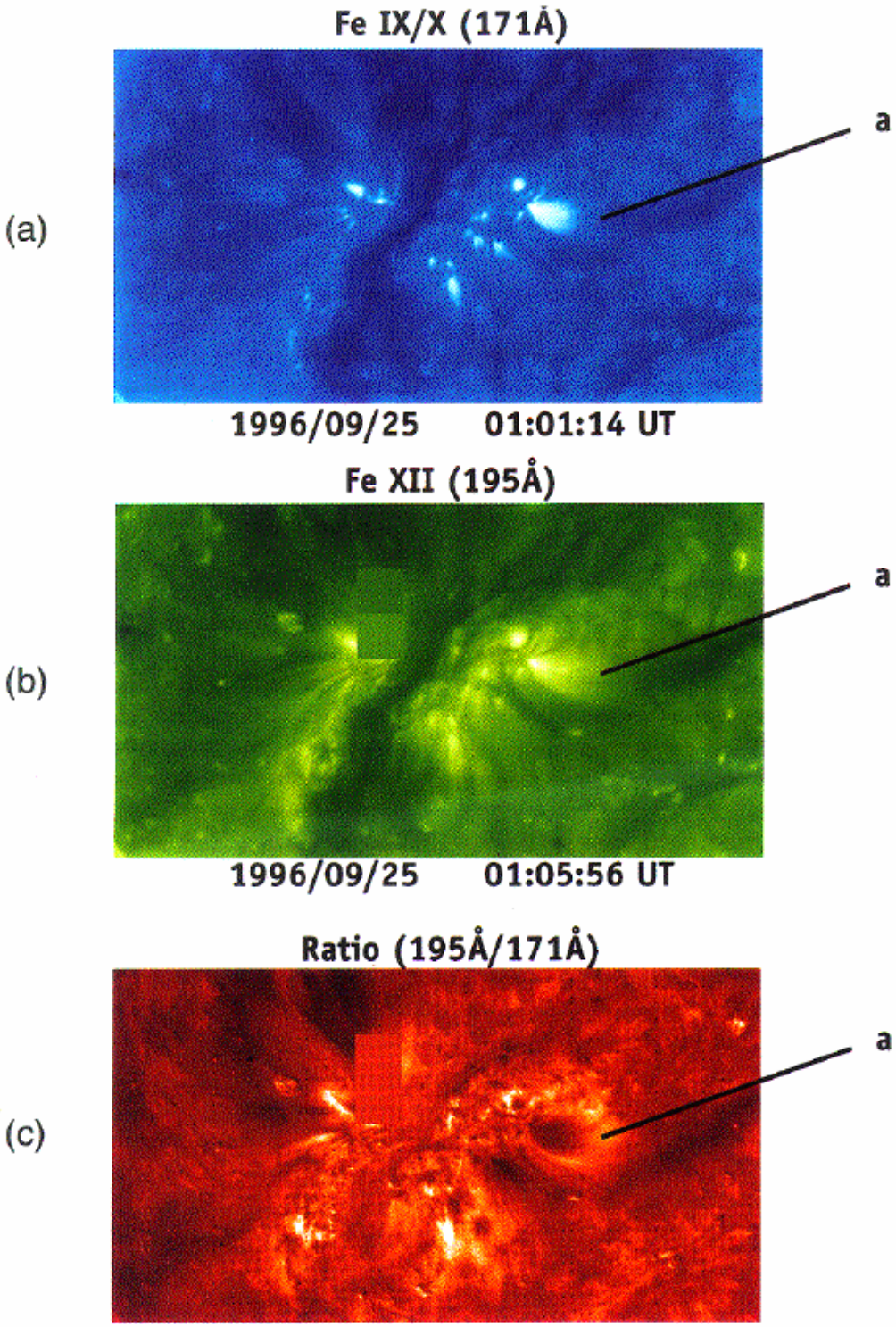

Figure 1. Observations of a decaying active region near the Central Meridian on 25 September 1996. (a) Fe IX/X emission; (b) Fe XII emission; (c) Ratio of the Fe XII and Fe IX/X images. The angular field of view of each image is 640 × 1140 arc sec. A coronal loop feature selected for analysis is indicated. Two blocks of uniform color near the centers of frames (b) and (c) are fillers for data that are missing.

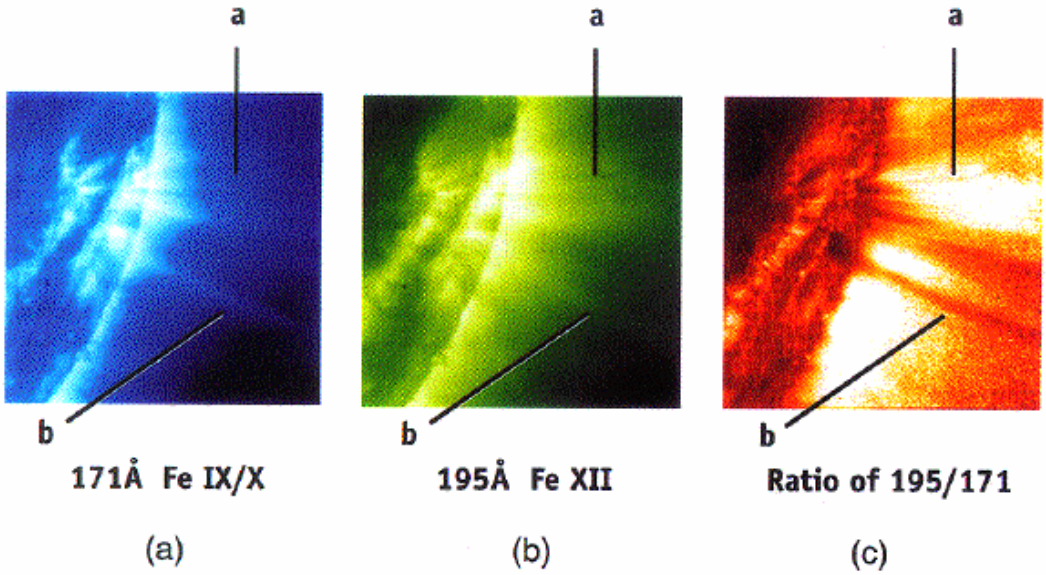

Figure 2. Observations by of a decaying active region approaching the west limb on 30 September 1996. (a) Fe IX/X emission; (b) Fe XII emission; (c) Ratio of the Fe XII and Fe IX/X images. As in Figure 1, increasing brightness in the ratio implies increasing T_e from approximately 1.0 MK to 1.6 MK. The angular field of view of each image is 582 × 582 arc sec. Two features selected for analysis are indicated.

of weakly enhanced magnetic field. Fe XV images were obtained about 5 hours prior to the 25 September data set and appeared to have a more diffuse morphology probably not cospatial with the Fe IX/X and Fe II features.

In addition to loops over the neutral line and the loops directed away from the region, EIT recorded during west limb passage of the region an extended ray-like feature with no obvious curvature or second footpoint. This feature is designated (b) in Figure 2. Its appearance in the limited EIT field of view was consistent with either an extended loop closing far above the field of view or a near-radial open field region, as might be present at the base of a helmet streamer. The latter interpretation is supported by data returned from the LASCO CI coronagraph (S. Plunkett, 1996, private communication). Feature (b) was observed as a darker feature (diminished emission) in Fe XV, indicating that its T_e could not have exceeded approximately 2×10^6 K.

3. Analysis

3.1. Calculation of Coronal Temperatures and Emission Measures

As the formation temperatures of lines in the Fe IX/X and Fe XII bands are similar (ionization peaks near 0.8–0.9 and 1.4 MK), the ratio of these bands can provide an estimate of T_e, given the assumption that the plasma is near-isothermal and

cospatial. These ratios are displayed in frames (c) of Figures 1 and 2 where increasing brightness implies increasing T_e. Newmark (1996) has convolved hypothetical EUV spectra provided by the CHIANTI program (Dere *et al.*, 1997) with the measured passbands of each of EIT's three coronal channels to derive T_e and emission measure of an assumed isothermal plasma as functions of the signal levels in pairs (171 Å and 195 Å or 195 Å and 284 Å) of EIT images. The 'eit-temp' routine in the EIT data analysis library was used for determination of temperatures and emission measures. Several sources of uncertainties in the results must be addressed first, however.

3.2. Error analysis

Klimchuk and Gary (1995) have made an error analysis of both random and systematic errors associated with the SXT measurements (as have Kano and Tsuneta, 1995; Porter and Klimchuk, 1995). Application of a similar approach is appropriate for the EIT image ratios and we base our error estimates on Equations (3.1)–(3.5) of their paper. Tarbell (1996) has determined that the photon noise is between $0.7(DN)^{1/2}$ and $0.95(DN)^{1/2}$ as each data unit (DN) corresponds to more than one arriving photon, the actual value being between 4 and 6. As a conservative approach we adopted a value of $1(DN)^{1/2}$. In addition there is a residual noise level of approximately $7^{1/2}$ due to readout noise and unsubtracted cosmic rays associated with each data readout, so that

$$(\text{noise})^2 = 7 + S\,, \tag{1}$$

where S is the signal level. The uncertainty associated with each emission ratio and hence temperature includes contributions from four data values (two for each wavelength – a feature signal and a fore/background signal from the adjacent corona).

Systematic errors in the analysis of EIT data include (a) uncertainties in the initial calibration, particularly in determining the spectral response in the far wings of the instrument's spectral passbands, (b) time-dependent EUV absorption at the surface of the cold CCD due to adsorption of volatiles, and (c) uncertainty in the location-dependent electron/photon production ratio in the CCD and its degradation with time (Defise *et al.*, 1997). The calibration used in this paper is based on the preflight calibration, flatfielding corrections to remove artifacts produced by the filter support mesh, and adjustments of up to 30% to compensate for estimated in-orbit degradation. At present, the uncertainty in sensitivity may be as high as a factor of four (yielding factors of two uncertainties in density estimates). Work is in progress to improve the EIT calibration using data from a recent EIT calibration rocket flight.

Additional sources of uncertainty are the result of EIT's limited spatial resolution, uncertainties in the geometries of features, and subtraction of emission along the same line of sight but not emanating from spatially resolved feature

fore/background emission. We assumed the level of this extraneous emission to be the same as emission from adjacent regions that appeared to be structureless but not anomalously faint. An accurate subtraction of the ambient (i.e., unenhanced) corona is especially difficult above the solar limb because of the steep radial gradients in coronal emission and the lack of nearby featureless regions. For that reason disk observations were preferable for analysis of feature (a). For near-radial features, as our feature (b) appears to be, only limb observations can provide the required spatial distribution of emission. With diminishing feature brightness (as may occur with increasing distance from the solar limb), the nominal fore/background correction becomes comparable (up to 80%) to the total signal which introduces a major uncertainty at low signal levels.

4. Results

4.1. Electron Temperature and Density Distributions

4.1.1. *High Loop System*

A qualitative distribution of temperature (within the limited 1–2 MK range) for feature (a) is displayed in Figure 1(c). Darker areas correspond to cooler regions ($\simeq$ 1.0–1.2 MK) while the brightest regions are in the 1.4–1.6 MK range. Observations on both 25 September and 30 September for feature (a) display a gradient from darker to light shades along its length, indicating increasing temperature as the line of sight moves away from the loop footpoint, with most of the increase appearing in the upper $\frac{1}{3}$ of the feature. Fluctuations across the feature were minor compared to the longitudinal change. The inferred coronal temperatures as a function of distance from the active region footpoint (derived from disk observations) of feature (a) are shown in Figure 3 together with a hand-fitted (dashed) curve. The plot assumes a semicircular loop of height 100 000 km with a temperature maximum at its apex. Temperature gradients range from 0.41 K km^{-1} at the lowest coronal heights observed to 10 K km^{-1} immediately below the loop apex. To provide an estimate of the impact that the uncertainty in fore/background coronal correction may have on our results, we also indicate in Figure 3 the temperature that would be inferred if no correction for fore/background emission were applied. Vertical error bars for points that include a fore/background correction are ± 3 standard deviations. Horizontal (dashed) error bars represent estimated positional uncertainties of ± 5 pixels (9100 km) in footpoint location and ± 10 pixels (18 200 km) in apex location). These uncertainties are equivalent to uncertainties in loop radii and apex heights of $\pm 20\,000$ km. The error in relative calibration between the 171 Å and 195 Å channels is estimated to be no greater than 40%. An error of that magnitude would correspond to a temperature shift of approximately 100 000 K for all points because of the near-linearity of signal ratio with T_e. An additional uncertainty in establishing the spatial scale is the unavoidable summation of emission

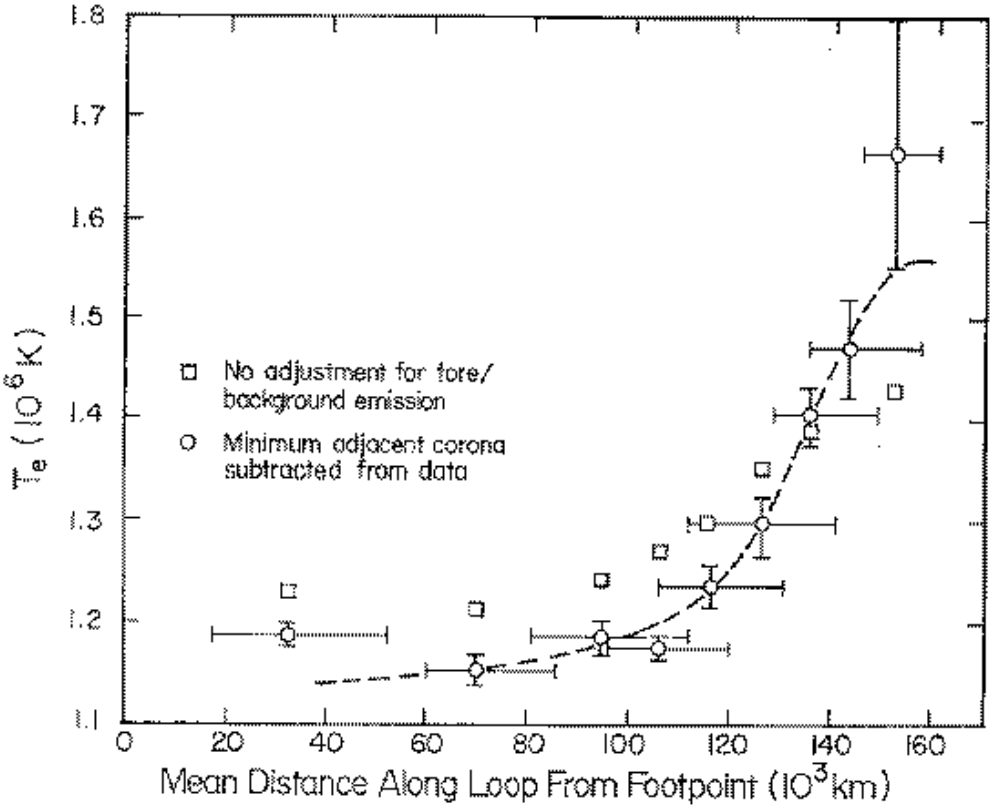

Figure 3. Temperature as a function of distance along loop feature (a), for an assumed semicircular loop of height 100 000 km, from disk observations in the Fe XII and Fe IX/X bands on 25 September 1996. Circular data points include a correction for fore/background emission along each line of sight whereas the open squares do not.

along oblique lines of sight through the feature and therefore over a range of heights and, in our models, a range of distances from the assumed footpoints. That range corresponds to 60–70% of the nominal footpoint distance for the lowest data point and 30% for the highest. These ranges are not included in the error (uncertainty) bars for distances shown in Figure 3. The distances used in that figure correspond to distances along the assumed axis of the broad observed feature.

The average electron density along a line of sight through the modeled loop is assumed to be

$$n_e = (\mathrm{EM}/L\phi)^{1/2} \quad [\mathrm{cm}^{-3}], \tag{2}$$

where EM is the line-of-sight emission measure from the eit-temp data analysis routine, L is the distance through the loop along the line of sight, and ϕ is the fill factor, the fraction of the observed volume that contains emitting material (Cargill and Klimchuk, 1997). As mentioned in Section 1, feature (a) may be interpreted as a single loop or as an ensemble of unresolved loop structures within the envelope of the observed feature. In the latter case, we assumed an ensemble of loops or strands

tightly bunched together at the bright footpoint only and connected to widely separated distant footpoints so that the fractional volume, ϕ, actually occupied by the ensemble of strands decreased with increasing distance from the footpoint, depending on the expansion factors of the individual strands. That geometry is consistent with early results from *Skylab* (Sheeley, 1980) and with observations of loops rooted in the penumbra of a large sunspot (Sam, Golub, and Weiss, 1992; Figure 5(a)). We will examine both hypotheses as a means of estimating the likely range of loop densities and local heating requirements.

For both cases the total width of the loop system, w, as a function of distance, s, from the footpoint was modeled from observations near central meridian as:

$$w = 11\,000 + 0.32s \quad [\mathrm{km}] \,. \tag{3}$$

Table I summarizes coronal densities assuming the feature is a single semicircular expanding loop with a circular crossection corresponding to its observed width. The obliquity of the line of sight through the loop for each observation was taken into account. This model is not likely to be realistic as we observe no symmetry of emission about a loop apex. Furthermore, the expansion factor (ratio of thickness at apex to thickness at footpoint) of 5.6 is far larger than would be expected for a dipole magnetic configuration (Klimchuk *et al.*, 1992). It does, however, represent a hypothesis for which we can evaluate the terms of the energy equation. Table II summarizes fill factors and densities as a function of distance from the footpoint for the multiple loop hypothesis, assuming that the loops originated in a footpoint area with a diameter of 6 EIT pixels (11 000 km) and that they diverged with height (each maintaining a constant crossectional area) so as to be spaced uniformly within the entire volume that we associate with the feature (i.e., the cross-sectional areas used in Table I). Such a hypothesis would explain the apparent brightness asymmetry of feature (a) as being the result of EIT's limited spatial resolution combined with a rapidly diminishing fill factor.

The densities given in Tables I and II are subject to limitations in determining the sizes of the emitting structures. An estimated error of two pixels (33%) in the six-pixel footpoint diameter has no impact on the single-loop densities in Table I, where loop dimensions above the footpoint are measured independently (again with an estimated error of two pixels – about 20% – resulting in a density uncertainly of 10%). In the case of multiple loops – Table II – the greater error in the footpoint diameter propagates to all heights as an error in the fill factor. The effect of these uncertainties on estimated densities is small compared to the present factor of four uncertainty in the EIT calibration (and hence a factor of four in radiative losses) discussed earlier and will not alter the conclusions regarding energy balance to be discussed in Section 4.2.

The inferred pressure scale height is dependent on the details of the assumed model. For the single loop model the inferred pressures are consistent with a scale height of $50\,000 \pm 10\,000$ km. For the multiple loop hypothesis, the densities (and pressures) within the compact loops remain approximately constant with height.

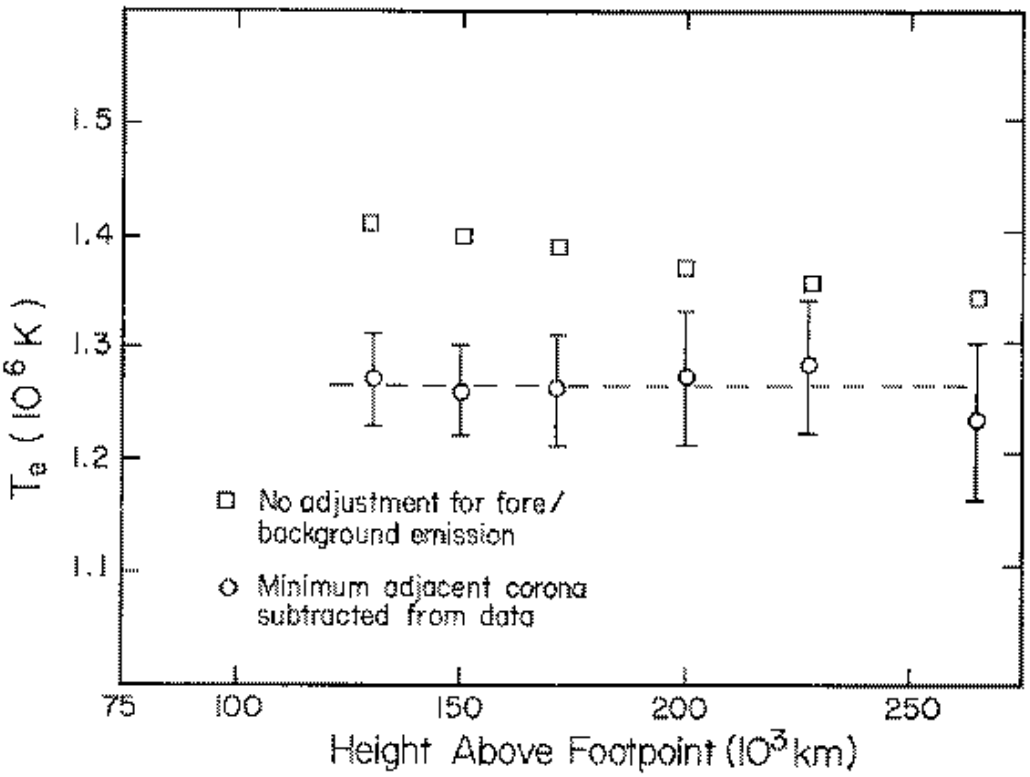

Figure 4. Temperature distribution along a near-radial feature as observed on the west limb on 30 September 1996. Circular data points include a correction for fore/background emission whereas open squares do not. The results are consistent with an isothermal distribution with height (or even a slight negative gradient, if no background correction is applied).

These results are to be compared with the expected scale height of 60 000 km ($(5000 \times T_e)$ km). By comparison, for loops hotter than the EIT loops but in the same range of heights (100 000 km), Kano and Tsuneta (1995) found densities and pressures to be 2–3 times higher at loop tops than at their bases.

4.1.2. *Extended, Near-Radial Feature*

In contrast to the T_e gradient found in the high loop system, the near-radial feature (b) exhibits no significant outwardly increasing temperature as may be seen qualitatively in Figure 2, frame (c), where the ratio appears as a nearly uniform dark feature out to the greatest distance observable by EIT.

Resulting temperatures are shown in Figure 4. There may even be a slight negative gradient of 0.6 K km^{-1} with height if no fore/background correction is applied. Feature (b) was not precisely aligned with any emission region on the solar disk and may have been rooted in an area already behind the west limb, making estimation of heights above the chromosphere somewhat ambiguous. That uncertainty is estimated to be $\pm 15\,000$ km and has negligible impact on the following discussion.

For an equatorial coronal hole Withbroe's radiative energy balance model (1988, his Figure 2) yields a broad temperature maximum near $R = 2\ R_\odot$, well beyond the heights of our observations. For the unstructured corona (his Figure 11), which may be more appropriate to the current observations, the maximum is near $R = 1.2\ R_\odot$ and not inconsistent with our data. Adopting a circular crossection with diameter increasing as $R/R_\odot$ and with an area of 1.37×10^{18} cm^2 at a height of 150 000 km, we find the properties listed in Table III. The results imply a pressure (and density) scale height of 170 000 km, far greater than is expected.

4.2. Local Energy Balance

We adopt the equations for energy and mass conservation in a coronal plasma as stated by Kopp and Orrall (1976) and Withbroe (1988), among others:

$$\Phi N_e N_p + \frac{1}{A(r)} \frac{\mathrm{d}}{\mathrm{d}r} \left\{ A(r)[F_c + F_m + F_A] + \lambda \left[\frac{5kT}{2m\mu} + \frac{V^2}{2} - \frac{GM_\odot}{r} \right] \right\} = 0 \quad (4)$$

and

$$\lambda = \rho V A(r)\ , \quad (5)$$

where the terms denote radiative losses, the divergence of the conductive, mechanical, and Alfvén wave fluxes, and the divergence of the enthalpy, kinetic energy and potential energy. ρ is the density in g cm^{-3} and V is the velocity through the area $A(r)$.

Evaluating all the possibly significant terms for EIT features is clearly impossible. Brekke *et al.* (1997) have used the CDS on SOHO to demonstrate the presence of flows in at least some coronal loops, but no data are available for the features that we discuss here. Although a mechanical flux is likely present (as evidenced by the ubiquitous non-thermal broadening of spectral lines), we have no information on changes of non-thermal broadening with height and hence the divergence of the mechanical flux. Downflows of 10 km s^{-1} at transition region temperatures have typically been observed and have been the basis for estimating downward enthalpy fluxes in the chromosphere – corona transition region (Pneuman and Kopp, 1977). However, their results have not been confirmed for the coronal components of a loop and we have therefore chosen to ignore possible enthalpy flows.

Local radiative losses were derived from:

$$\Phi N_e N_p = \Phi \frac{\mathrm{EM}}{\phi L} \quad [\mathrm{erg\ cm^{-3}\ s^{-1}}] \quad (6)$$

where Φ is the radiative loss function at T_e (we used $\Phi = 1.9 \times 10^{-22}$ erg cm^3 s^{-1} (Cargill and Klimchuk, 1997)).

Conductive losses were calculated by

$$\mathrm{div}\ F_c = \frac{\kappa_0}{A(s)} \frac{\mathrm{d}}{\mathrm{d}s} \left[A(s) T^{5/2} \frac{\mathrm{d}T}{\mathrm{d}s} \right] \quad [\mathrm{erg\ cm^{-3}\ s^{-1}}]\ , \quad (7)$$

TABLE I

Energy losses an input requirements assuming a single large loop (apex width / loop length = 0.2)

Distance from footpoint (km)	T_e (MK)	ϕ	n_e	$P^*_{\rm rad}$	div F_c^*	Nonthermal energy input rate*
45 000	1.14	1.0	1.2×10^9	3×10^{-4}	-3.4×10^{-6}	3×10^{-4}
70 000	1.15	1.0	1.2×10^9	3×10^{-4}	-4.4×10^{-6}	3×10^{-4}
100 000	1.185	1.0	0.9×10^9	1.6×10^{-4}	-2.5×10^{-5}	1.4×10^{-4}
130 000	1.34	1.0	0.6×10^9	5.9×10^{-5}	-10.5×10^{-5}	≈ 0

*Units of erg cm^{-3} s^{-1}.

TABLE II

Energy losses and input requirements assuming diverging loops of constant crosssectional area

Distance from footpoint (km)	T_e (MK)	ϕ	n_e	$P^*_{\rm rad}$	div F_c^*	Nonthermal energy input rate*
45 000	1.14	0.19	2.9×10^9	1.6×10^{-3}	-1.6×10^{-6}	1.6×10^{-3}
70 000	1.15	0.11	3.5×10^9	2.3×10^{-3}	-2.2×10^{-6}	2.3×10^{-3}
100 000	1.185	0.065	3.6×10^9	2.5×10^{-3}	-1.9×10^{-5}	2.5×10^{-3}
130 000	1.34	0.044	2.6×10^9	1.4×10^{-3}	-7.9×10^{-5}	1.4×10^{-3}

*Units of erg cm^{-3} s^{-1}.

where $\kappa_0 = 1.1 \times 10^{-6}$ and s is the distance along the feature from its base.

If a feature is magnetically open to the heliosphere, so that an outward flow is present, then work against gravity is given by

$$\frac{\lambda}{A(r)} \frac{\mathrm{d}}{\mathrm{d}r} \left(\frac{G M_\odot}{r} \right) = 2.25 \times 10^5 \left(\frac{R_1}{R} \right) \quad [\mathrm{erg\ cm^{-3}\ s^{-1}}] , \tag{8}$$

where G is the gravitational constant and $M_\odot$ is the solar mass. This term will be considered only for feature (b) and is discussed in Section 4.2.2.

4.2.1. *High Loop System*

The contributions of radiative and conductive losses to the energy balance for the two models of the loop system are summarized in Tables I and II. Uncertainties in the maximum height and T_e of the feature have little effect on its properties at intermediate heights as can be seen by inspection of the estimated error bars (Figure 3). Because of the near-linearity of temperature as a function of signal ratios between 1.0 and 2.0 MK, the impact of calibration errors on temperature gradients, hence conductive fluxes and div F_e is minor. The maximum (40%) error in relative calibration of the Fe IX/X channel relative to the Fe XII channel discussed earlier would result in a 10% error in F_e and a 20% error in div T_e. The resulting change

TABLE III

Energy losses and input requirements in a near-radial feature

Distance from footpoint (km)	T_e (MK)	n_e	Radiative loss*	Work against gravity*	Nonthermal energy input rate*
130 000	1.27	4.7×10^8	4.5×10^{-5}	2.4×10^{-5}	6.9×10^{-5}
150 000	1.26	4.2×10^8	3.3×10^{-5}	2.2×10^{-5}	5.5×10^{-5}
170 000	1.26	3.2×10^8	2.0×10^{-5}	2.0×10^{-5}	4.0×10^{-5}
200 000	1.27	2.9×10^8	1.6×10^{-5}	1.8×10^{-5}	3.4×10^{-5}
230 000	1.28	2.5×10^8	1.2×10^{-5}	1.6×10^{-5}	2.8×10^{-5}
265 000	1.23	2.2×10^8	0.92×10^{-5}	1.4×10^{-5}	2.3×10^{-5}

*Units of erg cm^{-3} s^{-1}.

in radiative flux would be negligible because of the near-constancy of the radiative loss function with temperature at these coronal temperatures. Adopting a coronal loop model with a fill factor less than one (Table II) increases radiative losses relative to conductive losses, but radiative losses are the major loss mechanism in both loop cases. Using the EIT observations with no adjustment for extraneous line of sight emission (Section 3.2) would reduce temperature gradients and conductive losses relative to radiative losses, thereby only re-enforcing the predominance of radiative losses. Wheatland, Sturrock, and Acton (1997) have argued that energy deposition at the tops of the hot loops recorded by SXT can by downward thermal conduction support energy losses below the loop apex. That conclusion is inconsistent with our present results for these cooler loops. A downward conductive flux does exist, but the divergence of that flux is adequate to heat the corona only immediately below the apex and then only in the low density case, as represented in our single loop model. Over the larger longitudinal extent of the loops only a volumetric heating rate distributed over the length of the loops and proportional to n_e^2 can match the energy requirements of these cool loops.

4.2.2. *Extended, Near-Radial Feature*

The significant terms in the energy balance for the apparently open feature are summarized in Table III. The lack of a temperature gradient in the extended ray implies that conductive losses again play a negligible role in coronal heating far above the transition region. To evaluate the work required to lift the plasma, if this feature does in fact extend to the heliosphere, we adopted a solar wind velocity of 10 km s^{-1} at $R_1 = 1.21\ R_\odot$ (about twice the value given by Withbroe (1988, his Figure 11 and Table II) for an unstructured region in the corona) and mass flux conservation in a ray whose crossectional diameter increased as $R/R_\odot$. We used a helium/hydrogen abundance of 0.1 giving $\rho = 1.17\ n_e m_p$. Under these assumptions energy requirements to lift the plasma become larger than radiation

losses at heights of $R \geq 1.24\ R_\odot$. Feldman *et al.* (1997) have proposed that far higher velocities may be present at these heights in a polar coronal hole if explosive jets of matter initiate the fast solar wind and if such were present here (none were observed in high rate observations of this feature) the energy balance would be appreciably altered. If a strong solar wind is not present, then the observations are again consistent with a volumetric heating rate proportional to the square of the local electron density.

5. Discussion

5.1. Energy input requirements

Any discussion of energy input hangs on the assumption that a quasi-steady energy deposition process (or possibly more than one) is present. Previous studies (Klimchuk and Porter, 1995; Yoshida and Tsuneta, 1995) have concluded that lifetimes of soft X-ray emitting loops are long compared to estimated energy loss times and the results of Arndt, Habbal, and Karouska (1994) indicate that coronal structures in the temperature range being discussed here (1–1.5 MK) may have less variability than either cooler (1×10^5 K) or hotter features. Aschwanden *et al.* (1998b) have discussed a statistical model for heating large EIT loops and concluded that localized transient heating at a mean rate of about 5 min at any location could maintain the temperature gradients they observe. The divergence of loops in feature (a) (or the broadening of a single loop) and their connections to distant and widely separated chromospheric regions would seem to be incompatible with a twisting together of field lines leading to reconnection and localized heating. We suggest that a process associated with the bright footpoint area, i.e., the active region end of the loops, is responsible for the propagation of energy into the coronal fields of the observed loop system.

Estimates of time-averaged total energy input rates at the bases of features (a) and (b) can be made by integrating estimated losses over the volume of each feature. For loop feature (a), the resulting estimate scales inversely with the base area adopted for the loop system. Taking into account the convergence of feature (a) with decreasing height (a factor of 42 in cross-sectional area between apex and base), we find that an energy input rate of 2×10^7 erg cm^{-2} s^{-1} at the base of corona is required to maintain the observed loop system. The estimated error in this result is the same as that of the base area, 75%, discussed earlier. Our result is greater than the early estimate of 5×10^6 erg cm^{-2} s^{-1} given by Withbroe and Noyes (1977) for radiative losses. The discrepancy could be due either to present errors in estimating the footpoint size, errors in EIT calibration, or the lower spatial resolution of observations on which the earlier estimates were based. Of course, another distributed heating process such as 'nanoflares' may satisfy the observed EIT loop characteristics and for such a process the estimation of mechanical energy flows at the coronal base made above would not be appropriate.

Energy requirements at the base of the near-radial feature depend strongly on whether or not an energy input to support the lifting of the plasma (and acceleration at higher levels in the corona) is required. The energy input to support radiative losses over the height range observed is about 1×10^6 erg cm^{-2} s^{-1}. Gravitational work to the greatest height observed is an order of magnitude less. This result is to be compared with Withbroe and Noyes' (1977) estimates of radiative and solar wind flux requirements of $1-2 \times 10^5$ erg cm^{-2} s^{-1} for the quiet Sun and 7×10^5 erg cm^{-2} s^{-1} for coronal holes.

5.2. Dependence of Energy Deposition on Ambient Pressure or Mass Density

Beginning with Rosner, Tucker, and Vaiana (1978) and Craig, McClymont, and Underwood (1978), and continuing through recent efforts by Klimchuk and Porter (1995), numerous authors have examined the dependence of various heating models in terms of observable coronal parameters. The single-loop feature that we have discussed falls consistently (particularly for model 1) at the extreme range of halflengths for SXT loops (Klimchuck and Porter, 1995, Figure 1) and we conjecture that our feature may follow the same functional relationship uncovered by Klimchuck and Porter (1995):

$$P \sim L^{\beta} , \tag{9}$$

where β has a most probable value of -0.96.

Klimchuck and Porter introduce the average volumetric heating rate:

$$\langle Q \rangle \sim P^{(4)/(11-2b)} L^{(4b-8)/(11-2b)} , \tag{10}$$

where $b = -\frac{3}{2}$ is appropriate for the EIT loops. Combining these relationships into the form

$$\langle Q \rangle \sim L^{a} , \tag{11}$$

they find that a has the most probable value of -1.95.

Combining these two results, we find:

$$\langle Q \rangle \sim p^{a/\beta} = p^{2.05} , \tag{12}$$

i.e., average energy deposition for an isothermal structure is approximately proportional to radiative losses. This result is consistent with our detailed analysis of the loop system, feature (a). If feature (b) is in fact the base of a very high loop so that the gravitational term is not required, then radiative losses also predominate at all locations and the above relationship also applies. A heating mode depending on the square of the local pressure is, however, not consistent with typical wave mode energy dissipation rates (Rosner, Tucker, and Vaiana, 1978; Craig, McClymont, and Underwood, 1978) nor with the constant volumetric heating rate adopted by Vesecký, Antiochus, and Underwood (1979).

6. Summary

We have examined a large and relatively cool coronal loop system associated with a decaying active region and a large near-radial feature that may be either the base of a very large loop or the base of a helmet streamer. In each case we find that radiative losses are far greater than the divergence of the conductive flux so that energy deposition proportional to the square of the electron density (or pressure) best fit the observations. This result imposes an additional constraint on possible heating processes for these cool coronal loops. Such heating must be distributed along the loops and not be localized to the loop tops. We also point out that observed geometry of diverging loops connecting to distant weak field regions appears to be incompatible with the twisting of magnetic field lines and subsequent reconnection and energy release.

Acknowledgements

WMN wishes to thank E. Hildner and his staff at NOAA's Space Environment Center for their hospitality and technical support to him as a guest worker. His work was supported by NASA Contract NAS5–32350 with the Raytheon STX Corp. We also thank the EIT and LASCO technical staff at SOHO's Experiment Operations Facility, with particular acknowledgment to E. Einfalt and S. Stezelberger, for their dedication in planning and executing the observational schedule for the EIT. We thank the anonymous referee whose comments improved the final manuscript. SOHO is a project of international cooperation between ESA and NASA.

References

Arndt, M. B., Habbal, S. R., and Karovska, M.: 1994, *Solar Phys.* **150**, 165.

Aschwanden, M. J., Neupert, W. M., Newmark, J., Thompson, B. J., Brosius, J. W., Holman, G. D., Harrison, R. A., Bastian, T. S., Nitta, N., Hudson, H. S., and Zucker, A.: 1998a, *Publ. Astron. Soc. Pacific*, to appear.

Aschwanden, M. J., Newmark, J. S., Delaboudinière, J.-P., Neupert, W. M., Klimchuk, J. A., Gary, G. A., Portier-Fozzani, F., and Zucker, A. : 1998b, *Astrophys. J.*, submitted.

Brekke, P., Kjeldseth-Moe, O., Brynildsen, N., Maltby, P., Haugan, S. W. H., Harrison, R. A., Thompson, W. T., and Pike, C. D.: 1997, *Solar Phys.* **170**, 163.

Cargill, P. J. and Klimchuk, J. A.: 1997, *Astrophys. J.* **478**, 799.

Craig, I. D., McClymont, A. N., and Underwood, J. H.: 1978, *Astron. Astrophys.* **70**, 1.

Defise, J. M., Clette, F., Moses, J. D., Hochedez, J.-F and the EIT Consortium: 1997, *Soc. Photo-Optical Instr. Eng.* **3114**, 598.

Delaboudinière J.-P., Artzner, G. E., Brunaud, J., Gabriel, A. H., Hochedez, J. F., Millier, F., Song, X. Y., Au, B., Dere, K. P., Howard, R. A., Kreplin, R., Michels, D. J., Moses, J. D., Defise, J. M., Jamar, C., Rochus, P., Chauvineau, J. P., Marioge, J. P., Catura, R. C., Lemen, J. R., Shing, L., Stern, R. A., Gurman, J. B., Neupert, W. M., Maucherat, A., Clette, F., Cugnon, P., and Van Dessel, E. L.: 1995, *Solar Phys.* **192**, 29.

Dere, A., Landi, E., Mason, H. E., Monsignori-Fossi, B. C., and Young, P. R.: 1996, *Astron. Astrophys. Suppl. Ser.* **125**, 149.

Feldman, W. C., Habbal, S. R., Hoogeveen, G., and Wang, Y.-M.: 1997, *J. Geophys. Res.* **102**, (A12), 26905.

Golub, L., Herant, M., Kalata, K., Lovas, I., Nystrom, G., Pardo, F., Spiller, E., and Wilczynski, J.: 1990, *Nature* **344**, 842.

Kano, R. and Tsuneta, S.: 1995, *Astrophys. J.* **454**, 934.

Klimchuk, J. A. and Gary, D. E.: 1995, *Astrophys. J.* **448**, 925.

Klimchuk, J. A. and Porter, L. J.: 1995, *Nature* **377**, 131.

Klimchuk, J. A., Lemen, J. R., Feldman, U., Tsuneta, S., and Uchida, Y.: 1992, *Publ. Astron. Soc. Japan* **44**, L181.

Kopp, R. A. and Orrall, F. Q.: 1976, *Astron. Astrophys* **53**, 363.

Moses, D., Clette, F., Delaboudinière, J.-P., Artzner, G. E., Brunaud, J., Carabetian, C., Gabriel, A. H., Hochedez, J. F., Millier, F., Song, X. Y., Au, B., Dere, K. P., Howard, R. A., Kreplin, R., Michels, D. J., Defise, J. M., Jamar, C., Rochus, P., Chauvineau, J. P., Marioge, J. P., Catura, R. C., Lemen, J. R., Shing, L., Stern, R. A., Gurman, J. B., Neupert, W. M., Newmark, J., Thompson, B., Maucherat, A., Portier- Fozzani, F., Berghmans, D., Cugnon, P., Van Dessel, E. L., and Gabryl, J. R.: 1997, *Solar Phys.* **175**, 571.

Newmark, J.: 1996, EOS **77** (46), F557.

Plunkett, S.: 1996, private communication.

Pneuman, G. W. and Kopp, R. A.: 1997, *Astron. Astrophys.* **55**, 305.

Porter, L. J. and Klimchuk, J. A.: 1995, *Astrophys. J.* **454**, 499.

Portier-Fozzani, F., Neupert, W. M., Aschwanden, M., Sheeley, N. R., Thompson, B., Maucherat, A. J., Newmark, J., Klimchuk, J. and the EIT Team: 1998, Publ. Astron. Soc. Pacific, to appear.

Rosner, R., Tucker, W. H., and Vaiana, G. S.: 1978, *Astrophys. J.* **220**, 643.

Sams, B. J. III, Golub, L., and Weiss, N. O.: 1992, *Astrophys. J.* **399**, 313.

Sheeley, N. R., Jr.: 1980, *Solar Phys.* **66**, 79.

Tarbell, T.: 1996, private communication to the EIT Team.

Vesecky, J. F., Antiochus, S. K., and Underwood, J. H.: 1979, *Astrophys. J.* **233**, 987.

Walker, A. B. C., Barbee, T. W. Jr., Hoover, R. B., and Lindblom, J. F: 1988, *Science* **241**, 1781.

Webb, D. F.: 1981, in, E. Q. Orrall (ed.), *Solar Active Regions, A Monograph from Skylab Solar Workshop III*, Colorado Associated University Press, Boulder.

Wheatland, M. S., Sturrock, P. A., and Acton, L. W.: 1997, *Astrophys. J.* **482**, 510.

Withbroe, G. L.: 1988, *Astrophys. J.* **325**, 442.

Withbroe, G. L. and Noyes, R.: 1977, *ARA&A* **15**, 363.

Yoshida, T. and Tsuneta, S.: 1995, *Astrophys. J.* **459**, 342.

V.2 Comparaison UV/Radio

Afin de mieux comprendre les structures coronales et leurs évolutions, nous avons corrélé les observations du radiotélescope de Metsähovi avec les images de SOHO/EIT.
Le premier article a été publie dans le NRO Report.
Le second article vient d'être soumis a A&A Supp.

- **Radio Bright Structures near the Solar Poles at Millimeter Wavelengths**
- by Pohjolainen S., Portier-Fozzani F., Ragaigne D.
- Accepted by NRO (Dec 1998)

Les structures coronales observées en radio à hautes fréquences sont comparées à celles observées par SOHO/EIT.

Radio Bright Structures near the Solar Poles at Millimeter Wavelengths

Silja Pohjolainen,[1,2] Fabrice Portier-Fozzani, [3] and Delphine Ragaigne[4]

[1] *DASOP, Observatoire de Paris, Meudon, France*
[2] *Metsähovi Radio Observatory, Kylmälä, Finland*
E-mail: Silja.Pohjolainen@hut.fi
[3] *Equipe SOHO/EIT, Laboratoire d'Astronomie Spatiale, Marseille, France*
E-mail: fpf@astrsp-mrs.fr
[4] *DEA, Observatoire de Paris, Meudon, France*

Abstract

Polar radio brightenings have previously been observed in the wavelength range 15-48 GHz, but at higher frequencies the observations have not been so clear: besides local brightenings, also depressions and uniform brightness areas have been reported. In this study high frequency solar radio maps, observed at 87 GHz (3.5 mm) at the Metsähovi Radio Observatory, were analysed and compared with the SOHO/EIT EUV-images. The data consisted of nearly simultaneous radio and EIT maps observed during 1996 and 1997. Some radio enhancements were found to have polar plume bases, but most often the polar radio brightenings corresponded to coronal hole-like structures and bright diffuse sources seen in the EIT images. The radio depressions near the solar poles corresponded well with mini-coronal holes and coronal holes seen in EUV. However, only a few of the many – and sometimes large – low density regions seen in EUV were seen as depressions at millimeter waves. Therefore the conception of coronal hole brightenings can be extended to higher frequencies.

Key words: Sun: quiet — Sun: corona — Radio: Sun — EUV: Sun

1. Introduction

Radio brightenings near the solar poles were first analysed in the 1970's, after polar-cap brightenings had been observed at 13.5 and 8 mm with the Crimean 22-m telescope, see review in Kosugi et al. (1986). It has since become a well established fact that between 15 and 48 GHz the poles of the Sun seem brighter than the rest of the quiet Sun. At frequencies less than 15 GHz dark features are observed, probably due to the deficit of coronal material. At higher frequencies (from 85 to 105 GHz; the small frequency range is due to lack of observations and instruments available), uniform brightness as well as local brightenings and/or depressions have been reported.

Uniform brightness at microwaves and millimeter waves could be explained by similar chromospheric structure, as the emission has its origin deeper down in the solar atmosphere, in the upper chromosphere. However, when discussing polar brightenings one should bear in mind that they are based on a large variety of observations, ranging from very high latitude polar cap brightenings to individual 'polar sources' seen anywhere from about 40 degrees up to the poles. The polar cap brightenings have been connected with atmospheric structure (Hiei 1987) and observed or predicted limb brightening (Hiei 1987; Shibasaki 1997). The polar sources with enhanced radio emission have been connected with coronal hole brightenings (Brajša et al. 1996; Gary et al. 1997; Gopalswamy et al. 1997,1998) that could be caused by network features and unipolar magnetic fields (Kosugi et al. 1986; Gopalswamy et al. 1998), faculae (Riehokainen et al. 1998), plumes (Gopalswamy et al. 1992), and possibly even with the formation of fast solar wind (Gary et al. 1997; Gopalswamy et al. 1998).

Solar maps at millimeter wavelengths are rather rare: the Nobeyama 45-m telescope has sometimes been used for solar mapping at high frequencies (98 GHz - see Kosugi et al. 1986), the Nobeyama Radioheliograph works daily at 17 and 34 GHz, and the Metsähovi 14-m telescope is used for solar observations at intervals (within the antenna allocation schedules, see e.g. http://kurp-www.hut.fi/current/ant-schedule.shtml) at 37 and 87 GHz. After the Metsähovi antenna upgrade in 1992-1994, with the improvement of surface accuracy and adjustments made to the

Wavelength	Frequency	Temperature	Observation
3.5 mm	87 GHz	7200 K	upper chromosphere/corona

Wavelength	Ion	Temperature	Observation
304 Å	He II	8.0×10^4 K	chromospheric network
171 Å	Fe IX,X	1.3×10^6 K	transition region
195 Å	Fe XII	1.6×10^6 K	quiet corona
284 Å	Fe XV	2.0×10^6 K	active regions

Table 1.. Radio observations and EIT bandpasses

85-115 GHz tunable receiver, the millimeter wave solar radio maps have created growing interest. The possibility of comparing the data with the SOHO EIT-instrument made our data set start from April 1996.

2. Observations

2.1. Radio observations

The 14-m single dish antenna at Metsähovi gives 1.0 arc min spatial resolution (HPBW) at 87 GHz. The antenna was upgraded in 1992-1994, which made it better for high frequency observations. The maps are made by scanning the Sun in right ascension, by changing declination between scans. Fairly good temporal resolution is obtained by making "fast maps", i.e., the full solar disk is scanned in 9 minutes, see e.g. Urpo et al. (1997). The flux resolution in this study was estimated by using nearby tracking data. Track files are made by pointing the beam to a selected region on the solar disk and by measuring the flux density. The sampling rate in this mode is 20 samples per second. The noise level was determined from active region track files, which should give the maximum noise level as fluctuations in the active region itself are included. An alternative would be to track the sky and determine the noise level from there, but this is not a routine procedure during the observations. With this error analysis the flux resolution in the radio maps was determined to be between 0.3% and 0.5% of the quiet Sun flux, depending on the observing run in question. The variation is most probably instrumental and depends on the set-up at the given time. No absolute flux calibration is done during the Metsähovi observations, but the quiet Sun brightness temperature has previously been estimated (see e.g. Pohjolainen and Urpo, 1997) to be around 7200 K at 87 GHz, giving a brightness temperature resolution of 22—36 K for this study.

The solar maps that were analysed are "raw" maps, i.e., without any deconvolution methods applied. Because the beam is not sharp but more like a broad Gaussian with wings (sidelobes), an artificial limb darkening and an artificial sky brightening are observed near the true edge of the solar disk, see Lindsey and Roellig (1991). Because of the tilt in the solar B_0 angle we are still able to see up to 70 degrees towards the solar poles (at central meridian), but the view depends on the time of the year. For the near-limb sources to show up, deconvolution methods would be needed. We analysed here only those brightenings and depressions that were well outside this effect (i.e. well inside the solar disk). The exact shapes of these sources are still ambiguous without further knowledge of the beam profile, but on the other hand deconvolution can sometimes overestimate/underestimate the excess brightness temperatures.

Quiet Sun radio emission at 87 GHz (3.5 mm) originates from chromospheric heights – from a brightness temperature of about 7200 K – and it is mostly due to thermal bremsstrahlung. However, radio emission can be produced at greater heights if the plasma density and temperature are high enough in e.g., coronal loops. Also non-thermal emission mechanisms may be present.

2.2. EUV observations

The Extreme Ultraviolet Imaging Telescope (EIT) onboard the *SOHO* spacecraft images the corona in four EUV wavelengths with a pixel resolution of 2.6 arcsec (Delaboudinière et al. 1996). From EUV lines – which represent different ion transitions – the chromosphere (He II), transition region (Fe IX/X) and corona (Fe XII, Fe XV) are imaged, see Table 1. Temperature diagnostics are made by wavelength ratios (Neumark et al. 1997), and 3-D coronal structure evolution is studied by comparing filter images (Portier-Fozzani et al. 1996).

2.3. Selection of data

We went through the radio maps measured at Metsähovi at 87 GHz (3.5 mm) in 1996 and 1997, and selected the ones that had close in time observations at one of the EUV wavelengths. In this way radio and EIT maps from 9 days were selected: April 12, 1996 (radio map at 13:57-14:05 UT), April 15, 1996 (radio at 12:05-12:13 UT), August 9, 1996 (radio at 07:23-07:32 UT), August 13, 1996 (radio at 12:31-12:39 UT), August 14, 1996 (radio at 12:55-13:03 UT), May 20, 1997 (radio at 13:03-13:12 UT), August 8, 1997 (radio at 11:30-11:39 UT), August 27, 1997 (radio at 12:13-12:22 UT), and August 28, 1997 (radio at 07:16-07:24 UT). The EIT Fe IX/X filter (171 Å) was mainly used to compare structures, as it is an intermediate temperature that shows well narrow shapes like loops. A lot more radio maps are available when nearness in time is not a requirement. In our position measurements the maximum time difference between a radio and an EUV map was 1.5 hours, but in that case more close-in-time observations were available at one of the other three EUV wavelengths.

In comparing features in radio and EUV one should be aware of the fact that the spatial resolution with a 14-m telescope at 87 GHz is rather poor, about 1 arcmin. This means that the true brightness is convolved with the beam, and therefore the given radio coordinates can be off the real source if the true brightness has complicated distribution within the beam. Also, a small bright point is not necessarily detected due to the dilution effect of the large radio beam. If sources looking similar in EUV are not both detected in radio, one must look for differences in temperature and/or density.

3. Observed features in millimetric radio and EUV

In the millimetric radio maps both radio brightenings and depressions could be seen. The radio brightenings were typically 0.5–1.5% (±0.3...0.5%) above the quiet Sun level (35–110 K if the quiet Sun is at 7200 K). The radio depressions were 0.5–2.0% below the quiet Sun level (corresponding to 35–145 K if quiet Sun at 7200 K). Sometimes diffuse brightness temperature enhancements (no peaks) were lying near the poles. With the articifial limb darkening effect we were not able to see further than 70 degrees towards the poles, at 0 longitude.

From the EIT images we were able to classify areas of different nature, mainly coronal holes, mini-coronal holes (small less dense regions), active regions, bright points, polar plumes, and diffuse structures that are generally thought to be non-resolved in the images.

As an example, a radio map from August 13th, 1996 and the corresponding SOHO EIT FeIX/X image are presented in Figure 1. The radio enhancements 2N and 3N near the solar north pole are clearly correlated to polar plumes in the EIT image, but for 1N the corresponding area could also be a bright point or an active region. The source 4N is a radio brightening, and 5N is a radio depression, that are located at coronal hole borders. In the southern hemisphere 1S and 2S are most probably active regions. The brightenings 3S and 4S, as well as the depression 6S, are connected to mini-coronal holes. The brightening 5S and the depression 7S are connected to bright diffuse sources.

To measure the uncertainties of position due to the different resolutions, we plotted the EIT image with resolution degraded to radio resolution (Figure 1). This confirmed that in some cases there is structural mixing and that the true locations of bright sources can be located nearby the peak intensities seen in the degraded image.

The temperature map derived from the EIT map on August 14, 1996 shows hot points and structures, presented in Figure 2. The radio map from the same day shows that some of the radio features are not only temperature dependent, but may be caused by density enhancements at lower/higher atmospheric heights (Figure 3).

4. Summary of statistical results

In the 9 radio maps observed at 87 GHz (3 mm) altogether 99 locations of radio features were determined. Of these 81 were brightness temperature enhancements and 18 were radio depressions (brightness below quiet Sun level). For 36 locations of brightness enhancement more than one EUV feature could be the counterpart. For the 45 radio bright locations where only one EUV feature could be identified within the radio beam area, the number of counterparts for the radio brightenings were the following:

- Active regions (9/45)
- Plume or plumes (3/45)
- Diffuse bright structures (11/45)

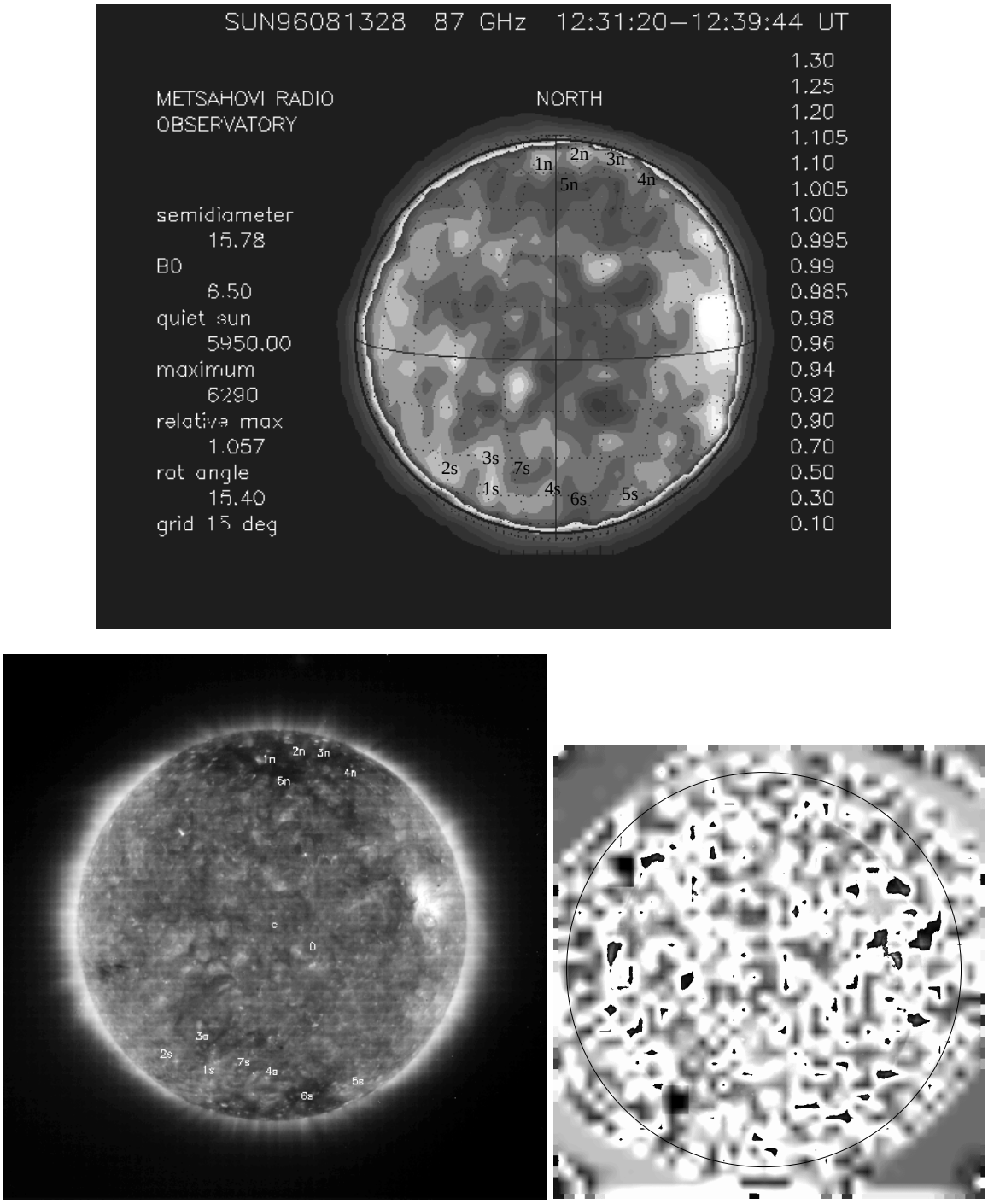

Fig. 1.. Metsähovi solar radio map at 87 GHz (3.5 mm) from August 13th, 1996, at 12:31-12:39 UT (**top**), and SOHO/EIT Fe IX/X from August 13th, 1996, at 12:30:13 UT (**bottom left**). The correlated features are marked by numbers 1n...5n (northern hemisphere) and 1s...7s (southern hemisphere). See text for more detailed explanations on the sources. In **bottom right** is the EIT image with resolution degraded to radio resolution. The method was to do a mean average of the 2.6×2.6 arcsec^2 EIT pixels over 1×1 arcmin^2 radio resolution. A consequence of the method is a small dilatation, as is usual in that kind of imaging. The circle plotted over the image represents the new averaged limb position.

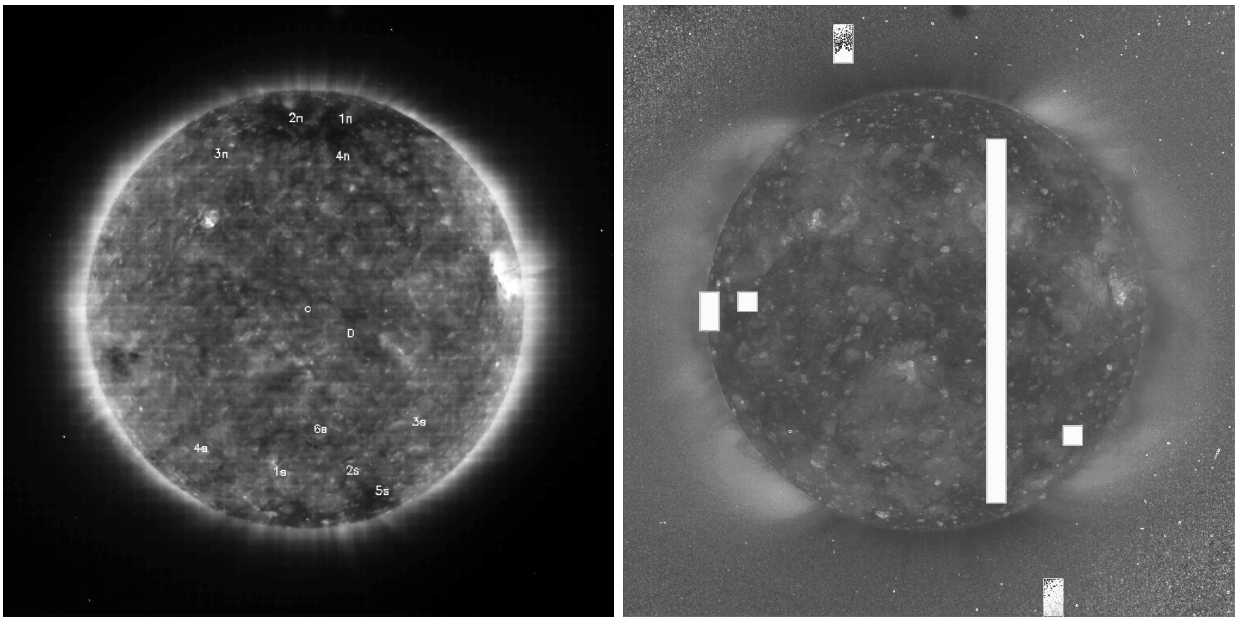

Fig. 2.. SOHO/EIT Fe IX/X image at 12:30 UT on August 14, 1996 (**left**). Temperatures derived from SOHO/EIT for August 14th, 1996 (between 0.8 – in black – and 1.6 MK – in white – except for the missing block due to low telemetry at that time) (**right**).

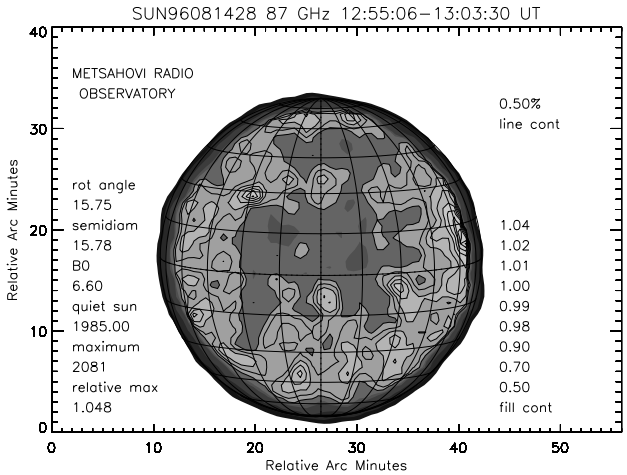

Fig. 3.. Metsähovi 87 GHz radio map at 12:55-13:03 UT on August 14th, 1996. The radio enhancements near the north pole were determined to have polar plume bases.

- Mini-coronal holes (13/45)
- Coronal holes (9/45)

The observed radio depressions (18 altogether) corresponded to:

- Mini-coronal holes (9/18)
- Coronal holes (2/18)
- Bright diffuse sources (2/18)
- A mixture of coronal hole/mini-coronal hole/border of coronal hole (5/18)

So the coronal holes seen in the EIT images corresponded to:

- Radio depressions (2)
- Radio enhancements (9),

and the EIT mini-coronal holes corresponded to:

- Radio depressions (9)
- Radio enhancements (13).

5. Discussion

We found that the millimeter wave radio depressions are very well correlated to coronal holes and other smaller less dense regions seen in EUV. We checked the locations of the radio depressions to see if there were any filaments present, but none were found – H_α dark filaments are known to cause radio depressions at mm-waves, see e.g. Vršnak et al., 1992. Low temperature filament plasma in the corona could also give signatures in the EUV emission, but we did not study this further.

Not all coronal holes or less dense regions looked as depressions in radio. In fact, the 'coronal hole brightening' can be stretched into millimeter waves by saying that some coronal holes look bright in radio and some not. This is in agreement with Gopalswamy et al. (1998), who suggest that only when enhanced magnetic flux is present in a predominantly unipolar region can radio enhancement (at microwaves) be seen. The SOHO EIT images analysed in this study did not show any features that could cause the brightenings at millimeter waves, but the magnetograms for these days are still to be analysed. Also the structures of polar plumes have to be studied in more detail, taking into account the possible differences (observed density, temperature) from line of sight variations.

The analysis presented here is in progress, and will be presented in a later paper. The analysis also has to take into account a possible selection effect because the radio features were selected first from the maps. Next step will be to reanalyse the data set by selecting the EIT features first. The difference of resolution between the two instruments is rather large, and by making an EIT image with the radio resolution we concluded that some artefact could be the result of structural mixing.

Acknowledgements Part of this work was done at Metsähovi Radio Observatory, during D. Ragaigne's training period. S. Pohjolainen is supported by the Academy of Finland Contract No. 42576. SOHO/EIT was build by an international consortium involving ESA and NASA, under the supervision of J.P. Delaboudinière (PI). F. Portier-Fozzani was supported in his work also by private foundations.

References

Brajša R., Pohjolainen S., Ruždjak V., Sakurai T., Urpo S., Vršnak B., Wöhl H. 1996, Sol. Phys. 163, 79
Delaboudinière J.-P. et al. 1996, Sol. Phys. 162, 291
Gary D.E., Enome S., Shibasaki K., Gurman J.B., Shine R.A. 1997, Bull. Am. Astron. Soc. 29, 8.01
Gopalswamy N., Schmahl E.J., Kundu M.R. 1992, Proc. First SOHO Workshop: Coronal Streamers, Coronal Loops, and Coronal and Solar Wind Composition, 113
Gopalswamy N., Shibasaki K., Thompson B.J., Gurman J., DeForest C. 1998, JGR, in press
Gopalswamy N., Thompson B.J., Shibasaki K. 1997, in K.S. Balasubramaniam, J. Harvey, and D. Rabin (eds.) Synoptic Solar Physics, ASP Conf. Ser. 140, 401
Hiei E. 1987, Publ. Astron. Soc. Japan 39, 937
Kosugi T., Ishiguro M., and Shibasaki K. 1986, Publ. Astron. Soc. Japan 38, 1
Lindsey C.A., Roellig T.L. 1991, ApJ 375, 414
Neumark J. et al. 1997, Am. Astron. Soc. Meeting 191, 73.07
Pohjolainen S., Urpo S. 1997, Fifth SOHO Workshop ESA SP-404, 619
Portier-Fozzani F., et al. 1996, PASP Conf. Ser. 111, 402
Riehokainen A., Urpo S., Valtaoja E. 1998, A&A 333, 741
Shibasaki K. 1997, in K.S. Balasubramaniam, J. Harvey, and D. Rabin (eds.) Synoptic Solar Physics, ASP Conf. Ser. 140, 373
Urpo S., Pohjolainen S., Heikkilä J., Wiik K. 1997, Solar Observations at Metsähovi in 1994-1995, Helsinki Univ. of Tech., Metsähovi Radio Res. Stat. Rep. 26
Vršnak B., Pohjolainen S., Urpo S., Teräsranta H., Brajša R., Ruždjak V., Mouradian Z., Jurač S. 1992, Solar Physics 137, 67

- **Comparison of 87 GHz solar polar structures with EUV emission**
- by Pohjolainen S.,Portier-Fozzani F., Ragaigne D.
- Submitted to A&A Sup. Ser. (Mai 1999)

La comparaison des observations radio à hautes fréquences avec celles de SOHO/EIT pose le probleme de la redéfinition de certains objets analysés.

ASTRONOMY & ASTROPHYSICS
SUPPLEMENT SERIES

Astron. Astrophys. Suppl. Ser. **143**, 227-263 (2000)

Comparison of 87 GHz solar polar structures with EUV and soft X-ray emission

S. Pohjolainen[1,2], **F. Portier-Fozzani**[3], **and D. Ragaigne**[4]

[1] DASOP, Observatoire de Paris, Meudon, France
[2] Metsähovi Radio Observatory, Helsinki Univ. of Technology, Espoo, Finland
[3] Equipe SOHO/EIT, Laboratoire d'Astronomie Spatiale, LAS-CNRS, Marseille, France
[4] DEA, Observatoire de Paris, Meudon, France

Received April 21, 1999; accepted January 21, 2000

Abstract. Polar radio brightenings at 87 GHz (3.5 mm) are compared for the first time with features seen in EUV and soft X-rays. The data consist of nearly simultaneous full disk images and maps from Metsähovi Radio Observatory, SOHO/EIT, and Yohkoh/SXT on 9 selected days near the solar minimum (1996-1997).

The observed radio brightenings corresponded to various features seen in EUV, such as diffuse or localized intensity enhancements (e.g., bright points and bases of polar plumes), and intensity depressions of varying sizes (e.g., coronal holes). Some of these features were also visible in soft X-rays. The visibility of radio bright coronal holes seemed to depend on how much of the polar area was exposed, due to the variation of the B_0-angle.

The observed radio depressions near the solar poles were very well correlated with coronal holes and other EUV and/or soft X-ray intensity drops. More than half of the coronal holes, or coronal hole-like intensity drops in EUV and soft X-rays, had radio brightenings inside them. Therefore coronal holes do not have uniform radio brightness at 87 GHz.

Many of the bright points seen at lower latitudes in the EIT and SXT images had no, or just faint, counterparts in the millimeter radio maps. It appears that for an EUV bright point to show up at 87 GHz it has to be bright and/or spatially large also in soft X-rays.

Key words: Sun: chromosphere — Sun: transition region — Sun: corona — Sun: radio radiation — Sun: UV radiation — Sun: X-rays

Send offprint requests to: S. Pohjolainen,
e-mail: pohjola@mesopy.obspm.fr

1. Introduction

Polar-cap brightenings in solar radio maps were first discovered in the 1970's (Babin et al. 1976; Efanov et al. 1980a, 1980b). Subsequently several studies were done using cm- and mm-wavelength data from, e.g., the Nobeyama 45-m telescope, the Nobeyama Radioheliograph, and the Metsähovi 14-m telescope. It has been claimed that the brightenings are restricted to a certain wavelength range, from 15 to 48 GHz (Gary et al. 1997), but the upper limit may simply be due to the lack of good quality observations at higher frequencies. Below 15 GHz the solar poles have been observed to appear darker, but at frequencies higher than 48 GHz both uniform brightness and local depressions have been observed (Gary et al. 1997; Kosugi et al. 1986), as well as the above mentioned brightenings (later paper by Moiseev & Nesterov 1987).

The studies of polar brightenings and depressions have included a variety of observed features, ranging from high-latitude polar-cap brightenings to any features observed above about 40 deg latitude. Also the appearance of coronal holes is very important in polar regions. Along with the question whether polar brightenings do appear at high frequencies (shorter than 6 mm), a puzzle exists on the origin of the brightenings: are they associated with limb brightening (Shibasaki 1997), coronal holes (Brajša et al. 1996), faculae (Riehokainen et al. 1998), magnetic features (Kosugi et al. 1986; Gopalswamy et al. 1999), atmospheric structures (Hiei 1987), polar plumes (Gopalswamy et al. 1992), or something else?

The starting point of this study was the fact that for the first time at 87 GHz (3.5 mm), the solar radio maps observed with the upgraded Metsähovi Radio Observatory 14-m telescope showed polar brightenings and depressions. We present here an analysis of data from 9 separate days

observed near the solar minimum (1996-1997), with good imaging capabilities at 87 GHz.

2. Observations

2.1. Metsähovi observations

The Metsähovi radio telescope was upgraded in 1992-1994, and at present the surface accuracy is 0.1 mm (rms). The 14-meter antenna gives 1.0 arcmin spatial resolution (i.e. HPBW beam size) at 87 GHz (3.5 mm). The maps are made by scanning the Sun in right ascension, by changing declination between the scans. The full solar disk is scanned in 9 minutes in the "fast map" mode, which makes 29 scans, 91 samples each. The flux resolution for this study was estimated from nearby active region track files. Track files are made by pointing the beam to a selected region on the solar disk and by measuring the flux density (sampling rate 20 samples/s). By using active region track files we get a maximum amount of noise fluctuations, as fluctuations from the active region itself are included. Large noise levels can therefore be the result of very active regions on the disk. A large noise level can affect the quality of the map (i.e., the dynamic range). An example of a low-quality radio map is in Fig. 8, from May 20, 1997. The variation in this case is most probably instrumental, and depends on the set-up. Set-ups may be changed between the days or between the observing runs. In the analysed radio maps the flux resolution varied from 0.3% to 0.5% of the quiet Sun flux, depending on the observing run in question.

No absolute flux calibration is done during the Metsähovi solar observations, but the quiet Sun brightness temperature has previously been estimated to be around 7200 K at 87 GHz (see Pohjolainen & Urpo, 1997), giving a brightness temperature resolution of $22 - 36$ K for this study. The observed flux density, which is directly related to brightness temperature, is expressed in the tables as a percentage of the quiet Sun level, which is determined from the A/D converter counts. For example, on April 12, 1996 the quiet Sun level was estimated to be at 7240.0 A/D count units, which is equivalent to the estimated 7200 K brightness temperature. A bright area showing a 1.009 relative intensity is therefore 0.9% above the quiet Sun level, i.e., is showing a brightness enhancement of 64.8 K.

The solar maps that are presented here are the "raw" maps, without any deconvolution methods applied. Because the beam is not sharp but more like a broad Gaussian with wings (sidelobes), an artificial limb darkening and an artificial sky brightening are observed near the true edge of the solar disk (see Lindsey & Roellig 1991). The effect can be seen as the dark ring in the 87 GHz radio maps inside the circle which marks the optical solar limb, and as additional emission outside the solar limb. We analyse here only those brightenings and depressions that were well outside this effect (i.e. well inside the solar disk). The artificial limb darkening makes it impossible to see the features as high as the polar caps, but because of the changing B_0 angle, features up to 70 deg in latitude (at 0 longitude) can be discerned.

Table 1. EIT bandpasses for the observations

Wavelength	Ion	Temperature
304 Å	He II	8.0 10^4 K
171 Å	Fe IX, X	1.3 10^6 K
195 Å	Fe XII	1.6 10^6 K
284 Å	Fe XV	2.0 10^6 K

2.2. SOHO-EIT observations

The Extreme Ultraviolet Imaging Telescope (EIT) onboard the *SOHO* spacecraft, images the corona in four EUV wavelengths (Delaboudiniere et al. 1996). From EUV lines – which represent different ion transitions – the chromosphere (He II), the transition region (Fe IX/X) and the corona (Fe XII, Fe XV) are imaged, see Table 1. Temperature diagnostics are made by wavelength ratios (Neumark et al. 1997), and 3-D coronal structure evolution is studied by comparing filter images (Portier-Fozzani et al. 1996).

The selected four EIT images per day – observed as close as possible to the radio observations – were taken with filter Clear or Al+1. The EIT pixel resolution is 2.6 arcsec. The full Sun images were either 1024×1024 (full resolution, denoted "F" in Table 2) or 512×512 (half resolution, denoted "H" in Table 2).

The EIT images were calibrated using the usual software methods described in Moses et al. (1997). To remove the shadow of the tiny grid that supports an aluminium filter standing in front of the CCD camera, included in all EIT images, smooth filtering using a local median filter was preferred (Portier-Fozzani et al. 1996). More details concerning the EIT calibration and in flight use can be found in Moses et al. (1997), Newmark et al. (1997), Defise (1999), and Portier-Fozzani (1999).

2.3. Yohkoh SXT observations

The Soft X-ray Telescope (SXT) onboard the Yohkoh satellite observes the solar corona through several different filters (Tsuneta et al. 1991). The broad-band instrument is sensitive over a range of energies between 0.25 and 4 keV. The corresponding coronal temperatures are in the range of $2 - 20$ MK. In the case of the quiet solar corona, the temperatures are at the lower end of this scale.

We used SXT full frame images, taken with the AlMg and Al.1 filters near the times of the radio observations,

with the longest available exposure times, in order to get the faint features visible. The full frame SXT images were observed either in Half resolution (denoted "H" in Table 2) with 4.9 arcsec pixel size, or in Quarter resolution (denoted "Q" in Table 2) with 9.8 arcsec pixel size. The exposure times varied between 0.6 s (August 13, 1996) and 30.2 s (April 12, 1996). The SXT images were corrected for dark noise and particle hits.

2.4. Other wavelength data

As it is well known than H_α dark filaments can cause radio depressions (Vršnak et al. 1992), we checked from the H_α images in the Web (http://sohodb.nascom.nasa.gov/cgi-bin/synop_query_form) that no filaments were present where we had radio depressions. Therefore the radio depressions analysed in this study must be caused by some other mechanism than an overlaying absorbing dark filament.

Coronal holes and their borders are sometimes difficult to define. We used also other wavelength data from the Web, when available, to check the locations under study. Especially He I (10830 Å) images were useful for this purpose.

2.5. Selection of data and error analysis

We went through the radio maps measured at Metsähovi at 87 GHz (3.5 mm) in 1996 and 1997, and selected the ones that had close-in-time observations at least with one of the EUV wavelengths, observed by the EIT. In this way 9 radio maps from 9 days were selected, see Table 2. A lot more radio maps are available if nearness in time is not a requirement.

All four EIT wavelengths were then analysed, to confirm the structural classification in EUV. In the analysis the maximum time difference between a radio and an EUV map was 1.5 hours, but in that case more close-in-time observations were available at the other three EUV wavelengths, and we checked that the observed features were consistent. SXT maps were selected on the basis of being taken as near as possible to the selected radio and EUV maps, and with the longest available exposure times.

The tops and the bottoms of the selected radio brightenings and depressions, respectively, were given heliographic coordinates. The positions (latitude, longitude) and intensities (relative to the quiet Sun level) for altogether 104 radio sources are given in Tables 3–11, for each of the days separately. In the tables, EIT and SXT structures are defined for the radio locations and their surrounding area.

In comparing the features in radio and in EUV one should be aware of the fact that the spatial resolution at 87 GHz is rather poor, about 1 arcmin (HPBW). Radio emission sources that are located within the 1 arcmin beam area will be convolved, and this means that the true peak brightness can be "off" the given coordinates. The scanning technique poses problems as well: pointing errors are common when using heavy antennas at high speed. To overcome the "off" pointing, all features within the 1 arcmin beam were classified and listed.

The Metsähovi scan map method was originally developed for 37 GHz, with a much larger beam size. At 87 GHz the beam size is smaller than the separation between scans, 1.2 arcmin. This can mean missing some flux, if a very small point source is located just in between the scan paths. However, the non-symmetrical main beam and strong sidelobes usually reduce this problem. Atmospheric changes between separate scans can also cause defects, which are usually seen as the sawed edge of the solar limb.

Another, a much larger error, comes from the determination of the center of the radio Sun. Due to the non-symmetrical beam and errors in scanning, the radio Sun is not a perfect circle, and the person making the data reduction is very much responsible for putting the center point to the "right" position. Our data set was analysed separately by two different people, and the maximum difference in coordinate determination was 10 degrees in heliographic longitude, which was caused by moving the center point in an East-West direction. However, this kind of difference in coordinates was extremely rare.

Also, a small bright point in a cool dense region will be diluted in a large radio beam, and will not necessarily show up. If sources looking similar in EUV are not both detected in radio, one must look for differences in temperature and/or density. The basics of radio emission and antenna beams can be found in, e.g., Dulk (1985) and Pohjolainen (1996). To explore the effects of the different resolutions of the two instruments, a test was made by plotting EIT images degraded into radio resolution. It was found that structural mixing was present in some cases, but also good fit to the radio images was found (Pohjolainen et al. 1999a).

3. Analysis and results

Nine solar radio maps, from 9 different days, observed in 1996–1997 were analysed for this study. The coordinates and fluxes of radio bright and depressed (relative to the quiet Sun level) areas near the polar zones were listed, as described in Sect. 2.5. Also some strong active regions at lower latitudes were given coordinates, mainly to check the accuracy of the radio coordinate determination.

The listed radio source locations were analysed in all EUV wavelengths, and all EUV features seen within the 1 arcmin radio beam were listed. The identification of EUV features was mainly based on coronal images (171/195/284 Å). The Fe IX/X line (171 Å) was usually checked first, and then compared with images at other

Table 2. Selected radio, EIT, and SXT maps for comparing polar structures

Date	87 GHz radio map UT	EIT map UT				SXT map UT	
		He II	Fe IX/X	Fe XII	Fe XV	AlMg	Al.1
Apr. 12, 1996	13 : 57 − 14 : 05	14:50(F)	14:28(F)	15:12(F)	14:06(F)	13:52(H), 14:23(Q)	13:55(H)
Apr. 15, 1996	12 : 05 − 12 : 13	13:12(F)	12:14(F)	12:20(F)	13:01(F)	11:18(H), 13:13(H)	
Aug. 09, 1996	07 : 23 − 07 : 32	07:40(H)	07:24(H)	07:34(H)	07:30(H)	07:00(H)	06:48(H)
Aug. 13, 1996	12 : 31 − 12 : 39	12:35(H)	12:30(H)	12:34(H)	12:32(H)	12:39(Q), 12:48(Q)	
Aug. 14, 1996	12 : 55 − 13 : 03	12:35(H)	12:30(H)	12:34(H)	12:32(H)	12:53(H)	12:39(H)
May 20, 1997	13 : 03 − 13 : 12	13:18(F)	13:00(F)	13:12(F)	13:06(F)	12:53(Q), 13:15(Q)	
Aug. 08, 1997	11 : 30 − 11 : 39	13:28(F)	13:10(F)	11:47(F)	13:16(F)	11:04(Q), 12:17(Q)	
Aug. 27, 1997	12 : 13 − 12 : 22	13:19(F)	13:01(F)	12:15(H)	13:07(F)	12:10(H), 12:55(H)	12:53(H), 13:08(H)
Aug. 28, 1997	07 : 16 − 07 : 24	07:18(F)	07:00(F)	07:12(F)	07:06(F)	07:06(H), 07:23(H)	07:04(H), 07:21(H)

wavelengths. The same procedure and listing was done with the soft X-ray images.

The classification of EUV and soft X-ray features was based on intensity, spatial scale, and general "lookout". We determined the quiet Sun level in each of the images, and the enhanced/reduced brightness was determined relative to this. One effect of this method was that very few of the analysed locations were determined to be "quiet Sun", as it was defined to be practically one intensity value. Also, as the radio beam area consists of 30 − 400 SXT or EIT pixels (depending on the observing mode), we did not try to give any "average" intensity value for the EUV/soft X-ray features.

With this method each radio location could have more than one possible counterpart in EUV and soft X-rays (indicated by "/" in Tables 3–11). The problem of multiple sources within the radio beam is clearly seen in the polar region EUV blow-up image, in Fig. 1. Tracking problems with radio antennas can sometimes cause displacements in the beam position, and therefore we also looked for strong emission sources nearby the assumed antenna beam position. The "nearby" features are also listed in Tables 3–11. The radio maps are presented in Figs. 2, 5, ... 26, the soft X-ray images in Figs. 3, 6, ... 27, and the EIT images in Figs. 4, 7, ... 28.

The quiet Sun radio emission at 87 GHz (3.5 mm) originates from chromospheric heights, and has an estimated brightness temperature of 7200 K. The emission is mostly due to thermal bremsstrahlung. However, radio emission can also be produced at greater heights if the plasma density and temperature are high enough in, e.g., coronal loops. Besides thermal emission, other emission mechanisms may also be present. There has been some discussion on possible synchrotron sources and plasma emission connected with coronal holes (e.g. Shevgaonkar et al. 1988).

In EUV coronal lines, the intensity is proportional to the emission measure, which is related to the temperature and the density. The iron lines are optically thin. With the iron lines different temperatures of the corona can be observed. The image appears darker where the temperature is lower (e.g., filament channels) or the density is smaller (e.g., coronal holes, where the plasma can escape along the open magnetic field lines). Fe XII is adapted to observe the "usual" corona, while Fe XV observes the more hot temperatures. Structures in Fe IX/X always appear with narrow shapes (such as loops). This transition region line is very important for the analysis, as it shows the evolution of the topology and the morphology at intermediate temperatures between the photosphere and the corona. The He II line at 304 Å is an optically thick line. This chromospheric line is mixed with a coronal Si IX line.

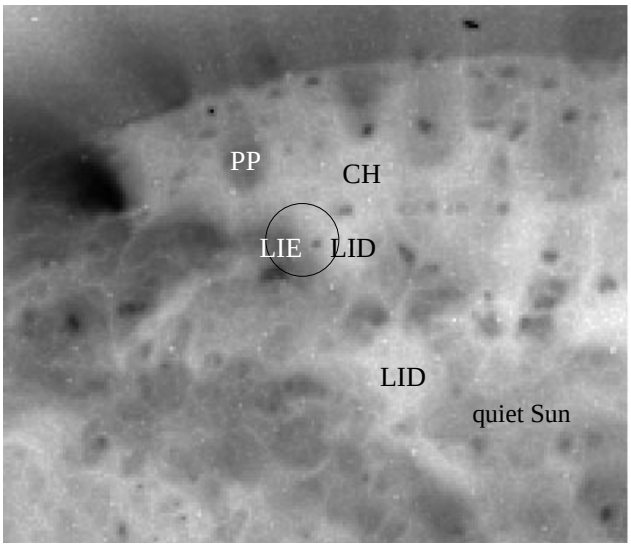

Fig. 1. Polar region on August 27, 1997, at 13:01:03 UT in Fe IX/X line (reversed colours). The cicle has 1 arcmin radius and shows the size of the radio beam. Depending on the location, there is a possibility of having several EUV structures within the beam. This location was classified as a local intensity enhancement (LIE, in dark colour), although it is nearby a local intensity decrease area (LID, in white colour). The contrast in the image has been enhanced, to show more clearly all the tiny EUV structures

The Yohkoh/SXT was mainly designed for observing flares and other transient phenomena. The quiet Sun

emission, with changing features but low count rates, is therefore more difficult to analyse. Some studies of polar coronal holes have been made with the SXT (see, e.g., Foley et al. 1997), but these have required longer than normal-mode exposure times and summing up of images over long periods. Coronal hole temperatures in soft X-rays have been found to be similar to the values for the nearby quiet corona, but with electron density values about 3 times lower (Hara et al. 1994). We did not do any temperature or emission measure analysis because of the long image intervals and low count rates in some of the individual images.

One should also note that no comparison of features was done between the EIT and the SXT images. We compared only radio and EUV, and radio and soft X-ray emission sources in the given solar coordinates, but within the radio beam. Since the radio resolution is so different from the two others, comparison of a single location in high resolution images might give different results.

Quiet Sun structures are usually considered to be very stable, and not change much in time. Polar plumes may stay the same for hours, and radio depressions and brightenings have been used for, e.g., determining the solar rotation rate at high latitudes. However, when comparing the radio and soft X-ray images we found that the borders of coronal holes can change their position within some tens of minutes. On April 12, 1996, at 13:52 UT the radio brightening 3S was situated in the coronal hole border area, near a soft X-ray brightening, but in the later SXT image at 14:23 UT the radio position had moved inside the coronal hole area. On August 9, 1996, the radio bright position 4N moved from coronal hole border area to a diffuse bright area within 12 minutes, and on August 8, 1997, positions 1N and 6N moved from the coronal hole border area to inside the coronal hole, within about an hour. Therefore one should be very careful in comparing coronal hole border areas when the time differences between images are larger than the order of tens of minutes.

3.1. Radio – EUV

The radio locations included 81 brightness peaks and 23 depression centers. For half of the radio locations (51/104) it was possible to determine a sole counterpart from the EIT images. For the rest of the cases two or possibly more different features were present within the estimated radio beam. We would have to know the temperatures and densities of each of these features to be able to determine how much they contributed to the radio emission.

The EUV regions listed in Tables 3–11 were classified as:

- AR = Active Region,
- BP = Bright Point,
- PP = Polar Plume (or a group of plumes),
- LIE = Localized Intensity Enhancement,
- LID = Localized Intensity Decrease,
- CH = Coronal Hole.

Active regions (AR) were classified with the help of NOAA active region listings from the Solar Geophysical Data. Also large EUV and radio bright regions with complex loop structure were classified as ARs, even if they were not listed by NOAA. These regions were much larger than bright points and much more intense than localized intensity enhancements (see below). The tops of the hot loops in ARs usually show thermal radio emission. During long duration events and flares, also footpoint brightening is observed at cm wavelengths (Hanaoka 1994).

Bright points (BP) are bright individual features sometimes seen in coronal holes. Bright points can also be seen over diffuse bright structures, all over the solar disk. The sizes of BPs are usually $10 - 50''$. Simultaneous EUV and soft X-ray observations have shown that the regions of peak emission are not always cospatial, suggesting a complex structure of small-scale loops, at different temperatures (Habbal et al. 1990). EUV and soft X-ray bright points have been found to be associated with magnetic bipolar regions, but cm-radio observations have shown some association between radio bright points and unipolar magnetic structures (Kundu et al. 1988). EUV bright points have not been studied much at radio wavelengths.

Polar plumes (PP) are bright individual features seen in polar coronal holes (DeForest et al. 1997), and sometimes in coronal holes that extend to equatorial heights (Allen et al. 1997). They can also appear in groups. The 3-D structures of polar plumes are very well seen with EIT. Polar plumes have not been detected previously at millimetric radio wavelengths. A study by Nindos et al. (1999) discovered centimeter radio emission arising between the plumes in polar regions.

Localized intensity enhancements (LIE) are brighter than the quiet Sun and less bright than ARs. They are also larger than BPs. They exist outside coronal holes and active regions, and include sometimes diffuse areas like the borders of coronal holes. Magnetograms for these areas give no definite polarities. The brighter features could be loop structures that are not seen due to the EIT spatial resolution. Temperatures given by EIT for these structures are between $1 - 1.6$ MK.

Localized intensity decreases (LID) are small – a few arcmin diameter – regions that are less bright than the quiet Sun. These small "holes" can be found all over the solar surface. The existence of small coronal holes has been suggested previously by Bohlin (1976).

Coronal holes (CH) are seen as dark regions in EUV and soft X-rays, and as bright regions in the He I absorption line. The density and/or temperature is usually lower than in the surrounding corona. There has been some debate on whether CHs can be identified as open field line areas (Obridko & Shelting 1999), but at least for statistical purposes this definition can be used. Coronal holes are usually seen as depressions at centimeter

wavelengths, but several studies have shown radio bright coronal holes (Gopalswamy et al. 1999; Brajša et al. 1996).

The radio brightness enhancements (81) correlated with the following EUV features: active regions (3), polar plumes (3), localized intensity enhancements (17), localized intensity decreases (12), coronal holes (9), and mixtures of features (37).

The radio depressions (23) correlated with the following EUV features: localized intensity enhancements(2), localized intensity decreases (13), coronal holes (2), and mixtures of features (6).

3.2. Radio – soft X-rays

The structures seen in the Yohkoh SXT images were listed similarly, but to avoid confusion between the EUV and soft X-ray features we named some of the soft X-ray features differently. Brightness enhancements and less bright regions in soft X-rays are usually spatially larger (reflecting also the instrument resolution) than in EUV, and therefore we dropped the term "localized". The soft X-ray features were listed as follows:

- AR (as in EUV),
- BP (as in EUV),
- enhanced brightness (above the quiet Sun brightness),
- reduced brightness (below the quiet Sun brightness),
- CH (as in EUV).

The radio brightness enhancements (81) correlated with the following soft X-ray structures: active regions (4), bright points (8), enhanced brightness (39), reduced brightness (5), coronal holes (16), and a mixture of features (9).

And the radio depressions (23) correlated with the following soft X-ray structures: enhanced brightness (2), reduced brightness (9), coronal holes (8), quiet Sun (3), and a mixture of structures (1).

4. Summary of comparisons

We have observed polar brightenings at 87 GHz (3.5 mm wavelength), with a typical $0.5-1.5\%$ brightness enhancement over the quiet Sun. Taking an average quiet Sun brightness temperature of 7200 K at 87 GHz, we get brightness enhancements in the scale of $35-110$ K. In comparison, the active regions observed at $20-30$ degrees in latitude in the same solar maps showed $1-4\%$ brightness enhancements.

Radio brightenings were found to correlate with several different types of structures seen in EUV (see Sect. 3 for the exact numbers).

- Localized intensity enhancements (LIE – 17 locations): At 87 GHz, they often showed a brightness enhancement of about 1%. The borders of coronal holes often show diffuse emission, as the open field line areas change into a border of closed lines.
- Localized intensity decreases (LID – 12 locations): Surprisingly many of the radio enhancement peaks were located inside the small less bright regions. The corresponding radio brightenings varied in intensity, between 0.2% and 2.4%. However, these EUV reduced brightness areas usually had very small spatial size, and were often surrounded by diffuse matter or small bright areas that could contribute to the radio flux, so the connection can be ambiguous.
- Coronal holes (CH – 9 locations): In our study the radio brightenings for coronal holes were between 0.4% and 2.3%. Radio brightenings inside coronal holes were linked with the changes in B_0 angle: when more of the polar regions and coronal holes were visible, the clearer were the radio brightenings inside them. On April 12, 1996, on April 15, 1996 (see Figs. 29 and 30 for close-ups), and on May 20, 1997, radio bright regions were located inside the southern CHs, and on August 9, 1996, and on August 8, 27, and 28 the radio bright regions were detected in the northern CHs.
- Polar plumes (PP – 3 locations): The radio enhancements for the three locations that corresponded to plumes were 1.0% (location 3N on August 13, 1996), 1.4% (location 2N on August 13, 1996), and 1.5% (location 2N on August 14, 1996). The fact that plumes are inside coronal holes, which are cool and less dense, and that the plumes may not fill the whole radio beam area and may be diluted within the beam, make this radio signature even more significant.
- Active regions (AR – 3 locations): The tops of the loops in EUV were seen as radio brightenings, as expected. Active region loops showed higher brightness temperature in radio $(3.6-4.0\%)$ than, e.g., the plumes.
- Bright points (BP – no definite detections): Three radio bright polar locations could be correlated to EUV bright points, with the help of soft X-ray images (EUV-only analysis classified them as mixed features). These were location 2S on August 9, 1996 (2.1% enhancement), location 1N on August 13, 1996 (1.3% enhancement), and 1S on August 14, 1996 (2.1% enhancement). Yohkoh SXT also showed 4 bright points that were not classified as those in EUV, on April 12, 1996 (locations 3N with 0.6% and 4N with 0.4% radio enhancements), on August 9, 1996 (location 2S with 2.1% radio enhancement), and on May 20, 1997 (location 3S with 0.6% radio enhancement).

Radio depressions (23 altogether) at 87 GHz showed $0.5-2.0\%$ ($35-145$ K) brightness drops, and were clearly correlated with coronal holes, localized intensity decreases, coronal hole borders seen as intensity enhancements, or a combination of these three features in EUV. The soft X-ray images confirmed the correlation: of the 23 radio depressions 17 were located within coronal holes or reduced brightness regions. And further, if we look at the

classifications in both EUV and soft X-rays, only one location (7S, on August 13, 1996) was not connected to coronal holes. Therefore we can say that radio depressions in 3.5 mm are connected to the coronal hole phenomenon.

However, this is not so in the reverse situation: coronal holes and local less bright regions seen in EUV, and in soft X-rays, were often seen as brightenings at 87 GHz. This study showed 15 radio depressions vs. 22 radio brightenings for coronal hole-like EUV sources, and 17 radio depressions vs. 21 radio brightenings for coronal hole-like soft X-ray sources.

X-ray bright points have previously been detected at cm-wavelengths, using observations made with the Nobeyama Radioheliograph and the VLA (Nitta et al. 1992; Kundu et al. 1994). We now report detection of bright points also at 3.5 mm wavelength. A few radio brightenings correlated with bright points that were strong both in EUV and soft X-rays. Besides the 3 that were reported earlier, there were some found at lower latitudes: location S22W06 on August 9, 1996, and location N35E33 on August 13, 1996.

However, many of the bright points seen on the solar disk in the EIT and SXT images had no, or just very faint, counterparts in millimeter waves. By looking at some low latitude bright points we were able to conclude that even if the bright points were strong in EUV, they would not show up in millimeter radio if they were not strong enough (N56E30 on August 9, 1996), or spatially large enough (S42W26 and S57E24 on April 15, 1996 – see Figs. 29 and 30), in soft X-rays.

Also, if the bright points lie inside coronal holes instead of bright diffuse sources, their radio flux will be diminished (N16W17 and S30E33 on April 12, 1996). There were also cases where no obvious reason could be found for why some bright points showed up in radio (S27W13 and S30W30 on August 28, 1997) and some did not (S15W13 on the same day), see Fig. 31.

5. Discussion

Quiet Sun radio emission at 87 GHz originates from the upper chromosphere, as free-free emission from a plasma at a temperature of about 7200 K. Thermal radio emission corresponds to the density and temperature of plasma, and the source height for radio emission can only be determined if the source is located over the limb. Also, radio brightening can be suppressed by cool dense material high in the corona, as is the case for the locations of H_α dark filaments.

In our study a large number of coronal holes appeared as brightness enhancements in radio. However, many coronal holes appeared also radio depressed. Therefore coronal holes in general cannot be defined as radio bright at 87 GHz. Many of the localized intensity decreases (LIDs) seen in EUV also appeared radio bright – but not all of them. In many cases structural mixing was present, i.e., more than one EUV feature appeared within the radio beam. In some of the EIT maps it was possible to see a patchwork of small "holes", and the radio enhancement peaks were located inside them. The observed diffuse bright soft X-ray emission over the EUV LIDs could be explained by hot coronal material, or by time differences in the observations, or by projection effects that could change the soft X-ray source positions.

Thermal radio emission is enhanced with growing density and/or temperature, and can be formed at any height in the solar atmosphere above the critical plasma density level. Therefore local dense and relatively hot (but cooler than needed for EUV lines), or less dense and very hot (possible to see in soft X-rays) regions would show out as radio brightenings. In our data a few locations were seen as dark coronal holes in the hot Fe lines, but when viewed in the chromospheric He II line, small local brightenings were found. Some of the coronal hole radio brightenings could therefore be formed at temperatures below the He II line.

In a recent paper Gopalswamy et al. (1999) suggest that coronal holes are seen as radio brightenings only if there are flux concentrations present in unipolar magnetic regions. The authors connect microwave enhancements with a combination of a smooth component, which probably comes from network cell interiors, and other more compact sources. Unfortunately the spatial resolution is too poor in our case to be able to separate the possible different components. The magnetograms for our data set are to be analysed, to see if there is a difference between the radio enhancements and depressions for coronal hole-like areas.

A study by Nindos et al. (1999), comparing 17 GHz radio brightenings with EIT features, did not find a one-to-one correlation between compact radio sources and bright EUV features either. They also suggested an association between the He II and diffuse polar cm-wave emission, which would mean that the radio emission comes from heights below the 80000 K layer, and not from the corona. The suggestion that in some cases the cm- and mm-wave radio emission has its origin at relatively low heights in the solar atmosphere has also been supported by the recent finding that 87 GHz radio bright regions are often associated with EUV, and even UV bright points, observed with the 0.5 arcsec pixel resolution of the TRACE satellite (Pohjolainen et al. 1999b).

Our data set showed that bright points, and sometimes even plumes, can be detected at 3.5 mm wavelength. However, many of the plumes were too high in latitude to be visible in the radio maps (limit of about 70 degrees). The bright points that did show up well in the mm-radio maps were intense both in EUV and soft X-rays. Also some indication of emission below 80 000 K was detected inside the coronal holes.

It has been suggested that cm-wave radio brightenings near the solar poles and inside coronal holes – as they are most probably connected to temperature enhancements in the chromosphere – may be related to the origin of solar wind. Millimeter wave emission has its origin even deeper down in the chromosphere, and our finding of mm-wave coronal hole brightenings may be a further proof of heating processes taking place in the chromosphere, that are necessary for solar wind plasma flows.

Due to the low spatial resolution of the available mm-wave radio observations it is difficult to determine any single feature to be the cause for radio brightenings. Our study suggests that bright points and polar plumes, as well as unresolved EUV and soft X-ray brightenings could be associated with radio brightenings. We also discovered radio bright regions inside coronal holes, with no obvious features causing them. This suggests that a closer look with good spatial resolution will be needed in the whole spectral range – from UV to soft X-rays – combined with magnetograms, to discover the physical counterparts for the brightenings.

Acknowledgements. We thank the anonymous referee for his constructive suggestions and helpful comments that improved the paper significantly. Part of this work was done at Metsähovi Radio Observatory, during D.R.'s training period. S.P. is supported by the Academy of Finland Contract No. 42576. F.P-F was supported in his work also by private foundations. SOHO/EIT was build by an international consortium involving ESA and NASA, under the supervision of J.P. Delaboudinière (PI). Yohkoh is a Japanese solar mission, with several internationally operated instruments. The SXT images were analysed using the Yohkoh Data Archive Centre (YDAC) at Mullard Space Science Laboratory. The alignment of multi-wavelength images for some of the figures was done with the help of Object-Based Methods for Analyzing Solar Images developed by D. Zarro.

References

Allen M.J., Oluseyi H.M., Walker A.B.C., Hoover R.B., Barbee T.W., 1997, Solar Phys. 174, 367
Babin A.N., Gopasyuk S.I., Efanov V.A., Kotov V.A., Moiseev I.G., Nesterov N.S., Tsap T.T., 1976, Izv. Krymsk. Astrofiz. Obs. 55, 3
Bohlin J.D., 1976, Natural History 85, 68-70
Brajša R., Pohjolainen S., Ruždjak V., Sakurai T., Urpo S., Vršnak B., Wöhl H., 1996, Solar Phys. 163, 79
Defise J.M., 1999, Ph.D. Thesis, Belgium
DeForest C.E., et al., 1997, Solar Phys. 175, 393
Delaboudinière J.-P., et al., 1996, Solar Phys. 162, 291
Dulk G., 1985, ARA&A 23, 169
Efanov V.A., Labrum N., Moiseev I.G., Nesterov N.S., Stewart R., 1980a, Izv. Krymsk. Astrofiz. Obs. 61, 52
Efanov V.A., Moiseev I.G., Nesterov N.S., Stewart R., 1980b, in Kundu M.R. and Gergely T.E. (eds.). Radio Physics of the Sun, IAU Symp. No. 86. Reidel, Dordrecht, p. 141
Foley C.R., Culhane J.L., Acton L.W., 1997, ApJ 491, 933
Gary D.E., Enome S., Shibasaki K., Gurman J.B., Shine R.A., 1997, BAAS 29, 8.01
Gopalswamy N., Schmahl E.J., Kundu M.R., 1992, Proc. First SOHO Workshop, Coronal Streamers, Coronal Loops, and Coronal and Solar Wind Composition, p. 113
Gopalswamy N., Shibasaki K., Thompson B.J., Gurman J., DeForest C., 1999, JGR 104, 9767
Habbal S.R., Dowdy J.Jr., Withbroe G.L., 1990, ApJ 352, 333
Hanaoka Y., 1994, Proc. of Kofu Symp., NRO Report 360, 181
Hara H., Tsuneta S., Acton L., et al., 1994, PASJ 46, 493
Hiei E., 1987, PASJ 39, 937
Kosugi T., Ishiguro M., Shibasaki K., 1986, PASJ 38, 1
Kundu M.R., Schmahl E.J., Fu Q.-J., 1988, ApJ 325, 905
Kundu M.R., Shibasaki K., Enome S., Nitta N., 1994, Proc. of Kofu Symposium, NRO Report No. 360, 79
Lindsey C.A., Roellig T.L., 1991, ApJ 375, 414
Moiseev I.G., Nesterov N.S., 1987, Izv. Krymsk. Astrofiz. Obs. 77, 83
Moses D., et al., 1997, Solar Phys. 175, 571
Neumark J., et al., 1997, Am. Astron. Soc. Meeting 191, 73.07
Nindos A., Kundu M.R., White S.M., Gary D.E., Shibasaki K., Dere K.P., 1999, AAS 194, 32.07
Nitta N., Bastian T.S., Aschwanden M.J., Harvey K., Strong K., 1992, PASJ 44, 167
Obridko V.N., Shelting B.D., 1999, Solar Phys. 187, 185
Pohjolainen S., 1996, Metsähovi Radio Res. Stat. Report Series A 24, 4
Pohjolainen S., Portier-Fozzani F., Ragaigne D., 1999a, Proc. Nobeyama Symp. 1998, NRO Report (in press)
Pohjolainen S., Riehokainen A., Valtaoja E., 1999b, Proc. EPS 1999 Meeting, ESA-SP 448 (in press)
Pohjolainen S., Urpo S., 1997, Fifth SOHO Workshop, ESA SP-404, 619
Portier-Fozzani F., et al., 1996, PASP Conf. Ser. 111, 402
Portier-Fozzani F., 1999, Ph.D. Thesis, University of Nice Sophia Antipolis
Riehokainen A., Urpo S., Valtaoja E., 1998, A&A 333, 741
Shevgaonkar R.K., Kundu M.R., Jackson P.D., 1988, ApJ 329, 982
Shibasaki K., 1997, in Balasubramaniam K.S., Harvey J. and Rabin D. (eds.). Synoptic Solar Physics, ASP Conf. Ser. 140, 373
Tsuneta S., Acton L., Bruner M., Lemen J., Brown W., et al., 1991, Solar Phys. 136, 37
Vršnak B., Pohjolainen S., Urpo S., et al., 1992, Solar Phys. 137, 67

Table 3. April 12, 1996: The radio Quiet Sun Level (QSL) was 7240.0 A/D converter count units (1.000 ± 0.003) in the Metsähovi 87 GHz map at 13:57 − 14:05 UT (Fig. 2). The radio source location is within the one arcmin beam. The Yohkoh SXT map was taken at 13:54:59 UT (Fig. 3), and the SOHO EIT Fe IX/X image at 14:27:41 UT (Fig. 4)

Point	Lat Deg	Long Deg	87 GHz Relative Intensity	Radio structure	EIT structure within 1 arcmin	SXT structure within 1 arcmin
1N	51.1	20.4	1.009 ± 0.003	brightening	LIE	enhanced brightness
2N	43.4	5.1	1.010 ± 0.003	brightening	LID	enhanced brightness
3N	56.8	9.4	1.006 ± 0.003	brightening	LID (He II: near LIE)	near BP
4N	31.3	−5.5	1.004 ± 0.003	brightening	LID	BP
1S	−67.0	5.0	1.017 ± 0.003	brightening	CH (He II: BP)	CH
2S	−55.8	35.0	1.012 ± 0.003	brightening	LID/BP nearby	BP
3S	−58.2	−41.2	1.010 ± 0.003	brightening	LID/BP nearby	enhanced brightness/CH
4S	−61.9	26.9	1.011 ± 0.003	brightening	LID/LIE nearby	enhanced brightness
5S	−47.3	−56.0	1.010 ± 0.003	brightening	LIE	CH/enhanced brightness

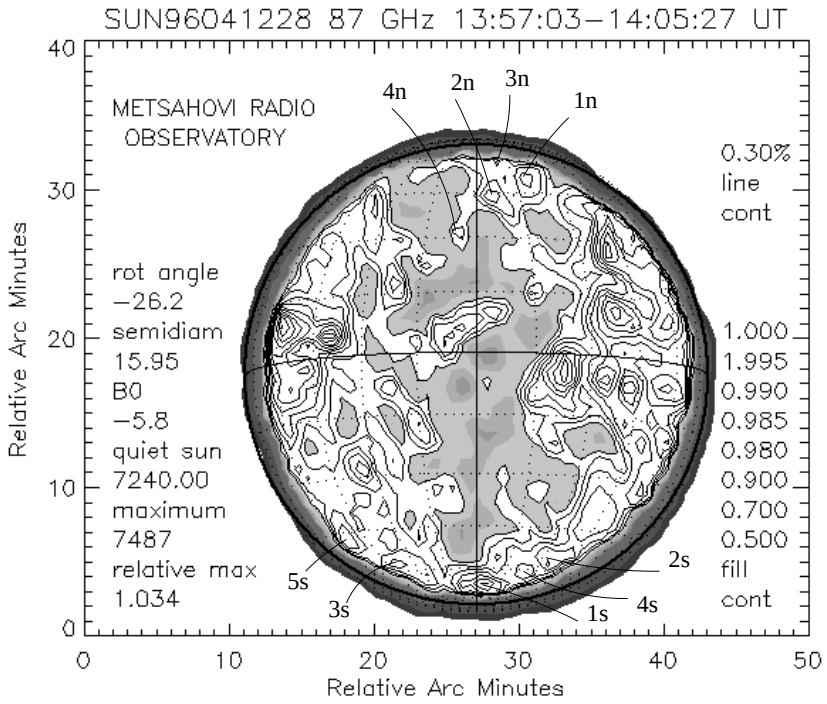

Fig. 2. Solar radio map at 87 GHz (3.5 mm) for April 12, 1996 at 13:57 − 14:05 UT. The greyscale contours (0.5, 0.7, 0.9, 0.98, 0.985, 0.99, and 0.995) represent levels below the quiet Sun. The quiet Sun (level 1.000) is plotted in white color, over which are the enhanced levels plotted in contour lines. The contour line level difference (0.3% of the quiet Sun in this case) is also the flux resolution

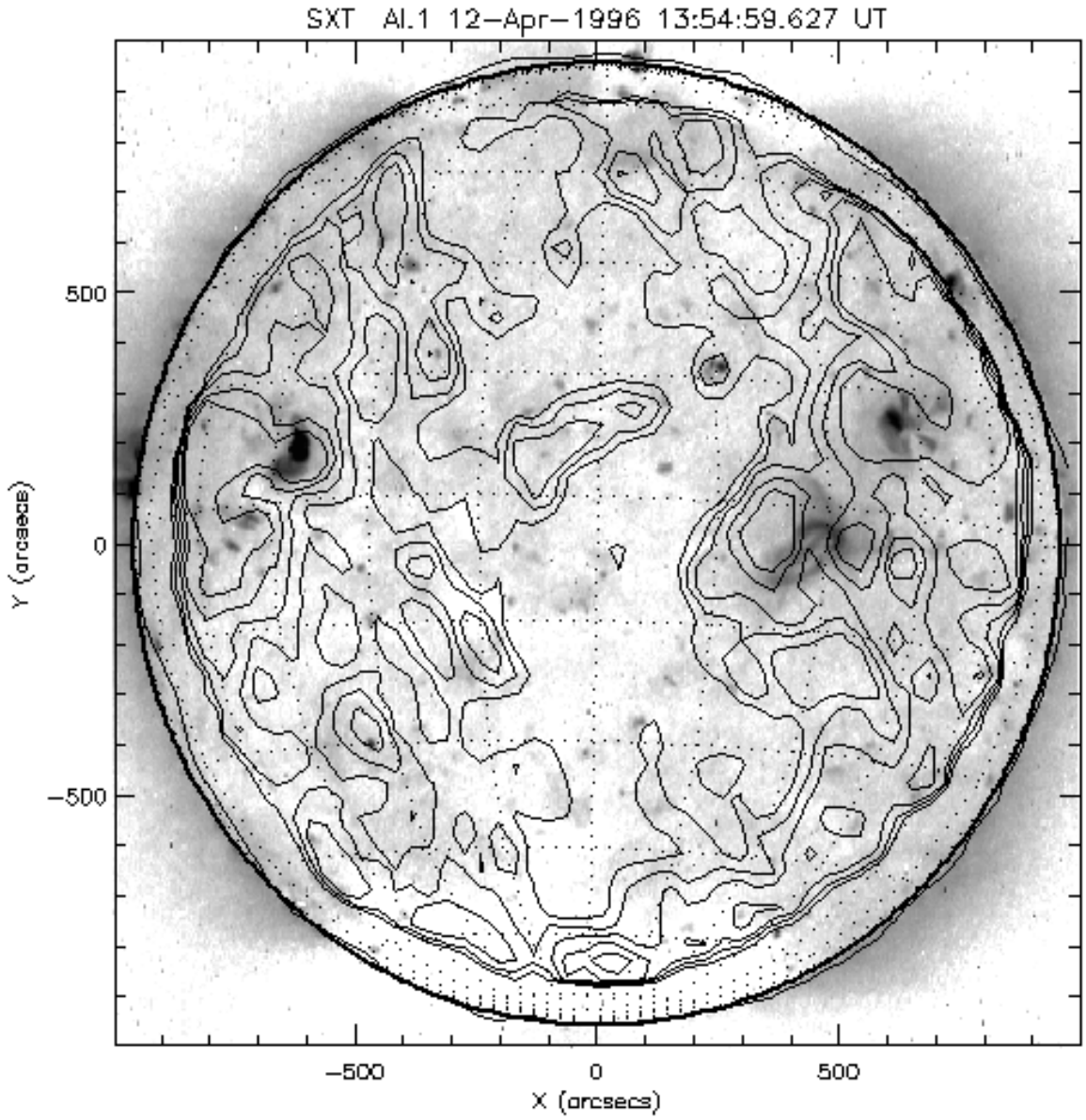

Fig. 3. Yohkoh SXT Al.1 image from April 12, 1996 at 13:54:59 UT (reversed colors). Overplotted are some selected radio contours (above the quiet Sun level only) of the 13:57 − 14:05 UT map

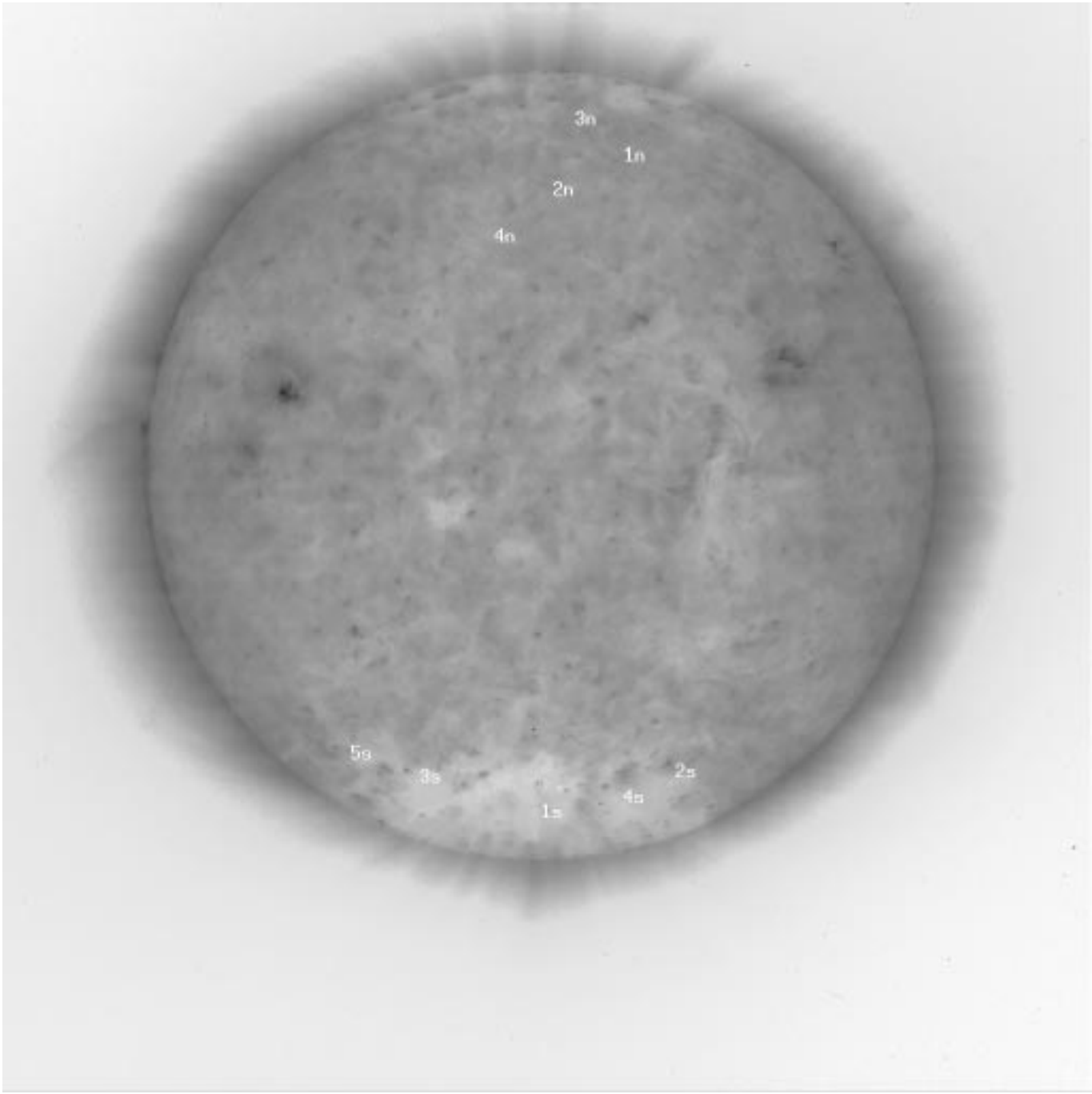

Fig. 4. SOHO/EIT Fe IX/X (171 Å, filter Al+1) image for April 12, 1996 at 14:27:41 UT (reversed colors)

Table 4. April 15, 1996: The radio Quiet Sun Level (QSL) was 7360.0 A/D converter count units (1.000 ± 0.003) in the Metsähovi 87 GHz map at 12:05 − 12:13 UT (Fig. 5). The radio source location is within the one arcmin beam. The Yohkoh SXT map was taken at 11:18:47 UT (Fig. 6), and the SOHO EIT Fe IX/X image at 12:14:16 UT (Fig. 7)

Point	Lat Deg	Long Deg	87 GHz Relative Intensity	Radio structure	EIT structure within 1 arcmin	SXT structure within 1 arcmin
1N	55.5	22.8	1.010 ± 0.003	brightening	LID	enhanced brightness
2N	40.2	4.5	1.007 ± 0.003	brightening	LID/LIE nearby	enhanced brightness
3N	53.2	−13.9	1.004 ± 0.003	brightening	LID/LIE nearby	enhanced/reduced brightness
4N	35.1	−10.1	1.009 ± 0.003	brightening	LIE	enhanced brightness
5N	52.8	33.8	1.011 ± 0.003	brightening	LID	enhanced brightness
6N	31.5	−20.4	1.010 ± 0.003	brightening	LIE	enhanced brightness
7N	53.7	0.4	0.995 ± 0.003	depression	LID	enhanced brightness
8N	45.1	−18.5	0.997 ± 0.003	depression	LIE	reduced brightness
1S	−63.5	−0.3	1.011 ± 0.003	brightening	CH	CH
2S	−64.5	20.6	1.009 ± 0.003	brightening	CH/LIE	CH
3S	−60.7	−36.5	1.014 ± 0.003	brightening	CH/LIE	CH/enhanced brightness
4S	−52.5	43.1	1.010 ± 0.003	brightening	LIE	enhanced brightness
5S	−46.3	48.9	1.010 ± 0.003	brightening	LID/LIE nearby	enhanced brightness
6S	−47.5	6.6	1.007 ± 0.003	brightening	LID/LIE nearby	enhanced brightness

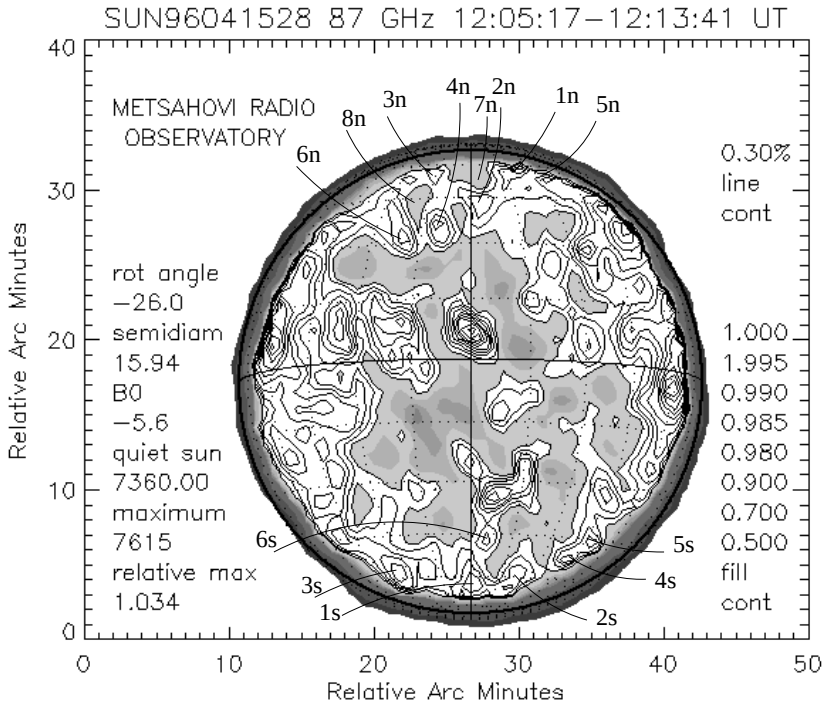

Fig. 5. Solar radio map at 87 GHz (3.5 mm) for April 15, 1996 at 12:05 − 12:13 UT. The greyscale contours (0.5, 0.7, 0.9, 0.98, 0.985, 0.99, and 0.995) represent levels below the quiet Sun. The quiet Sun (level 1.000) is plotted in white color, over which are the enhanced levels plotted in contour lines. The contour line level difference (0.3% of the quiet Sun in this case) is also the flux resolution

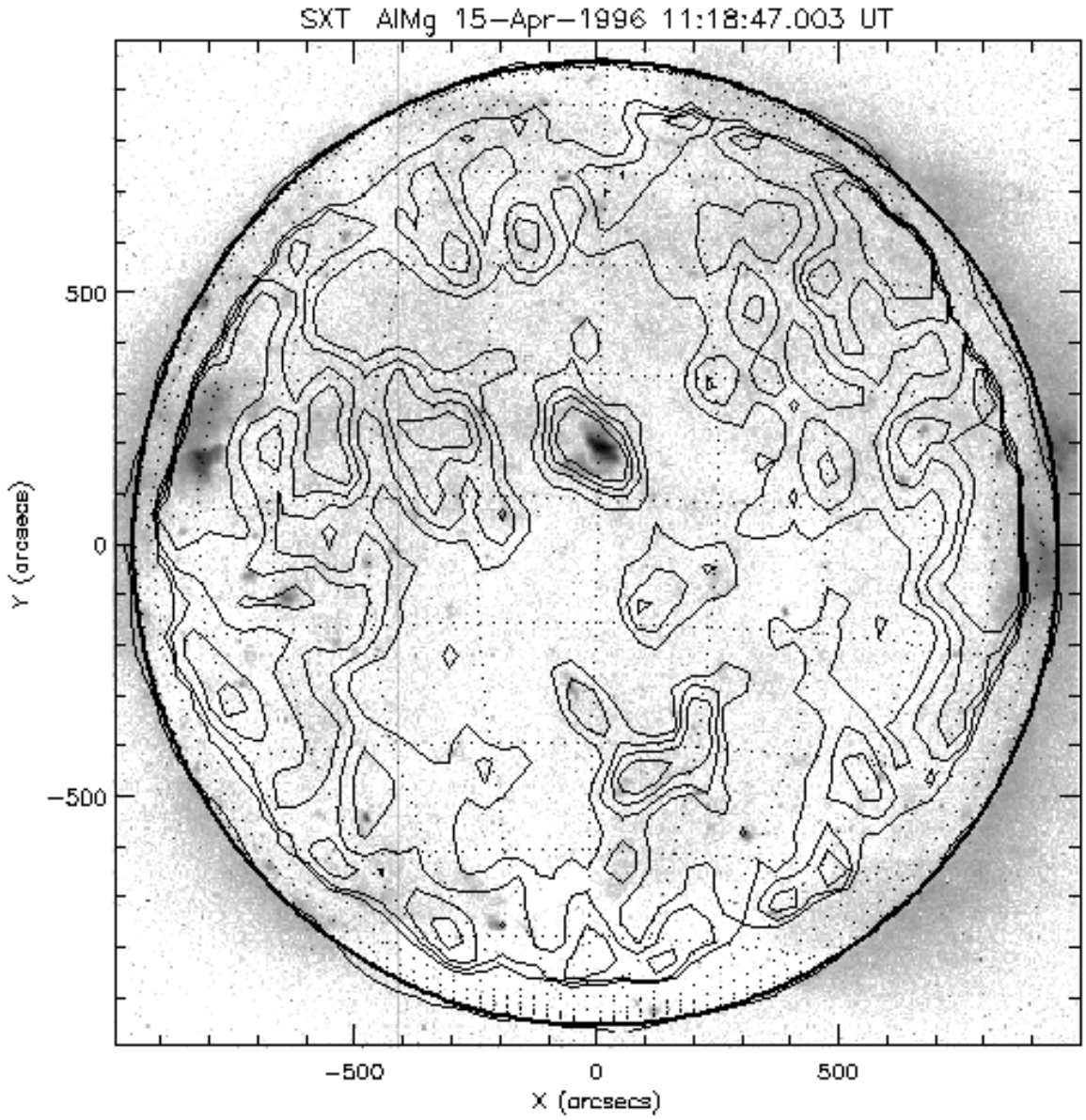

Fig. 6. Yohkoh AlMg image from April 15, 1996 at 11:18:47 UT (reversed colors). Overplotted are some selected radio contours (above the quiet Sun level only) of the 12:05 − 12:13 UT map

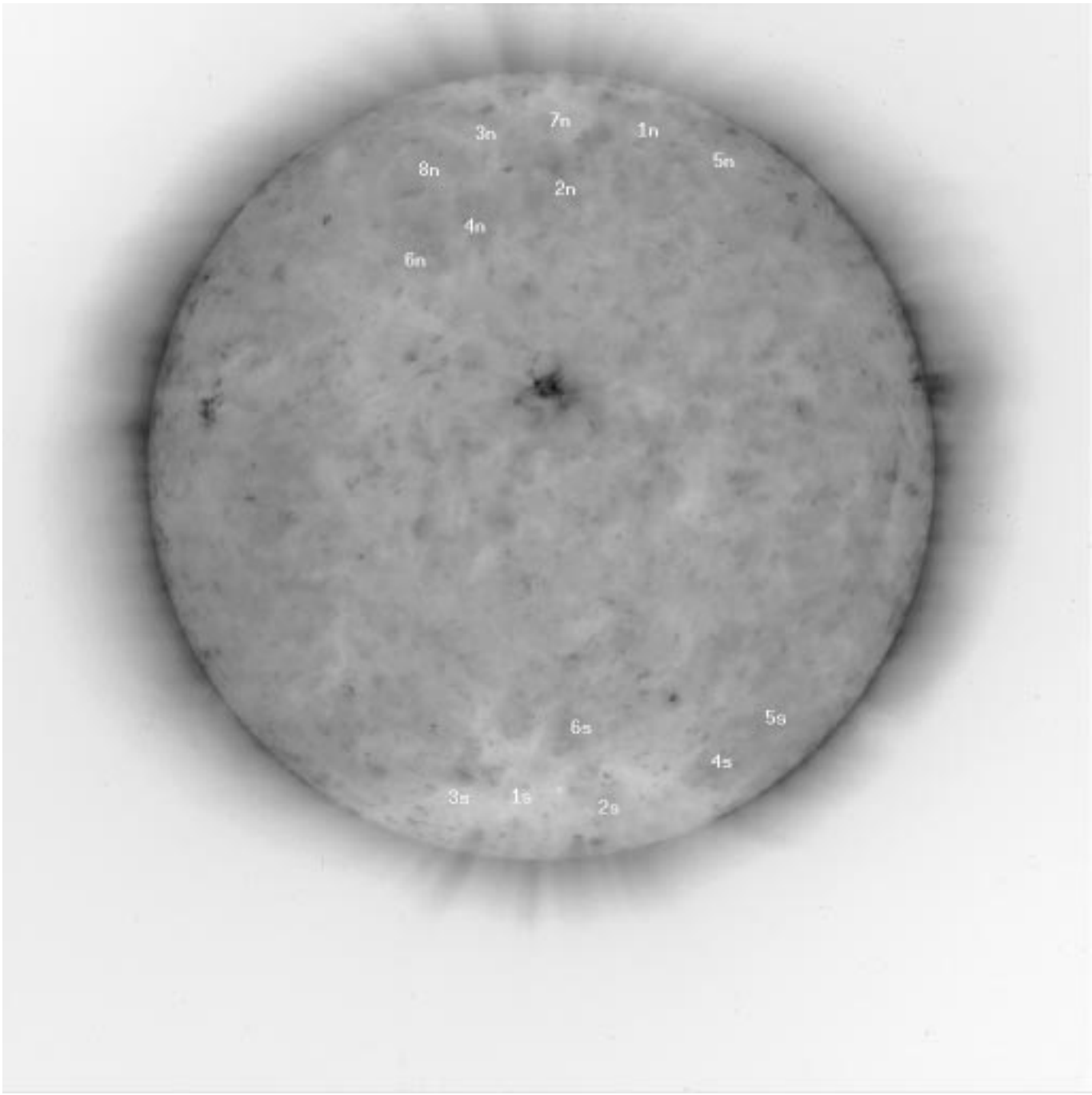

Fig. 7. SOHO/EIT Fe IX/X (171 Å, filter Al+1) image for April 15, 1996 at 12:14:16 UT (reversed colors)

Table 5. August 9, 1996: The radio Quiet Sun Level (QSL) was 5380.0 A/D converter count units (1.000 ± 0.003) in the Metsähovi 87 GHz map at 07:23 − 07:32 UT (Fig. 8). The radio source location is within the one arcmin beam. The Yohkoh SXT map was taken at 07:00:00 UT (Fig. 9), and the SOHO EIT Fe XII image at 07:34:25 UT (Fig. 10)

Point	Lat Deg	Long Deg	87 GHz Relative Intensity	Radio structure	EIT structure within 1 arcmin	SXT structure within 1 arcmin
1N	70.1	16.7	1.015 ± 0.003	brightening	CH	CH
2N	62.1	−27.0	1.019 ± 0.003	brightening	LID/LIE	CH
3N	52.2	3.9	1.013 ± 0.003	brightening	LID/LIE nearby	enhanced brightness
4N	47.4	−42.2	1.013 ± 0.003	brightening	LID	CH/enhanced brightness
5N	58.4	49.1	1.010 ± 0.003	brightening	LIE	enhanced brightness
6N	42.4	−16.7	0.986 ± 0.003	depression	LID	CH
7N	42.5	12.5	0.989 ± 0.003	depression	LID	quiet Sun
8N	37.6	1.7	0.988 ± 0.003	depression	LID	quiet Sun
1S	−52.0	−9.4	1.013 ± 0.003	brightening	LIE	enhanced brightness
2S	−42.4	42.8	1.021 ± 0.003	brightening	BP/LID nearby	BP nearby
3S	−34.9	−9.2	0.986 ± 0.003	depression	LID	reduced brightness

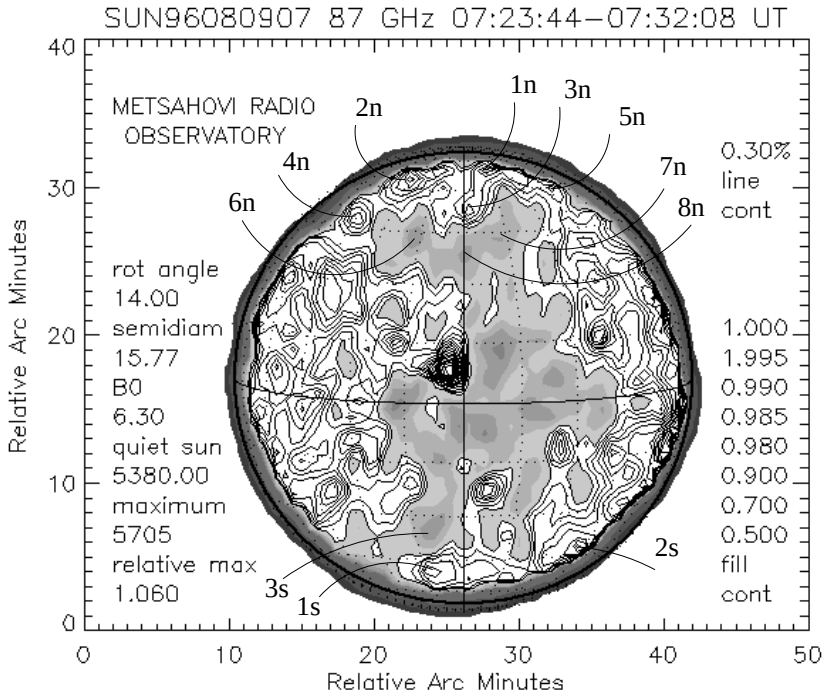

Fig. 8. Solar radio map at 87 GHz (3.5 mm) for August 09, 1996 at 07:23 − 07:32 UT. The greyscale contours (0.5, 0.7, 0.9, 0.98, 0.985, 0.99, and 0.995) represent levels below the quiet Sun. The quiet Sun (level 1.000) is plotted in white color, over which are the enhanced levels plotted in contour lines. The contour line level difference (0.3% of the quiet Sun in this case) is also the flux resolution

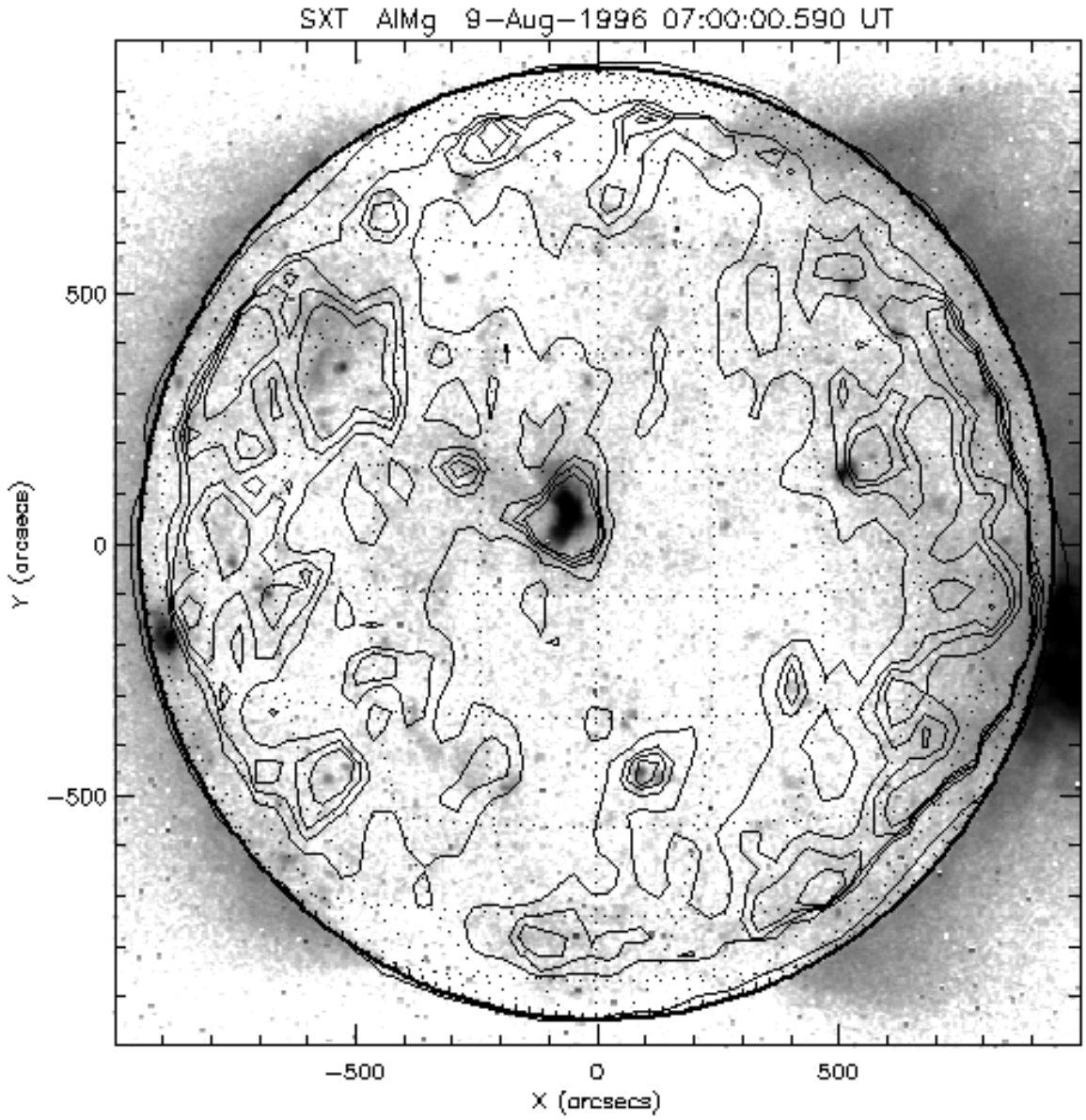

Fig. 9. Yohkoh SXT AlMg image from August 09, 1996 at 07:00:00 UT (reversed colors). Overplotted are some selected radio contours (above the quiet Sun level only) of the 07:23 − 07:32 UT map

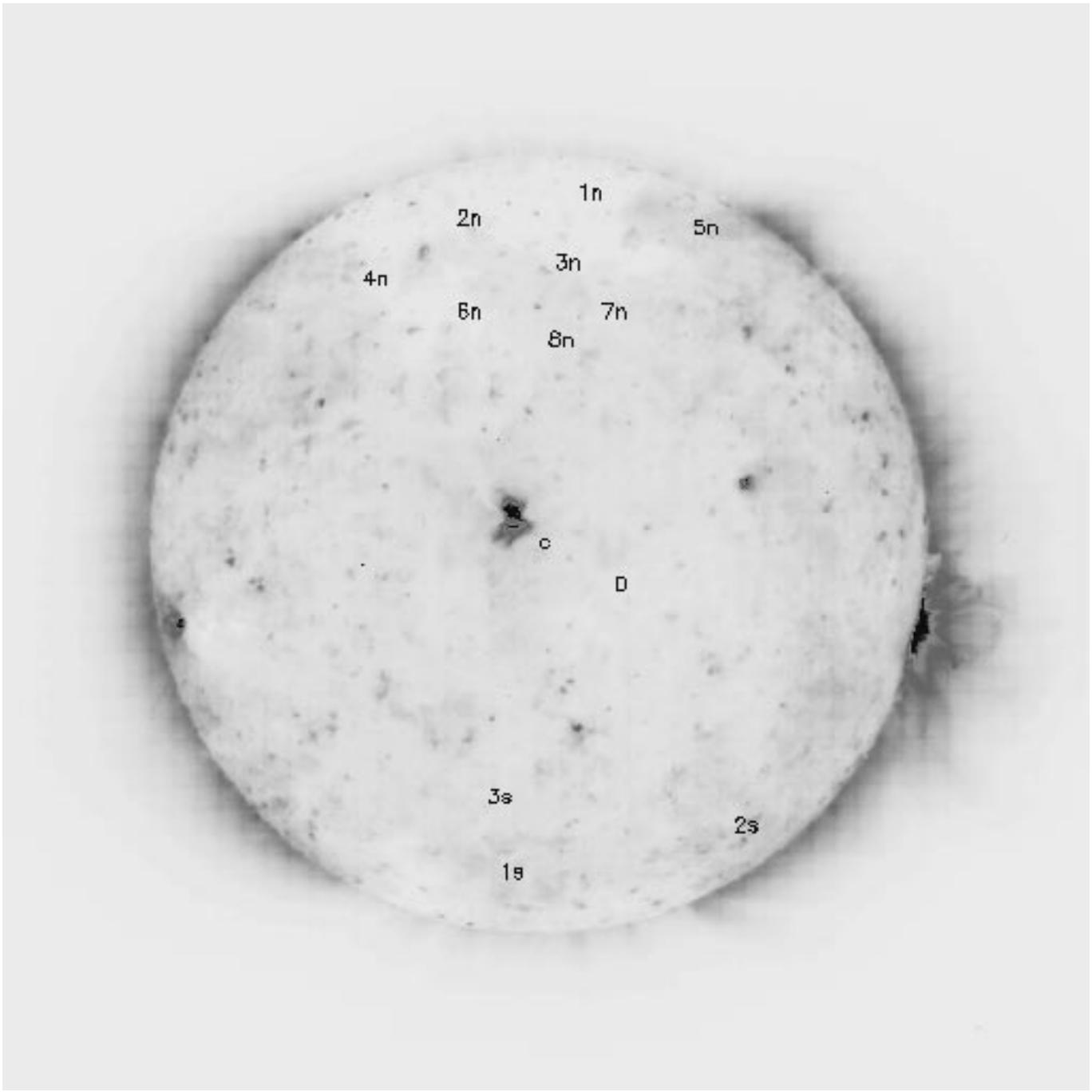

Fig. 10. SOHO/EIT Fe XII (195 Å, filter Clear) image for August 09, 1996 at 07:34:25 UT (reversed colors)

Table 6. August 13, 1996: The radio Quiet Sun Level (QSL) was 5950.0 A/D converter count units (1.000 ± 0.003) in the Metsähovi 87 GHz map at 12:31 − 12:39 UT (Fig. 11). The radio source location is within the one arcmin beam. The Yohkoh SXT map was taken at 12:39:53 UT (Fig. 12), and the SOHO EIT Fe IX/X image at 12:30:13 UT (Fig. 13)

Point	Lat Deg	Long Deg	87 GHz Relative Intensity	Radio structure	EIT structure within 1 arcmin	SXT structure within 1 arcmin
1N	64.7	−6.9	1.013 ± 0.003	brightening	BP or PP	BP
2N	68.5	21.6	1.014 ± 0.003	brightening	PP	CH
3N	64.3	47.8	1.010 ± 0.003	brightening	PP	CH
4N	55.5	50.8	1.005 ± 0.003	brightening	LID/LIE	CH
5N	52.4	5.1	0.989 ± 0.003	depression	LID/LIE	CH
1S	−45.2	−26.3	1.016 ± 0.003	brightening	LIE	enhanced brightness
2S	−40.1	−41.3	1.014 ± 0.003	brightening	LIE	reduced brightness
3S	−29.8	−22.9	1.011 ± 0.003	brightening	LID	enhanced brightnes
4S	−42.9	−1.6	1.011 ± 0.003	brightening	LID/BP nearby	enhanced brightness
5S	−50.5	35.7	1.006 ± 0.003	brightening	LIE	reduced brightness
6S	−53.1	13.6	0.992 ± 0.003	depression	CH	CH
7S	−38.0	−12.4	0.998 ± 0.003	depression	LIE	enhanced brightness

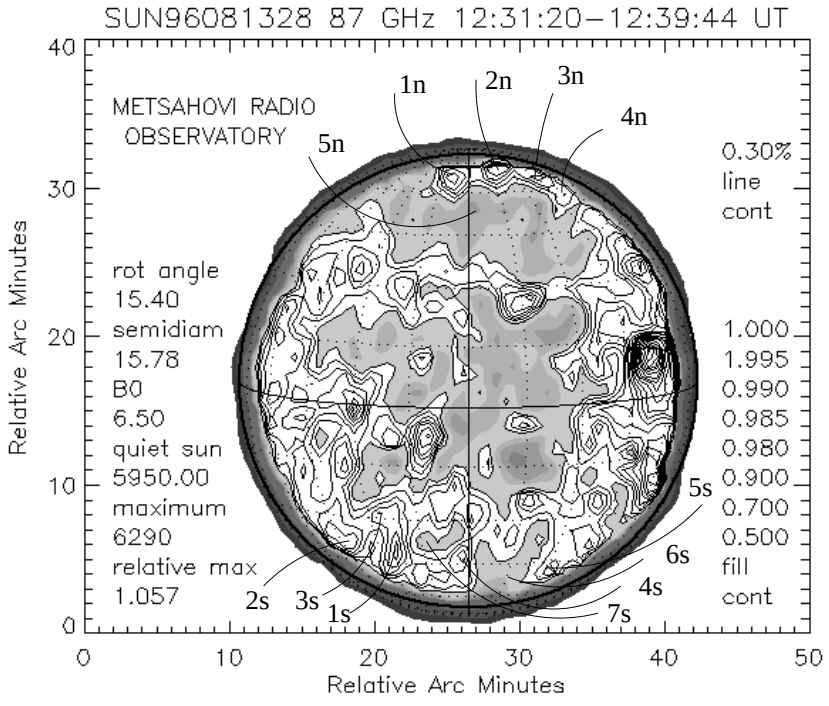

Fig. 11. Solar radio map at 87 GHz (3.5 mm) for August 13, 1996 at 12:31 − 12:39 UT. The greyscale contours (0.5, 0.7, 0.9, 0.98, 0.985, 0.99, and 0.995) represent levels below the quiet Sun. The quiet Sun (level 1.000) is plotted in white color, over which are the enhanced levels plotted in contour lines. The contour line level difference (0.3% of the quiet Sun in this case) is also the flux resolution

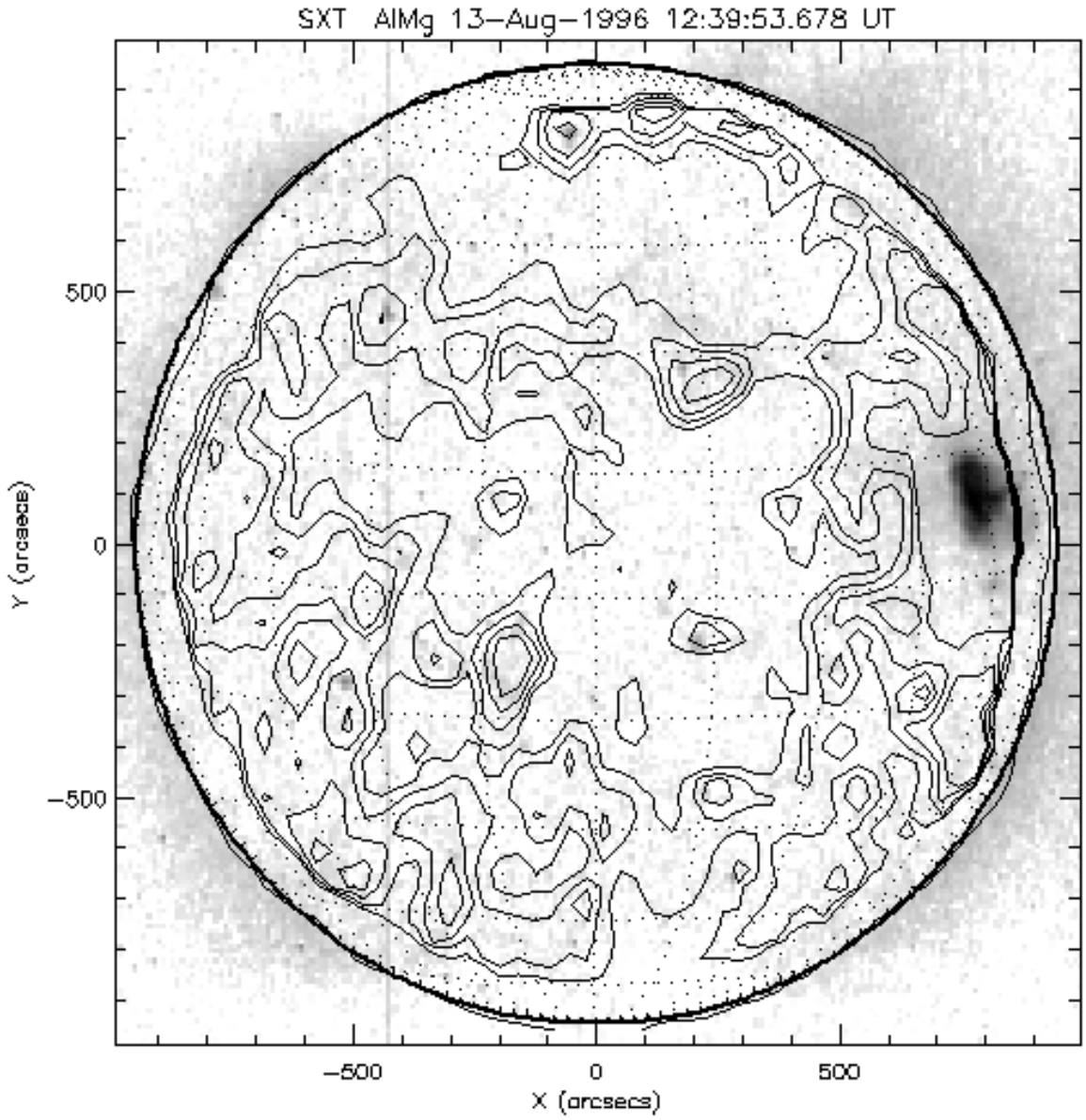

Fig. 12. Yohkoh SXT AlMg image from August 13, 1996 at 12:39:53 UT (reversed colors). Overplotted are some selected radio contours (above the quiet Sun level only) of the 12:31 − 12:39 UT map

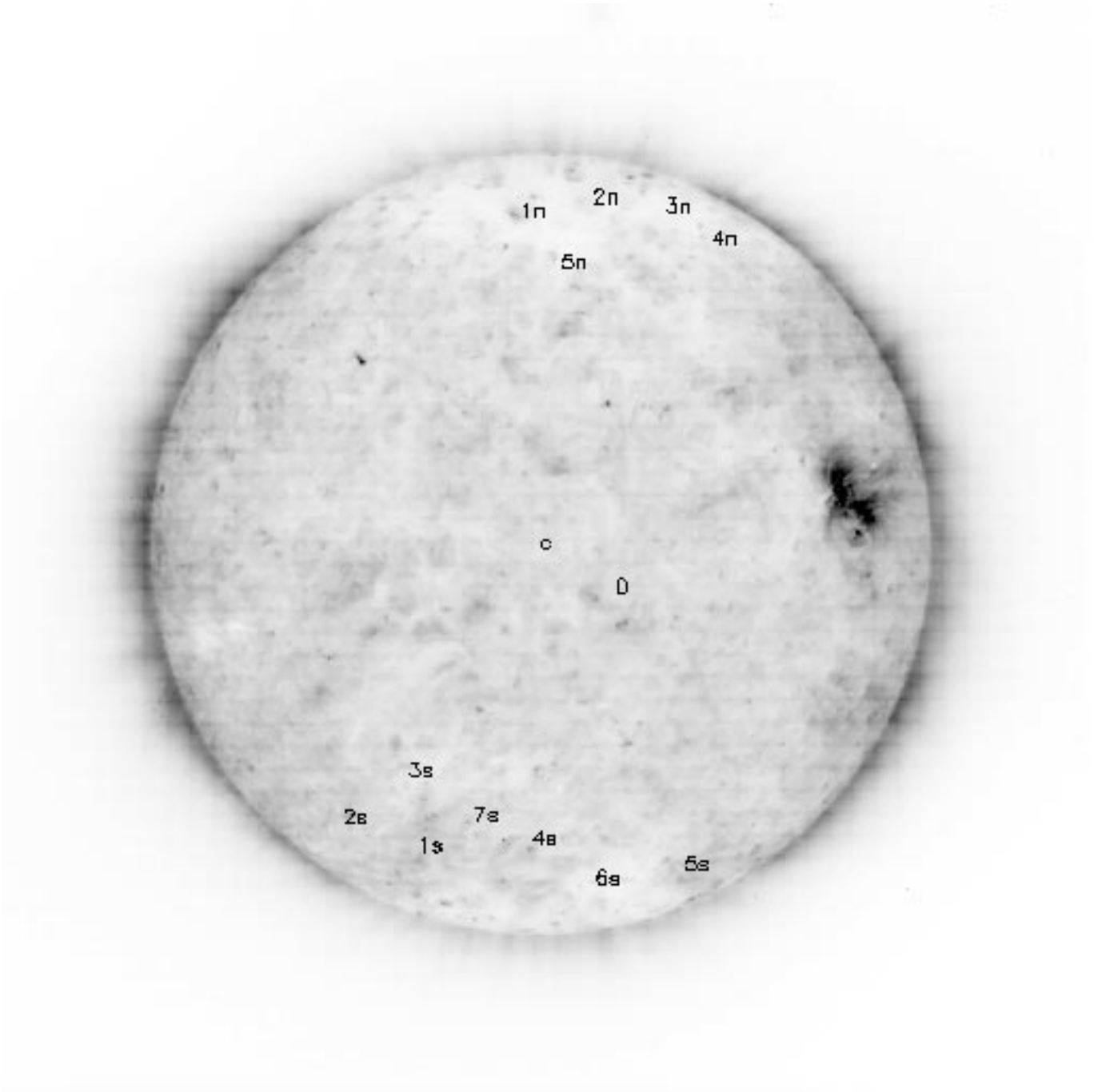

Fig. 13. SOHO/EIT Fe IX/X (171 Å, filter Clear) image for August 13, 1996 at 12:30:13 UT (reversed colors)

Table 7. August 14, 1996: The radio Quiet Sun Level (QSL) was 1985.0 A/D converter count units (1.000 ± 0.003) in the Metsähovi 87 GHz map at 12:55 − 13:03 UT (Fig. 14). The radio source location is within the one arcmin beam. The Yohkoh SXT map was taken at 12:39:41 UT (Fig. 15), and the SOHO EIT Fe IX/X image at 12:30:13 UT (Fig. 16)

Point	Lat Deg	Long Deg	87 GHz Relative Intensity	Radio structure	EIT structure within 1 arcmin	SXT structure within 1 arcmin
1N	67.5	30.0	1.018 ± 0.003	brightening	LIE	CH
2N	67.4	−11.5	1.015 ± 0.003	brightening	PP?	CH
3N	49.6	−47.0	1.006 ± 0.003	brightening	LID	enhanced brightness
4N	51.3	14.8	0.987 ± 0.003	depression	LID	CH
1S	−39.8	−9.4	1.021 ± 0.003	brightening	LID/BP nearby	BP
2S	−40.9	12.7	1.015 ± 0.003	brightening	LID	enhanced brightness
3S	−25.3	31.3	1.018 ± 0.003	brightening	LIE	enhanced brightness
4S	−35.1	−32.8	1.013 ± 0.003	brightening	LID/BP nearby	enhanced brightness
5S	−50.9	24.9	0.997 ± 0.003	depression	CH	CH
6S	−26.3	3.1	0.997 ± 0.003	depression	LID	quiet Sun

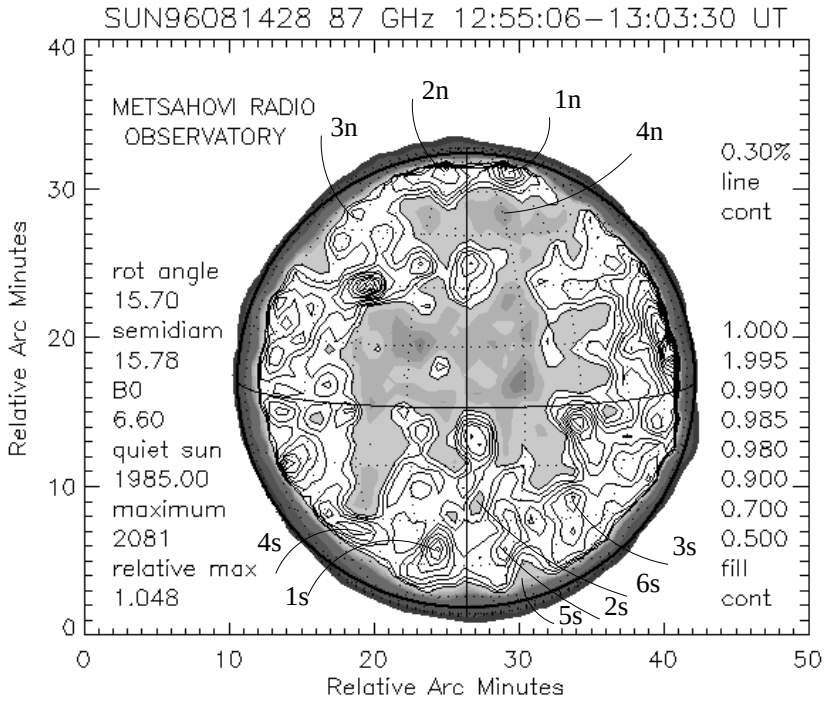

Fig. 14. Solar radio map at 87 GHz (3.5 mm) for August 14, 1996 at 12:55 − 13:03 UT. The greyscale contours (0.5, 0.7, 0.9, 0.98, 0.985, 0.99, and 0.995) represent levels below the quiet Sun. The quiet Sun (level 1.000) is plotted in white color, over which are the enhanced levels plotted in contour lines. The contour line level difference (0.3% of the quiet Sun in this case) is also the flux resolution

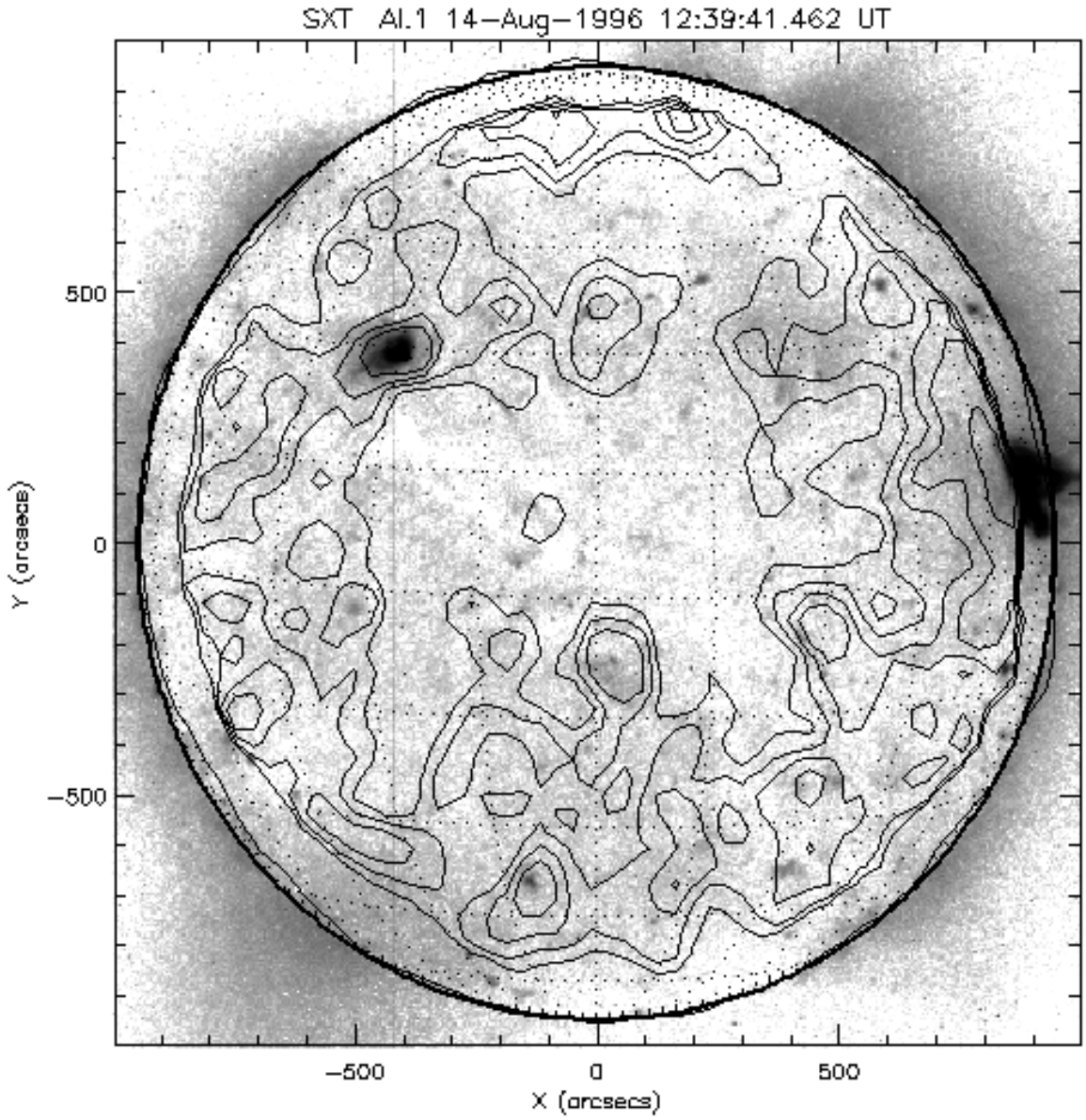

Fig. 15. Yohkoh SXT Al.1 image from August 14, 1996 at 12:39:41 UT (reversed colors). Overplotted are some selected radio contours (above the quiet Sun level only) of the 12:55 − 13:03 UT map

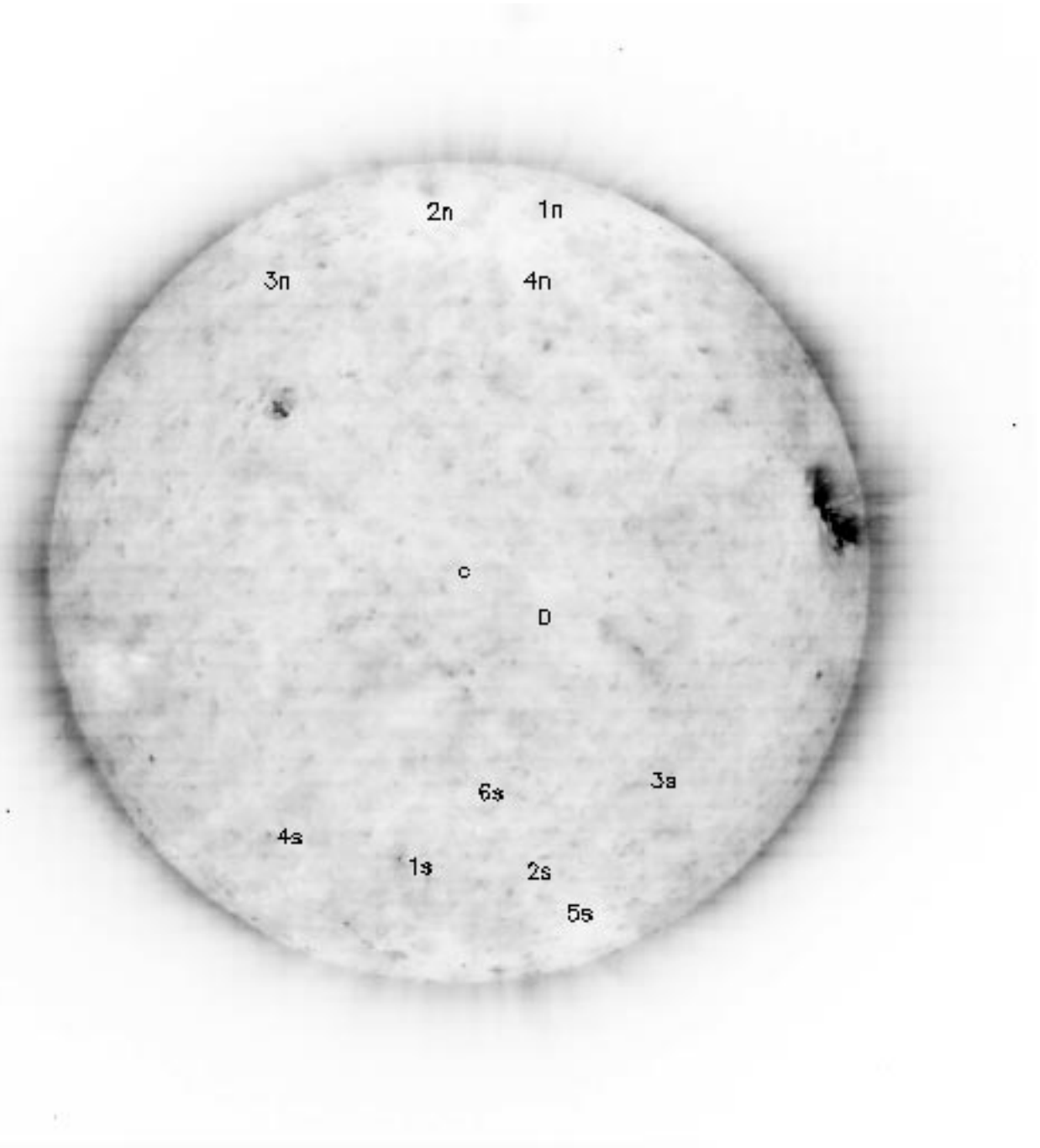

Fig. 16. SOHO/EIT Fe IX/X (171 Å, filter Clear) image for August 14, 1996 at 12:30:13 UT (reversed colors)

Table 8. May 20, 1997: The radio Quiet Sun Level (QSL) was 6910.0 A/D converter count units (1.000 ± 0.005) in the Metsähovi 87 GHz map at 13:03 − 13:12 UT (Fig. 17). The radio source location is within the one arcmin beam. The Yohkoh SXT map was taken at 13:15:13 UT (Fig. 18), and the SOHO EIT Fe IX/X image at 13:00:13 UT (Fig. 19)

Point	Lat Deg	Long Deg	87 GHz Relative Intensity	Radio structure	EIT structure within 1 arcmin	SXT structure within 1 arcmin
1N	58.7	−2.8	1.006 ± 0.005	brightening	CH/LIE	enhanced brightness
2N	47.8	−10.2	1.001 ± 0.005	brightening	LID/LIE	enhanced brightness
3N	44.4	26.7	1.011 ± 0.005	brightening	LID/LIE	enhanced brightness
4N	53.6	−22.9	0.997 ± 0.005	depression	LID/LIE	quiet Sun/CH
5N	54.8	18.1	0.993 ± 0.005	depression	LID/LIE	CH
6N	33.7	10.7	0.988 ± 0.005	depression	LID	reduced brightness
1S	−47.1	−29.6	1.013 ± 0.005	brightening	LIE	BP?
2S	−59.5	1.2	1.004 ± 0.005	brightening	LIE/LID	CH
3S	−53.3	28.4	1.006 ± 0.005	brightening	LIE	BP?
4S	−41.8	−4.4	1.006 ± 0.005	brightening	LID/LIE	reduced brightness
5S	−50.4	−9.0	0.993 ± 0.005	depression	LID/LIE	reduced brightness
6S	−43.8	28.1	0.997 ± 0.005	depression	LID/LIE nearby	reduced brightness

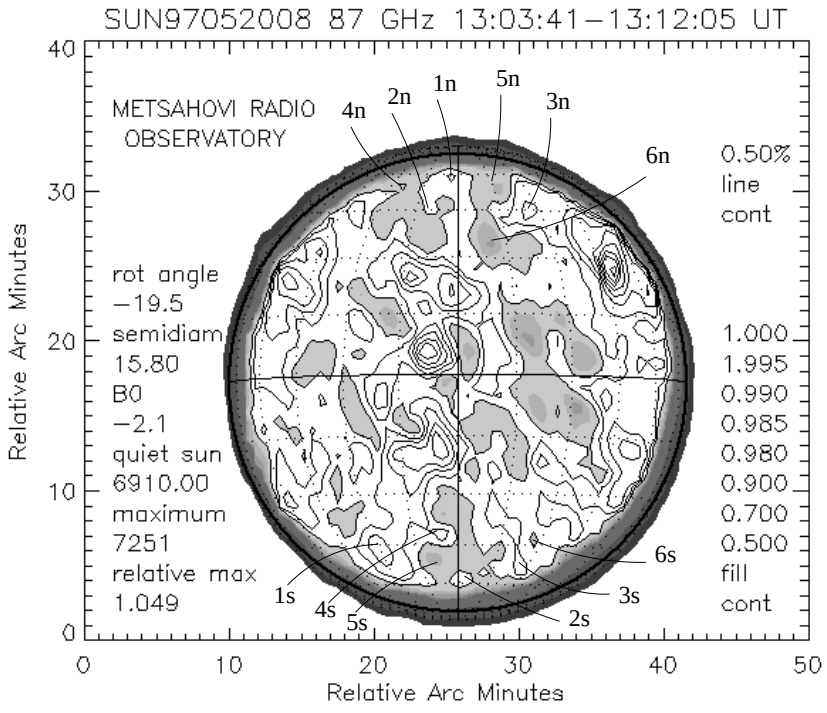

Fig. 17. Solar radio map at 87 GHz (3.5 mm) for May 20, 1997 at 13:03 − 13:12 UT. The greyscale contours (0.5, 0.7, 0.9, 0.98, 0.985, 0.99, and 0.995) represent levels below the quiet Sun. The quiet Sun (level 1.000) is plotted in white color, over which are the enhanced levels plotted in contour lines. The contour line level difference (0.5% of the quiet Sun in this case) is also the flux resolution

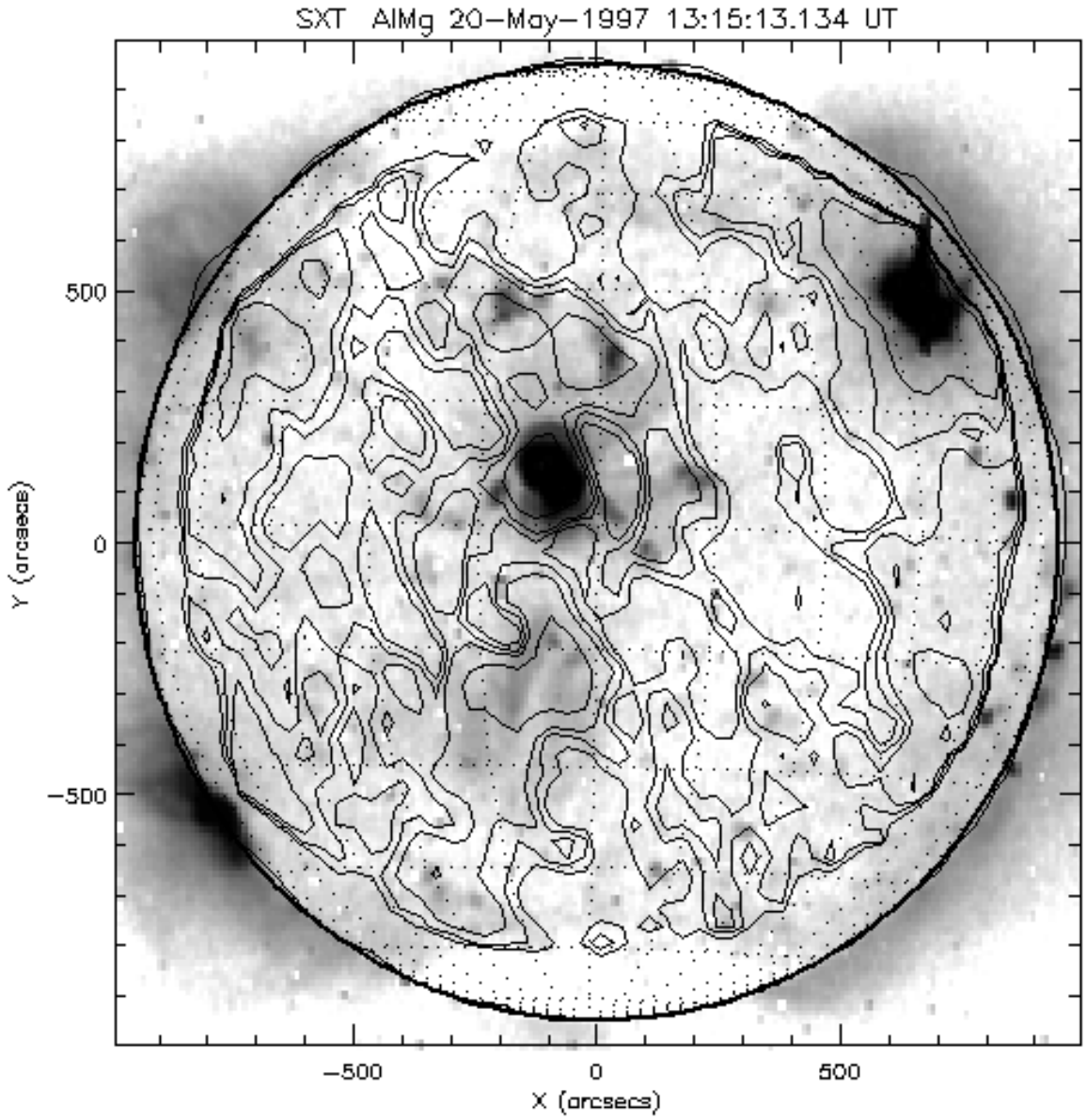

Fig. 18. Yohkoh SXT AlMg image from May 20, 1997 at 13:15:13 UT (reversed colors). Overplotted are some selected radio contours (above the quiet Sun level only) of the 13:03 − 13:12 UT map

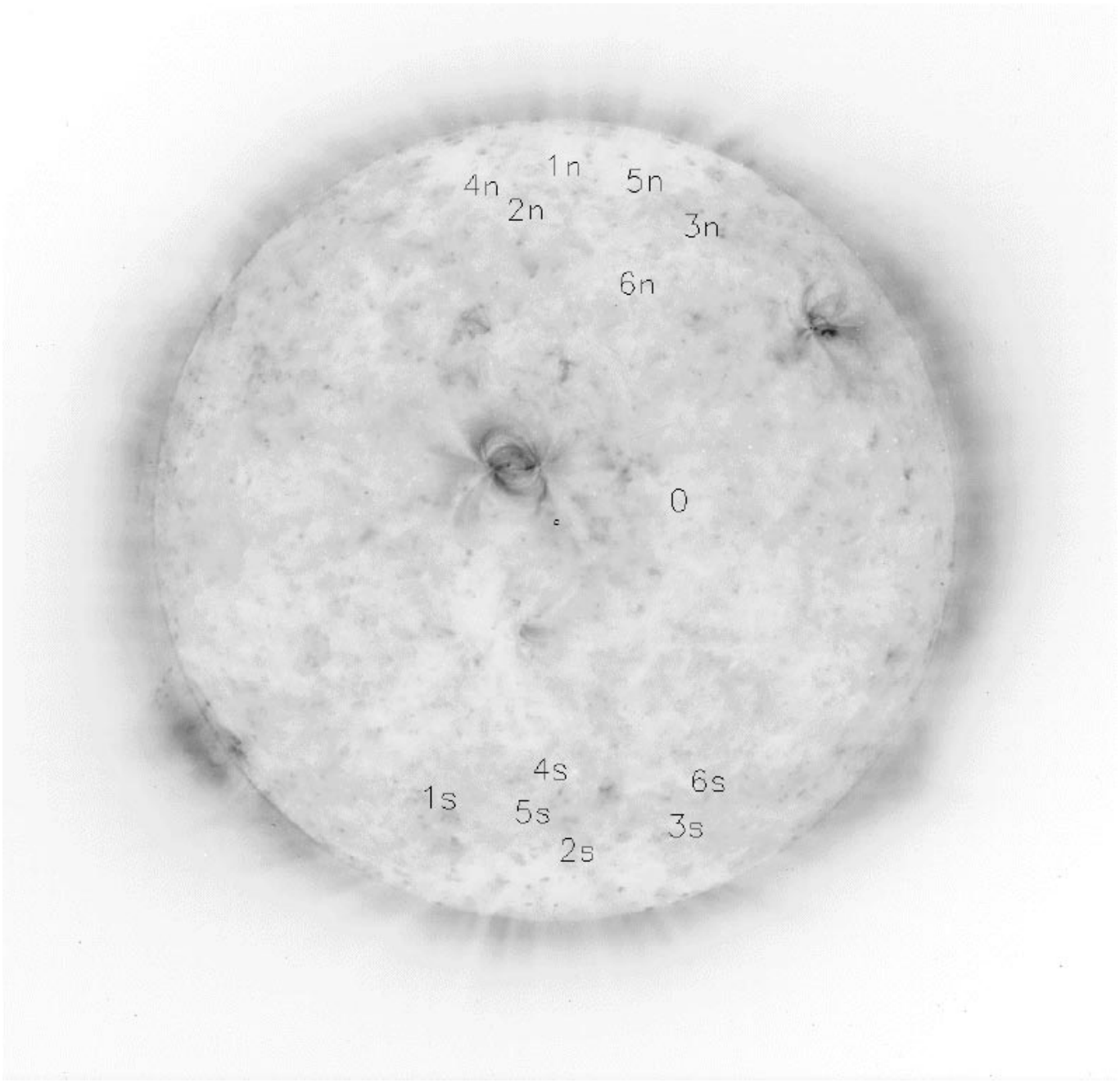

Fig. 19. SOHO/EIT Fe IX/X (171 Å, filter Clear) image for May 20, 1997 at 13:00:13 UT (reversed colors)

Table 9. August 8, 1997: The radio Quiet Sun Level (QSL) was 5350.0 A/D converter count units (1.000 ± 0.004) in the Metsähovi 87 GHz map at 11:30 − 11:39 UT (Fig. 20). The radio source location is within the one arcmin beam. The Yohkoh SXT map was taken at 11:03:59 UT (Fig. 21), and the SOHO EIT Fe IX/X image at 13:09:46 UT (Fig. 22)

Point	Lat Deg	Long Deg	87 GHz Relative Intensity	Radio structure	EIT structure within 1 arcmin	SXT structure within 1 arcmin
1N	65.6	38.9	1.009 ± 0.004	brightening	CH	CH/quiet Sun
2N	66.7	−8.3	1.004 ± 0.004	brightening	CH	CH
3N	51.8	43.7	1.005 ± 0.004	brightening	LID/LIE	enhanced brightness
4N	55.7	−39.9	1.007 ± 0.004	brightening	LIE/BP	enhanced brightness
5N	47.1	−22.7	1.003 ± 0.004	brightening	LIE/BP	enhanced brightness
6N	40.1	−10.9	1.002 ± 0.004	brightening	LID	CH/quiet Sun
7N	52.2	−9.5	0.982 ± 0.004	depression	LID/LIE	CH
1S	−37.5	−43.7	1.032 ± 0.004	brightening	LIE	enhanced brightness
2S	−30.9	−23.6	1.038 ± 0.004	brightening	LID/LIE nearby	AR
3S	−52.4	2.8	1.009 ± 0.004	brightening	LID/LIE	enhanced brightness
4S	−22.8	26.3	1.040 ± 0.004	brightening	AR	AR
5S	−21.0	−19.5	1.036 ± 0.004	brightening	AR	AR
6S	−35.2	−6.2	0.998 ± 0.004	depression	LID	reduced brightness

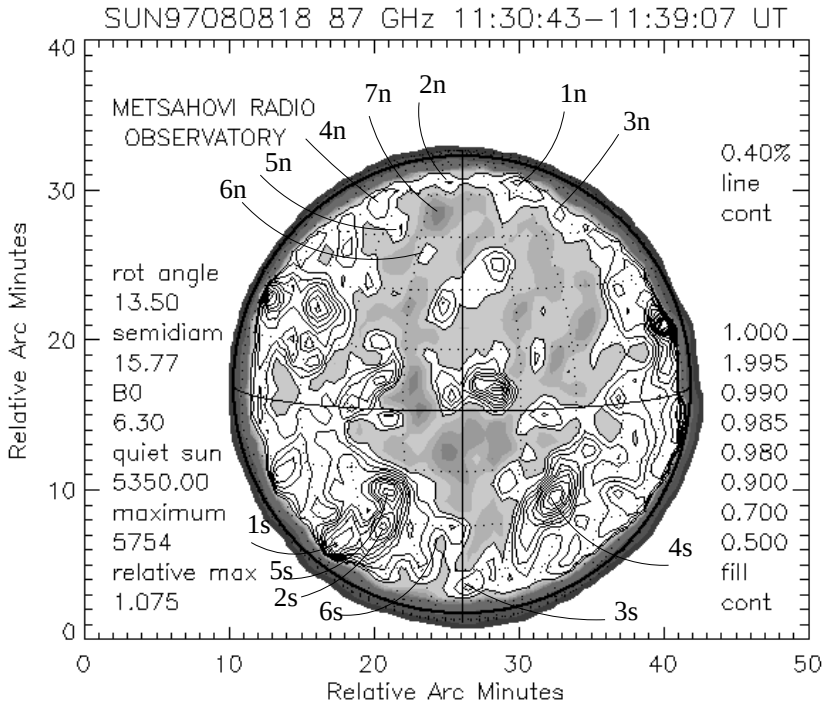

Fig. 20. Solar radio map at 87 GHz (3.5 mm) for August 8, 1997 at 11:30 − 11:39 UT. The greyscale contours (0.5, 0.7, 0.9, 0.98, 0.985, 0.99, and 0.995) represent levels below the quiet Sun. The quiet Sun (level 1.000) is plotted in white color, over which are the enhanced levels plotted in contour lines. The contour line level difference (0.4% of the quiet Sun in this case) is also the flux resolution

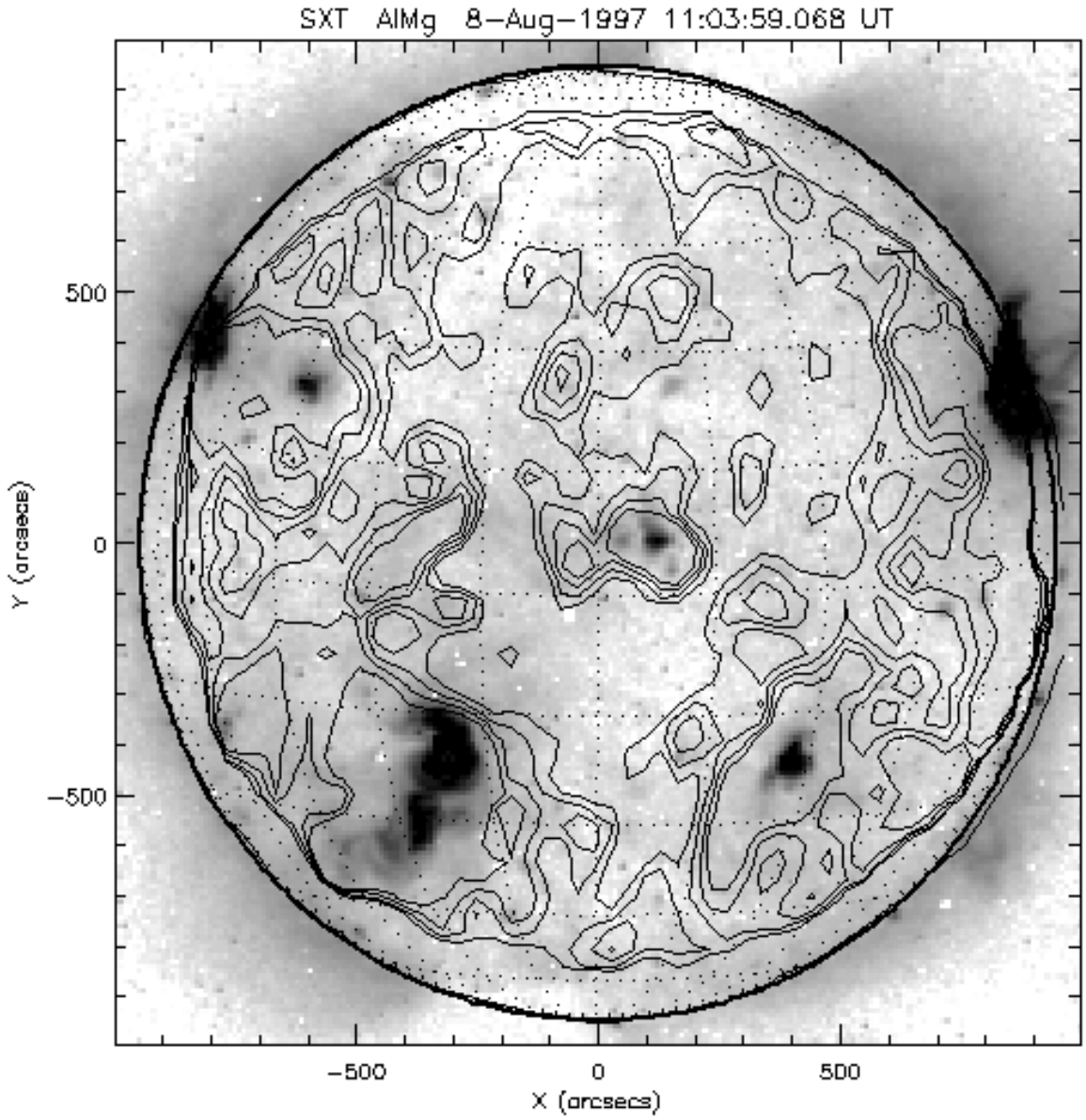

Fig. 21. Yohkoh SXT AlMg image from August 8, 1997 at 11:03:59 UT (reversed colors). Overplotted are some selected radio contours (above the quiet Sun level only) of the 11:30 − 11:39 UT map

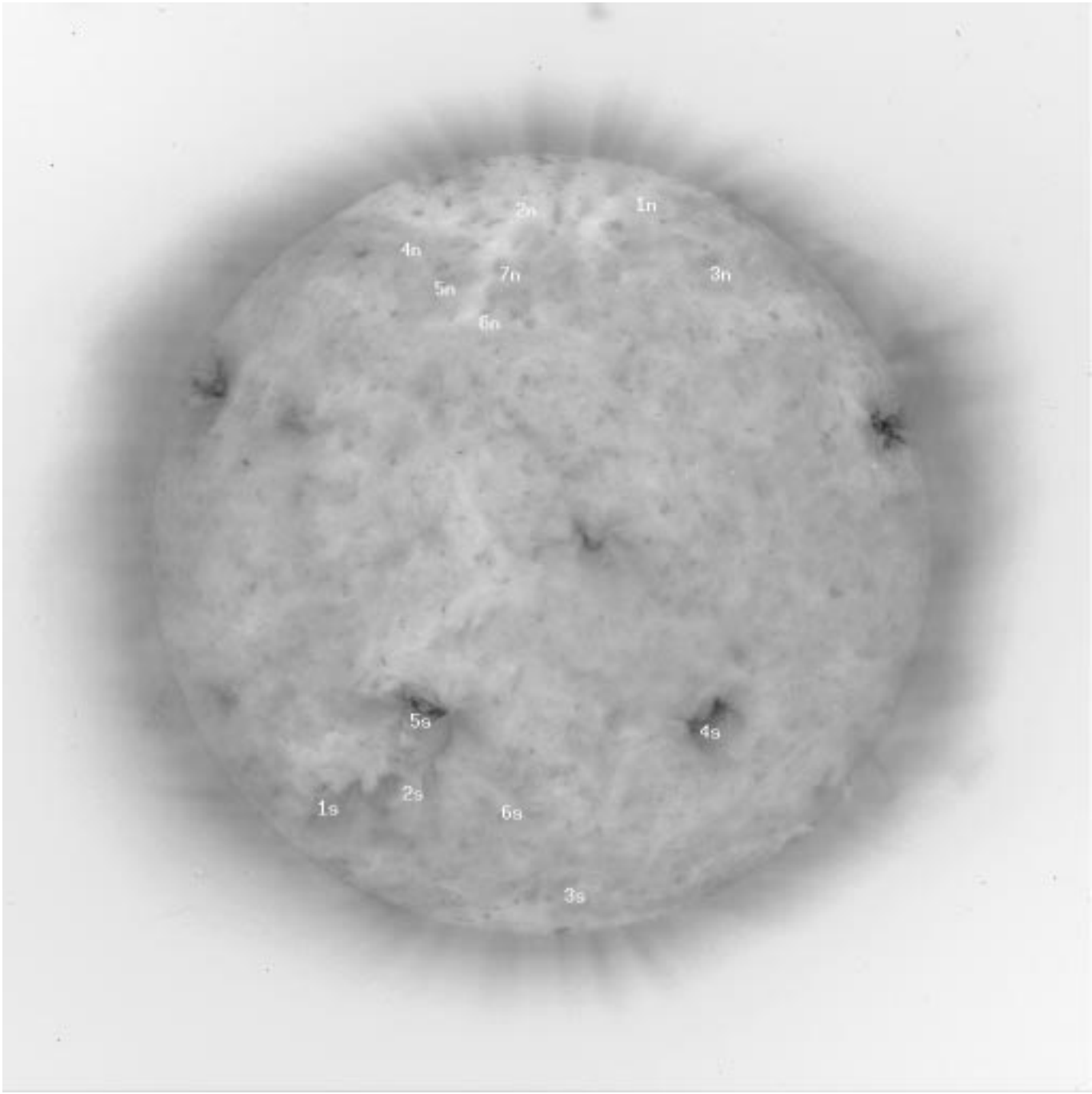

Fig. 22. SOHO/EIT Fe IX/X (171 Å, filter Clear) image for August 8, 1997 at 13:09:46 UT (reversed colors)

Table 10. August 27, 1997: The radio Quiet Sun Level (QSL) was 4560.0 A/D converter count units (1.000 ± 0.005) in the Metsähovi 87 GHz at 12:13 − 12:22 UT (Fig. 23). The radio source location is within the one arcmin beam. The Yohkoh SXT map was taken at 12:53:45 UT (Fig. 24), and the SOHO EIT Fe IX/X image at 13:01:03 UT (Fig. 25)

Point	Lat Deg	Long Deg	87 GHz Relative Intensity	Radio structure	EIT structure within 1 arcmin	SXT structure within 1 arcmin
1N	68.4	−7.1	1.018 ± 0.005	brightening	CH	CH
2N	65.8	−27.2	1.026 ± 0.005	brightening	LIE	enhanced brightness (large loop)
3N	66.9	13.4	1.015 ± 0.005	brightening	CH	CH
4N	62.3	41.5	1.012 ± 0.005	brightening	LID/LIE	CH
5N	56.5	−40.9	1.018 ± 0.005	brightening	LIE	enhanced brightness
6N	55.2	11.1	0.991 ± 0.005	depression	LID	CH
1S	−42.0	27.6	1.025 ± 0.005	brightening	LID/LIE	enhanced brightness
2S	−35.6	40.2	1.024 ± 0.005	brightening	LID	reduced brightness
3S	−48.5	−14.8	1.014 ± 0.005	brightening	LID/LIE nearby	enhanced brightness/CH
4S	−36.6	−2.8	1.014 ± 0.005	brightening	LID/LIE	enhanced brightness
5S	−42.1	−29.1	1.021 ± 0.005	brightening	LID/LIE	enhanced brightness
6S	−31.7	9.1	0.987 ± 0.005	depression	LID	reduced brightness

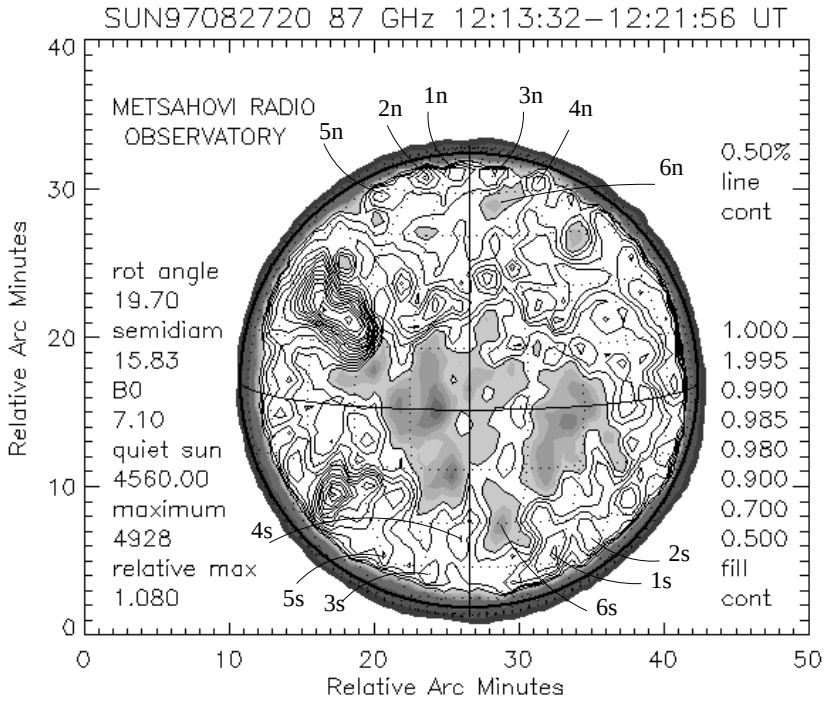

Fig. 23. Solar radio map at 87 GHz (3.5 mm) for August 27, 1997 at 12:13 − 12:22 UT. The greyscale contours (0.5, 0.7, 0.9, 0.98, 0.985, 0.99, and 0.995) represent levels below the quiet Sun. The quiet Sun (level 1.000) is plotted in white color, over which are the enhanced levels plotted in contour lines. The contour line level difference (0.5% of the quiet Sun in this case) is also the flux resolution

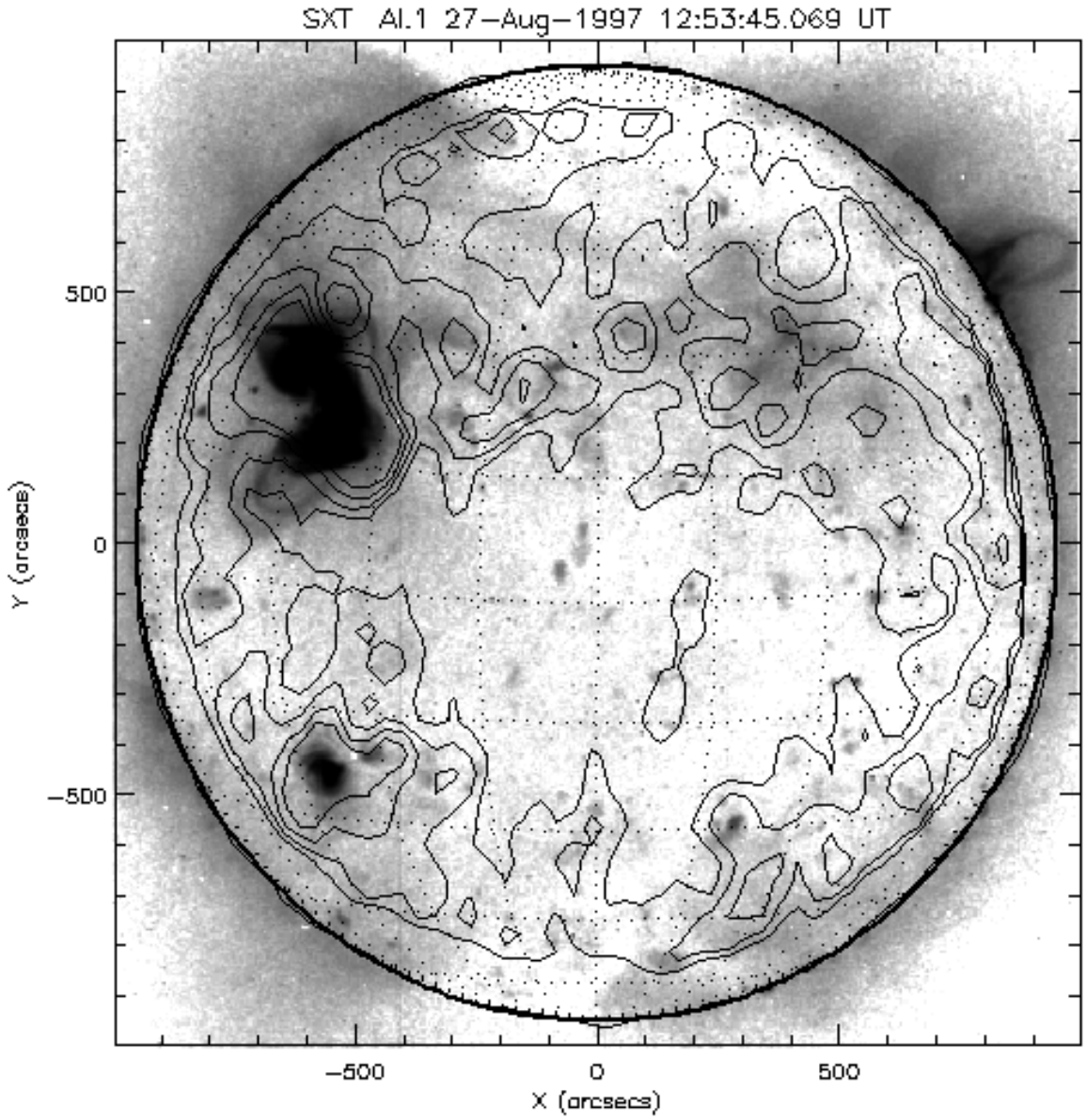

Fig. 24. Yohkoh SXT Al.1 image from August 27, 1997 at 12:53:45 UT (reversed colors). Overplotted are some selected radio contours (above the quiet Sun level only) of the 12:13 − 12:22 UT map

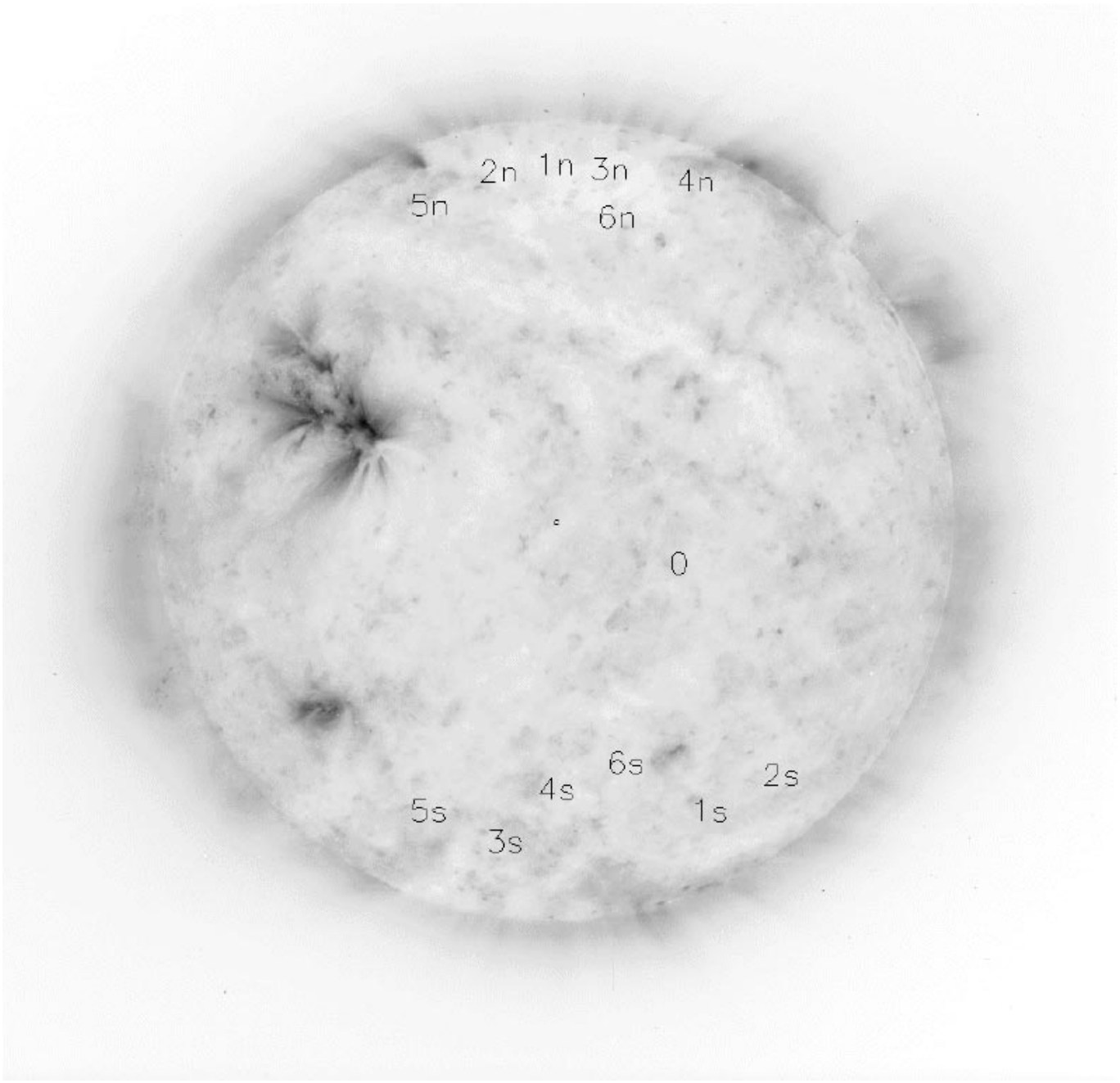

Fig. 25. SOHO/EIT Fe IX/X (171 Å, filter Clear) image for August 27, 1997 at 13:01:03 UT (reversed colors)

Table 11. August 28, 1997: The radio Quiet Sun Level (QSL) was 4480.0 A/D converter count units (1.000 ± 0.005) in the Metsähovi 87 GHz map at 07:16 − 07:24 UT (Fig. 26). The radio source location is within the one arcmin beam. The Yohkoh SXT map was taken at 07:23:28 UT (Fig. 27), and the SOHO EIT He II/Si XI image at 07:18:19 UT (Fig. 28)

Point	Lat Deg	Long Deg	87 GHz Relative Intensity	Radio structure	EIT structure within 1 arcmin	SXT structure within 1 arcmin
1N	64.5	24.3	1.012 ± 0.005	brightening	CH (He II: LIE)	CH
2N	64.3	−10.2	1.023 ± 0.005	brightening	CH	enhanced brightness (large loop)
3N	63.7	−26.9	1.033 ± 0.005	brightening	LID/LIE	enhanced brightness (large loop)
4N	57.6	−40.6	1.026 ± 0.005	brightening	LID/LIE	enhanced brightness (large loop)
5N	54.8	−5.1	1.013 ± 0.005	brightening	LID/BP nearby	enhanced brightness
6N	52.4	20.0	0.992 ± 0.005	depression	LID	reduced brightness
7N	41.1	−3.5	0.996 ± 0.005	depression	LID	reduced brightness
1S	−56.3	22.7	1.006 ± 0.005	brightening	LID/LIE	reduced brightness
2S	−30.4	8.9	1.008 ± 0.005	brightening	LID	enhanced brightness/BP nearby
3S	−25.0	−28.7	1.040 ± 0.005	brightening	AR	AR
4S	−36.5	48.7	1.021 ± 0.005	brightening	LID/LIE nearby	enhanced brightness

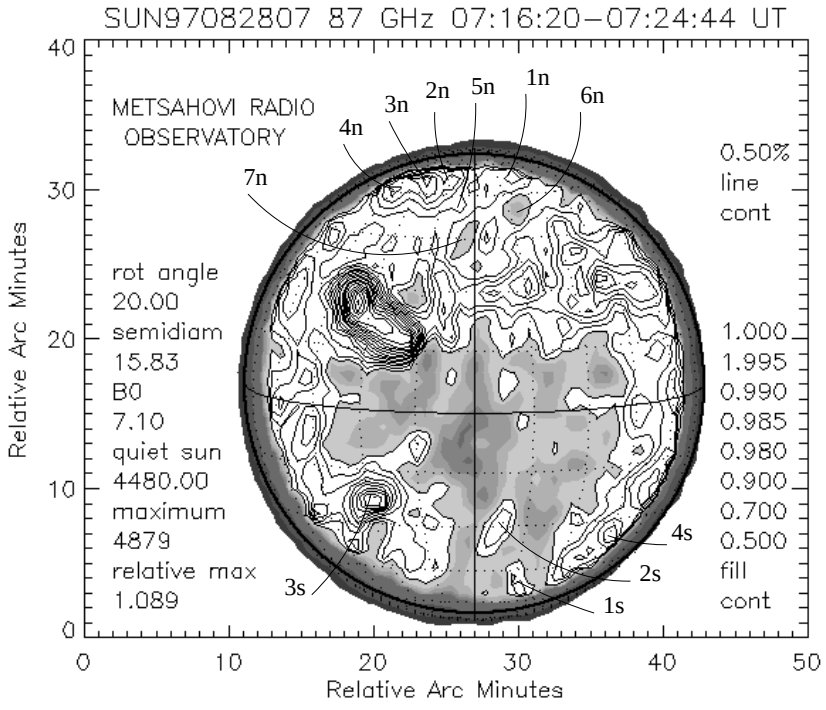

Fig. 26. Solar radio map at 87 GHz (3.5 mm) for August 28, 1997 at 07:16 − 07:24 UT. The greyscale contours (0.5, 0.7, 0.9, 0.98, 0.985, 0.99, and 0.995) represent levels below the quiet Sun. The quiet Sun (level 1.000) is plotted in white color, over which are the enhanced levels plotted in contour lines. The contour line level difference (0.5% of the quiet Sun in this case) is also the flux resolution

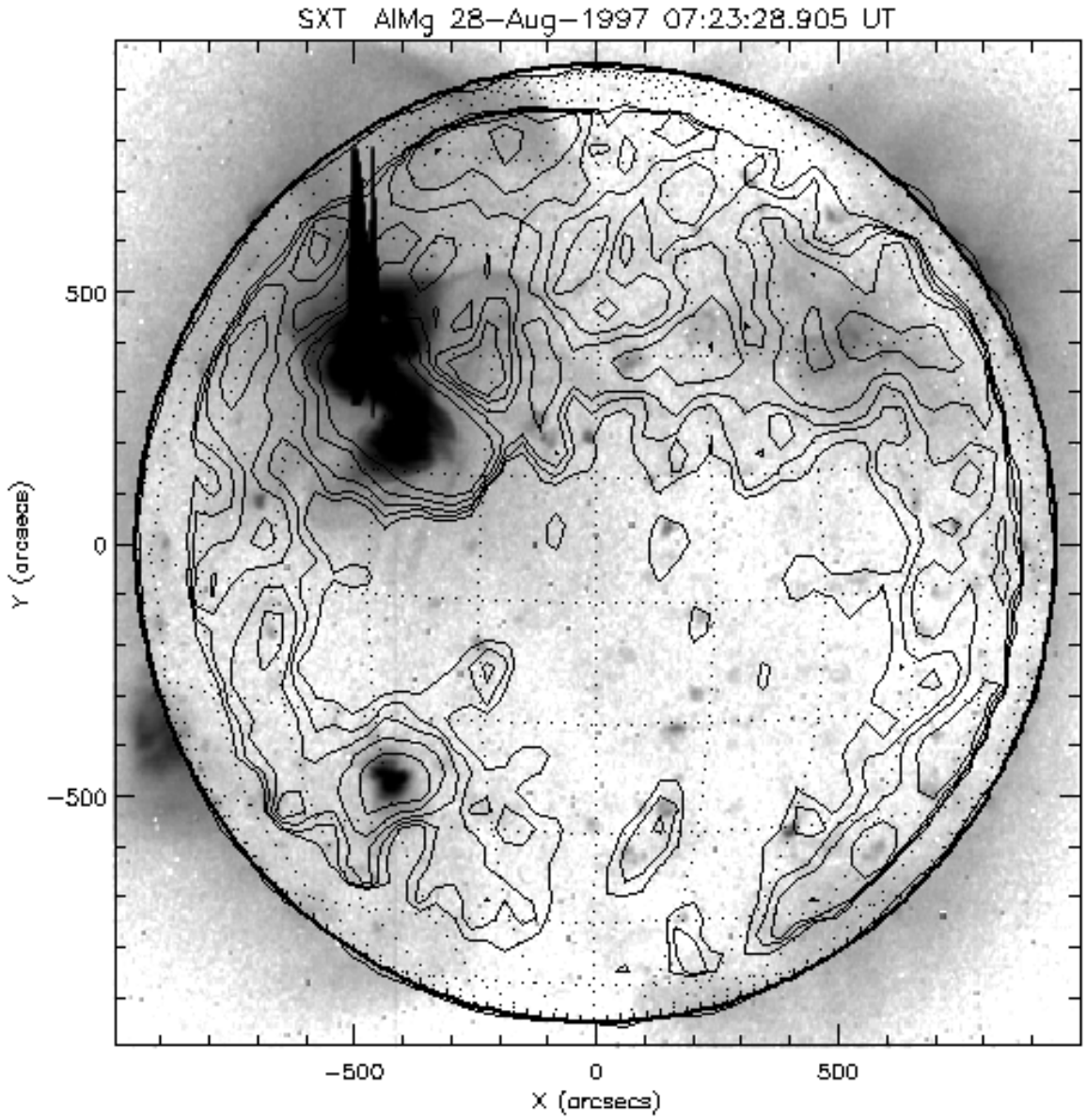

Fig. 27. Yohkoh SXT Al.1 image from August 28, 1997 at 07:23:28 UT (reversed colors). Overplotted are some selected radio contours (above the quiet Sun level only) of the 07:16 − 07:24 UT map

Fig. 28. SOHO/EIT He II (304 Å, filter Clear) image for August 28, 1997 at 07:18:19 UT (reversed colors)

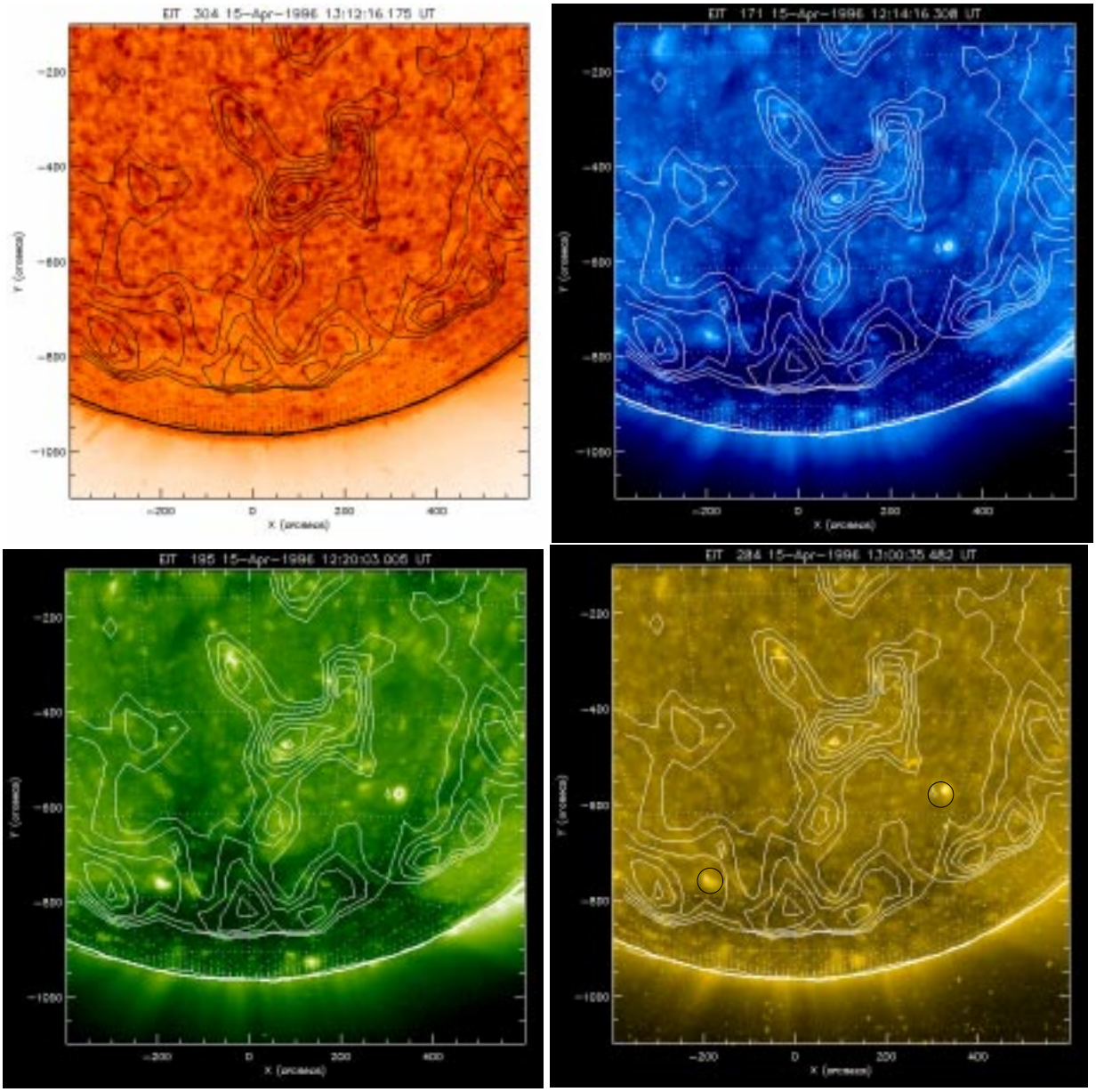

Fig. 29. SOHO/EIT images from the south pole region of the Sun on April 15, 1996: He II (304 Å, $T = 80000$ K, reversed colours) at 13:12 UT (top left), Fe IX/X (171 Å, $T = 1.3$ MK) at 12:14 UT (top right), Fe XII (195 Å, $T = 1.6$ MK) at 12:20 UT (bottom left), and Fe XV (284 Å, $T = 2.0$ MK) at 13:00 UT (bottom right). Superimposed are some selected radio contour lines (white), that show emission above the quiet Sun level (7200 K) at 3.5 mm wavelength at 12:05 − 12:13 UT. The black circles in the Fe XV image (bottom right) show the positions of the EUV and X-ray bright points mentioned in the text. The circles also represent the radio resolution, i.e., a beam size of 60 arcsec. Radio enhancements are seen over the coronal hole and diffuse emission regions, while the EUV bright points only have very faint radio signatures. The same regions are presented in soft X-rays in Fig. 30

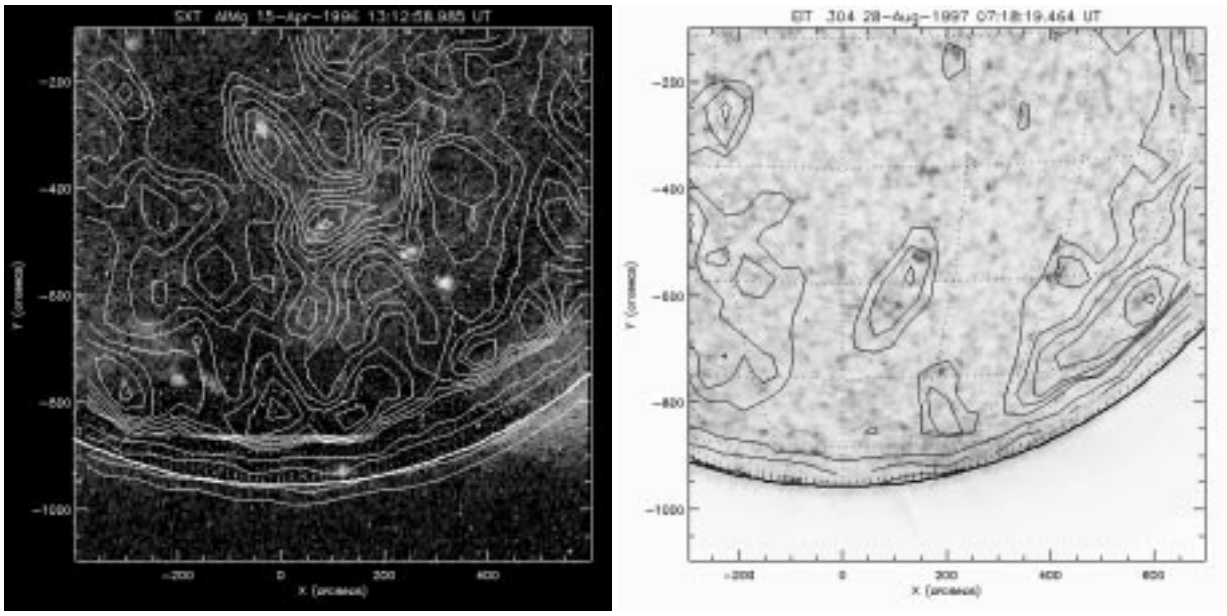

Fig. 30. Left: Yohkoh SXT AlMg image from April 15, 1996, at 13:12:58 UT. The southern coronal hole area is seen in black, and soft X-ray bright points bright. Superimposed are the 3.5 mm radio contours that are above the quiet Sun level, at 12:05 − 12:13 UT. Radio enhancements are seen over the coronal hole area, while the two X-ray bright points (seen in EUV in Fig. 29) only have very faint radio signatures. The emission areas of the two bright points are much smaller in X-rays than in EUV. **Right:** SOHO/EIT He II image on August 28, 1997 at 07:18:19 UT, with the radio map from 07:16 − 07:24 UT superimposed

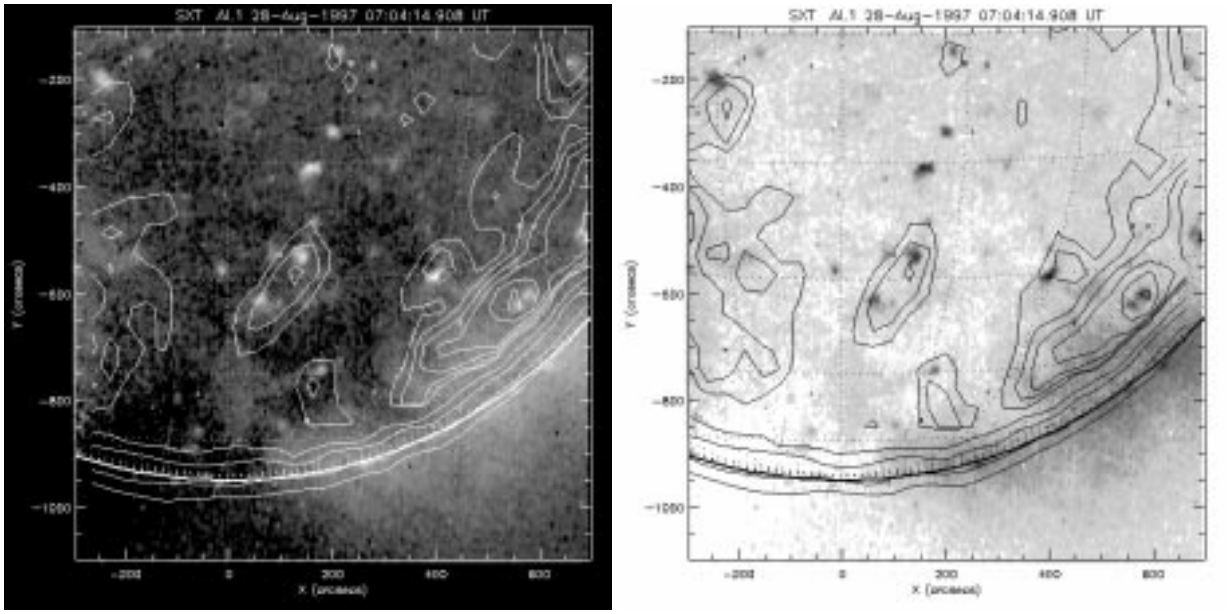

Fig. 31. Left: Radio map observed on August 28, 1997 at 06:56 − 07:05 UT superimposed on the Yohkoh SXT Al.1 image at 07:04:14 UT. **Right**: Radio map observed at 07:16 − 07:24 UT, superimposed on the same Yohkoh SXT map with reversed colors. Radio enhancements are seen in both of the radio maps, at approximately the same locations, that were scanned 19 minutes apart. The enhancements lie over or nearby some X-ray bright points, but the bright point in S16W13 shows no radio emission above the quiet Sun level. Grid spacing in the figure is 15 degrees

V.3 Stabilités des structures

V.3.1 Evolutions

L'article suivant résume l'importance des structures coronales que nous avons étudiées. Comprendre leurs évolutions nécessite de comprendre les critères de leurs stabilités. La formation de CMEs et des éruptions est ainsi discutée.

- **Eit Observations of the Extreme Ultraviolet Sun**
- by MOSES, D.; CLETTE, F.; DELABOUDINIERE, J.-P.; ARTZNER, G. E.; BOUGNET, M.; BRUNAUD, J.; CARABETIAN, C.; GABRIEL, A. H.; HOCHEDEZ, J. F.; MILLIER, F.; SONG, X. Y.; AU, B.; DERE, K. P.; HOWARD, R. A.; KREPLIN, R.; MICHELS, D. J.; DEFISE, J. M.; JAMAR, C.; ROCHUS, P.; CHAUVINEAU, J. P.; MARIOGE, J. P.; CATURA, R. C.; LEMEN, J. R.; SHING, L.; STERN, R. A.; GURMAN, J. B.; NEUPERT, W. M.; NEWMARK, J.; THOMPSON, B.; MAUCHERAT, A.; PORTIER-FOZZANI, F.; BERGHMANS, D.; CUGNON, P.; VAN DESSEL, E. L.; GABRYL, J. R.
- Solar Physics, v. 175, Issue 2, p. 571-599.
- Code ADS : 1997SoPh..175..571M

Cet article résume les résultats obtenus lors la première année de la mission SOHO/EIT. Il reprend ainsi de manière différente certains aspect concernant l'évolution de la couronne 3D (boucles, structures ouvertes et fermées, CMEs) ainsi que des aspects instrumentaux (dégrillage, ...).

EIT OBSERVATIONS OF THE EXTREME ULTRAVIOLET SUN

D. MOSES[1], F. CLETTE[2], J.-P. DELABOUDINIÈRE[3], G. E. ARTZNER[3], M. BOUGNET[3], J. BRUNAUD[3], C. CARABETIAN[3], A. H. GABRIEL[3], J. F. HOCHEDEZ[3], F. MILLIER[3], X. Y. SONG[3], B. AU[4], K. P. DERE[4], R. A. HOWARD[4], R. KREPLIN[4], D. J. MICHELS[4], J. M. DEFISE[5], C. JAMAR[5], P. ROCHUS[5], J. P. CHAUVINEAU[6], J. P. MARIOGE[6], R. C. CATURA[7], J. R. LEMEN[7], L. SHING[7], R. A. STERN[7], J. B. GURMAN[8], W. M. NEUPERT[8,a], J. NEWMARK[8,b], B. THOMPSON[8,b], A. MAUCHERAT[9], F. PORTIER-FOZZANI[9], D. BERGHMANS[10], P. CUGNON[10], E. L. VAN DESSEL[10] and J. R. GABRYL[10]

[1]*Naval Research Laboratory, Washington, DC 20375, U.S.A.*
[2]*Observatoire Royal de Belgique, Brussels, Belgium*
[3]*Institut d'Astrophysique Spatiale, Université Paris XI, 91405 Orsay Cedex, France*
[4]*Naval Research Laboratory, Washington, DC 20375, U.S.A.*
[5]*Centre Spatial de Liège, B4031, Liège, Belgium*
[6]*Institut d'Optique Théorique et Appliquée, 91403 Orsay, France*
[7]*Lockheed Palo Alto Research Laboratory, Palo Alto, CA 94304, U.S.A.*
[8]*NASA/Goddard Space Flight Center, Greenbelt, MD, U.S.A.*
[9]*Laboratoire d'Astronomie Spatiale, Marseille, France*
[10]*Observatoire Royal de Belgique, B-1180 Brussels, Belgium*

(Received 24 March 1997; accepted 17 June 1997)

Abstract. The Extreme Ultraviolet Imaging Telescope (EIT) on board the SOHO spacecraft has been operational since 2 January 1996. EIT observes the Sun over a 45 × 45 arc min field of view in four emission line groups: Fe IX, X, Fe XII, Fe XV, and He II. A post-launch determination of the instrument flatfield, the instrument scattering function, and the instrument aging were necessary for the reduction and analysis of the data. The observed structures and their evolution in each of the four EUV bandpasses are characteristic of the peak emission temperature of the line(s) chosen for that bandpass. Reports on the initial results of a variety of analysis projects demonstrate the range of investigations now underway: EIT provides new observations of the corona in the temperature range of 1 to 2 MK. Temperature studies of the large-scale coronal features extend previous coronagraph work with low-noise temperature maps. Temperatures of radial, extended, plume-like structures in both the polar coronal hole and in a low latitude decaying active region were found to be cooler than the surrounding material. Active region loops were investigated in detail and found to be isothermal for the low loops but hottest at the loop tops for the large loops.

Variability of solar EUV structures, as observed in the EIT time sequences, is pervasive and leads to a re-evaluation of the meaning of the term 'quiet Sun'. Intensity fluctuations in a high cadence sequence of coronal and chromospheric images correspond to a Kolmogorov turbulence spectrum. This can be interpreted in terms of a mixed stochastic or periodic driving of the transition region and the base of the corona. No signature of the photospheric and chromospheric waves is found in spatially averaged power spectra, indicating that these waves do not propagate to the upper atmosphere or are channeled through narrow local magnetic structures covering a small fraction of the solar surface. Polar coronal hole observing campaigns have identified an outflow process with the discovery of transient Fe XII jets. Coronal mass ejection observing campaigns have identified the beginning of a CME in an Fe XII sequence with a near simultaneous filament eruption (seen in absorption), formation of a coronal void and the initiation of a bright outward moving shell as well as the coronal manifestation of a 'Moreton wave'.

[a] Present address is SEL/NOAA 325 Broadway, Boulder, CO 80303, U.S.A.
[b] Space Applications Corp.

Table I
EIT bandpasses

Wavelength	Ion	Peak temperature	Observational objective
304 Å	He II	8.0×10^4 K	chromospheric network; coronal holes
171 Å	Fe IX, X	1.3×10^6 K	corona/transition region boundary; structures inside coronal holes
195 Å	Fe XII	1.6×10^6 K	quiet corona outside coronal holes
284 Å	Fe XV	2.0×10^6 K	active regions

1. Introduction

EIT is a new approach for imaging the EUV Sun on an extended spaceflight platform (Delaboudinière *et al.*, 1995). Normal incidence multilayer optics are used to image the Sun on an EUV sensitive 1024 × 1024 format charge coupled device (CCD) camera. With a telescope focal length of 1.652 m and a pixel size of 21 μm × 21 μm, the plate scale of the EIT images is 2.6 arc sec per pixel. The optics are divided into quadrants of matched multilayer pairs that are tuned to bandpasses selected for observation of the chromosphere and corona at all phases of the solar cycle. The quadrants are isolated by a rotating mask that permits only one bandpass to view the Sun at a time.

Images from the synoptic program are presented in Figure 1. The full details in these images are inadequately represented in the reduced journal prints, so full resolution digital images are included in the CD-ROM accompanying this volume. The in-flight observations of solar structures match the predictions of Table I (Delaboudinière *et al.*, 1995):

– The Fe IX, X image is generally less structured than the other coronal channels. Diffuse, unresolved emission is present over most of the quiet Sun, including coronal hole regions. Open field structures are seen in this bandpass as well as closed structures. Active region structures, as seen in this channel, are more confined to the core of the active region. Active region loops are narrow structures that in many cases are only filled at the base. These partially filled loops are similar to the 'spiky' Ne VII and Mg IX active region structures observed by *Skylab* (Sheeley, 1980; Webb, 1981). The primary difference is that the Fe IX, X structures do not appear to become narrower with height. A region of supressed emission is frequently observed surrounding an active region. X-ray bright points (XBP) are the most numerous in this channel (by 10%). Detection of faint structures in the Fe IX, X channel is more difficult than in the other coronal channels due to the relative intensity of the quiet corona (including coronal holes).

– The Fe XII image is more dominated by the closed field regions of the quiet-Sun. All but the hottest active region loops are visible in this wavelength. As in the Fe IX, X channel, some active region loops appear to only be partially filled. The appearance of some active regions in Fe XII is that the loops diverge more

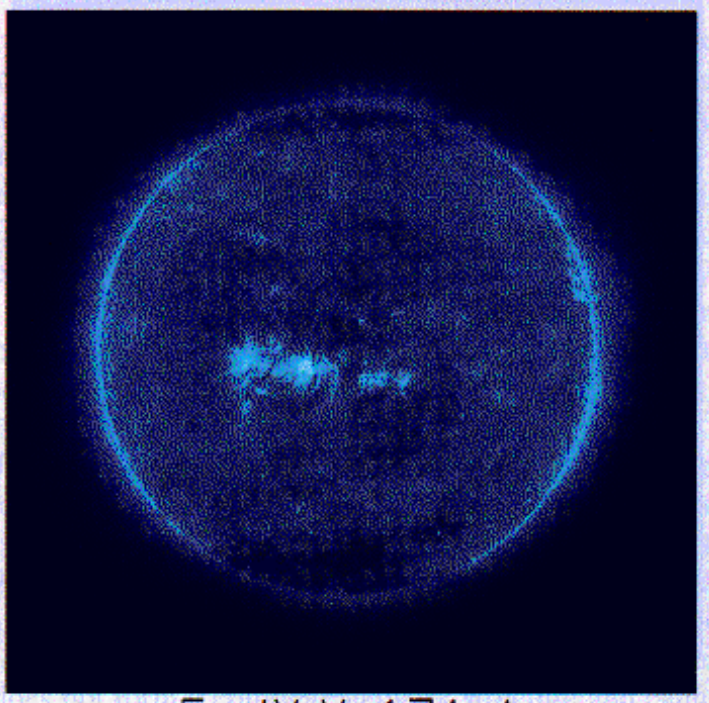

Fe IX,X 171 A

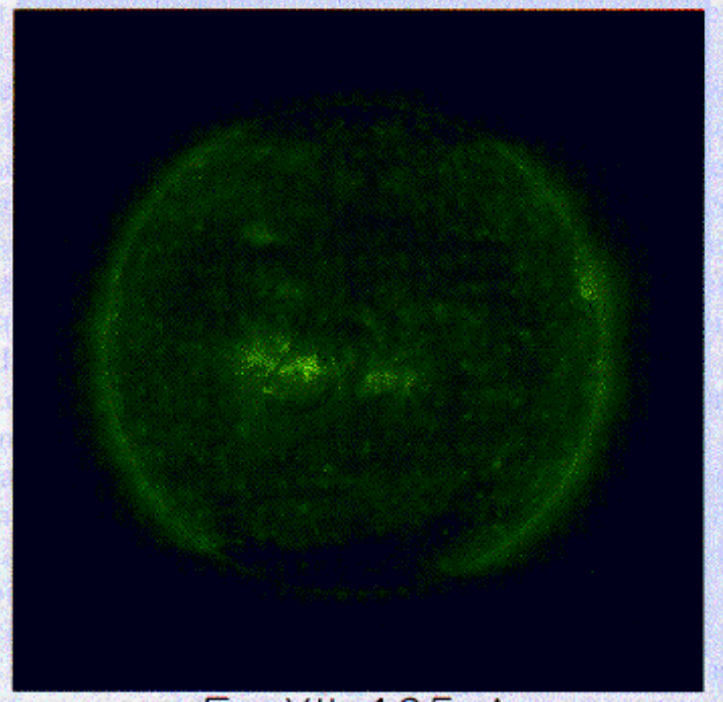

Fe XII 195 A

Figure 1a.

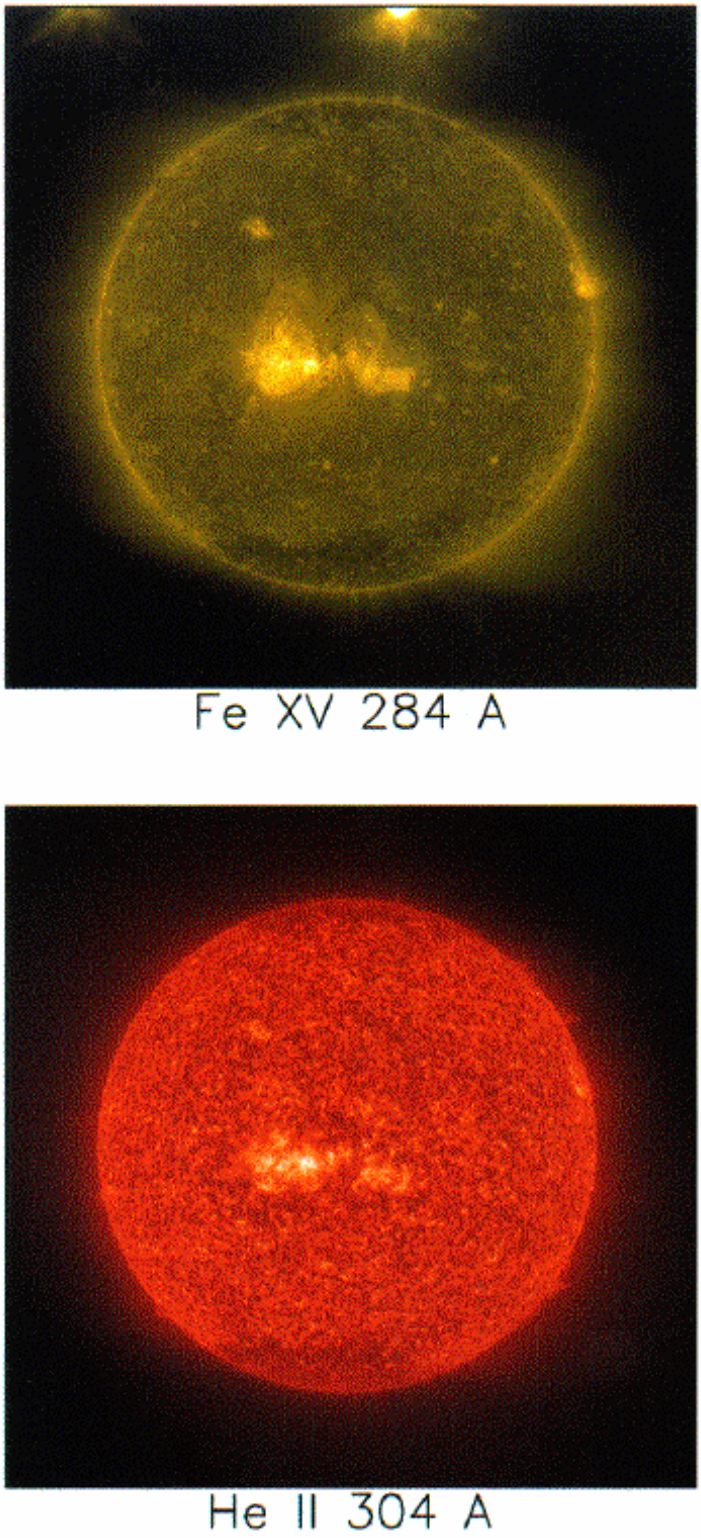

Figure 1b.

Figure 1. EIT synoptic images for 12 May 1996. Solar north is oriented up in this figure.

than higher-temperature active region loops (Fe XV and *Yohkoh* SXT). However, application of the technique of Klimchuk *et al.* (1992) on an isolated loop resulted in the same constant cross section for that loop as found at higher temperatures (Klimchuk, Moses, and Portier, 1997). Coronal holes are most easily visible in this channel because of the contrast between the emission intensity of the open field region and the closed field quiet Sun. Similarly, XBPs are most easily identified in this channel because of the contrast between the emission associated with the XBP magnetic bipole and the emission associated with the relatively weaker quiet-Sun magnetic regions or the coronal hole open field regions. Because of the high contrast and the high sensitivity to quiet Sun structures of the Fe XII channel, it is frequently used for movies of coronal evolution.

– The Fe XV image is dominated by the hot loops (e.g., active region loops). Of all the EIT observations, these most closely compare with the *Yohkoh* SXT images. Outside the active regions, this emission is obvious in the X-ray bright points, regions of erupting filaments and large-scale height loop structures. The large-scale height structures are best visible above the limb. In quiet Sun regions, there is also low level structure in Fe XV that maps out some of the internetwork field structure. The quiet-Sun Fe XV structure is not leakage of the He II into this channel as it does not form a complete network structure and cannot be removed by a normalized subtraction of a He II image. Instead, it is the high temperature component of the more general, diffuse emission seen in the other coronal channels. Also apparent in this channel is a visible light leak at the north edge of the field of view which is discussed in Section 3.

– The He II image is dominated by the transition region network structure. Bright network elements are visible throughout the region of closed loop structures. The coronal holes are marked by a reduction in the He II network elements. Active regions are generally bright in the He II image with a blending of Si XI emission. A region of supressed emission is frequently observed immediately around the active region enhancements. Macrospicules are apparent in the open field regions and along some large-scale closed regions. They are apparently aligned with the direction of the magnetic field. Prominences are always present. Filaments are slightly more difficult to identify because the contrast of the absorption features is frequently comparable to the contrast of the network structure.

Intercomparison of the images from the different coronal channels shows that, with increasing temperature, the plasma is more structured. As will be discussed in section 2.2, with increasing temperature for all channels, the emission exhibits greater variability with solar activity (time).

Detailed comparison of quiet Sun regions of coronal images and the He II images (e.g., Figure 11 in Section 3.2) shows that there is a transition region enhancement for every enhancement of coronal emission, but not the converse. This is in agreement with previous comparisons of X-ray bright points and He I 10830 Å emission (e.g., Moses *et al.*, 1994). With the availability of near-continuous photospheric magnetic field data from SOHO, the assumption that the relationship

between the coronal counterparts of transition region features and the connectivity of the magnetic field can now be addressed.

A comparison of the appearance of prominences and filaments in the four EIT channels can be made from Figure 2. On the equator, the prominence is aligned primarily perpendicular to the line of sight. This structure can be seen in absorption in the coronal channel due to a combination of H I, He I and He II continuum absorption (Cheng, Smith, and Tandberg-Hanssen, 1980; Fonkal, 1978; Schmahl and Orrall, 1979). The prominence in the south east can be seen to extend onto the disk as a polar crown filament in the He II as well as in the coronal channels. There is a coronal void around this prominence which reflects the temperature structure of the corona and is not due to absorption. The amount of absorption in the coronal lines depends upon the observed wavelength, the overall geometry of the observation, the relative elemental abundance, the density and the ionization balance of the cool material and thus can be used as a diagnostic of the plasma parameters of prominences.

2. Instrumentation

To move beyond a descriptive analysis of the data, several instrument issues must be addressed. These issues were either impossible to resolve pre-launch or their importance was not appreciated before the initial analysis began. This work has taken a large part of the EIT consortium effort during the first year of operations.

2.1. Imaging

The images obtained in-flight by EIT are consistent with the assertion by Delaboudinière *et al.* (1995) that the instrument resolution is limited by the plate scale of the CCD. Analysis of the off-disk images raises interesting questions about the extended distribution of He II in the solar atmosphere (Delaboudinière, 1998). In order to quantify these observations, the wings of the point response function (PRF) must be known in the EUV to better than the dynamic range of the CCD (1:5000). The PRF has been evaluated with wavefronts obtained with Zygo interferometer measurements of the telescope in each quadrant. The wavefronts obtained at 6330 Å were converted into optical path differences to obtain the complex pupil function. The Fourier transform of the complex pupil function gave the point spread functions of the optics in the four EUV wavelengths. The system PRF was obtained after convolution with the pixel size. Figure 3 is a plot of 2 perpendicular cuts in the PRF determined by the wavefront analysis for the 284 Å quadrant. (N.B. The quadrant structure of the telescope entrance pupil produces an asymmetric PRF.) To verify the Zygo measurements with measurements in the EUV, modifications were made in the IAS calibration facility in an attempt to produce a point source in the EUV with large angle scattering less than the level to be measured. The

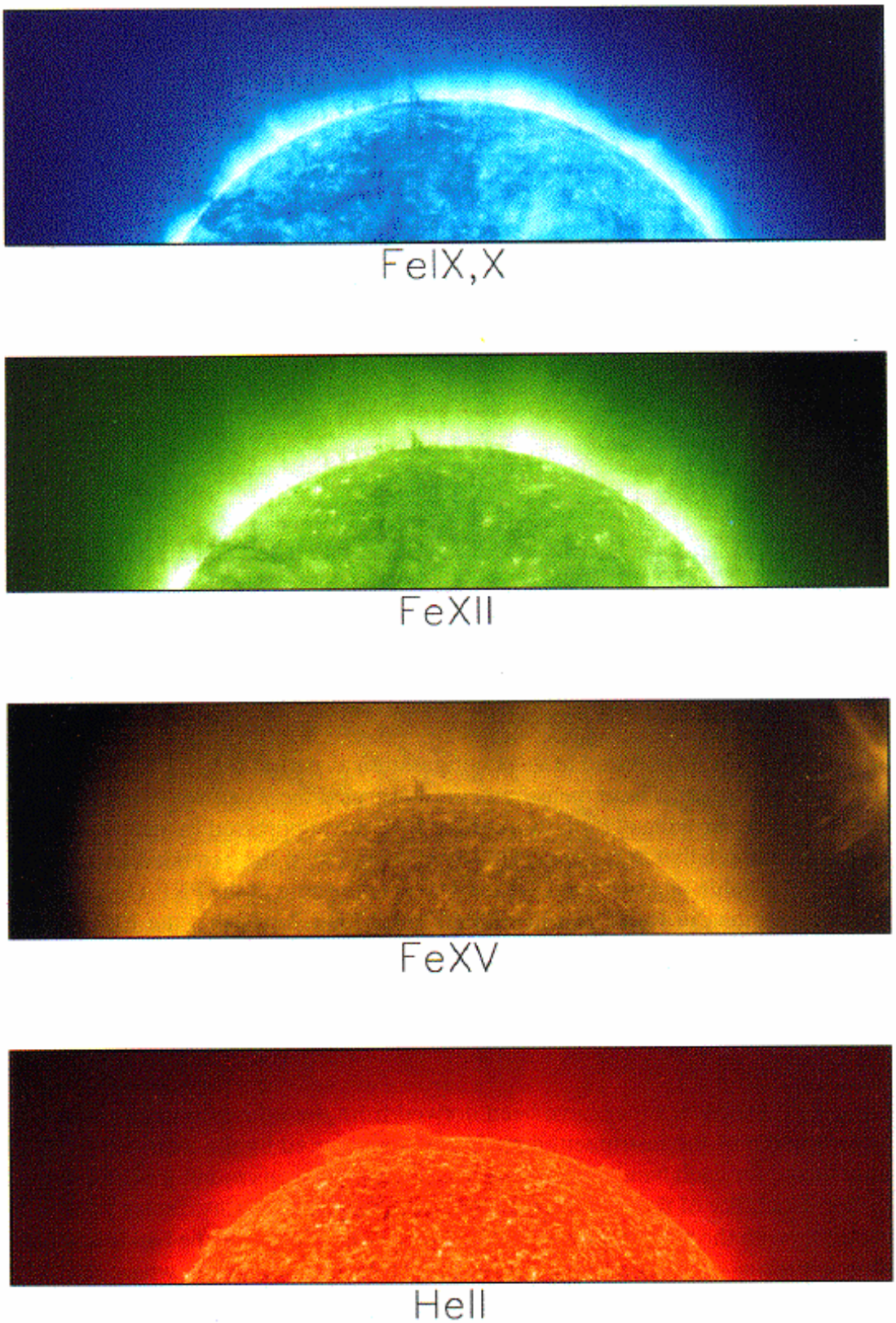

Figure 2. H I, He I, and He II absorption features in the EUV coronal images of the east limb on 28 February 1997.

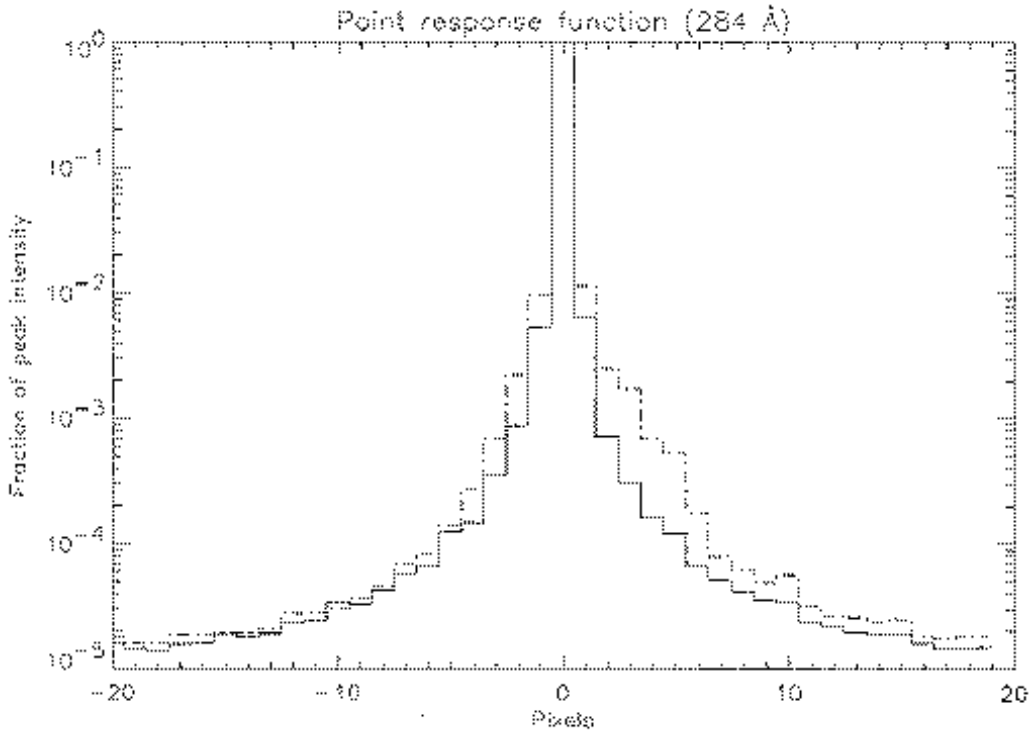

Figure 3. EIT extended point response function for the 284 Å quadrant from a wavefront analysis. The two lines represent perpendicular cuts through the peak of the response.

spare EIT optics were tested in this configuration as part of the EIT Calroc sounding rocket program. These measurements confirmed the Zygo wavefront analysis result that the far wings (1 arc min) of the PRF are suppressed by nearly 5 orders of magnitude relative to the core. However, vibration in the extended IAS facility prevented reliable measurement in the EUV near the core of the PRF. Observations of active regions in Fe XV just behind the solar limb verify that the EUV scatter measurements at IAS overestimate the spread of the PRF near the core.

2.2. EUV Response

Optimized exposure times have been derived from the inflight images (Table II). The variation of the instrument throughput is monitored by the total flux in a full field image for each bandpass (Figure 4). The utility of this monitor is determined by the variability of the solar flux in each waveband. The intrinsic solar variability increases with the temperature of the dominant emission line in the bandpass. Thus the monitor is very good for the He II and the Fe IX, X channels where the solar variability is low, while it degrades for the Fe XII channel and is poor for the Fe XV channel where changes in the instrumental response are masked by solar changes. Since the extremes of the wavelength regime are 171 Å (Fe IX, X) and 304 Å

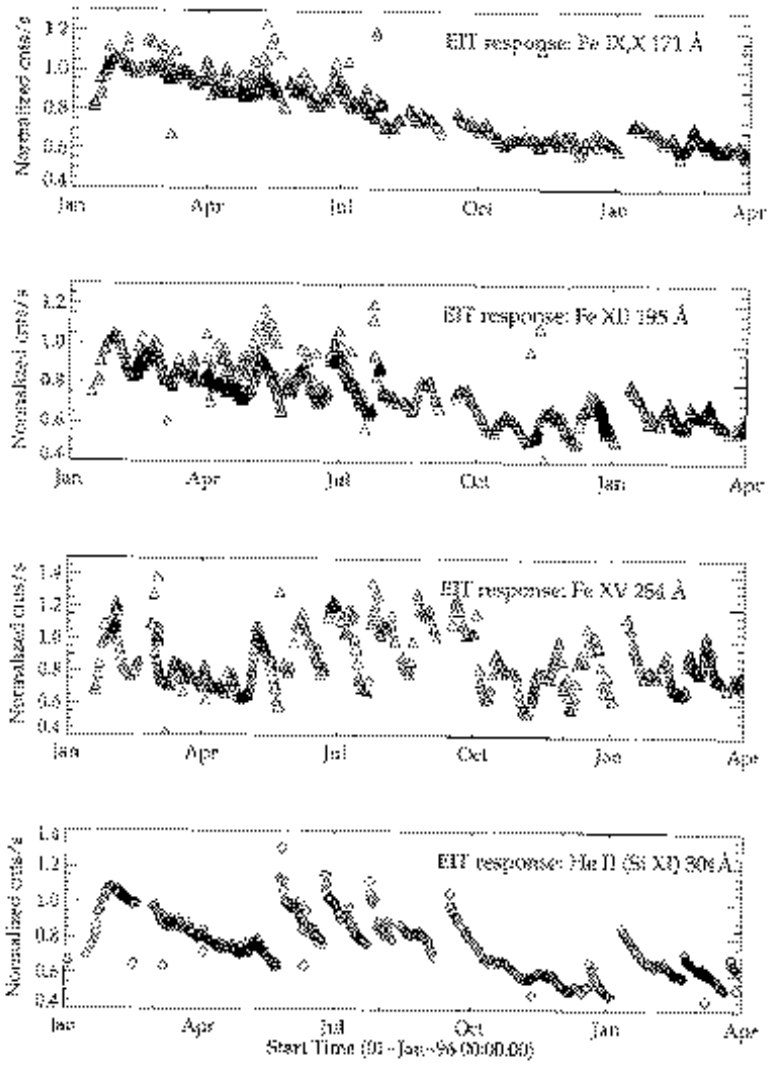

Figure 4. EIT response: total flux in each channel.

Table II
Nominal exposure times

Channel	Quiet Sun	Low activity	High activity
He II	32 s	25 s	18 s
Fe IX, X	7 s	5.5 s	2 s
Fe XII	12 s	9 s	4 s
Fe XV	102 s	62 s	47 s

(He II), this technique allows the full wavelength dependence of the degradation to be monitored.

Since the 304 Å radiation has the lowest penetration depth (range) of the wavelengths observed, the He II channel is the most sensitive to degradation asso-

Table III
EIT CCD temperature cycle history

Action	Date and Time	Duration
Heater on	1996 23 May 19:21	45 hr
Heater on	1996 23 June 19:10	24 hr
Heater on	1996 23 July 15:48	2.5 hr
Heater on	1996 5 Aug 18:50	15 hr
Heater on	1996 9 Aug 15:05	71.5 hr
Heater on	1996 6 Sep 19:49	236 hr
Heater on	1996 19 Dec 13:14	2.5 hr
Heater on	1997 3 January 21:50	156 hr
Heater on	1997 20 February 21:57	13 hr

ciated with evolution of surfaces and best illustrates the operative processes. The initial increase in response over the first month of observations is attributed to an overall cleanup of the optical surfaces and detector from the contamination associated with the launch and early spacecraft operations. Subsequently the response declined exponentially with an e-folding time of 210 days. In order to reverse the decline, the CCD was heated to 18C on 23 May 1996. Initial recovery was to the highest throughput observed in flight. Subsequent response declines have a shorter e-folding time (85 days) than the initial February to May interval. Successive heat cycles were conducted according to the requirements of the observing schedules and in exploration of the causes of the decline (Table III). An instrument failure occurred on 29 July that left the shutter open in the 304 Å channel for 7 hours. The total instrument response immediately declined 10 to 20% following this exposure. The response degradation was not uniform. Instead the degradation was patterned in proportion to the EUV exposure.

The degradation process consists of several components which are difficult to separate in detail. The two basic processes contributing to the degradation are (1) the absorption of EUV before it interacts with the CCD by a surface contaminant and (2) the reduction of charge collection efficiency (CCE) in the CCD due to EUV induced device damage.

The condensation of contaminant on the CCD is expected since the detector is one of the coldest surfaces in the instrument. In anticipation of in-flight contamination, (1) a cleanliness program was maintained in the construction of the instrument and (2) heaters for the CCD were included in the design. Accumulation of contamination at a constant rate will result in an exponential decline in response. If no polymerization of an organic component is involved, then the condensate will evaporate rapidly during temperature cycling. The straylight baffling around the CCD unfortunately reduces the vacuum conductance out of the vicinity of the CCD so that further outgassing during a temperature cycle is not feasible.

Reduction of the CCE is probably caused by the charging of the native backside oxide and the generation of interface trap sites. Since each interacting EUV photon generates more than one electron, the CCE can be determined by the comparison of the observed signal to the photon shot noise (Janesick, Klassen, and Elliott, 1987). The limitations of this approach are significant, but the degradation of the device for the 29 July event has been demonstrated to be totally CCE degradation. The proportion of the cumulative degradation from ordinary operations which can be attributed to CCE degradation is discussed in Defise *et al.* (1997). Although self annealing is observed, the rate of self annealing is dependent on the device temperature and possibly the level of prior damage. The self-annealing process during temperature cycling is at best 100 times slower than the condensate reversal.

2.3. Flat-Field Corrections

Spatial variations of the instrument response across the field of view must be corrected before performing almost any quantitative analysis of EIT images. These non-uniformities are produced by several independent contributions. Some of these flat-field components were known before SOHO launch, like the optical vignetting, the CCD flat-field and the grid pattern produced by the focal aluminum filter. However, the grid pattern could only be accurately measured after launch, using in-flight solar images. Moreover, during the course of the mission, two unpredictable artifacts appeared: a light leak affecting mainly the Fe XV images and a radiation induced non-uniform degradation of the CCD response. The characteristics of these last components can only be indirectly deduced from the affected solar images themselves, which limits the accuracy of any reconstruction due to the incomplete or distorted information available from flight data. Consequently, the ambitious 1% target for the accuracy of each flat-field component will not be met for some of them.

2.3.1. *The CCD Flat-Field*

A CCD flat-field calibration at EIT's working wavelengths was obtained on the ground with a monochromatic beam of synchrotron radiation using the method developed by Kuhn, Lin, and Loranz (1991). This analysis has been extended from the initial work reported in Delaboudinière *et al.* (1995). Figure 5 shows large-scale trends of the CCD flat field. Of particular interest is the steady gain enhancement towards the sensor edges, that reaches an amplitude of 10 to 15%. This last feature went unnoticed in a first partial analysis (Delaboudinière *et al.*, 1995). The accurate determination of these large-scale variations required special care, as the Kuhn, Lin and Loranz algorithm can produce false linear trends when intensities in the input images are improperly scaled. The accuracy of calculated large-scale variations was verified, but any residual edge-to-edge slope cannot be determined to better than about 10%. At smaller spatial scales, the accuracy of the results is close to 1%.

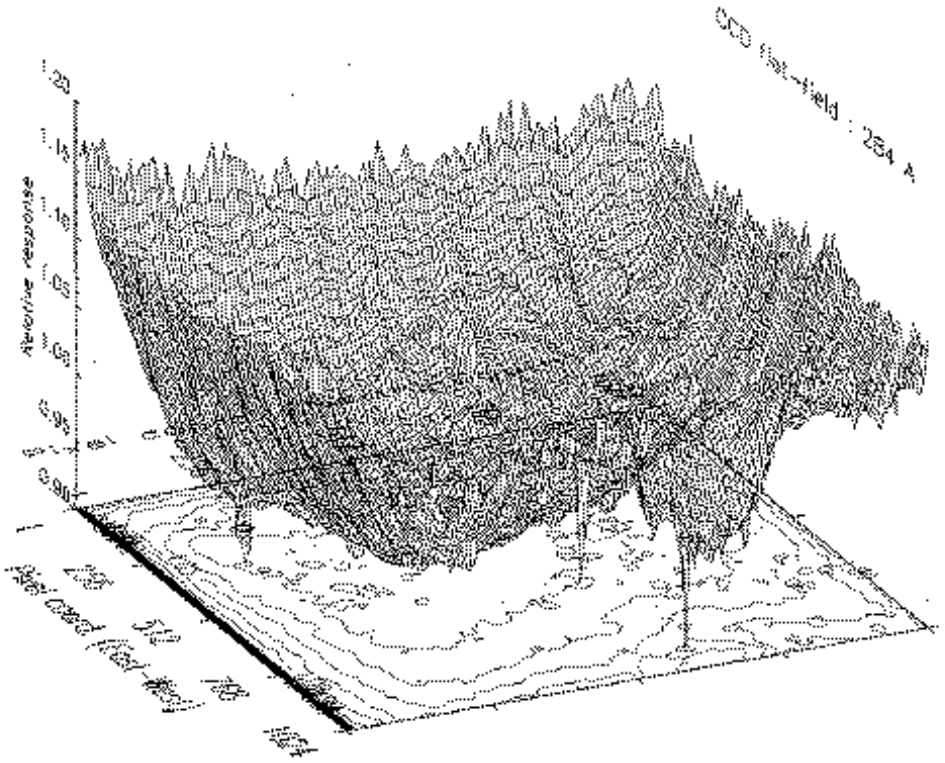

Figure 5. Three-dimensional plot of the CCD flat-field, showing the amplitude of the large-scale gain variations. The original map was smoothed over a 24 × 24-pixel domain to suppress local fluctuations.

Although the flat-field shows little change with wavelength, a systematic 10% increase in the amplitude of the defects can be measured from 171 Å to 304 Å. A comparison of the ground-based flat-fields with those deduced from the in-flight solar images shows a very good agreement over most of the sensor. However, significant discrepancies are observed inside some of the larger blemishes. Contaminants apparently interact preferentially with the surface defects. This could be interpreted in one of two ways: (1) the defects act as condensation nuclei or seeds for microcrystal formation or (2) the electronic properties of the defects are activated by chemical interaction with the condensate. Further analysis is needed to reconcile both measurements over the whole CCD within the 1% accuracy of the calculation. However, if we exclude the radiation induced aging described below, no change of the intrinsic CCD flat-field was detected in in-flight images during the first year in space.

2.3.2. *The Al-Filter Grid Pattern*

One of the redundant aluminum filters used to block long-wavelength radiation (mainly visible light) is located 14.5 mm in front of the CCD detector. Such Al filters are mechanically supported by a nickel grid (Delaboudinière *et al.*, 1995) which casts a shadow on the CCD. The finite extent of the asymmetrical entrance pupil of the telescope produces a smoothed out-of-focus pattern. The resulting

periodic intensity modulation, with an amplitude of about 15%, proved to be the main flat-field artifact. Another set of filters is located on a filter wheel, 35 mm in front of the CCD. When an additional Al filter is selected on the filter wheel, it produces an additional grid pattern, with different characteristics, as it is located at a larger distance from the focal plane.

In order to extract the grid pattern from the solar images themselves, we relied on the fact that the pattern is purely periodic, while the spatial distribution of the intensity on the EUV Sun is essentially random (Note that the Sun acts as a noise source in this problem). The extraction process consists of the following steps:

– Full-field full-resolution daily synoptic images are averaged over a period of several weeks (rotational averaging of activity features). The sensor noise is also reduced by this averaging.

– The average image is then submitted to a non-linear filtering: a running 2-dimensional median filter is applied to 5×5 pixel sets, with a 21-pixel spacing between sampled pixels in both dimensions. As this 21-pixel interval is a close approximation of the grid period, the filter selectively amplifies the grid signal relative to all other spatial fluctuations in the image, i.e., it acts as a morphological filter.

– The Fourier transform of the resulting image reveals about 30 peaks, corresponding to the harmonics of the grid pattern. Two numerical filters are then applied in the frequency domain : suppression of the low-frequency f^{-1} noise background (subtraction of a smoothed average radial profile) and rejection of high-frequency noise in regions where no harmonics are present (square domains with cosine edge tapers).

– An inverse transform is finally applied to the filtered spectrum to reconstruct a cleaned image of the grid modulation.

The resulting pattern has the regularity and uniformity expected from the grid specifications (mesh period: 440 μm, mesh width: 40 μm). The grid is detected up to the very corners of the field of view, despite the very low signal levels in that part of the solar images. The grid corrections, which are now integrated in the EIT image display software, are accurate to about 1% over most of the field of view.

Diffraction calculations indicate a slight wavelength dependency, with a 5% increase of the modulation amplitude between 171 and 304 Å. However, the 90° rotation of the pattern for each EIT bandpass, following the changing orientation of the entrance pupil, produces most of the observed differences. Comparative measurements do not reveal significant temporal changes in the grid pattern since the beginning of the mission.

2.3.3. *Filter Pinholes and Visible-Light Leak*

Two light leaks were discovered early in the mission. They affect mainly the Fe XV and also to a lesser extent (50 : 1) the Fe IX, X images in the 'Clear' filter wheel position. Both leaks are located near the northern edge of the images and consist a bright featureless core surrounded by fainter halos containing sharp rays and

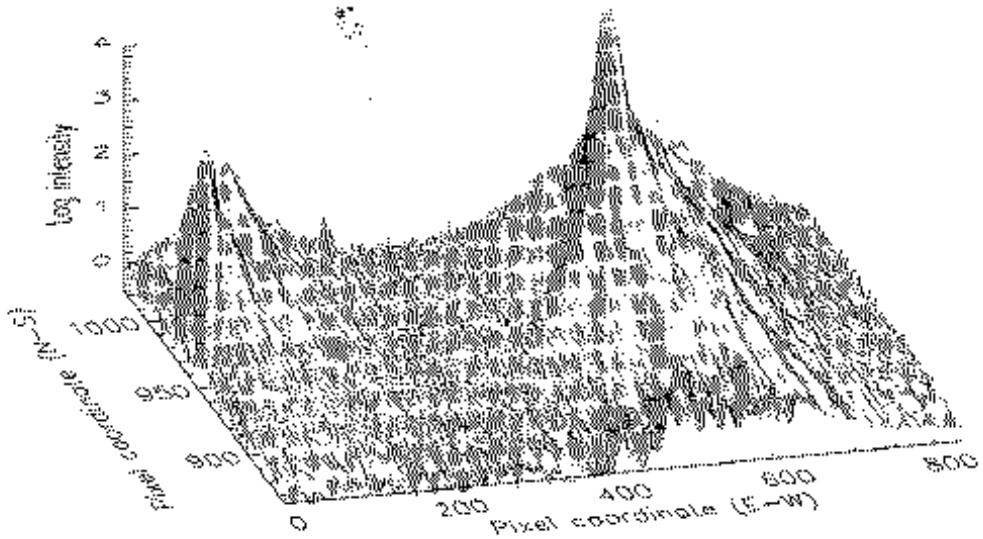

Figure 6. Two-dimensional distribution of the stray-light intensity produced by the light leaks in the 832×160 upper left area of the field of view, at 284 Å. To compensate the large intensity range between the core and faint extensions, several stepped exposures were combined and a logarithmic intensity scale is used. The intensities are scaled here according to the raw sensor output signal for a 10 s exposure.

extending up to 150 pixels from the core (Figure 6). No leak is detected in the Fe XII and He II images.

These leaks can be attributed to minute pinholes at the edge of the focal Al filter, and the light passing through these holes has been unambiguously identified as visible light reaching the CCD by study of the statistical fluctuations (photon shot noise dominated) of the signal. The visible light pattern is superimposed on the EUV solar image. The presence of visible light reaching the focal filter further implies the existence of visible light leaks in the entrance Al filters. Considering the large visible/EUV flux ratio and the limited intensity reaching the focal plane, both filter defects must affect only a small fraction of the filter area. These degradations probably occurred during SOHO's launch. The relative intensity of those leaks (50 : 1) at each of the two wavelengths, i.e., at each sector position, allow us to deduce that the tear in the front filter is located in the Fe XV sector near the edge adjacent to the neighboring Fe IX, X sector.

Being very bright and located in the dim and fairly uniform polar corona, this additive component can be extracted with a high accuracy from the Fe XV images. No significant changes in the pattern were observed in the course of the mission.

2.3.4. *Spatial Distribution of Radiation Induced Aging*

A degradation of the CCD response is induced by the radiation dose received by the detector, as explained in Section 2.2. As the average EUV intensity in the coronal and transition region images is highly non-uniform, the calculated flat-field is distorted by strong residuals of local solar activity features, especially outside the

disk area. Figure 7 illustrates the distribution of the radiation damage as it appeared in mid-December 1996. While the response remains largely unaffected far from the solar limb, the degradation is strong (50% in this case) over the solar disk, in the form of a negative imprint of an average solar disk. A slight limb darkening can be recognized as well as a single grid pattern, which coincides with the 304 Å (He II) grid pattern. All these properties indicate that most of the degradation was primarily produced by the long-wavelength radiation at 304 Å, with significantly less contribution from the exposures made in all three coronal lines. (The Fe XII and Fe IX, X exposures are at shorter wavelengths, and the total dose in the Fe XV is low in comparison to the other channels). Moreover, the localized damage due to the active region located near the S–E limb at the time of the 29 July 1996 shutter failure can also be recognized. The largest damages are found within this region, where the response falls to about 20% of its average value on the rest of the disk. Finally, as the radiation damage is averaged over long periods, the changing apparent solar radius produces a smoothed limb profile. As the integrated damage always lags behind the actual solar radius, this can produce a spurious limb brightening or darkening in uncorrected images.

The successive CCD bakeouts carried out since late May 1996 have shown that the damage can be partly cured by this method (cf., Section 2.2). However, the degree of recovery is variable over the field of view and also from one bakeout to the next. Indeed, from the limited information derived from the few bakeouts executed so far, we can already deduce that the CCD response is affected by different radiation-induced mechanisms having different properties. The magnitude of each effect also depends on the time span separating successive bakeouts and their response to bakeout is strongly variable. Some components disappear completely in a few hours (e.g., small off-limb effects), while others remain relatively unaffected (e.g., active region blemish).

Two techniques are now available to monitor changes in the spatial evolution of the radiation damage:

– Reconstruction of the EUV response from sets of solar images. An adaptive median filtering is applied, which again makes use of the rotational averaging effect. This the only way to extract the true EUV response. However, the accuracy of the reconstruction is low, due to the permanent changes in the solar images.

– Calibration lamp images. In this case, a diffuse illumination is provided by a lamp located next to the CCD. This illumination proved to be very stable with time, but it falls in the visible and near-infrared wavelength ranges. The CCD response can be very different at these long wavelengths, and comparisons with EUV results have even shown that some components affecting the EUV response escape detection in the calibration lamp images.

Considering their respective drawbacks, both approaches must be combined to improve the accuracy of the reconstruction. However, in view of the continuous evolution of this aging effect, it might be difficult to reach an accuracy better than 5%. For instance, preliminary EUV – visible comparisons also hint at the super-

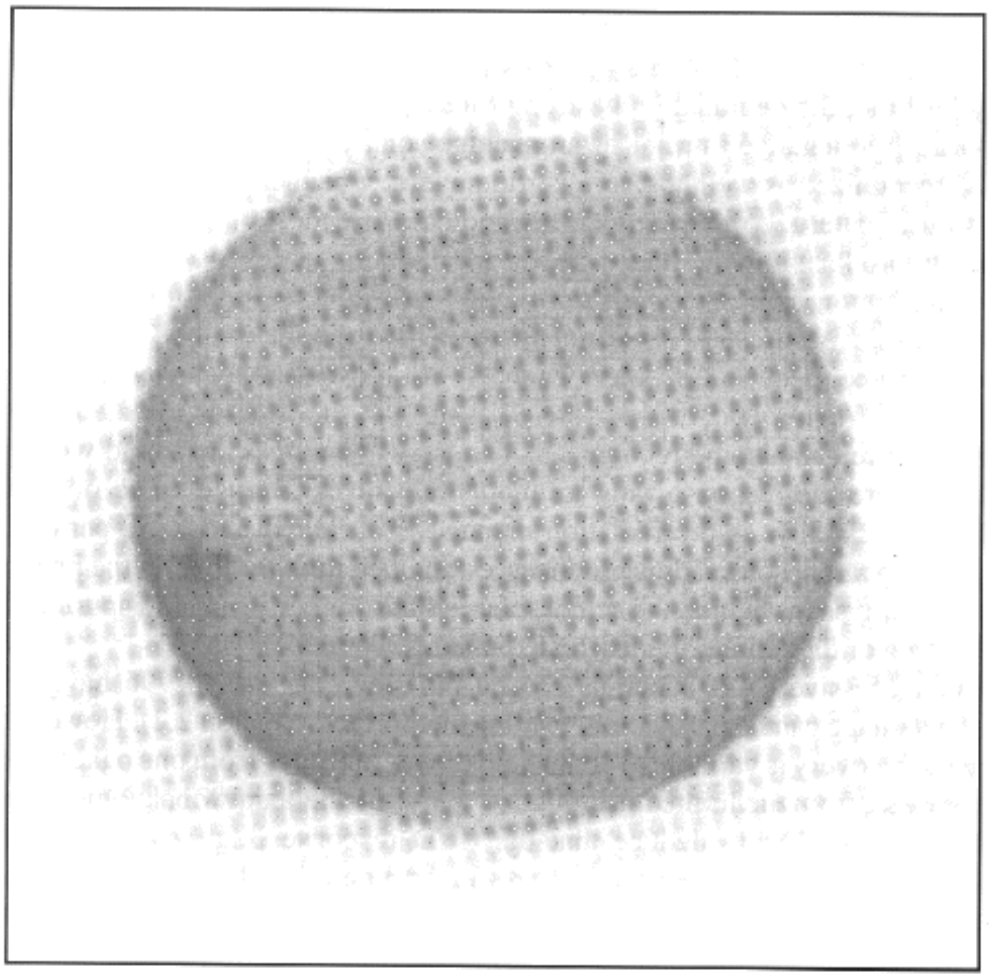

Figure 7. Distribution of the radiation induced aging of EIT's CCD sensor on 19 December 1996. This image was obtained by taking the ratio between calibration lamp images made in December 1996 and June 1996, when the response was still almost uniform.

position of different factors affecting differently the detector sensitivity in either wavelength range. Further analysis is in progress and should help in the identification of the underlying physical mechanisms (opacification of surface contaminants or degradation of the CCD charge collection efficiency: see Section 2.2). The ultimate goal of this effort would be to build a consistent model of the radiation damage. This fundamental undertaking will rely heavily on a permanent monitoring of the accumulated radiation dose and of the corresponding changes in the uniformity of the CCD response, which will be pursued until the end of the mission.

3. Observations

The versatility of the EIT instrument and the organization of the SOHO Experiment Operations Facility (EOF) allow a diverse range of scientific investigations. The

EIT synoptic program consists of one full frame full resolution image in each waveband each day. In addition, EIT supports SOHO Joint Operations Programs (JOPs) involving the coordinated observation of targets with the other SOHO instruments and outside observational facilities. EIT is deeply involved in the SOHO JOP program because of the context provided by a full disk EUV image. The results of the JOP participation are extremely diverse and are outside the scope of this paper. Beyond the synoptic program and JOPs, special EIT observing programs are conducted.

In this section we present reports of some of the new results from the EIT science investigations. The temperature structure of the corona is the subject of the first two sections. From the synopic program, the large-scale thermal structure of the corona in the temperature regime of 1 to 2 MK is described in Section 3.1. In order to investigate in detail the thermal structure with height of an active region, a special observing sequence was executed for an active region on the limb (Section 3.2).

The variability of the upper chromosphere and corona is well observed with EIT image sequences and is the subject of the last three sections. In Section 3.3, movies in the He II and Fe XII channels show the dynamics of the EUV Sun. An analysis of the variability in these channels during a special high-cadence observing program is presented in this section. Sequences dedicated to identifying outflows and eruptions are the subject of Sections 3.4 and 3.5. Programs searching for evolution of coronal plumes have recorded dynamic events in the polar coronal holes which are labeled 'EUV jets'. Programs searching for the initiation of coronal mass ejections have identified these events in the EIT images.

3.1. Coronal Temperature Diagnostics

Although many observations and much analysis exists on coronal structures at temperatures up to about 1 MK and above 2 MK, principally from EUV and soft X-ray observations by *Skylab*, SMM and *Yohkoh*, less attention has been directed toward the EUV structure of the corona between 1 and 1.5 MK where soft X-ray imagers have relatively little sensitivity. Initial observations from EIT confirm that this is an uniquely interesting temperature regime, particularly during the interval of solar minimum activity.

The three EIT coronal imaging channels were designed for optimum coverage of the temperature range of 1.0 to 2.5 MK. Each coronal bandpass was chosen to be dominated by a different ionization state of Fe under specific conditions (e.g., non-flaring structures in the Fe XII channel), so that abundance variations would not be a factor in the relative fluxes observed in each channel. The assignment of a plasma temperature value to a given set of fluxes observed in the three channels in a given pixel is, mathematically, a poorly constrained inversion problem requiring a set of assumptions, including the cospatiality of material being observed in optically thin lines. However, with sufficient attention to the limitations of this approach, the

thermal distribution and evolution of the corona in this temperature regime can be explored.

3.1.1. *Morphology of Line Ratio Maps*

Before quantitative analysis is presented, it is instructive to investigate the morphology of maps of the ratio of the Fe XII and Fe IX, X channels as a guide to the overall temperature distribution of 1 to 2 MK plasma in the corona. These two spectral bands have peak sensitivity at 1.2 MK and 1.5 MK, respectively, sufficiently close that cospatiality of at least some features can be expected. Even in the circumstance that the emission regions are not cospatial in the two channels, the relative intensity of the channels indicates the relative thermal distribution in the corona. The thermal distribution of coronal plasma in the 1 to 2 MK regime is presented for 12 May 1996 in Figure 8. Note the residual grid pattern in Figure 8. The aluminum filter support grid shadow discussed in Section 2.3 would dominate the ratio image without correction. This demonstrates the importance of the instrument work described in Section 2 even for qualitative analysis.

This ratio map generally outlines magnetically closed field regions. The diffuse, unresolved coronal regions in the Fe XII and Fe IX, X channels are cooler than the structures associated with stronger field regions and are thus also dark in the ratio image. For this reason, the ratio maps are sometimes used for enhanced contrast coronal displays for easy comparison with other data. X-ray bright points are associated with compact bipolar regions and are identified in the ratio image as bright compact structures. Active regions are indicated as the hottest structures observed on the disk by their intensity in the ratio image.

The coronal hole regions are clearly defined as cool, open field regions by the dark regions in the ratio image both on and off the disk. Polar plumes are identified in the ratio images as the darkest and thus the coolest structures in coronal holes. Plume-like structures have been observed outside the polar holes (see below for an example in a decaying active region) and they are some of the coolest extended coronal structures observed by EIT.

Closed off-limb regions in the ratio map are predominantly indicative of large-scale structures because the increased line of sight reduces the contribution of any given compact structure. In general, the extended, closed-field structures seen off-limb in the ratio images are hotter than the corresponding on-disk structures because the line of sight is primarily integrating through the region of higher temperature plasma which has a greater scale height. Extended structures outlined by the ratio maps include both high-latitude and low-latitude structures.

3.1.2. *Coronagraph Comparisons*

The hot high-latitude structures observed in the EIT temperature maps correspond to the persistent closed loop structures seen in the LASCO C1 green line (Fe XIV) coronagraph images as reported by Schwenn *et al.* (1997). These structures are of particular interest because of their role in determining the characteristics of the

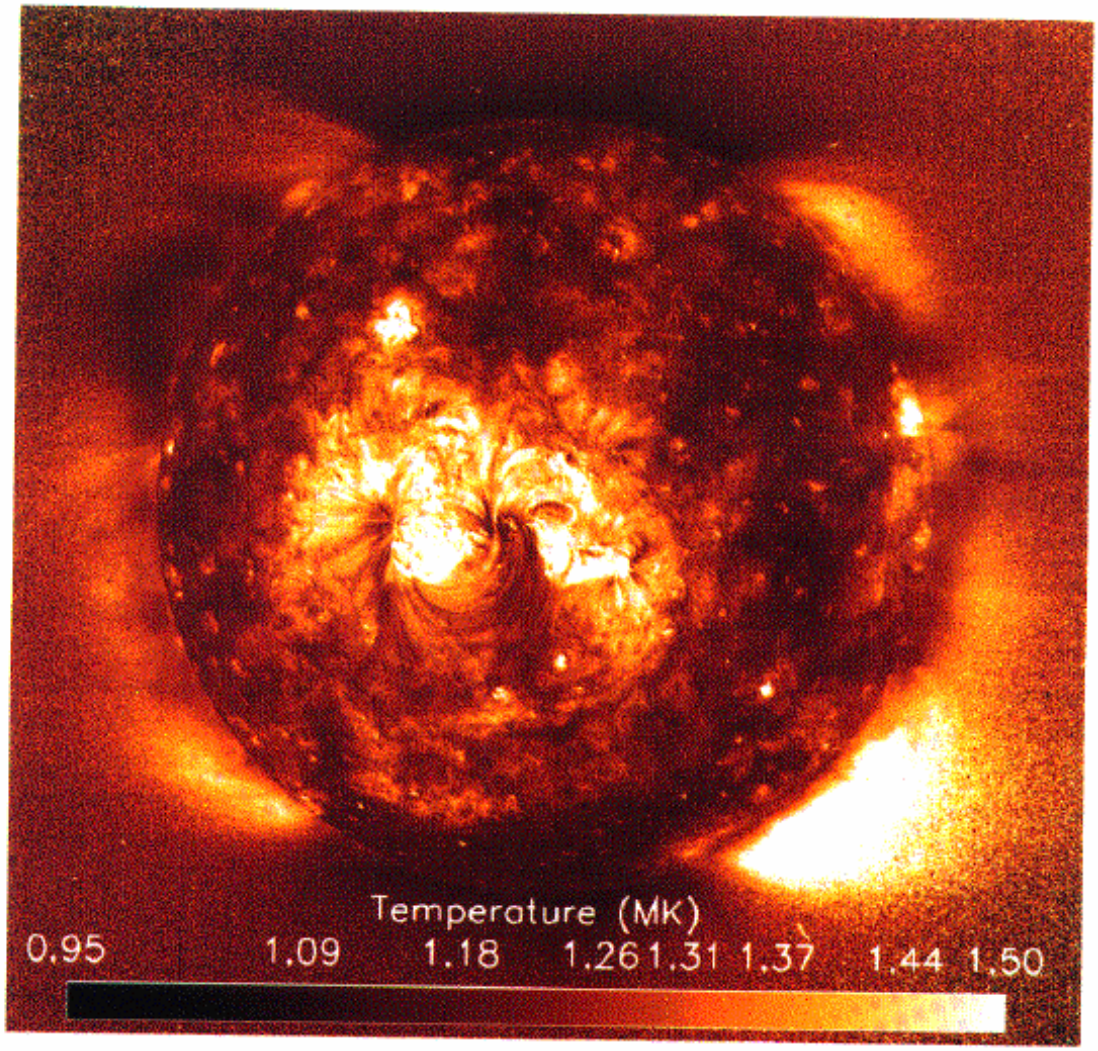

Figure 8. Temperature map derived from ratio of Fe XII and Fe IX, X from 12 May 1996

heliospheric current sheet. This correspondence directly links these high latitude structures with the large-scale high-temperature zones observed by Guhathakurta and Fisher (1994) using ground based green line (Fe XIV) and red line (Fe X) ratios. With the improved signal to noise ratio of the EIT temperature maps and the capability to follow a structure as it rotates on or off the solar disk, the EIT observations provide a valuable enhancement to the work with coronagraphs on this topic.

The *high-latitude* off-limb large-scale structures observed by EIT show a coupling of emission intensity and temperature. Comparable structures observed in the study by Guhathakurta and Fisher show the same coupling throughout most of the last solar cycle. With the low-noise EIT temperature maps, a temperature enhancement of these high-latitude structures at the boundary with the polar hole can frequently be observed. This can be seen in the both southern polar hole boundar-

ies and the westward northern polar hole boundary of Figure 8. These temperature enhancements are also identified as regions of enhanced emission. As such, this temperature enhancement is better interpreted as a high-latitude concentration of closed-field flux elements than as some example of increased heating in the region of transition from closed to open field magnetic geometry.

Also, as found in the Guhathakurta and Fisher study, the *low-latitude* large-scale closed field structures observed by EIT do not show as direct coupling of emission intensity and temperature. This is particularly true for the case of structures associated with an active region surrounded by a weak magnetic field region. Due to the higher density of the active region loops, this is observed on the disk as well as on the limb. With the on-disk view of these structures, their magnetic origins can be determined. The region of enhanced temperature associated with the active region on the disk in Figure 8 is clearly much larger than the region of enhanced emission associated with the active region in the Fe IX, X and Fe XII images. A close examination of the Fe IX, X images shows, in comparison to the intensity of the overall quiet-Sun emission in this line, an extended region of suppressed emission surrounding the active region. Interestingly, there is also a kind of 'moat' around the active region in He II suggestive of the Hα circumfaculaire described by Bumba and Howard (1965). Apparently, flux elements in an active region which have diffused far enough from the neutral line of the active region bipole form large-scale connections with opposite polarity flux elements in the surrounding mixed polarity region. The consequence is a region of large-scale structures beyond the temperature range of the Fe IX, X images.

3.1.3. *Quantitative Analysis*

For an initial estimation of the emission measure and temperature of the structures observed by EIT, the preflight calibration described in Delaboudinière *et al.* (1995) has been combined with the CHIANTI solar spectrum (Newmark *et al.*, 1996). The CHIANTI (Dere *et al.*, 1997) database is maintained on the world wide web for easy access by the astrophysical spectroscopy community:

– http://wwwsolar.nrl.navy.mil/chianti.html.

With the limitations in applicability of the pre-flight EIT calibration described in Section 2 above, the results of this calculation must be considered preliminary until the conclusion of inflight intercalibrations involving the EIT Calroc and SEM CALSO–3 sounding rocket programs and the SOHO CDS, SUMER, CELIAS/SEM and UVCS. At this stage of analysis, it is preferable to just consider ratios of bandpasses. The temperature sensitivity for a unit emission measure of ratios of the three coronal channels is presented in Figure 9. Although all of the curves become double valued at higher temperatures, the response of the instrument to these higher temperatures is so low (Delaboudinière *et al.*, 1995) that these regimes become important only for hot regions of very high emission (e.g., flares).

In the images of 12 May 1996 from Figure 8 above, one can identify several interesting regions in the Fe IX, X and Fe XII images that are straightforward to

Table IV
Plasma parameter calculations

Feature	Counts s^{-1} (195 Å)	Fe XII/Fe IX, X	Temp × 10^6 K	EM (cm^{-5})
Plume (base)	50	0.55	1.35	7×10^{27}
Coronal hole	20	0.67	1.4	2.7×10^{27}
XBP	175	2.0	1.7	3.7×10^{28}

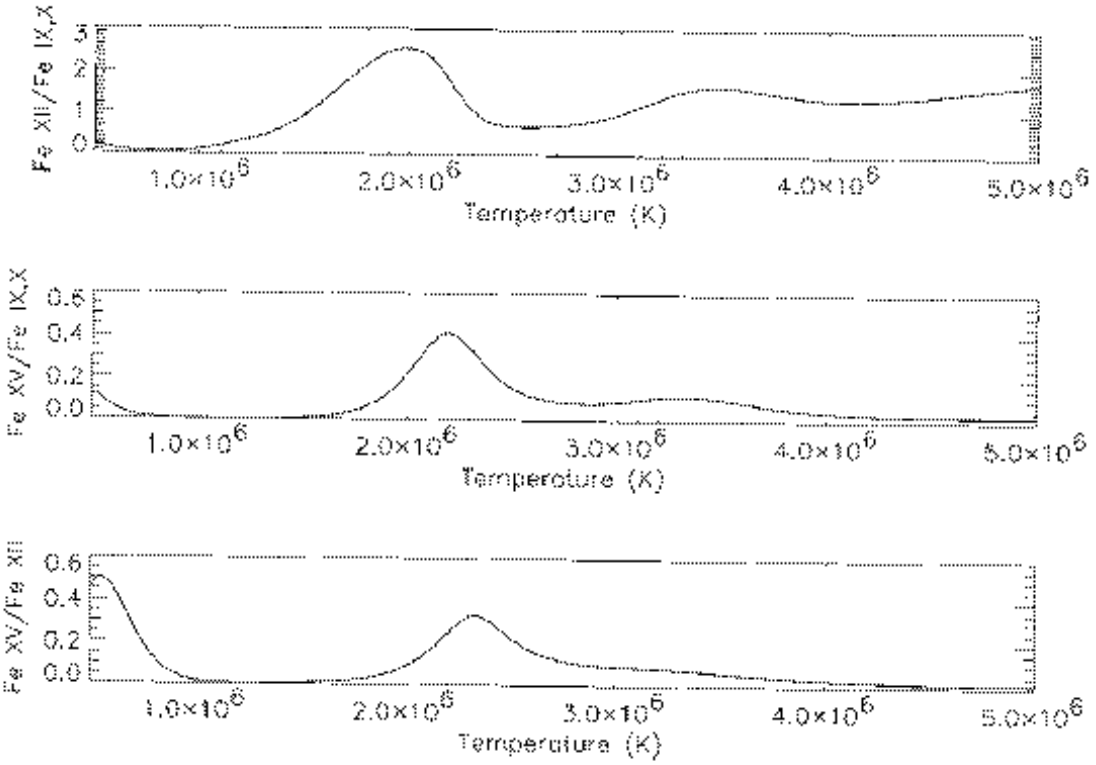

Figure 9. Temperature response of image ratios: Fe XII/Fe IX, X (*top*), Fe XV/Fe IX, X (*middle*), and Fe XV/Fe XII (*bottom*).

interpret. Since the emission is a slowly varying function of electron density, a value of 1×10^9 cm^3 is chosen for all the calculations. Values of temperature and emission measure for the polar coronal hole, the base of a plume in the coronal hole and an X-ray bright point are presented in Table IV. Analysis of other structures and other line ratios is not as straightforward.

3.1.4. *Temperature Structure of Active Region Loops*

An active region at latitude S 07° and heliographic longitude 260° was observed by EIT from May 1996 to September 1996 (Neupert *et al.*, 1997). By the end of this period it had decayed so that only a neutral line with a quiescent filament bisecting somewhat enhanced magnetic fields of opposite polarity remained. Figure 10 shows the appearance of this region in Fe IX, X and Fe XII as it approached the ... west limb

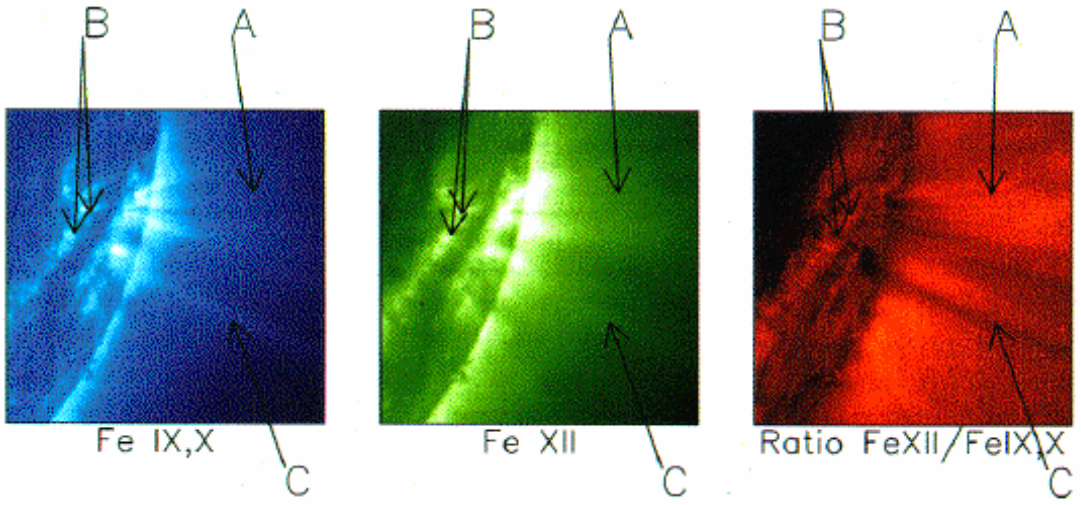

Figure 10. Fe IX, X, Fe XII and ratio images for 30 September 1996. Large-scale loops are identified as 'A', small scale loops are identified as 'B' and an extended feature is identified as 'C'.

on 30 September. A complex system of high (200 000 km) loops were present both over the major neutral line, and over leading and trailing portions of the region, where they may have connected to distant weak field regions of mixed polarities. A group of such features, observed most strongly in Fe IX, X and Fe XII, but to a lesser extent in Fe XV (not shown) is indicated as 'A' in the Figure. Smaller loop-like features (several indicated as 'B') were present at lower heights in the central portion of the region. A more nearly radial feature (designated as 'C'), for which only one footpoint was observed, may have been either a very high loop or the base of an open field region extending into the outer corona.

3.1.5. *Low Coronal Loops (Height Appreciably Less Than the Separation of Loop Footpoints and the Pressure Scale Height)*

Low loops (less than 10 000–20 000 km) have been observed in their entirety in a one or both spectral bands ('B' in the figure), suggesting that such features are nearly isothermal and in the range of 1.2–1.7 MK. Similar features, although at higher temperatures ($T_e > 2$ MK), have been well-observed by *Skylab*, SMM, and *Yohkoh*.

3.1.6. *Large-Scale Loops (Heights to 200 000 km and Comparable to or Greater than Footpoint Separation)*

EIT was able to track several features to heights well in excess of 100 000 km on the limb. The diminution in brightness with height for feature 'A' implies a density scale height of approximately 60 000 km. This result is comparable to the scale height expected at these temperatures. In 'A' the ratio of Fe XII to Fe IX, X increases to a maximum at a height of 190 000 km, suggesting the presence of coronal loops hottest ($T_e = 1.7$ MK) at their tops. Fe XV was also present, although more diffuse, so hotter plasmas may have been intermingled with the loops at 1.2–1.7 MK.

Table V

General characteristics of the 28 December 1996 image sequences (T: total duration, N: number of images, ΔT: average sampling time)

Sector	Begin	End	T	N	ΔT
He II	$16^h10^m21^s$	$19^h20^m56^s$	$3^h10^m35^s$	173	66.483 s
Fe XII	$20^h53^m26^s$	$21^h59^m08^s$	$1^h05^m42^s$	55	70.516 s

3.1.7. *Extended Features*

By comparison with large closed loop feature discussed above, the nearly radial feature denoted by 'C' may have been the base of a magnetically open field region. For this feature the Fe XII/Fe IX, X ratio was less than in the surrounding corona. Diminished emission of Fe XV (not shown) in this feature confirms the relatively low coronal temperature. The pressure scale height in this structure is in the range of 150 000 to 200 000 km. This result is significantly higher than the scale height expected at these temperatures. (N.B. This temperature structure is in contrast to the apparent positive gradient of the plumes in the polar coronal hole.)

3.2. Intensity Oscillations in the Transition Region and Corona

The EIT's ability to produce high-cadence images covering a wide field of view has brought the picture of a highly dynamical quiet corona, with small-amplitude variations of the local emission at all spatial and time scales. This small-scale activity is observed everywhere and can thus contribute significantly to the energy transfer from the photospheric and chromospheric levels into the corona through the transition region. Movies of the variability of the He II and Fe XII emission are presented in the CD-ROM.

3.2.1. *Image Data*

Subimages (320 × 320 pixel) of the central part of the solar disc were sampled every minute on average (unequal sampling) for a total duration of about 3 hours in the He II line and 1 hour in the Fe XII line (Table V). The intensity averaged over the whole data set, with compensation for solar differential rotation, is shown for both sequences in Figure 11. For this first analysis, these corrected images were submitted to a one-dimensional discrete Fourier transform for unequally spaced data (Deeming, 1975) along the time dimension, after an initial preprocessing.

3.2.2. *Initial Results*

The dynamics of the solar plasma is expected to vary according to the local state of the plasma, e.g., with magnetic field strength, density and temperature. Changes in these parameters are traced by spatial variations of the EUV brightness, allowing one to distinguish the dark cell interiors and bright cell boundaries in the transition region network, or dim loop patterns and bright points in the corona. In the time-

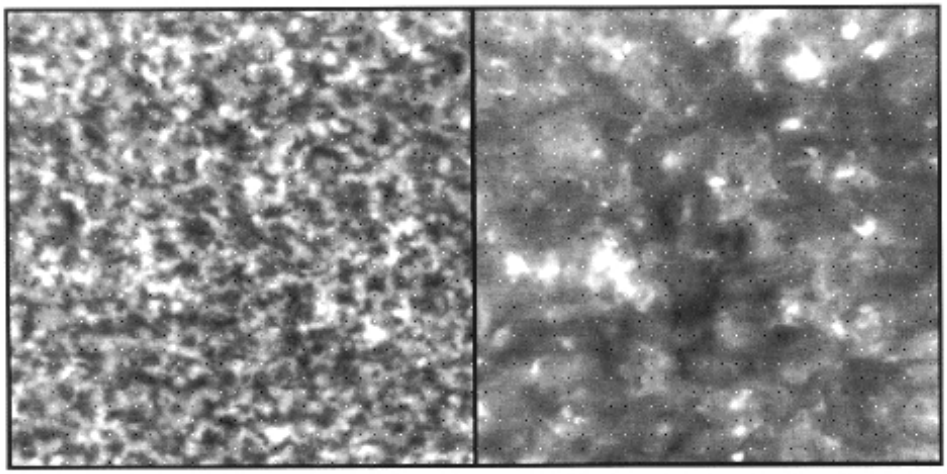

Figure 11. Spatial distribution of the average intensity in corrected and projected images of the He II image sequence (*left*) and the Fe XII image sequence (*right*).

averaged intensity maps (Figure 11), the observed contrast and sharpness of small-scale features (network, faint coronal loops) implies a relative stability of the medium-scale magnetic patterns over timescales of the order of the integration time, i.e., several hours.

Taking advantage of this property to improve the signal/noise ratio in the power spectra, individual spectra computed for single pixel locations were grouped by intensity ranges according to the local time-averaged intensity, which reflects the local plasma state. The resulting spectra are dominated by a smooth f^{-1} 'red noise' spectrum. They show only minor changes over the full intensity range, as well in the He II line as in the Fe XII line. The dynamical behavior thus seems largely independent of the local plasma state, and the amplitude of the fluctuations is simply proportional to the local average intensity. This invariance allows us to average out the spectra over the whole field-of-view, further reducing the uncertainty in the power estimates (Figure 12). In these global spectra, the noise background in the 0–2.5 mHz range is accurately reproduced by a $f^{-1.55\pm0.1}$ dependency in He II and $f^{-1.7\pm0.15}$ in Fe XII. These exponent values are close to the $-\frac{5}{3}$ value of the Kolmogorov turbulence spectrum (Landau and Lifchitz, 1971). Such an energy distribution corresponds to a fully developed turbulence (inertial regime) or to an intermittency mechanism in a non-linear system (Schuster, 1984). Spatial variation in the velocities exhibited by the C IV line formed at a temperature similar to the He II were studied by Dere (1989). He found that the power in the velocities varied with the wave number k as $k^{1.5}$ or $k^{5/3}$ as expected for the inertial regime of a turbulent plasma.

For the Fe XII coronal images, the power is falling off more rapidly with frequency, and beyond about 3 mHz the f^{-1} component merges with a uniform white-noise background, indicating the presence of a second noise contribution. Assuming that the fluctuations of the exposure times due to the shutter mechanism

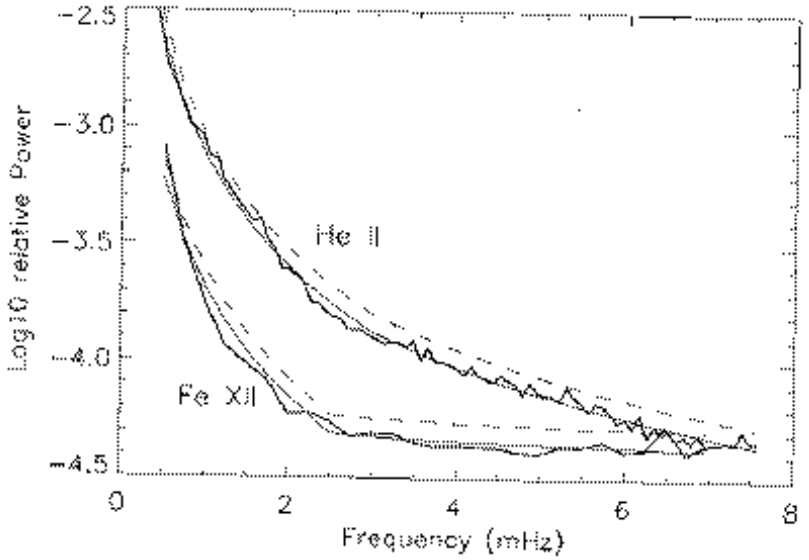

Figure 12. Average power spectra computed for the He II (304 Å) and Fe XII (195 Å) image sequences (full-field average). The thin lines represent the fitted f^{-3} profile, while the dashed lines show the 99.9 confidence levels.

are purely random, the associated 0.4 s standard deviation would correspond to a uniform noise background at a power of 5×10^{-5}. This is in good agreement with the high frequency part of the Fe XII power spectrum, indicating that this component has an instrumental origin. The same calculation shows that this background is 10 times lower in the He II power spectrum, which is one order of magnitude below the observed background. In this case, the noise background is produced by the Sun over the whole frequency range.

Using chi-squared statistics based on the dispersion of power estimates, the confidence levels (Groth, 1975) were also computed for the power estimates (see Figure 12). No significant local power excess is found, in particular within the 5-min and 3-min period ranges of photospheric and chromospheric oscillations. These oscillations are thus either fully reflected at the base of the corona or strongly attenuated, with residual amplitudes below our detection level. For the present data sets, this level equals 0.4% in relative amplitude. We must also stress that our preliminary study is based on a statistical approach and does not inform us about the spatial coherence of the detected waves. If waves originating in the low atmosphere can only propagate up to the corona along localized vertical magnetic field structures, their signature might elude detection in our spatially averaged spectra. A full 3-dimensional transform as well as the separate analysis of individual features, like single loops or bright points, is thus required and will be applied to the data in a subsequent analysis. Obviously, image sequences produced by EIT will deliver their full content of unique dynamical information only by applying such detailed analysis schemes involving jointly the spatial and temporal dimensions.

3.3. Dynamics of the Polar Coronal Hole

From previous space observations (e.g., Bohlin, Sheeley, and Tousey, 1975; Ahmad and Webb, 1978; Walker *et al.*, 1993) it was anticipated that EIT observations of structures within the polar coronal hole would contribute to the study of the dynamics of the polar coronal hole. A report by DeForest *et al.* (1997) on coordinated SOHO studies of polar plumes justifies this anticipation and can be found in this volume. The discovery (Gurman *et al.*, 1996) of EUV jetlike events in EIT Fe XII image sequences opens a new perspective on the study of polar coronal hole dynamics. These EUV jet events could be the 'building blocks' of dynamic phenomena in coronal holes.

Figure 13 shows a time series of images taken during the brightest EUV jet event observed so far. This jet begins in a bright, low-lying looplike feature some 1.3×10^4 km long and extends to the edge of the field of view, over 16.5×10^4 km above the surface, some 7 min later. During this time, the leading edge of the jet rises at an apparently constant speed of 400 km s^{-1}. Measurement of some 15 similar events yields a distribution of average speeds of 100–400 km s^{-1} and maximum observed lengths of 2 to 16.5×10^4 km. A movie showing an EUV jet eruption is included in the companion CD-ROM.

The EUV jetlike events are similar in appearance to the soft X-ray jets observed with the *Yohkoh* Soft X-ray Telescope (Shibata *et al.*, 1992). While the soft X-ray jets occurred predominantly in active regions and flaring, soft X-ray bright points (Shimojo *et al.*, 1996), the EUV jets appear to be confined to the polar coronal holes. The average speed of the EUV jets in the current (limited) sample, 325 km s^{-1}, is higher than that found for 100 soft X-ray jets by Shimojo *et al.* (1996). The maximum observed height of the EUV jets is about half that of the X-ray jets of Shimojo *et al.*'s study. Thus, the EUV jets appear to be a new regime of jet-like phenomena.

The EUV jets are not well observed in the Fe IX, X or the Fe XV channels. The contrast in EIT Fe IX, X images between structures in the coronal hole and the coronal hole itself limits the detection of faint structures. Exposure times in the Fe XV channel for quiet-corona structures are much longer than the other two coronal channels. Fe XV exposures long enough to show the EUV jets would blur these relatively faint features over several pixels, thus raising the brightness threshold for detection.

The footpoints of the microjets constitute a diverse collection of features: low-lying, bright loops as in Figure 13; unresolved structures that vanish as the microjet fades; supergranule-sized areas of emission that eject the microjet helically; and one case (so far) of what appears to be a thin flux tube breaking loose from the solar surface at one end while remaining fixed at the other. All these footpoints appear to have in common is that they occur within a coronal hole, where the magnetic field is diverging, and even small instabilities or eruptions are unlikely to be constrained magnetically.

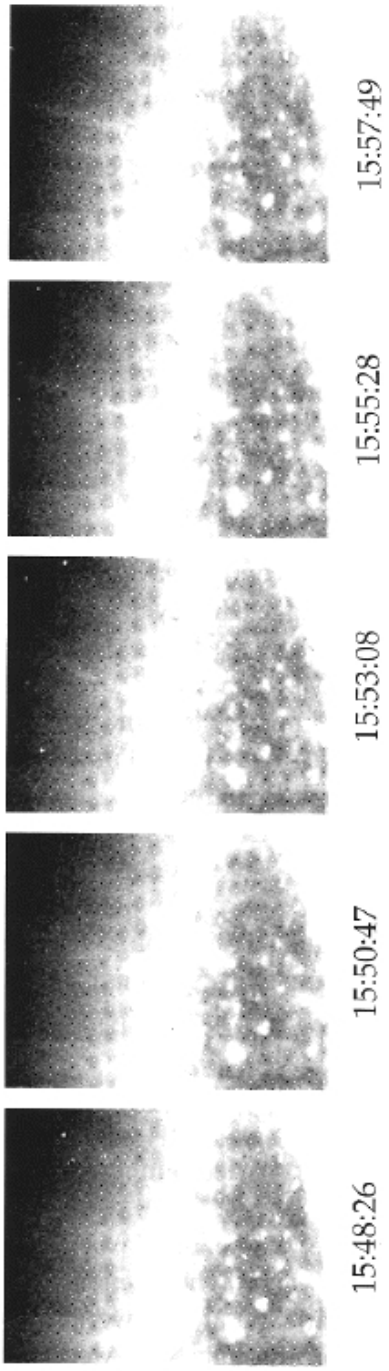

Figure 13. EUV jet in polar coronal hole.

3.4. CME WATCH

With the availability of flexibility in the SOHO telemetry resources beginning in December 1996, it has been possible to initiate sustained high cadence full disk imaging to search for large-scale coronal transients. The instrument is left in a single waveband in order to maximize temporal coverage of phenomena in a single temperature regime. To improve cadence in some circumstance, the resolution is reduced by on-chip binning to improve the cadence while supporting other programs.

During the first CME watch, a CME was observed in Fe XII on 23 December 1996 with full resolution from initiation (Dere *et al.*, 1997). The site of initiation was compact and simultaneously contained a filament eruption, a coronal void, and an outward propagating shock front. This front became the leading edge of the CME observed in LASCO. The evolution of these features is seen in the CME movie on the accompanying CD-ROM.

Associated with this CME was a disturbance tentatively identified as a coronal manifestation of a "Moreton wave". At the time of the initiation of the CME, the event began as a localized increase in emission propagating across the solar disk. The average increase over the entire wavefront began at greater than 10%, decreasing with each successive image. However, individual regions exhibited more than 100% increase in emission.

Based on the five 'coronal Moreton wave' events observed thus far, typical speeds range from 250–400 km s^{-1}, and the wavefronts which are initially propagating radially begin to break up and travel in separate fronts. The magnitude of the wave shows little correlation with the peak thermal X-ray flux of the associated event; in fact, the majority of EIT observations close to flare events do not show any evidence of these waves. The model of a weak fast-mode MHD shock developed by Uchida (e.g., Uchida, 1974) explains several features of the EIT observations, including the eventual localization of the wavefronts, the preferential direction of propagation (away from active regions) and the lack of correspondance with the peak thermal X-ray flux of the flare. A movie of a coronal Moreton wave is included in the CD-ROM.

Acknowledgements

NRL received support from the Office of Naval Research and NASA grants NDPRS-86759E and NDPRS-09930F. The French laboratories were supported by CNRS and CNES. The Belgian laboratories were supported by SPPS via PRODEX. LMPARL recieved support through NASA contract NAS5–32627 and the Lockheed Independent Research Program. We wish to acknowledge the assistance of Drs L. Acton, G. E. Brueckner, J. Cook, L. Floyd, N. R. Sheeley, O. C. St. Cyr, K. Waljeski, and Y. M. Wang. We are particularly indebted to the operations staff

including L. Allen, R. Doney, E. Einfalt, E. Larduinat, J.-P. Olive, S. Passwaters, K. Schenk, H. Schweitzer, S. Stezelberger, and D. Wang. Finally we would like to thank the LASCO team for cooperation in overall operations and the SUMER team for the critical telemetry bandwidth increases they have occasionally allowed EIT.

References

Ahmad, I. A. and Webb, D. F.: 1978, *Solar Phys.* **58**, 323.
Bohlin, J. D., Sheeley, N. R., and Tousey, R.: 1975, in M. J. Rycroft (ed.), *Space Research*, p. 651.
Bumba, V. and Howard, R.: 1965, *Astrophys. J.* **141**, 1492.
Cheng, C. C., Smith, J. B., and Tandberg-Hanssen, E.: 1980, *Solar Phys.* **45**, 393.
Deeming, T. J.: 1975, *Astrophys. Space Sci.* **36**, 137.
Defise, J.-M. *et al.*: 1997, *SPIE* **3114**, in preparation.
DeForest *et al.*: 1997, *Solar Phys.* **175**, 393 (this issue).
Delaboudinière, J.-P.:1998, *Solar Phys.*, submitted.
Delaboudinière, J.-P., Artzner, G. E., Brunaud, J., Gabriel, A. H., Hochedez, J.-F., Millier, F., Song, X.-Y., Au, B., Dere, K. P., Howard, R. A., Kreplin, R., Michels, D. J., Moses, J. D., Defise, J.-M., Jamar, C., Rochus, P., Chauvineau, J.-P., Marioge, J.-P., Catura, R. C., Lemen, J. R., Shing, L., Stern, R. A., Gurman, J. B., Neupert, W. M., Maucherat, A., Clette, F., Cugnon, P., Van Dessel, E. L. *et al.*: 1995, *Solar Phys.* **162**, 291.
Dere, K. P.: 1989, *Astrophys. J.* **340**, 599.
Dere, K. P. *et al.*: 1997, *Solar Phys.* **175**, 601 (this issue).
Foukal, P.: 1978, *Astrophys. J.* **223**, 1046.
Groth, E. J.: 1975, *Astrophys. J. Suppl.*, No. 286, **29**, 289.
Guhathakurta, M. and Fisher, R.R.: 1994, *Solar Phys.* **152**, 81.
Gurman, J. B. *et al.*: 1996, *EOS* **77**, (46), F557.
Janesick, J. R., Klassen, K. P., and Elliot, T.: 1987, *Opt. Eng.* **26** (10), 972.
Klimchuk, J. A., Moses, D., and Portier-Fozzani, F.: 1997, in preparation.
Klimchuk, J. A., Lemen, J. R., Feldman, U., Tsuneta, S., and Uchida, Y.: 1992, *Publ. Astron. Soc. Japan* **44**, L181.
Kuhn, J. R., Lin, H., and Loranz, D.: 1991, *Publ. Astron. Soc. Pacific* **103**, 1097.
Landau, L. and Lifchitz, E.: 1971, *Mécanique des fluides*, Editions de Moscou.
Moses, D. *et al.*: 1994, *Astrophys. J.* **430**, 913.
Neupert W. M. *et al.*: 1997, *EOS* **78** (17), S256.
Newmark, J.: 1996, *EOS* **77** (46), F557.
Schmahl, E. J. and Orrall, F. Q.: 1979, *Astrophys. J.* **231**, L41.
Schuster, H. G.: 1984, *Deterministic Chaos: An Introduction*, Physik-Verlag, Weinheim.
Schwenn, R. *et al.*: 1997, *Solar Phys.* **175**, 667 (this issue).
Sheeley, N. R.: 1980, *Solar Phys.* **66**, 79.
Shibata, K., Ishido, Y., Acton, L. W., Strong, K.T., Hirayama, T., Uchida, Y.: 1992, *Publ. Astron. Soc. Pacific* **44**, L173.
Shimojo, M., Hashimoto, S., Shibata, K., Hirayama, T., Hudson, H., and Acton, L. W.: 1996, *Publ. Astron. Soc. Pacific* **48**, 123.
Uchida, Y.: 1974, *Solar Phys.* **39**, 431.
Walker, A. B. C., DeForest, C. E., Hoover, R. B., and Barbee, T. D. W.: 1993, *Solar Phys.* **148**, 239.
Webb, D. F.: 1981, in F. Q. Orrall (ed.), *Solar Active Regions*, Colorado Associated University Press, Boulder, p. 165.

V.3.2 Filaments éruptifs

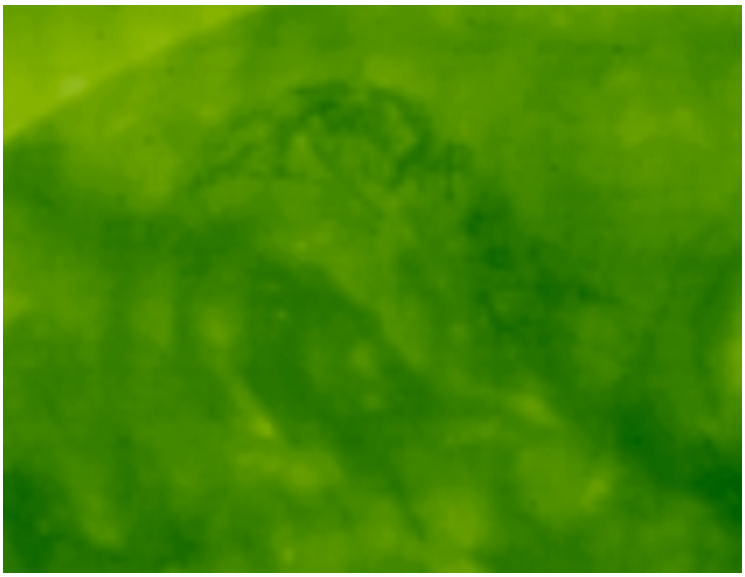

Figure V.1: Eruption du Filament du 13-10-99 : SOHO/EIT Fe XII à 08:48 TU

Nous avons étudié au chapitre IV comment des boucles d'une région active évoluent et en particulier le role du torsadage. Nous venons d'analyser au paragraphe précédent l'évolution de plusieurs structures vers des CMEs ou des éruptions. Nous allons revenir un instant sur les filaments. Souvent un filament est soutenu par des boucles transverses à son axe principal (*eg.* les "arch-filaments"). Il existe des cas où le torsadage est présent dans le filament sans que les boucles qui le soutiennent soient visibles. Le 13 Octobre 1999, durant la campagne MEDOC, un filament très torsadé éruptait (Fig. V.1). Le film EIT (cf. CD-ROM) montre qu'il est initialement très torsadé (07:00 TU) et se détorsade au fur et à mesure de son éruption ($\rightarrow\sim$ 10:00 TU). Les images du coronographe H_α du Pic du Midi viennent confirmer cette forte torsion encore présente à 10:35 TU (Fig. V.2).

La encore, le torsadage joue encore un rôle dans la stabilité des structures.

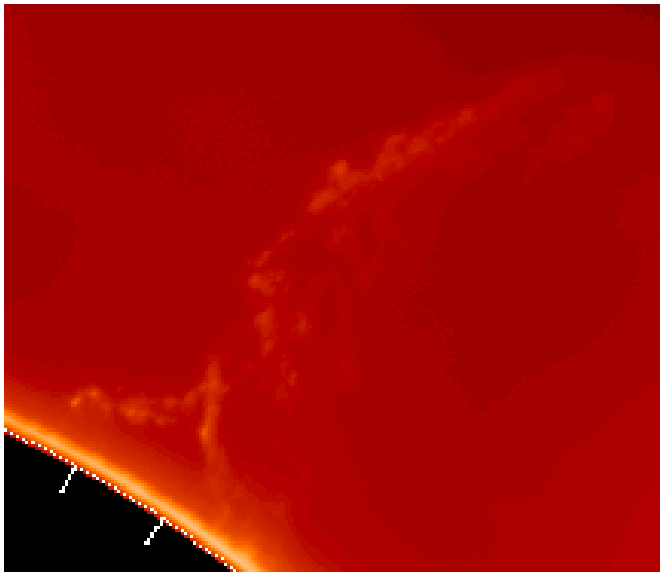

Figure V.2: Eruption du Filament du 13-10-99: Extrait de l'image du coronographe H_α du Pic du Midi prise à 10:35 TU

V.4 Une vision globale de ces études sur la couronne solaire

L'article suivant (publié pour le colloque de SOHO 8) résume en grande partie la thèse.

- **3D loops evolutions (twist and expansions) and magnetic fields interactions studied with SOHO/EIT**
- by F. Portier-Fozzani
- SOHO 8 meeting (Paris, June 1999)
- Paru dans ESA SP-446 (Oct. 1999)

3D LOOPS EVOLUTIONS (TWISTS AND EXPANSIONS) AND MAGNETIC FIELDS INTERACTIONS STUDIED WITH SOHO/EIT

F. Portier-Fozzani

Laboratoire d'Astronomie Spatiale, BP 8, 13376 Marseille Cedex 12, France

ABSTRACT

3D Technics were developed to study coronal structures evolution. Anaglyphs were used to analyse the global corona, and constraints for complete stereovision reconstruction were derived in the case of EUV wavelengths. Loops morphologies were succesfully described with a torus fit which includes twist evolution.
On a quick magnetic flux emergence (August 5th 1997), the loop twist is decreasing during its expansion. During a long time evolution (July - August 1996), flaring activities are well correlated with sudden twist decreases. These 2 results correspond to the evolution described by Parker's formula (1977).
Magnetic field lines interactions were also analyzed. From multi-wavelengths observations, some morphological and topological changes were interpreted as interactions between open and closed magnetic field lines (*ie.* between Coronal Holes and Active Region Loops).
Then, relationship between CME or Flares formation and our different instabilities studied were analyzed in the aim to find, in the future, good criteria concerning space weather.

Key words: SOHO; EIT ; Coronal loops.

1. INTRODUCTION

Due to the low value of the beta plasma parameter, the solar corona traces in 3D the very complex and hightly dynamical movement of the magnetic field. Solar Studies have taken profit of the launch of the SOHO spacecraft in December 1995 (Fleck *et al.*, 1995). Coronal events were then able to be followed 24h per day by space instruments and complementary ground based observations in the aim of better understanding the puzzle of the very hot temperature, flaring loops processes, and other not understood phenomena...

Aboard SOHO, the Extreme ultraviolet Imaging Telescope (EIT) images the Chromosphere (He II line : temperature $T \sim 8 * 10^4$ K), the Transition Region (Fe IX/X line : $T \sim 1.3$ MK) and the Corona (Fe XII — 1.6 MK — and Fe XV lines — 2 MK —) on a 1024x1024 CCD with a spatial resolution of 2.6 arcsec (Delaboudinière *et al.*, 1995 and Table 1). It is then possible to follow structure evolutions (Portier-Fozzani *et al.*, 1997) or calculates the temperature (Neupert *et al.*, 1998) for each structure.

This paper summarizes some results from my PHD/Thesis :

- 3D imaging technics were developed to understand the solar corona such as shape vision (Portier-Fozzani *et al.*, 1997) and anaglyph. A feasibility steady (Portier-Fozzani, 1999b) for complete computer stereovision inversion in thin optical lines was realised based upon INRIA results for solid reconstruction object from couple of images (Vezien, 1995).
- To study coronal loops, a fitting model using the *dynamic stereovision* (Aschwanden *et al.* 1999) were developed with M. Aschwanden to take into account the twist and shear for loops.
- Loops evolution were followed for emerging AR, and during long time evolution.
- Exemples of relations between loop anisotropies and flares or CMEs formation (as filaments are supported by loops) were made.

The aim of this paper is to present different technics to rebuilt the 3D aspect of the corona (stereovision, model for loop fitting,...), to analyse magnetic field evolutions (emerging flux, closed loops evolution, magnetic interactions) and to discuss the future possibilities of forecasting the space weather precisely from loops shear/twist measurement.

2. DEGRIDDING, SPATIAL WAVELETS AND OTHER IMAGERY ENHANCEMENT

Concerning the EIT instrument, a redundant aluminium filter used to block visible light, mechanically supported by a nickel grid casts a shadow on the CCD (Moses *et al.*, 1997). The usual method for degridding the EIT images is to take off a modelized grid pattern obtained by mean time average (Defise

et al., 1997). But the real grid is not uniform —due to the asymmetry of the entrance—, so a local median filter made on each image —which takes more time processing— is more efficient (Portier-Fozzani *et al.*, 1997, Moses *et al.*, 1997).

As multiscale visualization —based upon spatial wavelets (*cf.* Bijaoui *et al.* 1996)— are made for finding structure signal near the noise level (which is supposed to have no regular shape), the image dynamic has to be low, so it is better to zoom on the part of the image that we want to analyse. Image is cleaned before the wavelet treatment to avoid presence of a regular object which can hide some real structures. Technics and results are fully described in Portier-Fozzani *et al.* (1999c).

3. 3D CORONA

3.1. GENERAL 3D TECHNICS

To analyze solar corona, 3 dimensional technics were developed. The simplest was to study *steady structure* by using different angle of sight due to the solar rotation with time. For anaglyph, the image for one eye is colored in red (or in one polarization) while the other image (taken few hours later) is colored in blue (Portier-Fozzani, 1999b).
Another technics is to do real stereovision inversion. From calculations based on the INRIA reconstruction made on solid object (Vezien, 1995), we had extrapolated the theoretical amount of uncertainties on the reconstruction for the optical thin coronal lines studied. With the help of the anaglyph results, we conclude that for doing real 3D reconstruction we need to have simultaneously observation which should happen with STEREO (Portier-Fozzani, 1999b).
Other technics are to consider specific methods for each structures and to use "stereo-vision" as a modelised fit.

3.2. LOOPS ADJUSTEMENT : THE METHOD

Different studies of the 3D structures used the solar rotation to vary the aspect angle of otherwise *static* structures (e.g. Loughhead, Chen & Wang 1984; Berton & Sakurai 1985; Aschwanden & Bastian 1994a,b; Davila 1994; Aschwanden et al. 1995; Aschwanden 1995). A new method by Aschwanden *et al.* (1999) take into account the small variation of the magnetic field with time versus heating or cooling processes in coronal loop to consider some *Dynamic Stereoscopy*. Then, some EIT loops are fitted with a circular model. Different time projections give the unicity of the loop parameters derived.
For taking into account that the loop are sometimes twisted and sheared, the improved model considered the loop as a line over a torus (As in "plan parallel" model of atmosphere, a loop is represented by a straight line, a small perturbation for footpoints move the line inside a cylinder, so the line is inside a torus in the real 3D corona).
As magnetic field lines could be parabolic or with other shape for a magnetic bipole, twisted loops are an approximation —which is able to describe more cases than circular loops—.

4. STUDIES OF ACTIVE REGION LOOPS

Loops trace the magnetic field lines because the value of the beta plasma parameter is low in the corona. Many results concerning hot loops were obtained with Yohkoh (Klimchuk & Porter 1995, Porter & Klimchuk 1995), so different scaling laws were looked in EUV at lower temperature for cooler loops.

4.1. STATISTICS OVER CIRCULAR LOOPS

We studied (*cf.* Aschwanden *et al.* 1999) the 3D structure of the ARL NOAA 7986 on August 30th 1996. 30 circular loops were analysed. Radius ($R_0 = 93 \pm 23$ Mm), azimuth angle of loop baselines ($\alpha = -3^0 \pm 10^0$), inclination angle of loop planes ($\vartheta = 7^0 \pm 37^0$) were measured and temperature and density diagnostic were made. The conductive cooling time were found to be $\tau_{cond} \sim 10$ days, while the radiative cooling time were $\tau_{rad} \sim 40$ min.

To summarize some results, it was found that

1. these cool EUV and rather scale loops ($h \sim 30 - 225$ Mm) are in hydrostatic equilibrium
2. the loop width is found almost constant
3. the scaling laws obtained are different than the SXR loops

These statistics were compared with hotter loop analyzed by Kano & Tsuneta (1995, 1996) : Yohkoh measured loops with 4 times the EIT loops temperature, 1.5 times the density and 0.5 the loop half length.

4.2. EMERGENCE AND SHORT TIME EVOLUTION OF AN ARLs

Complete study of the area NOAA 8069 is done in Portier-Fozzani *et al.* (1999a). The area emerged in 1 day (August 5th-6th, 1997) and was enough far away from other Active Region to be considered as an emerging flux tube without interaction.
It has emerged in a previous activity location where, even if there were no NOAA number for few days (on July 30th it was NOAA 8066), there were some weak photospheric magnetic field.

It emerges twisted (Fig. 1) which confirms the extrapolations of Leka *et al.* (1996). It detwists as it expands which is coherent with the Parker formula (1977) for twisted flux tubes (radius R and $2\pi\delta$ the

λ_{EIT} (Å)	λ_{solar} (Å)	λ (Å)	Ion	Transition	Intensity	Atmosphere
171	170.600	170.577	Fe X	$3s^23p^5\ ^2P_{3/2}$ - $3s^23p^4(^3P)3d\ ^2D_{3/2}$	1.6e+02	Transition Region
.	171.073	171.073	Fe IX	$3p^6\ ^1S_0$ - $3p^53d\ ^1P_1$	2.8e+04	Transition Region
195	195.125	195.118	Fe XII	$3s^23p^3\ ^4S_{3/2}$ - $3s^23p^2(^3P)3d\ ^4P_{5/2}$	1.0e+04	Quiet Corona
.	.	195.131	Fe XII	$3s^23p^3\ ^2D_{3/2}$ - $3s^23p^2(^1D)3d^2D_{3/2}$	4.2e+02	Quiet Corona
.	196.640	196.648	Fe XII	$3s^23p^3\ ^2D_{5/2}$ - $3s^23p^2(^1D)3d\ ^2D_{5/2}$	8.0e+02	Quiet Corona
284	284.159	284.160	Fe XV	$3s^2\ ^1S_0$ - $3s3p\ ^1P_1$	4.4e+04	Corona
304	303.324	303.325	Si XI	$2s^2\ ^1S_0$ - $2s2p\ ^1P_1$	1.5e+04	Corona
.	303.782	303.780	He II	$1s\ ^2S_{1/2}$ - $2p\ ^2P_{3/2}$	6.1e+05	Chromosphere
.	.	303.786	He II	$1s\ ^2S_{1/2}$ - $2p\ ^2P_{1/2}$	3.0e+05	Chromosphere

Table 1. SOHO/EIT line list : —transitions from the atomic database CHIANTI (adapted from Deré *et al.* 1997)—

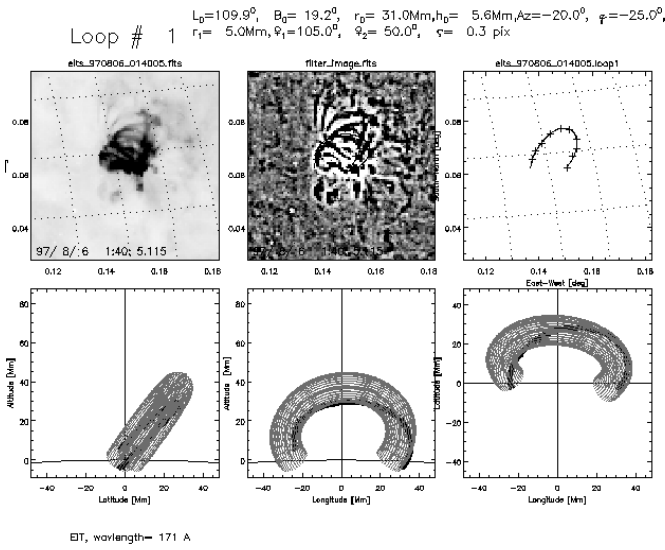

Figure 1. Loops Fitting : radius, altitude and twist measured for a loop on August 6th 1997 at 01:40 from a SOHO/EIT Fe IX/X image

helix wavelength) with $\omega = (x^2 + y^2)^{\frac{1}{2}}$ and the distance up to axe z,

$$B_z = B_0 . \frac{(1 + \frac{R^2}{\delta^2})^{\frac{1}{2}}}{(1 + \frac{\omega^2}{\delta^2})^{\frac{1}{2}}}$$

and $B_\Phi = B_z \frac{\omega}{\delta}$.
As helix step δ decreases while twist increases, and because energy is proportional to $|B|^2$ (Aly, 1991), a decrease in twist corresponds to a lost of energy. So energy is transformed into expansion. Loop expansion velocity ($\sim$ 10km/s) is less than the usual initial speed of CMEs. Flares happen in this AR only after August 6th 1997, long time after the emergence, when loops have almost constant size. This shows that other energy input than the twist exists at that time.

4.3. LONG TIME EVOLUTION OF AN ARLs

Summer 1996 was perfect to study long time evolution. The AR successively named NOAA 7978, 7981, 7986 was alone. Of course each loop could not be followed upon a so long time, but average tube flux parameters were obtained. Study is still in progress as some correlation were found between degree of non circularity of loops and flares. Shear and twist created this inhomogeneity.
With the time, the bipolar AR becomes wider (van Driel, 1998).

Even at the solar minimum cycle, the area topology was pretty complex. Multi-wavelengths observations (H_{alpha} for filament channel, He I for coronal holes and comparison with the Nobeyama Radio Heliograph) show that a positive polarity coronal hole preceded the ARL, a filament channel lies along the neutral line between the 2 polarities, and a negative polarity coronal hole follows the ARL (Fig. 2).

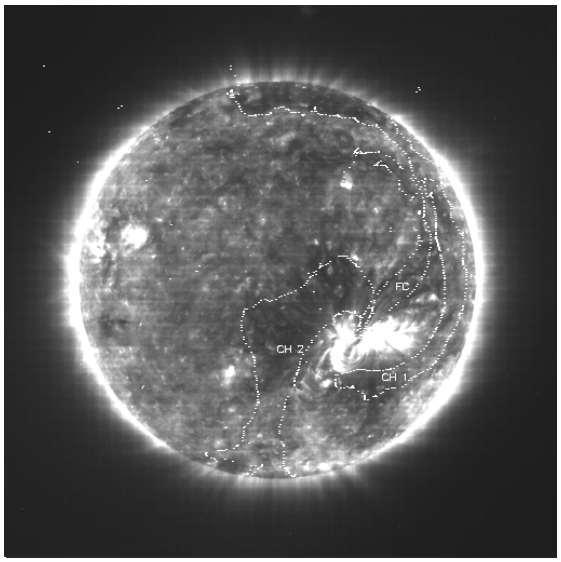

Figure 2. Topology of the area (neighbourhood of NOAA 7986) observed August 31st 1996 :
CH 1 is the famous elephant trunk Coronal Hole
FC is the filament channel following the neutral line between the 2 polarities of the ARL.
CH 2 is a coronal hole with opposite polarity versus CH 1 (also obtained by Sheeley *et al.* modelisation —in Wang *et al.* 1997 —).

As the Summer 1996 corresponds to the solar minimum cycle, the Sun gives a kind of symmetry aspect between the North West and the South East (*eg.* Au-

gust 29th, September 26th). The northern polar CH which comes upon equator (CH1) in front of the AR while it has a symmetric hole with opposite polarity related to the southern polar hole (CH2). These holes became structured when the AR had emerge. The filament channel separates the 2 CHs and the 2 polarities of the ARLs as a mirror (Fig. 2).

As Active Regions follow the differential rotation law and Coronal Holes follow more rigid rotation (Wang *et al.*, 1988), some of the morphological changes observed in loops where probably partly due to magnetic interactions.

4.4. COMPARING OPEN AND CLOSED STRUCTURES

In Neupert *et al.* (1998), we analysed 2 different coronal structures above an AR September 25th 1996. With SOHO/EIT Fe XI/X and Fe XII images and the CHIANTI atomic code we had estimated temperatures and densities of the structures. A closed loop and an extended coronal feature —which correspond to an open line— were fully studied.
We found that downward conductive losses were inadequate to support radiative losses which imply that energy deposition is approximately proportional to the square of the local density.

4.5. MAGNETIC INTERACTIONS

Effects of newly erupting flux on the polar coronal holes were previously analyzed by Sheeley *et al.* (1989). Magnetic interaction were derived from Skylab mission observations. Further interactions observed in EUV where then derived with SOHO/EIT. Interactions between magnetic field lines were studied in different cases :

1. between CH and ARLs : Observations such as May 16th 1997 conclude for possibilities of structurations of CHs by ARL (Portier-Fozzani, 1999b, Portier-Fozzani & Pohjolainen 1998b). Mini-CHs are then named when the field is weakly open and not very structured (Pohjolainen & Portier-Fozzani 1999)

2. between ARLs (reconnections known from 1996 by Yohkoh : Tsuneta 1996 and other authors) : several examples were found (*cf.* Portier-Fozzani 1999b)

3. between ARL and CH predicted in theory by Ruzmaikin (1998) : an opening of an ARL was probably due to magnetic reconnection (Portier-Fozzani 1998a)

5. CMES AND FLARES

Two classical CMEs and flaring events were studied.

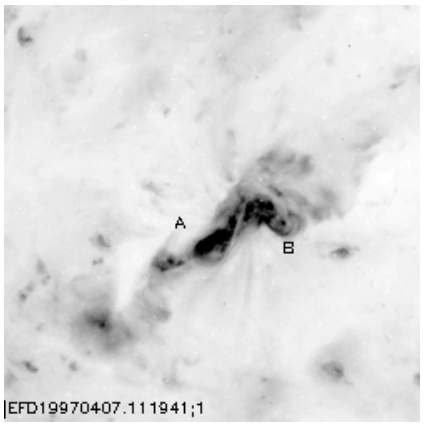

Figure 3. NOAA 8027 S shape on EIT Fe XII Image taken April 7th 1997 at 11h19mn

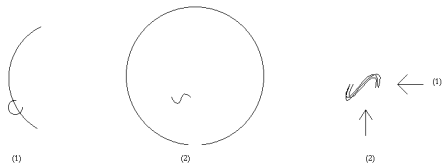

Figure 4. The 3D aspect of the NOAA 8027 deduced from the projection : (a) shape when the AR was at the limb : April 1st 1997, (b) AR on the disk

- April 7th 1997, the Active Region NOAA 8027 changed itself from an S shape to an arcade. The S shape was an highly twisted/sheared group of loops (Fig. 3, 4). Observations of post-eruption arcades are described in Klimchuk (1996).

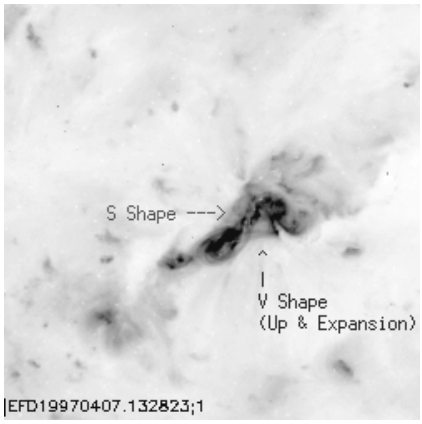

Figure 5. EIT Fe XII April 7th 1997 at 13h 28mn

A V shape is observed at 13h28mn (Fig. 5). A precise analysis with the help of stereovision shows that the V is expanding upward. A Filament Disparition Brusque is reported by the SEC at 13h54mn in the North West part of the Area with a flare. SOHO/EIT after 14h12mn —due to low temporal resolution— shows that the flare is progressing southward as it "creates" an arcade. This progression coincide with the "connection" of the V lines with S lines. It is coherent with the Amari (1999) model of CME formation which gives small loops at lower altitude. Magnetic re-

connection of the V lines (small loops which go upward) with the S loops change then the topology (Portier-Fozzani, Amari & Pick, 1999d).

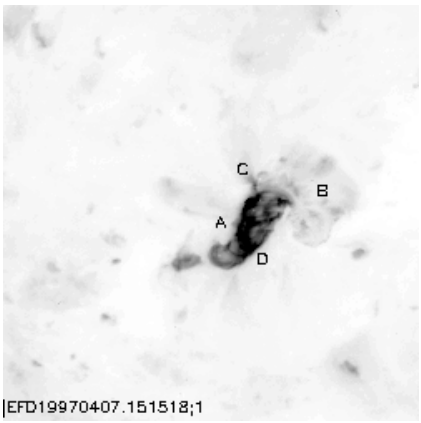

Figure 6. EIT Fe XII April 7th 1997 at 15h 15mn

The arcade —made with parallel loop (AD) up to (CB)— is formed (Fig. 6) in a transverse direction than the previous loop (AB). A CME is observed with SOHO/LASCO coronagraphs in relation with these events (Maia *et al.*, 1998).

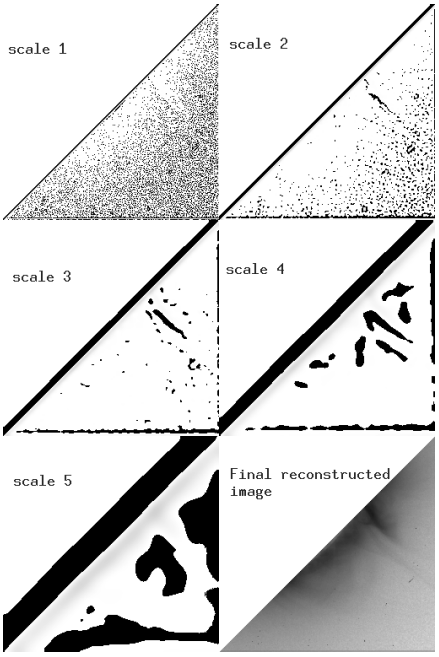

Figure 7. Wavelet reconstruction of the NOAA 8100, November 6th, 1997 :
The 5 wavelet transforms planes and the rebuilt object (double Y shape)

- Between November 5th 1997 at 22h00 and November 6th at 6h00 some plasma escape outward from an area located southward than NOAA 8100 —South West limb—. A flare occurred at 12h15mn, as the 2 opposite polarities of the AR were connected by a S shape loop. About 1 hour later, first particles were detected on the SOHO spacecraft (bright points everywhere on the EIT CCD). After 16h11, the southern loop

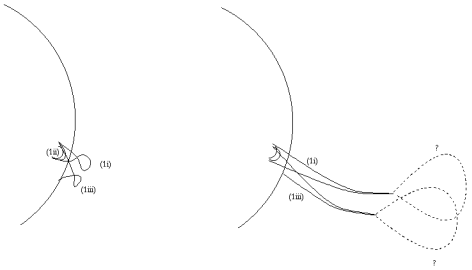

Figure 8. Possible scenario for the formation of a coat-hanger from highly twisted loop : From EIT images, aspect of the NOAA 8100 November 6th nearby 0h30

structures expand with a double V shape, as the other loops -even they had the same footpoints- kept their regular morphology (ie circular).

In the both case, the S shape is present. The loop becomes instable due to high twist or high shear. Reconnection needs to happen to create such amount of energy for the flare.

6. CONCLUSION

Different 3D Technics were developed to study coronal structures evolution. Anaglyphs and other stereovision methods were used to point out interresting global coronal changes (such as global interactions). Loops fitting were preferred to understand their 3 D geometry including twist and shear parameters.
Emerging magnetic flux was observed to appear highly twisted and expands as it detwist. It corresponds to the evolution described by the Parker formula. Statistics concerning circular loop were obtained and compared with hotter loops seen with Yohkoh. Long time evolution for cool loops were analysed too. Magnetic field interactions were also studied.

From the torus model, it is possible to propose a more precise analysis concerning the contribution for each group of loops to the space weather. While measuring the degree of non-circularity for loops (by twist or shear measurements), we obtain helicity measurement. As the helicity is supposed to be conserved, the twist and shear can be transformed in other type of energy. As high twist and shear in ARL creates instabilities and as filaments are supported by loops, we should be able soon to forecast CMEs formations from EUV loops fitting.

ACKNOWLEDGMENTS

SOHO/EIT is a ESA/NASA instrument headed by J. P. Delaboudinière. Many successfull collaborations (precised in the text) have participate to the success of these studies (Aschwanden M., Neupert W.,...).

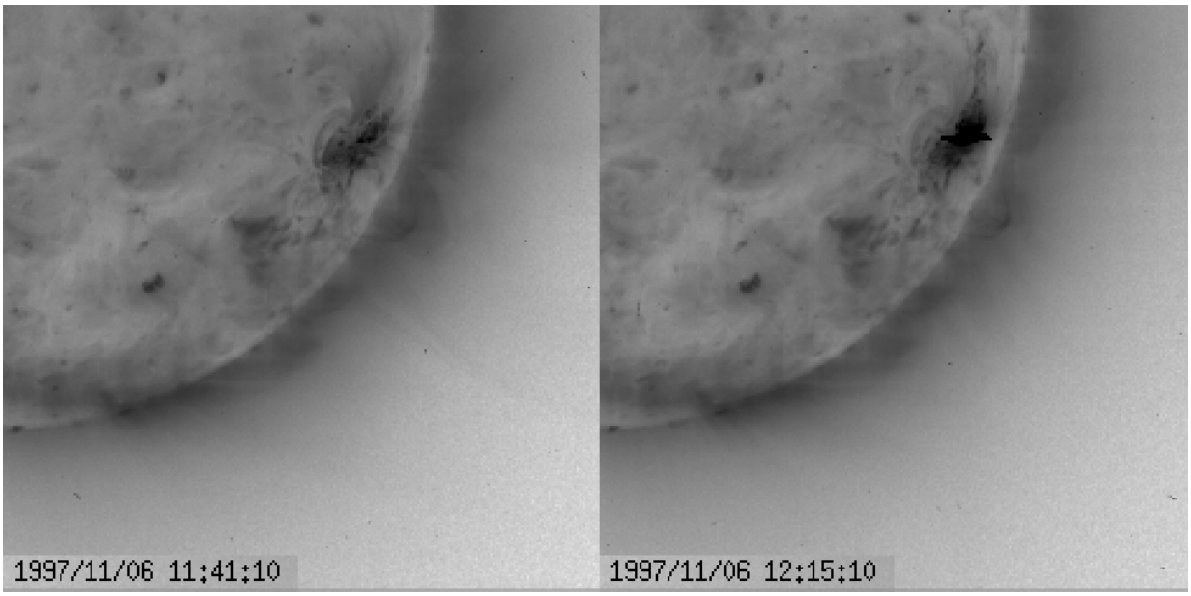

Figure 9. Flare in NOAA 8100 November 6th : SOHO/EIT Fe XII images at 11h41mn and 12h15mn

REFERENCES

Aly J.J., 1991, "Dynamics of solar flares", Flares 22 Workshop, p.29, Obs. Paris-Meudon DASOP Editors

Amari T., 1999, this proceeding

Aschwanden M., Newmark J., Delaboudinière J.P., Neupert W., Klimchuk J., Gary A., Portier-Fozzani F. & Zucker A. , 1999, ApJ. 515, 842-867

Aschwanden M.J. & Bastian T.S., 1994a, ApJ 426, 425

Aschwanden M.J. & Bastian T.S., 1994b, ApJ 426, 434

Dere K.P., E. Landi, H. E. Mason, B. Monsignori-Fossi & P. R. Young, 1998, A&A. Sup. Ser. 125, 149

Berton R. and Sakurai T. 1985, Sol. Phys. 96, 93

Bijaoui A., Slezak E. & Vandame B., 1998, in em Astrophysics and Algorithms: a DIMACS Workshop on Massive Astronomical Data Sets

Davila J.M. 1994, ApJ. 423, 871

Defise J.M., Clette F., Moses J.D., Hochedez J. F., & the EIT contorsium, 1997, SPIE 3114, 598

Deré K.P., Landi E., H. E. Mason H.E., Monsignori-Fossi B. and Young P.R., 1997, A&A Sup Ser 125, 149

Deré K.P., 1978, ApJ 221, 1062

Delaboudinière J.P. *et al.*, 1995, Sol. Phys. 162, 291

B. Fleck, V. Domingo & A. Poland, 1995, Sol. Phys. 162, n 1-2

Kano R. and Tsuneta S. 1996, P.A.S.J. 48,535

Kano R. and Tsuneta S. 1995, ApJ. 454, 934

Klimchuk J.A., 1996, PASP Conf. Ser. 111, 319

Klimchuk J.A. & Porter L., 1995, Nature 377, p.131

Leka *et al.*, 1996, ApJ. 462, 547

Loughhead R.E., Chen C.L., and Wang J.L. 1984, Solar Physics 92, 53

Maia D. *et al.*, 1998, Sol. Phys.,

Moses D. *et al.*, 1997, Sol. Phys. 175, 571

W. Neupert *et al.*, 1998, Sol. Phys., 183-2, 305-321

Parker, E.N, 1977, A.R.A.A. 15, 45-68

Pohjolainen S. & Portier-Fozzani F., 1999, A&A Sup., submitted

Porter L. & Klimchuk J., 1995, ApJ 454, 499

Portier-Fozzani F. *et al.*, 1999a, A&A, to be submitted

Portier-Fozzani F. *et al.*, 1999b, Thesis, to be submitted

Portier-Fozzani F. *et al.*, 1999c, Sol. Phys., to be submitted

Portier-Fozzani F., Amari T., Pick M. & al., 1999d, A&A, In preparation

Portier-Fozzani F., Neupert W., Aschwanden M., Sheeley N.R., Thompson B., Maucherat A., Newmark J., Klimchuk J.A., 1998a, 2nd ASPE meeting: Oral presentation, *3D Structures of the solar corona observed with SOHO/EIT*

Portier-Fozzani F. et Pohjolainen S., 1998b, CESRA meeting : poster contribution

Portier-Fozzani F. et *al.*, 1997, PASP Conf. Ser. 111, 402

Ruzmaikin A. & Berger M. A., 1998, A&A 337, L9

Sheeley N. R., Wang Y.-M., Harvey J. W., 1989, Sol. Phys. 119, 323.

Thomas & Neupert, 1994, ApJ. Sup. Ser. 91, 461

Tsuneta S., 1996, ApJ. 456, L63

Vézien J.M., 1995, Thèse de Paris VII, UFR Informatique, *Technique de reconstruction globale par analyse de paires d'images stéréoscopiques*

van Driel L., 1998, PASP Conf. Ser. 155, 202

Wang Y.M. *et al.*, 1997, ApJ 485, 875

Wang Y.-M., Sheeley N. R. JR., Nash A. G., & Shampine L. R., 1988, ApJ. 327, 427

Chapter VI

Synthèse

Je persiste à dire que la Terre tourne autour du Soleil,
et qu'il existe d'autres soleils semblables au nôtre dans l'Univers
Giordanno Bruno, lors de son procès devant l'Inquisition,
avant d'être brulé en 1600 à Rome en place publique.

Sommaire

Le lecteur trouvera dans ce chapitre un article (en préparation) de synthèse de la thèse.

VI.1 Article de synthèse de la thèse

Etude de la couronne solaire en 3 D et de son évolution avec SOHO/EIT

VI.1.1 Résumé

L'étude de la couronne solaire permet de mieux comprendre sa température élevée et d'analyser sa forte dynamique afin de faire de la météorologie spatiale. Le plasma coronal étant figé par le champ magnétique, les images EUV de SOHO/EIT sont donc particulièrement bien adaptées pour suivre les évolutions.

Après avoir mis en place des outils spécifiques à l'intrument SOHO/EIT pour développer les données (catalogue d'images, dégrillage, ...), nous avons utilisé les séquences temporelles dans les 4 longueurs d'ondes de SOHO/EIT pour étudier les évolutions morphologiques et topologiques de la couronne solaire.

Des techniques de stéréovision permettent la reconstruction en 3 Dimensions d'objets ordinaires à partir de 2 prises de vues du même objet depuis un angle différent. Après avoir pris en compte les contraintes inhérantes aux longueurs d'ondes utilisées —raies optiquement minces—, ainsi que les contraintes temporelles, nous nous sommes servis de la rotation solaire pour reconstruire en 3D la couronne. Pour une reconstruction précise il a parfois fallut considérer un modèle à priori (boucles circulaires par exemple).

La stéréovision avec contraintes a ainsi permis de déterminer la physique de 30 boucles d'une région active. Ces boucles EUV sont apparues comme étant en équilibre hydrostatique contrairement aux boucles plus chaudes en X.

La technique utilisée a ensuite intégré des asymétries telles que la torsion des boucles. Lors de l'émergence d'une région active, les boucles apparaissent torsadées. Ces observations confirment des observations précédentes. Les boucles se détorsadent ensuite au fur et à mesure de leur expansion. Cela s'explique par une conservation de l'hélicité.

D'autres techniques sont venues completer ces études.

VI.1.2 Introduction

Le Soleil, sa couronne, et intérêt de son observation en 3 dimensions

La température du soleil décroît depuis l'intérieur du Soleil (plusieurs millions de degrés) jusqu'à la photosphère (Température de 5800K). Cela est facilement compréhensible puisque la chaleur produite au centre par l'énergie des réactions nucleaires est transportée selon le moyen adéquat le plus efficace (radiation ou convection) vers l'exterieur. Par con-

tre, la spectroscopie a montré que la haute atmosphère solaire —aussi appelée couronne solaire à cause de son aspect lorsque la photosphère est cachée par la Lune lors d'une éclipse — a une température très élevée. Sa température atteint plusieurs millions de degrés, ce qui rend la couronne observable en EUV et rayons X. Ainsi, on recherche quels processus de chauffage peuvent être mis en jeu.

Depuis Galilée, avec des instruments optique adaptés, on observe sur la photosphère des parties sombres appelées taches solaires. Ces taches correspondent à un fort champ magnétique. Le nombre de taches varie avec une période de 11 ans. Durant la même période, elles migrent progressivement en latitude et inversent ensuite la polarité dans les 2 hémisphères. Ainsi le soleil est une étoile magnétique avec une période de 22 ans.

Dans la couronne solaire, le plasma est figé par le champ magnétique. Cela permet ainsi de visualiser en 3D les lignes de champs magnétiques. La seule méthode permettant d'imager les champs magnétiques coronaux en 3D, consiste à observer le plasma, les polarimètres étant inefficaces en EUV. Ainsi comprendre l'évolution des tubes de flux coronaux permet de mieux comprendre les mécanismes de chauffage supposés d'origine principalement magnétiques.

VI.1.3 La couronne : aspect général

De nombreuses structures en forme de boucles sont observées dans la couronne solaire (ex. Fig. II.5). Le plasma y suit alors des lignes de flux magnétiques fermées [125].

La couronne solaire apparaît comme extrêmement dynamique en 3 dimensions [157]. On observe ainsi des éruptions et des éjections de masses coronales (CMEs) qui traduisent des phénomènes très énergétiques [94],[177]. Des changements dans l'aspect des boucles correspondent à de nombreuses éruptions.

D'autres structures de lignes de champs magnétiques ouvertes appelées trous coronaux évoluent rotation après rotation.

Etudier la couronne nécessite donc de comprendre l'évolution de la morphologie (aspect) des structures qui la composent mais aussi les variations de la topologie (géométrie) magnétique. Ces différents aspects peuvent être liés. Comprendre l'évolution en 3D nécessite donc une compréhension globale et précise de ces différents éléments.

VI.1.4 Observation du soleil et de sa couronne

Lancé fin 1995, le satellite SOHO avec ses 12 instruments observe le soleil 24h sur 24 [79]. L'intéractivité entre ses différents instruments et les instruments terrestres permet de mieux comprendre le comportement du soleil dans sa globalité [181].
A son bord, l'imageur EIT observe en EUV 4 longueurs d'ondes bien adaptées de la chromosphère à la couronne [58].

- A 304A, la raie d'He II permet de voir la chromosphère (Température environ de

10^4 K). On y voit un bouillonnement. Des parties sont quelquefois visibles en émission, en dehors du limbe : les protubérances.

- A 171A, le Fe IX/X montre les structures de la région de transition (région intermédiaire ou le gradient de température est très important). Sa température est de 1.3MK. Les structures des boucles ont un aspect généralement plus fin. Différentes structures sombres existent à grandes échelles : les trous coronaux et les filaments.

- A 195A, le Fe XII image les structures de la couronne (environ 1.6MK).

- A 284A, le Fe XV image une couronne plus chaude à environ 2MK.

Pour produire ces images, l'instrument SOHO/EIT est un télescope de Ritchey-Chrétien. La résolution de sa CCD est de 1.62 x 1.62 $arcsec^2$ (1 arcsec représentant environ 730km sur le soleil) avec un champ de 1024 x 1024 pixels. Le choix de la longueur d'onde d'observation s'effectue par un quadrant cache ouverture.

D'autres instruments peuvent venir aider à l'analyse en complétant ces mesures soit avec d'autres longueurs d'ondes ce qui permet de mieux déterminer la nature physique des objets observés (Visible, H_α, Radio, X, coronographie), soit pour zoomer sur certaines structures (TRACE).

VI.1.5 Dégrillage des images de SOHO/EIT

Sur les images d'EIT apparaissent une surbrillance en forme de grille (Fig. III.2). La transformée de Fourier d'une image montre que les fréquences ne sont pas régulièrement espacées (Fig. III.4). Pour ôter numériquement ce défaut nous allons donc devoir faire un filtrage local. Le filtrage médian semble bien approprié puisqu'il remplace la valeur "anormale" par la médiane des points voisins. Ainsi pour enlever la grille qui est une anomalie du plan objet, nous allons faire un filtrage médian local.

Cette méthode a été intégrée au soft EIT sous le nom de eit_degrid_smooth.

Toutefois un filtre médian est un filtre non linéaire. Nous allons donc utiliser cette méthode pour extraire les grilles. Une fois extraites de chaque images, on somme ainsi ces grilles. L'image soustraite à cette grille moyenne obtenue permet d'obtenir une image calibrée dégrillée que l'on peut alors utiliser pour l'analyse physique.

VI.1.6 Catalogue par imagettes de SOHO/EIT

Afin de choisir les données adéquates, nous avons développé un code permettant de visualiser sur une seule image un catalogue d'imagettes obtenu selon des critères précis (Fig. III.1). Cela permet de faire des pré-études rapide de l'évolution des structures et des intéractions magnétiques.

VI.1.7 Les structures de la couronne

Les observations multi-longueurs d'ondes permettent de préciser la nature physique des régions observées. Sur la Figure II.13 nous pouvons distinguer les régions suivantes :

1. Les filaments (notés FC) apparaissent en sombre sur les images EIT (Fe X/X, XII, XV), en sombre sur les images radio de Nobeyama, ainsi que sur les images H_α [191]. Ils suivent les lignes de neutralité magnétique avec du plasma froid. A noter que les filaments peuvent être vus en émission lors de leurs éruptions mais aussi lorsqu'observés au bord du limbe. Dans ce dernier cas on parle aussi de protubérances.

2. Les régions actives les plus simples (notées ARL) correspondent à des bipolarités du champ magnétiques (cf. Fig. IV.1). Elles sont vues sous formes de boucles multiples en EUV, les magnétogrammes montrent les 2 polarités différentes de leurs pieds. Les régions actives peuvent aussi être davantage complexes en regroupant plusieurs couples de polarités. Nous reviendrons sur l'étude des boucles qui composent ces régions actives ultérieurement.

3. Les trous coronaux (notés CH) sont des régions où le champ magnétique est ouvert. Ils sont simultanéments sombre en EUV pour EIT, brillant dans les longueurs d'ondes radios de Nobeyama, et de polarité majoritaire quasi-uniforme dans les magnétogrammes.

VI.1.8 Stéréovision et vision 3D

La vision en 3 dimensions se fait en observant un même objet grâce à la différence d'angle entre 2 récepteurs. Pour reconstituer simplement le relief de la couronne, on prend des images de SOHO/EIT à des temps différents ce qui donne une différence de perspective sur une même structure stable [191].

En maintenant séparé le trajet optique (par exemple avec des couleurs différentes complémentaires), le cerveau interprète les différences dans cette superposition d'images (ie les anaglyphes) comme du relief. Des méthodes plus systématiques de reconstruction par stéréovision existent. Après avoir extrait de chaque image des primitives (cf. techniques d'analyse d'images dans [27]), on définit grâce à la géométrie projective les formules d'inversions qui vont permettre de paramétrer les objets en 3D (cf. [77] et références dans ce livre).

L'INRIA a réalisé une méthode d'inversion en 3D à partir d'objets optiquement épais (table, chaises,... [246]). Nous pouvons à partir de la différence entre les structures des objets initiaux et celles des objets reconstruits mesurer les incertitudes de la méthode dans la reconstruction dans le cas d'objet optiquement épais.

VI.1.9 Contraintes de vision 3D pour la couronne

Les images de la couronne prises par les raies du Fe avec SOHO/EIT sont optiquement minces. C'est à dire que l'émission correspond à l'intégration sur une ligne de visée (cf. Fig. III.25). En réalisant des films à partir des séquences temporelles d'images EIT, on se rend compte de la forte dynamique des structures de la couronne solaire. Ainsi l'étude d'images non simultanées introduit des incertitudes supplémentaires.

La dynamique de la couronne et le fait que les raies soient optiquement minces impliquent des incertitudes trop grandes pour réaliser une reconstruction totale par stéréovision. Pour diminuer ces incertitudes on peut :

- soit prendre des mesures simultanées (c'est le but de la mission STEREO qui sera lancée bientôt)
- soit considérer un modèle à priori qui définira des contraintes morphologiques. Nous allons donc définir des modèles géométriques à priori qui nous permettrons d'étudier la physique de ces objets.

Les boucles coronales peuvent être facilement observées avec différents angles de perpectives et donc sont bien adaptées pour chercher à être reconstruites.

VI.1.10 Reconstruction par stéréovision pour des boucles circulaires

Considérons dans un premier temps que les boucles sont circulaires. Sur une image EIT (ou sur une image filtrée en haute fréquence pour faire ressortir les gradients importants), on ajuste à la souris une boucle pour obtenir un tableau x(n), y(n) dans les coordonnées de l'image. Il nous faut donc définir les paramètres suivants : (Fig. 2 dans [15])

1. l'inclinaison
2. l'azimuth
3. le rayon
4. l'altitude du centre de la boucle
5. la position sur le soleil du centre de la boucle (longitude et latitude héliographique)

On obtient ainsi pour l'image i une solution s(i).

Pour chaque image, on minimalise la distance entre l'ajustement de la boucle fait à la souris et le modèle de boucle circulaire. Comme décrit sur la Figure IV.10, une seule projection donne plusieurs solutions (j) possibles pour chaque image s(i,j).

En considérant des angles de vues différents de même structures (stéréovision statique), on obtient une unicité de la solution (cf Fig IV.11). Cela se démontre aussi en utilisant les lacets de la topologie algébrique. On a ainsi une solution par stéréovision pour une structure statique avec contrainte à priori (boucle=cercle).
L'algorithme mis en oeuvre est ainsi le suivant

1. Sur une image 1
    - Ajustement à la souris de la boucle
    - Transformation des coordonnées
    - Recherche modèle circulaire donnant l'erreur minimale sur la projection s(1,j)
2. Sur l'image 2 (environ 3h plus tard)
    - mêmes calculs que pour l'image 1 s(2,k)

On compare alors les différentes valeurs trouvées. Comme il y a unicité de la solution, par continuité des paramètres, on trouvera alors la solution valable sur l'ensemble des images.

Des résultats obtenus sont présentés Fig IV.13.

VI.1.11 Stéréoscopie dynamique

La lenteur de la méthode donne alors l'idée d'une première amélioration en tentant de l'automatiser :
principe de la stéréovision dynamique dans le cas circulaire. Cette méthode est complètement décrite dans Aschwanden et al. 1999 ([15]). On considère la variation des boucles partiellement émissives dans un référentiel aplati en tenant compte de l'intégration sur la ligne de visée.

Cela nous permet d'obtenir les paramètres définis précédemment en permettant au boucles d'évoluer dynamiquement en se reremplissant ou non. Nous avons ainsi pu faire des statistiques sur les boucles de la région active NOAA 7986 du 30 Aout 1996.

Physiquement les résultats obtenus sur 30 boucles de SOHO/EIT sont les suivants :
Les tailles, les rapports entre les raies EIT de l'émission, et le code atomique CHIANTI permettent de déterminer la température et la densité des boucles.
Les boucles apparaissent être en équilibre hydrostatique.
En général, il n'y a pas de variation de la section transverse.

Les relations obtenues sont les suivantes :

- Pression proportionnelle
  à la longueur de la boucle à la puissance -0.41+/-0.12

- Champ magnétique proportionnel
  à la longueur de la boucle à la puissance -1.02+/-0.43

- Energie de Chauffage proportionnelle
  à la longueur de la boucle à la puissance -0.73+/-0.23

Différents résultats magnétiques sont résumes Table 2 de Aschwanden & al.[15].

Cela permet de comparer les résultats entre les mesures EUV et SXR Table 3 de Aschwanden & al.[15]. Le comportement des boucles tièdes (EUV) est donc relativement différent de celui des boucles chaudes (SXR).

Les boucles quelquefois sont non circulaires même dans les cas de modélisation MHD simples (Fig IV.8). Certaines boucles ne sont pas ajustables par des cercles (Fig. IV.14).

VI.1.12 Prise en compte des écarts à la circularité

Une manière simple de prendre en compte l'"acircularité" est de la considérer comme une torsion.

En effet, de manière naîve considérons un bout de corde. Si l'on exerce une torsion en un sens opposé de part et d'autre de cette corde, elle se raidit puis se déforme. Un calcul MHD montre que les contraintes sur les pieds impliquent les mêmes consequences sur le plasma qui est figé par le champ magnétique.

Ainsi, la représentation plan parallèle d'une boucle donne une ligne rectiligne, une déformation des pieds de cette ligne l'inscrit dans un cylindre, ce qui donne en 3 dimension une ligne se déplaçant à la surface d'un tore (Fig. IV.15).

Le paramétrage pertinent a donc 3 paramètres supplémentaires (Fig IV.16):

- le rayon secondaire du tore
- l'angle initial (ϕ_1)
- le nombre de tour (ψ) ou l'angle final (ϕ_2)

Validons tout d'abord la méthode en mesurant la sensibilité de la déviation suite à une variation des variables : les Figures IV.18 et IV.18 montrent que pour une différence de torsadage inférieure à 7 degrés on obtient une variation de 2.78 pixels au lieu de 0.32 pixel. La minimisation de cette variation est donc un bon critère pour une mesure précise des différents paramètres.

L'algorithme de la méthode dans le cas des boucles non circulaires est le suivant :

1. On recherche des solutions par minimisation avec la fonction POWELL d'IDL (méthode qui mélange les moindres carrés, les gradients et le minimum d'entropie). On obtient j solutions pour l'image i $s(i,j)$.

2. La variation avec l'angle de vue nous permet de trouver la solution en réalisant la stéréovision sur l'ensemble des $(s(i,j))$ possibles. En effet on suppose la continuité des paramètres physiques. Cela s'écrit $\|s(1,k1) - s(2,k2)\| = 0$ quand k1 et k2 correspondent à la bonne solution pour les images respectives 1 et 2.

On obtient ainsi une seule solution physique acceptable pour l'ensemble des images $s(i0,j0)$, $s(i1,j1)$, etc... avec i0 différent de i1,...

VI.1.13 Ajustement de boucles dynamiques

A partir de cela on peut considérer pour des boucles non circulaires les cas statiques et les cas dynamiques. En effet, les solutions $s_(i,j)$ dépendent de la position et de la boucle elle même. Cette dernière partie dépend de [Ar, theta , r0, h0, r1, ϕ_1 , ϕ_2] = G(i,j).

Quand k1 et k2 correspondent à la bonne solution pour les images 1 et 2 :

- $\|G(1,k1) - G(2,k2)\| = 0$ dans le cas statique puisque tous les paramètres de la boucle sont strictement les mêmes.
- $\|G(1,k1) - G(2,k2)\| \longrightarrow 0$ quand $\|temps(1) - temps(2)\| \longrightarrow 0$ dans le cas dynamique. On peut alors autoriser certains paramètres à varier (exemple phi1 et phi2,r0,h0 continu) afin de vérifier un modèle à priori (ex :expansion...).
  Cela constitue une généralisation dynamique de la stéréovision statique (qui constitue une méthode différente de la méthode de la "stéréovision dynamique")

Cette méthode permet l'étude de l'évolution dynamique de l'émergence d'ARL et de leurs évolutions.

Nous avons donc appliqué cette méthode pour mesurer la variation du torsadage et de la taille des boucles lors de l'émergence d'une nouvelle région active. La région NOAA 8069 émerge en un jour (5-6 Août 1997) et elle est suffisamment éloignée des autres régions pour pouvoir considérer que les tubes magnétiques ne subissent aucune interaction extérieure. Elle émerge à la place d'une ancienne AR. Les ajustements sont mesurés sur les Figures 5 et 8 de l'article [189].

La Table VI.1 reporte le résultat de ces mesures.

Il en ressort que l'émergence se fait avec des boucles déjà torsadées. Cela confirme les extrapolations de Leka & al. ([133]). Les boucles se détorsadent pendant l'expansion.

Jour	97-08-05	97-08-06	97-08-06	97-08-06
Heure	19:07 UT	01:40 UT	15:51 UT	23:25 UT
Altitude maximale ($r_0 + h_0$ en Mm)	34	37	40	46
Torsadage : $\Psi = \Phi_2 - \Phi_1$	210	55	27	10

Table VI.1: **Taille des boucles et de leur torsadage**. Les incertitudes obtenues sont de 2 Mm pour l'altitude et 5 degrés pour le torsadage. Le petit rayon du tore reste constant (5Mm)

La formule de Parker [173] dans le cadre d'une géométrie linéaire, nous montre que le détorsadage traduit que l'énergie est transformée en expansion. L'hélicité magnétique traduit -entre autres- la torsion du champ magnétique ($H = \int B.rot(B) = T.\Phi^2$ avec T le torsadage et Φ le flux magnétique). Ainsi la conservation de l'hélicité magnétique traduit la transformation de la rotation en expansion. Un trop fort torsadage peut conceptuellement créer une forte expansion ce qui peut être relié au départ de certaines CMEs en forme de boucles dans certains cas. La mesure du torsadage nous permet donc de comprendre l'altitude atteinte des boucles et les énergies mises en jeu.

VI.1.14 La vision multi-échelle de la couronne

Des structures de faibles intensités peuvent être mises en évidence par des techniques d'imagerie appropriées. Afin d'étudier leurs évolutions, nous allons, après avoir défini les contraintes, appliquer la méthode de vision multi-échelle développée par Bijaoui et al. [204]. La méthode MVM décompose l'image en différents plans ondelettes. Les "objets" se signent par une signature multifréquence spatiale tandis que le bruit ne serait présent aléatoirement donc dans un seul plan fréquence. Nous reconstruisons ainsi les objets même noyés dans le bruit. Pour les images SOHO/EIT, les critères de contraintes pour pouvoir appliquer la méthode ont été les suivants : tout d'abord dégriller finement les images (sinon la grille noie l'image), ensuite utiliser préférablement de petites images (car sinon le programme normalise les intensités et ne reconstruit pas tous les objets). La méthode s'applique particulièrement bien aux zones peu contrastées. Pour améliorer la reconstruction, il est possible de passer plusieurs fois MVM à différentes échelles d'arborescence et lissage.

Nous avons appliqué cette méthode à la formation de CMEs ce qui a montré le lien dans la continuité de la transformation du plasma qui suit des boucles très torsadées qui deviennent en forme de Y (NOAA 8100 le 6 nov 1997). L'étude de structures complexes a montré l'ouverture d'une ligne de champ fermée entre NOAA 8194 et NOAA 8195 le 6-7 avril 1998.

On a $\vec{rot}B = \alpha\vec{B}$ Le minimum d'énergie est obtenu pour un champ force free (c'est à dire α constant). Un champ ouvert dispose d'une énergie plus important qu'un champ fermé. Donc l'ouverture du champ observée nécessite un apport d'énergie. Nous avon-

s vu que le torsadage donnait de l'énergie. La torsion de lignes magnétiques fermées est susceptible de permettre leur ouverture ce qui expliquerait le processus physique de l'ouverture ci-dessus.

VI.1.15 Conclusion et perspectives

L'étude temporelle en 3D de la couronne permet de comprendre l'évolution de B. Afin d'étudier en détail la structure principale de la couronne (les boucles) nous avons mis au point de nouvelles méthodes d'ajustement. Nous avons trouvé que les boucles circulaires EUV étaient en équilibre hydrostatique.

Nous avons analysé l'émergence d'une nouvelle région active et constaté que les boucles émergeaient torsadées. Le torsadage diminue alors pendant l'expansion des boucles ce qui s'explique par la conservation de l'hélicité magnétique.

Cette méthode est très prometteuse pour étudier la dynamique des boucles et en particulier la formations d'instabilités. Cela peut permettre d'améliorer la précision de la météorologie spatiale.

Chapter VII

Conclusion et Perspectives

Science sans Conscience n'est que ruine de l'âme
Rabelais François (1490-1553), Pantagruel, Chapitre 8.

Sommaire

VII.1 Conclusion et Perspectives

L'objectif de ce travail était d'améliorer la compréhension de la structure 3D de la couronne solaire et de son évolution en utilisant l'imageur EUV de SOHO EIT.
Le plasma coronal étant figé par le champ magnétique et les polarisateurs EUV étant inefficaces, observer en 3D le plasma coronal est le seul moyen de comprendre le champ magnétique au niveau de la couronne. Ainsi, pour mieux comprendre la structure de la couronne différentes méthodes d'imagerie en 3D ont été développées. Les anaglyphes ont montré les interactions à grandes échelles entre les structures coronales.

Des méthodes basées sur la stéréovision ont permis le calcul des paramètres de certaines structures. En particulier, une méthode appelée *stéréovision dynamique* a été mise au point et appliquée avec succès sur 30 boucles d'une région active pour déterminer les paramètres géométriques des boucles. Ensuite, les paramètres physiques de ces boucles EUV de température proche du MK ont pu être déterminés. Il est apparu que ces boucles, contrairement aux boucles chaudes, étaient en équilibre hydrostatique.

Des modèles géométriques de boucles prenant en compte les asymétries comme le torsadage ont été appliqués à l'ajustement des boucles par stéréoscopie. Ainsi, l'émergence de nouvelles régions actives se traduit par un fort torsadage des boucles les composant. La conservation de l'hélicité permet de transformer le torsadage de boucles en grandissement de taille. L'hélicité et la mesure du torsadage apparaissent donc comme des termes

importants dans la prévision de l'évolution d'une région émergente.

A plus long terme - sur plusieurs rotations solaires -, les variations de torsions pour des tubes de flux magnétiques fermés d'une même région active ont pu être mesurées. Le torsadage apparaît comme pouvant varier à cause de la rotation différentielle et des mouvements stochastiques des pieds des boucles. Lorsqu'il devient trop important des instabilités peuvent se développer. Ainsi le détorsadage rapide a été observé comme corrélé positivement avec des éruptions.

L'étude sur les interactions entre lignes magnétiques fait apparaître que la reconnection ne se limite sans doute pas à des cas entre boucles mais peut aussi survenir entre des boucles (lignes fermées) et des trous coronaux (champ ouvert). Dans ce cas, l'hélicité intervient comme permettant l'ouverture du champ magnétique.

Il est apparu aussi que la structuration des trous coronaux dépend fortement de l'activité magnétique du voisinage géographique. La notion de mini trous coronaux pouvant se structurer en trou coronal a été confirmé par une comparaison EUV-Radio.

Des diagnostics de déposition d'énergie pour des régions ouvertes et fermées ont été réalisés. Des observations multi-longueurs d'ondes complétent l'analyse.

La formation de CMEs et d'éruption a été abordée sur un cas à partir de la vision stéréo des données SOHO/EIT et d'observations multilongueur d'ondes. Le fort torsadage des boucles (en forme de S), la haute altitude de celles ci et l'émergence de petites boucles qui se reconnectent avec les précédentes et forment une arcade, permettent de se demander si lorsque nous nous trouvons face à une morphologie en S, la place laissée libre favorise la possibilité d'émergence d'une nouvelle ARL. De plus l'éruption est sans doute facilitée par le fort torsadage qui rend déjà les boucles quasiment instables.

Dans l'avenir, les critères d'instabilités propres (cisaillement, torsadage) et d'instabilités de voisinage (reconnection) devront sans doute être pris plus systématiquement encompte afin de mieux décrire l'évolution 3D de la couronne.

Les méthodes d'analyses développées ici devrait permettre

1. de mieux modéliser les critères d'instabilités pour les boucles
2. de prendre en compte toutes les interactions dans la structuration de la couronne

Maintenant que les méthodes d'ajustement fonctionnent, d'avantages d'exemples sont nécessaires pour obtenir des critères observationnels en relation avec les modèles MHD. De tels critères peuvent permettre d'améliorer les prévisions de météorologie spatiale. Actuellement, nombre de ces critères sont empiriques et morphologiques. Les thèmes développés dans cette thèse montrent que des facteurs importants pour la météorologie

spatiale peuvent être mesurés à partir de la physique des tubes de flux magnétiques et des intéractions de manière plus formelle. En effet, la mesure des paramètres critiques de torsion et de cisaillement des boucles coronales peut permettre de définir le moment des éruptions et des départs de CMEs. De plus, d'autres circonstances peuvent aussi participer à ces événements comme les interactions de lignes magnétiques voisines (par exemple la reconnection,...). Tous ces phénomènes interviennent aussi pour le chauffage coronal et des observations sytématiques devraient permetttre de comprendre quantitavement leur apport.

Une mesure sytématique de critères observationnels tels que le torsadage des boucles permet donc une meilleure compréhension de l'évolution 3D de la couronne solaire.

Bibliographie

Bibliography

[1] Alexander D. and Katsev,S. 1996, *Solar Physics* 167, 153

[2] Allen C.W. 1973, Astrophysical Quantities, London:Athlone

[3] Aly J.J., 1991, “Dynamics of solar flares”, Flares 22Workshop, p.29, Obs. Paris-Meudon DASOP Editors

[4] Amari T., 1999, SOHO 8 Workshop

[5] Amari T, Luciani JF, Aly JJ, Tagger M., 1996, ApJ. 466, L39-L42

[6] Antiochos & Dalberg, 1997, *Solar Physics* 174, 5

[7] Arnaud J., 1983, Thèse de Paris VI, *Contribution à létude de la polarisation des raies interdites de la couronne solaire*

[8] Aschwanden M.J. and Bastian T.S. 1994a, ApJ 426, 425

[9] Aschwanden M.J. and Bastian T.S. 1994b, ApJ 426, 434

[10] Aschwanden M.J. 1995, Lecture Notes in Physics 444, 13

[11] Aschwanden M.J., Lim J., Gary D.E., and Klimchuk J.A., 1995, ApJ 454, 412

[12] Aschwanden M. et *al.*, 1997, PASP Conf. Ser., 2nd ASPE meeting

[13] Aschwanden M.J., Bastian T.S., Nitta N., Newmark J., Thompson B.J. and Harrison R.A. 1998a, in Proc. 2nd *Advances in Solar Physics Euroconference (ASPE), Three-Dimensional Structure of Solar Active Regions*, (eds. C.Alissandrakis and B.Schmieder), PASP, subm.

[14] Aschwanden M.J., Neupert W.N., Newmark J., Thompson B.J., Brosius J.W., Holman G.D., Harrison R.A., Bastian T.S., Nitta N., Hudson H.S., and Zucker A., 1998b, in Proc. 2nd *Advances in Solar Physics Euroconference (ASPE), Three-Dimensional Structure of Solar Active Regions*, (eds. C.Alissandrakis and B.Schmieder), PASP, subm.

[15] Aschwanden M., Newmark J., Delaboudinière J.P., Neupert W., Klimchuk J., Gary A., Portier-Fozzani F. & Zucker A. , 1999, ApJ. 515, 842

[16] Athay R. G., 1987, Nature 327, 685

[17] Thèse de G. Aulanier, Novembre 1998

[18] Batchelor D., 1994, Sol. Phys. 155, 57-61

[19] Baty H., Einaudi G., Lionello R. & Velli M., 1998, A & A,333, 313-321

[20] Bentley R. et *al.*, 1996

[21] Berger M., 1998, PASP Conference Series, Vol. 150, IAU Colloquium 167, p. 102

[22] Berger M., 1988, ApJ. 201, 355-361

[23] Berger M., 1985, ApJ. Sup. Ser. 59, 433-444

[24] Berger M., 1984, Ph.D. Thesis Harvard Univ., Cambridge, MA

[25] Berton R. and Sakurai T. 1985, *Solar Physics* 96, 93

[26] Betta R., Peres G., Reale R. & Serio S., 1997, A & A Supp. 122, p. 585B

[27] Bijaoui A., 1995, Cours de DEA sur l'imagerie, UNSA

[28] Boyd TJM & Sanderson JJ, 1969, *Plasma Dynamics*, London:Nelson

[29] Bohlin J.D. & Sheeley N.R., 1978, Sol. Phys. 56, 125

[30] Bray R.J. & Loughhead R.E., 1985, A&A, 142, 199-204

[31] Bray R.J., Cram L.E., Durrant C.J., and Loughhead R.E., 1991, *Plasma Loops in the Solar Corona*, Cambridge: Cambridge University Press

[32] Brekke P., Kjeldseth-Moe O., Brynildsen N., Maltby P., Haugan S.V.H., Harrison R.A., Thompson W.T., Pike C.D. 1997, *Solar Physics* 170, 163

[33] Brekke P., Kjeldseth-Moe O. & Harrisson R., 1997, Sol. Phys. 175, 511-521

[34] Bromage G.E., Cowan R.D., and Fawcett B.C.,1977 , Phys. Scripta, 15,177

[35] Bromage G.E., Cowan R.D., and Fawcett B.C.,1978 , MNRAS , 183, p 19

[36] Brosius J.W., Davila J.M., Thomas R.J., Saba J.L.R., Hara H. and Monsignori-Fossi B.C., 1997, ApJ 477, 969

[37] Brosius J.W., Willson R.F., Holman G.D., and Schmelz J.T. 1992, ApJ 386, 347

[38] Brown S.F. 1996, AA 305, 649

[39] Browning P.K. & Hood A., Solar Physics, vol. 124, no. 2, 1989, p. 271-288.

[40] Browning P.K. & Priest E., 1984, Sol. Phys.92, 173

[41] Canfield, 1997, PASP 111, 341

[42] Cargill P.J. 1994, ApJ 422, 381

[43] Cargill P.J. and Klimchuk J.A. 1997, ApJ 478, 799

[44] Carrington R. C., 1858, MNRAS, 19, 1

[45] Chabbi H., 1993, Thèse de l'institut polytechnique de Lorraine, *Construction de facettes 3D par stéréovision intégrant des principes de géométrie projective*

[46] Chen F., *Plasma Physics and controlled fusion*

[47] Chen J. et *al.*, 1997, ApJ. 490, L191

[48] Cheng C.C. 1980, ApJ 238, 743

[49] C. Chiauderi, R. Giachetti & G. Van Hoven, 1977, Sol. Phys. 54, 107-122

[50] Chianderi *et al.*, 1998, Conclusion du groupe detravail sur le chauffage coronal, CESRA

[51] Craig , ApJ., 296, 710

[52] A.N. Cox, W.C. Livingston & M.S. Matthews editors, 1991, *Solar Interior and Atmosphere*, The university of arizona press (Tucson)

[53] Cowley S., 1996, *introduction to the magnetosphere*, St Andrew Summer School

[54] Culhane J. L. *et al.*, 1991, Sol. Phys. 136, 89

[55] Davila J.M. 1994, ApJ 423, 871

[56] Defise J.M., 1999, These

[57] Delaboudinière J.P. et *al.*, 1997, COSPAR, Advances in Space Research, Vol 20, Issue 12, p. 2231-2237, (cf chapitre 3 de cette these).

[58] Delaboudinière J.P. et *al.*, 1995, Sol. Phys. 162, 291

[59] Demoulin P., Henoux J.C., Priest E.R., Mandrini C.H., 1996, A & A, 308, 643

[60] Dere, K. P.; Landi, E.; Mason, H. E.; Monsignori Fossi B.C.; Young, P. R., A & A Supplement series, Vol. 125, October 1997, 149-173.

[61] K.P. Dere, D. M. Horan and R. Kreplin, 1977, *structure and dynamics of a solar flare : Xray and XUV observations*, Ap.J. 217 , p 976

[62] K.P. Dere, H.E. Mason ,K. G. Widing and K. Bhatia, 1979 *XUV electron density diagnostics for solar flares*, Ap.J. Supp. 40 , p 341

[63] K. Dere, 1982, Sol. Phys. 75, 189-203

[64] Deré *et al*, 1997, Sol. Phys., 175, 607

[65] Dulk G.A. and McLean,D.J. 1978, *Solar Physics* 57, 279

[66] Dikpati D. & Charbonneau P., 1999, ApJ. 518, 508-520

[67] Dimitruck P., 1998, ApJ. 505

[68] Domingo V. *et al.*, 1995, Solar Physics, 162, 1-37

[69] Einaudi G, Lionello R., Velli M., 1997, Adv. Sp. Res.,19, 1875

[70] Site internet d'EIT, http://umbra.nascom.nasa.gov/eit

[71] ESA (european space agency) & NASA (national aeronautics and space administration), 1989, *The SOHO mission : Scientific and technical aspects of the instruments* esa sp-1104

[72] ESA , 1994, *3rd SOHO Workshop : Solar Dynamic Phenomena and Solar Wind Consequences*, SP-373, Estes Park, Colorado, USA, 26-29 septembre 1994

[73] *Solar Jets and Coronal Plumes*, 1998, *Solar Physics* 421, Note du meeting de l'éclipse de 1998 en Guadeloupe, ESA Edt.

[74] Ouvrage collégial, 1993, "La Peinture géométrique d'Escher", Taschen Edt

[75] Fainshtein V.G., Rudenko G.V. & Grechnev V. V., 1998, Solar Physics, 181, 133-158

[76] Fang C. *et al*, 1997, Sol. Phys., 176, 267-277

[77] Faugéras O., 1993, "3 Dimensional Computer Vision : A Geometric Viewpoint", Massachussetts Institute of Technology (MIT) Press

[78] Feldman, Doschek, and Widing *Electron densities in solar flare and active region plasmas from a density-sensitive line ratio of Fe IX*, Ap.J. 219, 304 , (1978)

[79] B. Flech, V. Domingo & A. Poland, 1995, *The SOHO mission*, book reprinted from solar physics vol 162 n 1-2, 1995, Kluwer Academic Publisher

[80] Flares, Numéro Spécial, 1989, Sol.Phys. 121

[81] Fludra A., Brekke P., Harrison R.A., Mason H.E., Pike C.D., Thompson W.T., and Young P.R. 1997, *Solar Physics* 175, 487

[82] Forbes T., 1996, St Andrew Summer School

[83] Foukal P. 1975, *Solar Physics* 43, 327

[84] Foukal,P. 1978, ApJ 223, 1046

[85] Gabriel A., Jordan ., 1975, MNRAS 173, 397

[86] Galeev A.A., Rosner R., Serio S., and Vaiana G.S. 1981, ApJ 243, 301

[87] Gallilee, 1613, *Etudes sur les taches solaires*

[88] Gary G.A. 1990, "Concerning the Extrapolation of Solar Non-Linear Force-Free magnetic Fields", Memorie della Societa Astronomica Italiana, 61, 457

[89] Gary G.A. 1997, *Solar Physics* 174, 241

[90] Gary G.A. and Alexander D. 1998, *Solar Physics*, subm.

[91] R. Giachetti, G. Van Hoven & C. Chiauderi, 1977, Sol. Phys. 55, 371-386

[92] Gibson S.E. & 13 co-authors, 1999, ApJ 520, 871

[93] P.Gidon, 1996, http://webhome.infonie.fr/alpes_stereo

[94] Golub L. & Pasachoff J.M., 1997, *The Solar Corona*, Cambridge University Press

[95] Golub L., Herant M., Kalata K., Lovas I., Nystrom G., Pardo F., Spiller E., Wilczynski J. 1990, Nature 344, 842

[96] Gopalswamy N., Hanoka, Y. & Lemen J. R., 1998, PASP Conference Series, Vol. 150, IAU Colloquium 167, p 358-365

[97] Gopalswamy N., Shibasaki K., Deforest C. E., Bromage B. & Del Zanna G., 1998, PASP Conference Series, Vol. 140,p. 363

[98] Habbal S.R., Ronan R., and Withbroe G.L., 1985, *Solar Physics* 98, 323

[99] Hale G. E. 1908, ApJ, 28, 315

[100] Hanaoka Y., 1996, Sol. Phys. 165, 275-301

[101] Hara H. *et al.*, 1991, PASJ 44, L135-L140

[102] Harrison, 1986, A&A 162, 283-291

[103] Harrison R., 1991, Adv. Spa. Res. 11, 25

[104] Harvey et *al.*, 1997

[105] Harvey K.L. and Hudson H.S. 1998, in "Observational Plasma Astrophysics: Five Years of Yohkoh and Beyond", Proc. Yohkoh Workshop, Yoyogi, Tokyo, Japan, Nov. 6-8, 1998, (eds. T.Watanabe, T.Kosugi, and A.C.Sterling), Astrophys. and Space Science Library, Dordrecht:Kluwer, 229, 315

[106] Heyvaerts J., 1996, Lectures during the St Andrew Summer School

[107] Heyvaerts J. & Hagyard, 1991, "Dynamics of solar flares", Flares 22 Workshop, p.1, Obs. Paris-Meudon DASOP Editors

[108] Heyvaerts J. & Priest E., 1984, A&A 137, 63

[109] Hochedez J.F., 1999, Document interne

[110] Hood A.W. & Priest E., 1979,Sol. Phys., 64, 303

[111] Howard R. *et al.*, 1997, European Geophysical Society, meeting in Vienna

[112] Hudson H.S., LaBonte B.J., Sterling A.C., and Watanabe T. 1998, in "Observational Plasma Astrophysics: Five Years of Yohkoh and Beyond", Proc. Yohkoh Workshop, Yoyogi, Tokyo, Japan, Nov. 6-8, 1998, (eds. T.Watanabe, T.Kosugi, and A.C.Sterling), Astrophys. and Space Science Library, Dordrecht:Kluwer, 229, 237

[113] Hundausen, 1997, Cosmic wind the Heliosphere, Jokipii *et al.* Edt., University Arizona Press, Tucson)

[114] Site internet ISTP, 1998, http://www-istp.gsfc.nasa.gov/istp/cloud_jan97/event.html

[115] Jakimiec J. *et al.*, 1998, A.& A. 334, 1112-1122

[116] C. Jordan, 1965, *The population of excited levels of the ground terms of ions Fe X, XI, XIV in the solar corona*, Physics Letters, vol. 18 n 3 , p. 259

[117] C. Jordan, 1966, *The abundance of iron in the Solar Corona*, MNRAS 132, p 515

[118] S.D. Jordan, 1994, *Line formation and intensity enhancement of the He II 304 A line in the solar atmosphere*, IAU Colloq. 144, p 415

[119] Kano R. & Tsuneta S., 1995, ApJ. 454, 934-944

[120] Kano R., 1996, PASP Conf. Ser. 111, 112

[121] Kano R. and Tsuneta S. 1996, Publ. Astron. Soc. Japan 48, 535

[122] Klimchuk J., Sturrock P.A., Yang W.H., 1988, ApJ. 335, 456

[123] Klimchuk J.A., Lemen J.R., Feldman U., Tsuneta S., and Uchida Y. 1992, PASJ 44, L181

[124] Klimchuk J.A., and Gary D.E. 1995, ApJ 448, 925

[125] Klimchuk J.A. and Porter L.J. 1995, Nature, 377, 131

[126] Klimchuk J. *al.*, 1997

[127] Kosugi *et al.*, 1991, Solar Phys. 136, 17

[128] Koutchmy S.*et al.*, 1991, in "solar interior and atmosphere", 1055

[129] Landini M. & Monsignori Fossi B.C., 1975, A&A 42, 213L

[130] Lang K.R. 1980, Astrophysical Formulae, Berlin:Springer

[131] *Lasco/EIT Science Contortium Meeting*, 10-13 september 1995, St Michaels, Maryland, USA

[132] LASCO-EIT meeting in Aix en Provence, 1997

[133] Leka et *al.*, 1996, ApJ. 462, 547

[134] Lenz D., Deluca E., Golub L., Rosner R., Bookbinder J., ApJ 517L, 155

[135] Levy Leblond J. M.,*physique quantique*, interedition

[136] Lionello R., Velli M., Einaudi G., Miric Z., 1998, ApJ. 494, 840-850

[137] Linker et *al.*, 1992, JGR, 97, 13733

[138] Linker J. & Mikić Z, 1995, ApJ. 438, L45-L48

[139] J.F. Linsky, 1985, *Nonradiative activity across the HR Diagram : Which types of stars are solar-like ?*, Solar Physics, 100, p. 333-362

[140] Lothian & Hood, 1989, Sol. Phys. 122, 227

[141] Loughhead R.E., Wang J.L., and Blows G. 1983, ApJ 274, 883

[142] Loughhead R.E., Chen C.L., and Wang J.L. 1984, *Solar Physics* 92, 53

[143] Lotti J.L., 1996, Thèse de l'UNSA (Essi Nice), *Mise en correspondance stéréo par fenêtres adaptatives en imagerie aérienne haute résolution*

[144] Maia D., Pick M., 1998,

[145] Malherbe J.M., 1987, Thèse d'Etat

[146] Martens P.C.H. and Kuin N.P.M. 1982, AA 112, 366

[147] Martin F., 1995, Cours de DEA sur la tomographie, UNSA

[148] H.E. Mason and B.C. Monsignori Fossi, 1994, *Spectroscopic diagnostic in the VUV for sollar and stellar plasmas*, A & A Rev., 6: 123-179

[149] Mason H. et *al.*, 1997

[150] Matthews S. & Harra-Murnion L.K., 1997, Sol. Phys. 175, 541-551

[151] McClymont A.N., Jiao L., and Mikić Z. 1997, "Problems and Progress in Computing Three-Dimensional Coronal Active Region Magnetic Fields from Boundary Data", *Solar Physics* 174, 191

[152] Merle, 1993, Cours de Géomtrie Projective en Maîtrise de Mathématiques Pures, UNSA

[153] Meunier *et al.*, 1991, Journal of Seismological Research

[154] Meyer, J.P. 1985, ApJ Sup., 57, 173

[155] Mikic Z., Schnack D.D., Van Hoven G., 1990, ApJ. 361, 690-700

[156] Moffatt, 1969

[157] Moses D. *et al.*, 1997, Solar Physics 175, 571, "Eit Observations of the Extreme Ultraviolet Sun"

[158] Neupert W., Delaboudinière J.P., Thompson B., Catura D., Moses D., Gurman J., Portier-Fozzani F., Gabricel A., Artzner G., Clette F., Cugnon P., Maucherat A., Defise J.M., Jamar C., Rochus P., Dere K.P., Howard R.A., Michels D., Freeland S., Lemen J.R., Stern R.A., 1998, Sol. Phys. 183, 305

[159] Newmark J.S., Delaboudinière J.P., Dere K.P., Gurman J.B., Lemen J.R., Thompson B.J. 1996, EOS, Vol.77, No.46, p.557

[160] Newmark J., Thompson B., Catura R., Moses J.D., Portier-Fozzani F., Delaboudinière J.P. et *al.*, 1997, B.A.A.S., SPD meeting 29, 01.15

[161] Newmark J.S., Thompson B., Gurman J.B., Delaboudinière J.P., Aschwanden M.J., and Mason H. 1997, BAAS 29/5, 1321, #73.07

[162] Newmark J. *et al.*, 1997, "Temperature and density with SOHO/EIT", EIT internal report

[163] Nitta N., White S.M., Kundu M.R., Gopalswamy N., Holman G.D., Brosius J.W., Schmelz J.T., Saba J.L.R., and Strong K.T. 1991, ApJ 374, 374

[164] Noens J. C. & J.P. Rozelot, 1974, A & A. 30, 81

[165] Noens J. C., Niot J.M., 1997, Solar Physics, v. 173, Issue 1, p. 53-66.

[166] Noens J. C., Tritakis V. P., Mavromichalaki H., Paliatsos A. G & Petropoulos B., Sol. Phys., soumis

[167] Ofman L., Klimchuk J.A. and Davila J.M. 1998, ApJ 493, 474

[168] Ogowara Y. *et al.*, 1992, PASJ, 44, L41-L44

[169] Orlando S. & Pérès G., 1995, A&A 294, 86

[170] O'Shea E. F., 1997, Thèse sur la dynamique du soleil en UV présenté à l'Université de Belfast, Irlande du Nord, Nov. 1997

[171] Pallavicini R., Serio S., and Vaiana G.S. 1977, ApJ 216, 108

[172] Parker E.N., 1974, Solar Physics 36, 249

[173] Parker, E.N, 1977, A.R.A.A. 15, 45-68

[174] Parker E.N. 1988, ApJ 330, 474

[175] Peres G. & Orlando S., PASP Conf. 109, 93, 1996

[176] Peres G. 1997, in Proc. 5^{th} SoHO workshop on *The Corona and Solar Wind Near Minimum Activity*, Oslo, Norway, 17-20 June 1997, ESA SP-404, in press

[177] K. Phillips, 1995, "A guide to the Sun", Cambridge University Press

[178] Plunkett et *al.*, 1997, (private communication)

[179] Pohjolainen S. *et al.*, 1992, Solar Physics137, 67

[180] Porter L.J.& Klimchuk J., 1995, ApJ. 454, 499-511

[181] F. Portier-Fozzani, 1996, *"Discovering" the Sun with SOHO*, Guest Seminar at the Center of Extreme Ultraviolet Astronomy, University of Berkeley, California, USA , january 19th 1996

[182] Portier-Fozzani F., intervention au groupe de travail EIT, NASA-Goddard, Janvier 1996

[183] Portier-Fozzani F., Malina R.F. & J. Maucherat, 1996, Poster SFSA sur comparaisons couronnes stellaires et solaires, http://cdsweb.u-strasbg.fr/sfsa/prog/node43.html

[184] Portier-Fozzani F. & Stern R., 1996, Internal Report, LAS edt.

[185] Portier-Fozzani F. et *al.*, 1997, *EIT images of the EUV solar atmosphere : initial data reduction*, PASP Conf. Ser., vol 111, p. 402-406

[186] Portier-Fozzani F., Neupert W., Aschwanden M.J., Sheeley N.R., Thompson B., Maucherat A.J., Newmark J., Klimchuk J., and EIT Team, 1997, talk in Proc. 2nd *Advances in Solar Physics Euroconference (ASPE), Three-Dimensional Structure of Solar Active Regions*

[187] Portier-Fozzani F., A. J. Maucherat & the EIT Team, 1998, PASP Conf. Ser., Vol. 150, IAU 167, p 41-44

[188] Portier-Fozzani F. & Pohjolainen S., 1998, CESRA meeting, Poster Session

[189] Portier-Fozzani F., A&A, submitted

[190] Portier-Fozzani F. *et al.*, 1999, A&A, in preparation

[191] Portier-Fozzani F., 1999, SOHO 8, ESA SP-446, 549-554

[192] Pottasch, 1964, Space Science Rev., 3, 816

[193] Pouquet A., 1997, Cours Post-Doctoral de l'UNSA, OCA (Nice) Editors

[194] Priest E.R., Foley C.R., Heyvaerts J., Arber T.D., Culhane J.L., and Acton L.W. 1998, Nature, in press

[195] Priest E. R. , 1996, Lectures during the St Andrew Summer School

[196] Priest E. & Forbes T., 1986, J. Geophys. Res., 91, 5579

[197] Priest E. R. , 1982, "Solar MagnetoHydroDynamics", Geophysics & Astrophysics Monographs, D. Reidel Publishing Company

[198] Priest E.R. 1981, "Solar Flare Magnetohydrodynamics", Gordon and Breach Science Publishers

[199] Rabbia Y., 1995, Cours de DEA sur l'optique de Fourier, UNSA

[200] Raymond J.C., Cox D.P, and Smith B.W. 1976, ApJ 204, 290

[201] Robertson, Hood et Lothian, 1992, SoPh 137, 273

[202] Rosner R., Tucker W.H., and Vaiana G.S. 1978, ApJ 220, 643

[203]) Roumeliotis G,.Sturrock P., Antiochos S., 1994, ApJ. 423, 847

[204] Rué F. & Bijaoui A., 1997, Experimental Astronomy, v. 7, Issue 3, p. 129-160.

[205] V. Rušin, P. Heinzel, & J.C. Vial (eds), 1994, *Solar Coronoral Structures"*, IAU Colloq. 144, Veda Publishing Company, Bratislava (Slovakia)

[206] Rust D., Nakagawa Y & Neupert W., 1975, Sol. Phys. 54, 403

[207] Rust D. & Kumar A, 1996, ApJ. 464, L199

[208] Sakurai,T. 1982, *Solar Physics* 76, 301

[209] Sakurai,T. 1989, *Computational Modeling of Magnetic Fields in Solar Active Regions*, Space Science Reviews 51, 11

[210] E. Schatzman & F. Praderie, 1990, *Les étoiles*, Savoirs actuels, InterEditions, éditions du CNRS

[211] Schmelz,J.T., Holman,G.D, Brosius,J.W., and Gonzalez,R.D. 1992, ApJ 399, 733

[212] Schmelz,J.T., Holman,J.D., Brosius,J.W., and Willson,R.F. 1994, ApJ 434, 786

[213] Schwabe S. H., 1843, Astron. Nachr. 20, 234

[214] Serio S., Peres G., Vaiana G.S., Golub L., and Rosner R. 1981, ApJ 243, 288

[215] Sheeley,N. 1980, *Solar Physics* 66, 79

[216] Sheeley, N.R., 1981, Skylab Workshop III

[217] Sheeley et *al.*, ApJ, 1997

[218] Scherrer P. H. *et al.*, 1995, Sol. Phys. 162, 129

[219] Schmieder B. et *al.*. 1998, 2nd ASPE meeting, PASP Conf. Ser.

[220] Schmieder B., Heinzel P., Wiik J., Lemen J., Anwar B., Kotrc P., Hiei E., 1995, Sol. Phys 156, 337

[221] B. Schmieder, L Golub, and S.K. Antiochos, 1994, *Comparison between cool and hot plasma behaviors of surges*, Ap.J. , vol 425, n 1, Part 1, 1994

[222] SEC, 1998, SEC web home page, http://www.sec.noaa.gov/

[223] Snodgrass, 1984, Solar Physics, 90, 199S

[224] SOHO EIT Users' Guide, http://umbra.nascom.nasa.gov/eit/eit_guide/guide.html

[225] SOHO-EXPLORE-1999 WEB SITE, http://sohowww.nascom.nasa.gov/explore/links.html

[226] : Solanki S., 1998, Space Solar Physics, Vial & al. Edt, Lecture Notes in Physics, Springer

[227] Solodyna C., Kriger A. & Nolte J., 1977, Sol. Phys. 54,123-134

[228] Song X., 1995, Thèse sur la calibration d'EIT présenté à l'Université d'Orsay le 21 Dec. 1995

[229] Spitzer,L. 1962, Physics of Fully Ionized Gases (Interscience, New York), p.144

[230] Stanford Solar Web, http://solar-center.stanford.edu/about.html

[231] Royal Society (London),Philosophical Transactions, Series A, vol. 281, no. 1304, May 6, 1976, p. 435-441.

[232] Taylor, 1974,

[233] Thonnat M., 1995, Cours de DEA sur la structure d'image, UNSA

[234] Thompson B., 1997, SOHO-Yohkoh Workshop, MEDOC-Paris

[235] Tomczyk S., Schou J., & Thompson M. J., 1995, ApJ 448, L57

[236] Site internet de Trace, http://sunland.gsfc.nasa.gov/smex/trace/index.htm

[237] Tsuneta *et al.*, 1991, Sol. Phys. 136, 37

[238] Tsuneta *et al.*, 1996, ApJ. 456, L63

[239] Tritakis V. P., Noens J. C., Paliatsos A. G, 1995, Sol.Phys. 156, 229

[240] Ulmschneider P, 1998, Space Solar Physics, Vial & al. Edt, Lecture Notes in Physics, Springer

[241] Ushida et *al.*, 1991

[242] Van Driel L. *et al.*, 1998, PASP Conf. Ser.

[243] N. G. Van Kampen & B. U. Felderhof, 1967, *Theoritical methods in plasma physics*, North Holland Publishing Company

[244] Velli M, 1997, Lecture at the SOHO-MEDOC Summer School

[245] Vesecky J.F., Antiochos S.K., and Underwood J.H. 1979, ApJ 233, 987

[246] Vézien J.M., 1995, Thèse de Paris VII, UFR Informatique, *Technique de reconstruction globale par analyse de paires d'images stéréoscopiques*

[247] Vigouroux A., 1996, Thèse de l'UNSA-OCA

[248] Vourlidas,A. and Bastian,T.S. 1996, ApJ 466, 1039

[249] Von Hoven et *al.*, PASP Conf. Ser., 68, 211-218

[250] Wang Y. & Sheeley N.R., 1994, Journal of Geophysical Research, 99, A4, 6597

[251] Wang H. and Sakurai T. 1998, PASJ 50, 111

[252] Wang Y., Sheeley N.R. *et al.*, 1997, ApJ. 485, 875

[253] Wang Y.M., Sheeley N.R. Jr., Hawley S.H., Kraemer J.R., Brueckner G.E., Howard R.A., Korendyke C.M., Michels D.J., Moulton N.E., and Socker D.G. 1997, ApJ 485, 419

[254] Waku Kouomou J., 1996, Thèse de l'Univ. Grenoble I-IMAG, *Ondelettes et applications en imagerie et en calcul de surfaces*

[255]) Walsh R., 1998, Space Solar Physics, Vial & al. Edt, Lecture Notes in Physics, Springer, p. 202

[256] Webb D.F., Holman G.D., Davis J.M., Kundu M.R., and Shevgaonkar R.K. 1987, ApJ 315, 716

[257] Whitbroe et *al.*, 1991

[258] Wheatland M.S., Sturrock P.A., and Acton L.W. 1997, ApJ 482, 510

[259] Wiik, Deré *et al* 1997, Sol. Phys., 175, 411

[260] Wilkinson D. et *al.*, NOAA web page, 1998

[261] Wilkinson, Esmilie & Gary, 1989, Sol. Phys. 119, 77-86

[262] Wolfson R. & Siddharth S., 1998, ApJ 499, 496

[263] Wragg M.A. and Priest E.R. 1982, AA 113, 269

[264] Wu D.J & Fang C., 1999, ApJ. 511,958-964

[265] Wu S.T. & Guo W.P., 1998, ApJ. 494, 419

[266] Wu *et al*, 1997, Sol. Phys., 175, 719-735)

[267] Yohkoh, 1992, Numéro spécial Yohkoh de *Publication of the Astronomical Society of Japon*, PASP, volume 44

[268] Yoshida & Tsuneta, 1996, Ap.J. 459, 342-346

[269] Yoshimori *et al.*, 1991, Sol. Phys. 136, 69

[270] H. Zirin, 1988, *Astrophysics of the Sun*, Cambridge University Press

[271] Zuccarello F., 1991, "Dynamics of solar flares", Flares 22 Workshop, p.33, Obs. Paris-Meudon DASOP Editors

Appendix A

Rappels de Physique des plasmas solaires

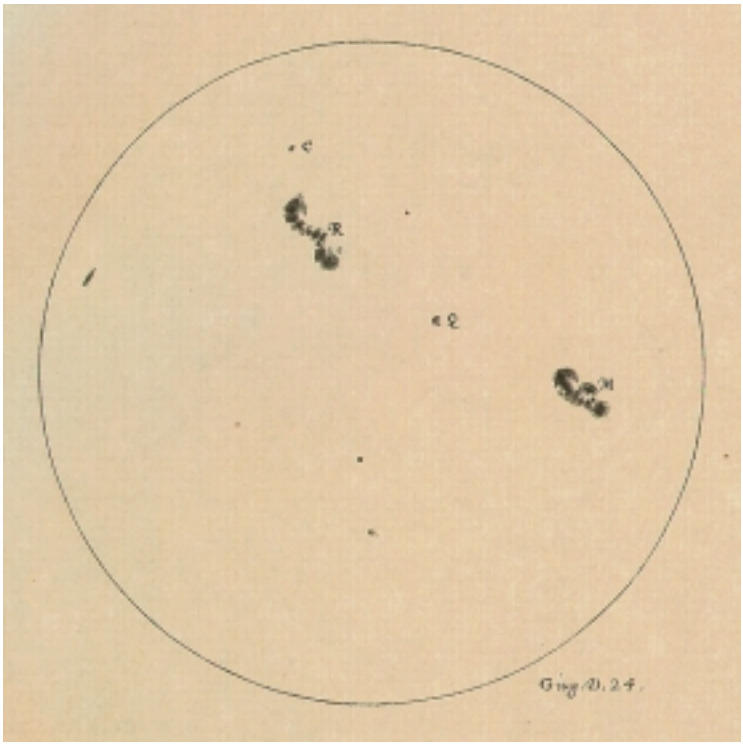

Figure A.1: Les taches solaires étudiées par Galilee du 24 Juillet 1613 : Non seulement elles tournent mais en plus le champ magnétique y est très complexe.

Sommaire

A.1 Différents ions présents dans la couronne solaire observés par EIT

A.1.1 Les raies EUV : Processus de formation des raies

Mason H. & Monsignori Fossi B.C. ([148]) rappellent les processus atomiques qui se produisent dans les plasmas chauds ($T > 2 \times 10^4 K$) et de faibles densités ($N_e < 10^{13} cm^{-3}$) avec des raies optiquement minces ce qui est le cas pour la partie externe du soleil. La somme totale de toutes les émissions provenant de transitions liées-liées (*ie* d'un niveau d'énergie à un autre pour un atome) plus les liées-libres (*ie* dans un état libre, l'électron se trouve au dessus du niveau d'ionisation de l'atome) et les libres-libres qui sont très importantes à hautes températures-, forme le spectre coronal. La partie continue du spectre provient des transitions libre-libre et libre-liées (dans ce dernier cas, un électron se déplaçant avec une vitesse $v. -^{+} \delta v$ va se recombiner sur les niveaux quantifiés d'un atome). Plus intéressant pour notre étude est l'émission liée-liée car comme on va le voir pour nos raies interdites cela va nous permettre de remonter aux températures et aux densités. Dans le cas de l'émission liée-liée un élément X passe du niveau i au niveau j avec création d'un photon d'énergie $\Delta E_{ij} = h\nu_{ij}$:
$X_j^{+m} \rightarrow X_i^{+m} + h\nu_{ij}$ (X_j^{+m} indique un atome X avec m électrons en moins, *ie* Xm+1 en notation spectrométrique).

Le bilan des ions se résume de la manière suivante :

- L'ion peut être formé par ionisation depuis un niveau d'énergie plus bas.
- L'ion peut disparaître par ionisation vers un niveau plus haut.
- L'ion peut descendre par recombinaison depuis un état plus haut.
- L'ion peut descendre par recombinaison vers un état plus bas.

Les plasmas considérés ici à basse densité ont une densité d'espèce déterminée par les ionisations électroniques plus les recombinaisons radiatives et électroniques.

A.1.2 Flux mesurés et calculs depuis les raies

Le flux reçu à une distance R est en ergs cm-2 s-1:

$$F_{ji} = \frac{\Delta E_{ji}}{4\pi R^2} A_{ji} \int_{\Delta V} n_j dV \tag{A.1}$$

avec A_{ji} la probabilité de transition et ΔV le volume où le plasma est formé. La densité de l'ion s'écrit :

$$n_j = \frac{n_j}{n_{ion}} \frac{n_{ion}}{n_{el}} \frac{n_{el}}{n_H} \frac{n_H}{n_e} n_e \tag{A.2}$$

où $\frac{n_j}{n_{ion}}$ est la population relative du niveau d'excitation, $\frac{n_{ion}}{n_{el}}$ est l'abondance relative de l'élément, $\frac{n_{el}}{n_H} = A_{el}$ est l'abondance relative de l'element par rapport à l'hydrogène et $\frac{n_H}{n_e}$ la densité d'hydrogène par rapport à la densité électronique.

Dans l'approximation coronale ([94]), on suppose que le niveau j est peuplé exclusivement depuis le niveau de repos g par des collisions avec des électrons thermiques. Le niveau j est dépeuplé uniquement par désexcitation radiative vers des niveaux plus bas. Ceci est vérifié dans les conditions ordinaires de la couronne à l'exception des éruptions (très énergétiques). On a donc

$$N_g(X^{+m}) N_e C^e_{gj} = N_j(X^{+m}) \sum_{k<j} A_{jk} \tag{A.3}$$

avec C le coefficient de desexcitation collisionnelle.

Comme la puissance totale (en ergs cm-3 s-1) s'écrit :

$$P_{ij} = N_j(X^{+m}) A_{ij} \frac{hc}{\lambda_{ij}} \tag{A.4}$$

avec

$$\lambda_{ij} = \frac{c}{\nu_{ij}} \tag{A.5}$$

On définit la fonction de contribution G(T) telle que

$$P_{gj} = 0.8 A_X G(T, \lambda_{gj}) \frac{hc}{\lambda_{ij}} N_e^2 \tag{A.6}$$

Elle s'écrit

$$G(T, \lambda_{gj}) = \frac{N(X^{+m})}{N(X)} C^e_{gj} \frac{A_{jg}}{\sum_{k<j} A_{jk}} \tag{A.7}$$

. Les formules peuvent être développées dans le cas d'une distribution maxwellienne de particules et en connaissant la section transverse de la structure. La fonction de contribution peut alors s'écrire dans ces cas simples comme

$$G(T) = \frac{n_{ion}}{n_{el}} . T^{-\frac{1}{2}} . e^{-h\nu} k T_e \tag{A.8}$$

fonction qui est très piquée en température à cause de l'abondance relative des ions. On se réferera à la température à laquelle la fonction G(T) est extrémale comme température de formation de la ligne (*c.f. e.g. [170]*). Le flux reçu est

$$I(\lambda_{ij}) = \frac{1}{4\pi R^2} \int_V P_{ij} dV \tag{A.9}$$

On appellera mesure d'émission différentielle la quantité

$$N_e^2 dV = Q(T) dT \tag{A.10}$$

qui se trouve dans l'expression précédente ([192]).

A.1.3 Relation intensité de l'image, densité de l'ion

L'intensité d'une raie i émise depuis un plasma optiquement mince d'un volume V s'écrit (cf. [61]) :

$$I_i = \int\int\int_V F_i[T(\vec{r}), n_e(\vec{r})] n_e^2(\vec{r}) d^3r \tag{A.11}$$

avec F la fonction spectrale de la raie i, fonction de la température T et de la densité électronique n_e.

Dans le cas des faibles densités, F dépend seulement de la température, d'où

$$I_i = \int F_i(T)\xi(T)dT \tag{A.12}$$

avec

$$\xi(T) = \int\int_{S_T} n_e^2 [\nabla T]^{-1} dS \tag{A.13}$$

Dans le cas général on a :

$$I_i = \int F_i[T, n_e]\xi(T)dT \tag{A.14}$$

Ainsi, l'intensité I_i de radiation émise par quelques raies spectrales i d'un plasma optiquement mince avec une température T, un volume V et une densité moyenne électronique n_e, est donnée par

$$I_i = F_i[T, n_e].n_e^2.V = F_i[T, n_e].EM \tag{A.15}$$

avec la mesure d'emission $EM = n_e^2.V$ D'où on a n_e par

$$n_e = (\frac{EM}{V})^{\frac{1}{2}} \tag{A.16}$$

Donc la mesure de l'intensité d'une raie donne la densité électronique dès que l'on connait par la physique atomique la fonction spectrale de la raie.

A.2 Le chauffage coronal

Les théories actuelles ne peuvent complètement expliquer la très haute température de la couronne. Des hypothèses pourtant existent.
La couronne étant très fortement magnétique et dynamique, la MHD permet de former des théories sur le mécanisme de chauffage. Ils sont principalement de 2 types

1. Les courants alternatifs (AC) : comme les ondes MHD
   Dans toutes structures peuvent se développer des ondes.

Transporteur d'énergie	Mécanisme de dissipation
Mécanismes magnétiques	**de chauffage**
1. Courant alternatif (AC)	*ou mécanismes ondulatoires*
Modes lents d'ondes MHD	
Ondes MHD longitudinales dans les tubes	dissipation par choc
Modes rapides d'ondes MHD	atténuation de Landau
Ondes d'Alfvén	couplage des modes
(transverses, ou de torsions)	chauffage par resonance
	chauffage par compression visqueuse
	chauffage par turbulence
	atténuation de Landau
ondes magnetoacoustiques de surface	couplage des modes
	mélange des phases
	absorption par résonance
2. mécanismes basés sur	*les courants directs (DC)*
nappes de courants	reconnection
	(chauffage par turbulence,
	chauffage par ondes)

Table A.1: Aspect Théorique des différents mécanismes possibles intervenant dans de chauffage coronal (adapté de Ulmschneider 1998, [240])

2. Les courants continus (DC) : comme la reconnection.
   La reconnection magnétique a été expliquée au chapitre V.1

Suivant si le temps dynamique est plus grand ou plus petit que le temps d'Alfven on se trouve en AC ou DC.

Différents mécanismes de chauffage coronal envisagés sont résumés Table A.1.

Bien que nous ne nous soyons pas explicitement exprimé sur ce point, nous avons au chapitre IV et V donné des exemples d'observations correspondant à chacun de ces cas possibles.

A.2.1 Les ondes MHD

Dans les plasmas traités par la MHD se développent des ondes. Les relations de dispersions des ondes sonores classiques sont trouvés à partir des équations de bilan de masse, de quantité de mouvement et la loi des gaz parfaits. Pour les ondes MHD, on considère les équilibres magnétohydrodynamiques. La force de Lorentz pouvant être interprétée comme la somme d'une tension et d'une pression magnétique, l'analyse dimensionnelle -par exemple- donne comme vitesse de propagation possible dans un tel milieu la vitesse de Alfvén

$$\vec{v_A} = \frac{\vec{B}}{\sqrt{\mu_0 . \rho}} \tag{A.17}$$

A.2.2 Les nappes de courants

D'après la loi d'Ohm, on a $j \sim \frac{B}{\mu L}$ où j est la densité de courant, B le champ magnétique, L la longueur caractéristique sur lequel il s'applique. Lorsque la densité de courant j est importante on a des nappes de courants [1] qui peuvent être vues comme des discontinuités séparant 2 régions où la MHD s'applique. Les équations d'équilibre s'écrivent pour les pressions $p_1 + \frac{B_1^2}{2\mu} = p_2 + \frac{B_2^2}{2\mu}$. Les nappes de courants sont généralement formées ([197] p 115) près des points X dans des régions en train de se rapprocher , à la frontière de parties topologiquement séparées se rapprochant l'une de l'autre (avec souvent des éruptions), et par dissipation topologique quand l'équilibre magnétostatique est rompu par une petite perturbation.

[1] ou "Current Sheet"

Appendix B

CD-ROM : Catalogue des images EIT, des principaux films préparés et d'images traitées utilisés dans cette thèse

Sommaire

Cette annexe comprend un CD-ROM. Ce CD-ROM contient le catalogue des images en (.gif) pour 3 années, les films (en .save —IDL—) et certaines images dégrillées et/ou traitées ayant servi dans ce document.

Il contient aussi la these version définitive en .pdf ainsi que les articles en .pdf

B.1 Le catalogue EIT

B.2 Le catalogue EIT en Fe IX/X : 1996-1997-1998

Les .gif sont dans /eitcatalogue171/1996 , dans /eitcatalogue171/1997 et dans /eitcatalogue171/1998 .

B.3 Les films et images

Les films sont respectivement sur /films/*date de la periode*. Idem pour les images (températures, ondelettes, ...).

Appendix C

Observations

Sommaire

C.1 Observations coordonnées avec Metsähovi

Des observations coordonnées avec l'observatoire radioastronomique de Metsähovi (Finlande) étaient programmés juin 1998. Malheureusement la perte temporaire de SOHO n'a permis de récuperer qu'un jour de donnée d'EIT. Le but de ces observations était de permettre de mieux comprendre la formation des CHs et les interactions avec les ARL.
EIT devait observer ces jours là selon son mode synoptique (images Full Disk Full Resolution toutes les 6h) ainsi que des images pleins champs en Fe XII pour recherche de formation de CMEs et quelques régions précises de campagnes.
En pratique, on se sert principalement du logiciel eit_display pour visualiser les images EIT en temps réel. Après avoir définit les zones d'intéret le logiciel image_tool permet de trouver les coordonnées exactes à pointer.
Le protocole d'observation que j'avais proposé était le suivant :

1. 1 Image de la totalité du disque
2. 1 Image Partielle se limitant au Trou Coronal Nord
3. 1 Image de la totalité du disque
4. 1 Image Partielle se limitant au Trou Coronal Sud
5. 1 Image de la totalité du disque

Auquels se rajoutent des sujets spécifiques :
• *Etudes des interactions entre AR et CH :*

Si des ARs qui évoluent sont décelées sur EIT avec des CH autour alors pour chacune de ces régions, on réalise
10 Images Partielles (en se limitant sur une région qui inclus le CH et l'AR) et
1 Image pleine résolution qui inclut le bord et la région

- *Comparaison entre les Plumes et les points brillants dans les CH:*

Cette étude provient des résultats de l'analyse précédente où l'on s'est aperçu que les EM en UV et brillance en radio étaient très semblables en valeurs. D'où la question de savoir si ces tubes de plasmas présents tous deux au voisinage de structures ouvertes n'avaient pas la même nature physique.
Pour cette étude pendant 10 fois on image
une région incluant un CH et des plumes polaires
une région incluant un BP dans un CH et un CH

Cela permet d'auto-calibrer les eventuelles fluctuations atmosphériques.

- *Evolution d'ARL, formations de CME:*

S'il existe une boucle très torsadée (*ie* vue en forme de S allongée ou calculée d'après l'ajustement des boucles) ou avec de nombreuses évolutions alors pour 20 fois il faut faire
1 Image Partielle : On zoome sur cette région
1 Image Disque entier (incluant le bord et les régions proches)
fin

Pour les observations EIT, il semble important d'observer dans les 4 longueurs d'onde (1024×1024) afin de pouvoir faire des diagnostics de températures. Essayer de comprendre si par exemple les différences en radio sur les CH proviennent de légères différentes de températures, de densités ou d'orientation du champ magnétique. La même question peut se poser par rapport aux activités magnétiques voisines.
Les protocoles explicités ci dessus peuvent être appliqué pour SOHO/EIT dans les 4 longueurs d'ondes.

C.2 Observations coordonnées avec les coronographes du Pic du Midi

L'article ci dessous, publié lors du colloque Thémis à l'obsevatoire de Paris-Meudon, rend compte des observations entre le HACO et EIT le 16 Aout 1996.

- *Coordinated Observations made with SOHO/EIT*
- by NOENS J.C. & PORTIER-FOZZANI, F.
- published in Themis meeting (1996)
  Edited by the Observatory of Paris Meudon.

FIRST RESULTS OBTAINED WITH SOHO/EIT IN COLLABORATION WITH THE Hα CORONAGRAPH OF THE PIC DU MIDI

F. Portier-Fozzani[1] and J.C. Noens[2]

[1] *Laboratoire d'Astronomie Spatiale, UPR 9019, Marseilles, France*

[2] *Observatoire du Pic du Midi, UMR 5572, Bagneres de Bigorre, France*

Abstract. The satellite SOHO (SOlar and Hellospheric Observatory) has been launched december 2nd 1995. It has reached its orbits around the Lagrangian L1 Earth-Sun on February,14th 1996. Aboard, the instrument EIT (Extreme ultraviolet Imaging Telescope) images the chromosphere, the transition region and sun's corona in 4 wavelengths of UV. Then it is possible in collaboration with others instruments to follow evolution and consequences of the magnetic fields from the photosphere to the upper corona. The Hα coronograph at the Pic du Midi observatory allows observations at very high frequency in real time which gives the ability to follow a short time phenomena (such as the development of ejection during 10 minutes). Comparison of the 2 instruments gives informations about short time and long time evolution.

Key words: Solar Corona – Chromosphere – UV – Hα

1. Introduction

On August 16th 1996, an eruption was observed in the West North West part of the H alpha coronagraph of the Pic du Midi observatory (France). At the same time , the SOHO/EIT instrument observed the same active region of the corona, on the limb. Lines observed shows different morphology versus temperature.

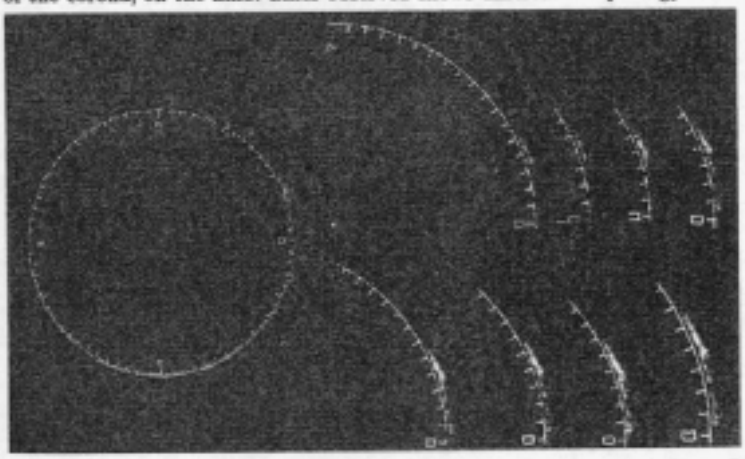

Figure 1. Evolution observed with HACOPIC (the H alpha coronagraph of the Pic du Midi observatory) : images taken on 1996-08-16 at respectively 06:05AM 06:12 06:16 06:32 06:37 06:47 06:59 07:17 (07:39 for the big image on the left hand side)

2. Analysis of the eruption of August 16th 1996

The observation of August 16th 1996 with the H alpha coronagraph of the Pic du Midi observatory gives important informations for the evolution of the structure with time. At 5:59 UT 4 jets at respectively 313,233,79, and 279 degrees are present with an active region (20° wide) between 283 and 303, a protuberance at 223 et 3 protuberances at 123 over 10 degrees. At 6:12 UT, fast evolution exists between 273 and 304. A protuberance appears at 44° and disappears 3 minutes later. At 6:19 UT the morphology changes at 284°. A bright point appears near 343° at 6:36

Proceedings : Forum Themis 1996, 7– 8

UT. There are some activity at the north pole at 6:47 UT, which disappears at 6:59 UT. At 7:39 UT an outward ejection and a jet at 314° and 2 brights points at 89 and 99° are present. At 8:01 UT some activity exists on south pole at 199°.

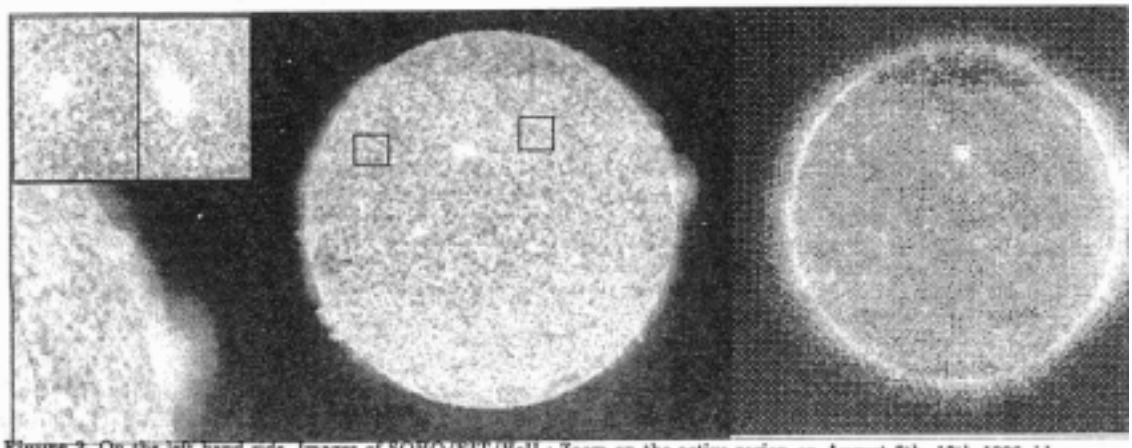

Figure 2. On the left hand side, Images of SOHO/EIT/HeII : Zoom on the active region on August 8th, 12th 1996, idem the 16th. On the right hand side, image of SOHO/EIT/FeXII : For this same active region, on August 16th 1996, the corona shows some differences with some open field lines presents

The same day, observations with SOHO/EIT shows details of the morphology of the active region and confirms important activity near the poles. Hα line as expected looks like the chromospheric He II. The observations of few days earlier (August 8th, and 12th 1996) in He II (304 A , 8.0×10^4 K) gives informations about the global chromospheric structure of this part of this active region. The observations in Fe IX/X (171 A, 1.3×10^6 K) which corresponds to the transition region shows some completely different morphology for the active region. It is also different for Fe XII (195 A, 1.6×10^6 K) which corresponds to the "quiet" corona and Fe XV (284 A, 2.0×10^6 K) which corresponds to the main corona with active regions.

3. Conclusion

Some part of the short time evolution observed in coronagraphs are due to the effect of the rotation of the active region with the sun but it can not explained all the observed phenomena. Little jets and bright points seems to appear like short time evolution of chromosphere. Concerning the corona, comparison with the different wavelengths of EIT show the relationships between the difference of morphology of structure due, partly, to the transmission of energy inside the corona.

Acknowledgements. J.-P. Delaboudinière is the PI of SOHO/EIT, that was realised by a consortium : Inst. d'Astrophysique Spatiale, Centre Spatial de Liège, Inst. d'Optique Theorique et Appliquee, Lab. d'Astronomie Spatiale, Obs. Royal de Belgique, Naval Research Laboratory, Lockheed Palo Alto Research Lab., NASA/Goddard Space Flight Center. "L'equipe des observateurs associes du HACOPIC" has made most of the coronographic observations. The CNRS/INSU inside the "programme sol air 1996" has support the project.

References

J.P. Delaboudiniere & al.: 1996, *COSPAR* , Imaging the solar corona in the EUV
F. Portier-Fozzani, & al.: 1996, *to appears in PASJ* , EIT images of the EUV solar atmosphere : initial data reduction
J.P. Delaboudiniere & al.: december 1995, *Sol. Phys.* **162**, 291
J.M. Niot & J.C. Noens: 1997, *accepted in solar physics* , An Hα survey of the polar corona at Pic du Midi

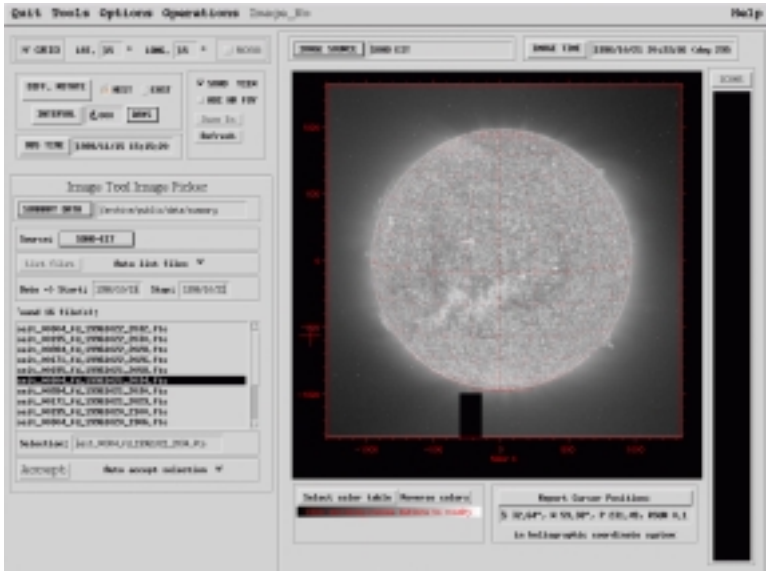

Figure C.1: Procédure image_tool qui permet de définir les coordonnées des objets à observer : Image SOHO/EIT du 21 Octobre 1996 He II

Le programme d'observation d'EIT est défini la veille au Goddard afin d'être téléchargé dans de bonnes conditions. Il comporte un programme synoptique de 1 (puis de 4 après l'augmentation de la télémétrie) images dans chaque filtre. A ce programme de base, vient se greffer des programmes scientifiques spécifiques comme le "CME watch" (Séquences permanentes d'observations en Fe XII), etc... Les 19, 21, 22, 23 Octobre 1996 les coronographes du Pic du Midi et SOHO/EIT observaient simultanément. Nous nous sommes servis des images EIT pour définir nos régions d'intérets à observer en détail avec le grand coronographe (Fig. C.1). Nous avons alors déplace la fente le long du bord du disque occulteur en nous limitant à ces régions afin d'obtenir sur la barette CCD les intensités dans chaque raie.
Ces données sont venues compléter les observations de la même région réalisées un mois plus tot par SOHO/EIT dans les 4 longueurs d'ondes ce qui a servi à mieux comprendre la région pour l'analyse des articles [158], [189],[190].

Appendix D

Notions mathématiques relatives à la méthode d'ajustement des boucles

Sommaire

D.1 Solutions pour chaque image du problème d'inversion

Soit $s_{(i,k)}(x,y,z)$ la kième solution à l'ajustement de la boucle dans l'image i.

On a l'application $s_{(i,k)} : \mathfrak{M} \longrightarrow \mathfrak{M}'$
avec i,k étant des paramètres fixés
et où $\mathfrak{M}$ et $\mathfrak{M}'$ sont des variétés différentielles de dimensions 3. Pour simplifier la suite on les prendra comme $\mathfrak{M} \simeq \mathfrak{M}' \simeq \mathbb{R}^3$.

On note p_i : la projection de l'espace $\mathfrak{M}'$ vers le plan image $\mathbb{R}^2$.

L'ajustement à l'écran se fait donc sur $p_i(s_(i,k)(x,y,z)) : \mathfrak{M} \simeq \mathbb{R}^3 \longrightarrow \mathbb{R}^2$.

1. Dans le cas du modèle circulaire, on a comme contrainte : $s_{(i,k)}(x,y,z) = (\alpha,\beta,\gamma)$ est sur un arc de cercle c'est à dire il existe un référentiel des coordonnées tel que $(\tilde{\alpha}-\tilde{\alpha 0})^2 + (\tilde{\beta}-\tilde{\beta 0})^2 = R0^2$ et (α,β,γ) appartiennent à un même plan. Le cercle étant un cercle de rayon R0, de centre qui s'écrit en fonction de h0 et x0 et y0 (cf. annexe de [15]), on peut donc l'écrire facilement en fonction des paramètres recherchés.

2. Dans le cas du tore, on écrit de même les équations d'un tore.

Avec une notation évidente, cela revient à s'écrire $s(x,y,z) = S(r0,h0,x0,y0,theta,var)$ dans le cas du modèle circulaire et $s(x,y,z) = S(r0,h0,x0,y0,theta,var,r1,phi1,phi2)$ dans le cas du tore et donc trouver alors les différents paramètres recherchés (Cf chapitre 4).

D.2 Recherche de la solution

On considère maintenant l'espace vectoriel de fonction des solutions pour l'ensemble des images = $\{i = 0,\ nombre\ d'images; k = 0,\ kmax(i);\ tels\ que\ s_(i,k)\ solutions\}$.
En considerant les variations avec le temps t (donc $\propto i$ le numéro d'image), on peut donc supposer que $R_0(t)$, $h_0(t)$, $x_0(t)$, $y_0(t)$, etc... sont continus ou constants. Le cas constant correspond à un objet statique qui ne varie pas entre 2 images. Le cas continu correspond au fait que la physique évolue généralement progressivement [135].

L'unicite des solutions est obtenu par stéréovision comme expliqué au chapitre 4. Ainsi finalement il est construit une relation biunivoque pour chaque i avec un seul k solution.

CQFD[1].

[1] *ie* Ce qu'il fallait démontrer pour notre recherche de solutions (existance et unicité dans l'espace des fonctions.

Appendix E

Programmes informatiques

Sommaire

De très nombreux programmes informatiques ont été développés. Certains outils maisons étaient adaptés au VMS utilisé localement. D'autres (comme le calcul des rapports Est-Ouest dans chacun des filtres) ont été développés sous Unix en se servant de la librairie solar soft d'IDL.

Dans cette annexe on présente sommairement quelques programmes "maison".

E.1 Catalogue d'imagettes

/pro/vince/lasession.vms2idl réalise automatiquement le catalogue d'imagettes en allant chercher sur le disque dur ou sur la DAT les données.
Au MEDOC par exemple, la version aout97-ias.env réalise automatiquement en Unix le catalogue d'imagettes en allant chercher sur la base de donnée les images EIT. Le programme IDL lz_f5f_imagettes_gif_unix.pro est alors utilisé en tant que sous-programme.
Le catalogue d'imagette est programmé de la manière suivante :
Pour chaque fichier, après lecture des paramètres des headers, prise en considération de l'image si elle correspond aux critères choisis et alors "redimensionnement" en imagette, repositionnement dans un panneau et redéfinition des contrastes. Sauvegarde en gif, en postscript Noir et Blanc ou couleur selon demande

E.2 Imagerie

E.2.1 Dégrillage

Dans le repertoire /pro/vence le programme decigalesession.idl2vms cherche sur la DAT les données correspondant aux critères d'entrées et lance depuis VMS le programme fourmi.pro pour effectuer le dégrillage.
Le programme decigalesessionfilm.idl2vms est plus adapté au nouveau codage de 1997 où plusieurs images peuvent être regroupées sous le même nom.
Enfin le programme lectgoddeg.vms2idl permettait du temps où l'on pouvait monter un disque par VMS a distance d'aller chercher uniquement les données correspondant aux critères d'entrées.

E.2.2 Fabrication de gif

defd2gif.pro dans le repertoire /pro/duction transforme les images dégrillées en images normalisées au format gif.
le programme film.pro montre les séquences d'images dégrillées en tant que films
film_idl2gif.pro permet de fabriquer les films au format VHS en les dégrillant. J'ai fait ce programme au Goddard pour réaliser des cassettes vidéos sans la grille des évolutions d'EIT.

E.3 Vision 3D

E.3.1 Fabrication d'anaglyphes

affiche2couleur.pro réalise les anaglyphes en attribuant à chacune des images dégrillées la bonne palette de couleurs.

E.3.2 Boucles 3D

Près de 48 programmes IDL "maisons" constituent la structure des ajustements des boucles.
La structure initiale est de M. Aschwanden ([8]). Les programmes ont été reécrits et repensés pour être utilisés pour l'analyse avec SOHO/EIT. Ils tournent sous IDL Unix (actuellement fonctionnels au Goddard -sur la machine penumbra- via telnet avec renvoi de fenêtre).

Il faut prélablement choisir les données EIT dans le catalogue puis utiliser la procédure eit_prep pour rendre les données utilisables.

Ensuite on entre les coordonnées de l'almanach et en lancant fab_loop_trace,instr,date,time,io,new on réalise le tracé des boucles.
Puis fab_loop_fit,instr,date,time,iloop,io,new permet de trouver les paramètres géométriques des boucles.

Enfin fab_loop_teem,instr,date,time,time2,iloop,io,wid,incr,niter,test permet de calculer les températures lorsque 2 boucles coincindent avec des filtres différents d'EIT.

L'utilisation de ces programmes se fait en utilisant les contraintes stéréographiques définies au chapitre IV.

Résumé : Pour mieux comprendre les structures de la couronne solaire —de température élevée— et leurs évolutions, des méthodes de vision à 3 dimensions à partir des images EUV de SOHO/EIT ont été développées. Des anaglyphes ont servi à mieux comprendre le rôle du champ magnétique et des intéractions entre champ fermés et ouverts. Il est apparu que la reconnection entre des trous coronaux (CH) et des régions actives (AR) peut expliquer certaines disparitions de boucles coronales fermées. De plus, des analyses multi-instruments ont montré que la structuration des CHs résulte parfois de changements dans l'activité magnétique voisine.

Les mesures d'incertitudes sur les reconstructions par stéréovision n'ont pas permis de valider une méthode générale pour visualiser la couronne globalement en 3D. Par contre, le principe a pu être utilisé avec succès pour la reconstruction en 3 dimensions de boucles coronales. Ainsi après analyse des paramètres physiques de 30 boucles EUV de températures intermédiaires d'une région active, il est apparu que contrairement aux boucles chaudes en X, elles étaient en équilibre hydrostatique.
Les boucles d'une région active émergentes sont apparues comme se détorsadant au fur et à mesure de son grandissement ce qui correspond à un transfert de l'hélicité.
Des corrélations entre des brusques détorsadages et des éruptions ont aussi été établis dans les cas où la torsion initiale est trop importante et permet le développement d'instabilités.

Ces études 3D vont pouvoir permettre de mieux contraindre les bilans énergétiques pour le chauffage coronal grâce à la conservation de l'hélicité et d'améliorer la prévision de la météorologie spatiale. L'utilisation de techniques d'imageries adaptées (comme le dégrillage ou le Modèle de Vision Multi-échelle) a permis de faire ressortir certains détails dans la formation de CMEs par exemple.

Summary This thesis deals with 3D evolution of coronal structures based upon the ultraviolet telescope of SOHO : EIT.
Anaglyphs and incertainties on a complete stereovision reconstruction are described. Stereoscopic methods for loop reconstruction were successfully made to find 3D parameters. With dynamical stereoscopy, physical conditions were derived for 30 loops of temperature around 1MK. A method which is able to derive twist variation were also built. Emerging loops were found highly twisted and they detwist as they grow. According to helicity conservation, this correspond to a transfert of twist into expansion.
Long time twist evolution of magnetic flux tubes are followed in relation with flares as relaxation.
Interaction between magnetic field lines were analysed. An example of reconnection between open and closed field line were observed. Other interactions were found with multi-wavelength observations : coronal holes borders (and thus CH) are better defined when an active region nearby is growing.
Other imaging techniques were used to better take profit as possible of SOHO/EIT. A multiscale vision model (MVM) was applied with success to show small coronal structures

evolutions hidden by the noise level.

Résumé : Pour mieux comprendre les structures de la couronne solaire —de température élevée— et leurs évolutions, des méthodes de vision à 3 dimensions à partir des images EUV de SOHO/EIT ont été développées. Des anaglyphes ont servi à mieux comprendre le rôle du champ magnétique et des intéractions entre champ fermés et ouverts. Il est apparu que la reconnection entre des trous coronaux (CH) et des régions actives (AR) peut expliquer certaines disparitions de boucles coronales fermées. De plus, des analyses multi-instruments ont montré que la structuration des CHs résulte parfois de changements dans l'activité magnétique voisine.

Les mesures d'incertitudes sur les reconstructions par stéréovision n'ont pas permis de valider une méthode générale pour visualiser la couronne globalement en 3D. Par contre, le principe a pu être utilisé avec succès pour la reconstruction en 3 dimensions de boucles coronales. Ainsi après analyse des paramètres physiques de 30 boucles EUV de températures intermédiaires d'une région active, il est apparu que contrairement aux boucles chaudes en X, elles étaient en équilibre hydrostatique.
Les boucles d'une région active émergentes sont apparues comme se détorsadant au fur et à mesure de son grandissement ce qui correspond à un transfert de l'hélicité.
Des corrélations entre des brusques détorsadages et des éruptions ont aussi été établis dans les cas où la torsion initiale est trop importante et permet le développement d'instabilités.

Ces études 3D vont pouvoir permettre de mieux contraindre les bilans énergétiques pour le chauffage coronal gràce à la conservation de l'hélicité et d'améliorer la prévision de la météorologie spatiale. L'utilisation de techniques d'imageries adaptées (comme le dégrillage ou le Modèle de Vision Multi-échelle) a permis de faire ressortir certains détails dans la formation de CMEs par exemple.

Les instructions relatives à l'utilisation du CD-Rom sont données dans les fichiers README de chaque répertoire

---

Summary This thesis deals with 3D evolution of coronal structures based upon the ultraviolet telescope of SOHO : EIT.
Anaglyphs and incertainties on a complete stereovision reconstruction are described. Stereoscopic methods for loop reconstruction were successfully made to find 3D parameters. With dynamical stereoscopy, physical conditions were derived for 30 loops of temperature around 1MK.
A method which is able to derive twist variation were also built. Emerging loops were found highly twisted and they detwist as they grow. According to helicity conservation, this correspond to a transfert of twist into expansion.
Long time twist evolution of magnetic flux tubes are followed in relation with flares as relaxation.
Interaction between magnetic field lines were analysed. An example of reconnection between open and closed field line were observed. Other interactions were found with multi-wavelength observations : coronal holes borders (and thus CH) are better defined when an active region nearby is growing.
Other imaging techniques were used to better take profit as possible of SOHO/EIT. A multiscale vision model (MVM) was applied with success to show small coronal structures evolutions hidden by the noise level.

Instructions to use the CD-Rom are given in each directory inside the README files